Dark Matter Constraints from High Energy Astrophysical Observations

Daniel Nieto Castaño

Departamento de Física Atómica, Molecular y Nuclear

Universidad Complutense de Madrid

Thesis advisor

Dr. Juan Abel Barrio Uña

A thesis submitted for the degree of

Doctor of Philosophy

January 2012, Madrid

A mis padres, Paqui y Pepe,
a mi hermano Ismael
y a ti, María.

Acknowledgements

I would like to warmly thank all the people that, directly or indirectly, helped me during these years of PhD studentship.

First of all, I would like to acknowledge my advisor Juan Abel Barrio Uña and thank him for his guidance and advice, but also for the freedom he offered to me since the first day, which is probably the best help one can get when joining the world of research.

I want to thank Victoria Fonseca for the opportunity she gave me to join the UCM-GAE group. I would like to thank all past and present members that shared these years with me: Miguel Cámara, Pedro Antoranz, Marcos López, and many other excellent collegues and friends. I owe special thanks to Igor Oya, Néstor Mirabal, José Luis Contreras, and Tarek Hassan, since this work as a whole is also theirs.

I can not forget to acknowledge those MAGIC Collaboration colleagues I worked and had fun with. Particularly, I would like to thank Michele Doro, Saverio Lombardi, Miguel Ángel Sánchez-Conde, Fabio Zandanel, and Jelena Aleksić, as well as Mattia Fornasa, external collaborator and colleague too.

Finally, my most intense gratitude goes to may family and to my partner María. Without their love and support this work would have never been possible.

This work has been funded through the MICINN's FPI scholarship BES-2007-16, the CICYT's program FPA2006-12383-C02-01, the MICINN's program FPA2009-08938, and the MICINN's MultiDark project CSD2009-00064.

Contents

Introduction

There is strong evidence for the existence of dark matter in the Universe. In the paradigm of the Concordance Cosmological Model, 83% of the mass density in the Universe cannot be explained with ordinary baryonic matter and requires an additional non-baryonic component. Without a doubt, understanding this dark matter is one of the most important topics of physics today.

In the standard scenario, the dark matter is considered to be a new type of massive particle which experiences low interactions with the ordinary matter and radiation. In the search for such a particle, three different strategies are being carried out in parallel: its direct production in collider experiments, its direct detection through scattering off ordinary matter, and its indirect detection based on the search for secondary particles produced by the annihilation or decay of the dark matter particle.

This work consists of indirect dark matter searches through the observation of astrophysical objects such as dwarf spheroidal galaxies, and possible dark matter subhalos of the Milky Way. These observation were performed in the high energy window of the electromagnetic spectrum, mainly in the high and very high energy γ-ray band, and to a less extent in the X-ray band.

In the following, the outline of the work is presented. Afterward, the selected publications that constitute this work are listed, accompanied by a co-authorship statement.

Outline: The structure of this thesis consists of two introductory chapters followed by three chapters containing the original scientific contributions conforming this work, a final chapter devoted to summarize those contributions, and a brief set of appendices.

Introductory chapters:

- Chapter 1: This first introductory chapter deals with the dark matter paradigm. The observational evidences of this component of the Universe are summarized, along with some notes on the Concordance Cosmological Model. The main dark matter particle candidates are presented too, particularly those of special interest for this work. This chapter ends with a state-of-the-art discussion about dark matter searches, paying a particular attention to indirect dark matter searches.

- Chapter 2: The second introductory chapter is devoted to the high energy astrophysics. After the introduction of the main messengers of this field, the discussion focuses on γ-ray astrophysics: the γ-ray production and absorption mechanisms, the γ-ray astrophysical sources, and the γ-ray detection techniques. Later, the principal detectors used for this work are introduced, namely the MAGIC Telescopes, the Fermi γ-ray Space Telescope. The MAGIC Telescopes are described into more detail, in either the technical and the data analysis descriptions, due to their specific weight within this work. The chapter finishes with a very brief introduction to X-ray astrophysics and to the Chandra X-ray Observatory, another relevant detector for this work.

Original scientific contribution:

- Chapter 3: This chapter deals with the indirect dark matter detection in dwarf spheroidal galaxies of the Milky Way. It starts with a brief introduction to such objects and the presentation of the two dwarf spheroidal galaxies that have been studied in this work, namely, Willman 1 and Segue 1. Then, the very high energy γ-ray observations of Willman 1 by MAGIC Telescope are detailed, along with an interpretation of the results in terms of annihilating dark matter. Afterward, observations of the same dwarf spheroidal galaxy, this time in the X-ray energy band by the Chandra X-ray Observatory, are used to search for decaying dark matter signatures. This chapter closes with the study of Segue 1 γ-ray emission at very high energies thanks to MAGIC Telescope observations. An interpretation of the results is the context of annihilation dark matter is later presented.

- Chapter 4: This chapter is devoted to the search of possible dark matter subhalos of the Milky Way in the population of unassociated Fermi objects, and their subsequent characterization with the MAGIC Telescopes. First, an exhaustive search over the Fermi catalog is detailed, including a dedicated multiwavelength counterpart search, and the analysis of Fermi high energy data, that eventually led to a list of reasonable targets. Second, the MAGIC Telescopes observations of the two best targets, namely, 1FGL J0338.8+1313 and 1FGL J2347.3+0710, are presented, and their results are discussed.

- Chapter 5: This chapter is based on the study of the dark matter detection prospects with the next generation of Cherenkov telescopes. The Cherenkov Telescope Array was taken as the particularization of such generation. The sensitivity of the future telescope to generic dark matter spectra was surveyed, being able to estimate the required astrophysical conditions that would generate a detectable dark matter signal in the context of annihilating dark matter.

- Chapter 6: This last chapter summarizes the main scientific production of this work, and presents an outlook, by reviewing the three previous chapters in a succinct way.

Appendices:

- Appendix A: In this first appendix, some brief notes about extended atmospheric showers theory are shown. Its intention is to help with the comprehension of that phenomena, cornerstone of the ground-based very high energy γ-ray astrophysics.

- Appendix B: This second appendix is a summary of the work in Spanish language.

- Appendix C: In this last appendix, the author's list of publications during his PhD studentship, by the thesis publication date is shown. It includes publications in refereed and non-refereed journals, as well as public conference contributions and internal MAGIC collaboration contributions.

Publications and co-authorship statement: The original scientific contributions that comprise this work are the outcome of fruitful collaborative efforts the author had the opportunity to participate in.

- The study of Willman 1 dwarf spheroidal galaxy with the MAGIC telescope was carried out in collaboration with Michele Doro, Saverio Lombardi, Miguel Ángel Sánchez-Conde,

and Fabio Zandanel. The author was responsible for the data analysis, and upper limits calculations. The results have been published as [1].

- The inspection of Willman 1 dwarf spheroidal galaxy with the Chandra X-ray Observatory was performed in collaboration with Néstor Mirabal. The author participated on the data analysis, the interpretation of the results, and the article writing. The results have been published as [2].

- The study of Segue 1 dwarf spheroidal galaxy with the MAGIC telescope was done in collaboration with Michele Doro, Mattia Fornasa, and Saverio Lombardi. The author cooperated on the data analysis, the mSUGRA dark matter simulations and upper limits calculations, the interpretation of the results, and the article writing. The results have been published as [3].

- The search for dark matter in unassociated Fermi objects was a project headed by the author. The search for possible dark matter clumps among the unassociated Fermi objects was performed in collaboration with Néstor Mirabal, Silvia Pardo, and Víctor Martínez, and it has been published as [4]. The data analysis of the two observed unassociated Fermi objects, 1FGL J0338.8+1313 and 1FGL J2347.3+0710, was performed in collaboration with Jelena Aleksić and Saverio Lombardi. The results have been published as [5].

- The study of the dark matter detection prospects for the next generation of Cherenkov telescopes was performed in collaboration with Tarek Hassan, Néstor Mirabal, and José Luis Contreras. The results have been published as [6].

Chapter 1

Dark Matter Paradigm

The following chapter intends to introduce the Dark Matter paradigm in a brief and succinct way. In section 1.1, the main observational evidences for a dark matter component in the Universe will be presented. Section 1.2 contains a summarized description of the current standard cosmological model, known as Concordance Cosmological Model or Λ-Cold Dark Matter Model, as well as its mayor challenges and possible alternatives. While the first two sections justify the need for the dark matter, section 1.3 shows the main requisites a particle must have in order to qualify as a dark matter particle candidate. A set of real and hypothetical dark matter particle candidates will be also described. Finally, the state-of-the-art in dark matter searches will be abridged in section 1.4, covering the direct and indirect searches, as well as its direct production in laboratories.

1.1 Dark matter observational evidences

Since Newton's law of universal gravitation was enunciated, the search for non-visible gravitating matter have been always pursued by scientist of all times. As an example, back in 1846, Neptune was discovered thanks to the gravitational perturbations it produced over Uranus orbit. At the beginning of the 20th century, many works tried to compute the total density of matter in the Solar vicinities, placing limits to possible non-visible matter, like asteroids or gas. While some results required just a tiny amount of matter to be non-visible [7; 8], some others were striking, suggesting that the amount of non-visible matter could be as large as twice the visible one [9]. As soon as the scientific community was able to study the dynamics of galaxies and cluster of galaxies through the inspection of the kinematics of their constituent members, some strong discrepancies between the observations and the predictions were highlighted. In 1933, a study of the radial velocities of a set of galaxies of the Coma cluster concluded that the gravitational mass of the system was ten times larger than its luminous mass [10]. Since those days up to now, the most clear evidences for the existence of the so-called dark matter come from the study of the dynamics of galaxies and galaxy clusters, and the gravitational lensing effects. Despite the strength of the aforementioned evidences, the enigma of the dark matter composition remains unsolved. In the following, both evidences will be commented.

1.1.1 Dynamics of galaxies and galaxy clusters

The velocities of stars belonging to a galaxy or galaxies belonging to a galaxy cluster can be expressed, as a function of the radial distance to the center of gravity of the system, in a rela-

tively straightforward manner under certain assumptions. First, the application of Newtonian dynamics at all scales is assumed, together with the hypothesis that the system is virialized, meaning that it is a stable bound system, so the virial theorem applies and thus the time average of kinetic $\langle K \rangle$ and potential $\langle V \rangle$ energies are related as $-\langle V \rangle + 2\langle K \rangle = 0$, without losses of energy to spin or shape modifications of the individual constituents of the system (star or galaxies respectively). Then, equating the gravitational force to the centrifugal force as

$$\frac{mv^2}{r} = \frac{mM(r)G}{r^2} \Rightarrow v = \sqrt{\frac{M(r)G}{r}}, \tag{1.1}$$

$v = v(r)$ is obtained. In the previous equation $M(r)$ is the mass of the system inside a radius r and G is the gravitational constant. Assuming a spherically symmetric system, in the case of a star in the galactic bulge, and considering that M stands for the visible mass, $M(r) \propto r^3$ and thus $v(r) \propto r$, while for a star located in the outskirts of the galaxy, $M(r) \sim$ constant and thus $v(r) \propto r^{-1/2}$ (see dashed line in Fig. 1.1). The first strong observational contradiction to the expected velocity behavior was the already mentioned study of the radial velocities of a set of galaxies of the Coma cluster, carried out by Zwicky in 1933 [10], and later rotational curves of galaxies (see, *e.g.*, [11]), which showed that the velocity tends towards a constant value at large radii instead of the velocity decrease predicted by Newtonian gravity if only visible matter is accounted. This inconsistency was firstly attributed to missing and non-visible baryonic mass like intragalactic gas, but after mapping the baryonic gas content of the problematic systems, the conclusion was that baryonic gassy alone could not justify the discrepancy (see dotted line in Fig. 1.1). The discrepancy is solved if a dark matter halo embedding the galaxies and galaxy clusters is added to the whole system (see dot-dashed line in Fig. 1.1).

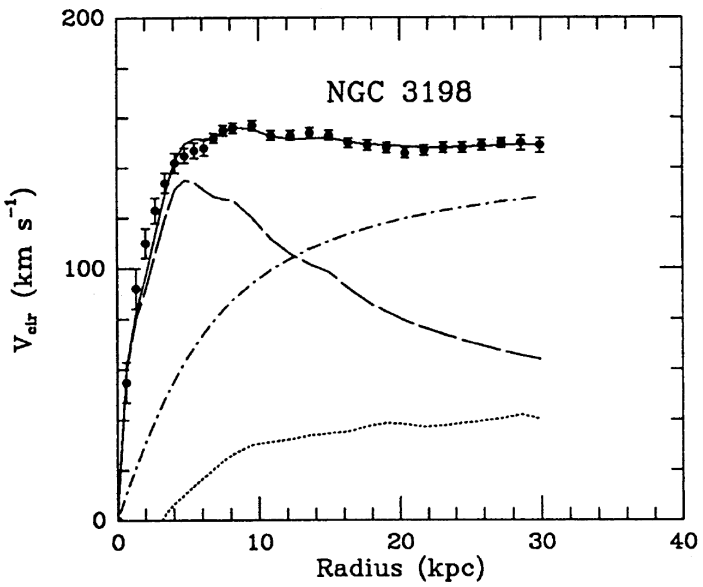

Figure 1.1: Rotation curve for the galaxy NGC 3198. The dashed line depicts the contribution to the velocity from visible baryonic mass distribution inferred for the galaxy disk, the dotted line corresponds to the contribution to the velocity from the baryonic gas component and the dot-dashed line shows the dark matter contribution required to match the observed velocities of the system. Figure extracted from [11].

In the case of galaxies, rotational curves can offer direct information of the dark matter halo

profile until the radius at which the kinematics of baryonic matter can be studied (via star motion or neutral hydrogen gas studies), namely, few tens of kpc. However, this can be considered only the inner part of the dark mater halo, since gravitational lensing studies (described below) concluded that the average size of galactic dark matter halos is of the order of few hundred kpc.

Other dynamical proves to the existence of the dark matter in our galaxy are the Oort discrepancy and the unusual velocity dispersions of the dwarf Spheroidal (dSph) galaxies. The first is based on the discrepancy between the luminous matter in the vicinities of the Sun and the observed gravitational potential [12]. The second shows that mass-to-light ratio[1] in the local neighborhood must be much larger than the unity in order to account for the high velocity dispersions of these satellites of the Milky Way [13].

1.1.2 Gravitational lensing

According to the theory of General Relativity, photons suffer from gravitational deflection due to the curvature of space-time, in turn produced by density distributions. As a consequence, massive objects may act as gravitational lenses which can modify the apparent flux and shape of astronomical objects when such lenses are placed between the objects and the observer. Gravitational lenses theory (see, *e.g.*, [14], and references therein) presents such a level of development that, together with the latest observational techniques, it is possible to infer many interesting facts about the gravitational lens mass and distribution from lensed images. Depending on the mass of the lens, there are three different types of lensing: strong lensing, weak lensing, and microlensing.

Strong lensing is produced by very massive objects like large galaxies or clusters of galaxies. Strong lensing effects include multiple imaged objects and arc-shaped and ring-shaped distortion of objects. Out of these images, the total matter content of the lens and, in some cases, the distribution of the same, can be reconstructed. Thanks to this technique, several interesting conclusions have been obtained, among them, that galaxies and galaxy clusters are dominated by dark matter, where large mass-to-light ratios of few tens and few hundreds respectively have been estimated [15]. Most of the best examples of strong gravitational lensing are provided by background quasar's light traveling through a foreground massive galaxy cluster. One of such examples is depicted in Fig. 1.2a, where a galaxy cluster mass distribution lenses a background quasar, multiplying its image, and partially distorting some of the multiplied images. Another striking evidence of dark matter existence is the matter mapping in the Bullet cluster of galaxies, shown in Fig. 1.2b. This galaxy cluster was formed by the collision of two previous galaxy clusters. The baryonic matter of the system was mapped by X-ray observations, while the gravitational mass was inferred by strong lensing. During the collision, the dark matter component of both clusters pass through each other interacting only weak and gravitationally, while the baryonic component was slowed down due to electromagnetic interactions. As a result, the baryonic and dark matter component of each initial cluster were separated. Consequently, the overall dark matter distribution appears to be two disjoint regions, separated as well from the two disjoint baryonic matter distributions. The Bullet cluster observations do not only provide a clear evidence of the existence of the dark matter in the Universe, but they are in strong contradiction to theories of modified Newtonian gravity at large distances.

[1] The mass-to-light ratio is defined as the quotient between the gravitational mass of a system, inferred through the dynamics of the system and gravitational lensing, and its luminous mass, inferred through photometric observations. It is usually expressed in units of $M_\odot/L_\odot$, where $M_\odot$ is the solar mass, and $L_\odot$ is the solar luminosity.

There are two other gravitational lensing effects that provide clues regarding the dark matter content of the Universe. Weak lensing is referred to the cumulative gravitational lensing effect produced by the overall distribution of matter in the Universe, also called gravitational shear, that slightly distort the images of distant galaxies. This effect provides many interesting information about the cosmological dark matter distribution [16]. In the so-called microlensing effect, gravitational lensing produced by small stellar-mass dark objects can be also observed through the amplification of the flux intensity of background objects. Thanks to this last technique, the contribution of dark baryonic objects, like the massive compact halo objects, other compact objects, and dark stars, to the total dark matter content of the Universe can be constrained [17].

(a) A five quasar gravitational lens

(b) The Bullet Cluster matter mapping

Figure 1.2: Dark matter. Fig. 1.2a: HST image of a five quasar gravitational lens in the galaxy cluster SDSS J1004+4112, about 7 billion light years distant toward the constellation of Leo Minor. The five bright white points near the cluster center are images of a single distant quasar. The arced galaxies at 2, 4, and 10 o'clock are gravitationally lensed images of the same galaxy. Credit: ESA, NASA. Fig. 1.2b HST and Chandra-XRO composite image of the 3.4 billion light-years away galaxy cluster 1E 0657-56 (also known as Bullet Cluster), formed by the collision of two previous galaxy clusters. The X-ray emitting gas, accounting for most of the cluster's baryonic matter, is shown in red color, while the dark matter distribution, reconstructed from gravitational lensing, is shown in blue color. This image proves that the majority of the matter in the system is unseen. Credit: NASA.

1.2 Concordance Cosmological Model

The Concordance Cosmological Model (CCM), also known as Λ cold dark matter model (ΛCDM) or standard model of big bang cosmology, is a well established cosmological paradigm, product of more than one hundred years of theoretical cosmology developments, strongly supported by the relatively recent explosion of observational cosmology (see, *e.g.*, [18], and references therein).

1.2.1 The CCM formalism

The main hypotheses of the modern cosmology are the validity of General Relativity at all macroscopic scales, plus the assumption of the *cosmological principle*, namely, that the Universe is homogeneous and isotropic (at Mpc scales and larger). It proposes that the Universe was originated out of a singularity, the so-called Big Bang, followed by a period of exponential

expansion, the so-called *inflation*, which also generated the seeds for structure formation in the shape of quantum fluctuations of the inflaton field. After the inflationary era, the Universe composition turned out to be radiation (photons), matter (dark matter, leptons, hadrons), and dark energy, each of them described by a different equation of state. The CCM is the simplest model fulfilling all the aforementioned conditions.

The first hypothesis provides a relation between the geometry and the density content of the Universe through the Einstein equations:

$$G^{\mu\nu} \equiv R^{\mu\nu} - \frac{1}{2} g^{\mu\nu} R = -\frac{8\pi G}{c^4} T^{\mu\nu} - \Lambda g^{\mu\nu}, \tag{1.2}$$

where $G^{\mu\nu}$ is the Einstein tensor, $g^{\mu\nu}$ is the space-time metric, G is the gravitational constant, $T^{\mu\nu}$ is the energy-momentum tensor describing the density content of the Universe, $R^{\mu\nu}$ and R are the Ricci tensor and scalar respectively, and Λ represents the cosmological constant.

In turn, the *cosmological principle* fixes a family of metrics, among which the Friedman-Lemaitre-Robertson-Walker (FLRW) is the simplest one:

$$ds^2 = -c^2 dt^2 + a(t)^2 \left(\frac{dr^2}{1 - kr^2} + r^2 d\Omega^2 \right). \tag{1.3}$$

Solving the Einstein equations with the FLRW metric, and considering the time components of the field equations, the temporal development of the Universe can be expressed as

$$H^2 \equiv \left(\frac{\dot{R}}{R} \right)^2 = \frac{8\pi G \rho_{tot}}{3} - \frac{kc^2}{R^2}, \tag{1.4}$$

known as the Friedmann equation, where $H = H(t)$ is the Hubble parameter, $R = R(t)$ is the scale factor, and k is the curvature of the Universe. ρ_{tot} is the total density of the Universe, which can be decomposed as

$$\rho_{tot} = \rho_m + \rho_r + \rho_\Lambda. \tag{1.5}$$

In the previous equation, $\rho_m = \rho_{dm} + \rho_b$ represents the matter density as the sum of dark matter and baryonic components, ρ_r is the radiation density, and ρ_Λ is the density due to to the cosmological constant, which can be introduced in the Friedmann equation as $\rho_\Lambda = \Lambda / 8\pi G$[1].

Attending to the curvature k, three types of universes would be possible: $k = -1$ implies an curved open Universe with infinite extent, $k = +1$ implies a closed finite Universe without boundaries, and $k = 0$ implies a flat Universe with infinite extent. Thus, there is a *critical density* for a flat Universe, ρ_c, defined as

$$\rho_c = \frac{3}{8\pi G} H_0^2, \tag{1.6}$$

where H_0 is the so-called Hubble constant, defined as the Hubble parameter evaluated at the present time. Thus, the *critical density* has a value of $\rho_c = 9.6 \times 10^{-27}$ kg m^{-3} ($\rho_c c^2 = 5.4$ GeV m^{-3}).

[1]The contribution of the cosmological constant can be regarded as a particular case of dark energy described by the following equation of state: $p_\Lambda = \omega \rho_\Lambda$, with $\omega = -1$, where p_Λ stands for the pressure of this component. So far, data from cosmological observations are compatible with this equation of state for the dark energy. Throughout the text this ρ_Λ can be generalized as the density of dark energy, thus not necessarily following the already mentioned equation of state (*i.e.* $\omega < 0$ with the possibility of being time variable too).

From Eq. 1.4 a new parameter can be now defined, the so-called *closure parameter* Ω, as

$$\Omega \equiv \frac{\rho_{tot}}{\rho_c} = \Omega_m + \Omega_r + \Omega_\Lambda = 1 + \frac{kc^2}{(H_0 R)^2}, \tag{1.7}$$

where the $\Omega_i \equiv \rho_i/\rho_c$ $(i = m, r, \Lambda)$ are the so-called *density parameters*[1].

Additionally, the curvature contribution in Eq. 1.7 can be expressed as

$$\Omega_k \equiv \frac{\rho_k}{\rho_c} = -\frac{kc^2}{(H_0 R)^2}, \tag{1.8}$$

in such a way that Eq. 1.7 can be rewritten as

$$\Omega_m + \Omega_r + \Omega_\Lambda + \Omega_k = 1. \tag{1.9}$$

1.2.2 Cosmological parameters

There is a collection of cosmological observations that are able to provide direct or indirect measurements of the *density parameters* in Eq. 1.9, thus shedding light over the Universe geometry and composition. The most accurate results so far are those obtained thanks to the study of the Cosmic Microwave Background (CMB) fluctuations, in combination with Baryon Acoustic Oscillations (BAO) data and supernovae type Ia observations.

The CMB, predicted as a consequence of Big Bang cosmology back in 1948 [19], is an almost isotropic background of microwave radiation, composed by the relic photons frozen-out at mass-radiation decoupling era and cooled down due to the expansion of the Universe. This radiation was not experimentally confirmed until 1965 [20]. Due to its importance, several satellites have been specifically designed to measure the CMB radiation: first, the Cosmic Background Explorer (COBE) satellite launched in the last decade of the 20th century, then the Wilkinson Microwave Anisotropy Probe (WMAP) [21], and the next generation, the Plank satellite [2] [22]. By the time this work was written, the best public CMB measurements are those from WMAP satellite. WMAP CMB data represent the most precise black body emission ever measured, with a black body temperature of 2.725 ± 0.001 K. Although the CMB is very isotropic, fluctuations of the order of 10^{-5} K are detected. These fluctuations provide an image of matter density fluctuations at the time of decoupling and are an excellent tool for the determination of the cosmological parameters. In Fig. 1.3a a whole sky map of the 7-year WMAP CMB radiation measurements is presented, where the tiny temperature fluctuations can be realized. The corresponding temperature and temperature-polarization power spectra are found in Fig. 1.3b, together with the extremely precise CCM fit to the data.

The study of the BAO is a technique that allows to constrain the cosmological parameters at the same time that provides information about the dark energy equation of state. It consist of the measurement of the peaks that are present in the power spectrum of baryonic matter distribution after the epoch of recombination up to the present time, being these peaks produced by acoustic waves in the baryonic matter-radiation fluid before the decoupling of these two components [25]. Additionally, the detailed observations of type Ia supernovae are the other major contributor to the study of the Universe expansion and the determination of the cosmological parameters [26; 27; 28]. Both techniques complement the analysis of CMB anisotropies in order to derive precise

[1] Equivalently to the case of ρ_Λ, Ω_Λ can be generalized as the dark energy *density parameter*.

[2] WMAP and Plank satellites were in operation by the time this work was written, but only WMAP data on CMB anisotropies were available.

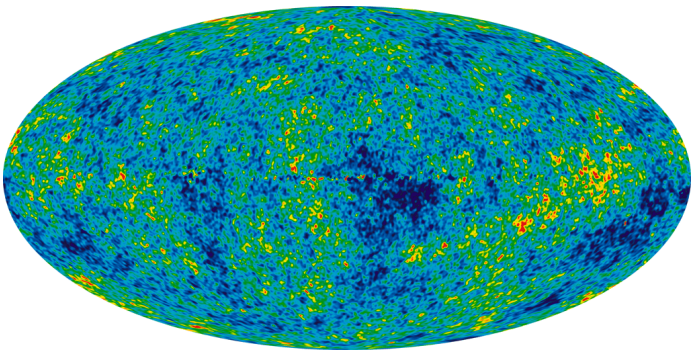

(a) WMAP temperature anisotropy map

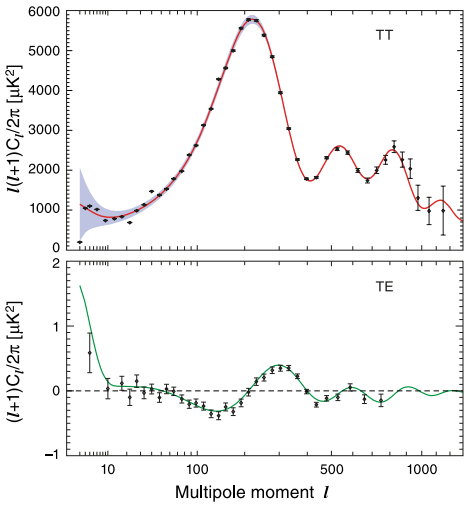

(b) WMAP temperature power spectrum

Figure 1.3: Fig. 1.3a: The 7-year temperature anisotropy map from WMAP, showing the temperature fluctuations in the early Universe. Map in Galactic coordinates (Mollweide projection). Linear color scale from -200 to 200 μK. Figure extracted from [23]. Fig. 1.3b: The 7-year WMAP temperature and temperature-polarization power spectra. The first acoustic peak is related to the total fraction of matter at the recombination era. The best-fit flat model is depicted by the solid lines. Figure extracted from [24].

values for the cosmological parameters via likelihood analyses. The current best-fit values for the CCM cosmological parameters [29] can be found in Table 1.1. To summarize the results, the best-fit model corresponds to a flat universe (-0.0133¡Ω_k¡0.0084, 95% confidence level) where the dark energy is compatible with the cosmological constant ($\omega = -1.1 \pm 0.14$), with a baryon *density parameter* of $\Omega_b = 0.0458 \pm 0.0016$, a dark mater *density parameter* of $\Omega_{dm} = 0.229 \pm 0.015$, and a dark energy *density parameter* of $\Omega_\Lambda = 0.725 \pm 0.016$ (all errors at 68% confidence level).

Consequently, the Universe is dominated at present by the dark energy, which drives the accelerated expansion of the Universe and contributes to the total density of the Universe with a $\sim$ 72%. As for the matter content, it represents the $\sim$ 28% of the total density of the Universe, out of which more than 80% is dark matter. The current contribution of radiation to the density of the universe is much less than a 0.1%.

It is worth mentioning that only a $\sim$ 4% of the total content of the Universe is formed by a known component, the baryons. Surprisingly, the visible density from stars, gas, and dust account for a total of $\Omega_{b,vis} \approx 0.01$. Thus, a large fraction of the baryonic content of the Universe is also dark. X-ray studies reveal that part of this baryonic dark matter is formed by intergalactic gas in galaxy clusters, as well as long filaments of warm-hot intergalactic medium connecting galaxies and clusters of galaxies. Massive compact halo objects, with stellar masses inferred and detected by microlensing techniques, also contribute to the total amount of baryonic dark matter.

1.2.3 Structure formation

It is widely accepted, in the context of the CCM, that the structures of the Universe were seeded by primordial perturbations in its density distribution. These primordial perturbations can be associated to the quantum fluctuations of the inflaton field and were imprinted in the density distribution after inflation. Right after the Matter Dominated era began, the tiny fluctuations in

Table 1.1: Summary of the cosmological parameters of the CCM.

Parameter	WMAP+BAO+H_0
$\Omega_b h^2$	0.02255 ± 0.00054
$\Omega_{dm} h^2$	0.1126 ± 0.0036
Ω_Λ	0.725 ± 0.016
n_s	0.968 ± 0.012
τ	0.088 ± 0.014
$\Delta^2_{\mathcal{R}}$	$(2.430 \pm 0.091) \times 10^{-9}$
σ_8	0.816 ± 0.024
H_0	70.2 ± 1.4 km s^{-1} Mpc^{-1}
Ω_b	0.0458 ± 0.0016
Ω_{dm}	0.229 ± 0.015
z_{reion}	10.6 ± 1.2
t_0	13.76 ± 0.11 Gyr

Values for the cosmological parameters of the CCM computed after the combined analysis of WMAP-7 years data, Baryonic Acoustic Oscillation data, and Hubble constant measurements. The six first parameters are the so-called primary parameters or fit parameters: $\Omega_b h^2$ is the physical baryon density, $\Omega_{dm} h^2$, is the physical dark matter density, Ω_Λ is the dark energy *density parameter*, n_s is the spectral index of density perturbations, τ is the reionization optical depth, $\Delta^2_{\mathcal{R}}$ is the amplitude of curvature perturbations. The rest of parameters are derived from the previous set: σ_8 is the amplitude of density fluctuations, H_0 is the Hubble parameter, Ω_b is the baryonic *density parameter*, Ω_{dm} is the dark matter *density parameter*, z_{reion} is the reionization redshift, and t_0 is the age of the Universe. Table adapted from [29]

the matter density were linearly amplified on all scales larger than the Jeans length at that time. When atoms began to form, the Jeans length dramatically reduced, and the fluctuations were amplified in a non-linear way (see, *e.g.*, [30], and references therein). Due to the overwhelming fraction of dark matter in the total matter content of the Universe, the structure formation was indeed driven by the dark matter component. Moreover, the dark matter freeze-out took place while the bosons and fermions were still in thermal equilibrium, thus strongly interacting. Consequently the dark matter dynamics were dominated by gravity before ordinary matter dynamics were. Once dark matter overdensities formed gravitational potential wells, baryons felt into them following the dark matter density distribution. Thus, the influence of the dark matter on the structure formation in the Universe is of singular importance, and so it is the physics of the microscopic dark matter constituent.

A density fluctuation will be gravitationally bounded, thus forming a structure whose characteristic size will be that of the fluctuation, if the free-streaming path of the massive particles is smaller than the fluctuation scale. Otherwise, the particles will efficiently free-stream and get scattered, diluting in that way the density fluctuation and preventing any structure formation on that scale. Attending to the effects over the structure formation, three possible types of particle dark matter can be distinguished: hot, warm, and cold dark matter.

- Hot dark matter particles would posses a very large free-streaming length, usually as a consequence of their relativistic nature at the time of dark matter freeze-out. A typical example of hot dark matter are the Standard Model neutrinos, whose free-streaming length, after considering the current bounds on the neutrinos masses, would be a few tens of Mpc. Consequently, density fluctuations below the Mpc scale, where galaxies and smaller objects

belong, would be erased. This fact implies that supercluster-scale structures would form first and then would fragment into smaller objects (the so-called top-down scenario). But this chronology is strongly disfavored by observations. Consequently, hot dark matter can not form the majority of the dark matter [31]. Some other hot dark matter candidates are hot *sterile neutrinos* and thermal axions.

- Cold dark matter particles would be non-relativistic particles with relatively small free-streaming lengths. Cold dark matter allows for density fluctuations down to Earth-like masses to form. From the point of view of structure formation chronology, the cold dark matter supports the observationally favored bottom-up scenario, where structures form hierarchically in time, from smaller to larger sizes. Cold dark matter simulations are in excellent agreement with the observational data [32]. There are some issues, though, coming from these simulations: the predicted number of satellite galaxies is larger than the observed population, the inner profile of the simulated dark matter halos is cuspier than the inferred profiles from kinematic data, and the loss of galactic angular momentum due to baryon in-fall is too large in the simulations to reproduce the observed thin galactic disks [33]. However, the first problem seems to disappear as more ultra-faint dSph galaxies are being discovered, while the last two problems are being reduced after the introduction of baryons in the simulations, and the improvement of the simulations resolution [34].

- Warm dark matter particles present velocities in between hot dark matter and cold dark matter. The warm dark matter typical free-streaming length is that of galaxy sizes. For galaxy sizes and larger structures, warm dark matter and cold dark matter behave quite similarly, but for smaller sizes, within the non-linear structure formation, big differences arise. Actually, the warm dark matter should not be too warm in order to predict the observable number of satellite galaxies in galactic halos [34]. More observational data in the non-linear large to small-scale clustering of matter may be able to tell the real warm or cold nature of the dark matter [35]. Typical warm dark matter candidates are particles with masses in the keV range, like the gravitinos or *sterile neutrinos*.

As already mentioned, N-body simulations of structure formation have been carried out on different scales. These simulations try to reproduce the large-scale structure formation [32; 36] and galactic halos formation [37; 38] considering different types of dark matter. An example on how well the CCM, which considers cold dark matter, matches the large scale structure of the Universe can be seen in Fig 1.4, where three different galaxy redshift surveys are compared to the corresponding region from N-body simulations.

1.2.4 Challenges to the CCM

Despite the extremely accurate match between the CCM and the aforementioned observations, there are still some data that could challenge the model (see, *e.g.* [43], and references therein).

- Large scale velocity flows: the CCM predictions for large scale flows differ significantly from observations. While flow motions up to the 50 Mpc scale and velocities of ~ 100 km s^{-1} are predicted, larger flow motions on the 100 Mpc scale and velocities of ~ 400 km s^{-1} are observed in a certain direction of the sky ($l = 282^\circ,\ b = 6^\circ$, galactic coordinates).

- Low multipoles in the CMB: attending to WMAP CMB data multipole analysis, the normal directions to the cuadrupole and octupole planes are aligned to the dipole plane normal in a way highly incompatible with a Gaussian isotropic sky.

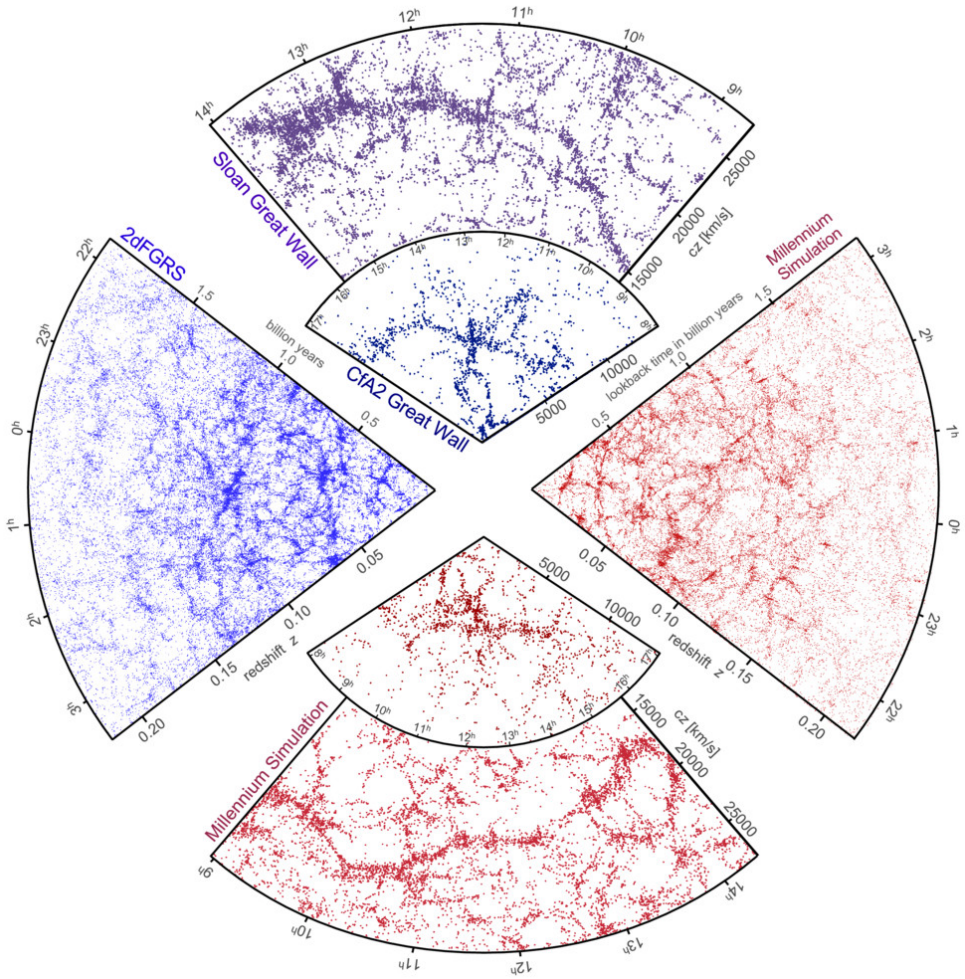

Figure 1.4: The large scale structure of the Universe mapped by the 2dF Galaxy Redshift Survey [39], the Sloan Digital Sky Survey [40] and the CfA Redshift Survey [41]. Each point represents a galaxy as a function of R.A. and redshift. The three redshift survey are accompanied by the corresponding N-body Millenium-II simulations considering the CCM. Figure extracted from [42].

- Quasars optical polarization alignment: The quasar optical polarization is not randomly oriented, but appears to be aligned with a particular axis in the sky ($l = 267°,\ b = 69°$, galactic coordinates).

- Halo profiles: the simulated CCM dark matter halo density profiles are not in full agreement with the observationally inferred dark matter halos. Galaxy cluster simulated halos are less concentrated than what is suggested by the observations. In galactic scales, the inner dark matter density profiles from simulations are cuspier than the observed cored profiles.

This last issue seems to be related to the technical limitations of CCM simulations. As the N-body simulations resolution gets improved, and the baryonic component and its interactions are included into the new data runs, the halo profiles tend to approach the observations. However, the three first issues still need to be addressed. Without a doubt, the confirmation of the

existence of a cosmological preferred axis would trigger a complete revolution in the history of cosmology.

1.2.5 Alternative cosmologies

There are many alternatives to the CCM, but none of them are as solid in their contrast with the observations or powerful in their predictive power regarding the generation of light elements, structure formation, CMB, and the expansion of the Universe. Some of these alternatives are:

- Modified Newtonian Dynamics: a phenomenological approach to the solution of the flattening of rotational curves of galaxies, which tries to eliminate the need for an additional hidden matter component, is the Modified Newtonian Dynamics (MOND) [44]. This theory states that the actual gravity deviates from the Newtonian gravity, magnifying its effects below a certain gravity scale a_0. Additionally to the explanation of the flattening of rotational curves of galaxies, the Tully-Fisher law can be derived within the MOND theory. However, MOND fails to explain the dynamics of large objects like galaxy clusters without adding a dark matter component, and the gravitational lensing effect. More over, MOND can not account for any relativistic phenomena.

- Tensor-vector-scalar gravity: as already mentioned, MOND is not a fully relativistic theory. In order to solve this problem, the Tensor-Vector-Scalar gravity (TeVeS) theory was developed, which recovers the MOND theory in the weak-field limit [45]. TeVeS inherit all the good properties of MOND, plus it is able to explain the gravitational lensing effect, although in an incompatible way with the galaxy rotational curves. TeVeS is also not compatible with stellar evolution theory and is not able to explain the Bullet cluster phenomena.

- Some non-standard cosmological models are the Gödel universe [46], the quasi-steady state cosmology [47], the Brans-Dicke cosmology [48], the Einstein-de Sitter universes [49], among others.

1.3 Dark matter candidates

There are certain characteristics a particle must hold in order to qualify as a viable dark matter particle candidate (see, *e.g.*, [50]). The main requirements, in the context of the CCM, are summarized in the following points:

- The dark matter particle must match the dark matter relic density[1]. Thus, an appropriate production mechanism that reproduces the given relic density and provides stability to the particle (meaning a decay lifetime larger than the age of the Universe) is needed. Nonetheless, in multicomponent dark matter scenarios [51], the relic density of a component can be lower than the total dark matter relic density (never higher).

- Usually, the particle is required to be electrically neutral, otherwise it would couple with photons and therefore would not be dark. On the other hand, it might be the case that the dark matter particle is electrically charged but forms electrically neutral bound states though. In either case the coupling between the electromagnetic sector and the dark

[1]The dark matter relic density is the value of the dark matter density at the time of freeze-out.

sector must be highly suppressed. Dark matter particle candidates strongly interacting with ordinary matter are extensively ruled out by the observations.

- The dark matter is supposed to rule the formation of structures in the Universe, since the evolution of perturbations in the Matter Dominated era is dominated by the fluctuations in the dark matter original density, which in turn depends on the dark matter particle physics. Thus any candidate must be able to produce the same structures observed in the Universe at all scales, as well as the structure evolution in time.
- The dark matter particle must preserve the observed abundances of light elements and leave untouched the Big Bang Nucleosynthesis (BBN) theory, which matches with great accuracy the observations. Thus, decays or catalytic reactions that might influence the formation of the light elements must be avoided. In the same way, the dark matter particle must not affect the stellar evolution.
- Any dark matter particle candidate must be experimentally verifiable, and as such it must be subject to experimental constraints, either from indirect or direct searches, or from direct production searches.

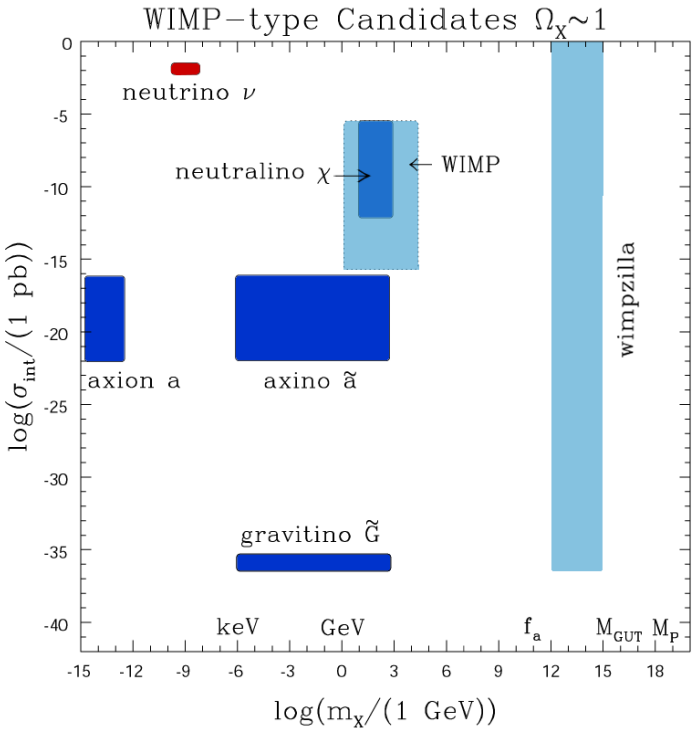

Figure 1.5: A representation of some well-motivated dark matter candidate particles as a function of their masses m_X and their typical interaction strength with ordinary matter σ_{int}. Within the WIMP region, possible candidates like the *neutralino* or Kaluza-Klein particles are found. Figure extracted from [52].

Besides, if the dark matter particle is a thermal relic, meaning that it was thermally produced in the early Universe, it is possible to infer some particle characteristics by applying statistical physics arguments at the particle's freeze-out, similar to those that allow to compute the density

and temperature of CMB photons today. If a massive generic particle p decouples from the rest of matter-radiation fluid without a change of entropy in such a fluid, one can relate the particle relic density to its annihilation cross section [53]. That relation reads

$$\Omega_p h^2 = \frac{s_0}{\rho_c/h^2}\left(\frac{45}{\pi g}\right)^{1/2}\frac{m_p}{T_0 M_{Pl}}\frac{1}{\langle\sigma_{ann}v\rangle} \approx \frac{10^{-27}\text{cm}^3\text{ s}}{\langle\sigma_{ann}v\rangle}, \tag{1.10}$$

where Ω_p is the relic *density parameter* of the generic massive particle p, m_p is the particle mass, s_0 is the current entropy density of the Universe, ρ_c is the critical density, h is the scaled Hubble constant, g are the relativistic degrees of freedom at the freeze-out, T is the temperature at freeze-out, M_{Pl} is the Plank mass, and $\langle\sigma_{ann}v\rangle$ is its thermally averaged product of the annihilation cross section times velocity. Consequently, for a monocomponent dark matter with $\Omega_{dm} \sim 0.22$, the expected values of its thermally averaged annihilation cross section will be $\langle\sigma_{ann}v\rangle \sim 10^{-26}$ cm^3 s. It is worth noting that this condition is fulfilled by the so-called Weakly Interacting Massive Particle (WIMP), with a mass around hundreds GeV. In turn, WIMPs typical temperature at freeze-out are a few percent of the typical particle mass, meaning that these WIMPs are non-relativistic at decoupling, and thus able to play the role of cold dark matter. These two characteristics, also known as the WIMP *miracle*, make this kind of hypothetical particles preferred dark matter candidates.

Many dark matter particle candidates have been proposed. Some of them arose as *natural* candidates in theories not intended to explain the dark matter problem, while some other are *ad hoc* candidates, explicitly designed to fulfill all dark matter particle characteristics. A brief compendium of the most studied candidates is presented in the following, without the intention of enumerating all proposed candidates. Some of these candidates can be found in Fig. 1.5, where they are represented as a function of their masses and interaction cross sections with ordinary matter. In the following, a special aim will be done for supersymmetric candidates, particularly the *neutralino*. Deeper and more complete descriptions of the plethora of dark matter particle candidates can be found in references [54; 55; 56; 57].

1.3.1 Supersymmetric dark matter

In the Standard Model of particle physics the matter basic constituent particles are fermions, while the mediators of the interactions are bosons. There exist the possibility to remove this compartmentalized picture through some kind of symmetry which could relate both fermionic and bosonic Standard Model elementary particles, thus providing a more unified picture of the particle physics world. The so-called supersymmetric extension of the Standard Model of particle physics (see, *e.g.*, [58; 59]) propose the following symmetry: for each Standard Model elementary particle, a particle with the same set of quantum numbers but the spin, which is increased by 1/2, is added. Supersymmetry is not only an elegant or aesthetic theory but a possible solution to some of the most important Standard Model theoretical problems:

- Supersymmetry allows to solve the so-called *hierarchy problem* by canceling the divergences in the radiative corrections to the Higgs boson mass, and thus to the masses of the rest of Standard Model particles [60].

- The inclusion of supersymmetric particles, also called sparticles, into the renormalization group equations allows for the unification of the gauge couplings of the Standard Model at a given unification scale [61].

- Under certain assumptions, the Lightest Super-Symmetric Particle (LSP) would be heavy, neutral and stable. Thus, supersymmetry provides a natural dark matter particle candidate [62].

Supersymmetry can be an arbitrarily complicated theory. Due to the fact that the number of supersymmetric transformations is not limited, theories with multiple symmetries besides the previously mentioned (extended supersymmetric theories) are allowed. Moreover, supersymmetric extra-dimensions theories are equally feasible. Thus, in order to start exploring supersymmetry, a minimum supersymmetric extension of the Standard Model is frequently considered.

- The Minimal Super-Symmetric Standard Model

  The Minimal Super-Symmetric Model (MSSM) extends the Standard Model particles with two extra Higgs doublets, to account for the up and down quark masses, plus the complete set of supersymmetric partners [63]. If the supersymmetry were not broken, the sparticles would have the same mass as their Standard Model partners and would have been already discovered in accelerators data. This symmetry breaking produces some critical effect over the proton lifetime, shortening it down to lower values than the age of the Universe. This effect is not compatible with the observed limits to the lifetime of the proton [64]. As a solution, a new symmetry called R-parity is introduced, which allows for supersymmetry breaking. The R-parity value is defined as

$$R \equiv (-1)^{3B+L+2s}, \tag{1.11}$$

  where B is the baryon number, L is the lepton number, and s is the spin number. Therefore, Standard Model particles have an R-parity value of +1, while the superpartners have an R-parity value of -1. This R-parity is a conserved quantum number in any reaction, thus Standard Model particles can only decay to Standard Model particles and the same applies for the sparticles. A significant corollary of R-parity conservation is that the lightest sparticle is stable, making it a viable dark matter candidate. The set of Standard Model particles and their corresponding superpartners in the MSSM can be found in Table 1.2.

- The constrained Minimal Super-Symmetric Standard Model

  Although being a minimal extension of the Standard Model, the MSSM has a large (above 120) number of free parameters. Thanks to phenomenological arguments and parameter relations to accomplish the unification at high energies, the number of free parameters can be significantly reduced, as in the case of the constrained Minimal Super-Symmetric Model (cMSSM). The cMSSM is built under the assumption that the soft supersymmetry breaking parameters present some universality properties at a certain energy scale, often chosen to be the grand unification scale, which fulfills some well established Standard Model observations like the absence of CP-violating terms and flavor-changing neutral-currents. This constraint allows the cMSSM to be described by only five parameters: four continuous parameters, namely, the universal gaugino mass $m_{1/2}$, the universal scalar mass (sfermions and Higgs masses) m_0, the universal trilinear coupling A_0, and the ratio of the vacuum expectation values of the two Higgs fields $\tan\beta$; and one discrete parameter, namely, the sign of μ, where μ is the higgsino mass parameter.

- The minimal Super-Gravity Model

  The so-called minimal SUper-GRAvity (mSUGRA) Model [59; 65] is a particular case of the cMSSM. If the supersymmetry breaking is mediated by the graviton and the gravitino mass is fixed to the universal scalar mass ($m_{3/2} = m_0$), the cMSSM shrinks to the mSUGRA, keeping the same free parameters than the cMSSM but reducing the hyperspace where the set of parameters can move in. Both, the cMSSM and the mSUGRA parameter spaces can, in turn, be bound by experimental constraints. Some of these constraints come from the measurements of the Standard Model decay $b \rightarrow s\gamma$, and the anomalous magnetic moment of the muon g_μ. Some others arise from experimental limits to the existence of supersymmetric particles in accelerator data, bounds on the relic density of dark matter particles from WMAP data, and limits from direct dark matter detection experiments. The resulting parameter spaces are usually simplified in terms of the (m_0, $m_{1/2}$) or ($tan(\beta)$, $m_{1/2}$) planes for graphical representation. Examples of cMSSM and mSUGRA parameter spaces in the light of 2010 LHC run and XENON 100 data can be found in Fig. 1.6.

- Other MSSM realizations

  If the universality assumptions of the cMSSM are abandoned, other realizations of the MSSM emerge. For instance, the non-universal Higgs masses model (NUHM), where the supersymmetry breaking contributions to the Higgs masses are not required to be universal, provides a relatively constrained parameter space, with only two more free parameters than the cMSSM [66]. Some other realizations of the MSSM do not drop the unification criterion, but consider different masses where this unification is accomplished, different than those proper from grand unification theories [67]. A particular example of this kind, where phenomenological constraints are added, is the so-called phenomenological MSSM (pMSSM), where the space parameter is reduced down to 19 free parameters [68]. Some other MSSM realizations can be found in the models of anomaly mediated supersymmetry breaking, gauge mediated supersymmetry breaking, gaugino mediated supersymmetry breaking, etc [56].

Table 1.2: Standard Model particles/fields and supersymmetric partners.

Standard Model particles/fields		Supersymmetric partners			
		Interaction eigenstates		Mass eigenstates	
quark	$u,\ d,\ t,\ b,\ c,\ s$	squark	$\tilde{q}_L,\ \tilde{q}_R$	squark	$\tilde{q}_1,\ \tilde{q}_2$
lepton	$e,\ \mu,\ \tau$	slepton	$\tilde{l}_L,\ \tilde{l}_R$	slepton	$\tilde{l}_1,\ \tilde{l}_2$
neutrino	$\nu_e,\ \nu_\mu,\ \nu_\tau$	sneutrino	$\tilde{\nu}$	sneutrino	$\tilde{\nu}$
gluon	g	gluino	$\tilde{g}$	gluino	$\tilde{g}$
W-boson	$W^{+,-}$	wino	$\tilde{W}^{+,-}$	chargino	$\tilde{\chi}^{+,-}_{1,2}$
Higgs-boson	$H^{+,-}$	higgsino	$\tilde{H}^-_1,\ \tilde{H}^+_2$	chargino	$\tilde{\chi}^{+,-}_{1,2}$
Higgs-boson	$H^0_{1,2,3}$	higgsino	$\tilde{H}^0_{1,2}$	neutralino	$\tilde{\chi}^0_{1,2,3,4}$
B-field	B	bino	$\tilde{B}$	neutralino	$\tilde{\chi}^0_{1,2,3,4}$
W^3-field	W^3	wino	$\tilde{W}^3$	neutralino	$\tilde{\chi}^0_{1,2,3,4}$

Standard Model particles and fields together with their corresponding supersymmetric partners in the MSSM. Table adapted from [63].

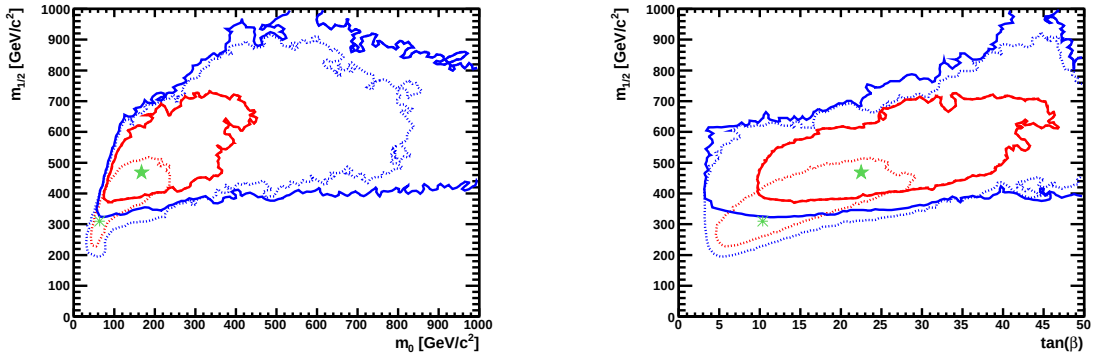

(a) CMSSM (m_0, $m_{1/2}$) plane

(b) CMSSM ($tan(\beta)$, $m_{1/2}$) plane

(c) mSUGRA (m_0, $m_{1/2}$) plane

(d) mSUGRA ($tan(\beta)$, $m_{1/2}$) plane

Figure 1.6: Examples of cMSSM and mSUGRA constrained parameter spaces in the light of 2010 LHC run and XENON 100 data. The (m_0, $m_{1/2}$) plane for the cMSSM and mSUGRA models is shown in Fig. 1.6a and Fig. 1.6c respectively. The ($tan(\beta)$, $m_{1/2}$) plane for the cMSSM and mSUGRA models is shown in Fig. 1.6b and Fig. 1.6d respectively. Red and blue contours define the 68 and 95% C.L. regions after including the 2010 LHC run and XENON 100 data constraints (solid lines) and only considering pre-LHC data (dotted lines). Best-fit points for pre-LHC data are depicted by the green open stars while best-fit points considering 2010 LHC run and XENON 100 data are depicted by solid green stars. Figures extracted from [69].

In the following, four different supersymmetric dark matter particles will be introduced, namely, the lightest *neutralino*, the gravitino, the sneutrino, and the axino. All of them can be realized within the MSSM, while only the first two are representative in the mSUGRA context.

1.3.1.1 Neutralino

The fermionic superpartners of the Standard Model bosons produce six different mass eigenstates as linear combinations of the interaction eigenstates. The so-called charginos $\tilde{\chi}^{+,-}_{1,2}$ are two charged supersymmetric fermions, linear combination of the charged winos $\tilde{W}^{+,-}$, and the charged higgsinos $\tilde{H}^{-}_{1}$, $\tilde{H}^{+}_{2}$. On the other hand, the linear combination of the neutral wino, the neutral bino, and the two neutral higgsinos give rise to the four different neutral supersymmetric fermions, called *neutralinos* $\tilde{\chi}^{0}_{1,2,3,4}$. In the vast majority of cMSSM and mSUGRA parameter

spaces, the role of the LSP is played by the lightest *neutralino* $\tilde{\chi}_1^0$, conventionally represented by the simple symbol χ:

$$\chi \equiv \tilde{\chi}_1^0 = c_1\tilde{W}^3 + c_2\tilde{B} + c_3\tilde{H}_1^0 + c_4\tilde{H}_2^0. \tag{1.12}$$

Being a stable, neutral and heavy particle, the *neutralino* emerges as a natural dark matter particle candidate.

The coefficients c_i in Eq. 1.12 are functions of the gaugino masses, the vacuum expectation values of the two Higgs fields $\tan\beta$, and the higgsino mass parameter μ. Concerning the relative weight of the coefficients c_i, a *neutralino* where c_1 is significantly predominant is called wino-like, bino-like in the case c_2 is dominant, and higgsino like for clear dominance of the $c_{3,4}$ coefficients. It can also be read that a *neutralino* is considered gaugino-like if $|c_1|^2 + |c_2|^2 > 0.9$, and higgsino-like if $|c_1|^2 + |c_2|^2 < 0.1$. The values that the coefficient c_i take, as well as the physical implications of the choice, depend on the particular point in the parameter space of the considered model.

Being a Majorana fermion, the *neutralino* is its own antiparticle, allowing for self-annihilation into Standard Model particles: fermions, photons, gauge bosons, and Higgs bosons. More specifically, the primary annihilation products, in the low velocity limit (well describing a cosmological *neutralino*), would be (see, *e.g.*, [56], and references therein):

- Fermions: Neutralinos can annihilate into fermion pairs via s-channel, thanks to the exchange of Higgs and Z bosons, or via t-channel, thanks to a sfermion exchange. In either case, the amplitude of the process is proportional to the mass of the fermion product. Consequently, the annihilation to fermions is dominated by heavy particles: $\tau^+\tau^-$, $b\bar{b}$, and $t\bar{t}$ (for sufficiently high masses). For large $tan\beta$, bottom-type fermion production dominate with respect to up-type ones, so the contribution of $t\bar{t}$ may not be significant.

- Photons: Since *neutralinos* do not couple to the electromagnetic sector they are not allowed to directly annihilate into photons. However, at one loop level there are interesting processes which could generate γ-ray lines, like $\chi\chi \to \gamma\gamma$ and $\chi\chi \to Z\gamma$, located at energies $E_\gamma = m_\chi$ and $E_\gamma = m_\chi + m_Z^2/m_\chi^2$ respectively. These lines represent invaluable features that would provide a strong dark matter smoking gun. However, the amplitudes of these processes are are strongly suppressed, being negligible with respect to the annihilation to fermions or bosons. Other mechanism which can provide photons in the final state from *neutralino* annihilation is the so-called internal QED bremsstrahlung [70]. If the annihilation final products are leptons, the annihilation exchange particle would be a charged sparticle able to emit a photon. This photon emission restores the helicity in annihilation processes like $\chi\chi \to l^+l^-\gamma$, thus allowing for previously forbidden processes. Photons from internal QED bremsstrahlung carry a significant amount of the available energy ($E_\gamma > 0.6m_\chi$) and would produce a distinctive bump in the end of the differential photon energy spectrum.

- Gauge bosons: In the low velocity regime, pure gaugino-like *neutralinos* can annihilate into Z and $W^\pm$ bosons via t-channel, through chargino or *neutralino* exchange. Pure higgsino-like and mixed *neutralinos* can annihilate into Z and $W^\pm$ bosons via s-channel.

- Higgs bosons: Neutralinos can annihilate into pairs of Higgs bosons or a Higgs boson and a gauge boson. The most favored channels are the annihilation to a light neutral Higgs and a Z boson ($\chi\chi \to h^0Z$), to a heavy Higgs and a Z boson ($\chi\chi \to H^0Z$), to a charged

Higgs and a W boson ($\chi\chi \rightarrow H^{\pm}W^{\mp}$), and to a light Higgs and a pseudoscalar Higgs ($\chi\chi \rightarrow h^0A^0$).

So far, no signs of supersymmetric particles have been found in accelerator data. Consequently, lower limits have been derived for the LSP mass. These limits, assuming the *neutralino* as the LSP, set a lower limit to its mass to $m_\chi > 46$ GeV [71]. The upper limit to the *neutralino* mass is theoretically motivated in the few TeV range. Higher masses would require a certain amount of fine tuning in order to maintain all the theoretical solutions supersymmetry offers, and are thus disfavored.

1.3.1.2 Other supersymmetric candidates

The *neutralino* is not the only supersymmetric particle that can play the role of dark matter. Depending on the parameter space region of the supersymmetric model, there are other supersymmetric particles well suited as dark matter particle candidates: the sneutrino, the gravitino, and the axino.Sneutrino The sneutrinos are massive and chargeless particles, superpartners of Standard Model neutrinos. In the MSSM, heavy sneutrinos with masses between $\sim$ 550 GeV and $\sim$ 2300 GeV are able to match the required relic density associated to the dark matter component. However, direct detection limits on the sneutrino scattering cross section are already below the theoretical expectations [72]. Gravitino The graviton boson has its superpartner in the gravitino. In some particular supersymmetric models like the gauge mediated supersymmetry, the gravitino qualifies as dark matter particle candidate due to its stability and for being the lightest supersymmetric particle within that scenario [73]. Although gravitinos are well theoretically motivated their detection prospects are not very promising since these particles interact only gravitationally. Due to the nature of their interactions, the main source of gravitinos would be the decay of the next-to-lightest supersymmetric particles. Thus, the dark matter characterization in the gravitino scenario would require the detection of the progenitor next-to-LSP signature. Axino The axion models (see Sec. 1.3.3) can be included within supersymmetry by introducing a full axion supermultiplet A. This supermultiplet is composed by the pseudoscalar axion a, its scalar superpartner saxion, and their fermionic superpartner axino. Depending on the specific model, axinos can play the role of hot, warm or cold dark matter particles [74]. Unfortunately, as in the case of gravitinos, their detection prospects are not very optimistic.

1.3.2 Sterile neutrino

The fact that neutrinos have non-zero mass is a solid experimental evidence that there must be physics beyond the Standard Model, which predicts these particles to be massless. A possible extension of the Standard Model that accounts for the masses of the neutrinos is the introduction of single Majorana fermions, also called sterile neutrinos, like in the case of the neutrino Minimal Standard Model (νMSM) [75]. In this picture, *sterile neutrinos* are weakly-interacting fermions which arise as the right-handed counterparts of the standard neutrinos. The lightest of these *sterile neutrinos* might lie in the keV range and would be compatible with a warm dark matter candidate [76], but can also be regarded as a cold dark matter candidate [77] depending on its production mechanism. The *sterile neutrino*, besides qualifying as a good dark matter particle candidate and resolving the neutrino mass problem, overcomes the puzzle of baryon asymmetry [78] and, in the warm dark matter scenario, may mitigate some of the shortcomings

of cold dark matter cosmologies including the apparent lack of dSph galaxies around the Milky Way [33].

As already mentioned, a dark matter particle must be stable over cosmological time scales. Due to the mixing between sterile and active (conventional) neutrinos, the former become unstable. For the lightest *sterile neutrino* (*sterile neutrino* from now on), the main decay channel is

$$\nu_s \rightarrow 3\nu, \tag{1.13}$$

where ν_s denotes the *sterile neutrino* and 3ν denotes three active neutrinos and antineutrinos. The decay width of this process is

$$\Gamma_{\nu_s \rightarrow 3\nu} = \frac{G_F^2 m_{\nu_s} \theta^2}{96\pi^3}, \tag{1.14}$$

where G_F is the Fermi constant, m_{ν_s} is the sterile neutrino mass, and θ is the mass mixing angle. With sterile neutrino masses of $m_{\nu_s} \sim \mathcal{O}(1 \text{ keV})$ the sterile neutrino lifetime reaches $\sim 10^{17}$ years, therefore being cosmologically stable [79]. The detection of the products from the previous dominant decay is extremely difficult due to the low energies of the resulting active neutrinos, and the intrinsic difficulty of detecting neutrinos. However, there is another possibility of *sterile neutrino* detection thanks to a subdominant decay channel which may provide a distinctive photon line:

$$\nu_s \rightarrow \nu\gamma \tag{1.15}$$

The width of that decay process is

$$\Gamma_{\nu_s \rightarrow \nu\gamma} = \frac{9}{256} \frac{\alpha_{EM} G_F^2}{4\pi^4} \sin^2(\theta) m_{\nu_s}^5, \tag{1.16}$$

where α_{EM} is the fine structure constant [80]. Photons contributing to such a line would have energies $E_\gamma = m_{\nu_s}/2$, and the line itself would be broadened due to the velocity dispersion of the *sterile neutrino* population. Therefore, compact regions with significant accumulations of sterile neutrinos could produce a detectable X-ray flux line in the 0.1–100 keV energy range [79; 81; 82].

The subsequent line flux is directly proportional to the density of the dark matter region $\rho(r)$, integrated along the line of sight. Hence, the expected line flux is related to the sterile neutrino parameter space (m_{ν_s}, θ) in the following way:

$$\Phi^{line}_{\nu_s \rightarrow \nu\gamma}(\Delta\Omega) = \frac{9}{256} \frac{\alpha_{EM} G_F^2}{4\pi^4} \sin^2(\theta) m_{\nu_s}^5 \int_{\Delta\Omega} \int_{los} \rho(r(s,\Omega))\, ds\, d\Omega. \tag{1.17}$$

So far, no X-ray line associated to the *sterile neutrino* has been clearly detected [83; 84; 85], although some possible hints have been shown [86]. Thus, flux upper limits to X-ray lines have been used to constrain the sterile neutrino parameter space. Other bounds to the lower mass limit to the *sterile neutrino* come from dSph galaxies kinematic phase-space density [87] and Lyman-α forest data [88]. The allowed *sterile neutrino* parameter space is shown in Fig. 1.7.

1.3.3 Other candidates

As already mentioned, there is an ample collection of dark matter particle candidates. It is out of the scope of this work to review all of them. Thus, only a brief selection of other candidates is presented in the following.

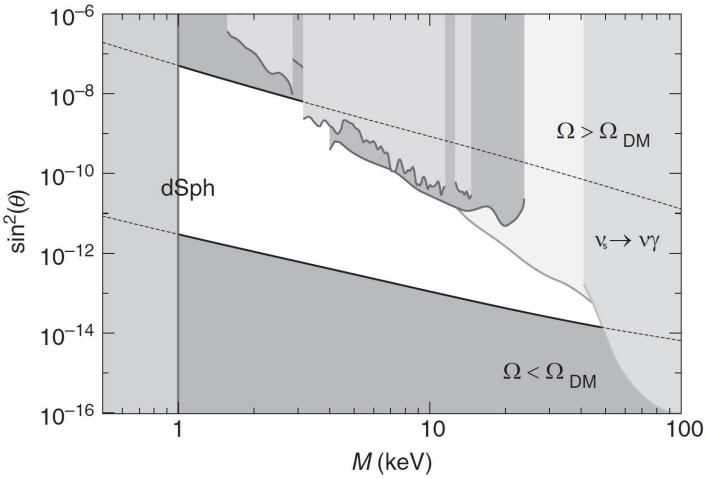

Figure 1.7: Parameter space of the *sterile neutrino* defined by its mass and its mixing angle $sin^2(2\theta)$. Regions which provide a non compatible dark matter relic abundance are excluded (denoted as $\Omega < \Omega_{DM}$ and $\Omega > \Omega_{DM}$). The constraints from X-ray astrophysical observations, searching for *sterile neutrino* decay lines, exclude almost the complete upper right part of the parameter space. The lower mass bound comes from the phase-space density of *sterile neutrinos* in dSph galaxies. Figure extracted from [57].

- Standard Model neutrinos

  The Standard Model neutrinos were proposed as dark matter particle candidates since they are massive and present weak interaction with baryonic matter. As their critical temperature at freeze-out was $kT \sim 3$ MeV, neutrinos were relativistic when they decoupled, and due to their large mean free path, they would represent a hot dark matter candidate. Nonetheless, their contribution to the total density of the Universe can not account for the total dark matter density. The neutrino number density after freeze-out is related to the precisely measured number density of CMB photons $n_\gamma = 413$ cm^3 as $n_\nu = 3/11 \times n_\gamma = 113$ cm^3 per neutrino flavor. Thus, if the neutrino was to account for the total dark matter density of the Universe $\Omega_{DM} = \Omega_\nu = \rho_\nu/\rho_c \approx 0.2$, the sum of neutrino masses must match $\sum m_{\nu_i} = 9.5$ eV where $i = e,\ \mu,\ \nu$. However, experimental bounds from neutrino flavor oscillations in detectors like Super-Kamiokande [89], place the neutrino masses below 0.1 eV, consequently ruling out the Standard Model neutrinos as the dark matter main component. In fact, WMAP data limit the contribution of neutrinos to the total dark matter *density parameter* to $\Omega_{nu}h^2 < 0.0067$.

- Dark Matter from Extra Dimensions

  Physical models based on extra dimensions propose that the 4-dimensional Standard Model is embedded into a higher dimensional space-time, like in the case of Kaluza-Klein models [90; 91]. These models offer a solution to the gauge hierarchy problem and, as a natural consequence, provide many dark matter particle candidates. In this framework, every multidimensional field is associated to a Kaluza-Klein tower of 4-dimensional particles with increasing masses. If the Standard Model is actually located into a higher dimensional space-time, there are towers of KK states for each SM particle. The characteristics of these KK states depend on the geometry of the extra-dimensions. Actually, in most extra-dimensional models, the KK states are not stable and thus can not play the role of dark matter particle, but new symmetries available in the extra-dimensions can stabilize the

KK states. This is the case of the Universal Extra Dimensions models [92], where the so-called KK-parity discrete symmetry brings stability to the lightest KK particle (LKP). One of the most studied LKP is the first KK excitation of the hypercharge gauge boson B^1, which qualifies as a viable dark matter particle [93]. Extra-dimensional models provide many other dark matter particle candidates. Only in KK-scenarios, there are many model-dependent stable LKPs: KK-Z boson, KK-Higgs boson, KK-neutrino, KK-graviton, Radion, Branons, superWIMPs, etc.

- Axions

  The axion particle was proposed as a solution for the strong CP problem in quantum chromodynamics [94]. This light and neutral boson of spin-0 arises after the spontaneous Peccei-Quinn symmetry breaking and represents a natural cold dark matter candidate. In the presence of electromagnetic fields, axions are predicted to couple with photons in such a way that a conversion is possible, leading to the so-called photon-axion oscillation. This effect may imprint a distinctive signature in the observed spectra of distant gamma-ray sources which could facilitate its discovery and characterization [95].

- Little Higgs

  In the so-called Little Higgs models [96] new particles must be introduced to cancel some quadratically divergent loops. After the introduction of T-parity, the lightest T-odd particle turns out stable. This particle is typically the T-odd heavy photon, which fulfills all the characteristics to play the role of dark matter.

- WIMPonium

  Most of dark matter candidates emerge after considering minimal dark sectors, *i.e.* neglecting possible WIMP interactions between themselves besides their annihilation. In non-minimal dark sector theories, WIMP bound states or WIMPonium have been proposed [97]. The amplification effect over the dark matter annihilation cross section arising from the inclusion of WIMPonium provides significant boosts to the possible annihilation flux [98].

- SuperWIMP and WIMPless Dark Matter

  Two examples of non-WIMP dark matter candidates can be found in the superWIMP and WIMPless particles. In superWIMP scenarios, WIMPs freeze out in the early Universe in the conventional way, but afterward decay to these even more weakly interacting particles [99]. This decay has predicted effects over the BBN and the CMB spectrum, as well as small-scale structure, which may provide a way for superWIMP detection. In WIMPless scenarios, the dark matter particle has no Standard Model gauge interactions, thus interacting in hidden sectors. It might be the case that connector sectors could mediate between the Standard Model and the hidden sector, producing detectable signals [100].

- WIMPzillas and super-heavy Dark Matter

  In some models of thermal inflation the dark matter particle is allowed to increase its mass after the freeze-out, reaching masses as high as 10^{10} GeV and fulfilling the correct cosmological abundance. These dark matter candidates, also known as WIMPzillas, suffer from severe problems as their detection appears rather difficult [101; 102]. Even heavier dark matter particles have been proposed, the so-called super-heavy dark matter particles, with

energies beyond 10^{13} GeV. These particles do not only qualify as dark matter candidates but also offer a solution to the problem of the creation of ultra-high energy cosmic rays thanks to their decay [103].

- Brane Dark Matter

  In the so-called brane-world scenario [104], the SM fields live on a three-dimensional hypersurface called brane and gravity propagates on a higher ($D = 4 + n$)) dimensional bulk space where the fundamental scale of gravity M_D is smaller than the Planck scale. The brane has a certain tension and its fluctuations are parametrized by the so-called branon fields, expected to be nearly weakly interacting at low energies, and massive due to spontaneous symmetry breaking of translational invariance. Thus, brane fluctuations could be a dark matter particle candidate also accounting for the local dynamics, that could be directly detected in accelerator laboratories [105].

- Others

  Some other interesting candidates are Q-balls, charged massive particles, self interacting dark matter, D-matter, radion dark matter, cryptons, fourth generation heavy neutrinos, minimal dark matter, technicolor models dark matter, mirror dark matter, among many others.

1.4 Dark matter searches

As in any search, there are some basic questions that should be addressed before attempting to detect the dark matter: what is searched for, where is it expected to be, and how is it planned to be detected. Depending on the answer to these questions the dark matter searches can be classified into three major approaches: direct production of dark matter in particle accelerators, direct searches through dark matter scattering off ordinary matter, and indirect searches for dark matter annihilation or decay into Standard Model products. In the following, these three approaches will be introduced, paying special attention to indirect dark matter searches.

1.4.1 Direct production

Assuming that the dark matter is actually a new type of particle, it would be subject to detection at particle accelerators with sufficient center-of-mass energy and luminosity: the accelerator must be able to provide center-of-mass energies larger than the new particle mass, at the same time that it generates a large quantity of events so the new signatures can be detected over the overwhelming background of purely Standard Model generated events. The dark matter particle would not leave any trace in the accelerator detectors, thus being invisible and only detectable through its associated missing momentum (see, *e.g.*, [57], and references therein).

Particularly, in supersymmetric scenarios, a mass spectrum of new particles is expected. For the case of hadron colliders, due to the absence of color charge in the LSP, its pair-production cross section is relatively low, of the order of 100 fb. On the contrary, color-charged supersymmetric particles present large pair-production cross sections, of the order of 10 pb, because it is a strong-interaction process. The posterior decay of these heavy color-charged particles goes through the new particles mass spectrum finally producing the LSP. Quarks and leptons with large transverse momentum are emitted through the decay chain down to the LSP. Thus, the typical event containing LSP signatures would consist of quark jets, hard leptons, and missing

transverse momentum, differing from typical quantum chromodynamics events. The expected rate of such a kind of events strongly depends on the mass of the LSP and is quite model-independent [106].

The Large Hadron Collider [107] and its accompanying detectors (ATLAS [108] and CMS [109] among them), are intensively testing the particle physics world at the weak-scale with unprecedented reach. Although no hints for the new physics have appeared by the time this work was written, results from the first $\sim$fb^{-1} of proton-proton collision data available. Based on these data, the parameter space of some of the most widely considered supersymmetric models are being constrained. In Fig. 1.8, a certain realization of the mSUGRA parameter space is constrained by ATLAS data by considering multijet events showing missing transverse momentum. Combined ATLAS and CMS data also allow for frequentist analyses of supersymmetric models, reducing their best-fit regions as shown in Fig. 1.6.

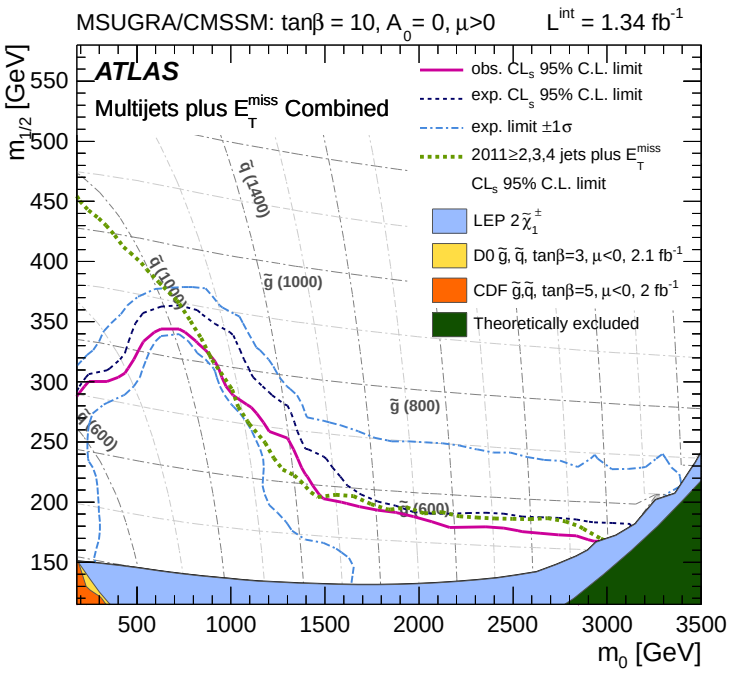

Figure 1.8: ATLAS exclusion limits over the mSUGRA parameter space after 1.34 fb^{-1} of accumulated data. The limits were computed by considering multijet events with missing transverse momentum. Limits from D0, CDF and LEP experiments are also shown. The mSUGRA (m_0, $m_{1/2}$) plane corresponds to tan$\beta = 10$, A_0=0, and $\mu > 0$. Figure extracted from [110].

The direct production of new particles offer very significant information like masses, annihilation and direct detection cross-section, as well as, in the case of dark matter candidates, the value for its thermal relic density. Nevertheless, such a set of characteristics must be confirmed by direct detection and indirect detection experiments in order to confirm the local and astrophysical existence of the particle. This condition is an unavoidable requirement to settle the particle as the real constituent of the dark matter in the Universe.

1.4.2 Direct searches

Despite the lack of coupling to the strong and electromagnetic sectors, the dark matter could still scatter off ordinary matter through weak interactions. The flux of dark matter particles at the Solar System can be estimated if its local density and mean particle velocity are known. Assuming the Milky Way to be embedded in a conventional dark matter halo, the local density of dark matter estimated from observational constraints is $\rho_0 \sim 0.3$ GeV s^{-1}. The velocity distribution of dark matter particles with respect to the Solar System is estimated to be of the order of $v \sim 100$ km s^{-1}. Thus, the local dark matter particle flux is expected to be around 10^5 cm^{-2} s^{-1} for hundred-GeV mass particles (see, *e.g.* [111], and references therein). Direct dark matter searches are based on the detection of nuclear recoils due to this large flux of dark matter particles elastically scattering off baryonic targets made of heavy nuclei.

The expected number of recoils per units of energy, time, and mass can be expressed as

$$\frac{dR}{dE} = \frac{\rho_0}{m_N m_{dm}} \int_{v_{min}}^{\text{inf}} v f(v) \frac{d\sigma}{dE}(E, v) dv, \tag{1.18}$$

where E is the recoil energy, ρ_0 is the local dark matter density, m_N is the nucleus mass, m_{dm} is the dark matter particle mass, $f(v)$ is the dark matter velocity distribution with respect to the detector, v_{min} is the minimum dark matter particle velocity that produces a recoil, and $d\sigma/dE$ is the dark matter-nucleus differential elastic scattering cross-section. After defining the dark matter-nucleus reduced mass $\mu = m_N m_{dm}/(m_N + m_{dm})$, and considering the non-relativistic scattering limit, the recoil energy can be calculated as

$$E = \frac{\mu_N^2 v^2 (1 - \cos\theta)}{m_N}, \tag{1.19}$$

where θ is the scattering angle in the center-of-mass reference system. Considering heavy nucleus and GeV-mass dark matter particles, the typical recoil energy is of few keV.

All the information about the dark matter microscopic properties is codified into the differential elastic scattering cross-section $d\sigma/dE$, conventionally separated into spin-independent and spin-dependent terms:

$$\frac{d\sigma}{dE} = \frac{d\sigma^{SI}}{dE} + \frac{d\sigma^{SD}}{dE}. \tag{1.20}$$

The spin-independent contribution comes from scalar and vector couplings to quarks while the spin-dependent one comes from axial-vector couplings to quarks. Depending on the dark matter type, the relation between both contributions is different and might help to distinguish different candidates.

Since the expected elastic scattering cross-section is of the order of $\sigma \sim 10^{-43}$ cm^2, the interaction rate of dark matter with ordinary matter is extremely low. The most challenging issue of direct dark matter searches is the background control and characterization. Therefore, extremely radio-pure elements are required for the target material, as well as for the rest of the detector parts. Direct dark matter detectors are placed underground so the cosmic ray background, mainly cosmic muons, is highly suppressed. On top of that, the target material is frequently surrounded by high-density stable metal shielding, like lead or copper. The electronic noise can also be a source of background and has to be as low as possible too.

The nucleus recoil energy can be deposited in the detector by different mechanisms: phonon production, ionization and scintillation. The phonons, vibrations of the crystal lattice, can

be detected through their thermalization via thermal sensors and mechanically via athermal sensors. The ionization can be detected through pair creation in semiconductors or electron drift due to strong electric fields in the detector. The scintillation arises from the de-excitation of electrons in the target producing the emission of optical photons. The fraction of recoil energy deposited in each mode, frequently referred as quenching, can be a distinguishing feature between background events and actual recoils originated by dark matter scattering of target.

There are many experiments searching for direct dark matter signals, each of them exploiting different techniques and energy deposit channels. Some examples, classified depending on their detection techniques, can be found in the following brief list:

- Ionization detectors: this kind of detectors are typically cryogenic germanium devices which detect the ionization effect measured in the semiconductor. Some examples are the IGEX [112], TEXONO [113], and CoGeNT [114] detectors.

- Scintillator detectors: these detectors use highly radio-pure inorganic scintillating crystals to detect the nuclear recoils via scintillation photons recorded by single-photon sensitive photodetectors. The DAMA/LIBRA [115] experiment falls into this category.

- Ionization-phonon detectors: in these detectors the recoil events are characterized through the measurement of both the ionization and phonons generated in the target material. The CDMS [116] and EDELWEISS [117] experiments belong to this type of detectors.

- Scintillation-phonon detectors: the CRESST [118] and ROSEBUD [119] experiments are examples of detectors exploiting the generation of phonons and photons in scintillation crystals acting as target material.

- Scintillation-ionization detectors: these kind of detectors consist of time projection chambers with a highly radio-pure liquid noble gas like Xenon or Argon as target material. There are single-phase detectors like XMASS [120], DEAP/CLEAN [121], while the most sensitives are two-phase detectors (target element in separated gas and liquid phases). There are Xenon-based two-phase detectors like XENON100 [122] and ZEPLIN [123] detectors, as well as Argon-based detectors like WArP [124] ArDM [125].

- Others: there are some other types of detectors, like the directional detectors, which are able to track the incident particle, like DRIFT [126], DMTPC [127], MIMAC [128], or NEWAGE [129] instruments. Bubble chamber detectors, which are able to distinguish signal from background, based of acoustic differentiation of ultrasound signals after bubble nucleization in the target material, are also efficient detectors. An example of the last group is the COUPP experiment [130].

The future of direct detection instruments goes in the direction of increasing the mass of the target materials above one ton, lowering the environment temperatures down to few mK, and detecting the signals from scintillation, ionization and phonon generation with the same detector. Examples of such future ton-scale cryogenic multisignal detectors are the planned EURECA [131] and DARWIN [132]. More details about the above-mentioned detectors can be found in [57] and references therein.

By the time this work was written, there was no strong evidence for a dark matter detection in direct searches. Nonetheless, some experimental groups have claimed positive signals, like the DAMA/LIBRA and CoGeNT collaborations. First, DAMA/NaI [115] reported

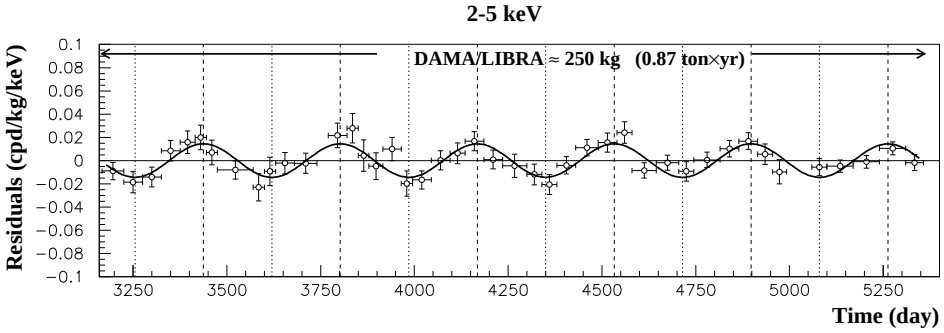

Figure 1.9: Residual rate of the scintillation events in DAMA/LIBRA experiment in the 2-5 keV energy range. The signal has a modulation period of 1 year at a 8.9σ CL. The data also include the DAMA/NaI exposure and accounts for a total cumulative exposure of ~ 1.2 ton yr. Figure extracted from [133].

a clear annual modulation signal in their detectors, later confirmed by the improved detector DAMA/LIBRA [133] at a CL of 8.9σ, as can be seen in Fig. 1.9. The COGeNT collaboration also reported the hint of a signal in the shape of an irreducible number of excess events over the background estimations [114] plus a posterior annual modulation of the signal at a 2.8σ confidence level [134]. Nevertheless, CoGeNT and DAMA/LIBRA results are not compatible, favoring different WIMP models, in the light of the existing bounds from other direct detection experiments [135; 136]. Actually, the annual modulation of the signal can be attributed to non exotic reasons, like the annual modulation of the muon background [137]. Moreover, the most stringent limits so far over the spin-independent elastic dark matter-nucleon cross-section, those published by the XENON100 collaboration, already exclude both, the DAMA/LIBRA and CoGeNT favored regions, as shown in Fig. 1.10.

1.4.3 Indirect searches

The indirect dark matter searches exploit the possibility that the dark matter particles annihilate or decay into Standard Model particles, and the fact that the detection of such products could help to infer dark matter particle properties and characteristics. Unfortunately, these Standard Model products are very frequently entangled with a large cosmic ray background which makes their identification extremely difficult. In principle, the fact that the dark matter particle could annihilate or decay might seem in contradiction with the requirement that it must be stable. This stability condition, as already mentioned, means that the particle must be *cosmologically stable*, namely, that its decay time must be larger than the Universe age or its annihilation rate small enough so the Universe amount of dark matter is not significantly reduced due to this two possible effects.

The expected signal depends on the dark matter particle candidate characteristics: its mass fixes the energy range where the products are expected, the signal strength depends on whether the particle decays or annihilates, and its mode to produce Standard Model particles is also strongly related to inherent particle properties. Due to the large variety of candidates and possible products, the list of detectors which could be well suited for indirect dark matter searches is proportional to that variety. Indirect dark matter searches are usually carried out by detectors on-board satellites and balloons, but ground-based experiments present also a great potential of discovery.

For a detailed discussion on indirect dark matter searches see [139] and references therein.

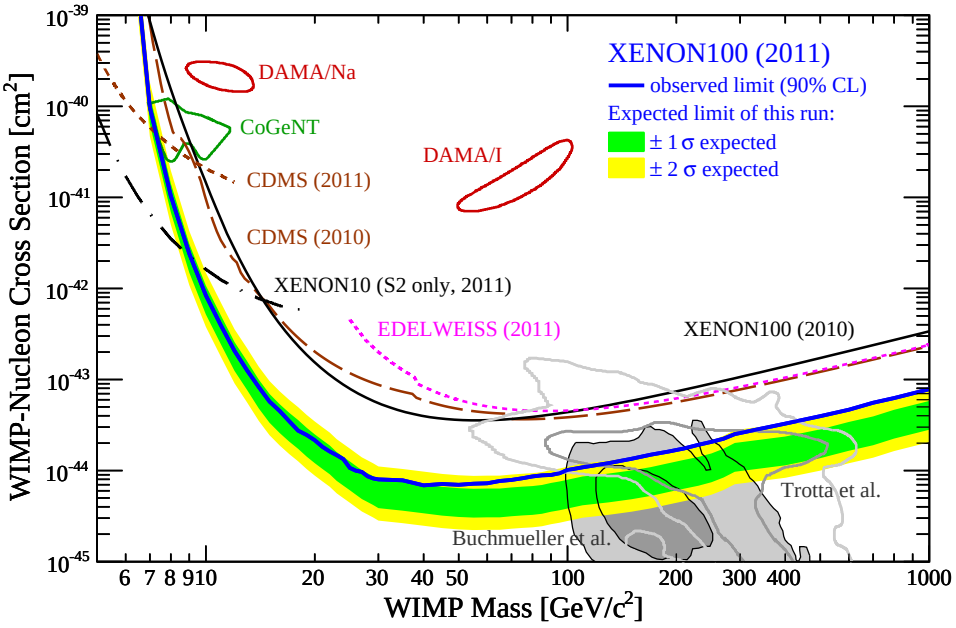

Figure 1.10: Spin-independent elastic WIMP-nucleon cross-section as function of WIMP mass m_χ. The 90% C.L. limits from XENON100, EDELWEISS, CDMS are shown together with the 90% C.L. areas favored by CoGeNT and DAMA results. Pre-LHC expectations for the cMSSM are shown as shaded and solid line regions. Figure extracted from [138].

1.4.3.1 Detectable products

As already mentioned, the annihilation or decay of dark matter particles would provide a distinctive flux of Standard Model products. Concerning detectable products, the indirect searches look for signatures through the stable final products: photons, neutrinos, electrons, protons, and their corresponding antiparticles.

- Photons: Among the possible products, photons are particularly important since they do not suffer magnetic deflection on their way to the observer, as charged particles do, and make possible to trace back their origin. The energy window where the photons from dark matter annihilation or decay are expected depends on the dark matter particle mass and the emission mechanisms.
  The γ-ray regime is very well motivated, since many of the possible dark matter particles, like WIMP-type candidates, posses masses in the GeV-TeV range, being most of them annihilating particles. The bulk of γ-ray emission from dark matter annihilating particles is expected to come from the hadronization of quarks, where the production of π^0 mesons (and their posterior decay into 2γ) is of particular relevance. Also final state radiation from charged particles plays a role. Direct annihilation into photons is a forbidden process, with a marginal incidence in the total γ-ray emission budget, but very interesting *per se*, since γ-ray lines would be generated. A third possible contribution comes from the already mentioned internal QED bremsstrahlung, of interest in *e.g.* certain *neutralino* annihilation processes. Eventually, the expected γ-ray emission from dark matter annihilation would show a hard spectrum with a sharp cut-off at the dark matter particle mass, as can be seen in the example of Fig. 1.11, where the spectra from different annihilation channels are found. As already proposed when describing keV mass candidates, a dark matter signal

in the X-ray band could be also expected. In the particular case of the sterile neutrino, a decaying particle, the photon flux would consist of a X-ray line without any continuum contribution. Going down to lower frequencies, the imprint of dark matter can could be also observed in microwave and/or radio emission. If the dark matter annihilation or decay produces a significant amount of electrons and positrons, the injection of such particles in the vicinities of the producing object may generate a low frequency photon emission, via synchrotron processes, if magnetic fields are present. Studies of the interstellar medium emission from WMAP data found an unexpected excess of microwave photons in the inner $\sim 20^{\circ}$ around the Galactic Center, the so-called WMAP haze [140], which has been interpreted in terms of annihilating dark matter [141], but also in terms of a conventional pulsar population [142]. The possible synchrotron radio signal has been also proposed, and studied for specific cases [143; 144]. However, a precise estimate of the radio emission is very difficult to obtain, since there are large uncertainties in the possible electron-positron population, the distribution of the magnetic fields in each target, etc.

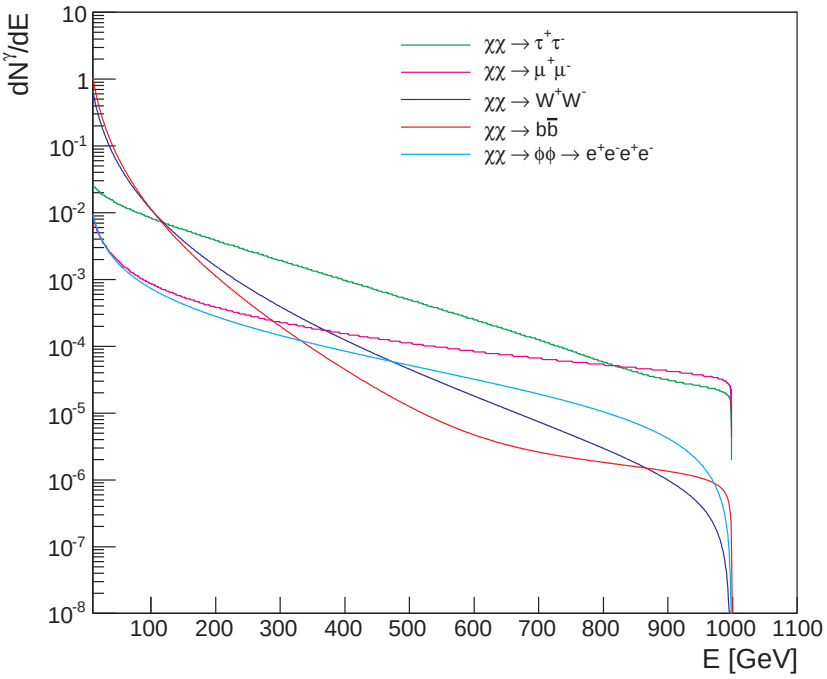

Figure 1.11: γ-ray photons yield from WIMP annihilation for different channels. For the channels $b\bar{b}, W^+W^-, \tau^+\tau^-, \mu^+\mu^-$ the fits from [145] were considered. For the channel $\phi\phi \rightarrow 4e$ the parametrization from [146] was used. Mass values for the WIMP of $m_\chi = 1$ TeV and for the mediator state of $m_\phi = 0.1$ GeV were assumed for the calculations.

- Neutrinos: a large amount of neutrinos are expected from dark matter annihilation or decay. If the dark matter is heavy enough, and the primary products of such processes are heavy leptons, neutrinos will be produced in their decay to lighter ones. For τ leptons, either for leptonic or hadronic decay modes, neutrinos are produced. In the case of muons, a pair of neutrinos are produced in almost all their decays to electrons (*e.g.* $\mu^- \rightarrow e^- \bar{\nu}_e \nu_\mu$, with a branching ratio of $\sim 100\%$). Neutrinos are also generated if the primary products are gauge bosons. If Z bosons are found among the primaries, there is a Z boson decay

channel directly to a pair of neutrinos. Additionally, Z bosons can produce neutrinos in their decay to $\tau^+\tau^-$, $b\bar{b}$, or $c\bar{c}$. In the case of W bosons, neutrinos are produced in the decay $W^\pm \rightarrow l^\pm\nu$. Thus, indirect dark matter searches by using neutrinos is a feasible strategy. Searches for neutrino signals from dark matter captured in the Sun have been proposed [147], and dark matter limits from neutrino observations of the galactic halo with the IceCube neutrino observatory have been already set [148].

- Other cosmic rays: Due to the fact that in the annihilation processes or decays the same amounts of matter and antimatter are produced, dark matter searches are usually conducted using antimatter as messenger particles because the astrophysical background is much lower. In this sense, the distribution of positrons is a very promising place where to look for deviations with respect to the conventional flux. Actually, if the dark matter is heavy enough so to produce W bosons on its decay or annihilation, and these bosons are expected among the final states, a positron excess will be found as a consequence of the aforementioned decay of these bosons. So far, some experimental results, with non-standard explanations, could be attributed to a dark matter particle annihilating producing positrons and electrons as final stable products. The INTEGRAL satellite reported the electron-positron annihilation line of photons with energies of 511 keV, from the central region of the galaxy [149] with a possible dark matter explanation [150]. The Advanced Thin Ionization Calorimeter (ATIC) balloon-borne experiment also reported an anomaly in the cosmic ray electron-positron spectrum, namely, a spectral bump in the energy range from 300 to 800 GeV [151]. Fermi-Large Area Telescope (LAT) results did not confirm the bump at such high significance level but also showed a deviation from the expectation in this energy range, converging at high energies with measurements the Major Atmospheric Imaging Cherenkov (MAGIC) and the High Energy Stereoscopic System (H.E.S.S.) telescopes [152] (see Fig. 1.12b). The Payload for Antimatter Matter Exploration and Light-nuclei Astrophysics (PAMELA) satellite also presented some striking results on the positron fraction [153], namely, a deviation with respect to the expected conventional behavior (see Fig. 1.12a). This deviation has been explained in terms of nearby population of positron injectors, like pulsars, or a more exotic explanation involving a dark matter origin[154]. In none of the aforementioned cases, a strong and unequivocal dark matter detection can be claimed. Another final stable product from dark matter annihilation or decay are antiprotons, which would be present via direct production, from the direct decay of other primary products like quarks, or from indirect decay (through quarks as well) of Higgs or gauge bosons. In the case of antiprotons, no clear deviation from the expected conventional behavior of their spectral distribution has been detected so far. More exotic signals are also expected, like an anti-deuterium production enhancement catalyzed by dark matter annihilation or decay [155].

1.4.3.2 Photon fluxes from dark matter annihilation and decay

Due to the importance of photons as possible dark matter identifiers and trackers, a brief introduction of the calculation of the expected fluxes from dark matter annihilation or decay is mandatory. Since most of the work to be presented in the forthcoming chapters deals with indirect dark matter searches in individual targets, photon fluxes from individual sources will be regarded. For the calculation of such an expected photon flux, instrumental effects will be taken into account, since the goal is to know how a dark matter generated photon flux would

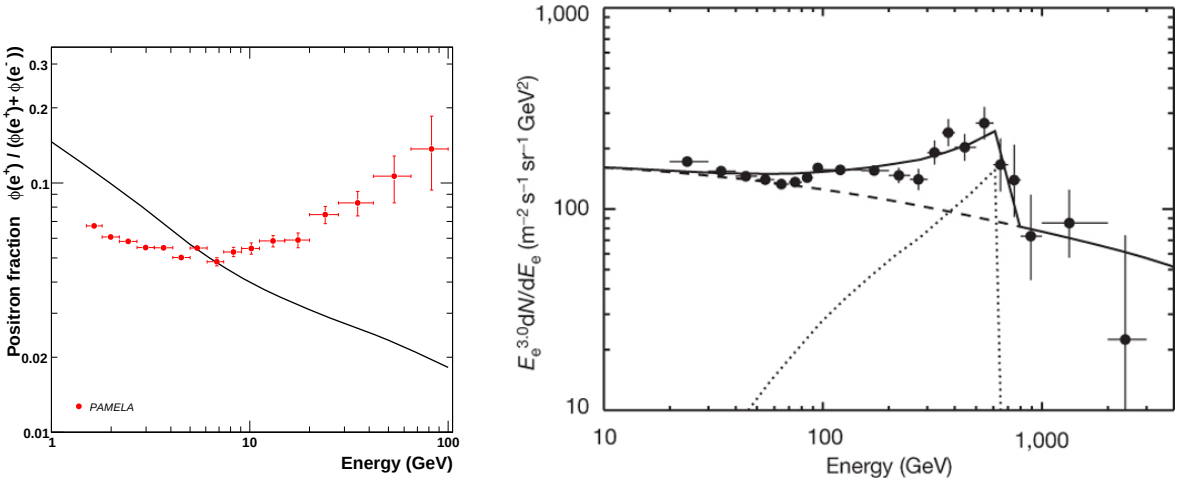

(a) PAMELA cosmic ray positron fraction

(b) ATIC cosmic ray electrons distribution

Figure 1.12: Fig. 1.12a: The PAMELA positron fraction. The solid line depicts the expected distribution of pure secondary production positrons from cosmic rays propagating in the galaxy. Figure extracted from [153]. Fig. 1.12b: The ATIC cosmic ray electrons distributions. The dashed lines represents the simulated general electron spectrum from galactic sources. The dotted line shows the generated electrons from a KaluzaKlein particle of 620 GeV mass. Figure extracted from [151].

look like in the considered detector. Consequently, a differential photon flux due to dark matter annihilation or decay depends on instrumental factors, namely, the angular resolution, the field of view, and the energy resolution of the detector (also the energy threshold for the case of integral fluxes). Such flux will also depend on physics factors as the intrinsic dark matter density distribution in the source, and the particle physics characteristics of the dark matter candidate. The calculation of the integral photon flux for the two considered cases will be described in the following.

Decaying dark matter case: When dealing with a two-body decay, the subsequent line flux can be conveniently described as the product of two factors:

$$\Phi(\Delta\Omega) = \Gamma \times J_{dec}(\Delta\Omega), \tag{1.21}$$

where Γ is the decay rate, which includes the particle physics contribution to the flux, and $J_{dec}(\Delta\Omega)$ is the so-called astrophysical factor, which includes the astrophysical target contribution to the flux. In the current case, the astrophysical factor is the integrated dark matter content along the line-of-sight s and inside a viewing cone $\Delta\Omega$, in such a way that the integral flux reads

$$\Phi(\Delta\Omega) = \Gamma \int_{\Delta\Omega} \int_{los} \rho(r(s,\Omega)) ds d\Omega. \tag{1.22}$$

Annihilating dark matter case: As in the previous case, the integral photon flux from dark matter annihilation can be factorized into two terms:

$$\Phi(>E_0, \Delta\Omega) = \Phi^{PP}(>E_0) \times J_{ann}(\Delta\Omega), \tag{1.23}$$

where $\Phi^{PP}(> E_0)$ is the so-called particle physics factor, which includes all the particle physics contribution, and reads

$$\Phi^{PP}(> E_0) = \frac{1}{4\pi} \frac{\langle \sigma_{ann} v \rangle}{2m_{DM}^2} \int_{E_0}^{m_{DM}} \sum_{i=1}^{n} B^i \frac{dN_\gamma^i}{dE} dE, \tag{1.24}$$

where E_0 is the integration lower energy, $\langle \sigma_{ann} v \rangle$ is the annihilation cross section, m_{DM} is the dark matter particle mass, and $\sum_{i=1}^{n} B^i dN_\gamma^i/dE = dN_\gamma/dE$ is the sum over all the n possible annihilation channels producing photons (B^i is the particular branching ratio for channel i).

The contribution from the astrophysical target is codified inside the astrophysical factor $J_{ann}(\Delta\Omega)$, which consist in the integration of the squared dark matter density over the line of sight s and the viewing cone $\Delta\Omega$:

$$J_{ann}(\Delta\Omega) = \int_{\Delta\Omega} \int_{los} \rho^2(r(s,\Omega)) ds d\Omega. \tag{1.25}$$

Consequently, the integral flux from dark matter annihilation can be expressed as

$$\Phi(> E_0, \Delta\Omega) = \frac{1}{4\pi} \frac{\langle \sigma_{ann} v \rangle}{2m_{DM}^2} \int_{E_0}^{m_{DM}} \sum_{i=1}^{n} B^i \frac{dN_\gamma^i}{dE} dE \int_{\Delta\Omega} \int_{los} \rho^2(r(s,\Omega)) ds d\Omega. \tag{1.26}$$

In order to take into account the energy resolution of the detector, the decay rate Γ in Eq. 1.22, and the particle physics term Φ^{PP} in Eq. 1.26, must be convoluted with the corresponding energy resolution function. In the same way, the dark matter density distribution must be convoluted with the angular resolution function of the detector, in both Eq. 1.22 and Eq. 1.26, in order to take into account this experimental effect in the final expected flux.

As it has been shown, the particle physics contribution to the photon flux is codified into the decay rate Γ or the particle physics term Φ^{PP}, for the decaying or annihilation dark matter respectively. Once a dark matter candidate is chosen, these factors are be fixed and universal. On the other hand, the astrophysical factor depends on each astrophysical target. This target is usually a dark matter halo, and the corresponding dark matter density distribution $\rho(r)$ can be described as such. To model the dark matter density distribution several profiles have been proposed, based on the results of N-body dark matter simulated halos. These theoretical profiles are later confronted to data, basically kinematic data of stars contained in known dark matter dominated systems. The most common profiles are the isothermal, Navarro-Frenk-White, Moore, and Einasto profiles.

The isothermal profile [156; 157] can be expressed as

$$\rho_{iso}(r) = \rho_s \left[1 + \left(\frac{r}{r_s} \right)^2 \right]^{-1}, \tag{1.27}$$

where ρ_s is the typical scale density, and r_s is the typical scale radius. The isothermal profile represents the so-called cored profiles, meaning that, at small radii, the density of dark matter approaches a constant value, forming a flat density core.

The Navarro-Frenk-White profile [158] reads

$$\rho_{NFW}(r) = \rho_s \left(\frac{r}{r_s} \right)^{-1} \left(1 + \frac{r}{r_s} \right)^{-2}, \tag{1.28}$$

representing cuspy profiles obtained by N-body simulations. The scale density ρ_s and the scale radius r_s are correlated with the halo virial mass, and depend on the epoch of halo formation. Unlike the isothermal profile, the dark matter density increases as a power law of radius when approaching the halo center, forming the so-called dark matter cusps.

The Moore profile [159] can be written as

$$\rho_{Moore}(r) = \rho_s \left(1 + \frac{r}{r_s}\right)^{-1} \left[1 + \left(\frac{r}{r_s}\right)^2\right]^{-1}, \tag{1.29}$$

being a phenomenological profile obtained from kinematic data of classical dSph galaxies. Like the NFW profile, the Moore profile is cuspy, not cored.

The Einasto profile [160] profile is described as

$$\rho_{Ein}(r) = \rho_s e^{-\frac{2}{\alpha}\left[\left(\frac{r}{r_s}\right)-1\right]}, \tag{1.30}$$

behaving almost like a NFW profile, but differently at the innermost radii. The Einasto profile presents a finite slope at the origin, unlike the NFW profile which has a divergent central density. The Einasto profile tends to better fit the dark matter halos of the latest N-body dark matter halo simulations [160].

The question of which dark matter density profiles better describe the actual dark matter halos is still open and subject to strong debate. Whether the dark matter profile is cuspy or cored is of crucial importance when dealing with annihilating dark matter, since cored profiles predict significantly lower photon fluxes that cuspy profiles, due to the dependence of the expected flux with the dark matter density squared. The difference is much less in the case of decaying dark matter, since the dependence is linear with the dark matter density profile.

It is worth mentioning that the integral fluxes described by Eq. 1.22 and Eq. 1.26 can be boosted by several mechanisms, like the so-called Sommerfeld enhancement and the consideration of substructures in the halo. The Sommerfeld enhancement is a non-relativistic quantum mechanical effect which boosts the annihilation cross section due to a resonance effect for certain dark matter masses, usually in the TeV region, under the condition that the dark matter velocity is small enough [161]. These conditions apply to heavy WIMPs representing cold dark matter candidates, and the boost effect have been studied for both, photons [162] and cosmic rays [163] as annihilation products. The inclusion of substructures in the calculation of the astrophysical factor through the dark matter density profile can also boost the expected overall flux. Detailed studies based on the results of cosmological N-body simulations conclude that boosts up to an order of magnitude can be obtained [38; 164]. Nevertheless, that estimate severely relies on the extrapolation of the simulated halos mass spectrum, and thus needs to be revisited once the numerical simulations reach better mass resolution.

1.4.3.3 Interesting targets

There are several parameters that must be taken into account in order for an astrophysical object to qualify as a good target for dark matter searches. First, as it has been shown in the previous section, the expected photon flux for dark matter decay is proportional to the dark matter density, and proportional to the dark matter density squared for the annihilating particle scenario (the same occurs for the expected neutrino flux). Consequently, astrophysical regions presenting high dark matter densities are favored. Nonetheless, the distance to the target plays a major role too, since the expected flux is inversely proportional to the distance squared. Besides

the previous considerations, the mass-to-light ratio of the system, and the possible background, must be regarded. Systems with large dark matter content but also large baryonic content present two drawbacks: first, the baryonic matter may disturb the dark matter profile through dynamical friction, smoothing out the central high dark matter density, and thus reducing the expected flux; second, these baryons may act as strong background for the dark matter signal, producing photons via conventional astrophysical processes in a much more numerous way than through dark matter annihilation or decay.

Attending to the previous criteria, the best targets proposed so far are the Galactic Center, the Galactic Halo close to its center, the dark substructures of the Galactic Halo, galaxy clusters, and dSph galaxies.

The Galactic Center and Galactic Halo: The Galactic Center is the closest (~ 8.5 pc) astrophysical region highly dominated by dark matter. However, the Galactic Center is a densely populated region. As a consequence, a large background from conventional sources is present in almost any wavelength. On top of that, the large baryon content of the inner part of the galaxy may have disturbed the dark matter distribution of the Galactic Center. Therefore, the characterization of the core region of the dark matter density profile is an extremely difficult task, full of uncertainties. At very high energies, where WIMPs signatures are expected, there have been observations of the Galactic Center by many Cherenkov telescopes: Whipple [165], CANGAROO [166], H.E.S.S. [167], and MAGIC [168]. These two last instruments have confirmed a non-variable signal (from hour to years timescale) with a power-law description of relatively hard spectral index ($\Gamma \sim 2.2$). The spectrum extends up to 20 TeV and it is very unlikely that it is due to dark matter annihilation although a signal in the low energy regime (~ 100 GeV) can not be ruled out by these observations. Studies of the spatial extension of the source are also not compatible with a dark matter profile density. On top of that, there are many possible conventional counterparts that can justify the emission: the super-massive black hole SrA, the supernovae remnant SgrA East, and the pulsar wind nebulae G359.95-0.04. Moreover, estimates of the possible dark matter signal from the Galactic Center are three orders of magnitude below the total flux detected by the before mentioned Cherenkov telescopes. Therefore, it would be very difficult to disentangle a dark matter component from the conventional astrophysical emission.
A way to overcome the background problem is to look for a dark matter signal in the Galactic Halo, far enough from the Galactic Center so to avoid the conventional High Energy (HE) emitters, but close enough to the Galactic Center so the dark matter density is sufficiently high. This kind of observations have been conducted by the H.E.S.S. telescopes[169], providing one of the best limits on the dark matter annihilation cross section so far (see Fig. 1.13).

Dwarf Spheroidal Galaxies: Satellite galaxies have been proposed to be the largest subhalos from a parent galaxy dark matter halo, which may have attracted baryonic matter along their evolutionary history, being able to form populations of star members [170], being therefore visible in the optical wavelength. Among them, the dSph galaxies, with luminosities from 10^2 $L_\odot$ to 10^8 $L_\odot$, are the most dark matter dominated systems known so far [13]. They represent an excellent population for indirect dark matter searches: their extreme mass-to-light ratio suggests that baryons are not expected to play a significant role in the dark matter distribution; they are expected to have a very low intrinsic background at high energies; and they are relatively nearby objects (closer than ~ 100 pc in most cases). A more complete motivation of dSph galaxies as good targets for dark matter searches can be found in Section 3.1.

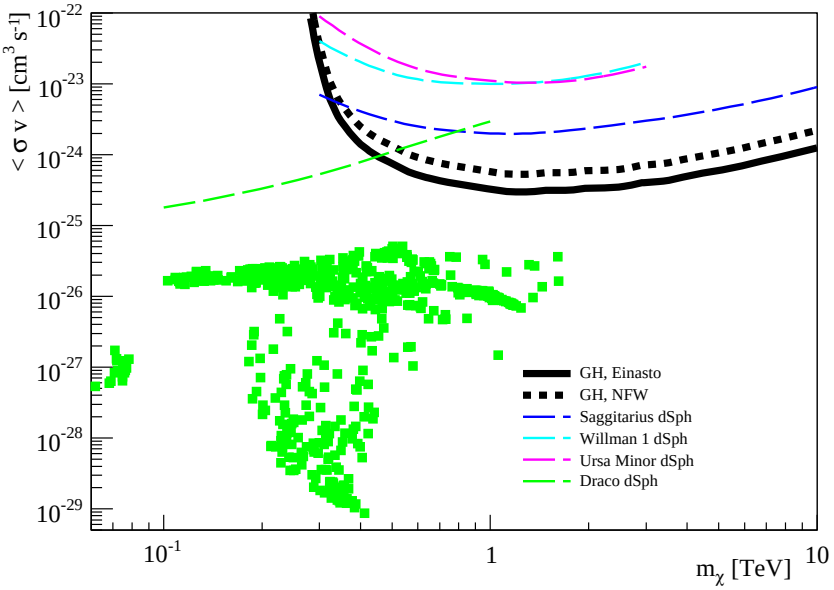

Figure 1.13: Upper limits at the 95% CL over the dark matter thermally averaged annihilation cross section from H.E.S.S. observations of the Galactic Halo for a fixed dark matter model. The corresponding upper limits from dSph galaxies observations are also shown for comparison purposes. Green points represent different simulated mSUGRA models. Figure extracted from [169].

Dark matter searches in the keV and GeV energy ranges have been conducted by X-ray telescopes, and γ-ray satellites and Cherenkov telescopes respectively. A brief summary of the main observations and instruments involved in dark matter searches in dSph galaxies can be found in Section 3.1 too.
The whole Chapter 3 is devoted to this topic, including detailed information on dark matter searches in Willman 1, in both, the Very High Energy (VHE) γ-ray band with MAGIC and the X-ray band with Chandra-XRO, and Segue 1, in the very high energy γ-ray band with MAGIC. These two candidates were selected due to their very large astrophysical factors.

Dark Matter Subhalos: the evolution of dark matter distribution in the Universe has been studied, from cosmological scales to galactic and subgalactic scales, by means of N-body cosmological simulations[171; 172]. The main conclusion out of these simulations is that dark matter hierarchically clusters, from smaller to larger scales, as already mentioned in Sec. 1.2.3. Therefore, dark matter halos should not be smooth but should rather present rich inner substructures, the so-called dark matter subhalos. In galactic terms, the largest of these subhalos may have attracted baryonic matter and have started start-formation, thus being visible as the previously mentioned dSph galaxies. On the other hand, it may be that these subhalos are too small to have attracted enough baryonic matter to start star-formation and are therefore invisible in the context of conventional emission mechanisms but may shine in the energy window where a dark matter signal is expected. The fact that they may be small can be compensated by the fact that a fraction of them might be nearby objects. In the framework of a GeV-mass WIMP, nearby subhalos could be bright emitters of VHE γ-ray radiation[173] and may appear in all-sky surveys performed by γ-ray satellite telescopes.

More information about the motivation of dark matter subhalos as excellent targets for dark matter identification can be found in Chapter 4. In the same Chapter, a search for possible dark matter subhalos in the Fermi-LAT point-like source population and the observation of two good dark matter subhalo candidates by the MAGIC telescopes is documented in-depth.

Galaxy Clusters: Attending to the theories of hierarchical formation of large scale structures in the Universe, the galaxy clusters are the latest to form and largest gravitationally bounded objects. These objects with radii of few Mpc and masses in the range from 10^{14} to 10^{15} $M_{\odot}$ are among the most dark matter dominated objects, with more than 80% of their total mass in dark matter form [174]. They have been extensively studied as targets for dark matter searches and compete with dSph galaxies providing similar expected photon fluxes from dark matter annihilation despite their huge distances (see, [175], and references therein). On the other hand, they present a large background for the possible dark matter signal due to the dominant emission from Active Galactic Nuclei (AGN) galaxy population, as well as a secondary component from cosmic ray induced radiation.
Among all the known galaxy clusters, the three most promising targets in terms of dark matter detection are the Perseus, Coma, and Virgo clusters. High energy γ-ray observations by Fermi-LAT, did not report any detection so far [176]. There have been Cherenkov telescopes γ-ray observations too, *e.g.* on Perseus [177; 178], and Coma [178; 179] clusters. The MAGIC telescopes detected two point-like sources in Perseus cluster, very likely associated to the central giant galaxy NGC 1275, and the radio galaxy IC 310, but none of the signals were compatible with a dark matter origin. Searches for decaying dark matter in the X-ray band have been also conducted in Coma and Virgo clusters by XMM-Newton [180], also without any detection.

Other interesting targets: The Sun is supposed to host a large amount of dark matter in its center due to gravitational in-fall of the local dark matter distribution. Observations of the expected photon flux with current instruments is not possible, but, as already mentioned, the neutrino signal could be detected by the current generation of neutrino telescopes [147]. If the dark matter is partly in some kind of axion-like particle, its imprint could be extracted from the study of AGNs VHE γ-ray attenuation due to the Extragalactic Background Light (EBL). Distinctive signals are expected if photons really convert into axion-like particles in the presence of magnetic fields [95]. Another hypothetical astrophysical objects which could produce detectable dark mater signal are the so-called intermediate massive black holes [181], where gravitational in-fall could have formed dark matter spikes of large central densities. There is also the possibility to detect a dark matter imprint in the AGN γ-ray spectra caused by the scattering of high-energy particles in the AGN jet off dark matter particles [182]. Indirect dark matter searches can be conducted not only on specific astrophysical objects but in the galactic and extragalactic background photons. For instance, in the γ-ray band, there have been searches for dark matter annihilation lines in the HE γ-ray background [183], and a possible detectable dark matter signature in the γ-ray background anisotropies has also been proposed [184] and is under study [185].

The bulk of this work consists of indirect dark matter searches in both, dSph galaxies and possible dark matter subhalos, considering observations performed in the X-ray, HE γ-ray and VHE γ-ray bands.

Chapter 2

High Energy Astrophysics

This chapter is devoted to the High Energy Astrophysics. A general overview of this field is of great interest, since the indirect dark matter searches to be presented in further chapters pursue the identification of products in the same energy window, thus being considered a significant portion of what can be defined as high energy astrophysics. In Sec. 2.1 a brief introduction of the high energy window to the Universe is done, where the non-electromagnetic messengers will be commented: cosmic rays, neutrinos, and gravitational waves. A special mention is done for the case of γ-ray astrophysics in Sec. 2.2, where the production mechanisms, main sources, and detection techniques are shown. More detailed descriptions of the γ-ray detectors used for this work are developed in Sec. 2.3 for the Fermi γ-ray Space Telescope, and in Sec. 2.4 for the MAGIC Telescopes. Finally, Sec. 2.5 closes the chapter with a brief mention to the X-ray waveband and a description of the Chandra X-ray Observatory, whose data is also exploited in Chapter 3.

2.1 Introduction to the high energy astrophysics

It was not until the 20th century that the observational window to the Universe was broadened, expanding the narrow band of the optical wavelengths down to the infrared, microwave, and radio, an up to the ultraviolet, X-ray, and γ-ray bands. Apart from the electromagnetic spectrum, more observational windows were open by means of new messengers, like the cosmic rays, and new ones are on the way, thanks to the neutrinos and the gravitational waves.

One of the main conclusions brought by the aforementioned step forward made by last century astronomy, mainly thanks to the discovery of radio, X-ray and γ-ray emission, is that there are extremely energetic processes in the Universe that can not be explained in terms of conventional thermal emission. The field of high energy astrophysics deals with the study of such non-thermal processes.

Due to the nature of the messenger particles, γ-rays and cosmic rays, high energy astrophysics is linked to high energy particle physics, and the former can study matter and radiation whose energies are currently unreachable by the latter. The synergy between both disciplines is usually denoted as astroparticle physics. Consequently, high energy astrophysics offers an exceptional field of research for fundamental physics. Open questions like the origin of cosmic rays, the properties of neutrinos, the stability of ordinary matter, the nature of gravity, and the identification of the Dark Matter constituents, may find an answer thanks to high energy astrophysical observations (see, *e.g.*, [186; 187], and references therein).

During this section, a brief summary of the non-electromagnetic messengers from the high

energy astrophysical processes will be given. A more detailed description of the γ-ray window will be developed in Sec. 2.2.

2.1.1 Cosmic rays

Cosmic rays are actually very energetic charged particles with extraterrestrial origin, whose discovery, dated the beginnings of the 20th century, is commonly attributed to Victor Hess [188]. This intriguing flux of particles has been deeply studied since then: their spectra and chemical composition has been characterized, but their origin is still under debate. Regarding their chemical composition, cosmic rays are basically 79% protons, 15% helium nuclei, while only a 6% can be found in the form of heavier nuclei and electrons [71]. The cosmic ray spectrum is characterized in a wide energy window that ranges 13 orders of magnitude, from 10^8 up to 10^{21} eV. It can be well fitted by a broken power-law presenting three spectral indices: 2.65 up to energies of 3×10^{15} eV (the so-called *knee*), then 3.1 up to energies of $\sim 10^{18}$ eV (the so-called *ankle*), and finally 2.7 up to the Greisen-Zatsepin-Kuzmin cut-off around $\sim 5 \times 10^{19}$ eV [71].

In the standard picture, there are two different populations of cosmic rays: galactic and extragalactic cosmic rays.

- Galactic cosmic rays: Particles with energies above 10^9 eV are unaffected by the Solar Wind, while lower energy cosmic rays are mainly produced in the Sun, showing chemical abundances according to those present in the star. Cosmic rays with energies up to $\sim 10^{18}$ eV are assumed a galactic origin and the *knee* is usually interpreted as the maximum energy most cosmic accelerators in the galaxy can reach. For instance, Supernovae remnants are estimated to be able to accelerate protons up to 10^{15} eV. Part of the released energy in such explosions can be used to accelerate particles up to relativistic regimes thanks to diffusive shock mechanisms of the gas expansion in the interstellar medium. Although the acceleration of particles in Supernovae is the most straightforward explanation for the origin of galactic cosmic rays, so far there is no conclusive prove of such an hypothesis. Other galactic high energy γ-ray emitters like pulsars or microquasars have been also proposed as contributors to the galactic cosmic ray budget.

- Extragalactic cosmic rays: The *ankle* of the cosmic ray spectrum is usually interpreted in terms of an extragalactic flux component overtaking the galactic flux. The extragalactic origin of particles with energies above $\sim 10^{18}$ eV is justified by the fact that, in that energy regime, these particles are no longer confined by the galactic magnetic fields. The proposed extragalactic particle accelerators able to provide the particles with such high energies are AGN, γ-ray bursts, radio galaxy lobes, and strong intergalactic magnetic fields in galaxy clusters. Due to their large energies, these high energy cosmic rays should not be significantly deflected by the magnetic fields in their way to the Earth, and thus they might carry directional information. Lately, certain anisotropies has been suggested in the arrival directions of the highest energetic cosmic rays detected by the Pierre Auger experiment, and associations with nearby AGN have been proposed [189; 190]. However, no correlation between ultra-high energy cosmic rays detected by the Auger experiment and Fermi high energy γ-ray sources has been found [191]. Thus, the origin of the extragalactic cosmic rays is still under debate. It is worth mentioning that there might be some other non-accelerating production mechanisms of cosmic rays of such high energies, namely, the annihilation or decay of dark matter particles, as already discussed in Sec. 1.4.3, or some others exotic generators like topological defects (*e.g.* monopoles, cosmic strings).

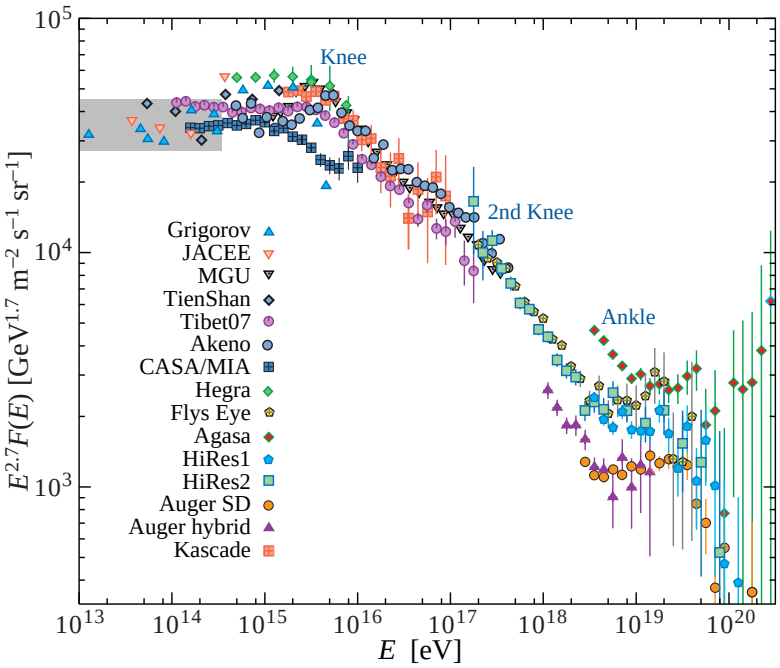

Figure 2.1: Cosmic ray all-particle spectrum from extended atmospheric shower measurements. The grey band depicts the range of the direct cosmic ray measurements. Figure extracted from [71].

2.1.2 Neutrino astrophysics

Neutrinos, being neutral particles, are not deflected by magnetic fields and thus allow to track their sources of origin, making these particles very appealing astrophysical messengers. However, neutrino detection is challenging due to their chargeless nature, their lack of coupling with the electromagnetic sector, and their weak interaction with matter. Originally, neutrino detectors were deployed in deep underground laboratories in order to get rid of the overwhelming background from cosmic rays (mainly muons). The first neutrinos whose origin was identified with an astrophysical source were those produced in in nuclear reactions in the Sun, by the Homestake experiment [192]. Later, a neutrino burst in the MeV energy range was detected in the direction of the supernovae SN1987A explosion by the Kamiokande-II detector [193] and the Irvine-Michigan-Brookhaven detector [194].

Higher energy neutrinos are expected to be produced in the vast majority of extreme astrophysical phenomena (see, *e.g.*, [195], and references therein), although no GeV or higher energy neutrinos have been detected so far. The two aforementioned major discoveries have motivated the construction of larger neutrino detectors with the capability of working as neutrino telescopes. Their locations in open water, like the ANTARES neutrino observatory [196], and open ice, like the IceCube neutrino observatory [197] exploit the same principle of detection: a three-dimensional array of photosensors embedded in a large volume of transparent media aimed to detect the Cherenkov light pulses from charged secondary particles, which are produced via neutrino interactions with the medium nuclei, either in the ice or in the rock below the ice. This new generation of neutrino telescopes cover the energy range from 10^{11} ev up to 10^{14} eV. In the case of IceCube, the first scientific data already put limits to the high energy neutrino flux from point-like sources, γ-ray burst, and *neutralino* annihilation in the Sun. They also show a

significant anisotropy in the cosmic ray background at many angular scales [198].

2.1.3 Gravitational wave astrophysics

Gravitational waves are predicted by the Theory of General Relativity. As a consequence of the weakness of the gravitational interactions their detection is very challenging and therefore the brightest sources of gravitational radiation are expected to be detected first. These sources must be compact and highly relativistic systems, thus involving high energy astrophysical systems. Promising sources of gravitational radiation are star core collapse in supernova explosions, collision and coalescence in binary systems containing neutron stars or black holes, neutron stars with irregular crusts, γ-ray burst, as well as a primordial gravitational radiation background analogous to the cosmic microwave background.

Currently, gravitational radiation detection is mainly based on laser interferometry. This technique consists on the detection of interferometric patterns, generated by gravitational-wave induced motion, in separated clone detectors acting as free masses. The distance between clone detectors is related to the gravitational wave frequency range that the complete experimental setup is sensitive to. The present generation of gravitational detectors, with the Laser Interferometer Gravitational-Wave Observatory LIGO [199] as principal experiment, are ground-based laser interferometers. Future experiments are planned to improve the already existing ground-based laser interferometers, but more ambitious projects are being planned: space-based laser interferometers like the Laser Interferometer Space Antenna (LISA, [200]), a three-spacecraft mission aimed to measure the fluctuations in the relative distances between them, placed in an equilateral triangle with 5×10^6 km separation between vertexes.

2.2 Gamma-ray astrophysics

In the present section the main γ-ray production mechanisms as well as absorption mechanisms are briefly commented. Some of these mechanisms are the basic principle on which the γ-ray detectors, also presented in a succinct way, are based. A set of the principal γ-ray astrophysical emitters, both extragalactic and galactic objects, is shown too.

2.2.1 Gamma-ray production and absorption mechanisms

Even for low energy γ-rays in the few MeV energy range, a significant thermal production would require extremely high temperatures, of the order of 10^9 K. Such a hot plasmas might be generated in exceptional phenomena, like Gamma-Ray Burst (GRB)s, but can not account for the total emission of γ-rays in the Universe and can not simply explain the generation of high energy γ-rays. Thus, the mechanisms involved in the generation of the majority of the γ-ray photons ought to be non-thermal processes. In the following, the most relevant γ-ray production mechanisms will be briefly commented.

Bremsstrahlung emission: This kind of emission is produced when a charged particle gets deflected by the electromagnetic field generated by a nucleus or ionized atom. The bremsstrahlung emission efficiency depends of the mass-to-charge ratio of the particle: for example, particles like electrons produce bremsstrahlung photons much more efficiently than protons do. If the electrons move at relativistic velocities in a gas, the produced bremsstrahlung photons will have energies of the order of the energy carried by the parent electrons. Consequently, the γ-ray spectrum will be produced with the same spectral shape than the original electron population presents.

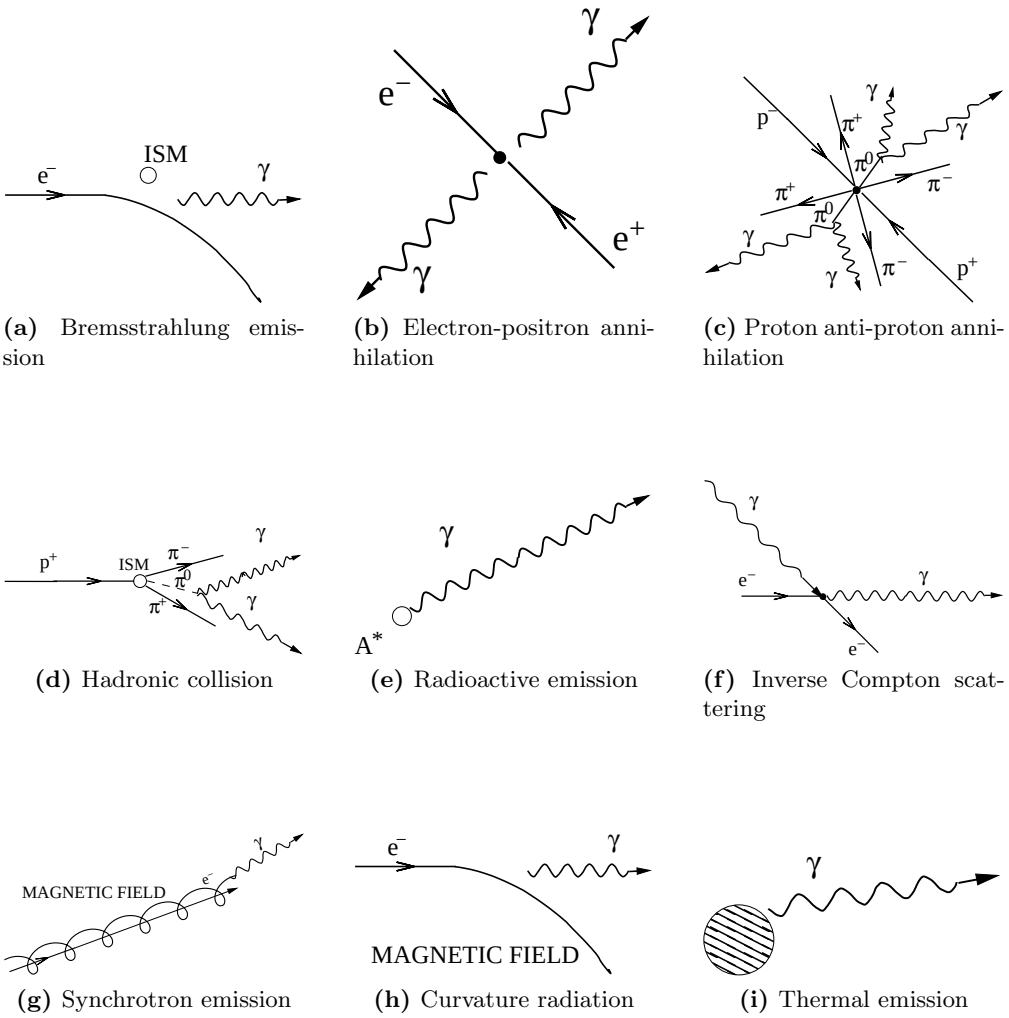

(a) Bremsstrahlung emission **(b)** Electron-positron annihilation **(c)** Proton anti-proton annihilation

(d) Hadronic collision **(e)** Radioactive emission **(f)** Inverse Compton scattering

(g) Synchrotron emission **(h)** Curvature radiation **(i)** Thermal emission

Figure 2.2: Simplified diagrams of γ-ray production mechanisms. All but the hot plasma production are non-thermal processes. ISM stands for any interstellar medium particle. A^* represents an excited nucleus. Figures extracted from [201].

Electron-positron annihilation: For a pair of electron and positron at rest, the annihilation $e^+e^- \rightarrow 2\gamma$ is a two-body final process with a final photon energy equal to the particle mass: $E_\gamma = m_e c^2 =$ 511 keV. For low velocity electrons and positrons, their annihilation processes produce a spectral line routinely detected, as in the already mentioned case of the Galactic Center region (see Sec. 1.4.3.3). There is an alternative way in which electron-positron annihilation can produce a continuum spectrum of MeV photons, namely, when positronium[1] states are formed and later decay into three final photons. These positronium states can be formed when a population of positrons interacts with cold thermal electrons. If the positron population presents relativistic energies, the bound states can be formed before the thermalization of the positrons. The subsequent continuum shows a steeper spectrum than the parent positrons spectrum, but keeping the same spectral features.

[1]The positronium is an unstable bound quantum system consisting of an electron and a positron.

Proton anti-proton annihilation: Contrary to electron-positron annihilation, γ-rays are not directly produced in proton anti-proton annihilation. However, γ-rays are produced as secondary products coming from the decay of neutral pions, which are dominant direct products of the annihilation. Anti-protons can be found as cosmological anti-matter or generated through interaction of energetic protons with nuclei. In either case the contribution to the total budget of γ-rays in the universe is not significant: the content of cosmological anti-protons is marginal and the production of anti-protons in collisions of protons with nuclei is sub-dominant with respect to the direct production of pions.

Hadronic collision: The inelastic collision between hadrons can be seen as a generalization of the previously shown proton anti-proton annihilation. The most frequent case consists on the collision between a high energy proton and a nucleus. The products of such a process are lighter nuclei, single nucleons, pions, and strange particles like kaons and hyperons. These pions, kaons, and hyperons are unstable particles that partially decay to photons. The strange particles are marginally produced, so the main contribution to the γ-ray production from hadronic collisions is due to pions. Among the pions, the decay of the neutral pion π^0, represents the largest source of γ-rays. Charged pions present basically leptonic decays ($\pi^+ \rightarrow \mu^+ + \nu_\mu$, $\pi^- \rightarrow \mu^- + \bar{\nu}_\mu$, branching ratio $\sim 99\%$) with a lifetime of 2.6×10^{-8} s, while neutral pions decay lifetime is 8.4×10^{-17} s with the two main channels being $\pi^0 \rightarrow 2\gamma$ (branching ratio $\sim 99\%$) and $\pi^0 \rightarrow e^+e^-\gamma$ (branching ratio $\sim 1\%$). Neutral pions will be produced if the available energy in the collision surpasses $E_{th} = 2m_{\pi^0}c^2(1 + m_{\pi^0}/4m_p) \simeq 280$ MeV. It is worth mentioning that the rest of products, nucleons and lighter nuclei, can provoke further collisions or generate more γ-rays via radioactive emission.

Radioactive emission: The production of low energy γ-ray lines is typical from radioactive emission. This radioactive emission has two main origins: nuclear radioactive decay and collisional excitation of nuclei. In order for the first to be significant, a large quantity of radioactive nuclei with short decay times are needed to produce a detectable emission. These conditions are found, *e.g.*, in explosive stellar nucleosynthesis, where the radionucleids are ejected from their sources, which favors a possible detection. Regarding collisional excitation, projectile and target can be a high energy proton and a nucleus, or two nuclei. The γ-ray emission is then produced by the de-excitation of the target (or projectile and target if both are nuclei), producing spectral lines broaden by the velocity distribution of the excited nuclei. Some relevant lines from collisional excitation are: ^{16}O (6.1 MeV), ^{12}C (2.3 and 5.1 MeV), ^{14}N (2.7 and 6.9 MeV), ^{26}Al (), ^{56}Fe (0.85 MeV), and $\alpha - \alpha$ (0.45 MeV). If the nuclei present relativistic velocities towards the observer, the emitted γ-ray lines can be boosted to higher energies.

Inverse Compton scattering: the so-called Compton scattering describes the possible interactions between an unbound electron and a photon: $e\gamma \rightarrow e\gamma$. Particularly, the Inverse Compton (IC) scattering takes place when a relativistic electron scatter a low energy photon to high energies: IC scattering is a very efficient way to produce high energy γ-rays if a population of relativistic electrons interacts with a population of low energy photons. Considering the case of a photon with initial energy E^0_γ such as $E^0_\gamma \ll m_e c^2$, in the center of momentum frame, that can be approximated to the rest frame of electron, the energy of the scattered photon will follow the relativistic Doppler shift formula:

$$E_\gamma = \gamma E^0_\gamma [1 + (v/c)\cos\theta], \tag{2.1}$$

where E_γ^0 is the initial energy of the photon, γ is the Lorentz factor of the electron in the laboratory frame, v is the velocity of the electron in the laboratory frame, and θ is the photon angle of incidence in the laboratory frame. Considering a population of relativistic electrons interacting with monochromatic photons (*e.g.* CMB photons) with characteristic energy E_γ^0, and boosting back to the laboratory frame, the average energy of the scattered photons as well as their maximum energy turn out to be $\langle E_\gamma \rangle \approx 4/3\gamma^2 E_\gamma^0$, and $E_\gamma^{max} \approx 4\gamma^2 E_\gamma^0$ respectively[1]. As for the spectral shape of the accelerated photons, if the population of relativistic electrons follows a power law distribution $dN_e/dE \propto E^{-\alpha}$, then the population of accelerated photons will follow a power law distribution $dN_\gamma/dE \propto E^{-(\alpha+1)/2}$.

Synchrotron emission: charged particles moving through a transverse magnetic field describe an helicoidal path along the lines of that magnetic field. The motion can be described in terms of two components: a parallel motion along the field line, and a circular motion around it. Only if the field lines are curved, the parallel motion will generate photons due to curvature radiation. The circular motion will always generate photons because it acts as a dipole. In the case of non relativistic electrons, the dipole frequency is that of Larmor precession:

$$\omega_L = eB/m_e v, \tag{2.2}$$

where B is the intensity of the magnetic field normal to the velocity vector v of the electron. In the relativistic case, the radiation gets beamed into a cone of angle $\theta \simeq m_e c^2/E_e$, and the emission follows a continuum spectrum with a maximum frequency of

$$\omega_{max} = (3/2)(eB/m_e c)\gamma^2 \sin\phi, \tag{2.3}$$

where ϕ represents the pitch angle between the direction of the magnetic field and the velocity vector of the electron.

Curvature radiation: As mentioned before, charged particles moving in parallel to a curved magnetic filed line will emit photons. The energy of the emitted photons is inverse proportional to the curvature radius of the field line. Thus, high energy photons from curvature emission will be relevant in extreme magnetic field environments, like pulsars. In these scenarios, charged particles are forced to move parallel to the magnetic field lines with almost zero pitch angle. The photons, which are emitted in the direction of the charge particle movement, will have energies

$$E_\gamma \approx \frac{3}{2}\frac{\hbar c \beta^3}{\rho_c}, \tag{2.4}$$

where ρ_c is the radius of curvature of the magnetic field line, $\beta = E_{cp}/m_{cp}c^2$, and E_{cp} and m_{cp} are the energy and the mass of the charged particles. Curvature radiation from electrons is produced in a much more efficient way than the one produced by protons due to the large mass-to-charge ratio of the last.

Thermal emission: Assuming the ideal case of a black body emission, where no absorption of the produced radiation is present, the distribution of photons depends exclusively on the temperature. Working out the Plank formula, the average photon energy can be expressed as

$$\langle E_\gamma \rangle = 2.7kT = 1.3 \times 10^{-10} T, \tag{2.5}$$

[1] As an example, a population of electrons with Lorentz factors $\gamma = 1000$ will boost optical photons to low energy γ-rays ($E_\gamma \sim$ MeV).

where the energy is given in MeV and the temperature in K. According to the Wien's law, the peak intensity of the black body emission corresponds to an energy of

$$E_{\gamma}^{peak} = 4.7 \times 10^{-10} T, \tag{2.6}$$

where the energy is given in MeV and the temperature in K again. Consequently, it can be seen that, in order to produce a significant flux in the few MeV energy range, extremely high temperatures of the order of 10^{10} K are required. Such a high temperatures can only be achieved in extremely energetic phenomena like GRBs or the very early Universe. However, this last option must be corrected by cosmological redshift, thus decreasing the energy of the originally produced γ-rays to a much lower energy window.

Of the same importance of the γ-ray production mechanisms are the antagonist absorption mechanisms. The main γ-ray absorption mechanism is the so-called pair production mechanism.

Pair Production: Two photons can produce an electron-positron pair through their annihilation if the available energy is larger than $2m_e c^2$. Two main scenarios of pair production can be distinguished: the classical pair production and the photon-photon pair production.

- Classical pair production: If a single photon energy is larger than $2m_e c^2$, it can produce an electron-positron pair in the vicinities of a charged particle, usually a nucleus, via annihilation of the real photon with a virtual photon of the charged particle field:

  $$\gamma\gamma_{\text{virtual}} \rightarrow e^+ e^-. \tag{2.7}$$

  The charged particle presence is also required to fulfill the energy-momentum conservation law. The classical pair production cross section increases with photon energy, reaching the following asymptotic value for energies larger than 30 MeV:

  $$\sigma_{pp} = \sigma_0 Z^2 \left[\frac{28}{9} \ln\left(\frac{183}{Z^{1/3}} \right) - \frac{2}{27} \right], \tag{2.8}$$

  where $\sigma_0 = (1/137)(e^4/m_e c^4) = 0.58$ mbarn, and Z is the atomic number. Classical pair production is responsible of the atmospheric opacity to γ-rays and it is exploited as a direct detection technique, in the case high energy pair production telescopes like Fermi-LAT. Classical pair production mechanisms also triggers the generation of electromagnetic atmospheric showers.

- Photon-photon pair production: In this case, the electron-positron pair is produced in the annihilation of two real photons with an available energy larger than $2m_e c^2$. In the case of VHE γ-rays, the photon-photon cross section acquires its maximum when the second photon is a low energy (soft) photon with energies from the ultra-violet to the far infrared:

  $$\gamma_{\text{VHE}}\gamma_{\text{soft}} \rightarrow e^+ e^-. \tag{2.9}$$

  This process is of special importance in VHE γ-ray astrophysics, since there is a significantly large pool of soft photons in the Universe. The EBL, consisting of three main cosmological components, the cosmic infrared background, the cosmic optical background, and the cosmic microwave background, attenuates the intrinsic flux of distant sources via this mechanism. This attenuation can be described by an optical depth $\tau_{\gamma\gamma}$, as a function of the redshift z and the energy of the γ-ray (see, *e.g.*, [202]), of the form

  $$F(E) = F_0(E) e^{-\tau_{\gamma\gamma}(E,z)}, \tag{2.10}$$

where $F(E)$ is the measured flux and $F_0(E)$ is the intrinsic flux of the source. If the intrinsic flux of the source is known, very high energy observations of distant sources can help in the EBL characterization The attenuation of VHE γ-rays implies the existence of a γ-ray horizon beyond which the γ-ray Universe is obscured.

A more detailed description of the aforementioned γ-ray production and absorption mechanisms can be found in, *e.g.*, [186] and references therein. A set of simplified diagrams which illustrates the principal γ-ray production mechanisms is found in Fig. 2.2.

2.2.2 Gamma-ray sources

The γ-ray sky has suffered a revolution in the last decade, when the number of γ-ray sources have exploded, in both the high and very high energy bands, thanks to the last generations of both, pair-production space-based telescopes and imaging Cherenkov ground-based telescopes. By the time this work was written, the number of HE γ-ray emitters was 1873 [203] (see Fig 2.7), and the number of VHE γ-ray sources was 131 [204].

For a significant γ-ray flux to be produced, very extreme regions are required where the aforementioned production processes can take place. In the following, the main types of sources confirmed or expected to produce high and VHE γ-rays, will be briefly mentioned, classified in galactic and extragalactic sources. This set contains conventional sources. If the production mechanism is the annihilation or decay of a possible GeV-mass dark matter particle, the set should be enlarged by adding the sources presented in Sec. 1.4.3.3.

It is worth mentioning that the association or identification of γ-ray sources is not always successful. By the time this work was written, 576 HE γ-ray sources [203] and 27 very HE γ-ray sources [204] remain unassociated to any known astrophysical source.

2.2.2.1 Galactic gamma-ray sources

There is a large collection of galactic objects which are confirmed γ-ray emitters: supernova remnants, pulsars, γ-ray binary systems, and globular clusters. The Galactic Center must be also included, although its real γ-ray emitter is unknown.

Galactic Center: as it has been already mentioned, the Galactic Center is a very crowded region which contains a noteworthy amount of possible γ-ray emitters, among them: the compact radio source Sgr A*, likely associated to a central super-massive black hole; young supernova remnants like Sgr A East; massive stellar clusters; and non-thermal radio arcs. If the emission was originated by Sgr A*, two possible explanations are possible: first, the Milky Way is an AGN and the emission comes from the base of the AGN jets; second, the emission comes from the central super-massive black hole accretion disk.

Fermi-LAT HE γ-ray data have shown the multiplicity of emitters in this region, detecting a bright source positionally coincident with Sgr A* [205]. The Galactic Center has also been detected in VHE γ-rays by all the current generation of Cherenkov telescopes: Very Energetic Radiation Imaging Telescope Array System (VERITAS) [165], H.E.S.S. [206], and MAGIC [168]. All observations coincide on their conclusions: an observed flux of of 0.15 normalized to the Crab Nebula flux, which can be considered steady in a time scale of years.

Supernova remnants: Conventionally, supernova remnants are classified into two different types, although no clear distinction can be made in some cases and mixed types exist. These

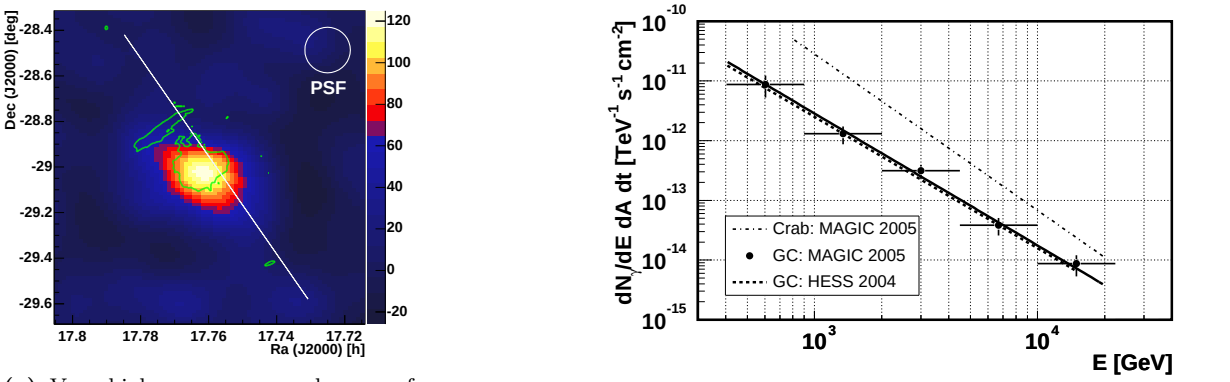

(a) Very high energy γ-ray skymap of the Galactic Center

(b) Very high energy γ-ray spectrum of the Galactic Center

Figure 2.3: The VHE γ-ray emission from the Galactic Center. Fig. 2.3a: MAGIC skymap for γ-rays events with energies above 1 TeV from the Galactic Center region. The green contour corresponds to 90 cm VLA radio data (0.3 Jy beam1). The white line depicts the galactic plane. Fig. 2.3b: Differential spectrum from the Galactic Center region from H.E.S.S. and MAGIC data. Both figures extracted from [168].

types are the pulsar wind nebulae and the shell-like supernova remnants. The pulsar wind nebula type is characterized by the presence of a central pulsar which emits a continuous flux of ultra-relativistic charged particles, the so-called pulsar wind. When the pulsar wind balances the total pressure of the pulsar surrounding medium a stable shock front is created. In such shock front the charged particles loose their energy through synchrotron emission (dominating the MeV range), and through IC scattering off those synchrotron photons and other ambient low energy photons (dominating the GeV range). On the other hand, the shell-like supernova remnants are only characterized by the shock wave from the supernova explosion, which heats the interstellar medium, thus producing a big shell of hot material where charged particles are accelerated due to Fermi acceleration processes. These diffusive shock processes originated by supernova explosions are considered the main accelerator mechanisms for the vast majority of galactic cosmic rays. The inelastic collisions of those cosmic rays with the rest of shell material then produce huge amounts of neutrinos and γ-rays, the later mainly originated though hadron collision and further π^0 decay.

Concerning the HE γ-ray band, Fermi-LAT has detected a large amount of galactic objects associated to supernova remnants. Moreover, Fermi-LAT observations have eventually shown that supernovae are the main producers of galactic cosmic rays [207]. As for the VHE γ-ray band, by the time this work was written, 44 sources likely to be associated with supernova remnants were detected, 13 being shell-type remnants, and 31 being pulsar wind nebulae [204]. It is worth mentioning that the first detection of a source in the VHE γ-ray band was that of the Crab pulsar wind nebula (Crab Nebula hereafter) by the Whipple telescope back in 1989 [208].

Gamma-ray binaries: These binary systems are formed by two gravitationally bound objects, one being a star of several solar masses and the other being a few solar masses compact object, either a neutron star or a black hole, which accretes mass from the first. These systems are also X-ray bright, and were first detected in this energy band.

There are two possible explanations for the origin of the γ-ray emission from this objects.

The first postulates a certain analogy with the γ-ray AGN production mechanism and suggests that the γ-ray binaries emit from an accretion disk around the compact object plus jet-like structures created following the same principia as in the AGNs. This analogy named this kind of objects as *micro-quasars* (see, *e.g.*, [209], and references therein). In the second scenario the compact object turns out to be a pulsar, whose pulsar wind shock interacting with the massive star material produces the γ-ray emission as explained before in the case of supernova remnants [210].

Four of this kind of objects have been detected in the VHE γ-ray band by the current generation of Cherenkov telescopes: LS 5039 and B1259-63 by H.E.S.S. [211; 212], and LS I+61 303 and Cygnus X-1 by MAGIC [213; 214]. In the HE γ-ray regime, Fermi-LAT has reported the detection of the binary systems LS I+61 303 [215], and Cygnus X-3 [216].

Pulsars: Pulsars are very exact periodic emitters whose signals are found from radio up to the highest photon energies. The standard picture is that pulsars are rotating neutron stars, with typical radii of $\sim$ 10 km and masses of $\sim$ 1.4 $M_{\odot}$, with spin periods in the range 1.4 ms to 8.5 s, thus generating extremely strong magnetic fields. The origin of the pulsed γ-rays is usually attributed to three different emission regions: the pulsar magnetosphere, the unshocked relativistic wind, and the synchrotron nebula. The first region produces γ-rays due to synchrotron and curvature radiation from charged particles accelerated by the pulsar, while the production in the last two regions will be dominated by IC scattering. However, pulsar emission models are very sophisticated and involve many production mechanisms under different environment conditions. The HE γ-ray band is usually explained by the so-called magneto-hydrodynamic model [217], while several models try to justify the VHE γ-ray emission. The first pulsed signal detected in the VHE domain was the Crab pulsar by MAGIC [218] for energies below 60 GeV. The pulsed emission spectrum at higher energies was extended by both, VERITAS and MAGIC, up to 400 GeV [219; 220]. These new data ruled out the super-exponential cut-off spectral behavior suggested by Fermi-LAT data, and pointed to models where very high energy γ-rays are generated in the outer magnetosphere, very close to the light cylinder, as proposed by the outer gap [221] or slot gap [222] models. Fig. 2.4 shows the Crab pulsar Spectral Energy Distribution (SED).

So far, only the Crab pulsar periodic signal has been detected at very high energies. The situation at high energies is very different, since the number of detected pulsars in this range has been noteworthy increased by Fermi-LAT, reaching a population which surpasses the 100 objects. It has to be noted that blind searches have provided with many new millisecond pulsar discoveries (see, *e.g.*, [223], and references therein).

Globular clusters: These very old systems harbor very high densities of starts in their cores. Due to these large densities, stellar encounters are very frequent, and thus the formation of binary systems [224]. Millisecond pulsars are also routinely detected in globular clusters. Apart for the inherent γ-ray emission from binary systems and pulsars commented before, production of γ-rays is also expected from IC scattering of seed photons by relativistic electrons generated in the pulsars and binary systems. The population of seed photons is formed by the photons, the optical starlight and thermal photons from the intracluster medium.

In the HE γ-ray range, Fermi-LAT has detected a numerous population of γ-ray emitting globular clusters [225]. In the VHE γ-ray band, there have been many globular cluster observations by all the current generation of Cherenkov telescopes, but only recently H.E.S.S. finally detected the first VHE γ-ray emission coincident with this kind of objects, corresponding to the

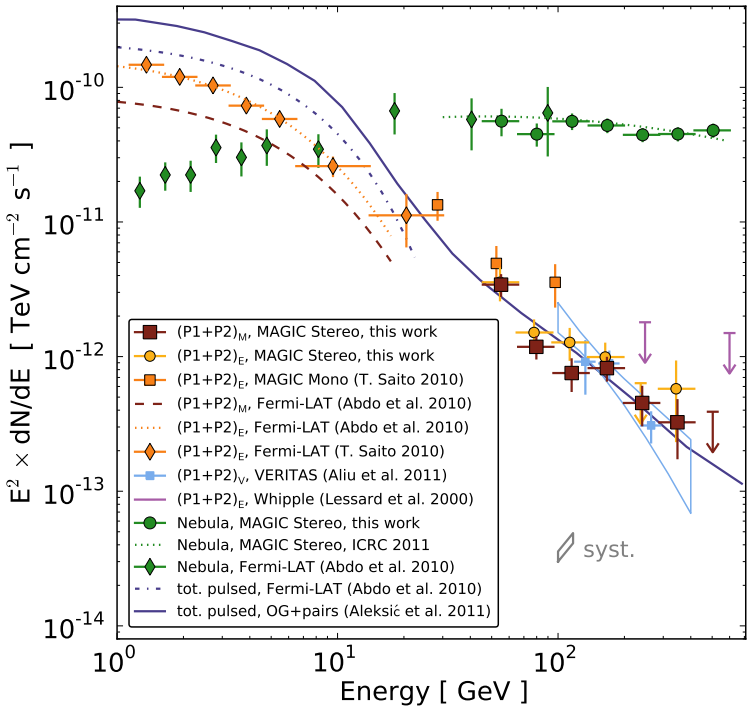

Figure 2.4: SED of the Crab pulsed γ-ray emission from Fermi-LAT, MAGIC, and VERITAS. P1 and P2 refer to the first and second pulses present in the pulsar phaseogram as shown in [219]. It can be seen that a super-exponential cut-off is clearly ruled out. Figure extracted from [219].

globular cluster Terzan 5 [226].

2.2.2.2 Extragalactic gamma-ray sources

There are several extragalactic objects characterized as γ-ray sources: AGN, γ-raybursts, and starburst galaxies. Galaxy clusters are also expected to be γ-ray emitters.

Galaxy clusters: According to the standard picture of structure formation, the larger the structure the later the collapse occur. Galaxy clusters are the largest gravitational bound systems of the Universe, with radii around few Mpc and masses around $10^{15} M_{\odot}$, and are currently being assembled. Galaxy clusters are experiencing the most energetic phase of structure formation, and large and powerful shocks of matter are expected to be consequently produced. These giant shocks are proposed as large sources of cosmic rays. On top of this contribution to the cosmic ray energy density, it has to be added the cosmic rays produced by AGNs and supernova explosions within the cluster. Due to their large sizes and to the intracluster magnetic fields, the cosmic rays are confined inside the cluster for cosmological times, thus increasing the number of proton-proton inelastic collisions, and then the number of γ-rays from π^0 decays. Besides the former contribution to the γ-ray production, the shocks produced by large structure formation would also accelerate electrons up to relativistic energies, consequently generating γ-rays by IC scattering of , optical photons from star emission, and thermal photons from the heated

intracluster gas (see [227], and references therein). So far, no γ-ray emission has been detected in any galaxy cluster, although this type of objects is a common target for the current generation of Cherenkov telescopes, and they are obviously covered by the full sky surveys of γ-ray satellites. Fermi-LAT data have placed strong limits to the GeV γ-ray emission from the total population of galaxy clusters [228]. MAGIC data are placing competitive upper limits to the cosmic ray induced TeV γ-ray emission from Perseus galaxy cluster, which are already probing the emission models, thus constraining cosmic ray density and magnetic fields within the system [229].

Active galactic nuclei: AGNs are very bright objects in many different wavelengths. The main AGN paradigm explain these objects through the existence of a central massive black hole (CMBH) in the host galaxy that powers the emission engine of the whole system. The gravitational attraction of the CMBH forms an accretion disk by in-falling galaxy matter, like interstellar medium, star members, and, in some special cases, even other cannibalized galaxies. The acceleration and dynamical friction of matter in the accretion disk is able to increase the energy of the particles up to relativistic regimes. Usually, AGNs are classified in two big groups: radio-loud and radio-quiet AGNs, the first being much brighter than the second in the γ-ray band. Radio-loud AGNs are characterized by two giant jet-like structures, perpendicular to the plane of the accretion disk and originated at the center of the same, consisting of particles accelerated up to ultra-relativistic energies that favor the generation of γ-ray emission (see, *e.g.*, [201], and references therein). These jets are extremely powerful emitters over the entire electromagnetic spectrum. Radio-loud AGNs are, in turn, classified into different categories, depending on the measured SED. In the standard picture, these differences do not arise from intrinsic properties of the objects, but are rather related to the pointing direction of the jets with respect to the observer [230]. The jet direction is parallel to the line-of-sight in the case of blazars. These objects are the most frequent γ-ray source, as can be seen from the collection of HE γ-ray emitters: out of the total population of associated and identified objects in the latest Fermi-LAT catalog, a 72% (917 sources) are AGNs-like sources, out of which 894 are blazars, 9 are radio galaxies, 5 are Seyfert galaxies, and 9 are other AGN types [203]. The situation is similar in the VHE γ-ray band, although the total number of detected sources is downscaled [204]. AGN observations in the γ-ray band offer information about the emitters themselves, but also about more fundamental physics. In general terms, AGNs are unstable γ-ray emitters, showing flare states which deviate from their quiescent flux levels. For distant AGNs showing short flares (in the time-scale of few minutes), it is possible to test the Lorentz invariance principle in VHE γ-ray observations, checking for time delays between different photon energies [231]. AGNs are also used to constrain EBL models through the VHE γ-ray absorption in the high end of AGN spectra [232].

Gamma-ray bursts: GRB are extremely powerful short-lived phenomena consisting on an outburst of radiation at all wavelengths, assumed to be the most energetic explosions in the Universe. The energy released by a typical GRB, under the caveat of isotropic emission, lays on the range from $\sim 5{\times}10^{51}$ erg to $\sim 3{\times}10^{54}$ erg, approximately the energy emitted by a Milky Way-like galaxy over few years, and the duration of the event is on the time-scale of seconds. These extraordinary events were first detected in the γ-ray band by the Vela satellite back in 1967 [233], but it was not until 1997 that they were detected in X-rays by the Beppo-SAX satellite [234]. The positional accuracy of the X-ray data made possible follow-up observations at other wavelengths, finally allowing for redshift determination. GRBs are assigned an extragalactic origin, since their redshift distribution ranges from $z = 0.0085$ up to $z = 6.7$, with an average of $z = 2.3$–

2.7. According to the current instrumental sensitivity, GRB are detected with an incidence of more than one per day. The GRB light-curves are characterized by a prompt emission of γ-rays, followed by the so-called afterglow emission that covers the rest of the electromagnetic spectrum, from X-rays to radio, and that can last significantly more than the γ-ray pulse (up to weeks). Although there is no apparent pattern in the GRBs' light-curves, a classification can be made attending to their prompt emission duration in the sub-GeV energy range: long and short GRBs. Short GRBs present durations below 2 seconds and their origin is commonly attributed to black hole coalescence or, more generally, to compact binary merging. On the other hand, long GRBs present a prompt emission which lasts more than 2 seconds and are usually attributed to the collapse of a rapidly rotating very massive star. There are many models that try to explain both types of GRBs (see, *e.g.*, [235], and references therein). One of them is the so-called fireball model, in which a cataclysmic event releases its energy mainly through gravitational waves and high energy neutrinos, plus a very high temperature fireball consisting of thermal γ-rays, and ultra-relativistic particles. These thermal γ-rays would generate the prompt emission, while the fireball shocks expanding against the external medium would generate the afterglow emission. The first detection of a GRB in the HE γ-ray band was done by the CGRO instrument on board EGRET satellite. Since then, the number of GRBs detected in the HE range has exploded thanks to the Gamma-ray Burst Monitor (GBM) detector on board the Fermi satellite (see Sec. 2.3) and its synergy with Fermi-LAT (see, *e.g.*, [236]). So far, there has been no conclusive detection of individual GRBs in the very high energy γ-ray band. Due to the EBL extinction, and the typical GRB redshift, VHE emission is significantly absorbed. Consequently, the detection of GRB VHE γ-ray emission would be restricted to seldom nearby events. Among the current generation of Cherenkov telescopes, MAGIC was specifically designed to promptly react to GRB alarms, but only upper limits have been reported up to date (see [237], and references therein). At TeV energies, the TIBET array provided with a 7σ detection significance from the stacking of data taken during time windows containing GRB events [238].

Starburst galaxies: Starburst galaxies harbor the so-called starburst regions, which are characterized by a high star-formation rate due to unusual concentrations of gas, which are normally attributed to effects of galaxy-to-galaxy collisions or bar instabilities in barred galaxies. Consequently, the starburst regions are also characterized by a high rate of supernovae explosions in volumes of localized high proton and gas densities. As a consequence of the numerous supernovae remnant shocks, the large concentration of cosmic rays and a dense medium of seed photons, a large production of γ-rays from IC scattering and π^0 decay is expected. There are two archetypal starburst galaxies, NGC 253 and M82. These galaxies have been detected in the VHE γ-ray range: NGC 253 by H.E.S.S. [239], and M82 by VERITAS [240]. Fermi-LAT has confirmed HE γ-ray emission in both objects too [241]. There is another class of star-burning regions, the so-called ultra-luminous infrared galaxies, being the galaxy Arp220 the most representative. Although γ-ray emission is expected from this kind of objects as well, no significant VHE γ-ray detection has been reported so far [242].

As an example of the variety of γ-ray emitters, Fig. 2.5 depicts a skymap of the VHE γ-ray sky, including both galactic and extragalactic sources, and their classification.

2.2.3 Gamma-ray detection techniques

The γ-ray window to the Universe is wide. Conventionally, the lines from electron-positron annihilation and nuclear reactions are considered to start it, thus placing its low energy limit

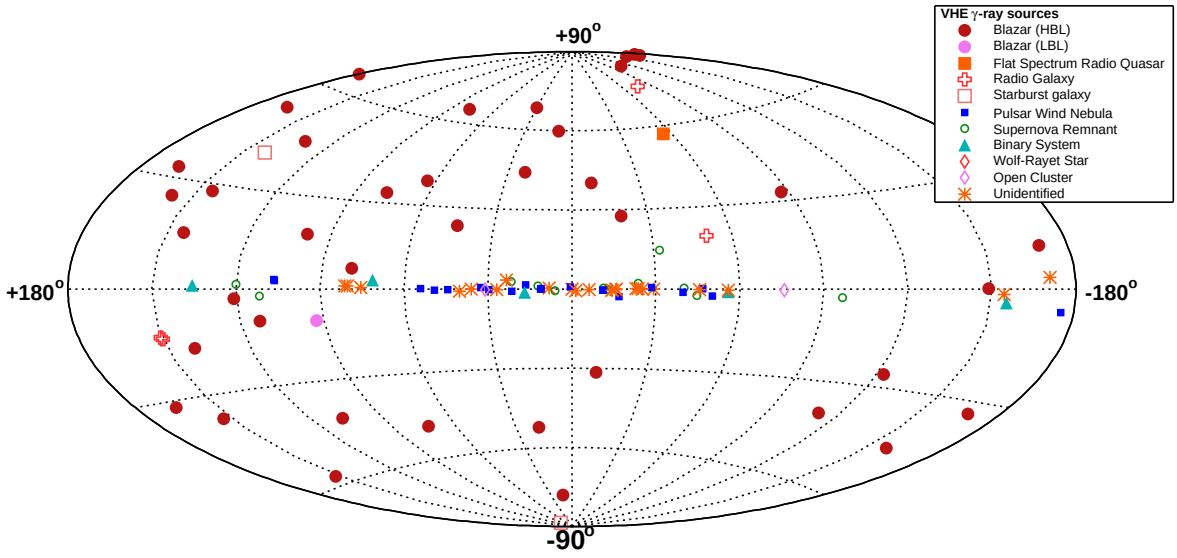

Figure 2.5: Skymap, in galactic coordinates, showing all VHE γ-ray sources ($E_\gamma > 100$ GeV) detected so far. Figure taken from [243].

around the ~ 0.5 MeV ($\sim 0.5 \times 10^6$ eV). In principle there is no upper limit to γ-ray energies, although the highest reported so far by cosmic ray experiments reach values ~ 100 EeV ($\sim 10^{20}$ eV). These more than 14 orders of magnitude wide waveband requires some convenient segmentation. This separation in narrower bands roughly corresponds to the different detection techniques and is marginally associated to different production mechanisms (see Table 2.1).

The Earth's atmosphere is opaque to γ-rays. Consequently, direct γ-ray detection must take place outside the atmosphere, by satellites and balloons. This is only feasible for low and HE γ-rays. Due to the limited effective area of these detectors, and the low fluxes beyond the HE range, the exploration of the more energetic γ-rays requires different techniques. Those techniques, exploited by ground-based experiments, rely on the detection of the products generated by the interactions induced by the γ-ray in the atmosphere, and the further reconstruction of the primary γ-ray properties out of it.

Table 2.1: Different γ-ray observational subranges.

Range	Notation	Detection mechanism	Type of detector
< 30 MeV	LE	Photoelectric, Compton	Space-based
30 MeV-100 GeV	HE	Pair-production	Space-based
100 GeV-30 TeV	VHE	Cherenkov (atmosphere)	Ground-based
30 TeV-30 PeV	UHE	Cherenkov (water)	Ground-based
> 30 PeV	EHE	Fluorescence, hybrid	Ground-based

Convenient segmentation of the γ-ray band, together with the corresponding type of detector and detection mechanism they use for the exploration of each subrange. LE, HE, VHE, UHE, and EHE stand for low, high, very high, ultra high, and extremely HE. Adapted from [244].

2.2.3.1 Space-based detectors

The detection of γ-rays from low to high energies is carried out by balloon-borne or satellite-borne experiments. These instruments exploit detection methods closer to particle physics experiments rather than typical astronomical instruments.

In the low energy γ-ray range, the detection is based on the γ-ray Compton scattering of electrons or the photoelectric effect. The typical detector consists of two planes: in the first plane, the crossing position of the impinging γ-ray is recorded and, a slight deflection of its trajectory is produced by Compton scattering of atomic electrons of the medium; in the second plane, the γ-ray is absorbed in a calorimeter via photoelectric effect, and its energy is reconstructed, at the same time that the final position of the γ-ray is recorded. Compton effect formulae allow to reconstruct the arrival direction out of the deflected direction and the energy of the γ-ray. The INTEGRAL satellite [245] is the latest detector exploiting this technique.

In the HE range, the main detection principle is the pair production. The main working idea is that, when a γ-ray impinges in the detector, an electron-positron pair is created: out of the paths followed by the electron and positron, the γ-ray arrival direction is inferred; and out of the energy of the same electron and positron, the γ-ray energy is reconstructed. A practical realization of this idea consists on layers of a high density material where the pair creation is produced (frequently tungsten), interleaved with track detectors, plus a scintillation calorimeter where the energy of the pair is deposited and measured. Possible background from charged particles is usually reduced by an anti-coincidence veto surrounding the whole device. The LAT on-board Fermi-Gamma-ray Space Telescope (GST) [246] is the most modern representative of this kind of detectors. A brief description of Fermi-GST can be found in Sec. 2.3.

2.2.3.2 Ground-based detectors

The detection of γ-rays from very high to extremely high energies is carried out by ground-based experiments. As already mentioned, these experiments do not directly detect the γ-ray, but the products generated by the absorption of the γ-ray in the atmosphere. When a cosmic ray or γ-ray impinges the atmosphere, its interaction with the medium nuclei initiates a huge chain of charged particles, and photon production called Extended Atmospheric Shower (EAS) (an introduction to the EAS physics can be found in Appendix A). Subsequently, the generated particles travel faster than light in the medium, thus producing Cherenkov radiation. It is worth mentioning that cosmic ray induced EASs present some differences with respect to γ-ray induced EASs that allows for discrimination. This is crucial, since cosmic ray induced EASs are much more numerous that γ-ray induced EASs, constituting the main background in ground-based γ-ray astronomy.

There are many different experiments and techniques aimed to detect γ-rays through the characterization of EASs. A brief summary of some particular relevant ones is presented in the following.

- Atmospheric Cherenkov detectors: These kind of instruments detect the Cherenkov photons produced in the atmosphere by charged particles from EASs. There are two different types of atmospheric Cherenkov detectors: sampling detectors and imaging detectors. Sampling detectors consist on matrices of detectors which sample the shower's Cherenkov photons front, mapping its intensity and arrival time, and then reconstructing the primary γ-ray energy and arrival direction out of these data. An example of sampling atmospheric Cherenkov detectors is HAGAR [247]. On the other hand, imaging atmospheric Cherenkov

detectors are able to record the image of the EASs itself from the emitted Cherenkov radiation, and then infer the arrival direction and energy of the primary γ-ray out of the image information. The current generation of atmospheric Cherenkov telescopes is represented by the MAGIC [248], H.E.S.S. [249] and VERITAS [250] telescopes, which are sensitive to γ-rays from $\sim$ 50 GeV up to few tens of TeV energies. The next generation is currently being planned and will significantly improve current generation sensitivity and will extend the covered energy range to both lower and higher energies (see Chapter 5 for more details). In Sec. 2.4 a more complete description of the Cherenkov telescope's technique is shown, as well as a detailed description of the MAGIC telescopes.

- Water Cherenkov detectors: The Cherenkov effect can also be exploited to detect the EASs particle front. The water Cherenkov detectors register the Cherenkov photons produced by the EASs particle front traveling through lightproof water tanks. This technique provides a large Field of View (FoV) but limited angular resolution, and is more sensitive to the TeV regime, although it can reach energy thresholds as low as few hundreds of GeVs. The detector can consist of a single large water tank, like the already decommissioned MILAGRO experiment [251], or an array of smaller water tanks distributed over a large surface, like the future HAWC [252], planned to improve MILAGRO sensitivity by a factor of 15.

- Particle counter matrices: This kind of detectors are able to map the intensity and arrival time of the EASs particle front, being able to reconstruct the primary particle (either γ-ray or cosmic ray) energy and arrival direction. Consequently they are not only γ-ray detectors but also cosmic ray detectors. They consist of a grid of individual particle counters covering large surfaces, like Tibet-AS [253], whose lattice of 789 plastic scintillator counters covers more than 36.000 m^2. However, some of them consist of detectors which completely fill the detection area, like the Argo-YBJ [254], whose resistive plate counters cover a surface of $\sim$ 6700 m^2. The aforementioned detectors are sensitive to cosmic rays or photons with energies ranging from few TeV up to several hundred TeV.

- Fluorescence detectors: there is another different way EASs can produce photons besides the Cherenkov effect. The shower's charged particles can ionize or excite atmospheric molecules, mainly nitrogen molecules. These molecules further de-excite or reionize, emitting fluorescence photons in the ultra-violet and optical wavelengths along the shower's path. This fluorescence signature can be measured by separated telescopes in coincidence, being able to reconstruct the arrival direction and energy of the primary cosmic ray from the differences in intensity and arrival times at the telescopes. This technique is effective for cosmic ray detection in the ultra high and extremely high energy regime, and is thus able to detect γ-rays of those energies too. A successful example of this detection method is the HiRes experiment [255], specifically designed to study the chemical composition and spectra of the highest energy cosmic rays.

- Hybrid detectors: This kind of instruments are those where two or more of the before shown techniques coexist. The Pierre Auger Observatory [256], the largest cosmic ray detector so far, is an example of such hybrid instruments: it consists of both, particle counter matrices and fluorescence detectors. Auger was designed to study the ultra high and extremely high energy component of the cosmic ray spectrum. It consists of 1600 water Cherenkov detectors covering an area of $\sim$ 3.000 km^2 plus a set of 27 optical telescopes

to measure the EASs induced fluorescence. Although it has been designed for cosmic ray detection, EASs from ultra high and extremely high energy γ-rays can be detected too.

2.3 Fermi Gamma-ray Space Telescope

Fermi-GST [246] is a satellite designed to study the GeV sky with unprecedented sensitivity and angular resolution. Fermi-GST was launched on 2008 aboard a Delta II rocket, and placed in a low-earth circular orbit at an altitude of 550 km (28.5° inclination, 0.93 h orbital period). Fermi-GST is a five-year lifetime mission, however its design allows for another extra five years of operations.

Fermi-GST carries two scientific instruments, the LAT and the GBM. Both instruments are described in the following, paying special attention to the LAT, on which part of the current work relies.

- Large Area Telescope: The LAT [257] is a pair-conversion instrument able to detect photons in the energy range from 30 MeV up to 300 GeV, with a large FoV which covers $\sim$ 20% of the sky. The γ-ray characteristics are inferred from the tracks of the produced electron-positron pair and the energy they deposit in the instrument. The LAT is a modular detector made out of several subsystems: a converter-tracker, a calorimeter, an anti-coincidence detector, and a trigger and data acquisition subsystems.

  The converter-tracker consists of a 4×4 array of modules, each of them made out of 16 tungsten planes, for efficient pair-conversion, interleaved with 18 silicon-strip detectors planes in order to track the produced particles. The arrival direction of the primary γ-ray is reconstructed from the detected tracks. Consequently, the angular resolution of the instrument depends on the silicon-strip detector positional resolution, but is also limited by multiple scattering and bremsstrahlung production.

  The calorimeter is also arranged in a 4×4 array of modules, each of them made out of 96 optically independent CsI(Tl) scintillating crystals, set into 8 layers. Once the e^+e^- pair reaches the calorimeter, electromagnetic showers are generated and the produced scintillation photons are detected by photodiodes at both extremes of each crystal. Due to the segmentation of the crystals, the spatial evolution of the showers are registered allowing for enhanced energy estimation and background rejection.

  An anti-coincident detector, consisting of 89 tiles of plastic scintillator, covers the top side and lateral sides of the LAT, allowing for a background rejection of 99.97%. The main LAT background are charged cosmic rays which produce a signal when crossing the anti-coincident detector, unlike the γ-rays, thus vetoing the event to be recorded.

  Finally, the data acquisition subsystem collects data from the subsystems of LAT after a three-level trigger (one hardware and two software triggers) which filters out background and accidental events, providing a downlink event rate of $\sim$ 450 Hz. An additional on-board science analysis platform allows for quick response to fast transient events. A schematic diagram of the Fermi-LAT can be found in Fig. 2.6.

- Gamma-ray Burst Monitor: The GBM consists of two sets of scintillators sensitives to the 150 keV to 30 MeV energy band, having an almost full coverage of the sky. The purpose of the GMB is the detection of bright transient events, particularly GRBs. The first set of detectors are 12 NaI(Tl) scintillators, sensitive from few keV to $\sim 1MeV$,

which provide the burst trigger and location. The second set of detectors are two Bismute–Germanate detectors, sensitive from 150 KeV to 30 MeV, thus overlapping with the NaI(Tl) scintillators at lower energies and with the LAT at higher energies.

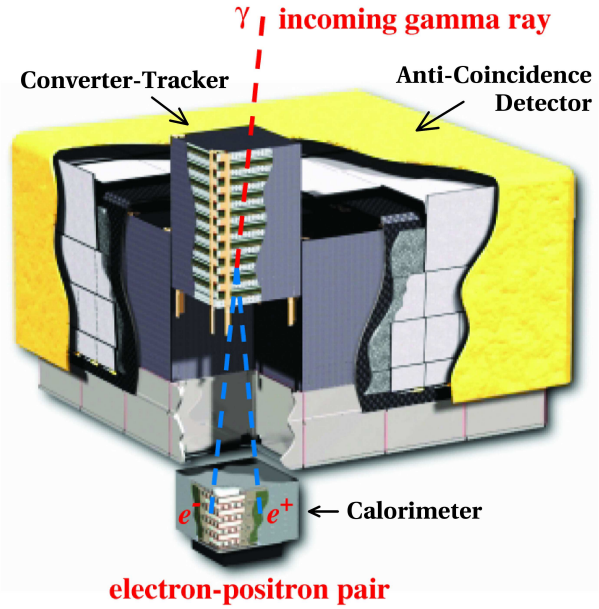

Figure 2.6: Schematic diagram of the Large Area Telescope on-board Fermi satellite. The principle of detection is also illustrated: the impinging γ-ray is converted into an electron-positron pair in the tracker and the arrival direction is inferred from their tracks. The pair of charged particles deposits its energy in the calorimeter so the energy of the primary γ-ray could be estimated. Figure extracted from [258].

Several scientific motivations aimed the construction of the Fermi-GST: the understanding of acceleration mechanisms in AGNs, pulsars, and supernova remnants; the explanation of the γ-ray diffuse emission; the characterization of previously unidentified HE γ-ray emitters, GRBs and other transient sources; and the study of possible dark matter signals and some other fundamental physics topics like the Lorentz invariance and quantum gravity.

Fermi-LAT has a very fruitful scientific production including new discoveries and unexpected detections. Its last catalog, named Fermi-LAT Second Source Catalog [203] and depicted in Fig. 2.7, contains 1873 sources, all of them characterized in the 100 MeV to 100 GeV. 127 sources are firmly identified and 1170 are associated with known counterparts, thus leaving 576 sources with an unassociated origin. There are many other noteworthy scientific results generated thanks to Fermi-GST data (see [246] for a more complete overview). Some examples are: the discovery of two 25.000 light years γ-ray bubble-like structures extending above and below the Galactic Center [259] whose intriguing origin is still under debate; the confirmation of supernova remnants as sources of galactic cosmic rays [207]; the detection of γ-ray flares in the Crab Nebula [260]; the discovery of a large population of γ-ray millisecond pulsars [261]; the discovery of γ-ray radiation from globular clusters [262]; the observation of GRB 080916C, the largest apparent cosmic energy release measured yet [262]. Although optimized for γ-ray detection, Fermi-LAT is able to measure cosmic rays too. In particular it has produced separated cosmic ray electron and positron spectra, having determined that the positron fraction continues rising up to 200 GeV [263].

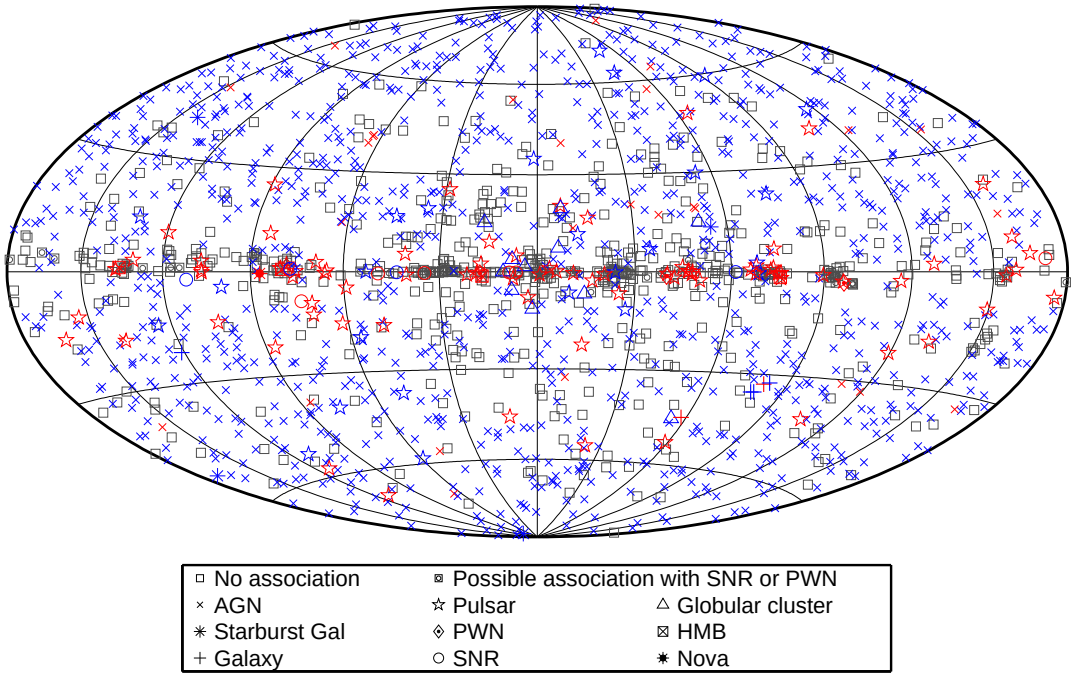

Figure 2.7: Full skymap in galactic coordinates showing the complete Fermi-LAT Second Source Catalog. Identified sources are shown in red symbols while associated sources are shown in blue symbols. Figure extracted from [203].

Fermi-LAT has also significantly contributed to indirect searches of GeV-mass dark matter particles. One of the first remarkable results of Fermi-LAT was the discovery that AGNs can account for just a small fraction ($\sim 16\%$) of the extragalactic diffuse background, when they were assumed as the main contributor to such a radiation [264]. This result leaves room for a dark matter-based explanation for the rest of that background. There are many works exploiting this possibility, like the ones dedicated to dark matter detection through anisotropies in the Fermi-LAT extragalactic diffuse background [185], and through its continuum emission imprint [265] or its line emission [266] in the overall isotropic diffuse background. Taking advantage of its full sky view, the Fermi-LAT is able to stack data from the most promising dark matter targets. That is the case for the stacking of galaxy clusters data [267], and the stacking of dSph galaxies data [268], the last one providing the most competitive limits so far in the few GeV energy regime. Fermi-LAT data has been also used for dark matter searches in the high energy cosmic ray electron spectrum from the Sun [269].

2.4 The MAGIC Telescopes

The *Florian Goebel* Major Atmospheric Gamma-ray Imaging Cherenkov telescopes [248], consist of two 17 m reflector diameter Imaging Atmospheric Cherenkov Telescopes (IACTs) (see Fig. 2.8). They are located at El Roque de los Muchachos Observatory in the Canary island of La Palma (28.8° N, 17.9° W), at an altitude of 2.200 m above the sea level. The system is able to reach the lowest energy threshold among the current generation IACTs ($E_{th}\approx$25 GeV) operating in stereoscopic mode.

The first of the telescopes (MAGIC-I from now on) has been operating since 2004. The second telescope (MAGIC-II from now on), was successfully constructed and commissioned during 2009, allowing for full stereo observation since then. By the time this work was written, MAGIC was undergoing an ambitious upgrade in both telescopes.

In the following, the basics of IACTs technique will be briefly explained, accompanied by a technical description of the MAGIC telescopes in short, and a section where the MAGIC data analysis is summarily presented.

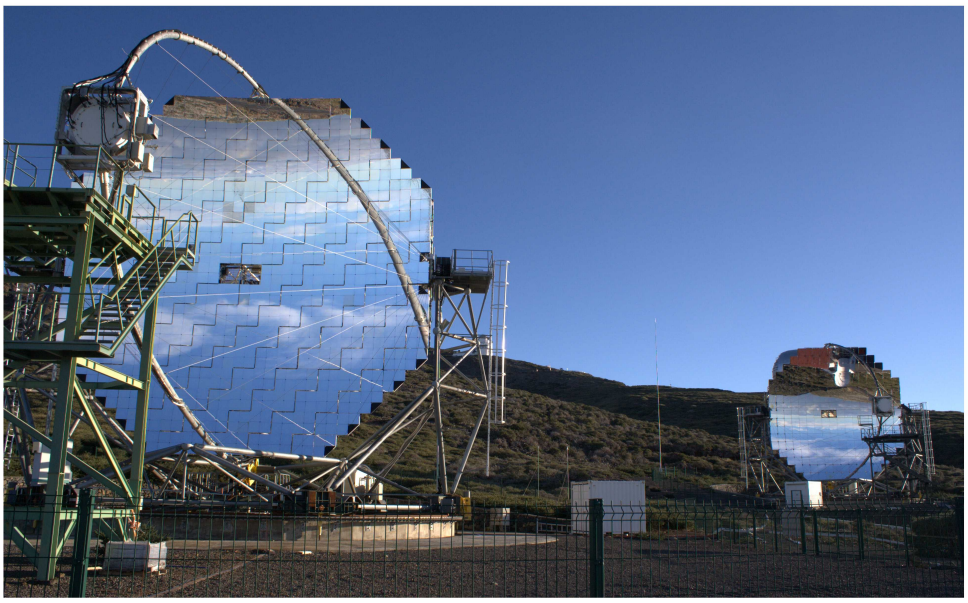

Figure 2.8: Picture of the MAGIC telescopes. MAGIC-I telescope on the foreground, MAGIC-II telescope on the background.

2.4.1 Imaging atmospheric Cherenkov telescopes

As already outlined in Sec. 2.2.3 the technique is based on the imaging of the EASs produced by the absorption of γ-rays in the atmosphere. The particle content of γ-ray induced EASs is formed by electrons and positrons. These charged particles travel through the atmosphere and polarize the medium. When the particle speed is larger than the speed of light in the medium, the polarization gets asymmetric, creating a net electric field, and the further emission of photons due to the in-phase depolarization of the medium. These photons are the so-called Cherenkov photons. Thus, EM-showers initiated by γ-rays emit during their developments a large amount of Cherenkov photons. The typical Cherenkov photon spectrum ranges from infrared to ultraviolet energies, but due to absorption and scattering of atmospheric particles, the infrared and part of the ultraviolet component are suppressed from the spectrum at ground level, which acquires a maximum around blueish wavelengths. A brief description of γ-ray and cosmic ray induced EAS, as well as the Cherenkov effect, can be found in Appendix A.

If a parabolic reflector is located within the Cherenkov photon yield at ground, and part of these photons are reflected onto its focal plane, an image of the shower is formed. Out of the shower image, recorded by extremely sensitive cameras of high efficiency photodetector pixels,

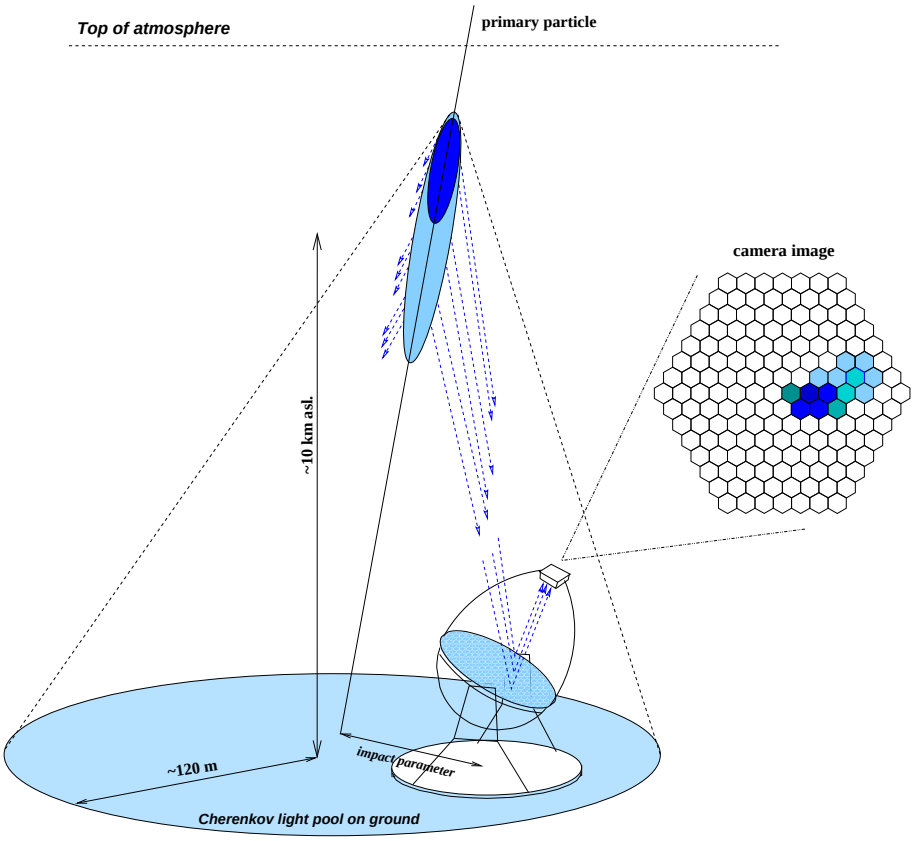

Figure 2.9: Schematics of the technique used by imaging atmospheric Cherenkov telescopes. When the primary particle impinges the atmosphere, it is absorbed producing an extended air shower. Charged particles from the shower emit Cherenkov photons (blue dashed lines) which are focused by a reflector onto a pixelized camera, thus imaging the shower Cherenkov photon yield. Figure extracted from [270].

the arrival direction and energy of the primary γ-ray can be reconstructed. If two or more of these detectors record the same event, a stereo image of the shower can be obtained, thus allowing for a better reconstruction of the event. In Fig. 2.9, a schematic description of the technique can be found.

However, the IACT technique is not background free. The understanding of the IACTs' inherent background is crucial to take full advantage of the capabilities of the technique, and to push the instrument sensitivity to its limit. There are many events that can trigger an IACT, mimicking a γ-ray induced signal:

- Hadronic showers: These showers, initiated by cosmic rays, are the main source of background. When a cosmic ray hits an atmospheric particle a particle shower is produced, containing neutral pions among its population. These neutral pions immediately decay into a pair of γ-rays ($\pi^0 \rightarrow 2\gamma$), consequently generating secondary EM showers, and the subsequent Cherenkov photons that image the hadronic shower into the camera. For conventional sources, the ratio between hadronic showers and EM showers in the acquired data is ~ 1000. This overwhelming fraction of background is further reduced by selection algorithms able to discriminate between both population of events with efficiencies higher than 99%, based on image properties.

- Electron induced EM showers: Electrons are also a significant component of the cosmic ray population. When electrons are absorbed in the atmosphere the generate purely EM showers, thus indistinguishable from a γ-ray induced shower. Consequently, the background from electron induced showers can not be suppressed. However, the smaller electron flux as compared to the typical γ-ray flux above 100 GeV, plus the fact that electron flux is approximately isotropic, strongly reduce the impact of this background.

- Diffuse γ-ray background: As in the previous case, the diffuse γ-ray background turns out to be irreducible. Strictly speaking, this background is not inherent to the technique but to the physics case itself, and it is also present in the HE γ-ray regime. It consists of two components, the extragalactic and the galactic γ-ray background. Fortunately, none of them are very significant in the VHE γ-ray regime, although its importance increases in the HE γ-ray regime, specially the galactic component in regions within the Galactic Bulge.

- Cherenkov photons from muons: Muons are produced routinely in hadronic showers, and usually reach the ground before decaying into an electron and the corresponding neutrino. Muons do not generate EM-showers like electrons, since the bremsstrahlung emission is not as efficient in their case due to their larger mass, but do emit Cherenkov photons. Their emission at moderate altitude can mimic the image of a low energy EM-shower, while muons reaching the ground nearby the telescope can create the so-called muon rings in the camera. The incidence of either case can be highly suppressed with the use of stereoscopic observations, and with further image analysis.

- Night-sky background light: low energy γ-ray events project very small images into the camera, consisting of few pixels reading a modest number of Cherenkov photons. These images can be mimicked by fluctuations of the Night-Sky Background Light (NSBL), which is the ambient light produced by the diffuse scattered light from stars, the Moon, or human activities in the vicinities of the observatory. This NSBL can be amplified in the presence of clouds or air pollution.

- Electronic noise: The camera pixels as well as the readout chain show intrinsic electronic noise that must be taken into account when analyzing the data. This noise is present even when the camera is not illuminated, and is sometimes referred as dark noise. Under certain circumstances, high electronic noise in a cluster of pixels is able to trigger the telescope as if it was a low energy γ-ray shower image. In order to suppress the electronic noise, it has to be well characterized through dedicated data runs.

The IACT technique is relatively new, as compared to other astronomical techniques like optical or radio telescopes. The first VHE γ-ray source ever detected was the Crab Nebula [208] by the Whipple telescope [271; 272] back in 1989, after more than 20 years of technical improvements over the camera of the original 10 m reflector diameter telescope. Since then, there has been other generation of IACTs, like HEGRA CT system [273; 274] or CAT [275; 276] telescopes, until the current generation, best represented by MAGIC [248], H.E.S.S. [249], and VERITAS [250] telescopes. The main characteristics of the aforementioned set of IACTs can be found in Table 2.2.

Table 2.2: Main characteristics of a selection of IACTs.

Instrument	Lat.	Long.	Alt.	Telescopes		Pixels	FoV	E_{th}	ΔE	$\Delta\Omega$	Sensitivity
				Units	Area						
	[°]	[°]	[m]		[m^2]		[°]	[GeV]	[%]	[°]	[% Crab]
MAGIC	29	18	2225	2	234	576/1039	3.5	50	15	0.07	0.8
H.E.S.S.	-23	16	1800	4	107	960	5	100	15	0.1	0.7
VERITAS	32	-111	1275	4	106	499	3.5	100	15	0.1	0.7
Whipple	32	-111	2300	1	75	379	2.3	300	30	0.1	15
HEGRA	29	18	2200	5	8.5	271	4.3	500	15	0.1	5
CAT	42	2	1650	1	17.8	600	4.8	250	20	0.14	15

Properties of the current generation of imaging atmospheric Cherenkov telescopes. The telescopes' areas are referred to the reflectors surface. The energy resolution ΔE, the angular resolution $\Delta\Omega$, and the sensitivity depend on the energy and are given for the optimum values for each telescope. The HEGRA, Whipple, and CAT telescopes are included for historical interest and their latest values for the selected parameters are shown. Adapted from [277].

2.4.2 Technical description of the MAGIC Telescopes

The MAGIC Telescopes are characterized by a continuous improvement of the system through the implementation of novel technologies that allow for a better performance. As already mentioned, by the time this work was written, both telescopes were experiencing a significant upgrade, mainly affecting the cameras and the readout systems. The technical descriptions presented in the following correspond to the pre-upgrade situation. On the other hand, it is worth mentioning that the data analyzed in this work was taken under these circumstances.

2.4.2.1 Mounting, drive, and mirrors

The mounting structures of the MAGIC telescopes are made by carbon fiber reinforced plastic (CFRP), weighting ∼5 tons each. The CFRP structures are three times stiffer and one third as heavy as a conventional steel-made structure. This fact allows the telescopes for fast repositioning, that together with the fast and accurate reaction of the drive systems make MAGIC suitable to promptly track any point in the visible sky in less than one minute.

The reflector dishes have a diameter of 17 m, with a focal distance to diameter relation of $f/(D) \approx 1$. MAGIC-I reflector 239 m^2 surface consists of 956 0.5 m × 0.5 m aluminum honeycomb mirrors of high reflectivity (80% – 90%) [278]. MAGIC-II reflector is composed by 1 m × 1 m, 143 full-aluminum mirrors and 104 glass-aluminum mirrors, accounting for a total surface of 247 m^2 [279]. The geometric shape of the reflectors is parabolic in order to minimize the spread on the Cherenkov photons arrival times on the focal plane. The benefit of this shape is two-folded: first, it reduces the time window required to extract the signal, thus reducing the integrated noise; second, it allows to use the time evolution of the showers as a discrimination parameter between hadronic and EM-showers. The structures of the telescopes are not completely rigid but slightly deform depending on the pointing position. In order to guarantee the parabolic shape of the reflectors, and thus the telescopes' optical performance, against these structural changes, a set of actuators are able to re-align each mirror panel independently during operation time. This system is named Active Mirror Control [280].

The mount of MAGIC telescopes is of Alt-Azimuth type and allows for continuous observation of a given source without reaching any end position in either Altitude or Azimuth

coordinates thanks to their wide range of movements: the Altitude range spans from $-70°$ to $105°$, while the Azimuth range spans from $-90°$ to $318°$. Each telescope has two azimuthal servo-motors and one servo-motor for the elevation axis, monitored by three absolute 14-bit shaft encoders, and limited by mechanical end-switches [281].

The pointing accuracy of each telescope is monitored by a *starguider* system, allowing for further misspointing correction via software. The *starguider* system consists of a $4.6°$ FoV CCD camera installed close to the center of the reflector which points toward the telescope camera. A set of LEDs, placed on the telescope camera frame, allow to compare the camera position to the star background, and later crosscheck the bright stars positions with their catalog coordinates, inferring the actual pointing direction of the telescope. Additionally, the number of detected starts as compared to the number of catalog stars in the FoV, provides with information about the atmospheric conditions [281].

2.4.2.2 Cameras and calibration systems

The IACT camera is of crucial importance, since its performance conditions the overall sensitivity of the instrument. MAGIC-I and MAGIC-II cameras are not exact copies. However, they share many design concepts: both cameras record the Cherenkov photons from EASs by means of Photo-Multiplier Tube (PMT) based pixels, amplify the signals and convert them into analog electric signals to be optically transmitted to the readout systems, placed in a separate building named counting house. The separation between the camera and the readout system lightens the weight of the focal plane instrumentation, thus allowing for lighter mounting structure, and also for faster movements without risking the integrity of the mounting.

- MAGIC-I camera: with 1.2 m diameter, corresponding to a $3.5°$ FoV, the pixel region of MAGIC-I camera presents a hexagonal shape and two different populations of pixels, made out of 577 hemispherical PMTs. The inner hexagonal region of the camera accounts for a total FoV of $\sim 2.4°$, and is equipped with 397 30 mm diameter PMTs equivalent to a $0.1°$ pixel diameter. This inner $1.2°$ diameter region constitutes the trigger area. The outer region of the camera consists of 180 60 mm diameter PMTs. The peak Quantum Efficiency (QE) of these PMTs is of 25% – 30%. The photon entrance of each PMT is equipped with a hexagonal light collector (Winston cones) in order to increase the entrance window for each pixel, and to increase the double-crossing probability of photons with large incidence angles. These Winston cones also limit the stray light not coming from the reflector entering the PMTs. The hemispherical PMT photocatode is coated with a wavelength shifter that decreases the Cherenkov photon frequencies in order to enhance the overall QE. MAGIC-I camera central pixel has been specifically designed to perform optical measurements. It is basically used to measure the optical pulsation of the Crab Nebula pulsar in order to cross-check the time stamp of the overall system.
  MAGIC-I camera is calibrated by means of an optical calibration system installed in the center of the reflector. The system consists of ultra-fast LEDs (in order to emulate the fast timing behavior of the Cherenkov pulses) with different characteristic wavelengths (frequencies of 370 nm, 460 nm and 520 nm), able to uniformly illuminate the whole camera with light pulses of custom frequency and intensity.

- MAGIC-II camera: the pixel region of MAGIC-II camera is circular-shaped (1.2 m diameter) and covers the same FoV of $3.5°$ than the MAGIC-I camera. The camera is uniformly equipped with 1039 30 mm diameter ($0.1°$ FoV) PMTs, forming 169 independent clusters.

MAGIC-II camera trigger area comprises the inner 2.5° diameter region. The peak QE of these pixels is of ∼35%, and, differently to MAGIC-I PMTs, no wavelength shifter is needed. Similarly to MAGIC-I camera pixels, MAGIC-II PMTs are equipped with Winston cones. Further details on the MAGIC-II camera con be found in [282]
The calibration system of MAGIC-II camera is installed in the center of its reflector too. It consists of a frequency tripled passively Q-Switched Nd-YAG laser able to produce subnanosecond pulses at 355 nm wavelength. The laser beam goes through two filter wheels with different attenuator filters, so the intensity of the pulse is highly customizable. After attenuation, the beam is diffused via an integrating (Ulbricht) sphere providing a homogeneous illumination of the camera.

2.4.2.3 Data readout

For both telescopes, the electric pulses at the base of the PMTs are amplified and converted into optical pulses by mean of vertical cavity surface emitting laser diodes (VCSELs). The VCSELs are coupled to optical fibers which transmit the optical signal to the counting house, 160 m away from the telescopes. This optical transport prevents the signal from the attenuation and electromagnetic interference an electric signal would experience. Once in the counting house, the optical signals are treated differently depending on the telescope, but in both cases they are split into two branches. One branch is directed to the trigger system while the other is digitized by the Data Acquisition System (DAQ).

MAGIC I: The readout of MAGIC-I data (see Fig. 2.10 for a schematic representation) for an schematic representation) split the optical signal before entering the receiver boards. Half of the signal is sent to the trigger system, where it is converted back to an analog electrical pulse by means of GaAs PIN photodiodes. The other half of the signal is sent to the fiber-optic multiplexing readout system (MUX) which concatenate the optical signals of 16 different pixels consecutively in one single channel, by delaying the pixel signals by multiples of 40 ns. The optical signals are converted back to analog electric signals by means of the aforementioned GaAs PIN photodiodes, concatenated in two active summation stages, and further digitized by ultra-fast Flash Analog to Digital Converter (FADC) at 2GSample/s. The multiplexing technique is possible due to the short duration of the pulses, of the order of few ns, and the trigger rate of few kHz at most. The digitized data are stored in a buffer which consists of an on-board RAM per channel. There are five FADC crates mounting a couple of four-channels boards each, in order to sample all MAGIC-I channels. In each of the crates a data acquisition program records the digitized signals which are stored in a 2000 event deep ring buffer. Each crate data is sent to a central MUX data acquisition computer, where the daq software merges the data from the different crates, building the events and recording them into the storage system. The readout of MAGIC-I data is explained in detail in [283][1].

MAGIC II: Contrary to MAGIC-I readout system, the MAGIC-II readout first convert the optical signal back into an analog electrical signal by means of a GaAs PIN photodiode and then split it into two branches. This is done by a high bandwidth programmable receiver boards (so-called MONSTER boards), able to process up to 24 channels each. One branch is sent to a discriminator with a software adjustable threshold. If the signal pulse surpasses the threshold,

[1]Previous to the 2GSample/s MUX-FADC, the readout system mounted 300 MSample/s FADC. Data presented in this work were taken with the MUX-FADC system.

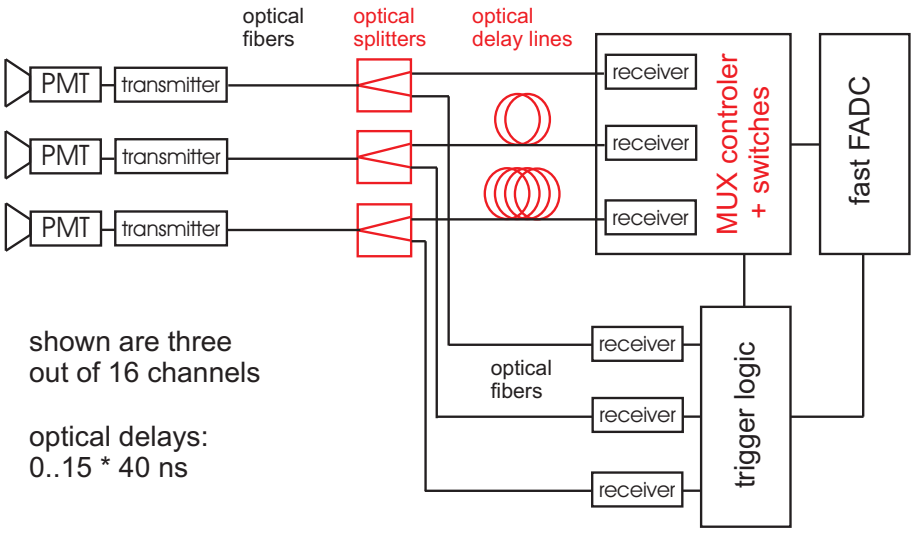

Figure 2.10: Schematic representation of the MAGIC-I readout system, where the optical splitting of the signal and the introduction of the optical delays are shown. Figure extracted from [283].

it is digitized and routed to the trigger system. Thanks to this adjustable threshold, the trigger rate for each channel can be controlled and stabilized. The other branch is routed to the digitizing units. The signals are sampled by low-power Domino Ring Sampler chips (DRS2) at the ultra-fast speed of 2 GSample/s, using an array of 1024 capacitors, acting as a ring buffer. After a trigger signal is produced, the sampling is stopped and the signal stored in the buffer is read out and digitized at 40 MHz rate by an external ADC with a nominal resolution of 12-bits. The DRS2 chips are integrated in mezzanine boards hosted in PULSAR boards. Each PULSAR board is able to deal with 80 channels, so 14 of these boards are used to readout the complete camera. Eventually, the data are sent via an S-LINK optical interface to a single computer. A VME interface controls the whole DAQ hardware, and it is steered by a slow control software named MAGIC Integrated Readout. The event building and data storage is managed by the DAQ software. The readout of MAGIC-II data is explained in detail in [284].

Trigger: The trigger system evaluates individual events and decides whether to store the digitized signals or not, being its main purpose to discriminate the Cherenkov showers from the NSBL. It is composed by four different trigger levels which select only fast pulses detected simultaneously in a compact region of the camera. The first three trigger levels work over individual telescope data, and are implemented in different units for each telescope, while the fourth trigger level unit is shared by the two telescopes. As already mentioned, MAGIC-I trigger region has 1.2° diameter while MAGIC-II trigger region has 2.5°, as shown in Fig. 2.4.2.3.

- Level 0 (L0): This trigger evaluates every single channel and digitize its signal if it surpasses a certain discriminator threshold (DT). These DTs can be individually controlled by software and can be tuned so to provide with a stable pixel rate under different light conditions.

- Level 1 (L1): Digitized signals from L0 are sent to the L1 trigger, which examines the channels looking for spatial and temporal correlations over the decomposition of the trigger region in 19 overlapping macrocells. The topological classification of events attends to the

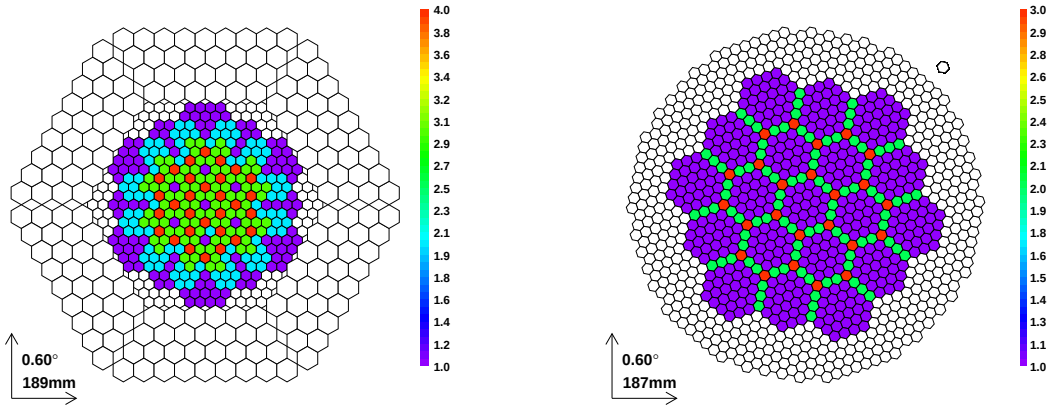

(a) MAGIC-I trigger area

(b) MAGIC-II trigger area

Figure 2.11: Schematic representation of the MAGIC cameras where the L1 trigger area is represented by the colored pixels. The color coding indicates the number of macrocells each pixel belongs to, illustrating the macrocell overlapping level. MAGIC-I camera is represented in Fig. 2.11a, while MAGIC-II camera is shown in Fig. 2.11b.

close compact next neighbor (CCNN) logic. The L1 trigger accepts those events which present N adjacent pixels forming a compact group. The standard CCNN logic applied in MAGIC observations is 4NN, but 2NN, 3NN, and 5NN are also available.

- Level 2 (L2): L1 triggered events enter the L2 trigger unit, which in principle allows for further discrimination of events based on their shapes. L2 trigger is not enabled for the usual data taking modes of MAGIC, although the L2 trigger unit is used for event rate monitoring, rate scaling, L1 trigger coordination with the calibration system, and merging with the stereo triggers.

- Level 3 (L3): For stereoscopic observations a stereo trigger or L3 trigger can be enabled in such a way that only events triggering both telescopes during a certain time window are recorded. In order to minimize the coincidence time window, the individual telescopes L1 events arrival times are delayed by a time interval depending on the pointing positions of the telescopes.

The aforementioned trigger levels are standard in MAGIC observations. However, there is another trigger concept specially designed to improve the trigger threshold by a factor of two at the lowest energies ($\sim$25 GeV). This is the so-called Sum Trigger (ST) [285], whose trigger logic is based on the sum of several analog signals, in such a way that the signal-to-noise ratio of low energy showers is minimized over the NSBL. This trigger scheme has proved very successful for the search of low energy pulsed signals, as the case of the Crab Nebula pulsar detection in the VHE γ-ray regime [218].

2.4.2.4 Data taking modes and type of runs

There are two observation modes which are widely implemented in the IACT telescopes: the *on–off*, and the *wobble* modes. These modes can be used indistinctly for single telescope or stereo observations.

- *On–off* mode: In this observation mode the telescopes are pointing directly to the target, in such a way that the target's nominal position is located at the center of the cameras. Data recorded in this configuration is called *on* data. To properly subtract the background from the expected signal in the *on* data, and in order to do it without any bias, the observation of dedicated *off* regions is required (thus recording the so-called *off* data). Such *off* regions are dark patches in the VHE sky, namely, fields where no very high energy sources are expected. On top of that, *off* regions must share the same observational conditions as the *on* region, namely, the same zenith angle range, the same background light (galactic or extragalactic field present different values of NSBL), and the same atmospheric conditions.

- *Wobble* mode: This mode, also known as *false source tracking* mode [286], consist of the observation of the source pointing to a slightly offset position with respect to the source nominal position. Conventionally in MAGIC, this is translated into the tracking of the source placing its nominal position at an angular distance of 0.4° from the camera center. In order to reduce possible bias, this position is alternated to the symmetric equivalent each 20 minutes of observation. The main advantage of this technique is the simultaneous measurement of the signal and the background. The background region can be extracted from the opposite region to the source position in the camera, also called the anti-source position (that would work as the equivalent to the previously introduced *off* region). Such a position turns to be the source nominal position rotated by 180° around the camera center. More background regions can be obtained as long as they do not overlap with the signal extraction region around the source's nominal position. For instance, the amount of background data can be increased by a factor of three if regions corresponding to the source's nominal position rotated by 90°, and 270° around the camera center are considered. *Wobble* observation render slightly less sensitive results, but profit from the fact that no extra time for dedicated background observations is needed.

Independently of the observation modes, there are three types of runs that are recorded during normal operations of the telescopes: the pedestal, calibration, and data runs. The pedestal and calibration runs are short runs taken right before the observation of a certain source is going to be carried out. The observation itself is recorded in the data runs.

- Pedestal run: This type of runs consist of a number of randomly triggered events which are digitized and recorded in order to evaluate the effect of the NSBL and the readout chain electronic noise. The contribution of both components is further extracted in the calibration of the data, in a pixel-by-pixel base. Pedestal runs typically contain 1000 events each. Due to the random nature of the trigger, the probability to record an actual shower is negligible.

- Calibration run: This type of runs contain events triggered by the calibration system of each telescope (see Sec. 2.4.2.2), which generates light pulses that try to mimic a Cherenkov light pulse in terms of duration and wavelength. The calibration events are further used in the calibration of the data. Out of them, the conversion factor from FADC counts to photoelectrons and the arrival time offsets are computed.

- Data run: This type of runs contain the digitized images of triggered cosmic events. These runs typically include pedestal and calibration events, which are interleaved with the cosmic events at a rate of 25 Hz thanks to dedicated trigger signals. These *interleaved*

events are further used to keep the pedestal values and calibration constants updated during the sequential calibration of the data.

Each telescope records its own pedestal, calibration, and data runs. For file management purposes, the data are grouped into sequences. Each observation night, the first sequence of a given source contains a pedestal run, a calibration run, and a data run, the last containing 20 minutes of data. The subsequent sequences of the same source consist only on data runs, each of 20 minutes long. In turn, data runs consists of several subruns, each of them corresponding to a single file. The size of the subrun file is limited by the filesystem type to 1.9 Gb. Thus, the number of subruns for each run depends on the acquisition rate and the number of pixels of each camera. In the case of MAGIC-II one more type of run is recorded twice per observation night, one at the beginning and one at the end of the night, the so-called linearity run. These runs are used to correct for the non-linearity of the DRS2-based readout system.

2.4.3 MAGIC data analysis

The data from the MAGIC telescopes are analyzed by means of the official MAGIC Analysis and Reconstruction Software (MARS) [287; 288]. It is a dedicated software package written in C++ language, embedded in the ROOT data analysis object-oriented framework [289].

The main steps that configure the MAGIC data analysis chain are carried out with the help of programs and classes within MARS. These steps are summarized in the following and expanded later on.

- Data calibration: It consists of the determination of the charge content in photoelectrons and the Cherenkov pulse arrival time for each pixel of the camera of a triggered event.
- Image cleaning and parametrization: The image cleaning removes pixels that contain no information from the shower image, based on the pixels charge content and arrival times. After the image cleaning, the parameters that describe the shower image are computed.
- Data selection: A quality control of the data is performed in a subrun-by-subrun basis, checking the acquisition rate stability, the atmospheric conditions, the deviations of the image parameters with respect to the average, among other quantities. Data subruns not fulfilling the quality test are rejected.
- Event characterization: For each event, its energy and its likelihood to represent a γ-ray induced shower are estimated, as well as its arrival direction.
- Signal significance calculation: The number of excess γ-ray events coming from the source position is obtained. Out of this number and the number of background events a significance of detection is computed.
- Higher level products generation: When the number of excess events produce a significant detection, higher level products can be computed. If the statistic of excess events allows for it, the differential and integral fluxes, the SED, and the light curve can be obtained. In case of no detection, integral and differential upper limits to the flux can be computed out of the excess events. Skymaps can be generated in either case.

If possible, the analysis of a given source is accompanied by a parallel analysis of a Crab Nebula data sample. The observational parameters of such a sample must coincide as much as

possible with the ones corresponding to the principal source, mainly the atmospheric conditions, and the zenith angle range. The purpose of this parallel analysis is to check the overall performance of the analysis chain. The Crab Nebula is the standard candle of VHE astrophysics due to its large and stable flux on this energy regime [290], although γ-ray flares have been detected at lower energies [291].

In the following, the MAGIC analysis chain for stereo data is presented in more detail. In order to illustrate the analysis chain, results from a Crab Nebula dataset are used throughout this section. Such a dataset was analyzed in parallel to the sources presented in Chapter 4. Since the analysis of single telescope data is also relevant for this work, the differences with the stereo analysis are properly mentioned.

2.4.3.1 Calibration

MAGIC raw data consist of the digitized pulses, in terms of amplitude in arbitrary FADC units versus time, for each pixel of each triggered event. All these raw data are initially stored in binary format that has to be translated into ROOT format. Afterward, the data from the Central Control of the telescope, which include relevant information from each of the telescope's subsystem, are merged with the already translated raw data. These two operations are performed by the Merging and Preprocessing Program (Merpp) program.

The pixel signal, also called the channel signal, occupies 80 FADC slices of 0.5 ns time window each. The signal extraction consist on the characterization of the signal pulse in terms of its arrival time, amplitude and charge given in FADC counts. Then the calibration itself is the conversion of the FADC counts, in arbitrary units, to equivalent photoelectrons, which are in turn proportional to the number of Cherenkov photons. In the case of MAGIC-II data, data are corrected prior to the signal extraction for the non-linearity of the DRS2 chip response. There are several algorithms that can be applied to perform the signal extraction [292]. Two of them have been adopted for the processing of MAGIC data: the cubic spline extractor, and the sliding window extractor.

- Cubic spline extractor: Adopted for the processing of MAGIC-I data, this extractor interpolates the FADC counts after pedestal subtraction by means of a cubic spline algorithm. The signal amplitude is then represented by the maximum of the interpolation function. The charge of the pulse is obtained as the interpolation function integral, in a window of fixed size, with variable integration limits depending on the position of the maximum. The position of the half maximum at the rising edge of the pulse fixes the signal arrival time.

- Sliding window extractor: Adopted for the processing of MAGIC-II data, this extractor maximizes the integral of consecutive FADC slices over a fixed time window and after pedestal subtraction, providing the charge of the pulse as such integral. The arrival time is then computed as the average of the FADC slices time weighted over the FADC slice counts.

After the signal is extracted, the charge in FADC counts is converted into the equivalent photoelectrons by means of the conversion factors. The main purpose of the calibration is the determination of such conversion factors, which are not constant but depend on the given channel. The conversion factors are obtained from the calibration events through the so-called F-factor method [293]. This method assumes an uniform photoelectron detection efficiency over the

the entire population of pixels, a number of incoming photons described by Poissons statistics, and a readout chain noise independent of the signal amplitude. The number of photoelectrons can be obtained as

$$N_{phe} = \frac{F^2 Q^2}{\sigma_Q^2 - \sigma_P^2}, \tag{2.11}$$

where Q is the mean reconstructed charge, σ_Q is the standard deviation of the reconstructed charge, σ_P is the resolution of the signal extractor obtained as the standard deviation of the pedestal, and F is the so-called excess noise factor. The F value is measured in the laboratory and has a value of $F^2 \approx 1.15$ for MAGIC-I and $F^2 \approx 1.10$ for MAGIC-II.

Consequently, the conversion factors C can be computed out of the calibration events, where all the aforementioned parameters are known, as

$$C = \frac{N_{phe}}{Q} = \frac{F^2 Q}{\sigma_Q^2 - \sigma_P^2}. \tag{2.12}$$

The conversion factors, which are channel dependent, also vary during the night due to the dependence of the VCSELs with the temperature. In order to keep the conversion factors updated, interleaved calibration and pedestal events are recorded during normal data taking with a frequency of 25 Hz for each type.

The calibration of the MAGIC data is performed by the CALibrate LIght Signals and Time Offsets (Callisto) program.

2.4.3.2 Image cleaning and parametrization

After the calibration the recorded images are characterized by the charge in photoelectrons and the arrival time of the pulse in each pixel. Using that information, an image cleaning is performed with the aim of removing the noise generated by the NSBL from the shower images. There are many possible image cleaning algorithms that try to discard those pixels of an image that do not provide information about the shower. Not all algorithms perform the same and their impact in the final sensitivity of the analysis is quite significant, specially at the lowest energies, where the shower images are small and faint, easily to be confused with NSBL fluctuations. For MAGIC data processing, the standard image cleaning is a two level absolute cleaning that make use of the arrival time information too. This cleaning defines two populations of pixels that form the final image, the so-called *core* pixels and *boundary* pixels, being the rest of pixels removed. In order to qualify as a *core* pixel, the charge of the pixel must exceed a certain threshold in number of photoelectrons q_c, and has to be adjacent to, at least, another pixel satisfying such condition. The group of pixels fulfilling those conditions form the so-called *core* of the image. Once the *core* of the image is determined the set of pixels surrounding the image *core* can qualify as *boundary* pixels. In order to do so, a *boundary* pixel charge is required to exceed a certain threshold in number of photoelectrons q_b always smaller than q_c, and the pixel has to be adjacent to, at least, another *boundary* pixel[1]. As for the time constraints, individual *core* pixels whose arrival time differs from the mean core pixel arrival time more than a certain Δt_c are excluded, as well as those individual boundary pixels whose signal arrival time differs from its core pixel neighbor arrival time more than a certain Δt_b. The standard values of the different cleaning parameters for MAGIC data can be found in Table 2.3.

[1]Since MAGIC-I has two pixel populations in term of their size, the thresholds q_c and q_b are correspondingly rescaled for the outer large pixels.

Table 2.3: Image cleaning parameters for MAGIC data.

Telescope	q_c [phe]	q_b [phe]	Δt_c [ns]	Δt_b [ns]
MAGIC-I	6	3	4.5	1.5
MAGIC-II	9	4.5	4.5	1.5

Standard image cleaning parameters for both MAGIC-I and MAGIC-II data. q_c is the *core* pixel threshold in photoelectrons, and q_b is the *boundary* pixel threshold in photoelectrons. Δt_c is the allowed time difference between individual *core* pixels and the image *core* mean arrival time, and Δt_b is the maximum arrival time difference between each *boundary* pixel and its *core* pixel neighbor.

In Fig. 2.12 the effects of two different cleanings applied to actual MAGIC-II events are shown.

The cleaned shower images are then parametrized in terms of the so-called Hillas parameters [294]. Some of these parameters are based on the fact that γ-rayshowers images typically present an elliptic-like shape, as illustrated in Fig. 2.13. This set of parameters is expanded by including time related parameters and head-tail discriminators. All these parameters are computed out of the single image of the shower and apply for both single telescope and stereo observation. For stereo observations a set of additional parameters can be obtained. Both, single telescope and stereo parameters are briefly explained in the following.

Monoscopic parameters: These parameters are obtained after the image cleaning of the single telescope data. They are obtained independently for each event image and telescope.

- *Size*: This parameter corresponds to the total charge in photoelectrons contained in the full cleaned image. Due to its strong correlation with the energy of the primary γ-ray, it is a good estimator of the energy of the event.

- *Length*: This parameter corresponds to the Root Mean Squared (RMS) spread of the light along the major axis of the shower image, thus being a measure of the longitudinal development of the shower itself. This parameter is usually larger for hadronic showers than for γ-ray induced showers.

- *Width*: This parameter correspond to the RMS spread of the light along the minor axis of the shower image, thus being a measure of the lateral development of the shower itself. A broader lateral development is present in hadronic event images as compared to γ-ray event images.

- *Conc(N)*: This parameter is defined as the fraction of the light concentrated in the N brightest pixels with respect to the total light content of the image, measured in photoelectrons. It is an estimate of the compactness of the shower image, being usually larger in γ-ray shower images than in the hadronic ones.

- *Dist*: This parameter depends on the position of the source in the camera, and thus needs the prior assumption of such. It is defined as the angular distance between the Center of Gravity (CoG) of the image and the source position in the camera, providing an estimator of the *impact parameter* of the shower.

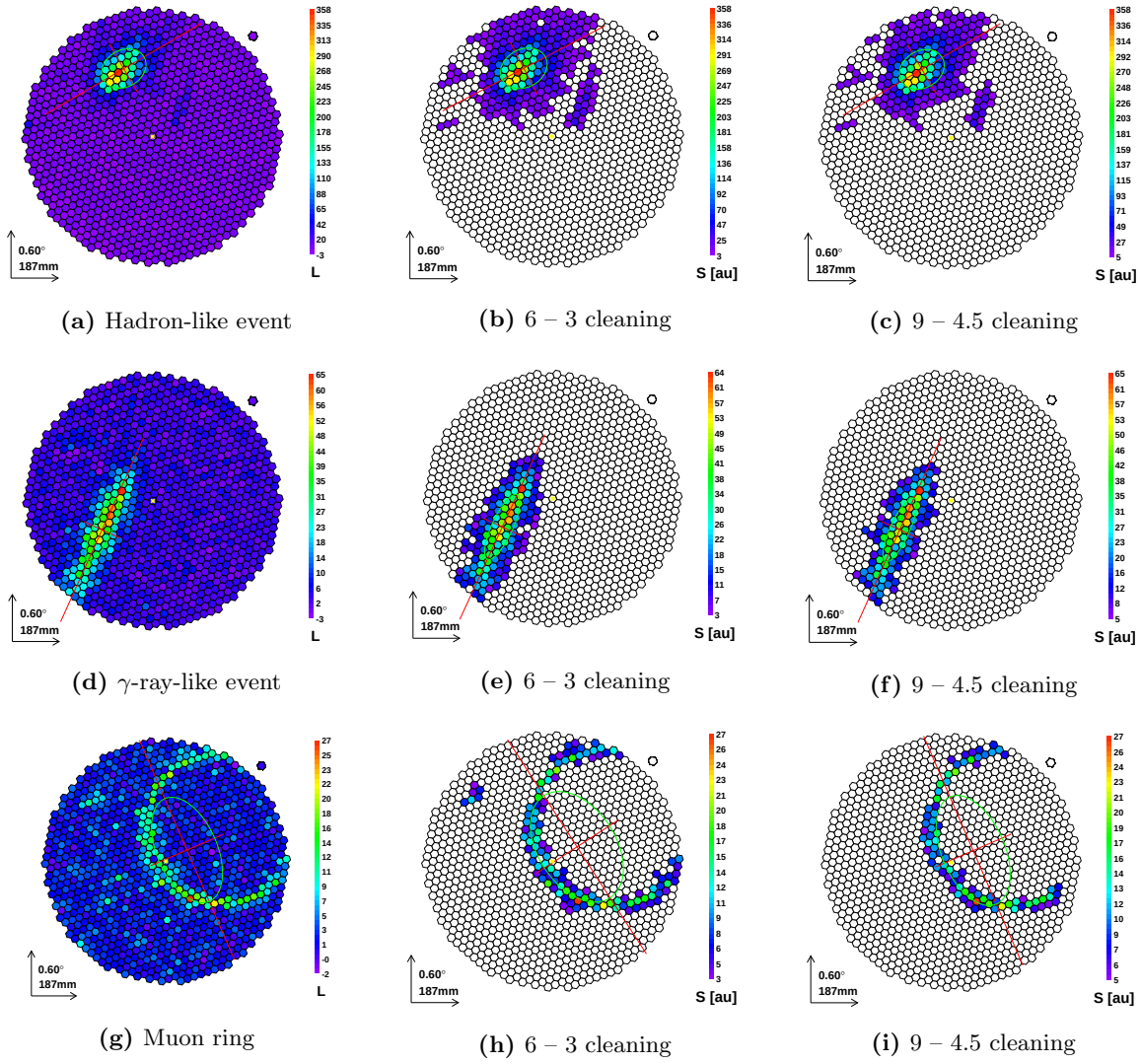

(a) Hadron-like event **(b)** 6 – 3 cleaning **(c)** 9 – 4.5 cleaning

(d) γ-ray-like event **(e)** 6 – 3 cleaning **(f)** 9 – 4.5 cleaning

(g) Muon ring **(h)** 6 – 3 cleaning **(i)** 9 – 4.5 cleaning

Figure 2.12: Actual events recorded by magic-II. Fig. 2.12a corresponds to the camera image of a hadron-like event after calibration. The same event is shown after two different image cleanings: absolute 6 – 3 (Fig 2.12b), and 9 – 4.5 (Fig 2.12c) cleaning levels. Equivalent images are provided for a γ-ray-like event 2.12d, and a muon ring 2.12g. The image parametrization of the showers in terms of the Hillas ellipse is superimposed. Keep in mind the slight differences in the outcome between different cleaning levels. Although apparently small, the differences have an impact on the overall sensitivity of the instrument. Absolute cleaning 9 – 4.5 is the one applied to MAGIC-II data by default.

- *Alpha*: This is another source position-dependent parameter. It is defined as the absolute value of the angle between the major axis of the shower ellipse and the connecting line between the CoG of the image and the source position in the camera. The major axis of images of showers whose primary γ-ray comes from the source will point to the source position in the camera, thus providing small *alpha* values. On the contrary, the isotropic distribution of hadronic showers and EM-showers generated by electrons provide with flat *alpha* distributions, consequently placing this parameter as an excellent background discriminator.

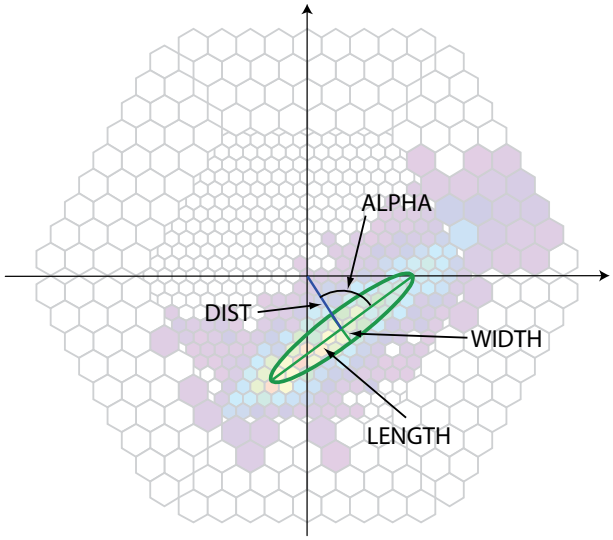

Figure 2.13: Image of an actual shower in the MAGIC-I camera after cleaning. The Hillas ellipse parametrization is superimposed. The main shower parameters for single telescope observations *width, length, alpha*, and *dist* are labeled.

- *TimeRMS*: This parameter corresponds to the RMS of the distribution of arrival times of all pixels that survived the image cleaning, regardless of the pixel position in the camera. Since the time development of γ-ray induced showers and hadronic showers is different, this parameter works as a good discriminator.

- *Time gradient*: This parameter is defined as the slope of the linear fit to the arrival time versus the spatial coordinate along the major axis line. This parameter is a source-dependent one, since its sign will be negative if the arrival time increases when moving towards the location of the source in the camera, and positive otherwise.

- *Asymmetry*: This parameter is defined as the distance from the pixel with the highest photoelectron content to the CoG of the ellipse, projected onto its major axis. It is used to characterize the head-tail arrangement of the shower image in the camera. It is positive when the shower image head is closer to the camera center than the tail. It corresponds to the fact that head and tail in the shower itself are asymmetric.

- *M3Long*: This parameter consist of the third moment of the image along its major axis. As the *asymmetry* parameter, it works as a head-tail discriminator and its sign follows the same convention.

- *LeakageN*: This parameter is defined as the fraction of cleaned image photoelectrons in the N-outermost ring of the camera to the total photoelectron content of the cleaned image. It helps to estimate the fraction of the shower image that spills over the camera. Events with large *leakageN* values are likely to undergo a bad reconstruction.

- *Number of islands*: This parameter corresponds to the number of isolated groups of pixels after the image cleaning. γ-ray induced showers generate single island images, while hadronic showers may generate several islands in one single event image.

The distributions of some of the aforementioned parameters, extracted from MAGIC actual data, can be found in Fig. 2.14.

Stereoscopic parameters: These parameters are obtained after the merging of the images from both telescopes corresponding to the same event. These stereoscopic parameters allow for a 3–dimensional description of the events [295].

- *Shower axis*: This parameter is characterized by an *arrival direction* and an *impact parameter*. The *arrival direction* is obtained as the crossing point between the major axes of the two images superimposed on a common camera plane. Once the *arrival direction* is known, the *impact parameter* with respect to each telescope can be obtained. The *impact parameter* is defined as the distance between the shower axis intersection with the ground and the telescope axis intersection with the ground. Thus, it is usually different between telescope.
- *Shower maximum height*: This parameter is an estimation of the height at which the maximum development of the shower took place. It is based on the *shower axis* characterization as the 3-dimensional geometrical location of the CoG of the image. This parameter is strongly correlated to the energy of the primary γ-ray and is a powerful discriminator at low energies.
- *Cherenkov radius* and *Cherenkov photon density*: Once the *shower maximum height* is obtained, then these two parameters can be computed as the density and radius of the Cherenkov light pool at ground. For that calculation, the Cherenkov emission from a single electron at the *shower maximum height* with an energy equal to the critical energy of 86 MeV[1] is assumed.

The MARS program, which performs the image cleaning and the single telescope image parameter calculation is the STandard Analysis and Reconstruction (Star) program. The stereo event images merging and the calculation of the stereo image parameters are carried out by the Superstar program.

2.4.3.3 Data selection

In order to obtain the best sensitivity of analysis, the quality of the data must be monitored, eventually discarding data whose quality could affect the final results. The data selection is performed in a subrun-by-subrun basis over the entire dataset, and it depends on two main factors: hardware performance, and atmospheric conditions.

Possible hardware malfunctions or failures are evaluated thanks to the electronic runbook information, provided every observation night by the telescopes' operators, and to the automated daily checks of the subsystems [296]. Data taken under non-optimal hardware conditions, and whose problems can not be corrected via software, are normally rejected.

The atmospheric conditions are the main source of data degradation. The propagation of Cherenkov light in the atmosphere is very sensitive to the transparency of the same. Aerosols, clouds, Calima[2], or any other particle pollutant reduce the amount of Cherenkov light arriving

[1] More details about shower developments and critical energy of the EM-shower constituents can be found in Appendix A.

[2] Calima, also known as Saharan Air Layer, is a high-altitude layer of suspended ultra-thin dust from the Sahara Desert, which occurs occasionally during the summer months.

to the reflector by means of photon absorption or scattering. The atmospheric conditions are monitored on-site by a dedicated weather station, which is complemented with a pyrometer (and a lidar system lately commissioned). The pyrometer provides an estimate of the sky quality through a *cloudiness* parameter. Data taken above a certain *cloudiness* threshold (usually a *cloudiness* of 50%) are rejected.

Additionally, the event analysis rate provides with a reliable estimator of the data quality. In an ideal situation, the event analysis rate only depends on the observation Zenith Angle (ZA) as $R = R_0 \times \cos(\mathrm{ZA})$. Thus, deviations from the expected value towards lower rates typically indicate bad weather conditions. On the contrary, deviations toward higher rates are produced when the cameras are accidentally illuminated by artificial light, like car flashes or torches. Usually, data differing from the analysis rate mean value more than a 15%–20% are discarded.

The quality of the data can be also inferred from some of the image parameters distributions, like *size*, *length* and *width*, which must be constant during data taking if the conditions are stable. The subrun image parameter's average is compared to the whole dataset average, and those subruns showing deviations above 5% are rejected.

Additionally, in case of *on–off* observations, the same quality selection applied to the *on* dataset must be applied to the *off* dataset. On top of that, and in order to check the suitability of the *off* dataset as background for the *on* dataset, the image parameter distributions from both datasets must be compared prior to any analysis cut. If the distributions from both populations match each other, then the *off* dataset can be used as background. Otherwise, the *off* dataset must be disregarded in order to avoid biases that could eventually spoil the analysis results. This check applies to either single telescope and stereoscopic observations. In the last case, the match between stereo parameters must be also checked. An example of matching *on* and *off* datasets for single telescope observations can be found in Fig. 2.14.

2.4.3.4 Monte Carlo simulations

The reconstruction of the primary γ-ray from its shower image characteristics, as well as the study of the telescopes performance require dedicated Monte Carlo (MC) simulations. This is due to the fact that telescopes lack of direct calibration, contrary to satellite γ-ray detectors that can be characterized in calibration γ-raytest-beams before being launched. Images from simulated γ-ray induced shower are compared to hadronic shower images to train the algorithms further applied to discriminate between actual γ-ray events and hadronic events. The simulated γ-ray events are also used to estimate the energy of the events classified as γ-ray induced showers, as well as to obtain the effective detection area of the telescopes. Besides the simulated γ-ray events, protons and helium nuclei induced showers are also generated for performance studies.

The MC simulations of γ-ray and hadronic events for MAGIC is carried out in three different stages: the shower simulation, the reflector simulation, and the camera and readout simulation:

- Shower simulation: The γ-ray and hadronic induced showers are simulated by means of the CORSIKA code [297] and considering the so-called US standard atmosphere model. The obtained Cherenkov photons reaching the ground serve as input for the next stage.

- Reflector simulation: At this stage the effect of the Cherenkov light attenuation due to both Rayleigh and Mie scatterings is computed, considering the same atmospheric model as in the previous step. Then the reflection and absorption of photons in the reflector mirrors is simulated, eventually obtaining the distribution of Cherenkov photons and their

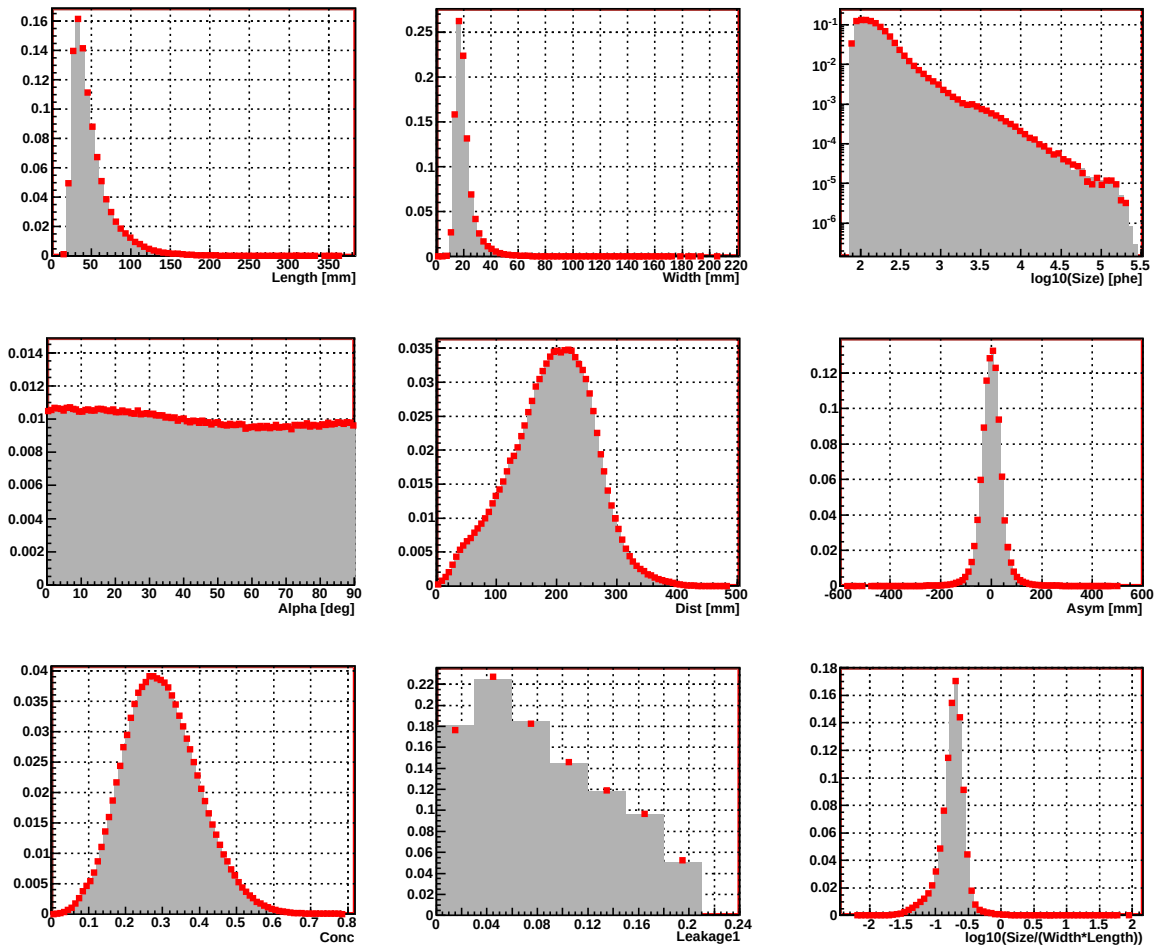

Figure 2.14: Distribution of some representative image parameters, or arithmetic combinations of the same, after image cleaning and data quality selection for Willman 1 *on* and *off* datasets. Grey bars and red dots represent *on* and *off* datasets respectively (Y-axis in arbitrary units). The match between the two populations is a significant indicator of the suitability of the *off* sample as background for the *on* sample.

arrival times on the focal plane. The optical Point Spread Function (PSF) of the system is not simulated at this stage but in the next, in order to keep the simulations more flexible.

- Camera and readout simulation: At this stage the response of the telescope's camera and the readout is simulated, including the trigger and DAQ systems. At this step the smearing of the shower image according to the optical PSF of the telescope is included. Thus, the final product turns out to be the digitized signals from the Cherenkov pulses for each pixel, ready to be processed by the same MAGIC analysis chain applied to real data.

There are different types of simulations according to the selected *arrival direction*. The standard simulations consider point-like sources, but there are also simulations of diffuse γ-rays in order to study extended sources. As for the energy distribution, typically power-law spectra are considered.

Since the data analyzed in this work were taken under different observation modes (*wobble* and *on–off*), some being single telescope observations, and some others being stereoscopic observations, different γ-ray MC simulated datasets have been used. It is worth mentioning that the optical PSF variations in different seasons were also considered at the time of selecting the appropriate MC production. More details into MAGIC MC simulation can be found in [298; 299].

2.4.3.5 Event characterization

The event characterization consist on an estimation of the nature of the primary particle which originated the air shower, its energy, and its *arrival direction*. In MAGIC, these main characteristics are inferred from the image parameters described in Sec. 2.4.3.2, following different algorithms: a Random Forest (RF) type decision trees [300], parametrization, and Look-Up Table (LUT)s.

The event characterization depends on whether the data is monoscopic or stereoscopic. In either case, the nature of the particle is estimated through a regression method. In the case of single telescope observations, the energy estimation makes use of this RF method too, while for stereoscopic observations both, the RF method and the use of LUTs are possible, the latter performing better. As in the case of the energy estimation, the arrival direction estimation can be obtained via a parametrization or through a RF method, but this time both approaches can be used for either monoscopic and stereoscopic observations.

A dataset of MC simulated γ-ray events is required in order to characterize the actual data, since it is not feasible to obtain a dataset of pure actual γ-ray events. Such dataset of simulated γ-ray events is split into two samples, the so-called *training* sample, used to train or tune the characterization algorithms, and the so-called *test* sample, used to test the performance of the algorithms once trained or tuned. Both subsets are independent, thus avoiding biased results.

Before the events are characterized, certain event-based quality cuts are applied in order to get rid of events whose parameters will not allow for a proper characterization. These cuts allow to reject the so-called *spark* events, produced by actual sparks generated by electric discharges between the PMT cathodes and the Winston cones. A minimum *size* value is also required, together with a small value of the *leakage* parameter (typically < 0.2), a reduced *number of islands* (typically < 3), and a minimum number of *core* pixels (typically > 3).

In the following, the estimation of the nature of the particle, its energy, and its *arrival direction* are briefly explained.

γ/hadron separation: IACT telescopes trigger on several types of events, namely, accidental triggers by NSBL fluctuations or artificial light sources, Cherenkov light from individual muons, extended air showers originated by γ-rays, and extended air showers originated by cosmic rays. While the accidental triggers are highly suppressed by the image cleaning, the showers originated by cosmic rays, also known as hadronic showers, are by far the most numerous population of triggered events, and thus the main background for the γ-ray originated showers.

It is worth mentioning that the incidence of hadronic showers in the recorded data of a typical VHE γ-ray source is around 10^4 times larger than the corresponding to γ-ray showers, and this happens in both monoscopic and stereoscopic observations. Additionally, Cherenkov light from individual highly-relativistic muons form complete or partial rings on the camera plane. The incidence of such rings is around five times lower than the incidence of hadronic showers, still much larger than the frequency of γ-ray showers. This value is significantly reduced is stereo

observation due to the nature of the muon rings, since the rings are formed by the light emitted at very low altitude and require very small *impact parameters*, disfavoring the stereo trigger. Muon rings are not only background, since can be used to estimate the telescopes optical PSF.

There are several methods which provide with the so-called γ/hadron separation. The so-called model analysis [301], or the static, dynamical, or scaled cuts on the image parameters can be used to discriminate background events from γ-rays events. The best performing method so far applied to MAGIC data is the RF method [302], which is the method used throughout this work.

The RF method is a multi-dimensional classification algorithm based on decision *trees*. These *trees* are trained with a sample of MC simulated γ-ray events and hadronic events from actual data samples, since unfiltered data consist, in an overwhelming fraction, of hadronic events. The *trees* are grown by considering a set of discriminating parameters among the image parameters. The *trees* grow through a dynamical evolution of the cuts, over the simulated γ-ray and hadronic samples, in terms of the mean decrease of the so-called Gini-index [303]: the process starts by subdividing the parameter space in two hypervolumes, setting a cut on one of the parameters, and subsequently repeating the process until the last discriminator parameter is considered. The mean decrease of the Gini-index thus provides with a measurement of the discriminating power of each of the selected parameters. An example of the differences between parameters can be found in Fig. 2.15.

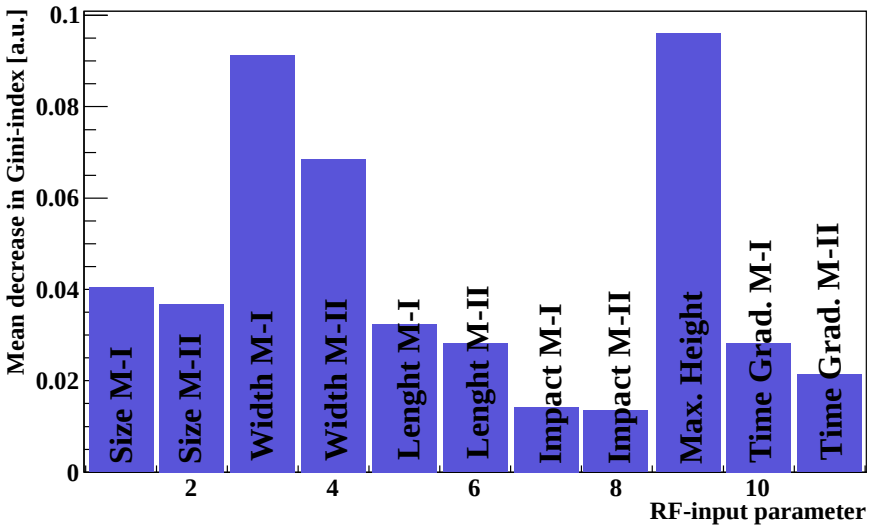

Figure 2.15: Mean decrease of the Gini-index for all the discriminator parameters considered for the training of the γ/hadron separation RF matrix. This quantity shows the discrimination power of each RF input parameter. The shower widths and its height of maximum development result the best discriminating parameters. This matrix was applied to the Crab Nebula dataset and the sources analyzed in Chapter 4.

In the classification step, each event is then characterized by the particular values of the selected image parameters. These values are introduced into the decision *tree*, and the first image parameter is compared to the corresponding cut value of the *tree*'s first node, determining a certain path of the two possible ones. The process is repeated on every node, with the corresponding discriminator parameter, until the terminal node is reached, and the path is completely determined. Each possible path ends in a certain dichotomous value l, fixed during

the training. A value $l = 1$ is assigned to the event if during the training the path was followed by hadronic events, and a value $l = 0$ is assigned if during the training the path was followed by simulated γ-ray events. The event goes through several independent decision *tress* (typically 100 for an standard MAGIC analysis), collecting all the final l values from each *tree*. Eventually, the so-called *hadronness* parameter is calculated as

$$h = \frac{\sum_{i=1}^{N_{trees}} l_i}{N_{trees}} \in [0, 1], \tag{2.13}$$

where N_{trees} is the total number of trees. Consequently, the *hadronness* parameter can be considered as the likelihood of an event to have a hadronic origin. *Hadronness* values close to 1 will be assigned to hadron-like events, while *hadronness* values close to 0 will be assigned to γ-like events.

The separation power of this *hadronness* depends on how well the image parameters are defined for each event. Thus, low energy events, producing small images on the camera, present larger uncertainties in their image parameter calculation, and so the separation power of the hadronness parameter is smaller. This particular effect can be seen in Fig. 2.16.

The RF decision *trees* are stored after the training in the so-called RF matrix for γ/hadron separation. This RF matrix is further applied to the data by means of the MErge and Link Image parameter Before Energy Analysis (Melibea) program.

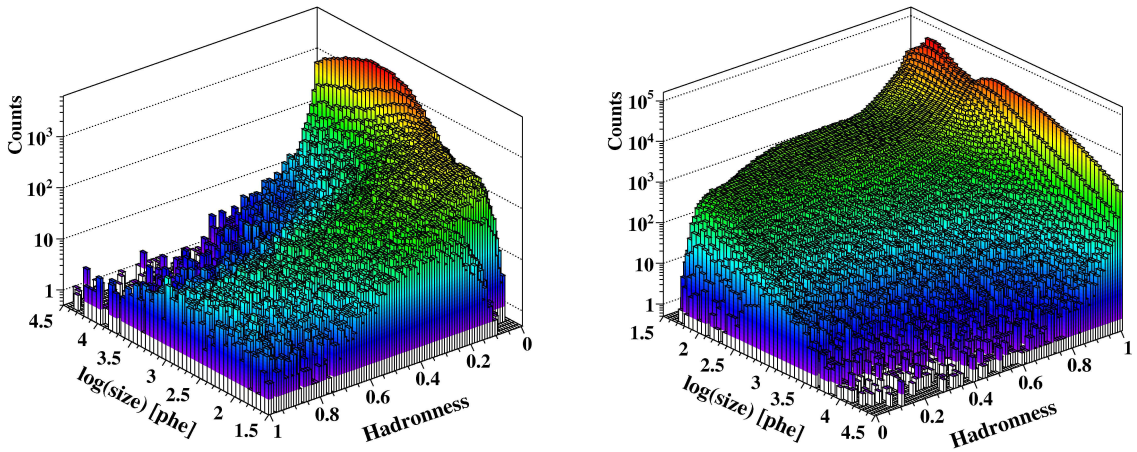

(a) Monte Carlo simulated γ-rays

(b) Hadron sample

Figure 2.16: Fig. 2.16a: Hadronness distribution corresponding to a MC simulated γ-ray sample. Fig. 2.16b: Hadronness distribution corresponding to a hadron sample.

Arrival direction estimation: The *arrival direction* of the primary γ-ray can be obtained geometrically in the case of an array of IACT telescopes, as shown in Sec. 2.4.3.2 where the stereo image parameters were commented. In the case of single telescope observations is more complicated, since no 3-dimensional reconstruction of the generated shower is possible. In either case, the shower major axis is the projection of the incoming direction of the primary γ-ray on the focal plane of the telescope, and thus the exact *arrival direction* must be located somewhere along this direction. Defining the parameter *disp* as the distance between the CoG of the

image and the *arrival direction* of the primary γ-ray, the source position can be determined by estimating that *disp* parameter for each γ-ray shower image [286].

There are two algorithms implemented in the MAGIC analysis chain that estimate the *disp* parameter: the *disp* parametrization, and the RF method for *disp* estimation (also known as *disp*-RF).

- *Disp* parametrization:

  The *disp* parameter can be estimated from the shower elongation by the following parametrization:

  $$disp = \mathrm{A}(size) + \mathrm{B}(size)\frac{width}{length + \xi(size) \times leakage2}. \tag{2.14}$$

  The introduction of the *leakage2* parameter try to correct the elongation of truncated images that may spill over the camera FoV, and the *size* dependent parameters A, B, and C are determined from a simulated γ-ray events sample, where the *disp* parameter equals the *dist* parameter. Once the *disp* value is obtained, then two possible solutions in the source position determination emerge, corresponding to the two possible orientations that can be adopted from the CoG of the image. The right position is chosen attending to the head-tail parameters of the image, described in Sec. 2.4.3.2.

  The effect of the truncation of the images introduces large uncertainties in this approach for the *disp* estimation, even if the *leakage2* correction is taken into account. This is one of the reason why the *Disp*–RF method was implemented in the MAGIC analysis chain.

- *Disp*–RF:

  The *Disp*–RF method makes use of multi-dimensional decision *trees*, based on the same working principle as explained before for the γ/hadron separation method. In this case, a set of image parameters correlated to the *disp* value, and required to be source-independent parameters, constitute the set of RF variables. The decision *trees* are trained over a simulated γ-ray events sample, where the *disp* value of each event is previously known, by minimizing the difference between the known and the estimated *disp* values.

  This *Disp*–RF method, together with the consideration of head-tail and time parameters into the RF set of variables, improved the sensitivity of MAGIC single telescope observations by a 20%–30% as compared to the *disp* parametrization [304].

  The *Disp*–RF method is also used for stereoscopic data. In this case, the *disp* parameters are estimated for each individual image. Then, if both images of the same stereo event are superimposed into a common focal plane, there would be four possible arrival directions, attending to the duplicity of possibilities for each image. Out of the four different combinations of position pairs the combination providing the shortest distance is chosen, and the reconstructed *arrival direction* is then obtained as the weighted average of such positions together with the crossing point of the two main axes of the images (see Fig. 2.17).

Any of the *disp* methods allows for an unbiased technique to estimate the source position into the camera FoV, since it does not make use of any source-dependent parameter. On top of that, the use of *disp* provides with a new powerful discriminator between γ-ray events coming from the observed source, and the rest of background events: the so-called θ^2 parameter. The θ parameter is defined as the angular distance between the reconstructed *arrival direction* of

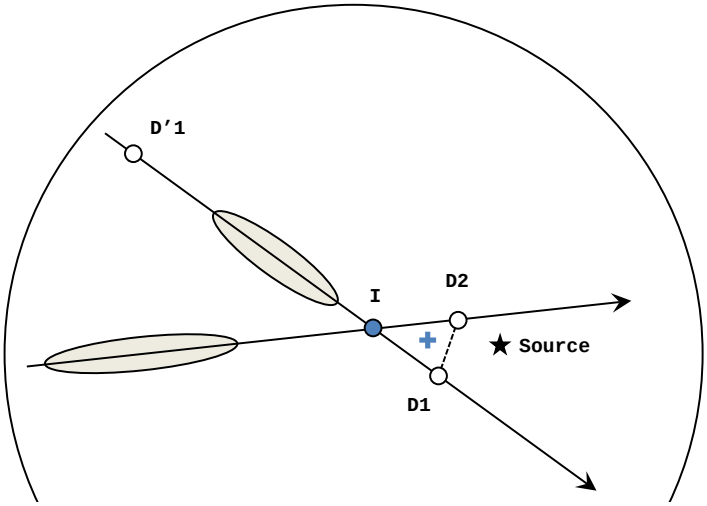

Figure 2.17: Principle of the *disp* method for stereoscopic observations. Two parametrized images for a stereo event are represented in a common focal plane. The crossing point of the two main axes is represented as a blue filled circle (I). The *disp* reconstructed positions are represented by open circles. For one of the images, the two possible *disp* reconstructed positions, D1 and D'1, are shown. D'1 is rejected by head-tail discrimination. The final reconstructed *arrival direction* is obtained by a weighted average of D1, D2 and I positions and is represented as a blue cross. The nominal source position is shown with a star. The angular distance between the nominal source position and the reconstructed *arrival direction* defines the θ parameter.

the event, and the source nominal position in the camera FoV. The distribution of this angular distance squared, θ^2, sharply peaks towards zero values for the population of γ-ray events coming from the source position, whereas the hadronic events, and the diffuse γ-ray events, which fall isotropically, originate a flat contribution to that distribution (see Fig. 2.20 for some examples of θ^2-distributions).

The estimation of the *disp* parameter of the actual events either through the application of the *disp*-RF matrices, or through the *disp* parametrization approach, is done by the Melibea program.

Energy estimation: The energy estimation can be performed by means of a dedicated RF method, or by considering LUTs. The first method performs better for single telescope observations while the second is the standard choice for stereoscopic observations.

- RF energy estimation: After dividing the energy range of MC simulated γ-ray events in logarithmic bins, the decision *trees* are trained to accommodate each event within its corresponding energy bin. Thus, after going through several decision *trees* (typically 100 *trees* in a standard MAGIC analysis), an *estimated energy* (E_{est}) is assigned to the event as the mean energy for each selected bin, averaged by the total number of *trees*.

- LUTs energy estimation: Due to the possibility of a 3-dimensional reconstruction of the shower from stereoscopic data, its energy estimation can be obtained by relating the image *size* on each telescope with the density of Cherenkov photons at ground in the position of the corresponding telescope. To do so, the *Cherenkov radius* (r_C), the *Cherenkov photon density* (ρ_C), and the *impact* stereo parameters, introduced in Sec. 2.4.3.2, are used. A

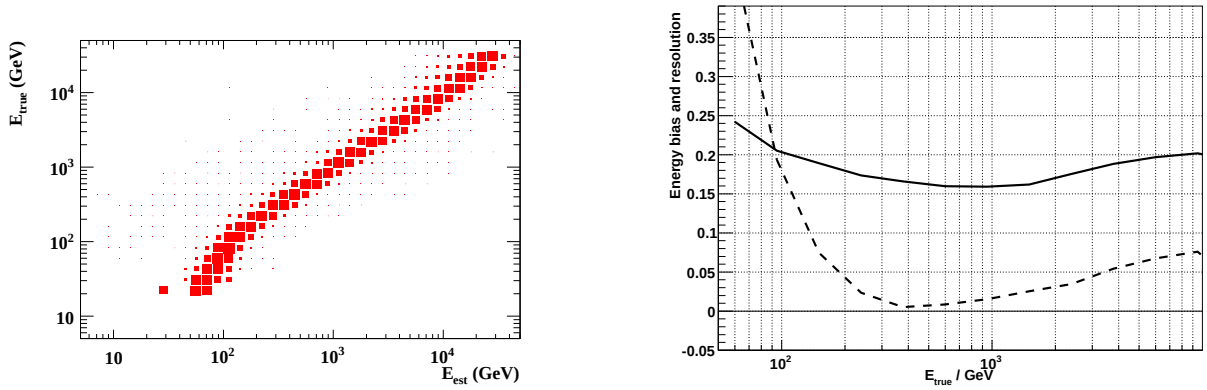

(a) Example of MAGIC migration matrix

(b) MAGIC energy resolution and bias

Figure 2.18: MAGIC energy estimation results. Fig. 2.18a is the corresponding migration matrix for the different analyses presented in Chap. 4. Fig. 2.18b, extracted from [305], depicts MAGIC energy resolution (solid line) and bias (dashed line) for stereoscopic observations. In both cases the energy is estimated by means of LUTs.

LUT is built for each telescope independently, by dividing the simulated γ-ray events *train* sample in bins of *size*, and in bins of the ratio *impact* to r_C. For each bin, the energy of the simulated γ-ray event is thus $E_{true} \propto size/\rho_C$. Consequently, the mean value and the error of the proportionality constant turns to be the mean value and the RMS of the distribution of $E_{true} \times \rho_C/size$ in that bin. Eventually, one LUT for each telescope is obtained, and thus two estimates of the energy are available for each stereo event. The final E_{est} is then the average of both quantities, weighted according to their errors, and corrected by the dependence through the empirical factor $0.4 \times \cos(\mathrm{ZA})$.

The analysis *energy resolution* is defined as the Gaussian width of the fit to the peak of the $(E_{est} - E_{true})/E_{true}$ distribution. The best resolution for single telescope observations reach the 25% in the energy range between 200 GeV and 1 TeV, whereas stereoscopic observations are able to improve the *energy resolution* down to a 15% in the same energy range. The *energy bias* is defined as the mean of the aforementioned Gaussian fit, being positive (*i.e.* overestimating the energy of the events) below 200 GeV and above some TeV. The *energy resolution* and *bias* for stereoscopic observations can be found in Fig 2.18, along with an example of an energy migration matrix[1].

The analysis *energy threshold* is conventionally defined as the maximum peak of the energy distribution from the simulated γ-ray *test* sample, once the background rejection cuts and the rest of analysis cuts are applied. The *energy threshold* strongly depends on the minimum cut in the *size* image parameter, as illustrated in Fig. 2.19.

The *estimated energy* of the events is assigned to the actual data via the *melibea* program in the case of the RF energy estimation, and via the Superstar program if LUTs are used.

[1]The energy migration matrix is a bi-dimensional histogram obtained from the MC *test* γ-rayevents sample. It illustrates the energy reconstruction performance by showing the relation between the simulated and the reconstructed energy of the MC γ-rayevents.

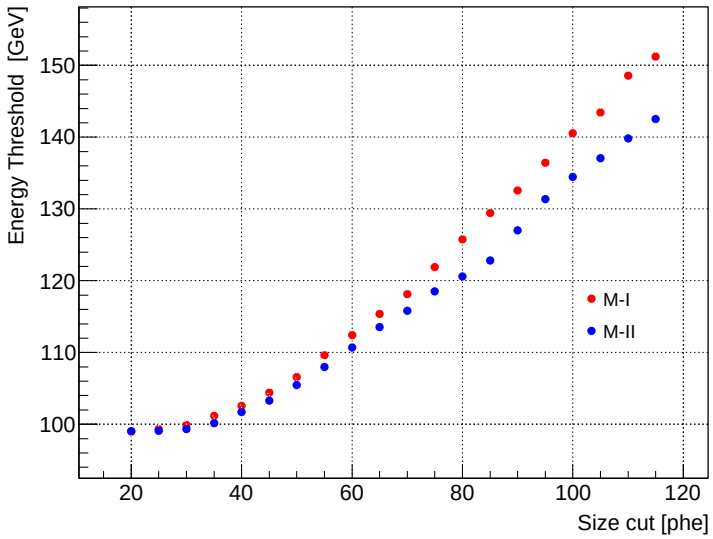

Figure 2.19: Energy threshold as a function of a lower MAGIC-I size cut (red dots; no MAGIC-II size cut) and MAGIC-II size cut (blue dots; no MAGIC-I size cut) over the MC γ-ray *test* sample. The final analysis energy threshold is computed by applying both cuts in MAGIC-I and MAGIC-II sizes to the MC γ-ray events *test* sample.

2.4.3.6 Signal extraction

In order to reduce the overwhelming population of hadronic events from the total recorded events, a cut at low value of the *hadronness* parameter is done. For further background suppression, the angular parameters *alpha* or θ^2 are used. As already mentioned, the distributions of the angular parameters *alpha* and θ^2 (represented by the so-called *alpha*-plot and θ^2-plot respectively) peak around zero values for γ-ray events coming from the source, whereas such distributions are flat for background events due to their isotropic arrival directions. Consequently, these angular parameters turn to be excellent discriminators of signal events from background events by defining a signal region for values below a given cut in the corresponding *alpha* or θ^2 range (see Fig. 2.20).

IACT data analysis does not allow to decide whether the recorded events come from the observed source in an event-by-event basis, as satellites do, but only allows to compute how many of those events represent an excess over the background. In order to obtain the number of *excess events*, the selected angular parameter distribution of the *on* data is compared to the equivalent distribution of the *off* data (see Sec. 2.4.2.4). Sufficiently away from the signal region both, *on* and *off* distributions are flat. This region serves for normalization purposes (thus being named normalization region) whenever the amount of *on* data is not equal to the *data*. Defining N_{on} as the number of events in the signal region of the *on* distribution, and N_{off} the number of events in the same region of the *off* distribution, the number of *excess events* is then computed as

$$N_{exc} = N_{on} - \kappa N_{off}, \tag{2.15}$$

where κ is the normalization factor between *on* and *off* distributions. The quantity κN_{off} is also referred as the number of *background events* (N_{bkg}).

Now, the significance level of detection of a given source S, can be defined in a straightforward way as the ratio between the number of *excess events* and its standard deviation:

$$S = \frac{N_{on} - \kappa N_{off}}{\sqrt{N_{on} + \kappa^2 N_{off}}}. \tag{2.16}$$

A more refined way to compute the significance level is by means of a statistical test, where the null hypothesis consists on the assumption that the expected signal is not different from the background: *i.e.* all the observed photons are due to background [306]. The significance is then determined by the expression

$$S = \sqrt{2}\left\{ N_{on} \ln\left[\frac{1+\kappa}{\kappa}\left(\frac{N_{on}}{N_{on}+N_{off}}\right)\right] + N_{off}\ln\left[(1+\kappa)\left(\frac{N_{off}}{N_{on}+N_{off}}\right)\right]\right\}^{\frac{1}{2}}. \tag{2.17}$$

Unless otherwise stated, this last formula of significance computation is henceforth applied when dealing with MAGIC data.

As a convention, the detection of a source can be stated if its significance level equals or surpasses the value of 5σ. This significance level has to be corrected by the number of trials generated if different sets of cuts were applied to the data, in order to avoid false detections coming from possible background fluctuations.

Cuts optimization: The optimization of the cuts on the *hadronness* and the signal region depends on the type of analysis to be performed: a detection analysis or a spectral analysis. A detection analysis requires a set of cuts with the best detecting power possible, sacrificing the γ-ray events statistics in order to be able to perform the best background rejection. On the contrary, the spectral analysis looks for the largest γ-ray events statistics possible, always fulfilling the 5σ condition, allowing for looser cuts and thus providing a smaller analysis sensitivity.

The analysis presented in the following Chapters focus on the detection strategy. There are two main approaches in order to optimize the cuts for a detection analysis:

- Optimization over a strong source: This approach can be carried out if there is a strong source dataset which shares the same observational characteristics that the dataset where the signal wants to be searched. The strong source, ideally the Crab Nebula, is then used to optimize the cuts through the maximization of the significance of detection from a scan over the cuts' parameter space. If the source to be detected is expected to show a very faint flux, then the signal of the strong reference source can be scaled down before the optimization.

- Optimization of the quality factor: This approach, which relays on MC simulated γ-ray events, looks for the best relation between background rejection and γ-ray acceptance. Considering the efficiency ϵ of the cuts in *hadronness* and signal region as

$$\epsilon_{\gamma,\ had} = \frac{N^{\text{After cuts}}_{\gamma,\ had}}{N^{\text{Before cuts}}_{\gamma,\ had}}, \tag{2.18}$$

  then the *quality factor* Q can be defined as:

$$Q = \frac{\epsilon_\gamma}{\sqrt{\epsilon_{had}}}. \tag{2.19}$$

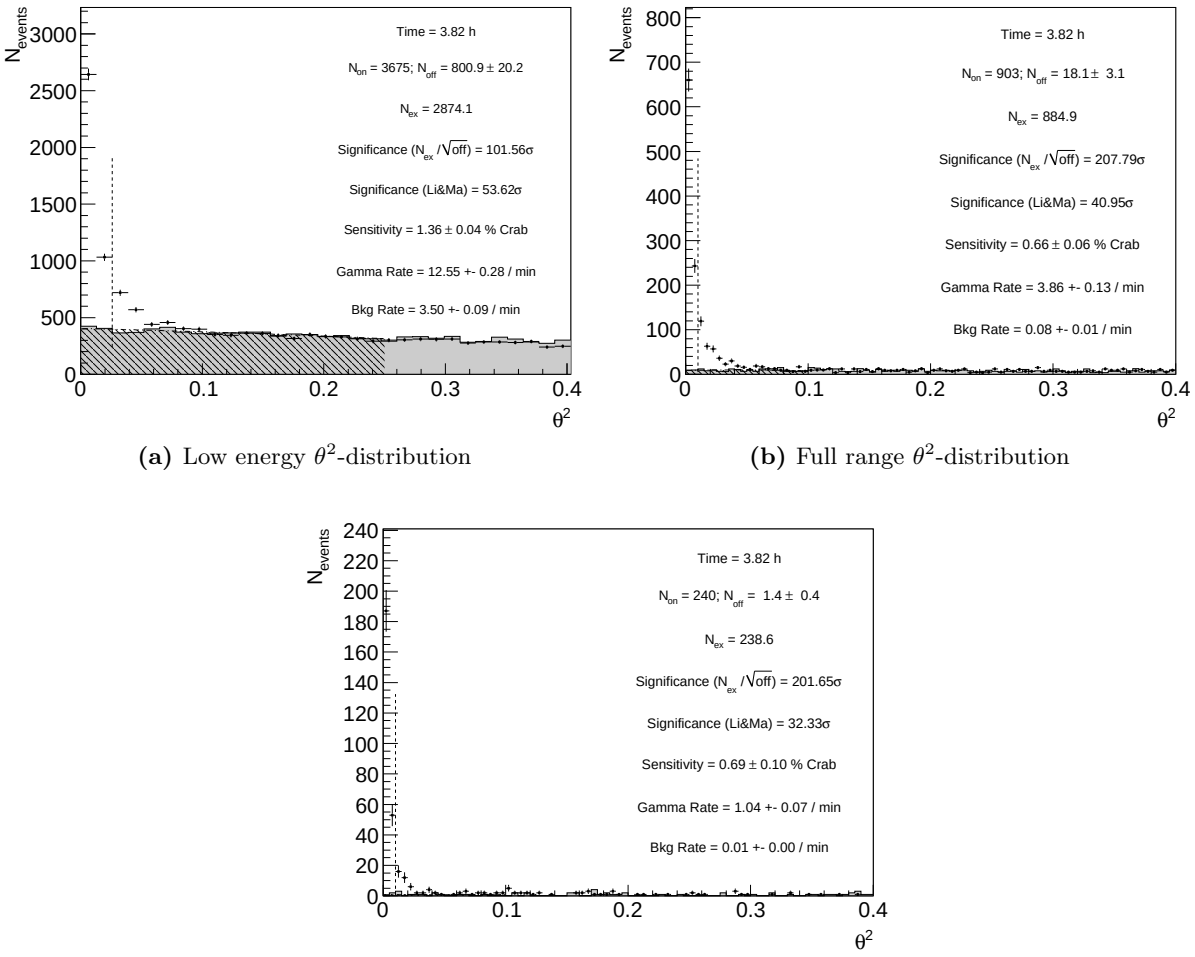

(a) Low energy θ^2-distribution

(b) Full range θ^2-distribution

(c) High energy θ^2-distribution

Figure 2.20: Crab Nebula θ^2-distribution from MAGIC data for several sets of cuts which optimize the sensitivity in three different energy ranges (see Table 4.5). 2.20a Low energy range cuts provide an analysis energy threshold of 120 GeV; 2.20b full range cuts consider $E > 250$ GeV; 2.20c high energy range cuts consider E>1 TeV. Dots are ON events, dots accompanied by gray filled areas represent off events. The dashed line shows the θ^2 cut which defines the signal region. All the energies are referred to the estimated energy of the events.

The efficiencies are then computed from the MC simulated γ-ray events sample, and a background sample, scanning as well the cuts parameter space, eventually selecting the set of cuts that maximize the Q factor.

The cuts optimization can be done over the entire MAGIC energy range or over bins of energy.

Sensitivity: The significance of detection of a stable VHE γ-ray source scales with the square root of time. Consequently, the sensitivity of an IACT telescope can be provided in units of $S/\sqrt{t}$, where S is the significance of detection in σ from the analysis of a Crab Nebula sample, and t is the total observation time of such sample.

The integral sensitivity above a certain analysis threshold E_{th} is defined as the minimum integral flux above E_{th} that would be detected at a 5σ level by MAGIC in 50 hours of observation time if the source spectrum had the same spectral shape as the Crab Nebula one. It is usually expressed as a total fraction of the Crab integral flux, also called Crab Nebula Units (CU).

Assuming a Gaussian approximation of the significance level (Eq. 2.17), and a normalization factor of $\kappa = 1$, the integral sensitivity of a certain analysis can be computed as

$$\Phi^{min}_{>E_{thr}} = 5\frac{\sqrt{N_{bkg}}}{N_{exc}}\sqrt{\frac{T_{obs}\ [\mathrm{h}]}{50\ \mathrm{h}}}\Phi^{Crab}_{>E_{thr}}, \tag{2.20}$$

where N_{exc}, N_{bkg} (both computed above the energy threshold), and the observation time T_{obs} refer to a Crab Nebula sample. If the integral sensitivity is expressed in CU, then it reads

$$I.S.^{50\ \mathrm{h},\ 5\sigma}_{>E_{thr}} = 5\frac{\sqrt{N_{bkg}}}{N_{exc}}\sqrt{\frac{T_{obs}\ [\mathrm{h}]}{50\ \mathrm{h}}}. \tag{2.21}$$

The same can be applied to the differential sensitivity, if the number of *excess events* and *background events* are extracted in bins of *estimated energy*. In this case the spectral dependence disappears if a fine binning is considered. Fig. 2.21 shows an example of MAGIC integral and differential sensitivity.

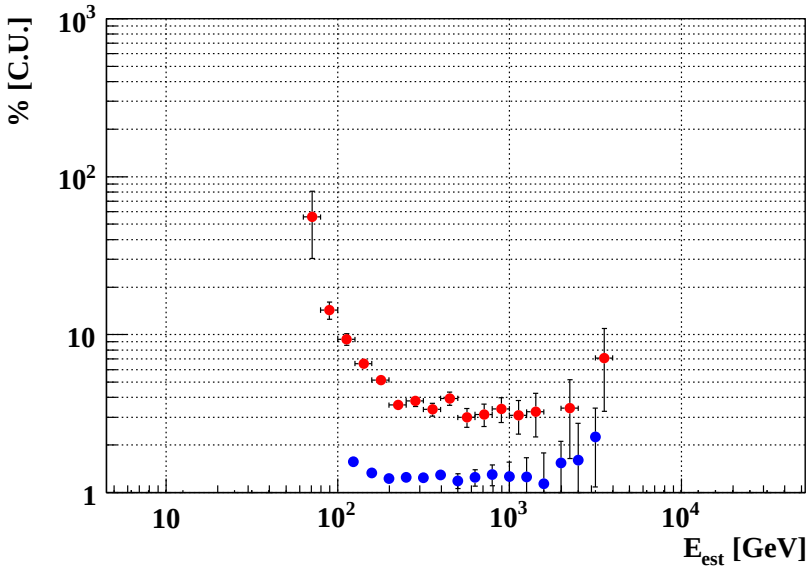

Figure 2.21: MAGIC integral (blue dots) and differential (red dots) sensitivities computed from the selected stereo Crab Nebula data sample.

2.4.3.7 Higher level products

There are several higher level products that can be obtained from MAGIC observations, namely, skymaps, differential and integral spectra, and light curves. In case of no signal detection, upper limits to the differential and integral spectra can be computed. In the following all these products are briefly explained.

Skymaps: The *disp* method allows for an unbiased reconstruction of the *arrival direction* in the camera plane coordinates of the γ-ray-like events. Thus, if the distribution of background events over the camera is modeled, a map of *excess events* can be obtained in the shape of a bi-dimensional histogram covering the camera. Such a bi-dimensional histogram can be converted to sky coordinates, consequently producing a *skymap* of excess events.

Although the estimation of the *disp* parameter for γ-ray-like events is relatively straightforward, the modelling of the background is complicated. The cameras acceptances are not homogeneous. Besides, other factors like field stars, malfunctioning pixels, and trigger inefficiencies can magnify such inhomogeneities. The zenith angle dependence of the instrument sensitivity must be also taken into account. There are different background estimation methods depending on the observation mode. For *on–off* observations, the background model is built from the *off* data assuming an isotropic *arrival direction* of the events. In the case of *wobble* observations, where the background is estimated from the same dataset, the effect of the cameras inhomogeneities is smoothed. The camera is divided into two halves, one containing the source position and the other containing only background events; then, the background model is built from the alternating halves of the camera that contain only background, so the inhomogeneities are significantly compensated.

The obtained bi-dimensional histogram of *excess events* is eventually smeared by a bi-dimensional Gaussian function, with a σ equal to the angular resolution corresponding to the considered energy range.

The skymap of *excess events* can be translated into a skymap of Test Statistics (TS) values, computing the significance for each bin attending to Eq. 2.17. The null hypothesis distribution of the TS looks like a Gaussian function, but may have a slightly different shape or width. The null hypothesis distribution is built out of a small MC simulated γ-ray sample and the background model. Deviations of the distribution from the null hypothesis distribution at positive values my indicate the presence of a source in the FoV. Examples of TS skymaps and their corresponding TS distributions can be found in Fig. 2.22.

The angular resolution can be obtained out of the skymap (with no smearing) of a bright point-like source, either an actual source like the Crab Nebula or an artificial source from MC simulated γ-ray events. It is usually computed as the sigma of a 2-dimensional Gaussian fit, and it is sometimes referred as γ-ray PSF. In Fig. 2.23 the angular resolution from stereoscopic observations as well as the 68% γ-ray events containment radius are shown.

Spectra and light curves: The differential spectrum of a source can be defined as the total number of photons coming from the source and reaching the observer position, per unit or energy, area, and time. Thus, the observed spectrum, typically expressed in ph cm^{-2} s^{-1} TeV^{-1}, can be computed as

$$\phi(E) = \frac{dN_\gamma}{dt_{eff} dA_{eff}(E) dE}, \tag{2.22}$$

where N_γ is the number of *excess events*, t_{eff} is the effective observation time, and $A_{eff}(E)$ is the effective collection area. The differential treatment in Eq. 2.22 of the effective collection area is translated into a fine energy binning from the computational point of view. Assuming a steady emission from the source, the differential nature with respect to the effective time can be dropped, considering a single time bin encompassing all the observation, and with duration t_{eff}.

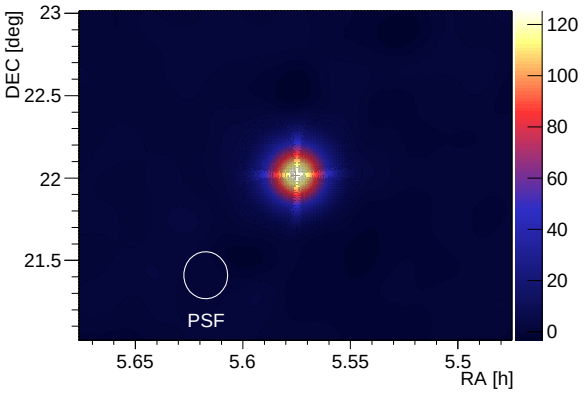

(a) Low energy skymap

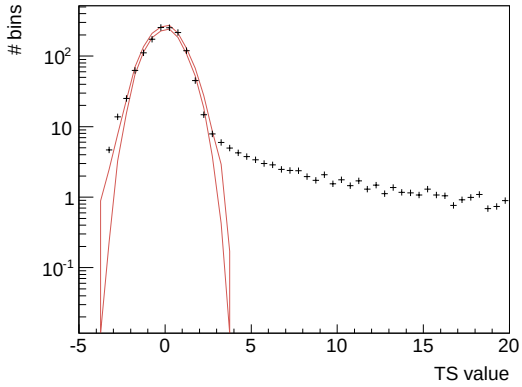

(b) Low energy significance distribution

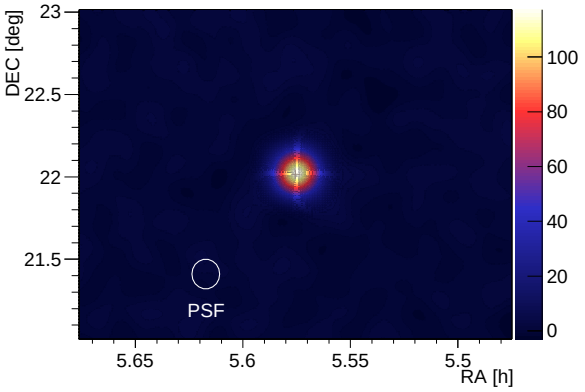

(c) Full range skymap

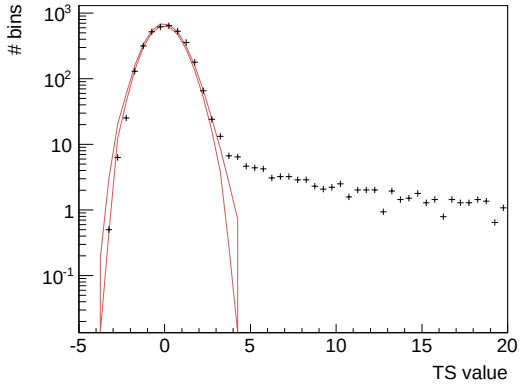

(d) Full range significance distribution

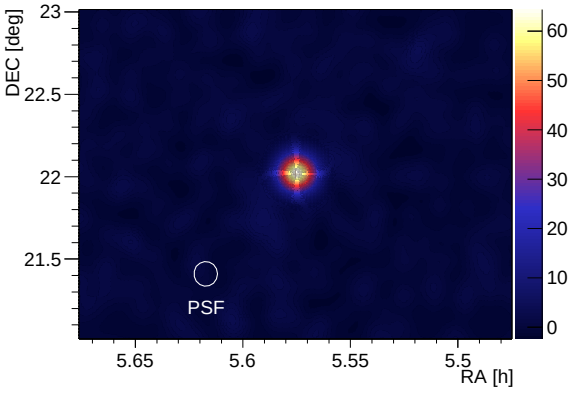

(e) High energy skymap

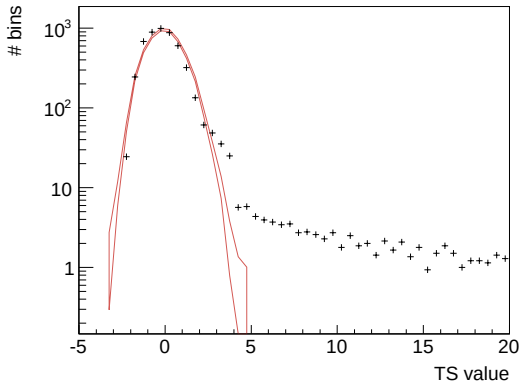

(f) High energy significance distribution

Figure 2.22: Crab Nebula TS skymaps from MAGIC data for several sets of cuts which optimize the sensitivity in three different energy ranges (see Table 4.5). Low energy range skymap considers an analysis energy threshold of 120 GeV (Fig. 2.22a). Full range skymap considers $E > 250$ GeV events (Fig. 2.22c). High energy range skymap considers E>1 TeV events (Fig. 2.22e). The white circle depicts MAGIC γ-ray PSF for the given energy range. The red line depicts the null hypothesis distribution. All the energies are referred to the estimated energy of the events.

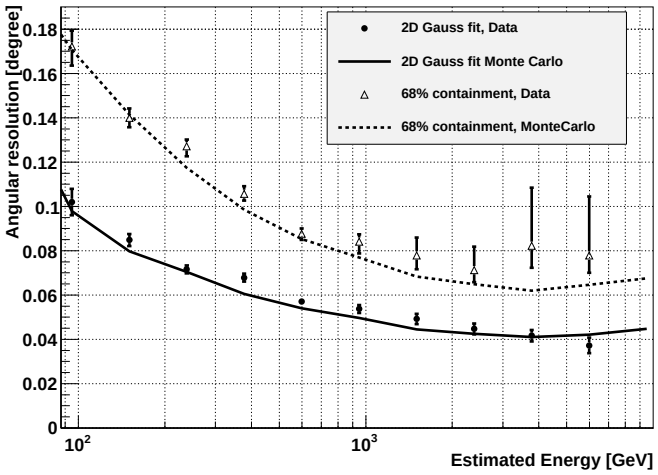

Figure 2.23: MAGIC angular resolution and 68% γ-ray events containment radius as computed from a MC simulated point-like source (lines), as well as from a Crab Nebula sample (dots and triangles). Figure extracted from [305].

In previous Sec. 2.4.3.6, the computation of the number of *excess events* out of the angular parameter's plot was explained. The computation of the effective collection area, and the effective observation time is explained in the following.

- Effective collection area $A_{eff}(E)$: This quantity is defined as the geometrical area around the telescope where any γ-ray shower of a given energy will be detected, folded with the trigger efficiency and the analysis efficiency after all analysis cuts:

$$A_{eff}(E,\theta) = \int_0^{2\pi}\int_0^{\infty} \epsilon(E,\theta,\phi,I) I dI d\phi, \tag{2.23}$$

  where E is the energy of the primary γ-ray, θ is the zenith angle, ϕ is the azimuthal angle, and I is the *impact parameter*. The efficiency $\epsilon(E,\theta,\phi,I)$ is computed from the MC simulated γ-ray events *test* sample as the ratio between the number of events surviving all the trigger and analysis cuts, and the total number of simulated events:

$$\epsilon(E,\theta,\phi,I) = \epsilon_{trigger}(E,\theta,\phi,I)\epsilon_{analysis}(E,\theta,\phi,I) = \frac{N_{\gamma}^{\text{After cuts}}}{N_{\gamma}^{\text{Total}}}. \tag{2.24}$$

  The effective collection area is smaller at low energies, since low energy events with large *impact parameters* will deposit few photons in the camera plane, and thus are more likely not to trigger the telescope or not to survive the image cleaning. On the contrary, high energy events with large *impact parameters* are more likely to survive the trigger and analysis cuts since they deposit more photons into the focal plane and form clearer images in the camera. An example of MAGIC effective collection area can be found in Fig. 2.24.

- Effective observation time t_{eff}: This quantity is defined as the the time the telescope was effectively recording events, namely, corrected from the dead time of the detector. This dead time is the duration of unavailability of the system to register any event while recording a triggered event. Assuming that the distribution of time differences between

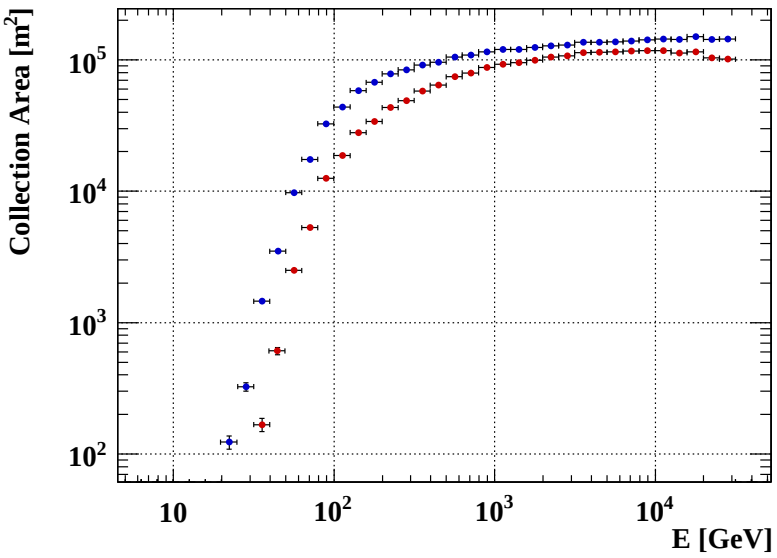

Figure 2.24: MAGIC effective collection area for stereoscopic observations. Blue dots represent the effective collection area if only the trigger efficiency is considered. Red dots represent the effective collection area if the rest of analysis cuts are also considered.

consecutive events is Poissonian, in the case of an ideal detector with negligible dead time, it can be expressed as

$$\frac{dN}{dt} = N_0 \tau e^{-\tau t}, \tag{2.25}$$

where τ is the ideal average rate, and N_0 is the total number of events the ideal detector would observe:

$$N_0 = \int_0^\infty \frac{dN}{dt} dt. \tag{2.26}$$

The total effective observation time is then

$$t_{eff} = \int_0^\infty t \frac{dN}{dt} dt = \frac{N_0}{\tau}. \tag{2.27}$$

Considering MAGIC as an ideal detector in terms of its dead time, the effective time is obtained from Eq. 2.27, where τ is obtained by fitting the data time differences to Eq. 2.25.

An example of a differential spectrum obtained from MAGIC Crab Nebula data can be found in Fig. 2.25, along with the corresponding SED.

In order to correct the obtained spectrum from the effect of the finite energy resolution of the telescope, as well as from the energy biases at the low and high end of the telescope's energy band, a spectral unfolding can be applied. Different unfolding methods have been implemented in the MAGIC analysis chain, namely, Tikhonov, Bertero, and Schmelling methods [307].

The variability of a source can be evaluated in terms of the so-called light curve. Such a light curve consists of the integral flux of the source in different time bins, hence all the points must share the same energy interval $[E_{min} - E_{max}]$. Each point i of a light curve can be computed,

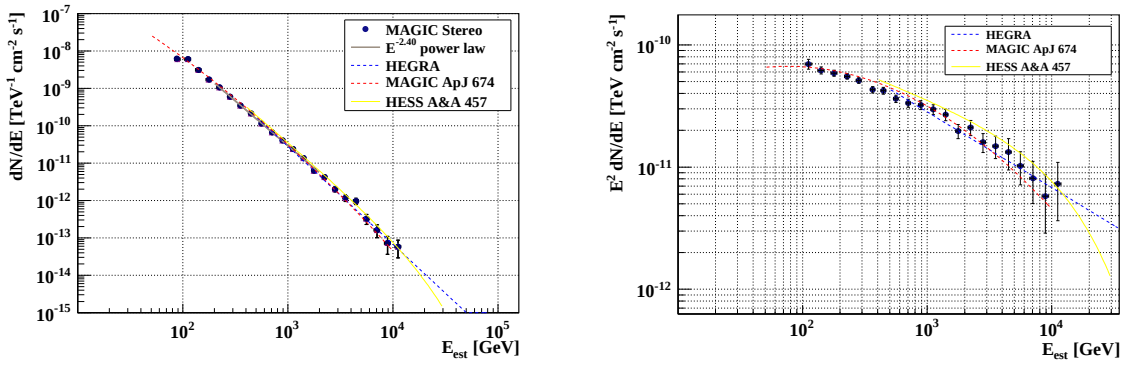

(a) Crab Nebula differential spectrum

(b) Crab Nebula spectral energy distribution

Figure 2.25: Crab Nebula differential spectrum (not unfolded) is shown in Fig. 2.25a. The corresponding SED is shown is Fig. 2.25b. In both cases the official fits from HEGRA, MAGIC and H.E.S.S. telescopes are shown.

after defining its time interval $[t_0^i - t_1^i]$, as

$$\Phi_{lc}^i = \int_{t_0^i}^{t_1^i} \int_{E_{min}}^{E_{max}} \phi(E) dE dt. \tag{2.28}$$

Eq. 2.28 only applies if the source is significantly detected in that energy bin and time interval. Otherwise, the corresponding light curve point is not an integral flux but and upper limit to the integral flux of the source.

Upper limits: Whenever no significant detection can be claimed, either in the complete energy range or in a certain energy bin, upper limits to the differential or integral flux can be computed at a certain CL.

The calculation of any flux upper limit requires the previous obtaining of the upper limit to the number of *excess events* N_{exc}^{UL} which, in the case of MAGIC analysis chain, is obtained through the so-called Rolke method [308]. Such a method computes the number of *excess events* for a given confidence interval assuming a Poisson distribution of the *excess events* and an approximately Gaussian distribution for the number of *background events*, both obtained from the angular parameter distribution (either *alpha* or θ^2 distribution, see Sec. 2.4.3.6). The Rolke method uses a fully frequentist treatment of the nuisance parameters, like the uncertainty on the background estimation and the efficiency of such estimation. In the particular case of MAGIC analysis, the uncertainty on the background estimation is set to a 30%, based on the systematic errors of the analysis method (see Sec. 2.4.3.8 below), and the efficiency is assumed constant and equal to 1.

In order to compute the flux upper limits certain assumptions must be made: first, that the source presents a steady emission; second, that the differential spectrum of the source can be expressed as a general function of the energy:

$$\phi(E) = K\ S(E), \tag{2.29}$$

where K is a normalization constant. The number of *excess events* expected in a certain bin of

estimated energy ΔE_{est} can be obtained as

$$N_{exc,\ \Delta E_{est}} = t_{eff} \int_0^\infty \phi(E) A_{eff}(E, \Delta E_{est}) dE, \tag{2.30}$$

where E refers to the true energy of the events, and the effective collection area depends on the true energy of the events but was obtained including the cuts in *estimated energy* that define the interval ΔE_{est}. From Eq. 2.30, the upper limit to the number of *excess events* can be translated into an upper limit to the normalization constant K as

$$K^{UL}_{\Delta E_{est}} = \frac{N^{UL}_{exc,\ \Delta E_{est}}}{t_{eff}} \frac{1}{\int_0^\infty S(E) A_{eff}(E, \Delta E_{est}) dE}. \tag{2.31}$$

If instead of the interval ΔE_{est}, only a lower limit for the *estimated energy* E_0 is imposed, then the integral flux upper limit can be calculated as

$$\Phi^{UL}(> E_0) = K^{UL}_{\Delta E_{est}} \int_{E_0}^\infty S(E_{est}) dE_{est} = \frac{N^{UL}_{exc,\ \Delta E_{est}}}{t_{eff}} \frac{\int_{E_0}^\infty S(E_{est}) dE_{est}}{\int_0^\infty S(E) A_{eff}(E, \Delta E_{est}) dE}, \tag{2.32}$$

where $S(E_{est})$ is the convolution of $S(E)$ with the energy resolution of the telescope.

Upper limits to the differential flux can be derived under the assumption that $S(E)$ can be locally described as a power law (where locally means within a given energy bin) of the form

$$S(E) = \left(\frac{E}{E_*} \right)^\Gamma, \tag{2.33}$$

where Γ is the spectral index and E_* is the pivot energy for the particular energy bin, defined as

$$E_* = \frac{\int_0^\infty E\ E^\Gamma\ A_{eff}(E, \Delta E_{est}) dE}{\int_0^\infty E^\Gamma\ A_{eff}(E, \Delta E_{est}) dE}. \tag{2.34}$$

Then, the normalization factor upper limit at the pivot energy can be expressed as

$$K^{UL}_{\Delta E_{est}}(E_*) = \frac{N^{UL}_{exc,\ \Delta E_{est}}}{t_{eff}\ \int_0^\infty A_{eff}(E, \Delta E_{est})\ (E/E_*)^\Gamma dE}\ . \tag{2.35}$$

Finally, since $S(E_*) = 1$ by construction, the upper limit to the differential flux at the pivot energy turns to be

$$\phi^{UL}_{\Delta E_{est}}(E_*) = K^{UL}_{\Delta E_{est}}(E_*) = \frac{N^{UL}_{exc,\ \Delta E_{est}}}{t_{eff}\ \int_0^\infty A_{eff}(E, \Delta E_{est})\ (E/E_*)^\Gamma dE}\ . \tag{2.36}$$

Additionally, it should be noted that the flux upper limit depends on the significance of the detection. The significance of detection has typically quite a strong impact on the upper limit to the number of excess events N^{UL}_{exc}, calculated with any statistical method, and in particular with the Rolke method. Quantitatively, a lower significance corresponds to a lower (thus more stringent) upper limit: *e.g.*, scanning values from $\sigma = -1$ to $\sigma = 1$, the upper limit worsens by a factor of ~ 2.5, as can be seen in Fig. 2.26. This is an intrinsic feature of the statistical method exploited in the analysis and it should be taken into account when comparing upper limits from different analyses and telescopes.

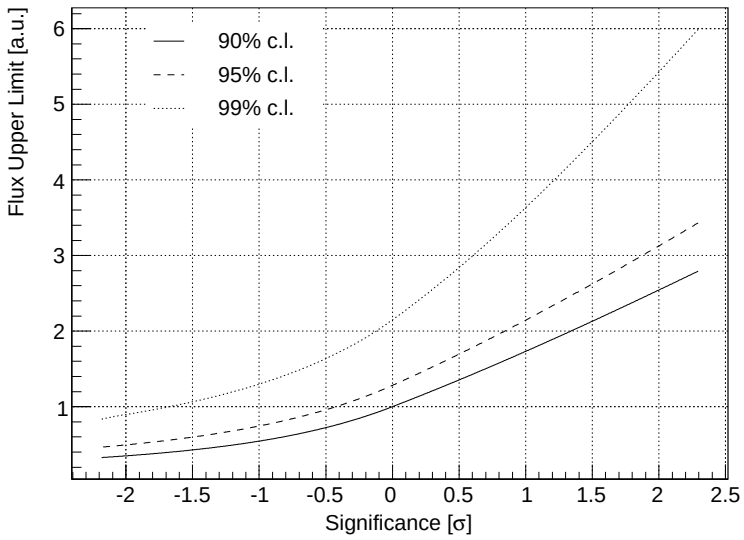

Figure 2.26: Flux upper limit dependence on the significance of detection σ, in arbitrary units. Three CLs are considered: dotted, slashed, and solid for 90%, 95% and 99% respectively.

2.4.3.8 Systematic uncertainties

While for weak sources the main uncertainty comes from the low statistic of excess events, strong sources allow for the estimation of systematic uncertainties due to the clear domination of the latter over the former. The systematic uncertainties of the MAGIC telescopes have been extensively studied and reported in [305]. Since the systematic errors are energy dependent, the uncertainties are studied in two different energy ranges: low energies corresponding to $E_\gamma \leq 100$ GeV, and medium energies corresponding to $E_\gamma \geq 300$ GeV. Three parameters are considered to illustrate the effect of the systematic uncertainties over power-law spectrum sources, namely, the energy scale, the flux normalization, and the spectral slope.

- Energy scale: the precision on the energy scale is of 17% at low energies and 15% at medium energies. The main sources of systematic uncertainties in this case are: the atmospheric transmission, the mirror reflectivity, the PMT electron collection and QE, the Winston cone collection efficiency, the signal extraction and the F-factor, and the temperature dependence of the channel gains.

- Flux normalization: the precision on the flux normalization is of 19% at low energies and 11% at medium energies. The main factors that contribute to this uncertainty are: the small discrepancies between MC simulations and data, the background subtraction, the camera inhomogeneity and broken pixels, the misspointing, the NSBL, and the readout dead time.

- Spectral slope: the systematic uncertainty on the spectral slope is estimated to be 0.15 and is estimated for the whole energy range. In this case, the uncertainty comes from the non-linearity of the readout, plus the unfolding of the energy spectra.

Finally, it is worth mentioning that the Crab Nebula spectrum measured by the MAGIC telescopes in stereoscopic mode is consistent with other experiments within 20–30%.

2.5 The X-ray waveband

The most energetic thermal processes in the Universe can be studied through X-ray photon emission. These photons, with energies between 0.1 and 500 keV, are expected from astrophysical regions containing extremely hot gas and plasmas, with typical temperatures ranging from $\sim 10^6$ K to $\sim 10^9$ K (see, *e.g.*, [309; 310], and references therein).

There are several mechanisms which can generate X-rays besides thermal black-body radiation: line emission, bremsstrahlung, synchrotron radiation, and IC radiation. Line emission is produced when atoms in a high temperature gas collide among them, promoting atom electrons to higher energy levels. The subsequent atomic de-excitations produce spectral lines whose energy denotes the gas temperature, while the intensity denotes the atomic abundances, and thus the gas composition. The collisions can also ionize the atoms, generating free electrons that emit bremsstrahlung radiation when accelerating around an already ionized atom. Part of these electrons can also reach relativistic velocities (*e.g.* through Fermi acceleration), and, if moving around magnetic field lines, can generate beamed X-ray radiation. Another mechanisms these relativistic electrons undergo to produce X-ray photons is IC scattering of low energy ambient photons, like the cosmic microwave background photons. Finally, atomic recombination is also a significant generator of X-ray radiation in these extreme environments.

The first detected source of extra-terrestrial X-ray radiation was the Sun, followed by Scorpius X-1 star. Since then, many stars have been studied in X-rays, like Hercules X-1 or Vela X-1, and even white and brown dwarf stars have been detected in X-rays. Type Ia supernova remnants have been also confirmed to be X-ray emitters. Black holes can be also bright sources of X-rays whenever an accretion disk of in-falling matter is present. Compact binary systems are also X-ray sources if part of the mass of the conventional star fall into the accompanying compact object, as in the case of accreting individual black holes. Some other sources of periodic X-ray emission, showing much higher frequencies, are the pulsars. Some less common galactic X-ray sources are magnetars and microquasars. Moving to galactic scales, AGNs present large accretion disks where X-rays are produced. Some other non-AGN galaxies are bright X-ray sources due to their hot gaseous corona. These hot gas reservoirs produce bremsstrahlung X-ray photons very efficiently. At even larger scales, galaxy clusters have been proved to be bright X-ray emitters due to the in-falling matter to the gravitational center of the system. This matter gains kinetic energy as it falls, eventually colliding with the already present matter in the center of the potential well. An example of an X-ray extended emission from a galaxy cluster is found in Fig. 1.2b.

Apart from these conventional sources and production mechanisms, there might a more exotic way of producing X-ray photons. As already mentioned, some dark matter candidates posses masses in the few keV energy range, like the case of the *sterile neutrino* (see Sec. 1.3.2). Consequently, X-ray telescopes can be also exploited for indirect dark matter searches. Besides this possibility, X-ray observations of large galaxies and galaxy clusters allow for the determination of the total baryonic content of such systems, unveiling large volumes of previously undetected hot gases. On top of that, the thermodynamic study of such gases provide information about the gravitational potential where they are embedded, and thus about the content of dark matter of the systems.

Due to the absolute opacity of the atmosphere to this type of radiation, astrophysical X-ray detectors must be space-based instruments. The history of X-ray astrophysics was initiated by balloon-borne experiments, followed by detectors on-board rockets. The first type of detectors is still used nowadays, but the field is now dominated by X-ray satellites. The current generation

of X-ray satellites is represented by the two fruitful space telescopes Chandra X-ray Observatory [311] and the X-ray Multi-Mirror Mission (XMM)-Newton [312]. In Chapter 3, a detailed search for *sterile neutrinos* is presented. Such a search is based on a deep Chandra-X-Ray Observatory (XRO) observation in the Willman 1 dwarf spheroidal galaxy core region. Thus, a brief description of the Chandra-XRO can be found in the following.

2.5.1 Chandra X-ray Observatory

Chandra-XRO provides sub-arcsecond imaging, spectrometric imaging, and high resolution spectroscopy over the energy range from 0.08 keV up to 10 keV. It was deployed by the Space Shuttle Columbia on 1999, and later placed in a highly elliptical orbit by an inertial upper stage (133.000 km apogee, 16.000 km perigee, 28.5° inclination, 64.2 h period). Chandra X-ray Observatory is technically described in terms of its X-ray telescope, and its science instruments (see [313], and references therein).

- X-ray Telescope: the High Resolution Mirror Assembly (HRMA) consists of four pairs of nested cylindrical paraboloid and hyperboloid, iridium and gold-coated mirrors. These mirrors are arranged in a Wolter type 1 geometry. The X-ray grazing angles range from $27'$ to $51'$ providing a good energy response for high energies, being able to focus X-rays up to 10 keV. The achieved angular resolution is of $0.5''$. The telescope focal length is of 10 m, providing an effective collection area of 0.04 m^2 at 1 keV.

- Science Instruments: there are two main detectors on-board Chandra, integrated in the so-called Science Instrument Module (SIM): the Advanced CCD Imaging Spectrometer (ACIS) and the High Resolution Camera (HRC). The SIM is located in the focal plane and is able to place into focus position, by request, either of the two instruments.
  The ACIS consists of two arrays of Charged Coupled Devices (CCDs): ACIS-I and ACIS-S. The first one is designed for imaging $16' \times 16'$ arc minutes fields while is optimized to be used together with the High Energy Transmission Grating (HETG). The ACIS-S3 chip has the best energy resolution of the system.
  As in the case of the ACIS instrument, the HRC comprises two different devices: the micro-channel plate imaging detectors HRC-I and HRC-S. The first has a FoV of $31' \times 31'$, being the largest among the Chandra imaging instruments. The second is optimized to be used together with the Low Energy Transmission Grating (LETG). The HRC has the best angular and time resolutions ($< 0.5''$ and 16 msec respectively).
  Between the HRMA and the SIM two transmission gratings are present. These set of gold gratings produce spectra dispersed in space at the focal plane where the SIM is located. The HETG is used for high-resolution spectroscopy of bright hard sources in the energy band from 0.4 keV to 10 keV, with an energy resolution varying from $\sim 0.12\%$ at 1.5 keV to $\sim 0.5\%$ at 6 keV. The LETG is used for high-resolution spectroscopy of bright soft sources in the energy band from 0.07 keV to 0.2 keV, with an energy resolution of $< 0.1\%$.

A schematic diagram of the Chandra X-ray Observatory can be found in Fig. 2.27, where the main subsystems are indicated.

With a very efficient duty cycle of $\sim 70\%$ and an already extended mission length of more than 12 years, the Chandra X-ray Observatory scientific impact represents, along with XMM-Newton results, a breakthrough in the history of X-ray astrophysics (see, *e.g.*, [314], and references therein). Due to its excellent sensitivity and energy resolution, the Chandra X-ray

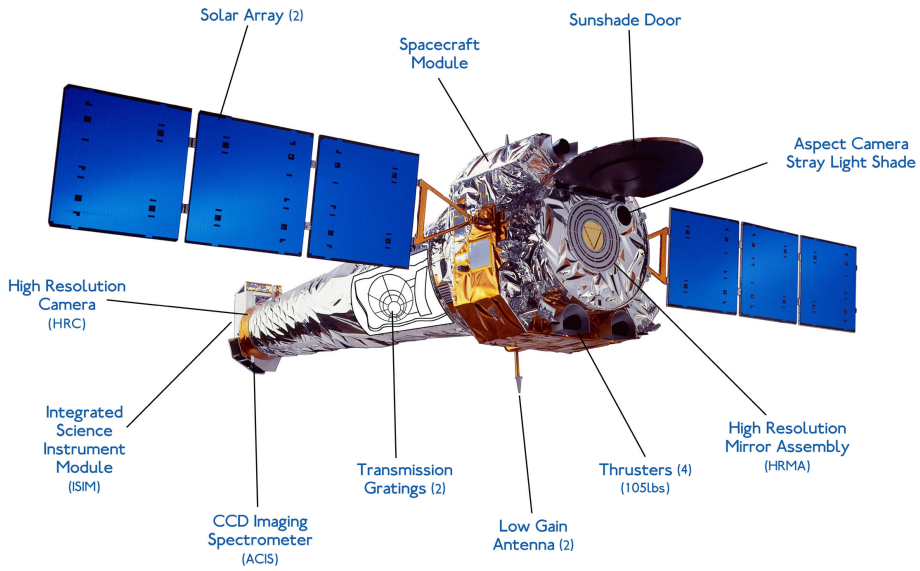

Figure 2.27: Schematic diagram of the Chandra X-ray Observatory. The main subsystems are labeled. Image credit: NASA/CXC/NGST.

Observatory is well suited for the searches of faint astrophysical lines as those predicted from decaying *sterile neutrinos*, as shown in the Chapter 3.

Chapter 3

Dark Matter searches in dwarf Spheroidal Galaxies

This chapter is devoted to indirect dark matter searches in dSph galaxies. Two different energy bands have been exploited: the X-rayband thanks to the Chandra-XRO satellite data, and the VHE γ-ray band thanks to the MAGIC-I telescope observations. In Sec. 3.2 the observation of the dSph Willman 1 with the MAGIC telescope and its interpretation in terms of dark matter searches in the γ-ray regime are presented. In Sec. 3.3 a Willman 1 Chandra-XRO observation was the starting point for a point-like source population study and a diffuse component analysis of the object which allowed to place constraints to the *sterile neutrino* as dark matter particle candidate. Finally, in Sec 3.4, an observation of Segue 1 dSph with the MAGIC telescope is presented along with a dark matter focused interpretation of the results thanks to extensive dedicated simulations. Conclusions and outlook are found in Sec. 3.5.

3.1 Introduction to dwarf Spheroidal galaxies

In the light of the CCM, N-body simulations show a hierarchical distribution of dark matter structures down to the mass-resolution limit of the simulations ($\sim 2 - -4 \times 10^3$ $M_\odot$), expected to extend to even smaller scales [38; 171]. Under this hypothesis, the Milky Way dSph galaxies have been proposed to be substructures of the Galactic dark matter halo which, along their evolutionary history, may have attracted the baryonic matter that nowadays form their star members[159; 170; 315; 316; 317].

DSph galaxies are, besides the globular clusters, the smallest astrophysical objects where the kinematics of their components allow to study their dark matter content and structure, pointing to these objects as the most dark matter dominated systems known so far [13]. DSph galaxies form a subcategory within the dwarf galaxies, by far the most numerous type of galaxies in the Universe. Due to their faint nature, with luminosities ranging from 10^2 $L_\odot$ to 10^8 $L_\odot$, these objects are relatively new discoveries. The first finding of this type of astrophysical objects was made in 1938, when Sculptor and Fornax dSph were identified [318] as new satellite galaxies of the Milky Way. From this date up to 1994, when Sagittarius dSph was identified, seven other dSph were discovered, the faintest of them being Ursa Minor with a magnitude of $M = -8.9$. It was not until the Sloan Digital Sky Survey (SDSS) [40] started to provide new data, that fainter dSph galaxies could be discovered. From 2005 on, when Willman 1 [319] and Ursa Major I [320] discoveries were made public, more than a dozen new dSph have been found

down to a magnitude of $M = -1.5$ in the case of Segue 1 [321]. The pre-SDSS dSph galaxies were distinguished from the globular cluster population based on the relation between absolute magnitude and half light radius: for a given magnitude, a typical globular cluster half light radius is much smaller ($r_h \gtrapprox 10$ pc) than the typical dSph one ($r_h \gtrapprox 100$ pc). Although for most of the new SDSS dSph galaxies this relation still holds, some ultra-faint objects like Willman 1 and Segue 1 have half light radii of some tens of pc which makes its classification harder. In these cases, the distinction is made based on kinematics and chemical composition. Despite the fact that velocity dispersion ranges in the interval from 5 to 15 km s^{-1} for both, globular cluster and dSph galaxies, it can be inferred that, due to their characteristic r_h, the dynamic mass of globular cluster is dominated by stars while for the dSph is strongly dominated by dark matter [322]. As for their chemical composition, globular cluster present metal-rich stars with a small metallicity spread while dSph galaxies star members are metal-poor and show a larger metallicity spread [323].

The population of ultra-faint dSph galaxies is very interesting in terms of indirect dark matter searches as well as for galaxy formation studies at small scales. The discovery of this new class of dSph galaxies might also contribute to the solution of the so-called missing satellite problem [170; 315; 322; 324] by partially filling the gap between the observed satellite galaxies and the predictions from N-body cold dark matter simulations.

Several reasons place dSph galaxies as excellent targets for indirect dark matter searches, namely:

- The kinematics of their star members allow to study their dark matter content and structure, pointing to these objects as the most dark matter dominated systems known so far in our Universe [13].

- Due to their large mass-to-light ratio and their relatively large half-light radius, as compared to the population of star members, the effect of the baryonic matter is not expected to play a crucial role on the dark matter distribution.

- They are expected to have very low intrinsic background at high energies. Their low baryonic content disfavors the chance to find conventional X-ray and γ-ray sources (*e.g.* binary systems containing compact objects, supernova remnants, pulsar wind nebulae). Moreover, no gas has been found in their interstellar medium so far, consequently preventing emission from cosmic rays interaction with the dSph medium. These facts turn dSph as background free targets for dark matter searches in the X-ray and γ-ray energy band [2; 325].

- Their location is sufficiently well known so their observation with different current instruments is much easier than in the case of completely dark substructures, which would require a serendipitous discovery[1].

- They are relatively nearby objects, most of them closer than 100 kpc from the Galactic Center. Thus, albeit their low intrinsic flux from dark matter annihilation or decay, the expected flux at the observer position is the largest among the known targets [175].

- Some dSph are located at high galactic latitudes, where a possible X-ray or γ-ray contamination by Galactic background is sub-dominant.

[1] A systematic search for such dark substructures is presented in Chap. 4 of this work.

Indirect searches for dark matter particle candidates in the γ-ray band (as WIMPs in the GeV-TeV mass range) have been conducted in those dSph galaxies which presented the most favorable detection prospects. So far, the contribution from IACTs have been the following: MAGIC observed Draco [326], Willman 1 (this work, [1]), and Segue 1 (this work, [3]); VERITAS observed Draco, Ursa Minor, Bootes 1 and Willman 1 [327]; H.E.S.S. observed Sagittarius [328], Sculptor and Carina [329]; Whipple observed Ursa Minor [272]. Fermi-LAT data have been also used for indirect dark matter searches in dSph galaxies. Due to its full-sky coverage, a wider set of dSph galaxies have been studied: Bootes I, Carina, Coma Berenice, Draco, Fornax, Sculptor, Segue 1, Sextans, Ursa Major II, and Ursa Minor [268].

As for the X-ray regime, indirect dark matter searches have been conducted in several dSph galaxies considering the dark matter to be formed of *sterile neutrinos* in the few keV mass range. The current generation of X-ray space telescopes has observed several of these objects: XMM-Newton observed Fornax [83], Suzaku observed Ursa Minor [84], Swift observed Segue 1 [85], and Chandra-XRO observed Draco [330] and Willman 1 [86] and [2] (this work).

In the following, two of these dSph galaxies will be introduced, namely Willman 1 and Segue 1, accompanied by a detailed description of indirect dark matter searches in the VHE γ-ray band for both sources, as well as in the X-ray band for the first of them.

3.1.1 Willman 1

Willman 1 object was discovered in the SDSS data as a faint overdensity of resolved stars in the R-band [319] towards the constellation of Ursa Major, at a distance to the observer of 38 kpc. Its classification has not been free of debate due to the fact that Willman 1 main characteristics lie between those typical for globular clusters and those expected in faint dSph galaxies, as shown in Table 3.1.

Table 3.1: Willman 1 main characteristics

Coordinates (R.A., Dec.)	$10^h40^m22.3^s$,$51°03'03.6''$
Year of discovery	2004
Distance to the observer	38 ± 7 kpc
Magnitude (M_V)	~ -2.5
Number of resolved stars	45
Half-light radius (r_h)	21 ± 7 pc
Luminosity	855 $L_\odot$
Mass	6×10^5 $M_\odot$
Mass-to-light	~ 700 $M_\odot/L_\odot$
Systemic velocity (v_{sys})	-12.3 ± 2.5 km s^{-1}
Velocity dispersion (σ)	$4.3\pm^{+2.3}_{1.3}$ km s^{-1}

Willman 1 main characteristics extracted from [331; 332].

After its discovery, deeper observations with the Keck II telescope and its DEIMOS spectrograph [333] were performed, and a very high mass-to-light ratio (~ 700) was inferred [331]. The source was considered by that time the most dark matter-dominated dSph satellite galaxy of the Milky Way, and consequently an attractive target for indirect dark matter searches [13; 334]. Further studies cast some doubts over the established nature of Willman 1 as a dSph galaxy, and suggested the hypothesis that the source might be a tidally disrupted metal-poor globular

cluster instead [335]. The latest observations and spectroscopic data from Willman 1 member stars strongly favored the dSph galaxy nature of the object, although they also suggested that Willman 1 may not be in dynamical equilibrium [332], and therefore its gravitational modelling should be revised. Deeper observations which could eventually increase the number Willman 1 star members, and consequently the statistics of the kinematic data, would be required in order to tell apart the dynamical status of the source, though. Due to the luminosity of the object, Willman 1 is currently considered within the subset of ultra-faint dSph galaxies. An SDSS optical image of Willman 1 region is shown in Fig. 3.1, where the object star members are highlighted.

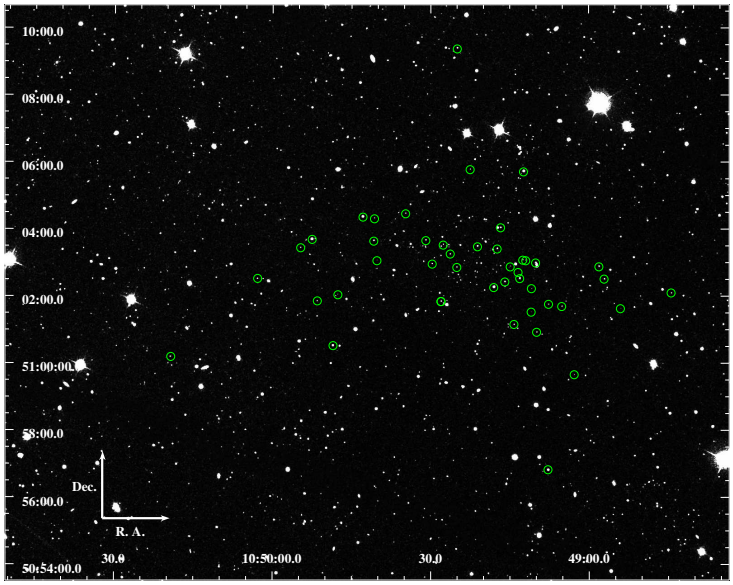

Figure 3.1: Willman 1 optical image in the R-band from the SDSS. Willman 1 star members are circled in green and have been extracted from [332]. Equatorial coordinates are used.

3.1.2 Segue 1

Segue 1 was discovered in the Sloan Extension for Galaxy Understanding and Exploration (SEGUE) [336], later observed with the Subaru [337] telescope, and initially classified as an unusually extended globular cluster [321]. It is located towards the constellation of Sagittarius, at a distance to the observer of 23 kpc. Its close proximity to the Sagittarius stream makes that the kinematic study, and even the identification of its star members, a very delicate issue. The actual nature of Segue 1 was a matter of controversy [321; 338; 339; 340], since the main astrophysical characteristics of the object (see Table 3.2) lay in the frontier between dSph galaxies and globular clusters.

More sensitive observations with the Keck II optical telescope and its DEIMOS spectrograph [333] allowed to extend the set of Segue 1 star members from 24 up to 71 (see Fig. 3.2). These new data allowed a clearer classification for Segue 1 as an ultra-faint dSph galaxy, placing Segue 1 as the most dark matter-dominated astrophysical object known so far, with a mass-to-light ratio estimated to be 3400 $M_{\odot}/L_{\odot}$ [341; 342]. Despite this impressive figure, the uncertainties in the total mass estimation ought to be taken into account. Therefore, an extension to the star members set would be desirable in order to further investigate the enigmatic

Table 3.2: Segue 1 main characteristics

Coordinates (R.A., Dec.)	$10^h07^m03.2^s$,+16°04′25″
Year of discovery	2006
Distance to the observer	23 ± 2 kpc
Magnitude (M_V)	$-1.5^{0.6}_{0.8}$
Number of resolved stars	71
Half-light radius (r_h)	28^{+5}_{-4} pc
Luminosity	340 $L_\odot$
Mass	$5.8^{+8.2}_{-3.1}$ $M_\odot$
Mass-to-light	$\sim$ 3400 $M_\odot/L_\odot$
Systemic velocity (v_{sys})	208.5 ± 0.9 km s^{-1}
Velocity dispersion (σ)	$3.7\pm^{+1.4}_{-1.1}$ km s^{-1}

Segue 1 main characteristics extracted from [322; 341].

source dynamics and shed more light about its dark matter distribution.

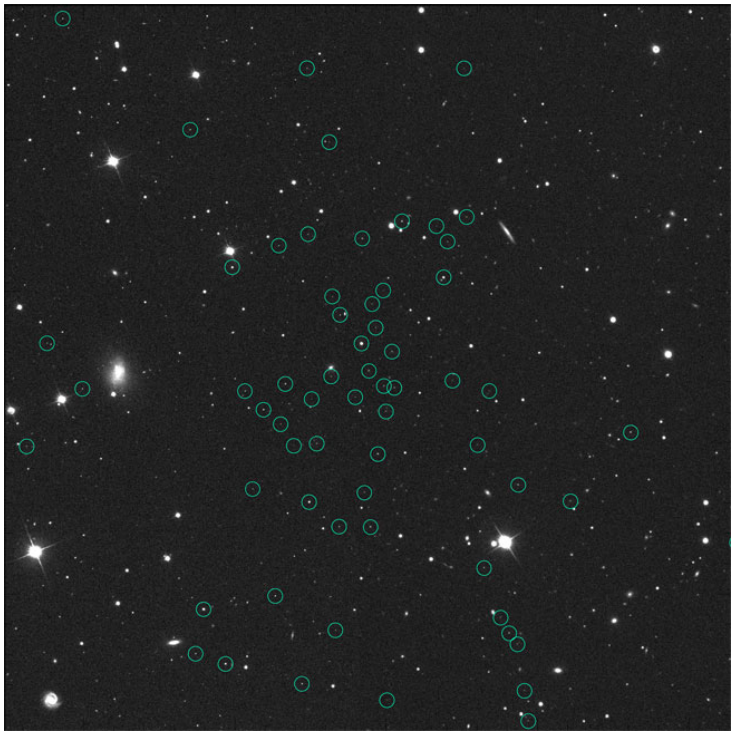

Figure 3.2: Segue 1 image from Keck II 10m-telescope. The image accounts for a total exposure of 5400 seconds in the 6400-9100 $\AA$ waveband. Segue 1 star members are circled in green. Credit: Marla Geha & W. M. Keck Observatory.

3.2 Dark matter searches in Willman 1 with MAGIC

As already mentioned in Sec. 3.1.1, Willman 1 is a good target to expect a dark matter originated γ-ray signal. The MAGIC observations of this object and its data analysis are described below. Next, results in the context of dark matter annihilation γ-ray emission are presented.

3.2.1 Observations description and data analysis

Willman 1 was observed in single telescope mode with MAGIC-I, while the second of the MAGIC telescopes was still under construction. The observations took place from late January to early March 2008. The source was surveyed at zenith angles between 22° and 30°, which guarantees the lowest energy threshold considering Willman 1 declination. The dataset is divided into two different subsets: 16.8 hours were taken in the so-called ON observation mode, where the source nominal position coincides with the center of the MAGIC camera; another 9.3 hours were taken in the so-called OFF observation mode, where the telescope tracks a dark patch in the sky where no γ-ray emission is expected, close to the source nominal position, and used for background estimation purpose. More details in both subsets can be found in Table 3.3.

Table 3.3: Willman 1 *MAGIC* dataset

Date	$t_{eff}[h]$	Z.A. [°]
2008/01/17	0.5	24.5 – 27.5
2008/02/05	2.2	22.0 – 30.5
2008/02/07	1.2	23.0 – 29.0
2008/02/08	1.6	24.0 – 30.5
2008/03/28	1.0	22.5 – 27.0
2008/03/29	2.0	22.5 – 30.0
2008/03/30	2.0	22.5 – 30.0
2008/03/31	1.3	23.0 – 30.0
2008/04/02	1.0	23.0 – 31.0
2008/04/03	1.8	22.5 – 30.0
2008/04/04	0.6	22.5 – 25.5
2008/04/05	0.9	22.5 – 26.0
2008/04/06	0.9	22.5 – 26.0

(a) Willman 1 *MAGIC* ON dataset

Night	t_{eff} [h]	Z.A. [°]
2008/02/05	0.9	22.5 – 26.5
2008/02/08	0.9	22.5 – 26.5
2008/03/28	0.8	22.5 – 25.5
2008/03/29	0.9	22.5 – 24.0
2008/03/30	0.9	22.5 – 24.0
2008/03/31	1.0	22.5 – 25.0
2008/04/02	0.8	22.5 – 24.5
2008/04/03	0.7	22.5 – 23.5
2008/04/04	0.8	22.5 – 23.5
2008/04/05	0.8	22.5 – 23.5
2008/04/06	0.7	22.5 – 23.5

(b) Willman 1 *MAGIC* OFF dataset

As a convention within MAGIC Collaboration, the observation *night* refers to the date of dawn after regular observations. t_{eff} stands for the effective observation time (see Sec. 2.4.3.7). Z.A. holds for the zenith angle window of the observation.

Data were analyzed attending to the standard MAGIC analysis procedures for single telescope observations (for deeper details see Sec. 2.4.3). The data were calibrated and pixel signals were extracted and converted into a number of photoelectrons. Then, events likely to be triggered by the noise from the NSBL were discarded by means of an image cleaning: *i)* a minimum amount of six photoelectrons per *core* pixel and three photoelectrons for *boundary* pixels were required; *ii)* the pulse arrival time difference between adjacent pixels was required to be less than 7 ns. After the image cleaning, the surviving shower images were characterized based on the Hillas parameters. The same calibration, image cleaning and parametrization were applied

to both, ON and OFF datasets.

After the image cleaning and parametrization, all the data were subject to a quality selection process. Certain atmospheric conditions, like high humidity, have proven to affect the telescope overall response. Consequently, data taken under bad atmospheric conditions were rejected. The event rate after image cleaning is also a very significant quality estimator. Data showing fluctuations in the aforementioned parameter were disregarded. The distribution of the Hillas parameters also help to discriminate between good and bad quality data. Thus, data which presented deviations with respect to the mean dataset values of the Hillas parameters were also rejected. The same set of quality cuts were applied to both, ON and OFF datasets. Eventually, Willman 1 data showed an overall excellent quality, 15.5 hours (93% of the total dataset) surviving the quality cuts.

A further check that has to be done when dealing with ON-OFF mode observations is that both, ON and OFF datasets, match in their main characteristics. A comparison of the rates, image parameters distribution, and zenith angle ranges between both ON and OFF datasets was made. It was verified that the OFF dataset was a suitable background selection for the ON dataset since most of the before mentioned distributions were matching (see, *e.g.*, Fig. 2.14). The only exception is the zenith angle ranges, since the ON distribution has its upper limit at 31.0° while for the case of the OFF subset this limit is 26.5°. Although a full overlap is lost, that is not problematic since the zenith angle influence over the shower images is not significant below a zenith angle of $\sim 35°$.

The events characterization, which consist in assigning an estimated energy and a *hadroness* to each single event, was carried out following the methods presented in Sec. 2.4.3.5. The *hadroness* calculation was performed thanks to the RF method. The RF matrices were produced after training the algorithm with a subset of the OFF data sample, and a sample of MC simulated γ-ray events. Shower information for each event, like the Hillas parameters, were used to train the multivariate method. The following variables were considered: $Size$, $Width$, $Length$, $Size/(Width \times Length)$, $Conc$, $Dist$, $M3Long$, $RMSTime$, and $P1Grad$ (in Sec. 2.4.3.2 an explanation of each of the parameters can be found). The energy estimation also made use of a RF algorithm, in this case considering the following variables: $Size$, $Width$, $Length$, $Size/(Width \times Length)$, $Conc$, $Leakage1$, $Dist$, $P1Grad$, and the original MC energy of the events. As for the MC γ-ray events that were used in the production of both, hadroness RF and energy estimation RF matrices, it is worth mentioning that formed a subset of a MC γ-ray events production which shared the dataset zenith angle range and that considered the same PSF that characterized the telescope by the time the data was taken.

In order to check the validity of the event characterization and the proper performance of the analysis chain, the RF matrices were applied to a Crab Nebula dataset, also coming from ON mode observations, contemporaneous to Willman 1 data, and sharing the same zenith angle conditions as Willman 1. The same quality selection was applied to the Crab Nebula sample. After an analysis optimization, the estimated sensitivity of the analysis from these Crab Nebula data was $15\sigma/\sqrt{t}$ h] over a minimum analysis energy threshold of 100 GeV, supporting the proper functioning of the analysis chain.

3.2.2 Results

Willman 1 data was analyzed in a day-by-day basis, as well as in a cumulative basis. No significant VHE γ-ray signal was found in any of the analyses. The α-distribution plot corresponding to a cumulative analysis, and considering an analysis energy threshold of 100 GeV, is shown

in Fig. 3.3. Regarding the γ/hadron separation, a hadronness cut of 0.15 was applied to both ON and OFF datasets. This value optimized the sensitivity over the before mentioned Crab Nebula sample. For the significance computation, a signal region region $\alpha < 12°$ was considered. This signal region is slightly larger than for a point-like source to take into account a possible moderate source extension, as explained later. The OFF data were normalized to the ON data in the region where no signal is expected, i.e., between $\alpha = 30°$ and $\alpha = 80°$.

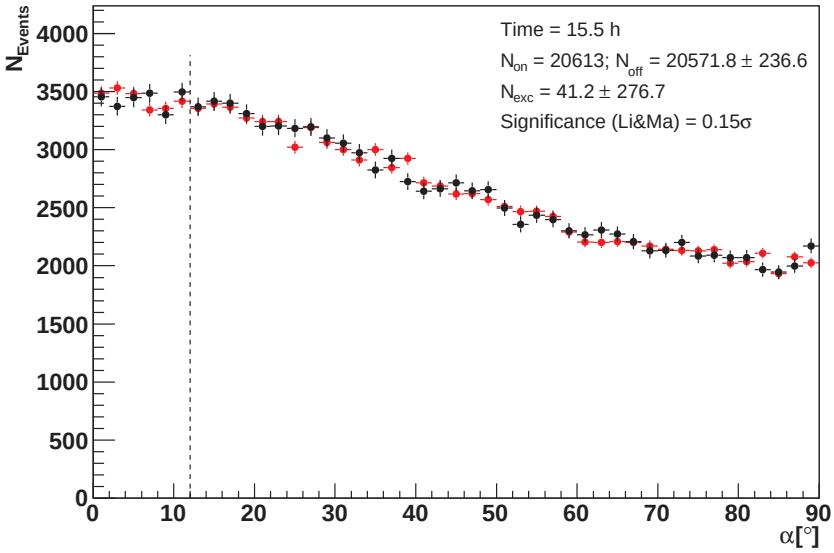

Figure 3.3: Willman 1 α-distribution as seen by MAGIC in 15.5 hours above an energy threshold of 100 GeV. The red dots represent the ON data events distribution and the black dots represent the OFF data events distribution normalized to the ON-data sample between $30° - 80°$. The signal region $|\alpha| < 12°$ where the signal is expected is limited by the vertical dashed line. An hadronness< 0.15 cut was applied to both ON and OFF data.

In Fig. 3.4 two significance maps for the sky region around Willman 1 position are shown. Fig. 3.4a considers a range in estimated energy from 200 to 342 GeV while for Fig. 3.4c the range from 342 to 585 GeV was considered. In both cases, the significance distributions are consistent with background fluctuations. The camera inhomogeneities at low energies, in single telescope observations, strongly affect the significance skymap production and its reliability. Thus, no energy skymap below 200 GeV is presented.

3.2.2.1 Upper limits for power-law spectra

Since no VHE signal was obtained, upper limits to the source's emission were obtained following the method outlined in Sec. 2.4.3.7. The upper limits to the number of excess events were obtained by means of the Rolke *et al.* method [308]. A systematic error of 30%, that accounts for the energy estimation and effective area calculation, was considered in the excess event upper limit calculation. The confidence level was fixed to a 95%.

Although the hypothetical Willman 1 spectrum is not known, certain assumptions on the spectral shape of the source must be assumed in order to calculate an upper limit to its flux. For the calculation of the flux upper limits presented in the current section, the hypothetical

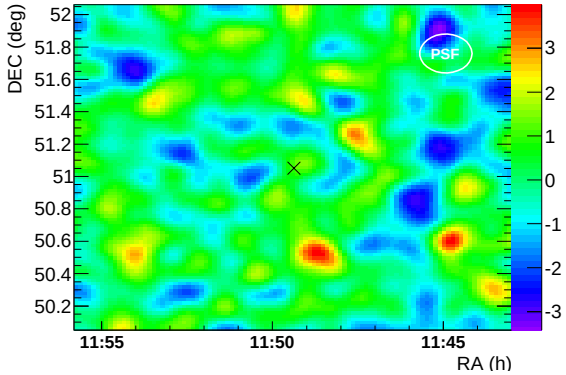

(a) Skymap between 200 and 342 GeV

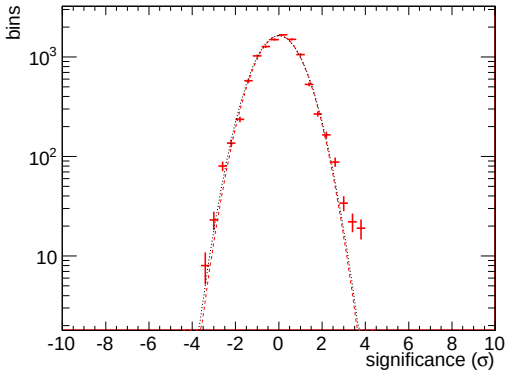

(b) Significance distribution between 200 and 342 GeV

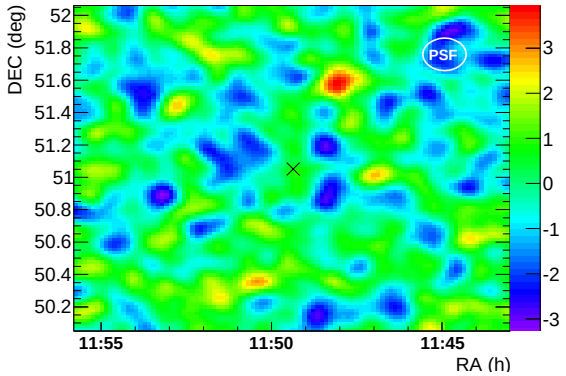

(c) Skymap between 342 and 585 GeV

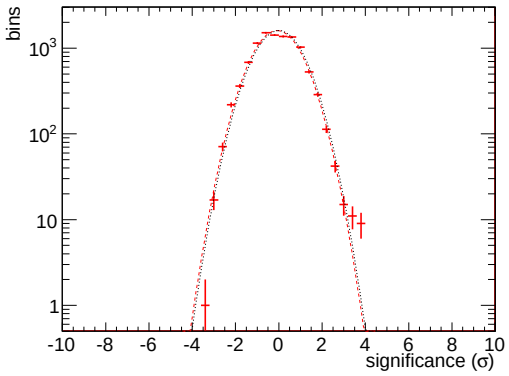

(d) Significance distribution between 342 and 585 GeV

Figure 3.4: Willman 1 MAGIC significance skymaps in two energy ranges: 200–342 GeV and 342–585 GeV. The significance distributions are compatible with the null hypothesis (meaning that no significant source is present in the region, depicted by the red dashed line) in both cases, therefore consistent with background fluctuations. The energy cuts are referred to the estimated energy of the events. The white circles in 3.4a and 3.4c depict MAGIC PSF for the given energy ranges.

source's emission was assumed to be described by a single power-law. A set of five different spectral indices running from $\Gamma = 1.0$ to $\Gamma = 3.0$ was used, wide enough so to accommodate most of the dark matter-like spectral slopes (see, *e.g.*, [343]).

Table 3.4 presents the differential spectrum upper limits, computed by means of Eq. 2.36, in four bins of estimated energy between 100 GeV and 10 TeV. Along with the upper limit in differential flux, the number of ON (N_{ON}) and OFF (N_{off}) events, the significance of detection, and the upper limit on the excess events are shown for each bin of reconstructed energy. In Fig. 3.5 these differential upper limits are shown together with the Crab Nebula differential flux (at 1%, 10% and 100% levels, extracted from [344]) for comparison purposes.

Integral flux upper limits were also computed following Eq. 2.32. The same set of spectral indices as for the differential flux upper limit calculation was assumed. The results, for six different thresholds in estimated energy, are shown in Table 3.5. These are presented in absolute flux terms as well as in a percentage with respect to the Crab Nebula flux. Beside these figures, the number of ON (N_{ON}) and OFF (N_{OFF}) events, the significance of detection, and the upper

Table 3.4: Willman 1 MAGIC differential flux upper limits.

ΔE [TeV]	$N_{\rm ON}$	$N_{\rm OFF}$	$\sigma_{\rm Li,Ma}$ 95% C.L.	N_{exc}^{UL}	$d\Phi^{UL}/dE$ [TeV^{-1}cm^{-2}s^{-1}]				
					$\Gamma=-1.0$	$\Gamma=-1.5$	$\Gamma=-2.0$	$\Gamma=-2.5$	$\Gamma=-3.0$
0.1, 0.32	53167	53555	-1.2	639.2	1.4×10^{-10}	1.5×10^{-10}	1.7×10^{-10}	2.1×10^{-10}	2.7×10^{-10}
0.32, 1	703	645	1.6	192	1.0×10^{-11}	1.1×10^{-11}	1.2×10^{-11}	1.4×10^{-11}	1.7×10^{-11}
1, 3.2	105	114	-0.6	26	6.0×10^{-13}	6.2×10^{-13}	6.8×10^{-13}	8.0×10^{-13}	1.0×10^{-12}
3.2, 10	8	8	0.0	10	7.1×10^{-14}	7.4×10^{-14}	8.1×10^{-14}	9.3×10^{-14}	1.1×10^{-13}

95% CL differential flux upper limits in units of TeV^{-1}cm^{-2}s^{-1} for five different power law γ-ray spectra with spectral index Γ, and four energy bins in TeV units.

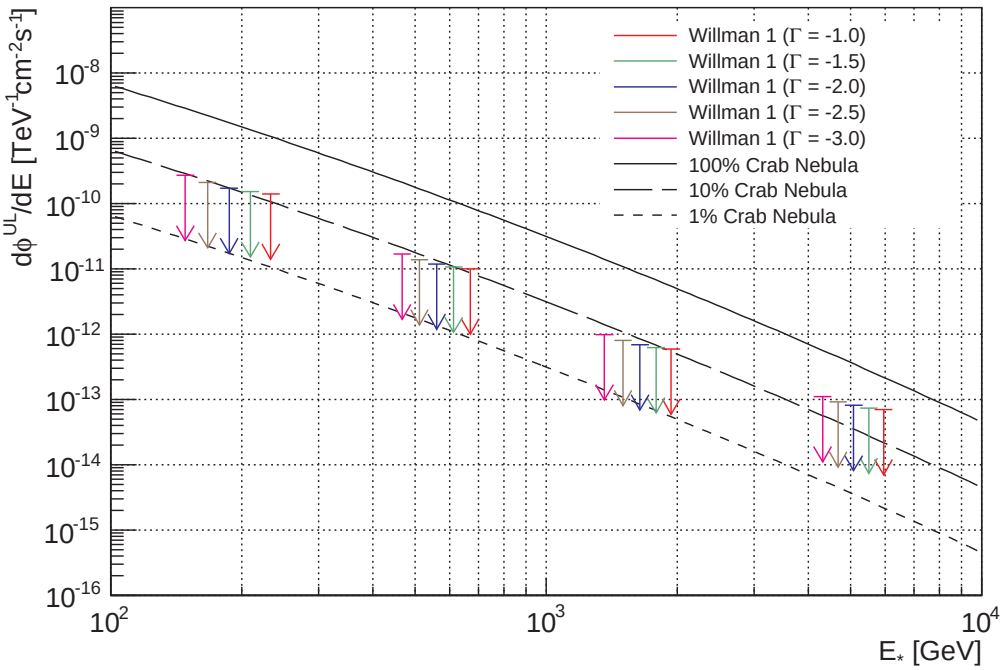

Figure 3.5: Willman 1 differential spectrum upper limits from MAGIC data as in Table 3.4. MAGIC Crab Nebula spectrum [344] at 100% (solid), 10% (long dashed), and 1% (dashed line) are depicted as reference.

limit on the excess events can be also found for each integral energy threshold.

As already pointed out, a noteworthy dependence between the significance of detection and the upper limit value (see discussion in Sec. 2.4.3.7) is manifested in Table 3.5. For this reason, in order to estimate the effect of the spectral slope and of the energy threshold on the value of the integral upper limit, without being biased by the fluctuation due to different values of the significance, the upper limits were recomputed again assuming a null value for $\sigma_{\rm Li,Ma}$. In Fig. 3.6 the experimental integral flux upper limits (i.e. number of ON events and number of OFF events independently extracted from the data) are depicted. In the same plot, equivalent flux upper limits obtained with a significance equal to zero (i.e. with number of ON events equal to the number of OFF events in the signal region of the $|\alpha|$-plot), are depicted as lines for

different values of the spectral index Γ. Thus, the dependence of the flux upper limit with the significance of detection is illustrated.

Table 3.5: Integral Willman 1 flux upper limits.

E_0 [GeV]	N_{ON}	N_{OFF}	$\sigma_{\mathrm{Li,Ma}}$ 95% C.L.	N_{exc}^{UL}	Φ^{UL} $\times 10^{-12}[\mathrm{cm}^{-2}\mathrm{s}^{-1}]$				
					$\Gamma=-1.0$	$\Gamma=-1.5$	$\Gamma=-2.0$	$\Gamma=-2.5$	$\Gamma=-3.0$
100	20613	20571	0.15	558	19.7 (4)	23.0 (4)	26.8 (5)	32.0 (6)	34.2 (6)
158	7687	7789	-0.82	189	6.7 (2)	7.2 (2)	7.5 (2)	9.0 (3)	9.7(3)
251	1321	1325	-0.07	154	5.0 (3)	5.1 (3)	5.9 (4)	6.1 (4)	6.2(4)
398	524	495	0.91	126	4.4 (6)	4.5 (6)	4.6 (6)	4.6 (6)	4.7 (6)
631	263	226	1.67	120	3.6 (9)	3.8 (10)	3.8 (10)	3.9 (10)	3.9 (10)
1000	104	124	-1.32	19	0.6 (3)	0.6 (3)	0.7 (4)	0.7 (4)	0.7 (4)

95% CL integral upper limits in units of $10^{-12}\mathrm{cm}^{-2}\mathrm{s}^{-1}$ for five different power law γ-ray spectra with spectral index Γ and several energy thresholds E_0. The numbers in parenthesis are the upper limits as a percentage of the Crab Nebula integral flux (extracted from [344]) above E_0.

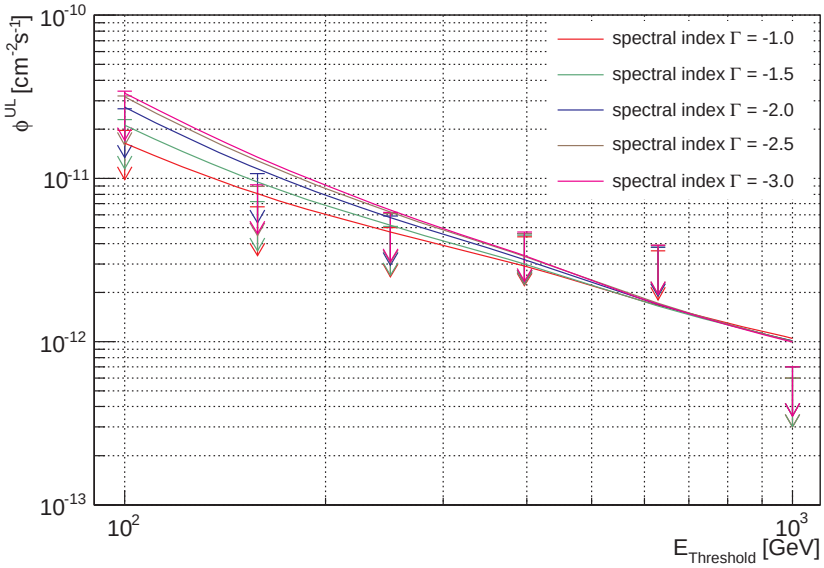

Figure 3.6: Integral flux upper limits from Willman 1 MAGIC data. The arrows indicate the integral flux upper limits as in Table 3.5 for different power-law spectra and energy thresholds. The dashed lines indicate the corresponding integral upper limits if zero significance $\sigma_{\mathrm{Li,Ma}}$ is assumed.

Concerning the dependence on the spectral index, it can also be seen that its change does not significantly vary the differential flux upper limits results. This is expected since the results should gradually converge, no matter the spectral index, if the energy binning goes finer (see Eq. 2.36). As for the integral flux upper limits, the spectral index change does vary the results, more significantly at low energies. This is due to the non-flatness of the effective collection area of the instrument (see Fig. 2.24 and Eq. 2.32). This effect can be found in all the flux upper limits computed for MAGIC data reported in this work. In the current case, the integral flux upper limits difference between the two extreme values of the spectral index, $\Gamma_{min} = -1$ and

$\Gamma_{max} = -3$, is a factor of 1.6 for $E_0 = 100$ GeV.

3.2.2.2 Upper limits for dark matter-like spectra

In the context of dark matter particle annihilation, and in order to place upper limits to a particular dark matter model, a spectral characterization of the possible γ-ray emission is required. Recalling Eq. 1.23, the integral photon flux due to dark matter annihilation is described as the product of two factors, namely, the astrophysical factor J, and the particle physics factor Φ^{PP}. In the following, the characterization of both factors is detailed.

As explained in Sec. 1.4.3.2, the astrophysical factor is determined by the dark matter density distribution in the object $\rho(r)$, and the field of view $\Delta\Omega$ that will fix the integration region. For the dark matter density distribution, the assumed parametrization was extracted from [13], where Willman 1 dark matter density distribution is described by a NFW profile (see Eq. 1.28) with a scale radius $r_s = 0.18$ kpc and a scale density $\rho_s = 4 \times 10^8$ $M_\odot kpc^{-3}$. Since Willman 1 is located at 38 kpc, the scale radius has an angular extension of $\sim 0.5^\circ$. Despite this extension, due to the steep nature of the NFW profile the source can be approximated as point-like for MAGIC-I telescope. Therefore, after inserting Eq. 1.28 into Eq. 1.25, and assuming an integration field of view defined by the telescope angular resolution (0.1° PSF), a final value of $J(\Delta\Omega) \sim 3.5 \times 10^{17} GeV^2 cm^{-5}$ was obtained.

As for the particle physics factor, four different mSUGRA models, with a *neutralino* as a WIMP, were exploited. These set of benchmark models were firstly proposed in [345] and refined in [346], where the *internal bremsstrahlung* contribution to the γ-ray emission was introduced. As already explained (a more detailed description of the mSUGRA theory can be found in Sec. 1.3.1), mSUGRA has five free parameters, namely, the scalar mass m_0, the gaugino mass $m_{1/2}$, the trilinear scalar coupling A_0, the ratio $\tan\beta$ of the Higgs vacuum expectation values, and the sign of the Higgs mass parameter sign(μ). Usually, this parameter space is represented as the plane defined by m_0 and $m_{1/2}$, after having fixed the other three free parameters. Within this plane, four regions can be identified: the *bulk region* (low m_0 and $m_{1/2}$, $m_\chi \sim 100$ GeV), the *focus point* (more massive m_0 and m_χ), the *funnel region* (large m_0 and $m_{1/2}$ values), and the *co-annihilation tail* (large $m_{1/2}$). The selected benchmark models are representative points of these four different regions in the mSUGRA parameter space. Denoted *I', F*, K', J'* for the *bulk, focus point, funnel,* and *co-annihilation* regions respectively, their characteristic parameters, and annihilation cross-section $< \sigma v >$, as well as their corresponding particle physics factor Φ^{PP} above 100 GeV (the energy threshold for Willman 1 MAGIC data analysis) can be found in Table 3.6. The differential particle physics factors as a function of the photon energy are depicted in Fig. 3.7 for each of the benchmark models. For the sake of completeness, it must be mentioned that the contribution of monochromatic lines to the annihilation spectrum were neglected in this study, due to its sub-dominant contribution as compared to the continuum emission.

Once both, the astrophysical factor and the particle physics factor were characterized, an estimated γ-ray flux for dark matter annihilation in Willman 1 could be computed following Eq. 1.26 as $\Phi^{est}(E > 100\ GeV) = J(\Delta\Omega)\Phi^{PP}(E > 100\ GeV)$. The integral flux upper limit from Willman 1 MAGIC data analysis was calculated for each of the benchmark models by introducing their particular spectral shapes in Eq. 2.32. In that way, a direct comparison between the expected γ-ray integral flux from dark matter annihilation and the integral flux upper limits could be done. Upper limits to the boost factor required to match both fluxes were obtained as $B^{ul} = \Phi^{ul}(E > 100\ GeV)/\Phi^{est}(E > 100\ GeV)$. Both, the estimated integral flux

Table 3.6: mSUGRA benchmark models for Willman 1 MAGIC data analysis.

	$m_{1/2}$ [GeV]	m_0 [GeV]	$\tan\beta$	A_0	$sign(\mu)$	m_χ [GeV]	$<\sigma v>$ [cm^3/s]	$\Phi^{PP}(E>100$ GeV) [cm^3 GeV^{-2} s^{-1}]
I'	350	181	35	0	+	141	3.62×10^{-27}	7.55×10^{-34}
F^*	7792	22100	24.1	17.7	+	1926	2.57×10^{-27}	5.98×10^{-34}
K'	1300	1001	46	0	−	565	2.59×10^{-26}	6.33×10^{-33}
J'	750	299	35	0	+	316	3.19×10^{-28}	1.23×10^{-34}

mSUGRA benchmark models as in [346]. *I', F*, K', J'* denote *bulk, focus point, funnel, and co-annihilation* regions respectively.

Φ^{est}, and the integral flux upper limit Φ^{ul}, together with the boost upper limit B^{ul} are presented in Table 3.7.

Table 3.7: Boost upper limits to Willman 1 dark matter γ-ray emission.

	$\Phi^{est}(E>100$ GeV) [cm^{-2}s^{-1}]	$\Phi^{ul}_{BM}(E>100$ GeV) [cm^{-2}s^{-1}]	B^{ul}
I'	2.64×10^{-16}	9.87×10^{-12}	3.7×10^4
J'	4.29×10^{-17}	5.69×10^{-12}	1.3×10^5
K'	2.32×10^{-15}	6.83×10^{-12}	2.9×10^3
F^*	2.09×10^{-16}	7.13×10^{-12}	3.4×10^4

Comparison of estimated integral flux Φ^{est} above 100 GeV for the benchmarks models shown in Table 3.6 and the integral flux upper limit Φ^{ul} above 100 GeV from MAGIC data analysis computed by considering each benchmark model spectral shape. The upper limit in the boost factor required to match both integral fluxes B^{ul} is also shown.

3.2.3 Summary and discussion

MAGIC single telescope observations in Willman 1 were carried out from January to March 2008. A total observation time of 16.8 hours was accumulated and a noteworthy fraction (93%) of the data survived the quality selection, ending up with a total effective time of 15.5 hours. No significant γ-ray excess was found after a thorough analysis of the data.

Upper limits to the differential and integral γ-ray fluxes were derived after assuming several power-law descriptions of Willman 1 emission in MAGIC energy range. The integral upper limits, of the order of 10^{-12} cm^{-2}s^{-1}, range from 2% to 10% CU depending on the energy threshold.

Integral flux upper limits were also computed for four different γ-ray spectra which characterize representative regions of the mSUGRA parameter space. After the calculation of Willman 1 astrophysical factor, and the particle physics factor for each of the aforementioned mSUGRA benchmark points, an estimation of the expected γ-ray flux from *neutralino* annihilation in the source could be obtained. The direct comparison between the integral flux upper limits and the estimated integral flux upper limits was then possible. As a conclusion, the required boost in flux, so the estimated flux matches the upper limit from MAGIC data, was constrained for each benchmark model.

Attending to those upper limits to the boost factors, it is clearly seen that the *funnel*

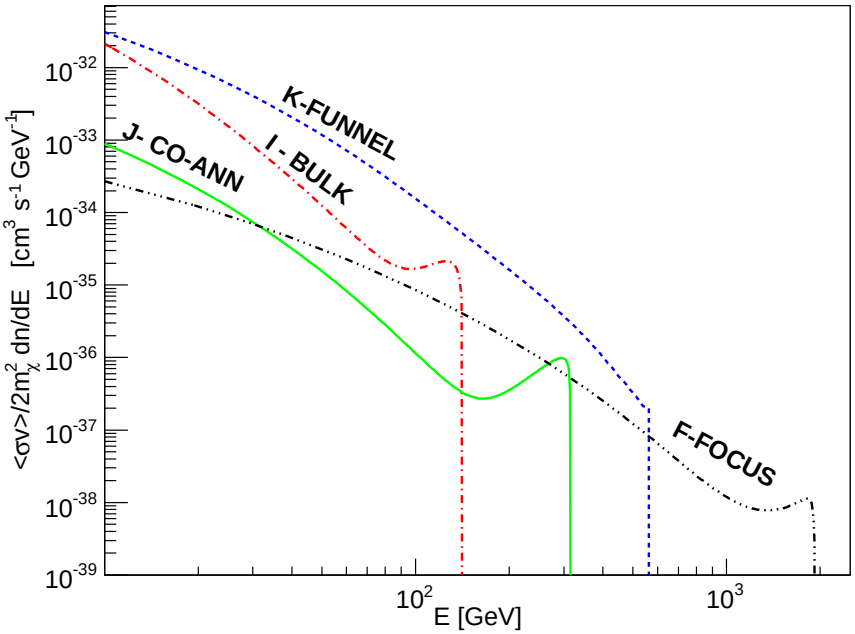

Figure 3.7: Differential particle physics factor (see Eq. 1.24) for the different benchmarks models from [346]. Line gamma emissions are not included, since their contribution to the flux is almost negligible.

region (labeled K' model) produced the smallest distance between flux upper limits and model estimations ($B^{ul} = 2.6 \times 10^3$) due to its larger particle physics factor contribution. This larger contribution is based on the equilibrium between the cut-off position, well inside MAGIC energy range, and its relatively low *neutralino* mass (since Φ^{PP} is modulated by the inverse of the of the *neutralino* mass squared, see Eq. 1.24). I' and F^* (*bulk* and *focus point* regions, respectively) models provided similar boost upper limits despite their significant differences in the spectral shape (see Fig. 3.7). I' model *neutralino* mass, and thus its spectral cut-off, are very close to Willman 1's analysis energy threshold. Nonetheless, this is compensated by the internal bremsstrahlung bump and the large photon yield of low *neutralino* masses models. On the contrary, F^* model photon yield is significantly lower, due to the high mass of the *neutralino* in this mSUGRA region, but this effect is reduced by the fact of the spectral extension into MAGIC energy range. Eventually, the $co-annihilation$ region provided the larger boost upper limit. Its photon yield is very scarce due to its low annihilation cross section.

It is important to bear in mind that the results above rely on a proper estimation of the expected γ-ray flux from *neutralino* annihilation, and should be critically analyzed. A noteworthy source of uncertainty in the flux estimation comes from the partial ignorance of the dark matter density distribution in Willman 1. The kinematic data from its stars is not sufficient to perfectly define the gravitation potential of the system. Thus, different dark matter density profiles are able to fit the data and may provide significantly different astrophysical factors. Moreover, the fact that Willman 1 could be affected by tidal disruption could dramatically change the dark matter density distribution of the system. Other effects that were disregarded are the inclusion of dark matter substructures in the density profile, which may increase the γ-ray flux by a factor from 2 [347] up to 20 [342], and the effect of baryons (although their influence in such a high

dark matter dominated system could be negligible). The so-called Sommerfeld enhancement was not taken into consideration either. This non-relativistic quantum effect can, in some cases, increase the annihilation cross section by several orders of magnitude [162]. However, its effect is significant only for WIMP masses on the TeV regime, thus none of the benchmark models would be affected. This fact also points to the need of considering a wider set of models, with a deeper study of the mSUGRA parameter space.

3.3 Dark matter searches in Willman 1 with Chandra-XRO

In this section, the indirect dark matter searches in Willman 1 presented so far, namely in the VHE γ-ray regime, are complemented with a search in the X-ray band. After some introduction about the scientific case, Willman 1 observations by Chandra-XRO are detailed below, followed by a description of the performed analysis. Eventually, results in the context of decaying dark matter are presented.

3.3.1 Observation description and data analysis

Willman 1 was observed by the Chandra-XRO during January 2010 (further details on the observation can be found in Table 3.8). The observations were conducted with the Advanced CCD Imaging Spectrometer (ACIS) in very faint (*VFAINT*) mode. Chips 0,1,2,3,6,7 were used with Willman 1 positioned near the ACIS-I aimpoint on the ACIS-I3 chip. Data reduction was performed using standard procedures [348] within the Chandra-XRO Interactive Analysis of Observations (CIAO) software. The level 1 event file was reprocessed to include grades 0,2,3,4, and 6. The total usable data is reduced to 100.68 ks after removing periods of potential flares and elevated background. Fig. 3.8 shows the resulting Chandra-XRO X-ray image in the 0.5–6.0 keV band. The X-ray image has been smoothed with a Gaussian kernel with radius $r_k = 2.5''$.

Table 3.8: Willman 1 Chandra-XRO observation summary.

Obs. ID	RA_{J2000} [^{hms}]	Dec_{J2000} [$^\circ$ $'$ $''$]	Date	Exposure [ks]
10534	10 49 21.00	+51 03 00.0	2010-01-27	102.75

The Chandra-XRO observation of Willman 1 were conducted with the ACIS-I in *VFAINT* mode.

3.3.2 Results

Two different types of analyses were conducted over Willman 1 X-raydata. A diffuse component analysis was performed with the aim of looking for possible X-raylines with a possible exotic origin, namely, *sterile neutrino* decay signatures. Besides the diffuse analysis component, Chandra-XRO position resolution allowed to carry out a point like analysis of X-raysources present in the FoV. Both results are detailed in the following sections.

3.3.2.1 Diffuse component analysis

In X-rays, it is expected that the diffuse emission from Willman 1 will be dominated either by an unresolved point source population or by a complex gaseous component [349]. However, there is also a possibility that the dark matter halo of Willman 1 produces a detectable X-ray flux via *sterile neutrino* decay (see Sec. 1.3.2 for more details). The principal decay channel for *sterile*

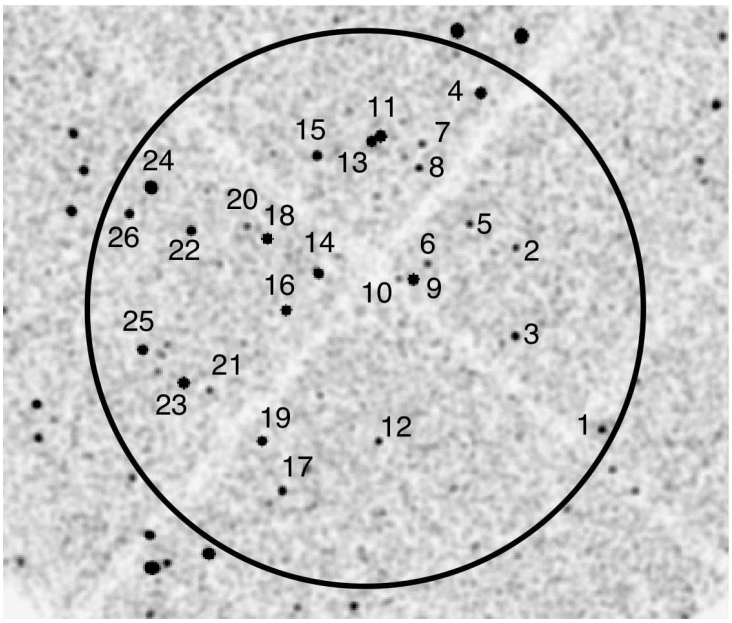

Figure 3.8: Chandra-XRO ACIS-I image of Willman 1 in the 0.5–6.0 keV energy range. The X-ray image has been smoothed with a Gaussian kernel with radius $r_k = 2.5''$. Identified sources are marked following the labels adopted in Table 3.9. The circle is centered on RA. $10^{\rm h}49^{\rm m}22\overset{\rm s}{.}3$, Dec. $+51°03'\ 03''$ and drawn with a $5'$ radius. The half-light radius corresponds to $r_{1/2} = 1.9'$. Notice that the placement falls near the intersection o the chip gaps.

neutrinos is into three light standard neutrinos. However, this decay channel is in practice impossible to detect. Nonetheless, there is a potentially detectable radiative decay channel in the X-ray band, where a standard neutrino and a X-ray photon are produced with a slow mean decay time of the order of the lifetime of the Universe. This decay is a two-body process, meaning that the resulting photon energy distribution is characterized by a spectral line with a broadening due to the velocity dispersion of the original *sterile neutrino* population[79; 81; 82]. Searches for this decay lines have been conducted in Fornax [83], Ursa Minor [84], Willman 1 [86], and Segue 1 [85]. In none of them a clear detection was claimed. However, a flux line pointing to a ~ 5 keV *sterile neutrino* was suggested in the analysis of Willman 1 data reported in [86].

In order to survey the diffuse emission, all point sources within the inner $5'$ of Willman 1 were removed (see Sec. 3.3.2.2 for further details). Due to an unfortunate placement of the object within the ACIS footprint, the diffuse emission is missing a critical section of the inner core of Willman 1 and extends over four distinct ACIS-I CCDs with distinct gains (see Fig. 3.8). In order to avoid significant intrachip variations, 32 pixels to each side of the CCD edges were excluded. Visual examination of the resulting X-ray image did not reveal prominent diffuse emission. Given the intrachip gain fluctuations across the CCDs, it is not straightforward to ascertain the significance of the counts within the inner $5'$ of Willman 1. It is worth noting that the limited signal-to-noise ratio and placement across four CCDs cannot ensure that the detected counts correspond to diffuse emission specific to Willman 1. Rather the counts might result from Poisson fluctuations in the background count rate.

On the other hand, it is possible to derive upper limits on the diffuse emission after subtracting the background contribution at this position. The spectrum of the diffuse emission was

obtained from a $5'$ radius circle at the nominal position of Willman 1 of RA. $10^{\rm h}49^{\rm m}22\overset{\rm s}{.}3$, Dec. $+51°03'\ 03''$ and corrected with the standard reprojected blank-sky background [350]. The final step consisted in a renormalization of the background spectrum to match the 9.0–12.0 keV count rate of the Willman 1 exposure. Fig. 3.9 shows the spectrum before and after subtraction of the background. Prior to subtraction, the spectrum is dominated by prominent instrumental line features that originate from fluorescence of material in the telescope including Si K α (1.74 keV), Au M α, β (2.1–2.2 keV), Ni K α (7.47 keV), and Au L α (9.67 keV). The instrumental features are largely removed after subtracting the background.

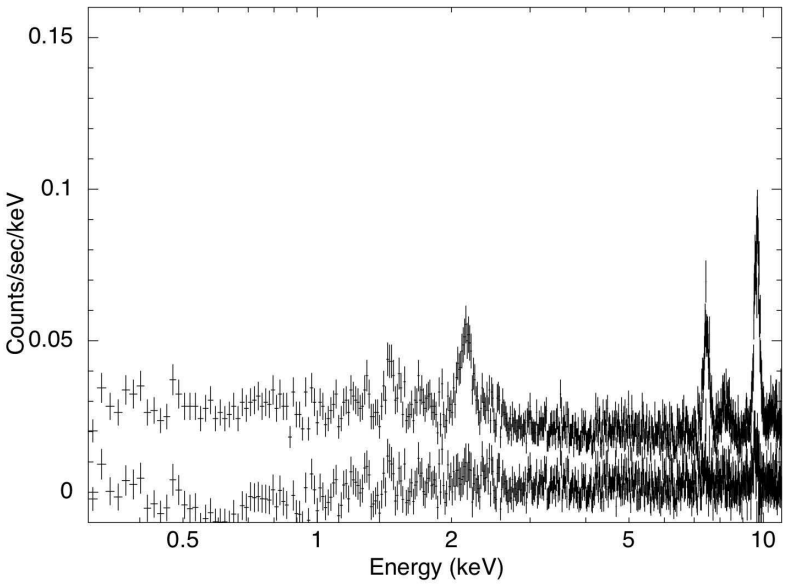

Figure 3.9: Chandra-XRO ACIS-I spectrum extracted from a $5'$ radius circle centered on Willman 1 as described in the text. Top: Data prior to removal of the background. Instrumental line features include Si K α (1.74 keV), Au M α, β (2.1–2.2 keV), Ni K α (7.47 keV), and Au L α (9.67 keV). Spectrum after background subtraction.

In order to establish upper limits to the emission of dark matter in the energy range covered by the observation, the spectrum was fitted in steps of 0.1 keV with the appropriate Gaussian width σ required to match the spectral resolution at each step. This emulates the procedure outlined in previous analyses of Chandra-XRO data (see, *e.g.*, [351; 352]).

The parameter space defined by the *sterile neutrino* mass m_{ν_s} and the mixing angle θ was constrained in the mass range from 1.6 keV up to 16.0 keV, by considering the following parametrization for the expected *sterile neutrino* decay line flux (given by Eq. 1.17, adapted following the formalism from [86]):

$$\Phi^{line}_{\nu_s \to \nu\gamma}(E = m_{\nu_s}/2) = 5.15 \sin^2\theta \left(\frac{m_{\nu_s}}{\rm keV}\right)^4 f_{\nu_s} M_7 d_{100}^{-2}\ {\rm cm}^{-2}\ {\rm s}^{-1}, \tag{3.1}$$

where M_7 is the projected dark matter mass of Willman 1 in units of 10^7 $M_\odot$, f_{ν_s} is the fraction of dark matter in *sterile neutrino* form and d_{100} is the distance of the observer to Willman 1 in units of 100 kpc. For the actual calculations, it was assumed that the dark matter is composed

exclusively by *sterile neutrinos* ($f_{\nu_s} = 1$), a distance to Willman 1 of $d_{100} = 0.38$ [319] and a projected dark matter mass for the object of $M_7 = 0.2$ [86]. Fig. 3.10 shows the resulting *sterile neutrino* parameter space ruled out by the Chandra-XRO observation.

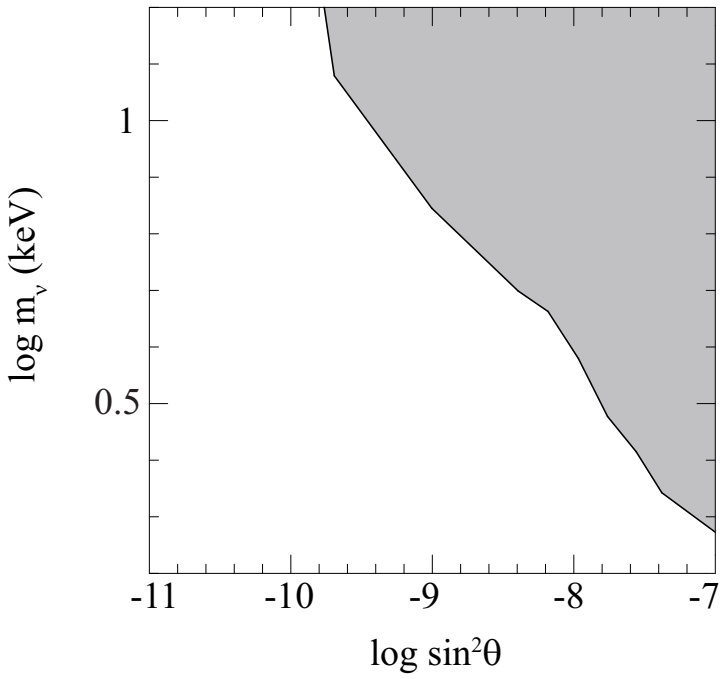

Figure 3.10: Parameter space constraints for the sterile neutrino. The grey filled region is ruled out by the Chandra-XRO observation of Willman 1.

Despite of being compatible with previous works regarding the constraints in the *sterile neutrino* parameter space, the current analysis found no evidence for exotic lines detection, contrary to [86], where the detection of a line at 2.51 keV was reported with a flux of $\Phi^{line}_{\nu_s \to \nu\gamma} = 3.53 \times 10^{-6}$ photons cm^{-2} s^{-1}. Fig. 3.11 shows this work background-subtracted ACIS spectrum in the 2.0–5.0 keV energy region. An absorbed power-law model fixed at the Galactic H I column density $N_{\rm H} = 1.2 \times 10^{20}$ cm^{-2} and photon index $\Gamma = 1.0 \pm 0.6$ fitted the data ($\chi^2_\nu = 0.86$). The inclusion of a Gaussian line with the properties reported in [86] did not improve the fit ($\chi^2_\nu = 0.85$) despite the fact that there is an apparent excess around 2.3–2.5 keV. Leaving the power-law index to be a free parameter, and allowing the Gaussian line centroid to take values in the 2.0–3.0 keV energy range, this provided an unrealistic $\Gamma = -1.2 \pm 0.7$ with a Gaussian line centered at 2.2 keV. The latter is most likely due to the instrumental Au M α, β (2.1–2.2 keV) line and highlights the difficulties with reported line detections in and around this region. Thus, while a weak emission between 2.3 and 2.5 keV cannot be ruled out, a power-law model provided a satisfactory fit without the need for any additional Gaussian line.

A closer inspection of the ACIS-I spectrum shown in Fig. 3.9 revealed spectral residuals in the vicinity of the aforementioned instrumental lines of Au M α, β (2.1–2.2 keV), Ni K α (7.47 keV), and Au L α (9.67 keV), also present in [86]. These features seem to be entirely consistent with a diffuse emission signal heavily dominated by background spectrum (see also [83]). In such circumstances, it is possible that a deficient subtraction of the Au M α, β (2.1–2.2 keV) instrumental line or calibration issues at $E < 2.3$ keV will start to produce the shape of a spectral line around 2.4–2.5 keV that might result in the finding reported in [86]. In addition,

it is difficult to discard that intrachip gain variations may conspire to mimic an emission line.

Even if one wants to advocate the reality of a line at 2.51 keV, a direct dark matter connection suffers from a fatal flaw in that it falls at a location matching the rest-frame of helium-like sulfur ion S XV α located at 2.45 keV [353]. This astrophysical line is routinely detected in plasmas with temperatures $\sim 10^{6-7}$ K [354; 355]. Consequently, it seems more plausible that one is detecting sulfur emission from a hot supernova remnant or a highly-ionized wind region either at Willman 1 itself or at an intervening location to the object, rather than the exotic signature of dark matter.

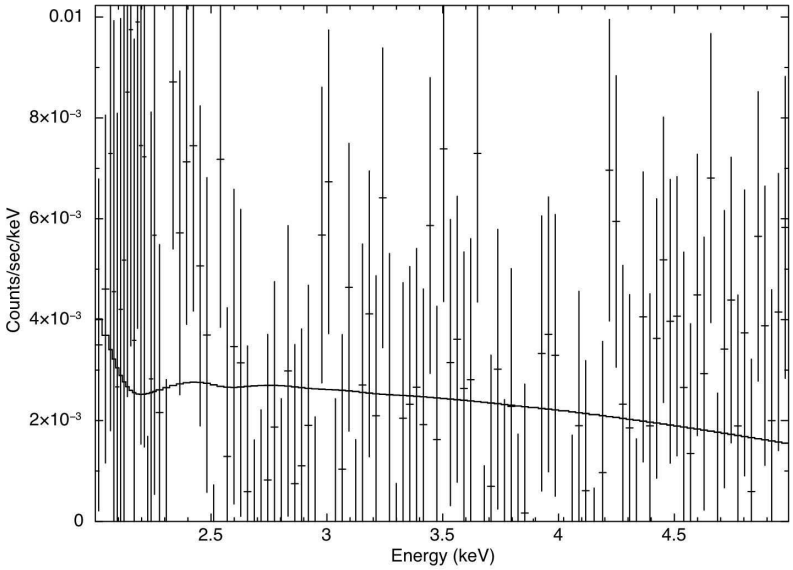

Figure 3.11: Chandra-XRO ACIS spectrum of the diffuse component of Willman 1 in the 2.0-5.0 keV energy range. The solid line depicts the best fit, which corresponds to an absorbed power-law model fixed at the Galactic H I column density $N_{\rm H} = 1.2 \times 10^{20}$ cm^{-2} with photon index $\Gamma = 1.0 \pm 0.6$ ($\chi^2_\nu = 0.86$).

3.3.2.2 Point-like population analysis

Apart from allowing access to the extended emission, the Chandra-XRO resolution is sufficiently accurate to study the X-ray point source population in the field of Willman 1. A search for point-like sources within the central $5'$ of Willman 1 was performed using the CIAO tool *celldetect*. This corresponds to a physical size of 55 pc assuming a distance for the observer to Willman 1 of 38 kpc. The region includes the half-light radius of Willman 1, estimated to be $r_{1/2} = 1.9'$ [319]. Fig. 3.8 shows all 26 detections with more than 15 net counts in the 0.5–6.0 keV energy range. Ten of the sources are on the I1 chip, seven on the I2 chip, six on the I0 chip, and three on the I3 chip.

X-ray counts were extracted within a $2.5''$ radius circles centered on the location of each source. The counts were then separated in three different energy ranges: a *soft* band (0.5–1.5 keV), a *medium* band (0.5–4.5 keV), and a *hard* band (1.5–6.0 keV). Finally, the net counts were estimated using source-free background regions in the corresponding individual chip. The

Table 3.9: X-ray sources identified within the central $5'$ of Willman 1

Source Label	Name	R.A. (J2000.0)	Dec. (J2000.0)	Net Counts 0.5 – 1.5 keV	0.5 – 4.5 keV	1.5 – 6.0 keV
1	CXOU J104855.4+510053	10 48 55.4	+51 00 53.0	1±1	14±4	20±5
2	CXOU J104905.1+510409	10 49 05.1	+51 04 09.6	1±1	16±4	20±5
3	CXOU J104905.2+510234	10 49 05.2	+51 02 34.5	15±4	29±5	17±4
4	CXOU J104909.1+510657	10 49 09.1	+51 06 57.1	94±10	171±13	83±9
5	CXOU J104910.3+510435	10 49 10.3	+51 04 35.8	15±4	20±5	5±2
6	CXOU J104915.1+510353	10 49 15.1	+51 03 53.2	6±3	14±4	9±3
7	CXOU J104915.9+510602	10 49 15.9	+51 06 02.2	9±3	17±4	8±3
8	CXOU J104916.2+510536	10 49 16.2	+51 05 36.6	18±4	26±5	10±3
9	CXOU J104916.8+510335	10 49 16.8	+51 03 35.6	89±9	161±13	83±9
10	CXOU J104918.5+510337	10 49 18.5	+51 03 37.0	7±3	12±4	8±3
11	CXOU J104920.6+510610	10 49 20.6	+51 06 10.6	183±14	291±17	124±11
12	CXOU J104920.8+510041	10 49 20.8	+51 00 41.3	15±4	22±5	10±3
13	CXOU J104921.6+510605	10 49 21.6	+51 06 05.1	46±7	81±9	39±6
14	CXOU J104927.7+510341	10 49 27.7	+51 03 41.5	27±5	66±8	39±6
15	CXOU J104927.8+510549	10 49 27.8	+51 05 49.3	28±5	55±7	33±6
16	CXOU J104931.4+510302	10 49 31.4	+51 03 02.5	58±8	100±10	47±7
17	CXOU J104931.8+505947	10 49 31.8	+50 59 47.0	12±4	33±6	24±5
18	CXOU J104933.6+510420	10 49 33.6	+51 04 20.0	48±7	112±11	70±8
19	CXOU J104934.1+510041	10 49 34.1	+51 00 41.1	28±5	61±8	39±6
20	CXOU J104935.9+510433	10 49 35.9	+51 04 33.2	4±2	13±4	11±3
21	CXOU J104940.2+510136	10 49 40.2	+51 01 36.0	4±2	13±4	14±4
22	CXOU J104942.3+510428	10 49 42.3	+51 04 28.1	36±6	57±8	24±5
23	CXOU J104943.1+510144	10 49 43.1	+51 01 44.1	34±6	178±13	157±13
24	CXOU J104946.9+510514	10 49 46.9	+51 05 14.7	154±12	316±18	193±14
25	CXOU J104947.8+510219	10 49 47.8	+51 02 19.7	31±6	78±9	57±8
26	CXOU J104949.4+510446	10 49 49.4	+51 04 46.8	26±5	43±7	19±4

All 26 point-like Chandra-XRO's source detections with more than 15 net counts in the 0.5–6.0 keV energy range. Ten of the sources are on the I1 chip, seven on the I2 chip, six on the I0 chip, and three on the I3 chip (see Fig 3.8). X-ray counts were extracted within a $2.5''$ radius circles centered on the source location.

source labels, positions, and net counts in three separate energy bands are listed in Table 3.9. A complementary search for optical counterparts was performed cross-checking source positions with SDSS-DR7 catalog [356]. The association required the angular distance between Chandra-XRO and SDSS catalog sources to be less than $2.5''$. This criterion produces 10 optical matches out of the total sample of 26 sources. According to SDSS object classification, 3 are categorized as stars and 3 as galaxies. The remainder 4 matches are listed as part of the *NBCK* catalog of photometrically selected quasar candidates [357]. Sources with optical matches are summarized in Table 3.10. It is important to emphasize that SDSS optical sources have been tentatively labeled based on colors and that no reliable spectroscopic classifications were available at the time of this writing.

The principal obstacle in sorting out whether any individual point source in the field represents a *bona fide* member of Willman 1 is the presence of background AGN and galaxies in the field [358; 359]. It turns out to be extremely difficult to distinguish the source identity whenever the number of predicted background AGN matches the observed number of sources in the field [360]. In this case, a detection limit of 15 net counts in the 0.5–6 keV energy range corresponds to a limiting flux 6×10^{-16} erg cm^{-2} s^{-1} in the 0.5–2.0 keV band, adopting an X-ray power

Table 3.10: X-ray sources with optical matches within the central 5′ of Willman 1.

Source Label	Name	Optical match	Offset (″)	Classification[1]	Redshift[2]
4	CXOU J104909.1+510657	SDSS J104909.10+510657.0	0.1	Star	-
8	CXOU J104916.2+510536	SDSS J104916.19+510536.6	0.1	Galaxy	-
11	CXOU J104920.6+510610	SDSS J104920.62+510610.5	0.2	Star	-
12	CXOU J104920.8+510041	SDSS J104920.85+510041.3	0.5	QSO[3]	2.8
13	CXOU J104921.6+510605	SDSS J104921.64+510605.1	0.4	QSO[3]	1.6
16	CXOU J104931.4+510302	SDSS J104931.40+510302.6	0.2	QSO[3]	2.1
17	CXOU J104931.8+505947	SDSS J104931.79+505946.9	0.1	Galaxy	-
24	CXOU J104946.9+510514	SDSS J104946.90+510514.3	0.4	QSO[3]	0.8
25	CXOU J104947.8+510219	SDSS J104947.85+510220.0	0.6	Galaxy	-
26	CXOU J104949.4+510446	SDSS J104949.36+510446.6	0.3	Star	-

[1] Classification according to [356]. [2] Photometric redshift from [357]. [3] Photometric classification as in [357]

spectral index $\Gamma = 1.4$ and a Galactic H I column density $N_{\rm H} = 1.2 \times 10^{20}$ cm^{-2}. Using the latest AGN counts from the Chandra-XRO Deep Field-South (CDFS) reported by [359], an average of 24 ± 3 background AGN are expected for a field of this size to the observation limiting flux in the 0.5–2.0 keV band. The detection of 26 sources does not exceed significantly the CDFS prediction. As a result, the majority of sources found are most likely background AGN.

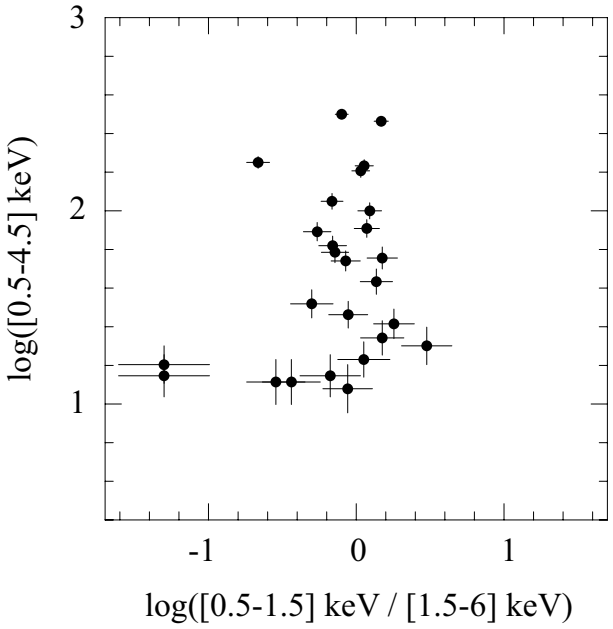

Figure 3.12: X-ray color-magnitude diagram for 26 sources detected within the inner 5′ of Willman 1.

Since this result relies on the adopted background source count, the variability and color of the sample were evaluated so to identify different kind of emitting objects. The presence of binary systems might be exposed through the detection of strong variability [361]. According to the CIAO tool *glvary*, there are no definite variables among the point sources. Similarly, the location of a source in an X-ray color magnitude diagram might be a powerful way to infer the presence of binary systems in a field [362]. In particular, certain cataclismic variables and low mass X-ray

binaries (LMXBs) will depart from AGN and become outliers in the color distribution. Fig. 3.12 shows the logarithm of the 0.5–4.5 keV counts versus the logarithm of the ratio of 0.5–1.5 keV and 1.5–6.0 keV net counts. Note that the majority of the sources tend to gather around the center of the diagram where it is difficult to tell binary systems and AGN apart. However, the void in the upper right corner of the diagram probably rules out the presence of LMXBs in quiescence [361]. The two hard sources to the left of the diagram could indicate heavily obscured AGN but the reduced number of counts prevents a formal identification. Therefore, the color analysis fails to discover any apparent binary system in the field as expected by the background AGN estimated population.

Additional clues about the nature of the point like population might be gained from the examination of the actual spectra of the sources. For this reason, spectra were extracted for all the sources with 50 or more detected counts in the 0.5–6.0 keV energy band. This criterion leaves 13 out of the total sample of 26 sources. The counts for each source were grouped using the CIAO tool *dmgroup* such that there are 10 counts per bin. By default, a power-law model spectral fit was adopted within XSPEC [363], with the absorption fixed at the Galactic value $N_{\rm H} = 1.2 \times 10^{20}$ cm^{-2}. Power law fits with indices $1.2 < \Gamma < 2$ were acceptable ($\chi^2_\nu < 1.5$) to all sources, except source 14. For the latter a black body or models with substantial internal absorption provided better fits. Overall, the spectral results are consistent with the properties of background AGN in such a field. It is worth mentioning that there is also a non-negligible probability that a handful of coronal emitting stars in the foreground could be superposed by chance along the line of sight [364].

Last but not least, the number of expected X-ray binary systems in Willman 1 can be estimated theoretically. The so-called encounter rate was computed following [365], considering a core radius $r_c = 1.5'$ and density $\rho_0 \sim 1 \times 10^{-2} L_\odot / pc^{-3}$ [331]. Applying the normalization in [224] a very low probability estimate ($p \sim \mathcal{O}(10^{-7})$) of finding X-ray binary systems at a luminosity over $4 \times 10^{30} ergs^{-1}$ was derived. Nevertheless the assumptions made in order to infer the binary rate are based on the daring hypothesis that Willman 1 density has remained constant throughout its evolution. Willman 1's unusual kinematics challenges any current model of tidally disrupted or ordered rotating system and point towards a significant tidal evolution which could have stripped a noteworthy fraction of its stellar component [332]. The initial stellar density of the system could have been such that binary systems were formed more efficiently in the past. Consequently the probability estimate should be taken *cum grano salis* since Willman 1 past evolution may have played a crucial role in binary formation. But since it might be nearly impossible to derive the past encounter rate from current dynamical structure, there is no reason to conclude that any significant fraction of the point source population in the field is associated with Willman 1.

3.3.3 Summary and discussion

The Chandra-XRO observed Willman 1 during January 2010. The observation were conducted with the Advanced CCD Imaging Spectrometer for a total effective time of 100.68 ks after data cleaning. Two complementary analyses were performed: a diffuse component analysis that allowed to constrain the *sterile neutrino* parameter space, and a study of the X-raypoint-like population in the FoV of the observations.

Regarding the diffuse component analysis and its interpretation in terms of dark matter constraints, and after assuming the *sterile neutrino* as the main component of the dark matter, a noteworthy part of the *sterile neutrino* parameter space was ruled out. As for the future

exploration of the parameter space with X-raydata, it might be wise to concentrate on the detectability of this hypothetical particle with forthcoming X-rayexperiments [366], since it will be difficult to improve current measurements with the existing instrumentation [81]. As for spectral lines with a possible exotic origin, no detection claim could be done. It has been shown that any viable indirect search for dark matter in this energy range must deal not only with possible overlap with instrumental lines in the spectrum (see also [352]), but also with possible contamination from intervening plasma lines that may mask a dark matter origin.

As for the point-like population analysis, and adopting a Willman 1 estimated distance of 38 kpc, it might be the case that the bulk of sources connected with the object lies below the observations luminosity limit of 10^{32} erg s^{-1} in the 0.5–2.0 keV energy band. However, the computed encounter rate indicates a very low probability of finding candidate binaries within Willman 1. Combined with existing optical imaging, the Chandra-XRO observation of Willman 1 could help to tell apart possible member stars from any AGN contaminants/stellar interlopers. Further analysis might help to investigate how will the X-raypoint source population influence the prospects of detecting a dark matter signal from Willman 1 with X-rayor γ-ray measurements, basically better constraining possible backgrounds, either from the object itself or from distant AGN.

It is worth noting that within the inner $5'$ radius circle of Willman 1, there are no radio sources at 1.4 GHz in the NRAO VLA Sky Survey (NVSS) source catalog [367]. Moreover, we have shown that the point source population to a limiting 0.5–2.0 keV X-ray flux of 6×10^{-16} erg cm^{-2} s^{-1} is consistent with background AGN and/or foreground stars. Pending a final verdict regarding the kinematic distribution of Willman 1 [332], the available data from radio through X-rays thus make Willman 1 a notable candidate for the eventual astrophysical verification of a dark matter particle.

3.4 Dark matter searches in Segue 1 with MAGIC

As already discussed in Sec.3.1.2, Segue 1 is the most promising target in terms of indirect dark matter detection in the VHE γ-ray regime due to its very large astrophysical factor (the largest up to now, excluding the Galactic Center one) and expected low background which might be produced by conventional very high energy emitters.

Segue 1 observations by the MAGIC telescope are reported below, including the description of the observations and data analysis, and also a detailed account of the results in the context of super-symmetric dark matter searches.

3.4.1 Observations description and data analysis

The observations of Segue 1 were performed in single telescope mode by MAGIC-I, since the second MAGIC telescope was not commissioned yet by that time. Data were taken from November 2008 until March 2009 during dark night conditions, and account for a total observation time of 43.2 hours. The source was surveyed in false tracking mode (so-called *w*obble mode) [286], defined by two different pointing positions, which alternate each 20 minutes, with an offset of $\pm 0.4^\circ$ in RA from the source nominal position. The zenith angle range of the observations extends from 12.7°, which corresponds to the source culmination at MAGIC latitude, and 33.9°. This zenith angle range provides a low energy threshold. Table 3.11 presents the effective observation time and zenith angle window of the whole Segue 1 dataset in a day-by-day basis.

Table 3.11: Segue 1 MAGIC dataset.

Date	$t_{eff}[h]$	Z.A. [°]
2008/11/27	0.4	13.0 – 16.5
2008/11/28	0.7	13.5 – 20.0
2008/12/01	0.8	13.0 – 19.0
2008/12/02	1.0	13.0 – 19.0
2008/12/03	0.6	13.0 – 15.0
2008/12/06	1.2	13.0 – 20.0
2008/12/07	0.9	13.0 – 16.5
2008/12/08	0.8	13.0 – 14.5
2009/01/04	2.0	13.0 – 30.0
2009/01/05	1.6	13.0 – 20.5
2009/01/19	0.9	18.0 – 25.5
2009/01/20	0.4	28.0 – 32.0
2009/01/21	1.6	13.0 – 20.5
2009/01/22	0.4	25.0 – 32.0
2009/01/23	1.6	13.0 – 19.5
2009/01/24	0.7	25.0 – 34.0
2009/01/25	1.7	13.0 – 22.0
2009/01/26	1.6	13.0 – 19.5
2009/01/27	3.7	13.0 – 32.0
2009/01/28	1.8	16.5 – 33.5
2009/01/30	0.5	25.0 – 31.5
2009/01/31	3.7	13.0 – 32.0
2009/02/01	0.5	21.0 – 32.5
2009/02/03	0.2	24.5 – 29.5
2009/02/25	0.6	25.0 – 32.0
2009/03/01	0.2	24.5 – 26.5
2009/03/02	1.4	13.0 – 17.0
2009/03/14	0.3	28.5 – 32.5
2009/03/15	0.6	25.0 – 32.0
2009/03/20	2.4	13.0 – 32.5
2009/03/22	2.6	13.0 – 34.0
2009/03/24	1.9	13.0 – 29.5
2009/03/30	0.8	13.0 – 15.0

As a convention within MAGIC Collaboration, the observation *night* refers to the date of dawn after regular observations. t_{eff} stands for the effective observation time (see Sec. 2.4.3.7). Z.A. holds for the zenith angle window of the observation.

The data analysis was performed by means of the standard MAGIC analysis procedure for single telescope observations (see Sec. 2.4.3). After the data calibration and signal extraction the noise from the NSBL was removed from the air-shower images thanks to an image cleaning. The algorithm applied to the event images was an absolute time image cleaning complying with the following conditions: *i)* a minimum amount of 6/3 phe for the *core/boundary* pixels were required; *ii)* individual core pixels whose signal arrival time differs from the mean *core* pixel

signal arrival time more than 4.5 ns were rejected. As for the individual *boundary* pixels, those whose signal arrival time differs from its *core* pixel neighbor signal arrival time more than 1.5 ns were also disregarded. After this NSBL suppression, surviving images were characterized by their image parameters, including their Hillas parameters [294].

Once the event images were characterized, the whole dataset went through a quality selection process. Data whose event rate presented significant deviations with respect to the average were discarded. The monitored atmospheric conditions were also used to identify and reject bad quality data, based on parameters like the cloudiness and humidity (high values of these parameters are related to a degrading telescope overall response). The distribution of the image parameters were also considered for data quality control, disregarding data which presented deviations with respect to the dataset mean values. Eventually, 29.4 hours of good quality data were remaining, meaning that a 32% of the initial dataset did not fulfill the data quality conditions.

After the image cleaning and parametrization, the events characterization was performed. The applied methods, which assign an estimated energy and a *hadroness* value to every single event, are detailed in Sec. 2.4.3.5. The *hadroness* value, used for hadronic background suppression, was computed by means of the RF method. In order to train the algorithm that eventually produced the RF matrices, samples of hadronic and γ-ray initiated events are required. A set of actual data were no γ-ray signal was previously found was used to represent a sample of hadronic event images. This set of data was chosen so its observational conditions, regarding zenith angle distribution, atmospheric situation and observation dates, were the most similar to the Segue 1 data's conditions as possible. For the γ-ray initiated events, a MC generated population was used. This population was simulated according to the actual telescope performance during Segue 1 observations. For the training of the RF multivariate method that eventually assigned to each event its *hadronness*, shower information from each image were used. The following variables were considered: $Size$, $Zenith$, $Width$, $Length$, $Size/(Width \times Length)$, $Conc$, $Dist$, $M3Long$, $RMSTime$, and $P1Grad$ (see Sec. 2.4.3.2 for an explanation of each of the parameters). As for the energy estimation, a RF algorithm was also applied. The variables used to train the algorithm and produce the corresponding matrices in this case were the following: $Size$, $Width$, $Length$, $Size/(Width \times Length)$, $Conc$, $Leakage1$, $Zenith$, and the original MC energy of the events.

The performance of the whole analysis chain, including that of the data quality selection and the proper behavior of the events characterization, was checked over a sample of Crab Nebula data, sharing the same observational conditions as Segue 1 data in terms of zenith angle, and being contemporaneous to Segue 1 observations. The check was satisfactory, reporting an analysis sensitivity of 2% CU above an analysis threshold of 200 GeV.

Unfortunately, the low energy range of Segue 1 observations, between 100 GeV and 200 GeV, suffered from the presence of the star $\eta-$Leonis (apparent magnitude $V = 3.5$) in the FoV. The light of the star, located at an angular distance of 0.68° with respect to the nominal position of the target, created camera inhomogeneities not suppressed by the normal analysis software. In order to suppress the negative effect of the star, some special *star-cuts* were applied to Segue 1 data. The same cuts were applied to the MC generated γ-ray events and to the Crab Nebula check sample which allowed to verify that the star suppression did not significantly degrade the sensitivity of the analysis chain at the affected energies. This novel technique of star suppression is extensively described in [368].

3.4.2 Results

Segue 1 data were analyzed in an night-by-night basis as well as on a cumulative basis. Different energy thresholds were considered, covering MAGIC best sensitivity range, from 100 GeV up to 1 TeV. The applied set of *detection cuts* were obtained from an optimization over the Crab Nebula data sample, assuming a point-like emitting source, and computed independently for each energy bin. No significant very high energy signal was found, either in the night-by-night analyses or the cumulative one. As an example, the cumulative $|\alpha|$-distribution for the lowest analysis threshold ($E_{th} = 100$ GeV) is shown in Fig. 3.13. For this energy threshold, the optimized signal region from the Crab Nebula analysis resulted to be $|\alpha| < 14°$, providing a number of excess events $N_{exc}(> 100 \text{ GeV}) = -279 \pm 329$. The corresponding significance, computed using Eq. 17 of [306], turned to be -0.85σ.

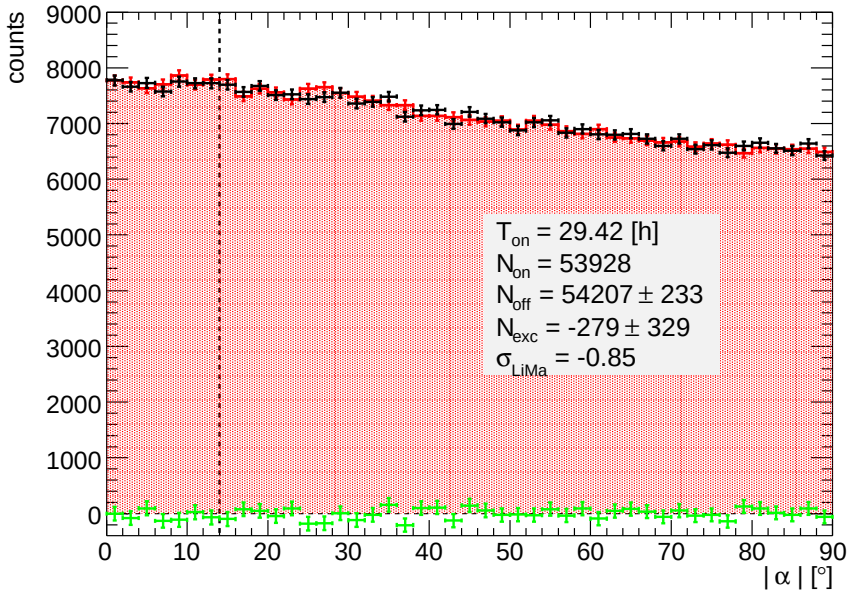

Figure 3.13: Segue 1 cumulative $|\alpha|-$distribution from 29.4 hours of MAGIC observation time. The energy threshold of 100 GeV is the lowest achieved for this data. The vertical dashed line depicts the signal region $|\alpha| < 14°$. Black points represent the background (OFF sample), red points the signal (ON sample), and green points their difference. The OFF sample was normalized to the ON sample in the region where no signal is expected, i.e., between $\alpha = 30°$ and $\alpha = 80°$.

In Fig. 3.14 three significance maps for the sky region around Segue 1 are shown. The generation of the maps made use of the source independent DISP method [369]. Due to camera inhomogeneities showing up in the data for the lowest energy images, plus the effect of the field star $\eta-$Leonis, the lowest event estimated energy was 200 GeV. Fig. 3.14a considers a range in estimated energy from 200 to 342 GeV. In Fig. 3.14c the range includes energies from 342 to 585 GeV. Fig. 3.14e considers energies between 585 GeV and 1 TeV. In all the cases, the significance distributions are consistent with background fluctuations, as shown in Figs. 3.14b, 3.14d, and 3.14f.

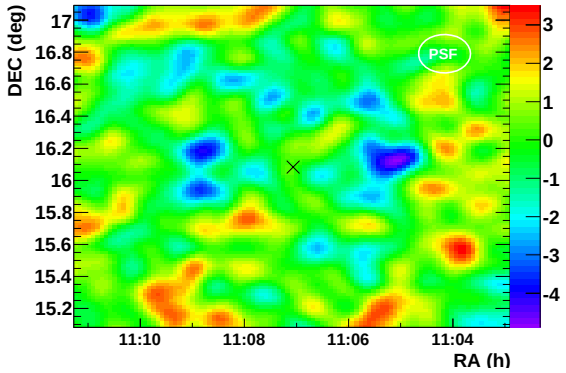

(a) Skymap between 200 and 342 GeV

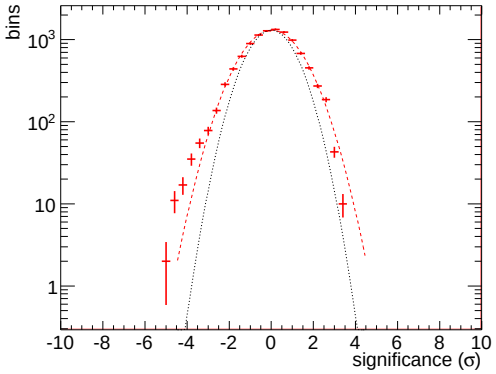

(b) Significance distribution between 200 and 342 GeV

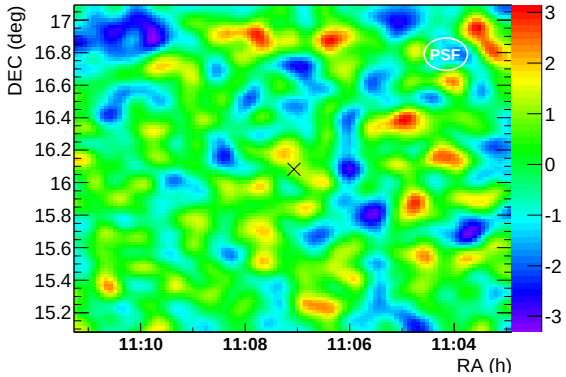

(c) Skymap between 342 and 585 GeV

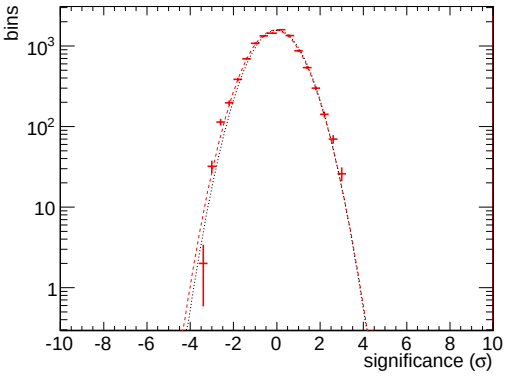

(d) Significance distribution between 342 and 585 GeV

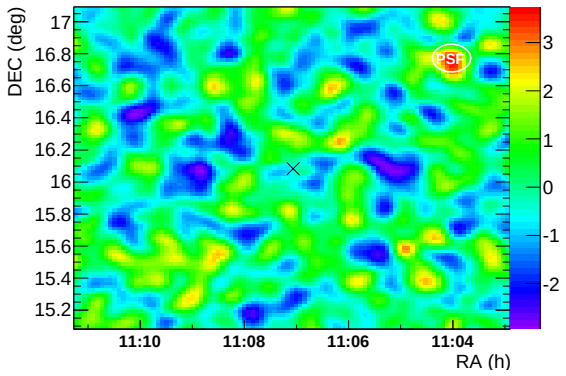

(e) Skymap between 585 and 1000 GeV

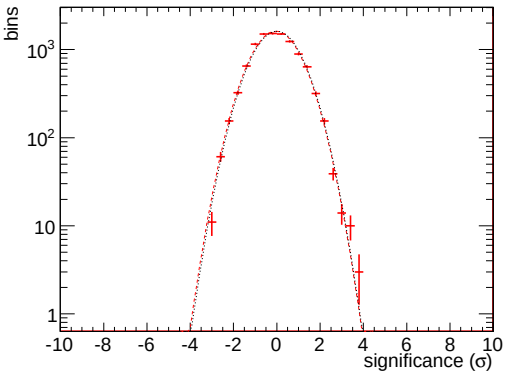

(f) Significance distribution between 585 and 1000 GeV

Figure 3.14: Segue 1 MAGIC significance skymaps in three energy windows: 200–342 GeV, 342–585 GeV and 585-1000 GeV. The significance distribution is compatible with the null hypothesis (meaning that no significant source is present in the region, depicted by the red dashed line) in all cases. The energy cuts are referred to the estimated energy. The white circles in 3.14a, 3.14c, and 3.14e depict MAGIC PSF for the given energy range.

3.4.2.1 Upper limits for power-law spectra

Given the fact that no VHE signal was found over the background in Segue 1 data, upper limits to the differential and integral flux were derived. In the current section, flux upper limits for general power-law spectra are shown, considering that the hypothetical Segue 1 spectrum can be described by such a function. The results were obtained following the instructions detailed in Sec. 2.4.3.7.

The Rolke *et al.* method [308] was used to compute the the upper limits to the number of excess events, considering a 95% confidence level. In order to reflect the uncertainty in the energy estimation and effective area calculation, a systematic error of 30% was assumed.

The upper limits to the differential flux were computed according to Eq. 2.36. The energy range was divided into four bins of estimated energy between 100 GeV and 10 TeV. Six different power-law indices were considered, namely, $\Gamma = -1.0, -1.5, -1.8, -2.0, -2.2, -2.4$.

Table 3.12 presents, along with the upper limit in differential flux, the number of ON (N_{ON}) and OFF (N_{off}) events, the significance of detection, and the upper limit on the excess events, for each bin of reconstructed energy. The results are also shown in Fig. 3.15, where these differential upper limits are shown together with the Crab Nebula differential flux (at 1%, 10% and 100% levels, extracted from [344]) for comparison purposes.

Table 3.12: Segue 1 differential flux upper limits from MAGIC data.

ΔE [TeV]	N_{ON}	N_{OFF}	N_{exc}^{UL} 95% C.L.	$\sigma_{\mathrm{Li,Ma}}$	$d\Phi^{UL}/dE$ [TeV^{-1}cm^{-2}s^{-1}]					
					$\Gamma = -1.0$	$\Gamma = -1.5$	$\Gamma = -1.8$	$\Gamma = -2.0$	$\Gamma = -2.2$	$\Gamma = -2.4$
0.1, 0.32	51871	52271	399	-1.2	4.9×10^{-11}	5.2×10^{-11}	5.5×10^{-11}	5.8×10^{-11}	6.1×10^{-11}	6.5×10^{-11}
0.32, 1	696	657	156	1.1	3.3×10^{-12}	3.4×10^{-12}	3.6×10^{-12}	3.8×10^{-12}	4.0×10^{-12}	4.2×10^{-12}
1, 3.2	99	77	72	1.7	3.5×10^{-13}	3.7×10^{-13}	3.9×10^{-13}	4.0×10^{-13}	4.2×10^{-13}	4.5×10^{-13}
3.2, 10	69	57	48	1.1	5.7×10^{-14}	6.0×10^{-14}	6.4×10^{-14}	6.6×10^{-14}	7.0×10^{-14}	7.4×10^{-14}

95% CL differential flux upper limits in units of TeV^{-1}cm^{-2}s^{-1} for six different power law γ-ray spectra with spectral index Γ, and four energy bins in TeV units.

Upper limits to the integral flux for Segue 1 were computed following Eq. 2.32 for different energy thresholds. As for the spectral indices, the same set as for the differential flux upper limit calculation was considered. The results are summarized in Table 3.13, where the upper limits are presented in absolute flux terms as well as in a percentage with respect to the Crab Nebula flux. The number of ON (N_{ON}) and OFF (N_{OFF}) events, the significance of detection, and the upper limit on the excess events are shown as well for each integral energy threshold.

Fig. 3.16 shows the integral flux upper limits from Table 3.13 (colored arrows) as well as the corresponding upper limits computed if the statistical significance $\sigma_{\mathrm{Li,Ma}}$ was zero, i.e. assuming $N_{ON} = N_{OFF}$ in the signal region of the $|\alpha|$-distribution (dashed lines). In this way, the remarkable dependence between the significance of detection and the resulting upper limit is shown, and the comparison between upper limits coming from different observations is made easier.

3.4.2.2 Upper limits for dark matter-like spectra

In order to place upper limits to the dark matter emission from Segue 1, it is mandatory to estimate the expected spectrum from the source (see Sec. 1.4.3.2 for a detailed description of the expected spectrum from dark matter annihilation). This requirement is due to the fact that the flux upper limit depends on the assumed spectral shape (see Eq. 2.32). Attending to Eq. 1.26

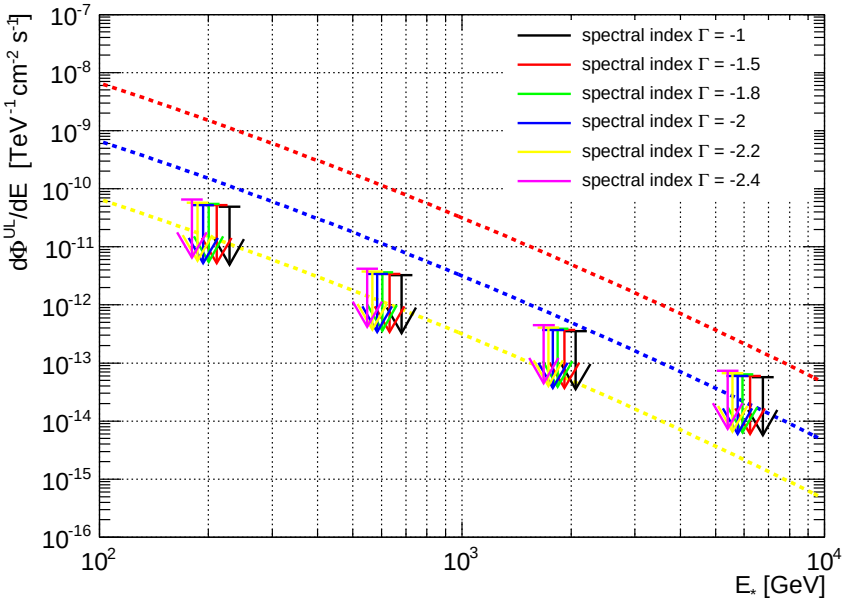

Figure 3.15: Segue 1 differential flux upper limits from MAGIC data as in Table 3.12. The Crab Nebula differential flux [344] (red dashed line) and its 10% (blue dashed line) and 1% (yellow dashed line) fractions are also depicted as reference.

Table 3.13: Segue 1 integral flux upper limits from MAGIC data.

E_0 [GeV]	N_{ON}	N_{OFF}	N_{exc}^{UL} 95% C.L.	$\sigma_{\mathrm{Li,Ma}}$	Φ^{UL} $\times 10^{-12}[\mathrm{cm}^{-2}\mathrm{s}^{-1}]$					
					$\Gamma=-1.0$	$\Gamma=-1.5$	$\Gamma=-1.8$	$\Gamma=-2.0$	$\Gamma=-2.2$	$\Gamma=-2.4$
100	52978	53301	453	-0.99	7.5 (1.4)	8.8 (1.6)	10.5 (2.0)	11.6 (2.2)	12.7 (2.4)	13.7 (2.5)
126	18835	19233	174	-2.04	2.8 (0.7)	3.2 (0.8)	3.6 (0.9)	4.0 (1.0)	4.3 (1.1)	4.6 (1.1)
158	6122	6374	93	-2.25	1.5 (0.5)	1.6 (0.5)	1.8 (0.6)	1.9 (0.6)	2.0 (0.7)	2.1 (0.7)
200	3012	3088	110	-0.97	1.7 (0.8)	1.7 (0.8)	1.9 (0.9)	2.0 (0.9)	2.1 (1.0)	2.2 (1.0)
251	1687	1654	194	0.57	2.9 (1.8)	3.0 (1.9)	3.1 (1.9)	3.2 (2.0)	3.4 (2.1)	3.5 (2.2)
316	1107	1030	250	1.67	3.6 (3.1)	3.7 (3.2)	3.8 (3.3)	3.9 (3.4)	3.9 (3.4)	4.1 (3.6)
398	792	761	147	0.79	2.0 (2.5)	2.0 (2.5)	2.1 (2.6)	2.1 (2.6)	2.2 (2.7)	2.2 (2.7)
501	613	580	140	0.96	1.9 (3.3)	1.9 (3.3)	1.9 (3.3)	1.9 (3.3)	2.0 (3.5)	2.0 (3.5)
631	536	509	124	0.84	1.5 (3.7)	1.5 (3.7)	1.6 (4.0)	1.6 (4.0)	1.6 (4.0)	1.6 (4.0)
794	486	445	146	1.34	1.7 (6.2)	1.8 (6.6)	1.8 (6.6)	1.8 (6.6)	1.8 (6.6)	1.8 (6.6)
1000	411	373	135	1.36	1.6 (8.6)	1.6 (8.6)	1.6 (8.6)	1.6 (8.6)	1.6 (8.6)	1.6 (8.6)

95% CL integral upper limits in units of $10^{-12}\mathrm{cm}^{-2}\mathrm{s}^{-1}$ for six different power law γ-ray spectra with spectral index Γ and several energy thresholds E_0. The numbers in parenthesis are the upper limits as a percentage of the Crab Nebula integral flux (extracted from [344]) above E_0.

it can be seen that the expected spectrum can be determined by fixing both, the contribution from the astrophysical factor J, and the contribution from the particle physics factor Φ^{PP}. In the current case, Segue 1 astrophysical factor took a constant value after its calculation, while the particle physics factor took a large variety of values thanks to the realization of a significant amount of simulations scanning the mSUGRA parameter space. These characterizations are detailed next.

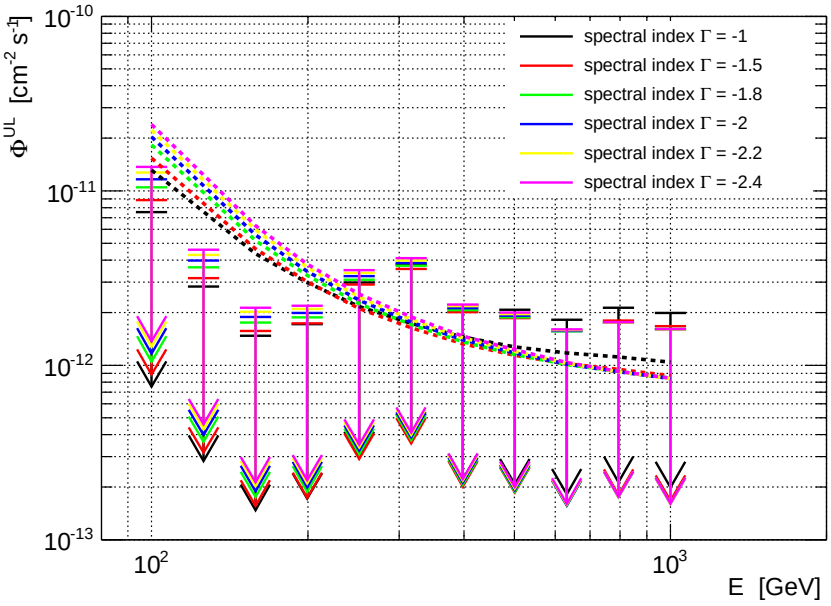

Figure 3.16: Integral flux upper limits from Segue 1 MAGIC data. The arrows indicate the integral flux upper limits as in Table 3.13 for different power-law spectra and energy thresholds. On the contrary, the dashed lines indicate the corresponding integral upper limits if zero significance $\sigma_{\mathrm{Li,Ma}}$ is assumed.

For the astrophysical factor computation, the dark matter density distribution in the object $\rho(r)$ has to be integrated along the line of sight considering a field of view $\Delta\Omega$ that will fix the integration region (see Eq. 1.25). In the case of Segue 1, the assumed dark matter density distribution profile was the so-called Einasto profile. As seen from Eq. 1.30, this profile is defined by the scale density ρ_s, the scale radius r_s and the index n. The particular values adopted for the Segue 1 dark matter density profile were $\rho_s = 1.1 \times 10^8$ $\mathrm{M_\odot kpc^{-3}}$, $r_s = 0.15$ kpc and $n = 3.3$ [370]. These values best fit the astronomical data used by [371], where the astrophysical uncertainty on the astrophysical factor has been estimated to be slightly larger than one order of magnitude at 2σ level. This large uncertainty is due to the scarce kinematic data from the dSph star members, as already mentioned in Sec. 3.1.2.

Concerning the integration region, Fig. 3.17 shows how the fraction of the integrated squared dark matter density (with respect to the total squared dark matter density) varies as a function of the integration angle Ψ for the considered Segue 1 profile. Since the expected flux from dark matter annihilation is proportional to the integrated squared dark matter density, the aforementioned figure could be interpreted in terms of the flux fraction coming from the solid angle defined by the integration angle Ψ. The flux fraction enclosed in the representative MAGIC angular resolution of 0.1° is only half of the total expected flux, so despite the peaked nature of the profile, the source can be considered as slightly extended from the analysis point of view. Therefore, a toy MC simulation for extended sources was generated, consisting on a distribution of γ-ray events whose arrival directions are scattered following the source dark matter density distribution profile. Out of this realization, the energy dependent $|\alpha|$ cuts are optimized, fixing the angular integration region (for further details on the method, see [368]). Eventually, the applied $|\alpha|$ cut corresponds to an angular integration region defined by a 0.14° radius around Segue 1 center. Therefore, as can be seen in Fig. 3.17, such an integration angle includes 64% of

the total flux. Consequently, this fact was taken into account by a proportional rescaling of the total astrophysical factor. Considering the aforementioned values for r_s and ρ_s which provide a total astrophysical factor of $J(\Delta\Omega) = 1.78 \times 10^{19}$ GeV^2 cm^{-5} sr, the *effective* astrophysical factor for the current analysis cuts turns out to be $\widetilde{J}(\Delta\Omega) = 1.14 \times 10^{19}$ GeV^2 cm^{-5} sr.

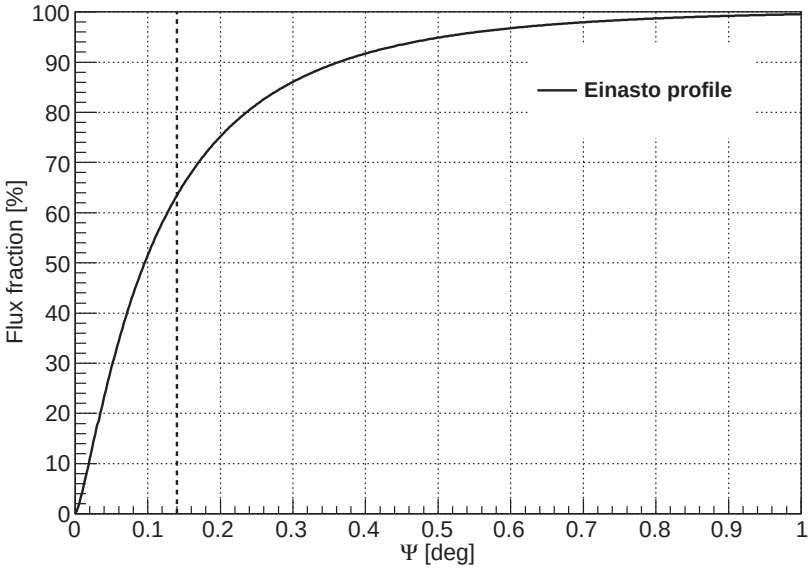

Figure 3.17: Fraction for squared dark matter density around Segue 1 integrated within an angular opening Ψ with respect to the total squared dark matter density, as a function of Ψ itself. The dashed line indicates the angular opening corresponding to the cut in the $|\alpha|$ plot used in the current analysis. Due to the fact that the total expected flux is proportional to this integral of the squared dark matter density, the aforementioned fraction can be interpreted in terms of flux fraction. An Einasto profile, as defined in the text, is assumed to describe the dark matter density distribution.

As for the particle physics factor, the LSP from a Super-Symmetry (SUSY) model, where the R-parity discrete symmetry provides the particle with cosmological stability, was considered. The chosen SUSY model was the highly-constrained mSUGRA model, a particularization of the cMSSM in the absence of CP-violating terms and flavor-changing neutral-currents, which requires a gravity-mediated SUSY soft-breaking term and the gaugino mass terms M_1, and M_2 to fulfill the relation $M_1 = 5 \tan\theta_W/3 \sim 0.5 M_2$ at the GUT scale. In this model, instead of the order of hundred free parameters required by the MSSM, there are only four free parameters and a free sign: the universal masses for gauginos $m_{1/2}$ and scalars m_0, the universal trilinear coupling A_0, the ratio between the vacuum expectation values of the two Higgs bosons $\tan\beta$, and the sign for the Higgs mass term μ. Concerning the LSP of the mSUGRA model, the lightest *neutralino* χ plays that role in most of the mSUGRA parameter space. More details on the mSUGRA model can be found in Sec. 1.3.1.

In order to investigate the phenomenology of the mSUGRA model, a grid scan over its parameter space was performed. The parameter space region defined in Table 3.14 was considered due to the fact that the subsequent covered *neutralino* mass range accommodates within MAGIC-I detection energy range. The sampling of the parameter space was performed according to the following instructions: for the cases of $m_{1/2}$, m_0, A_0, $\tan\beta$, each parameter interval was divided into 40 bins, and a randomly selected value, corresponding to each bin, was selected; as for the

μ sign, the two possible values were adopted. The sampling provided with a total of 5×10^6 points in the mSUGRA parameter space. Since not all the points represent valid mSUGRA models, the code `DarkSUSY`[1] [372] was used to test, for each of the generated points, whether the model was unphysical, and whether it passed the Standard Model experimental constraints implemented in the code (*e.g.* LEP bounds on Higgs mass $m_h > 114$ GeV, on chargino mass $m_{\chi^+} > 103.5$ GeV and constraints from $b \to s\gamma$). `DarkSUSY`, by means of the `Isasugra`[2] code [373], was also used to compute each model relic density. The figures out of this filtering are shown in Table 3.15.

Table 3.14: Ranges of the mSUGRA parameter space considered for the grid scan.

Parameter	Range	Steps
m_0	50 – 5000 GeV	40
$m_{1/2}$	0 – 5000 GeV	40
$\tan\beta$	2 – 62	40
A_0	−7000 – 7000	40
sign(μ)	$+, -$	2

These parameter space regions provide a *neutralino* mass range which accommodates within MAGIC-I detection energy range.

Table 3.15: Summary of the number of scanned models.

Conditions	Number of models
Total simulated models	5.12×10^6
Fulfilling SM bounds	2.42×10^6
SM bounds & $\Omega_{\rm DM}h^2 - \Omega_{\rm DM}^{\rm WMAP}h^2 < 3\sigma_{\rm WMAP}$	42427
SM bounds & $\lvert\Omega_{\rm DM}h^2 - \Omega_{\rm DM}^{\rm WMAP}h^2\rvert < 3\sigma_{\rm WMAP}$	4180

Values of $\Omega_{\rm DM}^{\rm WMAP}h^2 = 0.1123$ and $\sigma_{\rm WMAP} = 0.0035$ were considered. Extracted from [29].

All the models in the scan that correspond to a *neutralino* with a relic density smaller than the value derived by WMAP data plus three times its experimental error $\sigma_{\rm WMAP}$ [29] are plotted as crosses in Fig. 3.18. The crosses approximately cover the *neutralino* mass range between 100 GeV and 1 TeV, due to the before mentioned selection of mSUGRA parameters ranges. The values for the annihilation cross section are spread by many orders of magnitude, although they are mainly concentrated around a value of 3×10^{-26} cm^3 s^{-1}. However, there are models that, due to particular mechanisms, are characterized by lower values for the cross section. For instance, there is a prominent "strip" that crosses the plane from $\sim 10^{-27}$ cm^3 s^{-1} to $\sim 3 \times 10^{-29}$ cm^3 s^{-1} for *neutralinos* that co-annihilate with stops and staus, or the "tail" at low masses, for *neutralinos* close to the mass upper limits set by the LEP experiment (around 56 GeV). Among the models compatible with WMAP bounds, two representative subsets are also shown using a different color coding according to their main annihilation channel. Light brown crosses depict models characterized by a branching ratio $B(b\bar{b}) > 0.85$, while blue points represent models fulfilling $B(\tau^+\tau^-) > 0.7$). Both subsets are representatives of a soft and hard gamma-ray spectrum respectively.

[1] In its version `DarkSUSY 5.0.4.`

[2] In its version `Isasugra 7.78.`

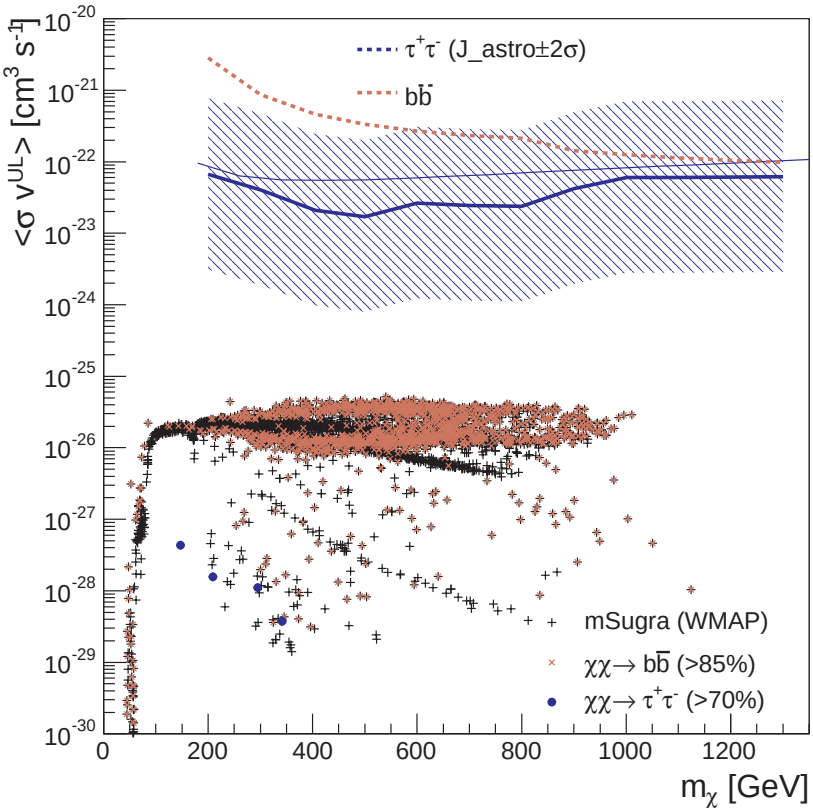

Figure 3.18: Annihilation cross section upper limits from Segue 1 MAGIC data considering *neutralino* annihilating entirely into $b\bar{b}$ or into $\tau^+\tau^-$. mSUGRA models with a relic density within $3\sigma_{\rm WMAP}$ from the WMAP value are plotted (black crosses). Among these, *neutralino*s annihilating mainly in $b\bar{b}$ and $\tau^+\tau^-$ are indicated with light brown crosses and blue points respectively. The dashed red line indicates upper limits for a *neutralino* annihilating entirely into $b\bar{b}$ while the solid blue lines the case of annihilation into $\tau^+\tau^-$. The blue thin line represents the integral upper limit for the $\tau^+\tau^-$ channel as if they were calculated (independently of the mass) with a fixed energy threshold of 100 GeV, while for the thick blue line the energy threshold is optimized for each value of m_χ. Finally, for annihilation into $\tau^+\tau^-$, the blue band covers the 2σ uncertainty on $J_\Theta(\Delta\Omega)$ estimated by [371].

For each mSUGRA model in the scan, integral upper limits $\Phi^{UL}(> E_0)$ can be derived following Eq. 2.32, using the Segue 1 data and the specific gamma-ray spectrum of the individual model. In Sec. 2.4.3.7 it was shown that the integral upper limits may change as a function of the energy threshold, with more stringent upper limits if E_0 is larger than the experimental one (see also [346]. While this variation is quite predictable in the case of power-law spectra, the situation may be less clear for annihilation spectra that contain features and terminate at dark matter mass. For the current analysis, analytical parametrization of dark matter annihilation spectra were considered. Spectra from WIMP annihilation into $\tau^+\tau^-$, $b\bar{b}$, W^+W^-, $\mu^+\mu^-$ were extracted from [145], where the dependence of the spectral shape with the WIMP mass is taken into account and the characteristic cut-off is included in the parametrization. WIMP annihilation via light intermediate states ϕ, which eventually decay in a pair of e^+e^-, was also considered. For this annihilation mode, the parametrization given in [146] was used. In Fig. 1.11

all these channels are depicted for $m_\chi = 1$ TeV and $m_\phi = 100$ MeV. The spectral shape does not significantly change in any channel when varying m_χ in the studied range. This fact permits to qualitatively interpret Fig. 1.11 in the context of IACTs detection prospects: in the region below $0.1m_\chi$ (which corresponds to 100 GeV in Fig. 1.11), $b\bar{b}$ and W^+W^- channels provide a noteworthy higher flux than the rest of channels. On the contrary, for energies above $0.4m_\chi$, the leptonic channels are the ones which provoke the largest photon yield. Therefore, considering an energy threshold of *e.g.* 100 GeV, heavy WIMPs, of the order of few TeV, will favor a detection if the annihilation spectrum is dominated by $b\bar{b}$ and/or W^+W^- channels whereas light WIMPs, of the order of few hundred GeV, will be more likely detected if $\tau^+\tau^-$ and/or $\mu^+\mu^-$ channels are prominent in the annihilation spectrum. The possible contribution of monochromatic lines to the annihilation spectrum was disregarded due to overwhelming contribution of the continuum emission, with respect to such lines.

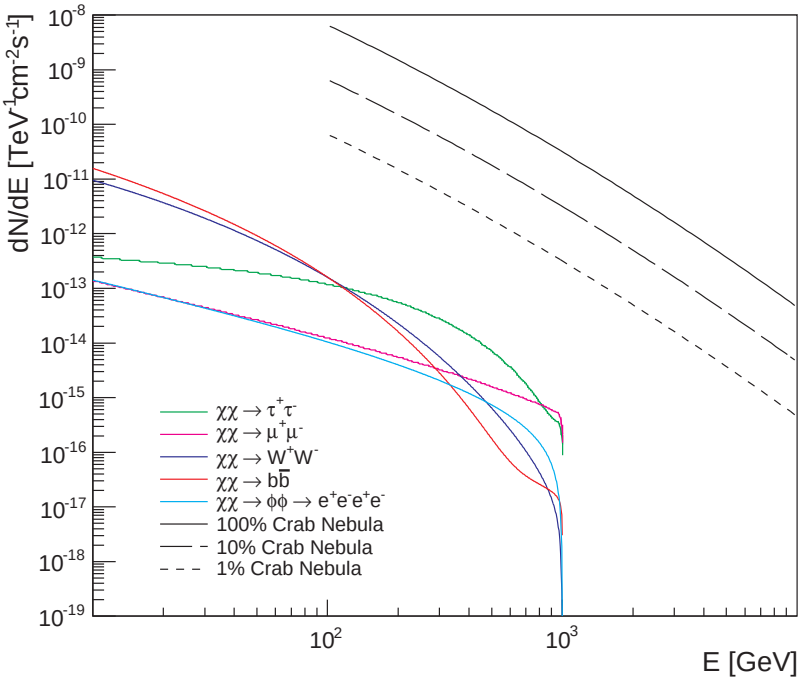

Figure 3.19: Expected Segue 1 differential flux from WIMP annihilation. A value of $< \sigma v >= 3 \times 10^{-26}$ cm^{3}s^{-1} was assumed, as well as an astrophysical factor of $J(\Delta\Omega) = 1.14 \times 10^{19}$ GeV^2 cm^{-5} sr and a WIMP mass of $m_\chi = 1$ TeV. Crab Nebula flux is depicted as reference.

Therefore, for each mSUGRA model, flux upper limits were computed for different values of energy thresholds E_0 among those listed in Table 3.13. To guarantee an unbiased comparison, the ideal case of null significance $\sigma_{\mathrm{Li,Ma}} = 0$ was considered. For each E_0 the appropriate average effective area above E_0 was used, weighted with the particular gamma-ray spectrum from dark matter annihilation. The value of the energy threshold producing the most stringent upper limit was then assigned to the particular dark matter model. Finally, the upper limits were computed again, for each model, by using the best E_0 and the actual analysis cuts, consequently abandoning the $\sigma_{\mathrm{Li,Ma}} = 0$ hypothesis.

To ensure a more direct comparison with the particle physics predictions, the results are presented in terms of upper limits to the annihilation cross section $\langle \sigma_{\mathrm{ann}} v \rangle^{UL}$. From Eq.1.24,

this upper limit can be computed as

$$\langle\sigma_{\rm ann}v\rangle^{UL} = \frac{8\,\pi\,m_\chi^2\,\Phi^{UL}(>E_0)}{\widetilde{J}(\Delta\Omega)\,\int_{E_0}^{m_\chi}\frac{dN_\gamma}{dE}dE}. \tag{3.2}$$

The effect of the energy threshold optimization can be seen in Fig. 3.18, where the two solid blue lines depict the upper limits on the annihilation cross section in the case of annihilation only into the τ channel (i.e. $B(\tau^+\tau^-) = 1$). The thin solid blue line represents the calculation of $\langle\sigma_{\rm ann}v\rangle^{UL}$ for a fixed energy threshold of $E_0 = 100$ GeV, while the thick blue line indicates the same upper limit after the optimization of the E_0. It can be seen that for WIMPs with masses around 500 GeV a factor of 3 in the upper limits can be gained if the optimized E_0 is considered. The same Fig. 3.18 also shows the upper limit dependence on the spectral shape. The dashed red line indicates the energy optimized upper limit in the case of annihilation only into $b\bar{b}$ (i.e. $B(b = 1)$. Differences can be larger than one order of magnitude (see also [374]) as can be seen by comparing the upper limits for annihilation to $\tau^+\tau^-$ and to b at low energies. Hard spectra are more constraining in that case, as expected. Finally, in the case of annihilation into $\tau^+\tau^-$, the effect of the astrophysical factor uncertainty is shown by means of a blue band. The upper (lower) band edge depicts the upper limits computed by considering an astrophysical factor minus (plus) its uncertainty at 2σ level (extracted from [371]), showing its dramatic influence for the upper limits calculation, and for the prospects for detection.

In Fig. 3.20 the $\langle\sigma_{\rm ann}v\rangle$ predictions for the points in the scan (full circles) are plotted, together with the corresponding upper limits after E_0 optimization (full squares). In addition, all the models in the scan that correspond to a *neutralino* with a relic density lower than the value derived by WMAP data plus three times its experimental error $\sigma_{\rm WMAP}$ [29] are also plotted as gray crosses. It can be seen that, for large *neutralino* masses, upper limits concentrate around 10^{-22} cm^3 s^{-1}, while at lower masses, the distribution is wider, because models with a low γ-ray flux above the threshold are able to produce only loose upper limits (as in the case of squares at low masses with upper limit of the order of $10^{-20} - 10^{-19}$ cm^3 s^{-1}). It is important to remark that each point in the scan should be compared to its own upper limit, so to avoid misinterpretations of the overlap in Fig. 3.20 between the upper limits (plotted as squares) and some models with a relic density below the WMAP value (gray crosses): this apparent overlap does not imply any exclusion. In order to avoid this possible misunderstanding the so-called enhancement factor (ENF), defined as the ratio between the upper limits on the averaged cross section and the value predicted by mSUGRA (see Eq. 3.3), was computed for each model:

$$\text{ENF} = \langle\sigma_{ann}v\rangle^{UL}/\langle\sigma_{ann}v\rangle. \tag{3.3}$$

The ENF indicates how much the cross section of the particular model should be increased in order to make it detectable. In these terms, models excluded by MAGIC-I data on Segue 1 would be associated with ENF smaller than one. In Fig. 3.20 the color coding is chosen in terms of the ENFs: yellow for points with an ENF smaller than 10^4, orange for models with $10^4 <$ENF$< 10^5$, red if $10^5 <$ENF$< 10^6$ and brown if ENF$> 10^6$.

In Fig. 3.21 the ENFs are also plotted as a function of the WIMP mass for models compatible (at 3σ level) with WMAP value of the relic density (red crosses) and below (black crosses). The panel in the upper right of the figure indicates the ENF distribution for the two sets of models. For those compatible with WMAP, the lowest ENF is of the order of 10^3. Fig. 3.20 shows that the models characterized by the lowest ENF are those with the largest annihilation cross section and a WIMP mass above 200 GeV. In contrast, the majority of the points in the scan have

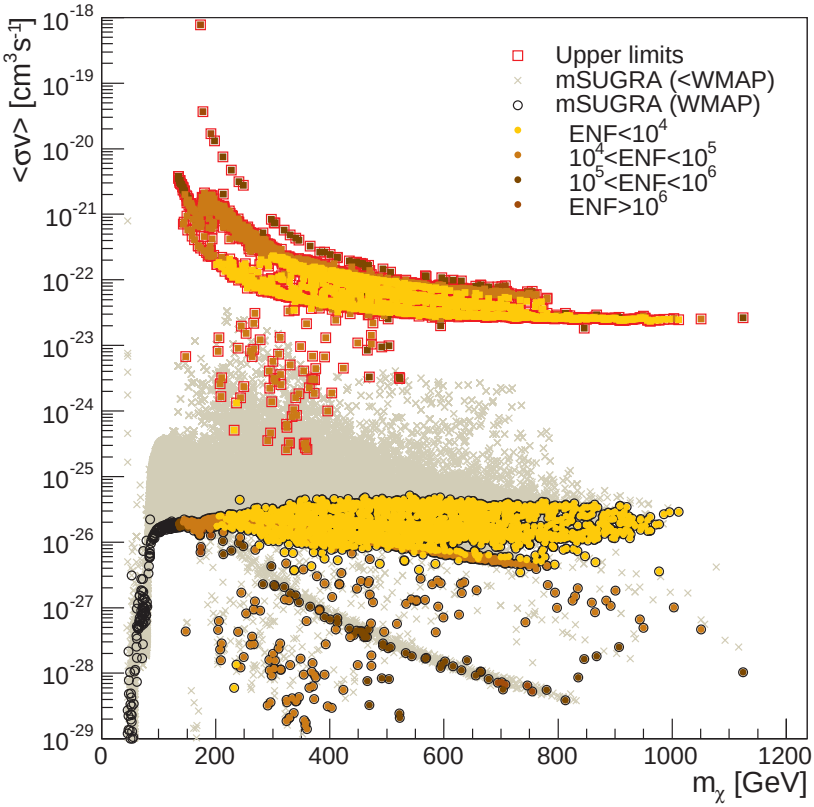

Figure 3.20: Annihilation cross section upper limits from Segue 1 MAGIC data computed for individual points in the scan. Grey crosses indicate the annihilation cross section value for those points in the scan (see Table 3.15) that pass the SM constraints and with a relic density lower than WMAP bound. The full circles only consider models within $3\sigma_{\rm WMAP}$ from WMAP. For each of these full circles the upper limit on the cross section can be computed from the Segue 1 data (after energy threshold optimization) and it is indicated here by a square. Circles and squared are color coded in terms of the enhancement factor (see Eq. 3.3).

an ENF $> 10^3$. Moreover, it can also be seen that the distribution of ENFs is quite wide. As commented before, this large spread is due to the very high, thus less constraining, upper limits relative to models with small WIMP masses, and, in general, to models with a low gamma-ray flux above the energy threshold. This fact was already pointed out by [1, 326].

In the case of models with a relic density below the WMAP value (black crosses), the situation is slightly better: their intrinsic higher cross sections make them closer to their corresponding upper limits, the ENF distribution peaks at values somewhat lower than those for points compatible with WMAP and it extends to lower values. In particular 211 models with an ENF<40, 106 with an ENF<20, 25 with and ENF<10 and 4 with ENF<5, are found.

For the sake of completeness, it is worth mentioning that the contribution of monochromatic lines to the annihilation spectrum was neglected in this study, due to the fact that their contribution is sub-dominant with respect to the continuum emission [375].

Beside the models that require the dark matter particle to be thermally produced in the early universe, and therefore request annihilation cross sections of the order of $\langle\sigma_{ann}v\rangle \sim$

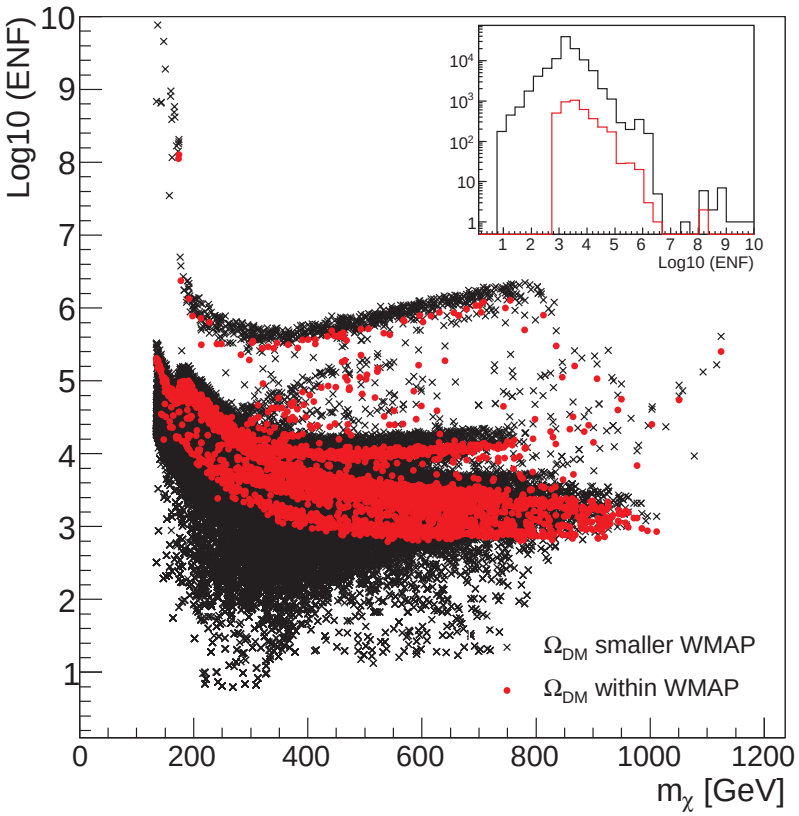

Figure 3.21: Enhancement factors as a function of the *neutralino* mass for models in the scan providing a relic density compatible with WMAP value (red crosses) or below (black crosses). The panel in the upper right part indicates the distribution of the ENFs for these two sets of models with the same color coding.

10^{-26} cm^3 s^{-1}, there are alternatives which could offer much larger values for this parameter, and consequently better detection prospects. One example are models where heavy dark matter particles annihilate mainly to leptons (frequently called leptophilic models). Many of these models can accommodate dark matter candidates able to describe the rise in the energy spectrum of the positron fraction $e^+/(e^+ + e^-)$ measured by PAMELA [153] and have been extensively studied (see, *e.g.*, [154; 163; 376; 377; 378; 379; 380; 381]). One possibility that has been largely studied is that the annihilation to leptons occurs through the production of an intermediate state ϕ, mediator of a new, long range, attractive force [376]. This type of annihilation provides a photon yield very similar to a direct annihilation to $\tau^+\tau^-$ or $b\bar{b}$, as can be seen from Fig. 1.11. However, a very large annihilation cross section is required, about a factor $100 - 1000$ larger than the canonical value derived for thermal production. Thus, the possibility to exclude those models with MAGIC-I Segue 1 was exploited. The regions in the $(m_\chi, \langle\sigma_{ann}v\rangle)$ plane that provide a good fit to the PAMELA data are shown in Fig. 3.22 for a dark matter candidate annihilating into $\mu^+\mu^-$, $\tau^+\tau^-$ and for the case of the intermediate state ϕ decaying to e^+e^-. These regions have been taken from [371] as well as the parametrization of the $\phi \to e^+e^-$ spectrum.

Using again the specific dark matter annihilation spectra, upper limits obtained from Segue 1

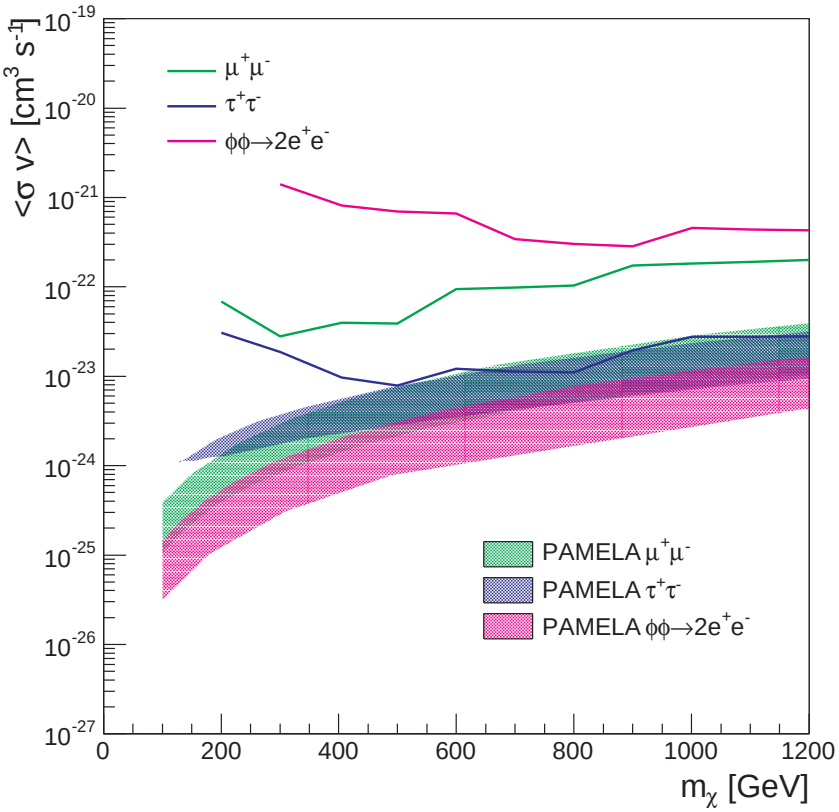

Figure 3.22: Exclusion lines for a *neutralino* dark matter annihilating exclusively into $\mu^+\mu^-$ (green line) or $\tau^+\tau^-$ (blue line) and for a dark matter candidate interacting with a light intermediate state ϕ decaying into a pair of electrons (pink line). The same annihilation channels (with the same color coding) are considered to draw the regions in the plane that provide a good fit to the PAMELA measurement of the energy spectrum of the positron fraction. The regions are taken from [371].

data are shown in Fig. 3.22. It can be seen that, in this case, the ENFs needed to meet the PAMELA-favored region are much smaller than for mSUGRA, and in the case of annihilation into $\tau^+\tau^-$ MAGIC-1 upper limits are marginally on tension with the allowed regions. However, it is worth mentioning that the uncertainty in the astrophysical factor (see Fig. 3.18) is large. Thus, no exclusion can be firmly stated until a more precise characterization of that parameter is done. If future kinematic data on Segue 1 member stars point to an astrophysical factor close to the upper end of the currently allowed range [371], MAGIC-I observations of Segue 1 might be able to confirm the exclusion of the PAMELA region for dark matter particles annihilating in $\tau^+\tau^-$, at least for massive dark matter candidates.

3.4.3 Summary and discussion

The ultra-faint dSph galaxy Segue 1 was observed by MAGIC-I telescope (single telescope observation) from November 2008 until March 2009, gathering a total exposure time of 43.2 hours out of which 29.4 hours qualified as good quality data. No significant γ-ray excess was found above an energy threshold of 100 GeV after a thorough analysis of the data.

Differential and integral upper limits to the source VHE flux were computed, considering several power-law energy spectra. The results, summarized in Table 3.12 and Fig. 3.15 for the case of differential upper limits, and Table 3.13 and Fig. 3.16 for the case of integral upper limits. In all cases, the effective area of the instrument was averaged by weighting it with the specific gamma-ray spectrum. This methodology allowed to determine how much the upper limits depend on the specific spectrum. The fact that one can get more stringent upper limits if computed above energies larger than experimental energy threshold, as a result of the interplay between the larger sensitivity of the experiment at moderate energies and the assumed spectrum, was also shown. These results are comparable with the ones already reported from other IACTs observations on dSph galaxies (see, *e.g.*, [326; 328]), including the results previously detailed in Sec. 3.2 about Willman 1 observations.

Furthermore, in the context of indirect detection of dark matter, upper limits to the *neutralino* annihilation cross section were computed for a large number of mSUGRA models. Each model, produced by an extensive simulation that scanned the IACTs region of interest out of the mSUGRA parameter space, were assigned its own upper limit to the annihilation cross section. Namely, the upper limits were derived separately for each point in the scan in order to completely account for the dependence on the specific spectral shape. This method provides a novel approach to the way results are presented in the field.

The results indicate that the upper limits are quite dependent on the energy spectrum and a general exclusion plot cannot be drawn to constrain the parameter space (see Fig. 3.20). For this reason, the results were provided in terms of enhancement factors, defined as the intrinsic flux boost needed to meet detection (see Fig. 3.21). A minimum enhancement factor of the order of 10^3 is found for models compatible with WMAP. On average, enhancement factors of the order of 10^{4-5} are found, though. However, by loosening the constraint and request only that the mSUGRA models do not exceed the WMAP upper limit considered throughout the text (meaning that smaller values than the 3σ WMAP lower limit to the relic density are also allowed), the situation is improved. In that scenario, enhancement factors as low as 3.9 are found. In these terms MAGIC-I data on Segue 1 are not so far from excluding portions of the mSUGRA parameter space.

Additionally, MAGIC-I data on Segue 1 was used to test leptophilic dark matter models able to accommodate the PAMELA results on electron-positron fraction. While current results are only marginally on tension with one of the models proposed to explain the PAMELA data (for dark matter annihilating through the $\tau^+\tau^-$ channel), if the most optimistic value for the current astrophysical factor within the uncertainties is considered (Fig. 3.18) and future improved Segue 1 kinematic data shifts its astrophysical factor towards this figure, MAGIC-I data might be able to confirm the exclusion of the PAMELA preferred region for this annihilation channel if the case of heavy dark matter particles.

The robustness of the upper limits to the annihilation cross section of the considered dark matter models strongly depends on the assumptions on the astrophysical factor, since an uncertainty of one order of magnitude (at 2σ level) remains, as estimated by [371]. The presented results can be considered conservative, since they do not take into account intrinsic contributions to the flux from the presence of substructures in the dark matter halo profile of Segue 1 (which is already *per se* a substructure of the larger Milky Way halo). The effects of substructures could boost the expected γ-ray flux from dark matter annihilation up to a factor of 15 [171] for an object like Segue 1. A second contribution to the flux, disregarded in these calculations, is the non-relativistic effect known as *Sommerfeld enhancement*, which may boost up the predictions for the γ-ray emission from dark matter annihilation [162; 382].

Comparing MAGIC-I results on Segue 1 with those of Fermi-LAT [374], the different energy range covered by the two experiments implies that the latter is more constraining for low mass dark matter candidates, while MAGIC-I can produce better upper limits only for dark matter particles heavier than few hundreds of GeV (which is also general for IACTs). For low mass dark matter particles, it is already possible for Fermi-LAT to exclude some of the mSUGRA models with a relic density smaller than what is compatible with WMAP [374]. With 5 years of data, Fermi-LAT may be able to probe some of the points of the parameter space considered here. In case of no detection, this will have the effect of excluding most of the models with large enhancement factors (see Fig. 3.21), which frequently correspond to low-mass WIMPs. On the other hand, for larger dark matter mass and in case of no detection, Fermi-LAT data will not have much influence on the prospects for IACTs.

3.5 Conclusions and outlook

Two different approaches to the indirect dark matter searches in dSph galaxies have been presented in this chapter: the search for cold dark matter particles in the VHE γ-ray band in Willman 1 and Segue 1 dSph galaxies, and the search for warm dark matter particles in the X-ray band in Willman 1 dSph galaxy. Both dSph galaxies were observed due to their promising expected fluxes, as compared to the rest of dSph population prospects, from dark matter annihilation or decay.

As for the searches in the VHE γ-ray band, data from the MAGIC-I telescope were exploited. No VHE γ-ray signal was detected for any of the surveyed dSph galaxies. Consequently, upper limits to their emission were obtained. After assuming a power law description of the possible emission, upper limits to the integral fluxes were computed: the limits, in the order of 10^{-12} $\mathrm{cm}^{-2}\mathrm{s}^{-1}$, range from 2% to 10% CU in the case of Willman 1, and from 0.5% to 9% CU in the case of Segue 1. These results are comparable with the ones already reported from other IACTs observations on dSph galaxies (see, *e.g.*, [272; 326; 327; 328; 383]). It is worth mentioning that MAGIC-I exposure on Segue 1 represents the deepest observation of a single dSph by IACTs so far, thus presenting very constraining VHE flux upper limits over this kind of objects. The aforementioned limits are unique in the low range of this energy band ($\sim$ 100 GeV) due to MAGIC-I lowest energy threshold among the current generation of IACTs.

The absence of VHE γ-ray signal was also exploited in terms of indirect dark matter searches. A common theoretical framework to describe a possible dark matter particle was chosen: namely, the mSUGRA model, a constrained particularization of the Minimal Super-Symmetry model. For Willman 1, four mSUGRA benchmark models were considered, each of them being representative points in the parameter space of the model. It was shown that the particular spectral shape, coming from the particle physics term of the flux, has a crucial importance on the detection prospects. Depending on the chosen model, the required boost factor to meet a detection varies from $B^{ul} = 2.6 \times 10^3$ in the case of the $funnel$ region to $B^{ul} = 1.3 \times 10^5$ in the case of the $co - annihilation$ region. One of the main conclusions out of these results was that a more ambitious parameter space sampling was needed. This requirement triggered a novel approach to present dark matter limits from IACTs observations that was eventually carried out with Segue 1 data. The main idea was to compute customized upper limits to the WIMP annihilation cross section in a model-by-model basis, where a large scan of the mSUGRA parameter space was conducted. In that way, the mSUGRA region which can provide a dark matter particle candidate whose mass lay in the typical IACTs energy range was completely surveyed. The results show that the annihilation cross section limits are quite dependent on the energy

spectrum of the model. Since a general exclusion plot cannot be drawn to constrain the parameter space, the results were given in the form of enhancement factors, defined as the intrinsic flux boost needed, for each model, to reach a detection. The distribution of these enhancement factors illustrates how far from constraining the mSUGRA parameter space Segue 1 data are: a minimum enhancement factor of the order of 10^3 was found, while this parameter ranges on average from 10^4 to 10^5 for models compatible with WMAP constraints. If those constraints are removed, the minimum enhancement factor turns to be as low as 3.9. Additionally to the mSUGRA models, Segue 1 data was used to probe some leptophilic dark matter models which accommodates PAMELA electron-positron fraction excess. It was shown, for leptophilic dark matter annihilating through the $\tau^+\tau^-$ channel, that Segue 1 upper limits are marginally on tension with the proposed model. An exclusion would be possible if updated kinematic data on Segue 1 star members shifted upwards the astrophysical factor of the source.

Concerning the search of dark matter in the shape of a *sterile neutrino*, Chandra-XRO observations of Willman 1 dSph galaxy were exploited. Both, the diffuse component and point-like population of the inner core of Willman 1 were studied.

As for the diffuse component, a thorough search for a possible spectral line from *sterile neutrino* decay was performed. As no detection of spectral lines with a possible exotic origin could be claimed, a significant part of the *sterile neutrino* parameter space was ruled out after assuming the *sterile neutrino* as the main component of the dark matter. It was shown that the main problem this kind of searches have to deal with is the control of the background, since many instrumental and even conventional astrophysical lines overlap with the region where the *sterile neutrino* signature is expected to be detected.

Regarding the study of the X-ray point-like population in Willman 1, and down to the luminosity limit of the observation, the probability of finding candidate X-ray binaries within its inner core was estimated to be extremely low. It might be the case that the majority of X-ray point-like sources located in the inner core of Willman 1 are background AGN.

It should be pointed out that all the results involving dark matter-motivated interpretations, rely on the assumptions made on the astrophysical factor and therefore on the dark matter modelling of the considered dSph galaxies. The strength of the presented upper limits to the WIMP annihilation cross section of the considered mSUGRA models or the excluded region of the *sterile neutrino* parameter space are significantly affected by the modelling of the dark matter content of the sources. For instance, in the case of Willman 1, the considered astrophysical factor was computed assuming a system in dynamical equilibrium, while some works cast the doubt that the system might be tidally disrupted. As for Segue 1, its nominal astrophysical factor has an uncertainty of one order of magnitude at 2σ level. Further studies about the dynamics of such objects should be carried out to better comprehend their dark matter distributions. Therefore, deepest optical observations on these objects are needed in order to refine their dark matter profiles, from both the spectroscopy of their star members as well as a better characterization of the dynamics of their surroundings.

In the case of *sterile neutrino* searches in dSph, deeper exposures on the best candidates are encouraged. Chandra-XRO and XMM-Newton are the best two instruments so far to study dSph galaxies in the X-rayband. Both instruments are complementary, though. Chandra-XRO is best suited to detect possible dark matter decay lines, due to its best PSF and energy resolution. On the other hand, XMM-Newton is more sensitive to extended emission, making the telescope best suited to check the variation of a possible dark matter signal as a function of the dark matter profile of the object. In any case, the control of instrumental lines and a fine characterization of the background would be key factors at the time of claiming a possible dark matter signal.

As an outlook to this work, in the VHE γ-ray band there have been many observations of dSph galaxies up to date. In the case of MAGIC, besides the two observations reported in the current chapter, Draco dSph galaxy was also observed. Although deeper observations on Segue 1 are being carried out by the MAGIC Telescopes, a stacking analysis of MAGIC data on dSph galaxies would provide very interesting results as well. It is worth mentioning that, in this VHE range, there are many other models offering dark matter particle candidates (see Sec. 1.3.3 for some examples) which could be probed with MAGIC data by applying the same methodology that was used for the mSUGRA *neutralino*.

To conclude, new dSph galaxies may emerge from current and future observational projects. The SDSS only covers a fraction of the northern hemisphere sky, but this fraction is constantly enlarged with new optical and spectroscopic data. Equivalent surveys in the southern hemisphere like the planned Skymapper [384] are going to increase the population of dSph satellite galaxies and might offer new candidates with even larger mass-to-light ratios and/or being at closer distances to the observer. With objects presenting larger astrophysical factors and more sensitive instruments in both, the x-ray band for warm dark matter particle candidates (like the International X-ray Observatory (IXO) [385]), and the VHE γ-ray regime (like the Cherenkov Telescope Array (CTA) [386]), the presented limits could be very much improved, and an eventual detection could be closer. The study of the prospect of detection in both energy bands is to be encouraged. Efforts on this direction have already started in the case of CTA, as can be seen in Chapter 5.

Chapter 4

Dark Matter searches in Unassociated Fermi Objects

According to current cosmological N-body simulations, the distribution of dark matter in a galaxy is not smooth but presents hierarchical and highly clustered state, therefore being able to form clumps. In the following chapter, galactic clumps of dark matter are proposed as targets for indirect searches in the context of annihilating dark matter. A selection criteria over Fermi-LAT data has been chosen as to elaborate a list of unassociated sources qualifying as good dark matter clump candidates. It was assumed that the mass of the dark matter particle is located beyond the energy range where Fermi-LAT can effectively detect the corresponding spectral cut-off, a smoking gun for dark matter detection. Therefore a different kind of detector more sensitive at higher energies is required. IACTs are very well suited for this kind of purpose. Consequently, the list of candidates is revisited, selecting the best targets to be observed by a MAGIC-like telescope. Two of the proposed sources were accepted for observation by MAGIC Telescopes. In section 4.2 the details of the dark matter clump candidates search are presented. Section 4.3 is devoted to the dark matter clump candidate 1FGL J2347.3+0710 and includes Fermi, MAGIC and Swift observational data, focusing on MAGIC data analysis and results. Section 4.4 deals with the source 1FGL J0338.8+1313 in the same way. Conclusions and outlook are presented in section 4.5.

4.1 Introduction

As already discussed in this work, a γ-ray signal in the VHE regime from dark matter annihilation would be characterized by a very distinctive spectral shape due to features such as annihilation lines [387] and internal bremsstrahlung [70] as well as a characteristic cut-off at the dark matter particle mass. Even if one can accommodate all these features in a single measured spectrum, not much could be said about the real nature of the dark matter. In order to shed light over the nature of the dark matter constituent the detection of several sources sharing the same spectral shape is mandatory. The dark matter spectrum must be universal; hence a forceful smoking-gun for dark matter would be the detection of several γ-ray sources, all of them sharing identical spectra [388; 389; 390; 391].

Astrophysical regions where high dark matter density is foreseen are the best candidates to expect γ-ray emission from dark matter annihilation or decay. No clear dark matter signal has been detected so far in any of the most promising targets, as was stated in Chap. 3 in the

case of dSph galaxies, nor in the case of VHE observations of the Galactic Center [167; 168]. Although galaxy clusters are very far objects VHE γ-ray emission of dark matter origin might be detectable. VHE observations in these kind of objects were performed and no dark matter signal was found so far [392]. Even if a VHE signal is detected, the hypothetical dark matter contribution may be over-shined by the emission from *e.g.* the AGN population.

Yet, there exist other possible regions of high dark matter density: in the last few years cosmological N-body simulations have successfully uncovered how the cold dark matter distribution evolves from almost homogeneous initial conditions into the present hierarchical and highly clustered state [171], [172]. Most recent high resolution simulations indicate that dark matter halos should not be smooth but must exhibit a wealth of substructure on all resolved mass scales [347], [393], as illustrated in Fig. 4.1. These subhalos could be too small to have attracted enough baryonic matter to start star-formation and would therefore be invisible to past and present astronomical observations. Overdensities or clumps are foreseen into these subhalos which can be nearby in our galaxy and therefore bright at VHE γ-rays by annihilation of dark matter. [173]. Also dark matter high density regions can develop around intermediate massive black holes, where a rather peaked VHE emission is predicted [394].These overdensities would most probably only be visible at HE and VHE and therefore not have shown up in any catalog yet. Since dark matter emission is expected to be constant, such hypothetical sources would pop-up in the all-sky monitoring programs [395], and this can be best provided by the Fermi-LAT [246] as Unassociated Fermi Object (UFO)s not detected at any other wavelengths. As already mentioned, the smoking-gun for dark matter detection could be a very distinct cutoff close to the dark matter particle mass. Most probably, this is too high an energy (typically > 50 GeV) [396] to be measurable by Fermi-LAT within reasonable time (if at all possible). Therefore the synergy between Fermi-LAT and the IACTs appears naturally. In addition, UFOs can provide a population of objects where to search for the universality or the dark matter spectrum.

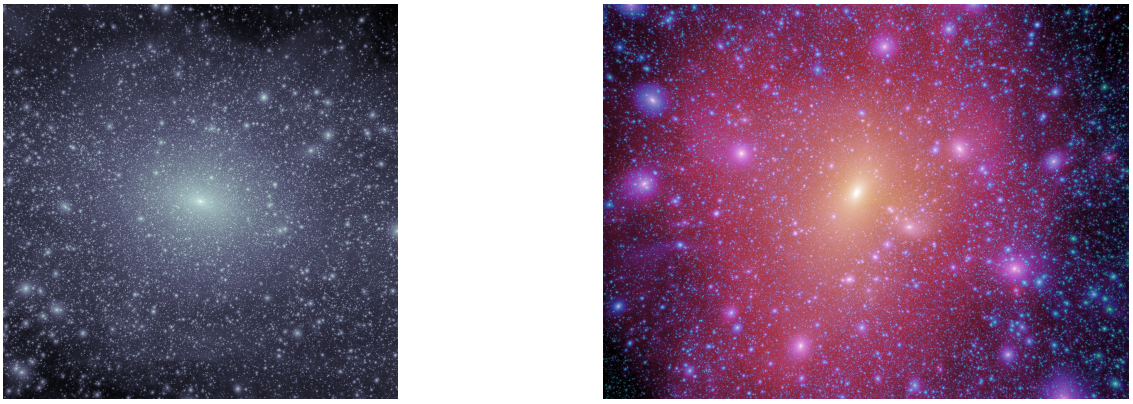

(a) Via Lactea II simulation

(b) Aquarius simulation

Figure 4.1: Examples of dark matter clumps in Milky Way-size hales at redshift $z = 0$ in different N-body simulation realizations. 4.1a Via Lactea II Project simulation. The projected dark matter density-square in a 800 kpc cube is depicted. This simulation has a mass resolution of 4100 $M_{\odot}$. The high resolution region is embedded in a 137 Mpc box to account for the large scale tidal forces. From [171]. 4.1b Aquarius Project simulation. The projected dark matter density-square in a 1084 kpc cube is depicted. This simulation has a mass resolution of 1712 $M_{\odot}$. This high resolution region is embedded in a 137 Mpc large scale simulation cube. From [172].

The work to be presented in the following sections consists on a practical realization of the

aforementioned line of research where: *i)* a search for good dark matter clump candidates in Fermi data has been performed together with a study on the detection prospects of detection by current IACTs for the selected sources, and *ii)* the data analysis and interpretation of the observed candidates by the MAGIC Telescopes.

4.2 Candidates search

Fermi-GST, already described in Sec. 2.3 is the most suitable tool to search for dark matter clump candidates due to its full sky coverage and sensitivity. Its positional resolution ($\approx 0.1^\circ$ for energies above 10 GeV) is similar to the current IACTs angular resolution, which is a mayor advantage since IACTs are mainly sensitive to well located point-like sources. In 2009, the Fermi-LAT Collaboration released a catalog of high energy γ-ray sources detected by the LAT instrument after having gathered data from the first 11 months of the science phase of the mission [183]. This catalog, dubbed First Fermi Catalog (1FGL), contains a total amount of 1451 sources over an average flux significance threshold of 4σ in the 100 MeV to 100 GeV energy range. For each source, positional and spectral information, as well as identification or possible associations with cataloged sources at other wavelengths, are provided. The 1FGL Catalog was the starting point of the search for dark matter clump candidates to be observed by IACTs. The search consisted on a consecutive four-step process that can be summarized as:

I. A thorough selection of sources out of the 1FGL Catalog based on the catalog information itself.

II. An extensive search for possible counterparts.

III. An independent and dedicated Fermi-LAT HE photons study.

IV. An IACTs detection prospects study based on MAGIC Telescopes characteristics.

4.2.1 Unassociated Fermi objects

The procedure to identify and associate Fermi-LAT sources to already observed objects at other wavelengths is complex. Although Fermi-LAT has a good angular resolution, a firm identification based on positional coincidence alone is not possible, since the typical Fermi-LAT error contour may contain more than one single object detected at different wavelengths. Thus, in order to infer the nature of Fermi-LAT sources more information is required: spectral information, time variability and the feasibility to produce the observed γ-ray emission in physical processes at the eventual identified source. A so-called identification demands a clear correlation of the flux timing characteristics between Fermi-LAT and observations at other wavelengths, like in the case of the periodicity of pulsars and X-raybinaries or the flaring states of blazars. Coincident angular extent with observations at other wavelengths can also establish an identification. If the identification is not possible, a so-called association can also be made if a positional coincidence is statistically unlikely to have occurred by chance. Source association is then provided by two different approaches: *i)* a test for statistically significant detection of sources of different types [397] or *ii)* an automated source association analysis [398]. The 1FGL automated source association algorithms used 31 different catalogs and observation archives for their purpose, finding most of the associations in the blazars catalogs (*e.g.* BZCAT produced 487 associations) and in the radio archives (*e.g.* VLBA Calibrator Survey provided 484 associations). If no

association was possible, then the source is classified as an UFO. It is worth noting that a lack of association might happen not only by a lack of candidates, but by an excess of likely candidates. Out of the 1451 sources that form the 1FGL Catalog, 630 of them are UFOs.

4.2.2 Selection of candidates out of the 1FGL Catalog

The collection of good dark matter clump candidates out of the 1FGL Catalog started with a thorough selection of sources attending to spectral characteristics, time variability, possible associations and position in the sky. The criteria, dubbed *catalog conditions*, that a source was requested to comply with in order to pass to the next step in the search procedure were the following:

- *To be an unassociated*: As previously mentioned, dark matter clumps could be small enough so their gravitational potential may have not accreted the sufficient baryonic matter to emit in a different energy range where γ-ray radiation from dark matter annihilation is expected. Moreover, if no other type of emitter is present in the vicinity of the γ-ray source it could be considered almost background free.

- *To lay outside the Galactic Plane*: Most of the UFOs are located in the Galactic plane. A noteworthy fraction of galactic baryonic objects are found in the Galactic Plane, unlikely the galactic dark matter substructures whose galactic latitude distribution is homogeneous [171; 172]. Source association in very crowded environments is more difficult for the association algorithms and therefore unassociations due to an excess of candidates is more common. Moreover, the galactic diffuse γ-ray background is much stronger at low galactic latitudes which makes Fermi-LAT data analysis more difficult. Therefore, detection of some faint UFOs, nearby or within the Galactic Plane, depends on the assumed galactic γ-ray background model. Consequently, UFOs with small galactic latitudes, precisely $|b| < 10\,\mathrm{deg}$, were discarded.

- *To be a hard source*: Several studies, including the computation of the expected photon yield from WIMP annihilation as a function of energy [145; 343], concluded with the idea that the corresponding spectra, which essentially follow the shape of the annihilation photon yield, are hard spectra until the WIMP mass cut-off. Additionally, 1FGL sources showing hard spectra are more likely to be detected beyond Fermi-LAT upper energy threshold by IACTs. Therefore only hard sources were selected, meaning that 1FGL sources whose spectral fitting power law index was above 2 were discarded. This figure was chosen because all the different annihilation spectra from [145] are harder than a power law with spectral index of 2.

- *To be non-variable:* As already mentioned, the photon flux from dark matter annihilation must be constant, and thus variable sources must be rejected. The 1FGL provides a *variability index* based on a month-by-month absolute flux statistical comparison. The corresponding light curve is significantly different from a flat one if that index is greater than 23.21. Therefore sources whose *variability index* surpasses that limit were discarded.

- *To follow a power law spectra:* Although it could appear counter-intuitive given the fact that dark matter spectra show prominent cut-offs at the dark matter particle mass, one of the main hypothesis that were assumed for this search is that the cut-off must lay outside Fermi-LAT energy range, sufficiently away from the cut-off energy the spectra can be well

described by a power law (see *e.g.* the asymptotic behavior of spectra in [343]). In order to quantify departures form a power law spectra, the 1FGL includes the so-called *curvature index*. When the value of that index is greater than 11 it means that the spectrum of the source significantly deviates from a power law. Consequently sources with a *curvature index* surpassing that limit were discarded.

Out of the total 630 UFOs only 93 of them fulfilled the *catalog conditions*.

4.2.3 Possible counterparts search

For each candidate from the above-mentioned subset of sources, an extensive and independent search for possible associations was performed. The main astronomical catalogs and missions archives were explored around the sources 1FGL nominal positions with a 20' conservative search radius corresponding to twice the Fermi-LAT PSF at 10 GeV [399]. The purpose of this search is neither to associate nor to identify counterparts for 1FGL sources, but better to discard objects whose Fermi-LAT γ-ray flux could be eventually attributed to an already present conventional source. In this way a list of unassociated and *clean* sources, with no X-raysources or bright radio sources (integral fluxes greater than 100 mJy) in their Fermi error region, was built. The search, performed with the help of the NASA's High Energy Astrophysical Archive [400], scrutinized the observation archives from current and past γ-ray missions like AGILE, INTEGRAL, CGRO, HETE-2, COS-B; X-raymissions like ROSAT, Chandra, XMM-Newton, Swift, Suzaku, RXTE; and radio catalogs like the NRAO VLA Sky Survey, Green Bank Survey, FIRST Survey. Infrared and ultraviolet missions archives like Spitzer, IRAS, FUSE, and GALEX were also considered when no γ-ray, X-rayor radio source was present in the field of study. In order to illustrate the results of the search some examples of $40' \times 40'$ regions centered on different UFOs are shown in Fig. 4.2 for both selected and discarded sources.

After this analysis, an additional search was performed. By the time this search was performed an ambitious program comprising X-rayobservations of several high galactic latitude UFOs with Chandra-XRO and Swift-X-Ray Telescope (XRT) [401] was ending. Although no published results were available, Swift-XRT data were made public and counterparts were searched for on them. Therefore analyses of these new Swift-XRT data were performed for each of the 23 sources, by means of the standard *HEASoft* Swift package tools [402]. UFOs containing X-raysources within Fermi error contour in Swift-XRT data were consequently discarded.

Finally, only 10 UFOs of of the 93 objects fulfilling the *catalog conditions* conditions survived the dedicated possible association search as *clean* sources. The list of sources can be found in Tab. 4.1.

4.2.4 High energy Fermi photons

Fermi-GST began its science phase on August 4, 2008. After 11 months of data taking, the 1FGL Catalog was compiled. However, a much richer photon statistic was available at the time this search for dark matter clumps candidates was performed. Therefore, a dedicated analysis of all the HE photons arriving from the *clean* sources and their surroundings was required.

Fermi-LAT data for all these 10 *clean* sources were analyzed using the latest version of *Fermi ScienceTools* [404]. The best suited event selection quality cuts for off-plane point source analysis were applied by means of the *gtselect* tool, namely, event class 3 and 4 were considered for photons below 20 GeV and class 4 beyond that energy. Additionally, a maximum zenith angle cut of 105° was applied and the latest Instrument Response Functions (*Pass6_v3*) were

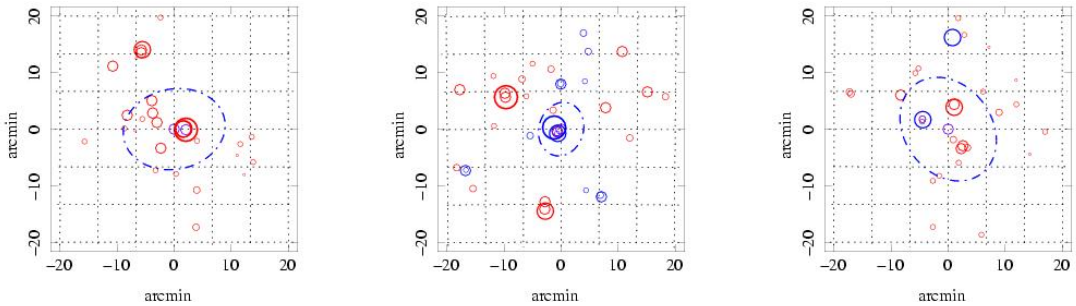

(a) 1FGL J0226.3+0937 **(b)** 1FGL J0537.7-5717 **(c)** 1FGL J1735.7+2031

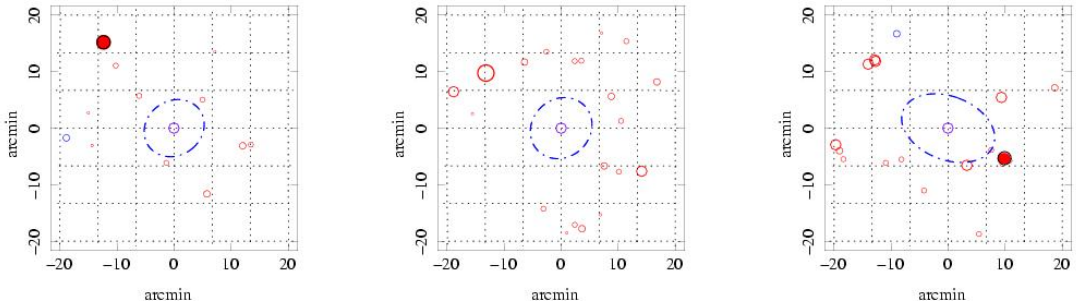

(d) 1FGL J0338.8+1313 **(e)** 1FGL J1351.8-1353 **(f)** 1FGL J2347.3+0710

Figure 4.2: $40' \times 40'$ regions centered on some representative sample of unassociated Fermi objects surviving the *catalog cuts*. Top three sources (4.2a, 4.2b, 4.2c) do not survive the dedicated counterpart search filter. Bottom three sources (4.2d, 4.2e, 4.2f) qualify as *clean* sources. The purple circles are centered on Fermi-LAT nominal position, surrounded by a dot-dashed line representing its 95% contour error. Red circles are radio sources, yellow circles are infrared sources, blue circles are X-raysources, and purple circles represent γ-ray sources. Circle radius is proportional to the source flux in the corresponding energy band. The maps (equatorial coordinates) were produced with the ASDC Data Explorer [403].

considered. Regarding the time selection, performed with the *gtmktime*, only good time intervals were considered. On top of that, photons arriving when the satellite was crossing the South Atlantic Anomaly were discarded as well as those recorded at a rocking angle greater than 45° . Regions of interest based zenith angle cuts were also applied. A more complete description of Fermi-LAT data analysis can be found in [405].

A large region of $20° \times 20°$ around the UFO nominal position was studied, in order to look for other possible HE sources or regions of high diffuse emission. The reason for this study was based on the fact that, for an eventual IACT observation, in order to obtain a significance of detection, regions where no γ-ray emission is expected are required for background subtraction. These background regions are usually extracted from nearby positions with respect to the source, some times even from the same IACT observation FoV (see Sec. 2.4.3 for more details). As a conclusion neither point-like sources nor strong background was found that could spoil an eventual IACT observation.

The total number of HE photons is a determinant quantity since it provides an evidence of the validity of the extrapolation of Fermi fluxes beyond the IACTs energy thresholds. Therefore, a smaller circular region of 1.5 times Fermi-LAT PSF radius (0.15°) was examined in order to get the HE photons over 10 GeV likely to have been emitted by the source. The diffuse HE γ-ray background at high galactic latitudes is expected to be almost negligible. In order to

evaluate its contribution to the total number of photons extracted from the 0.15° radius region centered around the sources, an estimate of the background flux was computed. All the 1FGL sources present in the large 20° × 20° regions were excised and the contribution of the diffuse background plus unresolved sources was obtained from the remaining photons in an annulus defined by an inner radius 1° and outer radius 6° . The adopted exposure time in the annulus was assumed to be homogeneous and equal to the candidate source position exposure, which is a good approximation considering the fairly uniform exposure of the instrument. The results of the γ-ray background flux estimation obviously depend on the source location, ranging from $\sim 7.5 \times 10^{-5}$ sr^{-1} s^{-1} to $\sim 3 \times 10^{-4}$ sr^{-1} s^{-1} in the set of considered sources. Therefore, the contribution of background photons over 10 GeV in the 0.15° radius extraction region was estimated to range from ~ 0.2 to ~ 0.8 photons.

After performing the extraction of the HE photons all the sources provided four or more of photons over 10 GeV. Attending to the estimated number of background photons in the extraction region it is clear that the majority of the extracted photons are unlikely to be background photons. The energies of the photons for each source are found in Tab. 4.1.

4.2.5 IACTs detection prospects

IACTs are able to detect sources with exposures of few minutes in the case of high fluxes like the Crab Nebula one or bright AGN in high or flaring states but usually the required observation time is much longer, from few to hundreds of hours. Since the total observation time is limited, the feasibility of detection of a certain source is crucial when proposing candidate targets for this kind of telescopes. For unexplored sources in the VHE regime, the spectral information, needed to compute the detection time, is obviously missing. In the case of well known sources with detailed spectral energy distribution information one can perform a model dependent extrapolation of the spectral behavior at very high energies and then estimate the detection time. This was not the case for the UFOs, where only Fermi-LAT spectral information was available. Therefore UFOs detection prospects for IACTs relied basically on Fermi-LAT spectral data. Given the hypothesis that the sources are located at galactic distances it was assumed that they do not suffer from EBL extinction and a direct extrapolation of Fermi power law differential flux to the VHE range was done.

As mentioned in Sec. 2.4, a signal detection in the IACT context is defined as a more than 5σ deviation of the number of excess events over the number of background events. If the total number of events is expressed in terms of their rates as $N_{on} = (R_{exc}+R_{bkg})t$ and $N_{off} = \kappa R_{bkg} t$, were t is the observation time, and the on-off ratio is assumed to be $\kappa = 1$, the detection time can be obtained working out Eq. 2.16 as

$$t = 25\frac{R_{exc} + 2R_{bkg}}{R_{exc}^2}, \tag{4.1}$$

where the excess rate over a certain energy threshold E_{th} can be estimated from the effective area of the instrument $A_{eff}(E)$ and the differential spectrum of the source $\phi(E)$ as

$$R_{exc} = \int_{E_{th}}^{\infty} \phi(E) A_{eff}(E)\, dE. \tag{4.2}$$

Consequently, the estimated detection time for a certain source depends only on its spectrum, the effective area and background rate of the instrument, and an energy threshold. In the current case, the effective area and background rate that were considered characterized the MAGIC Telescopes [406], and the very high energy UFO spectra were directly extrapolated from the 1FGL

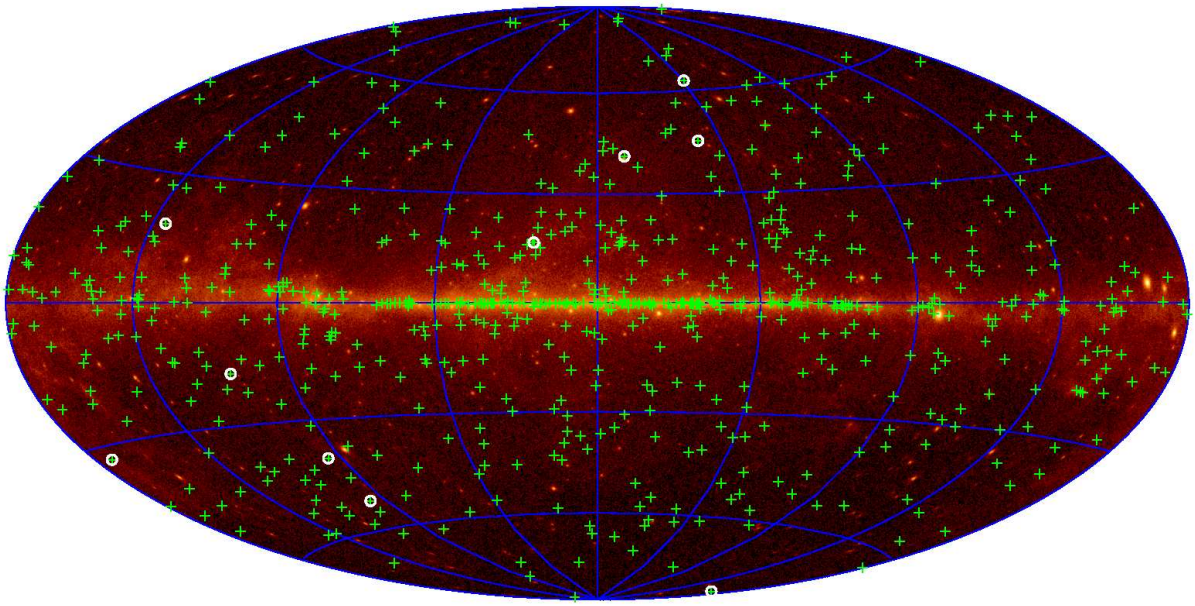

Figure 4.3: All sky Fermi-LAT Aitoff projection of photons over 1 GeV. Green crosses indicate the nominal position of the 630 unassociated Fermi objects. White circles are the final 23 selected dark matter clump candidates from table 4.1.

catalog. In a first step a *nominal case scenario* (NCS) is defined, where nominal normalization factors and spectral indices from the 1FGL Catalog are considered for flux extrapolation. In a second step, in order to estimate the effect of the uncertainty in the spectrum parameters provided in the 1FGL, the detection time was also computed in the case that of a 1FGL normalization factor one sigma below and a spectral index one sigma beyond the 1FGL nominal values, namely a pessimistic estimate of the detection time dubbed the *worst case scenario* (WCS). Regarding the energy threshold, two different ones were adopted. First, a conservative one, already achieved by MAGIC Phase-I (past single telescope observations), of E_{th} =100 GeV. Second, an expected E_{th} =50 GeV for MAGIC Phase-II (stereo observations). Eventually four different detection times were computed for each candidate source corresponding to the NCS and the WCS for both energy thresholds.

In the NCS, 8 out of 10 sources present an estimated detection time below 50 hours assuming an energy threshold of 100 GeV (7 out of 10 in the case of an energy threshold of 50 GeV) while only 3 out of 10 are estimated to be detected with less than 50 hours of observation in the WCS above 100 GeV (none of them would be detected in the WCS in less than 50 hours with an energy threshold of 50 GeV). The results are satisfactory since IACT detectability was not consider as a argument for candidate selection. Remarkably, to have a variety of dark matter clump candidates with such a detection prospects improves the probability to compare eventual HE γ-ray spectra looking for common spectral features. The results of the estimated detection time are detailed in Table 4.1.

4.2.6 Final candidates

The final set of dark matter clump candidates proposed as very interesting targets for IACT telescopes observation is found in Table 4.1. In such a table the significance of detection, the flux density and the spectral index from the 1FGL Catalog are shown, as well as the MAGIC detection prospects for both *NCS* and *WCS* scenarios for the two energy thresholds considered, namely 50 and 100 GeV. The lists of HE Fermi photons arriving from a 0.15° radius region around the sources nominal positions are also detailed. Six candidates are located in the northern celestial hemisphere and four candidates can be found in the southern celestial hemisphere. In Fig. 4.3 all the candidates can be found superimposed to an all-sky Fermi-LAT map of photons over 1 GeV.

4.2.6.1 MAGIC Telescopes candidates

Out of the list of good dark matter clump candidates not all of them could be observed by MAGIC telescopes. As already mentioned in Sec. 2.4 MAGIC Telescopes are situated at the Canary Island of La Palma, at an approximate latitude of $\sim 28.8°$ N. Therefore the maximum declination coverage from the telescopes latitude ranges from Dec.$\sim -61°$ to Dec.$\sim +119°$. None the less, as it was stated in Sec. 2.4.1, IACT telescopes' energy threshold is strongly dependent on the zenith angle of the observations. Consequently, the available declination window gets significantly reduced in the pursue to get the lowest energy threshold possible. This optimization of the energy threshold is required by the fact that the wider the energy range covered by the observation the wider the mass range of the WIMP that is tested. In the case of MAGIC telescopes the optimum energy threshold is obtained in observations performed below 35° in zenith angle. Thus, the optimum declination ranges from Dec.$\sim -6°$ to Dec.$\sim +64°$. Sources whose declination do not allow for observations in the aforementioned range were not considered.

At this stage of the search an ordering of the final candidates was required attending of the feasibility of detection by the MAGIC Telescopes. The ordering was based in two factors, namely, the total number and energies of Fermi-LAT photons over 10 GeV, and the detection prospects in both direct and conservative approaches. The total number of photons over 10 GeV is a determinant quantity since it provides an evidence of the validity of the extrapolation of Fermi fluxes to MAGIC energies. In that sense 1FGL J0338.8+1313, 1FGL J2347.3+0710, and 1FGL J1725.2−0509 present a noteworthy population of Fermi-LAT HE photons, the first two sources containing one photon over 100 GeV each. As can be seen in Tab. 4.1 the detection prospects for 1FGL J2321.4+1738 and 1FGL J2334.2+4319 are not the most promising ones since their expected detection time in the conservative approach overwhelmingly exceed the typical observation time that could be granted in a IACT telescope. On the other hand, 1FGL J2347.3+0710, 1FGL J1312.6+0048, 1FGL J0338.8+1313, and 1FGL J1725.2−0509 present reasonable expected detection times, below the reference 50 hours observation time in the case of an energy threshold of 100 GeV and the direct approach. In Tab. 4.2 an ordered list of the best dark matter clump candidates suitable to be observed by the MAGIC Telescopes is shown.

Table 4.1: 10 dark matter clump candidates out of the 630 unassociated Fermi objects.

Source	Significance	$F \pm \Delta F$	$\Gamma \pm \Delta\Gamma$	Detectability		$\gamma_{>10GeV}$
		$[cm^{-2}MeV^{-1}s^{-1}]\times10^{-11}$		$(E_{thr} = 50GeV)[h]$	$(E_{thr} = 100GeV)[h]$	[GeV]
1FGL J0136.3−2220	4.6	2.03±0.75	1.60±0.25	6 (154)	2 (35)	19.0, 25.0
1FGL J0336.0+7845	4.4	2.80±1.05	1.79±0.28	31 (1080)	7 (280)	43.7, 45.4, 171.5
1FGL J0338.8+1313	5.0	4.08±1.24	1.78±0.22	11 (167)	3 (41)	12.7, 14.0, 14.2, 18.2, 22.3, 23.7, 29.1, 133.5
1FGL J1312.6+0048	13.7	139.3±15.5	2.00±0.09	10 (34)	3 (9)	10.0, 10.6, 12.7, 27.0
1FGL J1351.8−1523	5.1	0.96±0.36	1.47±0.32	2 (50)	1 (11)	10.6, 24.4, 25.5, 49.2
1FGL J1509.7−0843	4.1	0.68±0.30	1.73±0.44	11 (930)	3 (256)	15.4, 18.0, 43.1
1FGL J1725.2−0509	6.3	17.06±3.92	1.99±0.14	20 (134)	5 (36)	14.5, 14.6, 22.4, 35.4, 42.5, 58.3
1FGL J2321.4+1738	4.2	2.04±0.86	1.86±0.38	107 (8770)	25 (2540)	13.8, 17.0
1FGL J2334.2+4319	4.1	3.71±1.30	1.98±0.34	170 (7720)	42 (2360)	18.6, 71.8
1FGL J2347.3+0710	5.5	1.13±0.38	1.54±0.35	2 (85)	1 (20)	15.6, 45.7, 20.4, 29.2, 86.8, 101.1

The source detection significance, in Gaussian σ units, is derived from the likelihood analysis Test Statistic. The flux density F and the spectral index Γ are derived from the likelihood analysis in the 100 MeV to 100 GeV energy range and referred to the pivot energy. The detectability was computed as explained in the text, the main values correspond to the direct calculation and values within parenthesis correspond to the conservative approach. The list of photons was obtained from Fermi-LAT data up to August 23, 2010.

Table 4.2: Best dark matter clump candidates observable by MAGIC Telescopes.

Order	Source	RA_{J2000} [^{h} ^{m} ^{s}]	Dec_{J2000} [$^\circ$ $'$ $''$]
1	1FGL J0338.8+1313	03 38 53.09	13 13 53.0
2	1FGL J2347.3+0710	23 47 19.92	07 10 26.0
3	1FGL J1312.6+0048	13 12 36.00	00 48 36.7
4	1FGL J1725.2−0509	17 25 13.20	−05 09 14.8
5	1FGL J2321.4+1738	23 21 26.16	17 38 47.4
6	1FGL J2334.2+4319	23 34 14.88	43 19 10.2

The top two candidates of the final list were proposed to be observed by the MAGIC Telescopes. Data were taken on both 1FGL J0338.8+1313 and 1FGL J2347.3+0710 UFOs. In the next Sec. 4.3 and 4.4 MAGIC data analyses and results are presented fro both sources, together with brief comments on Fermi-LAT HE photons and Swift observations on the aforementioned couple of good dark matter clump candidates.

4.3 1FGL J2347.3+0710 observations

4.3.1 Fermi high energy γ-ray data

The analysis of 1FGL J2347.3+0710 Fermi-LAT data presented hereafter considered LAT γ-ray events up to August 23, 2010 (304272002 s mission elapsed time MET) and followed the procedure described in Sec. 4.2.4. A $20^\circ \times 20^\circ$ region, centered in the source nominal position, of Fermi-LAT photons with energies larger than 10 GeV is shown in Fig. 4.4. The skymap provided relevant information for the subsequent observations by MAGIC Telescopes. It can be clearly seen that no bright HE γ-ray source other than the candidate is present in a region encompassing MAGIC FoV. Therefore, one can exclude contamination by a second HE γ-ray source in the background regions to be used in MAGIC data analysis.

The estimation of background events above 10 GeV arriving from the 0.15° radius region around the source nominal position is of 0.19 photons, as described above. This number is remarkably smaller than the total number of HE photons arriving from the same region, namely 6 photons with energies above 10 GeV (see Table 4.1). Thus, the probability of these events to be all of them background photons is negligible. This fact reinforces the hypothesis that the source does not present a sharp cut-off at energies of few tens of GeV.

4.3.2 Swift X-rayobservations

A total 4986 s exposure of 1FGL J2347.3+0710 was acquired during the end of January 2011 with the XRT [407] on board the Swift satellite. The observation, belonging to a wider program comprising X-rayobservations of several UFOs with Chandra and Swift telescopes [401], was divided into three different runs. In every run, the XRT operated in the so-called Photon Counting mode with full spectral resolution and a time resolution of 2.5 s. A brief summary of the observations can be found in table 4.3.

For the analysis, standard cleaned Level 2 events were used, meaning standard grade filtering (grades 0-12) and default screening parameters in the 0.3-10 keV energy range. Analysis of the data was performed with standard *HEASoft* Swift package tools [402]. Fig. 4.5 shows the XRT image of the field.

Within the 95% Fermi-LAT error contour, no point source brighter than 10 counts (0.0052 counts/s) in the 0.3-10 keV energy range were found. Using the web-based tool *WebPIMMS*

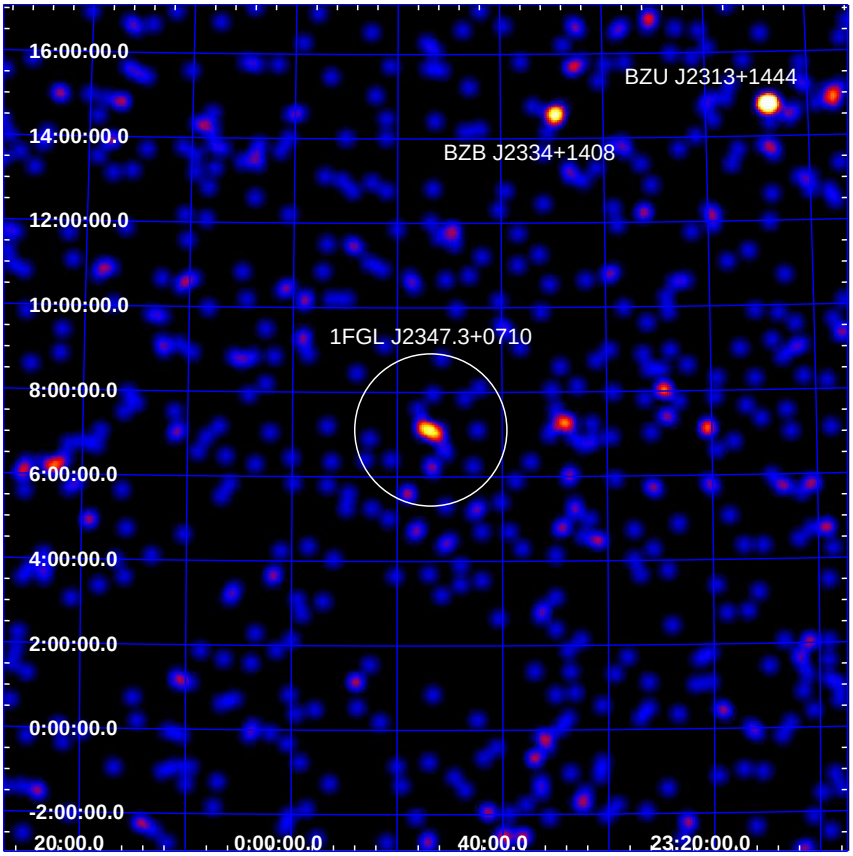

Figure 4.4: Fermi-LAT skymap over 10 GeV in a 20° × 20° region centered on 1FGL J2347.3+0710. The white 3.5° diameter circle depicts MAGIC FoV, where no other γ-ray source is present. Two bright objects are present in the region: the BL Lac BZB J2334+1408 and the blazar BZU J2313+1444, far enough from 1FGL J2347.3+0710 to spoil MAGIC observations. The image has been smoothed with a Gaussian kernel $r_k = 9'$. Fermi-LAT photons as of August 23, 2010.

Table 4.3: Swift-XRT 1FGL2347.3+0710 observations summary.

Obs. ID	RA_{J2000} [^{hms}]	Dec_{J2000} [° ′ ″]	Search Offset [']	Date	Exposure [s]
00041511003	23 47 07.01	+07 13 37.4	4.534	2011-01-29	1939

The exposure accounts for Photon Counting mode only.

[408] and the corresponding column density $N_H = 7.4 \times 10^{20}\ cm^{-2}$ and a photon index $\Gamma = 1.4$, an integral flux upper limit of $\Phi^{UL}(0.3 - 10keV) = 2.7 \times 10^{-13}\ ergs\ s^{-1}\ cm^{-2}$ is obtained. There is one point source outside the Fermi-LAT contour at RA_{J2000} $23^h46^m39^s.9$, Dec_{J2000} + 07°05′ 07″ .2 with a 0.017 counts/sec count rate in the 0.3-10 keV range. This corresponds to a 0.3-10 keV integral flux $\Phi(0.3{-}10keV) = (8.9{\pm}0.2){\times}10^{-13}\ ergs\ s^{-1}\ cm^{-2}$. Optical spectroscopy of this object taken by the Hiltner 2.4 m optical telescope hosted at the MDM Observatory [409] reveals a featureless spectrum possibly consistent with a BL Lac object [410]. A clear association with 1FGL J2347.3+0710 is not very likely assuming the current Fermi nominal position and 95% contour error. Refined positioning and error estimates in the forthcoming Fermi-LAT Second Source Catalog may contribute to clarify the situation.

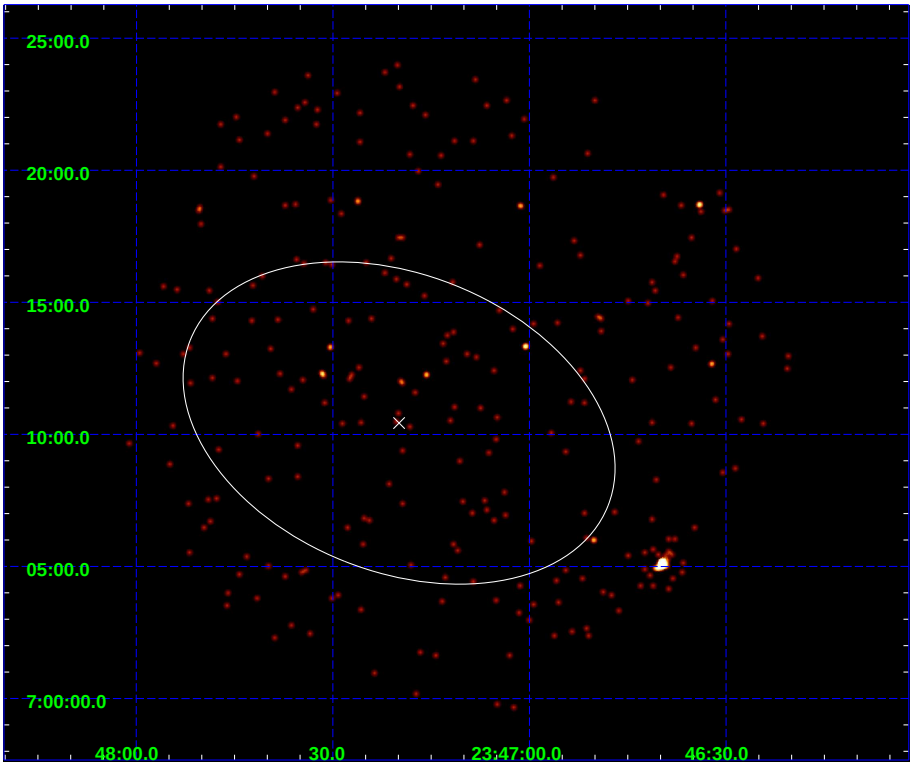

Figure 4.5: Smoothed Swift XRT 0.3-10 keV image in the direction of 1FGL J2347.3+0710. The white cross is 1FGL J2347.3+0710 Fermi-LAT nominal position. The white ellipse depicts Fermi-LAT 95% error contour for this source. The Swift XRT FoV is $26'$ $\times$ $26'$ in Photon Counting mode. The image has been smoothed with a Gaussian kernel $r_k = 4''$.

4.3.3 MAGIC very high energy gamma-ray observations

The observations of 1FGL J2347.3+0710 were performed with the MAGIC Telescopes in stereoscopic mode. Data were taken during October and November 2010 under dark night conditions. The source was surveyed in false tracking mode (the so-called *wobble* mode) [286], alternating the pointing direction every 20 minutes between $\pm 0.4^\circ$ offset in RA with respect to the source nominal position. The zenith angle window ranged from 21.5° (corresponding to the source culmination at MAGIC Telescopes latitude) to 30.0° , which ensures the lowest energy threshold for this source declination. The total exposure time was 13.3 hours. More details on the dataset can be found in Table 4.4.

Data were analyzed using the standard MAGIC analysis procedure for stereo observations (see Sec. 2.4.3). Data from each telescope were independently calibrated and signals were extracted. The noise from the NSBL was removed from the air-shower images independently as well. In the case of MAGIC-I Telescope, an absolute time image cleaning was applied to the event images: *i)* a minimum amount of 6 phe for the *core* pixels and 3 phe for the boundary ones were required; *ii)* individual core pixels whose arrival time differs from the mean *core* pixel arrival time more than 4.5 ns are excluded, as well as those individual *boundary* pixels whose signal arrival time differs from its *core* pixel neighbor arrival time more than 1.5 ns. In the case of MAGIC-II Telescope, an absolute time cleaning was also applied: while the time constraints were the same as in MAGIC-I image cleaning (since the trigger area pixels have the same geom-

Table 4.4: 1FGL J2347.3+0710 MAGIC dataset.

Night	t_{eff} [h]	Z.A. [°]
2010/10/06	1.3	21.5 – 30.0
2010/10/10	2.0	21.5 – 27.5
2010/10/11	2.0	21.5 – 27.0
2010/10/13	2.1	21.5 – 27.5
2010/10/31	2.0	21.5 – 30.0
2010/11/01	1.4	21.5 – 24.5
2010/11/04	1.3	21.5 – 30.0
2010/11/25	1.1	21.5 – 25.5

As a convention within MAGIC Collaboration, the observation *Night* refers to the date of dawn after regular observations. t_{eff} stands for the effective observation time (see Sec. 2.4.3.7). Z.A. holds for the zenith angle window of the observation.

etry in both cameras), the cleaning levels were different, namely, a minimum amount of 9 phe for the *core* pixels and 4.5 phe for the boundary ones were required. After the image cleaning, the image parameters were calculated.

The whole dataset was subject to a quality selection process. Data taken under bad atmospheric conditions, like high humidity or high cloudiness, proved to degrade the telescope overall response, were rejected. Data which presented fluctuations in the single telescope or stereo event rate were also discarded. Further quality cuts were done attending to the image parameters, disregarding data which presented deviations with respect to the dataset mean values. As a result of the quality selection, 37% of the total dataset was discarded, resulting in 8.3 hours of good quality data.

The events characterization, namely, the energy estimation and *hadroness* calculation, followed the methods outlined in Sec. 2.4.3.5 for stereo observations.

The *hadroness* calculation, used for the γ/hadron separation, was performed by means of the RF method. The corresponding matrices were trained over a 16 hours dataset composed by data where no significant γ-ray emission was found, and a subsample of MC γ-ray events. The aforementioned dataset shared similar observational conditions (atmospheric parameters, zenith angle range and instrument PSF), as both 1FGL J2347.3+0710 and 1FGL J0338.8+1313 datasets. Certain shower information for each event and telescope was used to train the algorithm: the image parameters *size, width, length,* and *p1grad* as well as the shower *impact parameter* and *maximum height*. The energy estimation made use of the LUTs that were constructed based on MC simulated γ-ray events. The arrival direction of the showers was calculated thanks to the DISP-RF method. The algorithm was trained using the image parameters *size, width, length, p1grad* and *dist*, the shower *impact parameter* and *maximum height*, as well as the observation *zenith angle*.

For all the event characterization methods, namely, the γ/hadron separation, energy estimation, and arrival direction calculation, a MC simulated γ-ray event population was needed. This population was chosen so to match the telescope behavior at the time the observations were performed (mainly driven by the PSF of the instrument). The zenith angle distribution of these MC events was chosen wide enough so the matrices could be applied to sources that were observed from zenith angles close to 0° up to 35°.

In order to verify the proper performance of the event characterization RF matrices and

LUTs, they were tested over a Crab Nebula data sample, contemporaneous to the 1FGL sources observations. The positive result from this check illustrates Sec. 2.4.3 as a practical example of the MAGIC analysis chain.

The analysis of 1FGL J2347.3+0710 data did not reveal any significant VHE signal in either night-by-night or cumulative analyses. In Fig. 4.6 three cumulative θ^2-distribution plots are depicted (see Sec. 2.4.3.6 for further details). They correspond to three different energy ranges probed to provide the best sensitivity based on Crab Nebula analysis. The explicit sets of cuts can be found in Table 4.5. The *low energy range* has an analysis threshold of $\sim$ 120 GeV and a sensitivity of $\sim$ 1.4% CU. The so-called *full range* cuts consider events above an energy of 250 GeV and provides the best sensitivity, $\sim$ 0.7% CU. The *high energy range* cuts allow for a sensitivity of $\sim$ 0.8% CU for events above 1 TeV. No γ-ray signal was found in none of the aforementioned energy ranges.

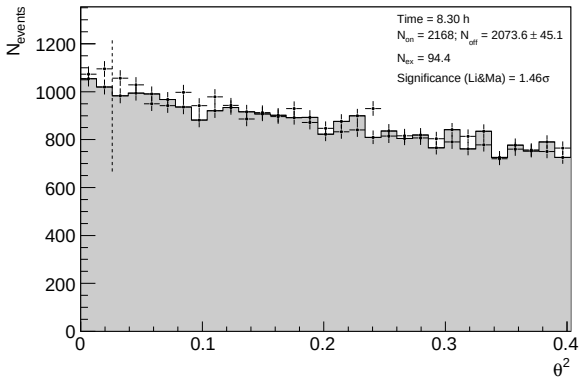

(a) Low energy θ^2-distribution

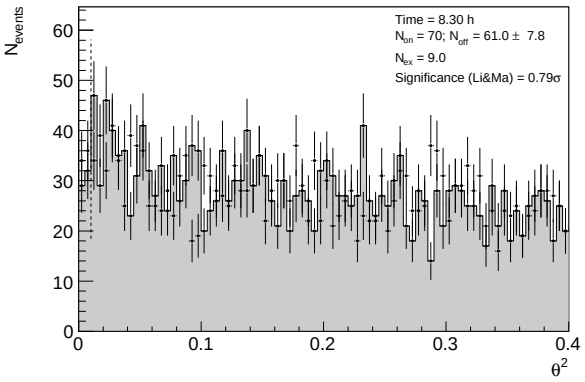

(b) Full range θ^2-distribution

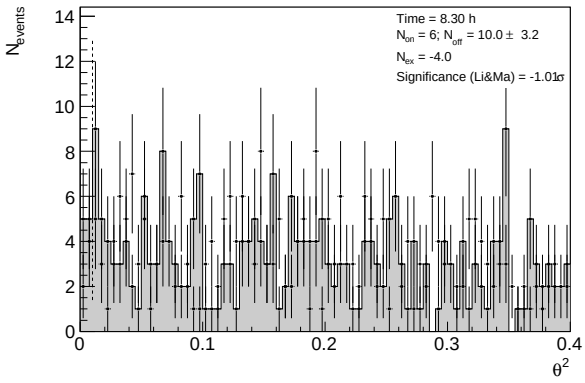

(c) High energy θ^2-distribution

Figure 4.6: 1FGL J2347.3+0710 θ^2-distribution from MAGIC data for several sets of cuts which optimize the sensitivity in three different energy ranges (see Table 4.5). 4.6a Low energy range cuts provide an analysis energy threshold of 120 GeV; 4.6b full range cuts consider $E > 250$ GeV; 4.6c high energy range cuts consider E>1 TeV. Dots are ON events, dots accompanied by gray filled areas represent off events. The dashed line shows the θ^2 cut which defines the signal region. All the energies are referred to the estimated energy of the events.

It is worth mentioning that in case a source is displaced from its assumed position, the significance of detection decreases. More over, if the actual position of the VHE source is

Table 4.5: 1FGL J2347.3+0710 MAGIC analysis set of cuts.

Type	$size_{MI}$ [phe]	$size_{MII}$ [phe]	*hadroness*	E [GeV]	Sensitivity [% C.U.]
Low energy	> 55	> 55	< 0.28	–	1.40 ± 0.05
Full range	> 125	> 125	< 0.16	250	0.68 ± 0.08
High Energy	> 300	> 300	< 0.17	1000	0.82 ± 0.30

All the energies refer to the estimated energy of the events. The low energy range provides a MC-based energy threshold of $E_{th} = 120$ GeV. The sensitivity is computed from a Crab Nebula dataset contemporaneous to 1FGL J2347.3+0710 observations.

offset by one telescope PSF it may happen, for faint sources, that the computed significance from the θ^2-distribution is even compatible with background fluctuations. Given the positional uncertainty of Fermi-LAT 1FGL nominal positions, a VHE γ-ray skymap is required in order to discard the possibility that the source may be slightly displaced from the catalog coordinates. Consequently, TS skymaps were performed in the three energy ranges characterized by the cuts shown in Tab. 4.5, and following the method described in Sec. 2.4.3.7. None of the TS skymaps presented any structure that could be compatible with a point-like source. Moreover, the actual distribution of TS values fitted reasonably well the null hypothesis distribution, namely, the absence of any VHE source in the skymap region. The TS skymaps together with the distribution of TS values can be found in Fig. 4.3.3 for all the considered energy ranges.

Since no VHE signal was confirmed, upper limits to the source's emission were computed following the prescriptions in Sec. 2.4.3.7. The upper limits to the number of excess events were obtained by means of the Rolke *et al.* method [308], assuming a systematic error of 30% that accounts for the energy estimation and effective area calculation. The considered CL was 95%.

As already mentioned, the upper limits depend on the assumed spectral shape. Despite the fact that 1FGL J2347.3+0710 has a catalog spectral index of 1.54 and a relative error of $\sim 30\%$ it may vary in the future as more photons statistics are collected. Therefore, five different spectral index were considered for the upper limits calculations, ranging from $\Gamma = -1.0$ to $\Gamma = -3.0$ in steps of $\Delta\Gamma = 0.5$. In that way, the 1σ error region in the nominal spectral index is taken into consideration, as well as softer indices for comparison purposes. This range of possible spectral indices also comprises the typical range where the dark matter-like spectra are expected [145; 343].

Table 4.6 summarizes the differential spectrum upper limits in four bins of estimated energies between 100 GeV and 10 TeV. Eq. 2.36 was used for the calculation. In Fig. 4.8 these MAGIC differential upper limits are shown. The 1FGL catalog spectrum, from 1 GeV to 100 GeV, is also depicted.

Additionally, Table 4.7 presents the integral spectrum upper limits considering different energy thresholds from 100 GeV to 1 TeV and the same set of spectral index as in the case of the differential spectrum upper limits. Eq. 2.32 was used for the calculation. In Fig. 4.9 these integral upper limits are shown, together with the corresponding results if zero significance $\sigma_{\mathrm{Li,Ma}}$ is assumed. As already mentioned, these artificial zero significance limits illustrate the noteworthy effect of the statistical fluctuations in the computations of upper limits, via its influence over the excess events upper limit calculation.

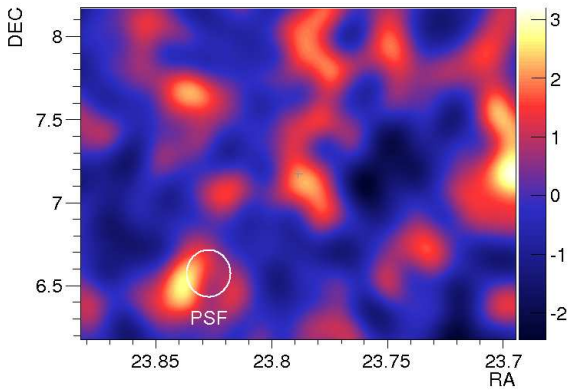

(a) Low energy skymap

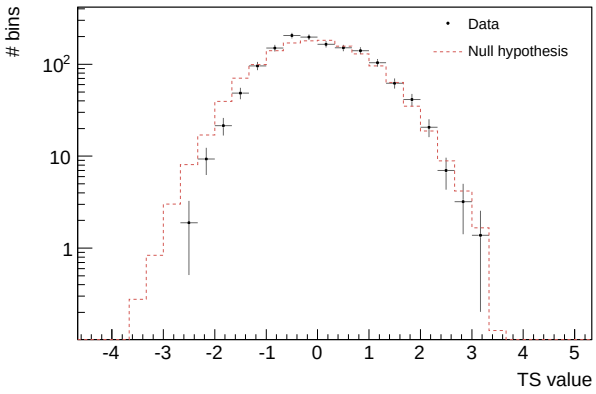

(b) Low energy significance distribution

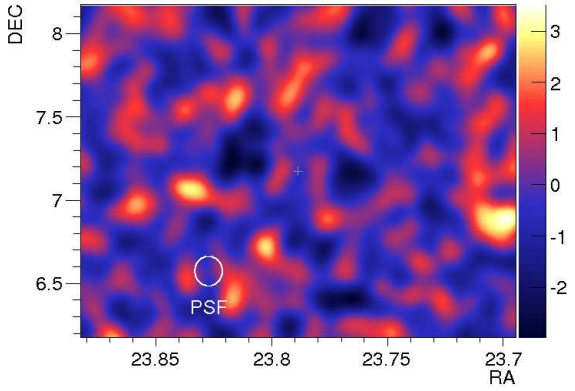

(c) Full range skymap

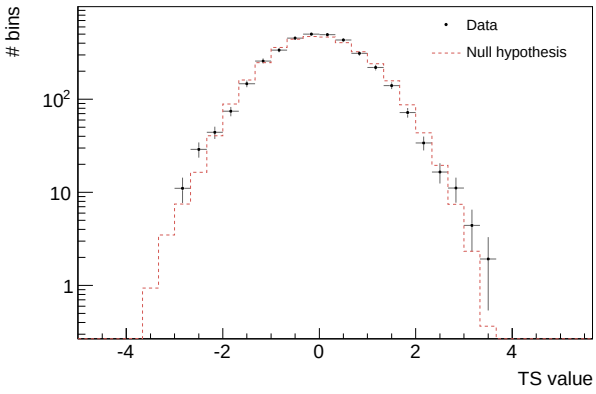

(d) Full range significance distribution

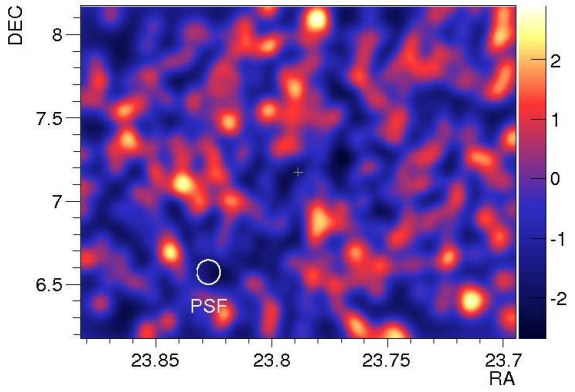

(e) High energy skymap

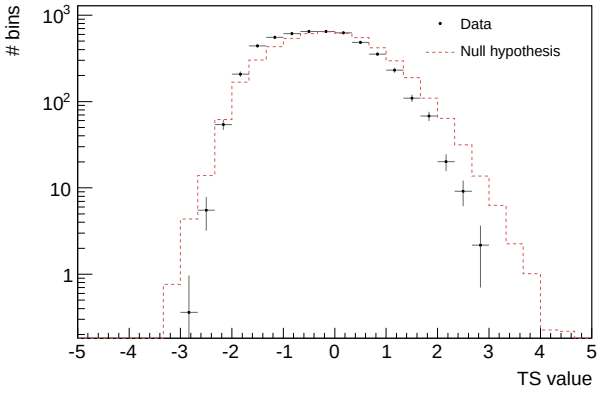

(f) High energy significance distribution

Figure 4.7: 1FGL J2347.3+0710 MAGIC skymaps from MAGIC data for several sets of cuts which optimize the sensitivity in three different energy ranges (see Table 4.5). 4.7a Low energy range skymap considers an analysis energy threshold of 120 GeV; 4.7c full range skymap considers $E > 250$ GeV events; 4.7e high energy range skymap consider E>1 TeV events. The white circle depicts MAGIC PSF for the given energy range. All the energies are referred to the estimated energy of the events.

Table 4.6: Differential 1FGL J2347.3+0710 flux upper limits.

ΔE [TeV]	$N_{\rm ON}/N_{\rm OFF}$	$\sigma_{\rm Li,Ma}$	N_{exc}^{UL} 95% C.L.	$d\Phi^{UL}/dE$ [TeV^{-1}cm^{-2}s^{-1}]				
				$\Gamma=-1.0$	$\Gamma=-1.5$	$\Gamma=-2.0$	$\Gamma=-2.5$	$\Gamma=-3.0$
0.1, 0.32	3519/3411	1.3	389	1.5×10^{-10}	1.6×10^{-10}	1.8×10^{-10}	2.1×10^{-10}	2.5×10^{-10}
0.32, 1	207/208	0.0	48	3.1×10^{-12}	3.3×10^{-12}	3.6×10^{-12}	4.0×10^{-12}	4.6×10^{-12}
1, 3.2	14/22	-1.3	8	1.3×10^{-13}	1.3×10^{-13}	1.4×10^{-13}	1.6×10^{-13}	1.8×10^{-13}
3.2, 10	3/5	-0.7	5	2.1×10^{-14}	2.3×10^{-14}	2.5×10^{-14}	2.9×10^{-14}	3.5×10^{-14}

95% CL differential upper limits in units of TeV^{-1}cm^{-2}s^{-1} for five different power law γ-ray spectra with spectral index Γ and four energy ranges in TeV units.

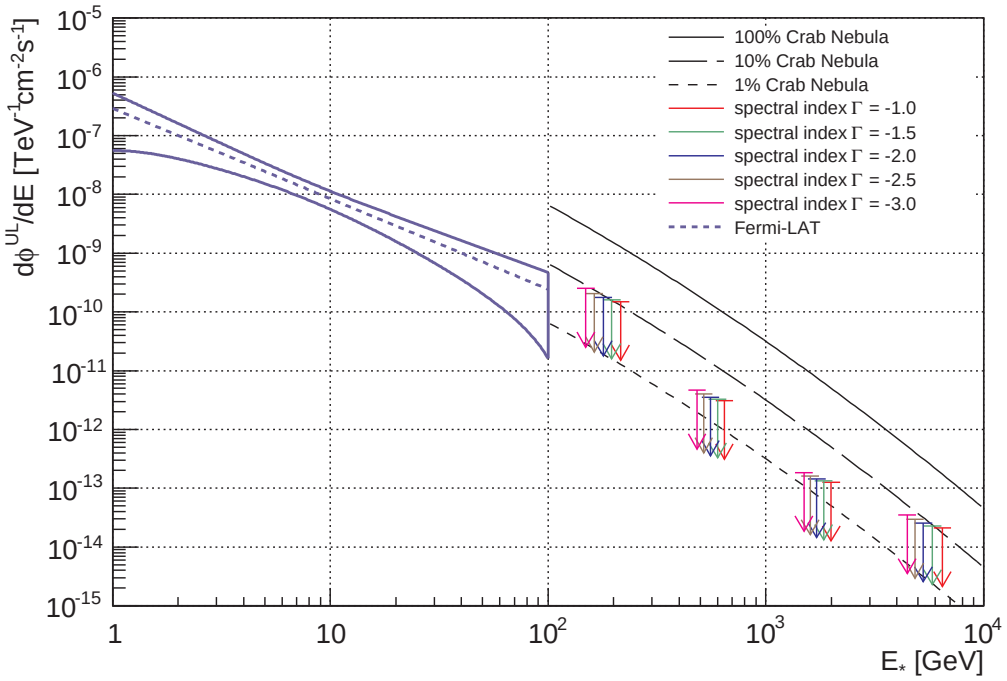

Figure 4.8: 1FGL J2347.3+0710 Fermi-LAT differential spectrum and MAGIC differential spectrum upper limits. MAGIC Crab Nebula spectrum [344] is depicted as reference. The Fermi-LAT differential spectrum error band was computed following the prescriptions from [411].

4.3.4 Summary and discussion

1FGL J2347.3+0710 qualified as a good dark matter clump candidate to be observed by MAGIC. It has no obvious counterpart after a dedicated search. Although a X-raypoint-like source is present in Swift-XRT data, very likely to be associated with a BL-Lac, its position is not compatible with Fermi-LAT error region. Refined positional information to be provided by the incoming Second Fermi Catalog (2FGL) Catalog will help to discern whether the Swift-XRT source could be a reasonable counterpart for 1FGL J2347.3+0710 or, on the contrary, both sources could have a different origin.

The analysis of Fermi-LAT HE photons ($E_\gamma > 10$ GeV) coming from 1FGL J2347.3+0710 coordinates also encouraged the observation of the source by MAGIC, due to both, its large

Table 4.7: Integral 1FGL J2347.3+0710 flux upper limits.

E_0 [GeV]	N_{ON}/N_{OFF}	$\sigma_{Li,Ma}$	N_{exc}^{UL} 95% C.L.	Φ^{UL} $\times 10^{-12}$[cm^{-2}s^{-1}]				
				$\Gamma = -1.0$	$\Gamma = -1.5$	$\Gamma = -2.0$	$\Gamma = -2.5$	$\Gamma = -3.0$
100	3744/3646	1.14	376	16.1 (3.0)	20.8 (3.8)	26.8 (5.0)	31.0 (5.7)	32.6 (6.0)
126	1762/1771	-0.15	132	5.5 (1.3)	6.8 (1.7)	8.4 (2.1)	9.6 (2.4)	10.1 (2.5)
158	960/970	-0.22	93	3.8 (1.3)	4.5 (1.5)	5.4 (1.8)	6.0 (2.0)	6.4 (2.1)
200	579/590	-0.32	69	2.7 (1.2)	3.1 (1.4)	3.6 (1.6)	4.0 (1.8)	4.2 (1.9)
251	369/372	-0.11	62	2.4 (1.5)	2.6 (1.6)	3.0 (1.9)	3.2 (2.0)	3.3 (2.1)
316	225/235	-0.47	40	1.5 (1.3)	1.6 (1.4)	1.8 (1.6)	1.8 (1.6)	1.9 (1.7)
398	137/156	-0.53	30	0.9 (1.1)	0.9 (1.1)	1.0 (1.2)	1.0 (1.2)	1.0 (1.2)
501	77/92	-1.15	18	0.6 (1.0)	0.6 (1.0)	0.7 (1.2)	0.7 (1.2)	0.7 (1.2)
631	42/61	-1.80	10	0.4 (1.1)	0.4 (1.1)	0.4 (1.1)	0.4 (1.1)	0.4 (1.1)
794	28/35	-0.88	12	0.4 (1.5)	0.4 (1.5)	0.4 (1.5)	0.4 (1.5)	0.4 (1.5)
1000	18/27	-1.34	9	0.3 (1.6)	0.3 (1.6)	0.3 (1.6)	0.3 (1.6)	0.3 (1.6)

95% CL integral upper limits in units of 10^{-12}cm^{-2}s^{-1} for five different power law γ-ray spectra with spectral index Γ and several energy thresholds E_0. The numbers in parenthesis are the upper limits as a percentage of the Crab Nebula integral flux above E_0.

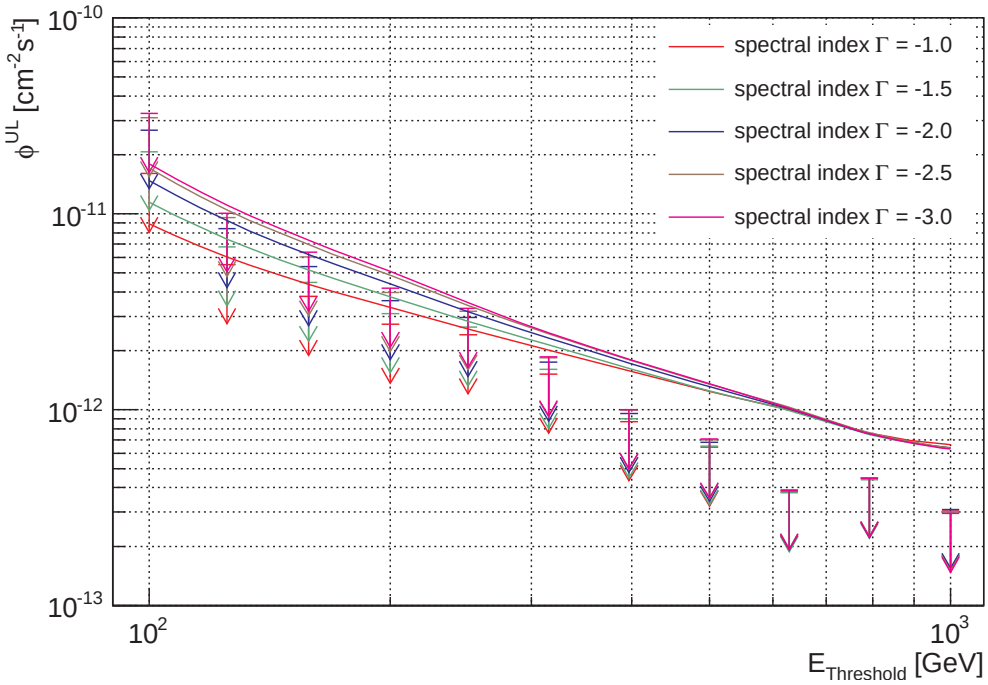

Figure 4.9: Integral flux upper limits from 1FGL J2347.3+0710 MAGIC data. The arrows indicate the integral flux upper limits as in Table 4.7 for different power-law spectra and energy thresholds. The dashed lines indicate the corresponding integral upper limits if zero significance $\sigma_{Li,Ma}$ is assumed.

population and the fact that neither other source of high energy Fermi photons nor a strong background was present in a celestial region corresponding to the MAGIC FoV and centered on

the UFO. Additionally, its prospects of detection based on Fermi-LAT 1FGL spectrum extrapolation up to MAGIC energy range indicated that the source could be detected, in the *worst case scenario*, in 20 hours.

The MAGIC observations of 1FGL J2347.3+0710 were performed during October and November 2010 and account for a total exposure time of 13.3 h. After data quality selection the exposure time reduced down to 8.3 h. No signal was found over the background. Consequently, upper limits to the differential and integral spectrum were derived.

Since the final good quality observation time reduced to 8.3 hours, less than half the 20 hours prescribed by the *worst case scenario* estimations, a complete exclusion of Fermi-LAT spectrum extrapolation cannot be claimed unless the uncertainties of the Fermi spectral parameters are ignored. Still, it can be seen from Fig. 4.8 that a direct extrapolation of 1FGL J2347.3+0710 Fermi-LAT power-law spectrum above 400 GeV is already ruled out by MAGIC observations, meaning that some kind of cut-off or spectral curvature may be taking place at energies between 100 and 400 GeV. Nonetheless, these conclusions should be taken *cum grano salis* for two main reasons. First, the results rely on 1FGL spectral information, and must be consequently revisited once the second version of the 2FGL Catalog is released. May it happen that the refined spectral information provides a softer spectral index, a possible claim of spectral curvature or cut-off will not stand. Second, because it was assumed that the source has a galactic location, thus the possible effects due to a possible EBL extinction are disregarded. In case the source has an extragalactic origin, its redshift could provoke the reported curvature or cut-off, bringing strong doubts about an intrinsic origin of such feature.

4.4 1FGL J0338.8+1313 observations

4.4.1 Fermi high energy γ-ray data

1FGL J0338.8+1313 Fermi-LAT data analysis considered LAT γ-ray events up to August 23, 2010 (304272002 s MET). The details in the analysis procedure are outlined in Sec. 4.2.4. Fig. 4.10 depicts a $20^\circ \times 20^\circ$ HE Fermi-LAT skymap centered on the source nominal position, where Fermi-LAT events with energies above 10 GeV are shown after smoothing. As in the case of 1FGL J2347.3+0710, the skymap does not reveal any bright HE γ-ray source other than the candidate within MAGIC FoV. Thus, one can again exclude contamination by a second HE γ-ray source in the background regions to be used in MAGIC data analysis.

Concerning the background estimation, a total number of ~ 0.22 photons with energies above 10 GeV are expected in the 0.15° radius region around 1FGL J0338.8+1313 nominal position. The number of high energy photons arriving from this same region is 8, as can be seen in Table 4.1. The probability of these events to be all of them background photons is consequently extremely low. As already mentioned in the case of 1FGL J2347.3+0710, this fact strengthen the hypothesis that the source spectrum may not suffer from a sharp cut-off at energies of few tens of GeV.

4.4.2 Swift X-rayobservations

A total 4138 s exposure of 1FGL J0338.8+1313 was acquired during October and December 2010 with Swift-XRT satellite. The observation belongs to the same observational program as 1FGL J2347.3+0710. It was divided into five different runs. In every run, the XRT operated in Photon Counting mode with full spectral resolution and a time resolution of 2.5 s. A brief summary of the observations can be found in table 4.8.

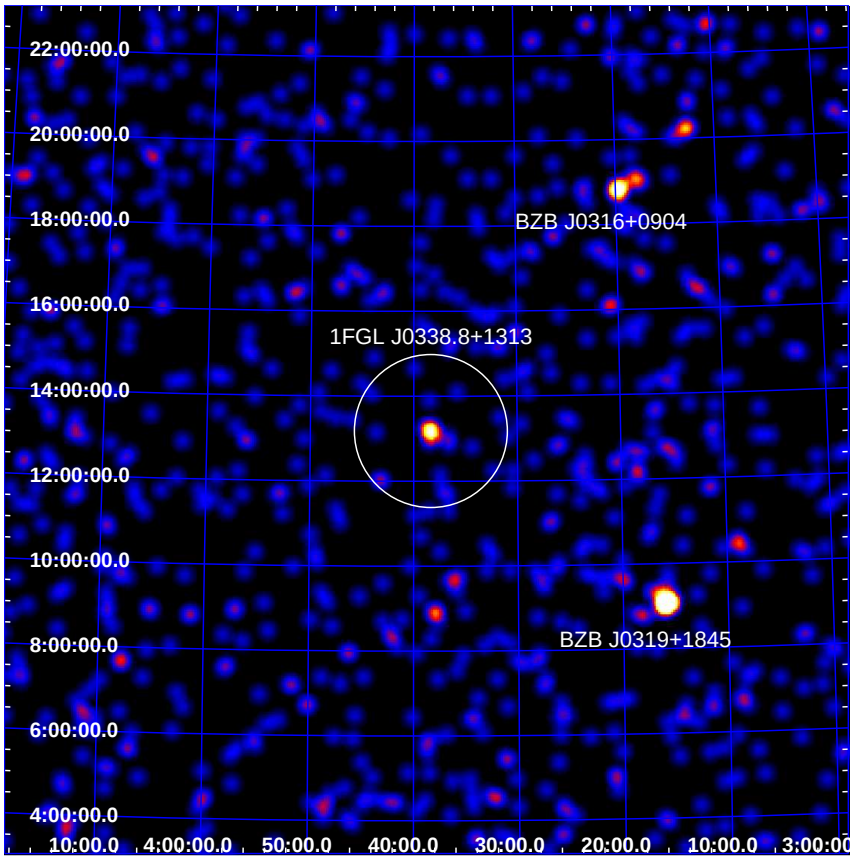

Figure 4.10: Fermi-LAT skymap over 10 GeV in a 20° × 20° region centered on 1FGL J0338.8+1313. The white 3.5° diameter circle depicts MAGIC FoV, where no other γ-ray source is present. Two BL Lac objects are present in the region: BZB J0316+0904 and BZB J0319+1845, far enough from 1FGL J0338.8+1313 to spoil MAGIC observations. The image has been smoothed with a Gaussian kernel $r_k = 9'$. Fermi-LAT photons as of August 23, 2010.

Table 4.8: Swift-XRT 1FGL J0338.8+1313 observations summary.

Obs. ID	RA_{J2000} [^{h} ^{m} ^{s}]	Dec_{J2000}[° ′ ″]	Search Offset [′]	Date	Exposure [s]
00041292005	03 38 43.38	+13 13 59.6	2.320	2010-12-22	1860

The exposure accounts for Photon Counting mode only.

For the analysis, the same procedure as with 1FGL J2347.3+0710 was followed. Standard cleaned Level 2 events, meaning standard grade filtering (grades 0-12) and default screening parameters in the 0.3-10 keV energy range were considered. Analysis of the data was performed with standard *HEASoft* Swift package tools [402]. Fig. 4.11 shows the XRT image of the field.

The main conclusion of the analysis is that there are no point sources brighter than 10 counts (0.0054 counts/s) in the 0.3-10 keV energy range within the Fermi-LAT error contour. With *WebPIMMS* [408], assuming a photon index $\Gamma = 1.4$ and column density $N_H = 1.5 \times 10^{21}\mathrm{cm}^{-2}$ an integral flux upper limit $\Phi^{UL}(0.3 - 10\mathrm{keV}) = 3 \times 10^{-13}\mathrm{ergs\ s}^{-1}\ \mathrm{cm}^{-2}$ was obtained. This observation also failed to discover any bright sources within the Swift-XRT FoV. This fact makes 1FGL J0338.8+1313 stand as a very interesting γ-ray source, free of possible X-raycounterparts

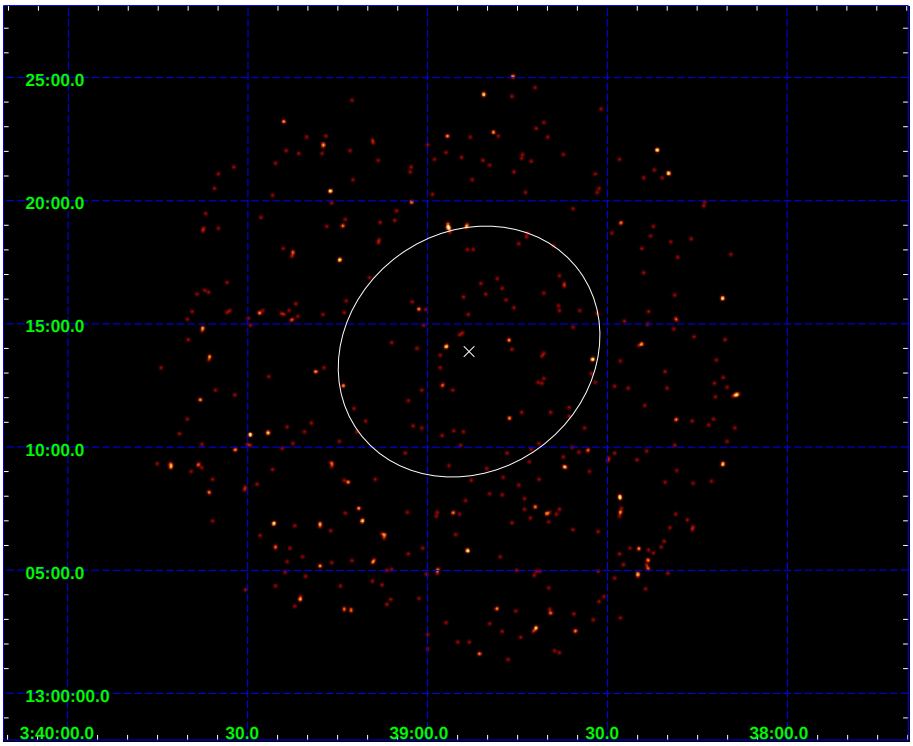

Figure 4.11: Smoothed Swift XRT 0.3-10 keV image in the direction of 1FGL J0338.8+1313. The white cross is 1FGL J0338.8+1313 Fermi-LAT nominal position. The white ellipse depicts Fermi-LAT 95%error contour for this source. The Swift-XRT FoV is 26′ x26′ in Photon Counting mode. The image has been smoothed with a Gaussian kernel $r_k = 4''$.

down to the flux limit of the observation.

4.4.3 MAGIC very high energy gamma-ray observations

The MAGIC Telescopes observed 1FGL J0338.8+1313 in stereoscopic mode during December 2010 and January 2011. The total exposure time was 15.3 hours under dark night conditions. The source was surveyed in false tracking mode (*wobble* mode) [286], alternating the pointing direction every 20 minutes between $\pm 0.4^\circ$ offset in RA with respect to the source nominal position, at zenith angles between 15.5° (corresponding to the source culmination at MAGIC Telescopes latitude) and 30.5° . The later zenith range provides the lowest energy threshold possible for the source's declination. More details on the dataset can be found in Table 4.9.

1FGL J0338.8+1313 MAGIC data were analyzed using the standard MAGIC analysis procedure for stereo observations (see Sec. 2.4.3). The calibration and the extraction of noise images produced by the NSBL was performed independently for each of the telescopes. The image cleanings to the event images that were applied are the same as for 1FGL J2347.3+0710 data: a time image cleaning characterized by a charge condition 6/3 phe and an arrival time condition 4.5/1.5 ns for *core/boundary* pixels in the case of MAGIC-I, and a time image cleaning characterized by a different charge condition 9/4.5 phe and the same arrival time condition for *core/boundary* pixels in MAGIC-II images. After the image cleaning, the image parameters were calculated.

The quality selection process that was applied to 1FGL J0338.8+1313 dataset attended to

Table 4.9: 1FGL J0338.8+1313 MAGIC dataset.

Night	t_{eff} [h]	Z.A. [°]
2010/11/15	0.2	22.0 – 23.5
2010/12/26	0.5	15.5 – 20.0
2010/12/27	2.7	15.5 – 28.0
2010/12/28	2.8	15.5 – 30.5
2010/12/31	0.5	16.0 – 20.5
2011/01/01	2.6	15.5 – 30.5
2011/01/02	1.4	15.5 – 20.0
2011/01/03	1.8	15.5 – 26.5
2011/01/04	1.5	15.5 – 20.5
2011/01/05	0.4	15.5 – 17.0
2011/01/06	0.9	15.5 – 17.0

As a convention within MAGIC Collaboration, the observation *Night* refers to the date of dawn after regular observations. t_{eff} stands for the effective observation time (see Sec. 2.4.3.7). Z.A. refers to the zenith angle window of the observation.

the usual parameters, *i.e.*, the atmospheric conditions (like humidity and cloudiness), the single telescope and stereo rate stability, and the image parameters distribution. After rejecting bad quality data which accounted for a 30% of the initial dataset, a final amount of 10.7 hours of data remained.

Given the fact that the 1FGL J0338.8+1313 observations are very close in time to the 1FGL J2347.3+0710 ones, and that no relevant changes were introduced in the system of telescopes between these two observations nor the PSF substantially changed, the event characterization (energy estimation and *hadroness* calculation) made use of the same set of RF matrices and LUTs that were produced for 1FGL J2347.3+0710 data analysis (more details about their generation can be found in Sec. 4.3.3). Nevertheless, these matrices were checked over a 1FGL J0338.8+1313 contemporaneous Crab Nebula data sample with positive results.

No significant VHE signal was found in 1FGL J0338.8+1313 data in either night-by-night or total cumulative analyses. Three total cumulative θ^2-distribution plots corresponding to the three energy ranges previously considered for 1FGL J2347.3+0710 analysis can be found in Fig. 4.12. The set of cuts that define the energy ranges can be found in Table 4.5 and details in the signal extraction method are explained in Sec. 2.4.3.6.

Comparing the Fermi-LAT error regions from both 1FGL J0338.8+1313 and 1FGL J2347.3+0710 (both of them depicted in Figs. 4.11 and 4.11) that the positional uncertainty of the first is smaller than the one of the second. Even though, the Fermi error region for 1FGL J0338.8+1313 has an approximately radius of 0.08°, thus the calculation of a VHE γ-ray skymap is recommended so to discard the possibility that the source may be slightly displaced from the catalog coordinates. TS skymaps were performed in the three energy ranges given by the cuts shown in Tab. 4.5 (see Sec. 2.4.3.7 for a description of the method). No point-like source structure was found in any of the three TS skymaps, whose significance distribution followed the null hypothesis significance distribution, *i.e.* no VHE γ-ray source in shows up in the surveyed region. Both, the TS skymaps and the the distribution of TS values per energy range are shown in Fig. 4.3.3.

After the confirmation that no VHE signal is present in 1FGL J0338.8+1313 MAGIC data, upper limits to the source's emission were calculated following the same methodology and as-

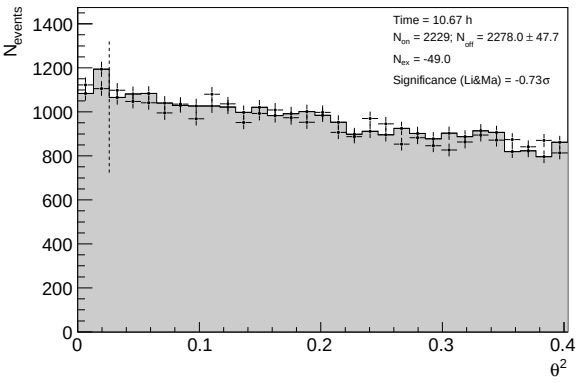

(a) Low energy θ^2-distribution

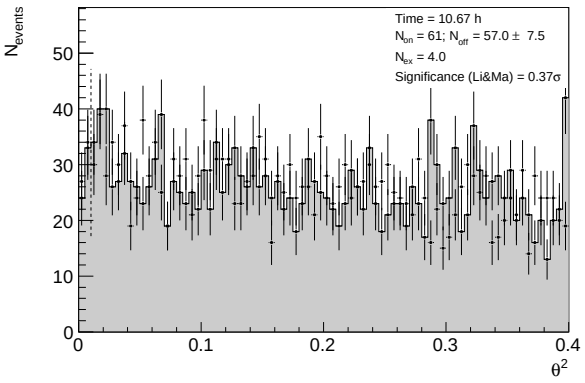

(b) Full range θ^2-distribution

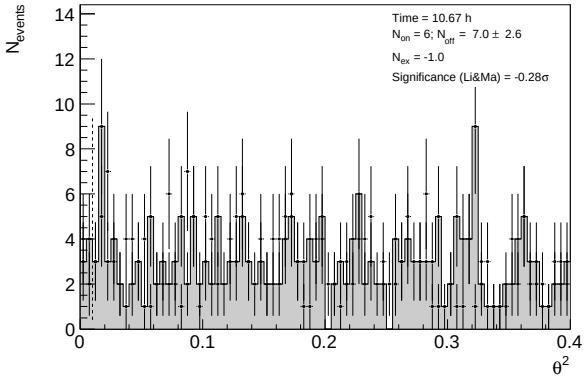

(c) High energy θ^2-distribution

Figure 4.12: 1FGL J0338.8+1313 θ^2-distribution from MAGIC data for several sets of cuts which optimize the sensitivity in three different energy ranges (see Table 4.5). 4.12a Low energy range cuts provide an analysis energy threshold of 120 GeV; 4.12b full range cuts consider $E > 250$ GeV; 4.12c high energy range cuts consider E>1 TeV. Dots are ON events, dots accompanied by gray filled areas represent off events. The dashed line shows the θ^2 cut which defines the signal region. All the energies are referred to the estimated energy of the events.

sumptions as in the case of 1FGL J2347.3+0710 (see Sec. 4.3.3).

Table 4.10 presents the differential spectrum upper limits. Four bins of estimated energies between 100 GeV and 10 TeV were considered. Eq. 2.36 was applied for the calculation, where different power-law spectra, with spectral indexes $\Gamma = -1.0, -1.5, -2.0, -2.5, -3.0$ were assumed. In Fig. 4.14 these MAGIC differential upper limits are depicted, together with the 1FGL catalog spectrum from 1 GeV to 100 GeV.

Furthermore, integral spectrum upper limits were derived. Several energy thresholds between 100 GeV and 1 TeV were considered, as well as the same set of spectral index as in the case of the differential spectrum upper limits. The results are presented in Table 4.11, and are depicted in Fig. 4.15. In this last figure, the integral upper limits computed assuming a zero significance $\sigma_{\mathrm{Li,Ma}}$ are also shown to illustrate the effect of the statistical fluctuations of the significance of detection in the computation of the limits.

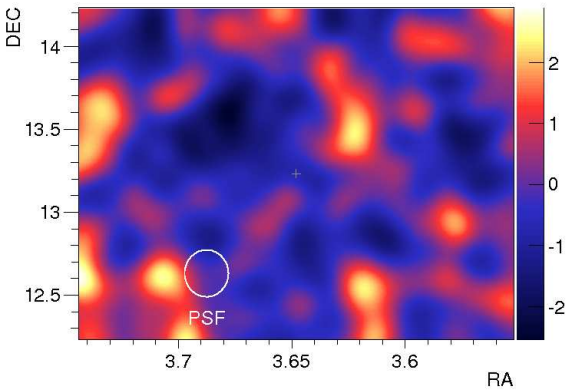

(a) Low energy skymap

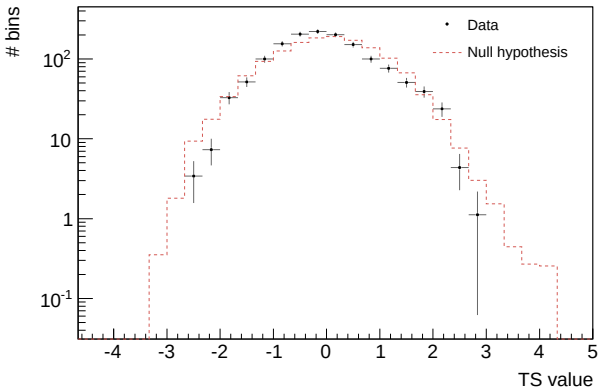

(b) Low energy significance distribution

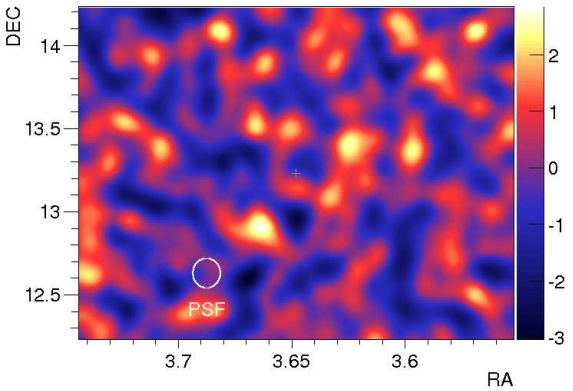

(c) Full range skymap

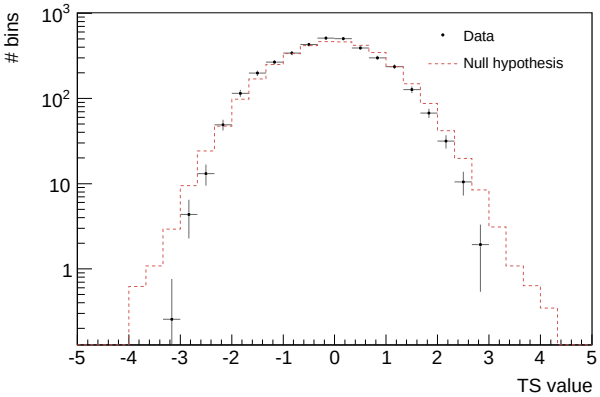

(d) Full range significance distribution

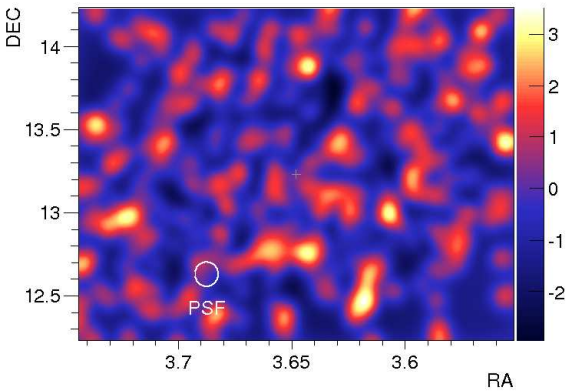

(e) High energy skymap

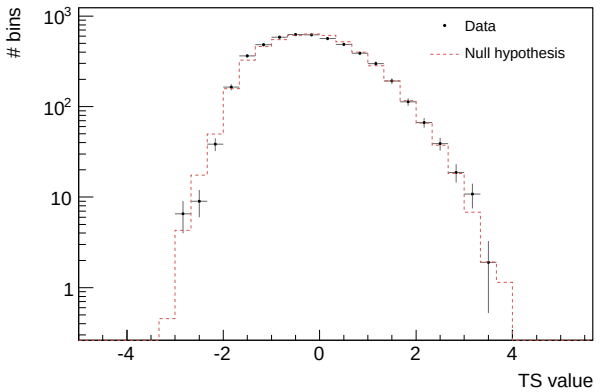

(f) High energy significance distribution

Figure 4.13: 1FGL J0338.8+1313 skymaps from MAGIC data for several sets of cuts which optimize the sensitivity in three different energy ranges (see Table 4.5). 4.13a Low energy range skymap considers an analysis energy threshold of 120 GeV; 4.13c full range skymap considers $E > 250$ GeV; 4.13e high energy range skymap consider E>1 TeV. The white circle depicts MAGIC PSF for the given energy range. All the energies are referred to the estimated energy of the events.

Table 4.10: Differential 1FGL J0338.8+1313 flux upper limits.

ΔE [TeV]	$N_{\rm ON}/N_{\rm OFF}$	$\sigma_{\rm Li,Ma}$	N_{exc}^{UL} 95% C.L.	$d\Phi^{UL}/dE$ [TeV^{-1}cm^{-2}s^{-1}]				
				$\Gamma=-1.0$	$\Gamma=-1.5$	$\Gamma=-2.0$	$\Gamma=-2.5$	$\Gamma=-3.0$
0.1, 0.32	3271/3342	-0.9	120	3.6×10^{-11}	3.9×10^{-11}	4.3×10^{-11}	5.0×10^{-11}	6.0×10^{-11}
0.32, 1	205/214	-0.4	39	1.9×10^{-12}	2.0×10^{-12}	2.2×10^{-12}	2.5×10^{-12}	2.9×10^{-12}
1, 3.2	18/16	0.3	18	2.2×10^{-13}	2.4×10^{-13}	2.6×10^{-13}	2.9×10^{-13}	3.3×10^{-13}
3.2, 10	1/3	-1.0	4	1.1×10^{-14}	1.2×10^{-14}	1.3×10^{-14}	1.5×10^{-14}	1.8×10^{-14}

95% CL differential upper limits in units of TeV^{-1}cm^{-2}s^{-1} for five different power law γ-ray spectra with spectral index Γ and four energy ranges in TeV units.

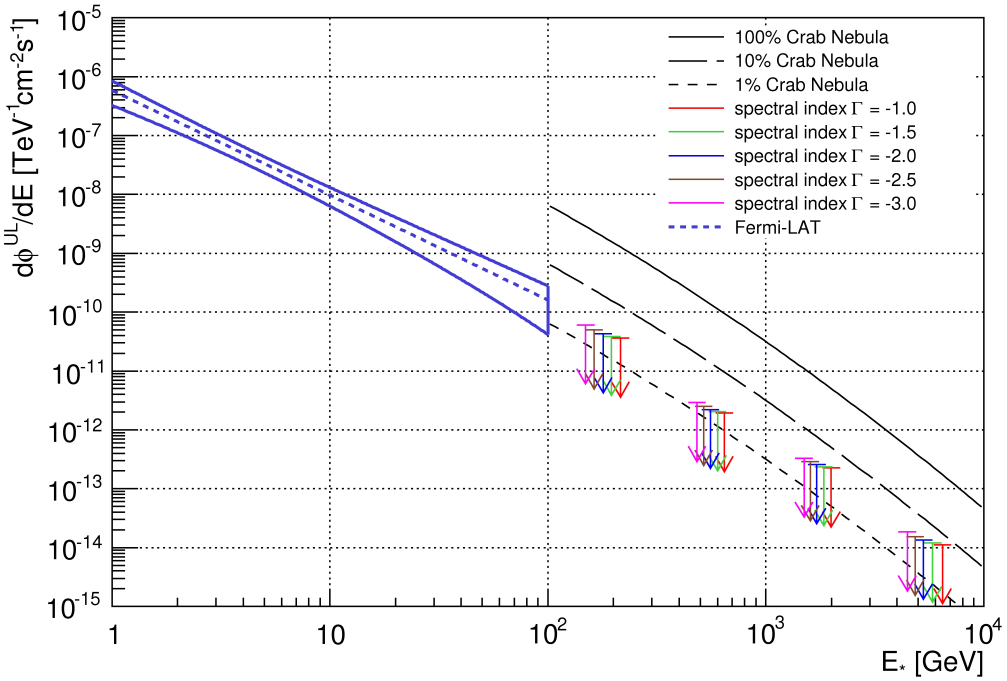

Figure 4.14: 1FGL J0338.8+1313 Fermi-LAT differential spectrum and MAGIC differential spectrum upper limits. MAGIC Crab Nebula spectrum(solid line 100%, half dashed line 10% and dashed line 1%) is depicted as reference. The Fermi-LAT differential spectrum error band was computed following the instructions from [411].

4.4.4 Summary and discussion

The selection of 1FGL J0338.8+1313 as a dark matter clump candidate suitable to be observed by MAGIC is well motivated. The source has neither an obvious counterpart after a thorough dedicated search nor in the analysis of Swift-XRT data.

Its large population of HE ($E_\gamma > 10$ GeV) Fermi-LAT photons coming from the source coordinates as well as the fact that there are neither other bright sources nor strong background in 1FGL J0338.8+1313 vicinities also encouraged MAGIC observations of this source. Furthermore, Fermi-LAT 1FGL spectrum extrapolation to MAGIC energy range provided a reasonable estimation of the detectability of 41 hours in the *worst case scenario*.

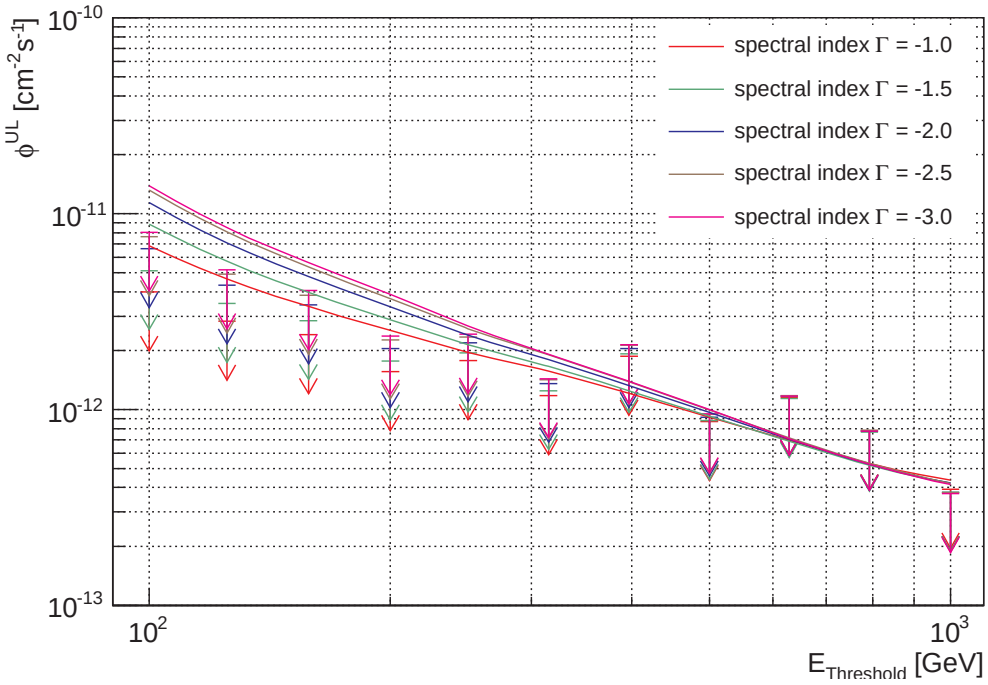

Figure 4.15: Integral flux upper limits from 1FGL J0338.8+1313 MAGIC data. The arrows indicate the integral flux upper limits as in Table 4.11 for different power-law spectra and energy thresholds. The dashed lines indicate the corresponding integral upper limits if zero significance $\sigma_{\mathrm{Li,Ma}}$ is assumed.

Table 4.11: Integral 1FGL J0338.8+1313 flux upper limits.

E_0 [GeV]	$N_{\mathrm{ON}}/N_{\mathrm{OFF}}$	$\sigma_{\mathrm{Li,Ma}}$	N_{exc}^{UL} 95% C.L.	Φ^{UL} $\times 10^{-12}[\mathrm{cm}^{-2}\mathrm{s}^{-1}]$				
				$\Gamma=-1.0$	$\Gamma=-1.5$	$\Gamma=-2.0$	$\Gamma=-2.5$	$\Gamma=-3.0$
100	3494/3575	-0.96	119	4.0 (0.7)	5.1 (1.0)	6.6 (1.2)	7.6 (1.4)	8.0 (1.5)
126	1666/1716	-0.86	87	2.8 (0.7)	3.5 (0.9)	4.3 (1.1)	4.9 (1.2)	5.2 (1.3)
158	920/944	-0.56	76	2.4 (0.8)	2.8 (0.9)	3.4 (1.1)	3.8 (1.3)	4.0 (1.3)
200	535/563	-0.84	50	1.6 (0.7)	1.8 (0.8)	2.0 (0.9)	2.3 (1.0)	2.4 (1.1)
251	346/350	-0.15	59	1.8 (1.1)	2.0 (1.2)	2.2 (1.4)	2.4 (1.5)	2.4 (1.5)
316	223/233	-0.47	40	1.2 (1.0)	1.2 (1.0)	1.4 (1.2)	1.4 (1.2)	1.4 (1.2)
398	156/143	0.75	64	1.9 (2.3)	1.9 (2.3)	2.0 (2.5)	2.1 (2.6)	2.1 (2.6)
501	81/82	-0.07	30	0.9 (1.6)	0.9 (1.6)	0.9 (1.6)	0.9 (1.6)	1.0 (1.8)
631	58/49	0.87	41	1.1 (2.8)	1.1 (2.8)	1.2 (3.0)	1.2 (3.0)	1.2 (3.0)
794	33/28	0.64	28	0.8 (2.9)	0.8 (2.9)	0.8 (2.9)	0.8 (2.9)	0.8 (2.9)
1000	18/19	-0.16	14	0.4 (2.2)	0.4 (2.2)	0.4 (2.2)	0.4 (2.2)	0.4 (2.2)

95% CL integral upper limits in units of $10^{-12}\mathrm{cm}^{-2}\mathrm{s}^{-1}$ for five different power law γ-ray spectra with spectral index Γ and several energy thresholds E_0. The numbers in parenthesis are the upper limits as a percentage of the Crab Nebula integral flux above E_0.

1FGL J0338.8+1313 was observed by MAGIC telescopes during December 2010 and January 2011 for a total exposure time of 15.3 hours which reduced down to 10.7 hours of good quality

data after quality selection. Their analysis did not reveal any significant VHE signal coming from the source. Hence, integral and differential spectrum upper limits were set.

As in the case of 1FGL J2347.3+0710, the final good quality observation time was significantly smaller than the predictions from the *worst case scenario* estimations. While the pessimistic prospects of detection asked for 41 hours in order to detect the source, only 10.7 hours of good quality data were available. Consequently, an exclusion of Fermi-LAT spectrum extrapolation to MAGIC energy range cannot be fully stated if the uncertainties of Fermi-LAT spectral parameters are taken into consideration. Yet, a direct extrapolation of the nominal spectral parameters stated in the 1FGL catalog is ruled out by MAGIC observations. Fig. 4.14 shows how MAGIC differential spectrum upper limits can conservatively rule out a direct extrapolation of Fermi-LAT spectrum above 200 GeV. This fact suggests a possible curvature or cut-off at Fermi-LAT high energy range. Same caution, as with 1FGL J2347.3+0710 results, has to be exercised at this point. It is worth mentioning that the conclusions presented above consider 1FGL spectral information, and must be revisited accordingly when the 2FGL catalog is made public. Again, the main hypothesis that 1FGL J0338.3+1313 is a galactic object and, as this, does not suffer from EBL extinction may play a role in the MAGIC limits interpretation. Anyhow, due to the fact that the curvature is already present around 200 GeV, a possible origin based on EBL extinction would require a redshift significantly larger than $z = 0.5$ (see *e.g.* [232]).

4.5 Conclusions and outlook

A dedicated search designed to select possible dark matter clump candidates out of the 1FGL Catalog has been presented, concluding with ten candidates out of the 630 UFOs. After studying the prospects of detection for each of these ten sources, six of them visible from MAGIC latitude, the two best candidates were observed by the MAGIC Telescopes.

Although no VHE γ-ray signal was detected for any of them, competitive upper limits to their differential and integral spectra were obtained.

It can be seen from Fig. 4.8 that a direct extrapolation of 1FGL J2347.3+0710 Fermi-LAT spectrum above 400 GeV is disfavored by MAGIC observations, meaning that some kind of cut-off or spectral curvature may be taking place at energies between 100 and 400 GeV. In the case of 1FGL J0338.8+1313, as illustrated in Fig. 4.14, the differential upper limits disfavor a direct extrapolation of Fermi-LAT spectrum above 200 GeV. This fact suggests a possible curvature or cut-off at Fermi-LAT high energy range.

Nonetheless, these conclusions should be taken *cum grano salis* since they rely on 1FGL spectral information, and must be consequently revisited once the second version of the Fermi-LAT Catalog is released.

Concerning deeper observations of these sources with MAGIC telescopes, they depend on incoming refined data from Fermi satellite. As for 1FGL J2347.3+0710, its condition as good dark matter clump candidate may be reconsidered once its possible association with the bright Swift-XRT source is solved. Regarding 1FGL J0338.8+1313, the source holds as a very promising dark matter clump candidate. Deeper observations should be encouraged if the source still qualifies after the candidate selection requirements are applied to its updated 2FGL characteristics.

Concerning the Swift-XRT data on high galactic latitude UFOs, one might consider to perform a similar analyses as the one presented in Sec. 3.3, where Willman 1 Chandra data were scrutinized in order to find evidences of a dark matter particle in the form of a *sterile neutrino*, eventually placing constraints in the *sterile neutrino* parameter space. Unfortunately, Swift-

XRT nominal point source sensitivity of $2 \times 10^{-14} erg\ cm^{-2}\ s^{-11}$ is above the Chandra-ACIS sensitivity of $4 \times 10^{-15} erg\ cm^{-2}\ s^{-12}$ and the average exposure time of Swift observations is around $2 - -3ks$ while Chandra Willman 1 observation was much deeper ($\sim 100ks$). Consequently, reliable spectral analyses of these UFOs Swift-XRT data are not possible due to low statistics. Currently, the best two instruments to study the UFOs in the X-rayband are XMM-Newton and Chandra satellites. Chandra has a better PSF and energy resolution while XMM-Newton has a much bigger effective area, a wider energy range, and is much sensitive to extended emission. Therefore Chandra is best suited to detect dark matter emission lines while XMM-Newton would be able to prove dark matter density profiles if a dark matter decay line is present, making both instruments complementary. As a conclusion, a systematic and deep search for X-rayemission lines in UFOs from dark matter decay is to be encouraged.

Eventually, it is worth pointing out that indirect dark matter searches can profit from coordinated multiwavelength campaigns. Past observation strategies dedicated to dark matter searches were mainly focused in a relatively specific energy band. With this work, it has been shown that the synergy between HE telescopes, like the Fermi-LAT satellite, and VHE telescopes, like MAGIC, was able to provide new interesting dark matter candidates to be explored. Moreover, astrophysical data from radio to X-ray significantly contributed to this task. Therefore, it is strongly recommended to widen the search energy windows and take advantage of all possible astrophysical data in the pursue for the dark matter particle identification.

[1] Swift-XRT sensitivity in $10^4 s$ exposure in the 0.2 to 10.0 keV energy range.
[2] Chandra-ACIS sensitivity in $10^4 s$ exposure in the 0.4 to 6.0 keV energy range.

Chapter 5

Dark Matter Prospects for the Next Generation of Cherenkov Telescopes

As it has been presented in previous chapters, the current generation of imaging atmospheric Cherenkov telescopes, illustrated by MAGIC results, have taken the indirect search for dark matter to competitive levels. The next generation of Cherenkov telescopes, which has a solid candidate in the planned Cherenkov Telescope Array (CTA), is expected to bring the potential of dark matter discovery of this technique to a new stage. Though still in the design phase, MC simulations already provide an idea about the sensitivity improvements this new instrument will bring as compared to its predecessors. In the following sections CTA predicted sensitivity will be exploited in the context of indirect dark matter searches. In Sec. 5.1 a brief introduction to CTA is presented. A method to probe CTA sensitivity to general dark matter point-like sources and is developed in Sec. 5.2. Finally, some conclusions and outlook for further steps are developed in Sec. 5.3.

5.1 The next generation of Cherenkov telescopes

Due to the great success of the current generation of Cherenkov telescopes, as a consequence of an already mature technique which has evolved during the last three decades, the next generation of instruments has been planned. CTA [412] is the global initiative to build this next generation ground-based γ-ray observatory (see [386] and references therein). When compared to current facilities such as H.E.S.S., MAGIC or VERITAS, a factor of 5-10 improvement in sensitivity is expected in the 100 GeV to some tens of TeV energy domain. In addition CTA sensitivity will extend to both lower and higher energies. This significant improvement in sensitivity will go accompanied by a much better energy and angular resolution. Besides the technical improvements, and the flexibility of operational modes that such an array could provide, CTA is planned to be an open observatory, thus able to serve a larger community of researchers for the first time in the field.

CTA will provide full-sky coverage since the observatory will consist of two arrays, one in each hemisphere. Due to the privileged situation of southern latitudes to observe the Galactic Center and Galactic Plane, the Southern hemisphere array will be mainly dedicated to Galactic sources and the central part of our Galaxy. The Northern hemisphere array will complement the Southern one, and will be dedicated to northern extragalactic objects namely, active galactic nuclei, gamma-ray bursts, and starburst galaxies, and in general, low energy threshold stud-

ies. Apart from this wide variety of conventional astrophysical objects, CTA will allow a deep exploration of an energy window where dark matter signatures are expected, via dark matter particle annihilation or decay as γ-ray by-products. Consequently, a dedicated study of the CTA response to possible dark matter signals is required.

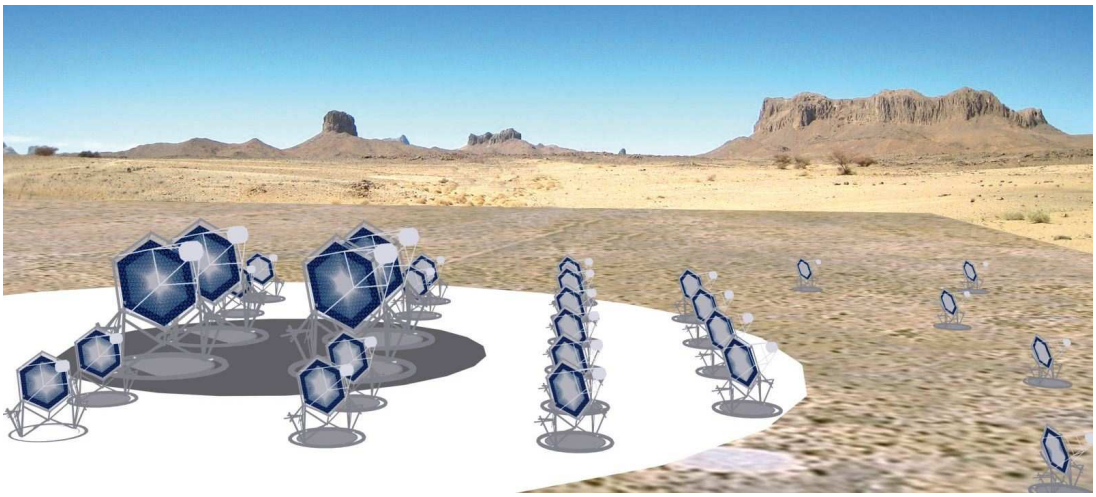

Figure 5.1: Conceptual layout of a possible Cherenkov Telescope Array. The telescopes are not to scale with the background. The proportions between telescopes are a good approximation to what planned in some proposed configurations. Figure extracted from [386].

CTA layout optimization is a very complex issue that must consider the instrument performance in different energy bands, and the costs of its realization. Typically, the energy range to be covered by CTA is divided into three subranges with different technical requirements: the low-energy range (E$<$ 100 GeV), covered by a small number of closely grouped large 20–30 m diameter telescopes; the core-energy range (100 GeV$<$E$<$10 TeV), covered by a grid of medium-size 10–15 m diameter telescopes with separations of $\sim$ 100 m; the high-energy range (E$>$ 10 TeV), covered by either a large (multi-km^2) grid of few m^2 mirror surface telescopes, or by several subclusters of $\sim$10 m^2 mirror surface telescopes separated several 100 m among them. By the time this work is written, the layout optimization was already under study and subject to discussion, although several possible array configurations are being explored. The arrays considered throughout this work have been studied in detail with the help of Monte Carlo simulations as described in [386]. The performance of the different arrays rely on several factors, besides the number and size of the telescopes and its geometrical arrangement: the FoV of each telescope, the pixelization degree of the camera, the signal recording, and the trigger conditions. Among the simulated arrays, the three typically considered CTA layouts consist on:

- Array B: 37 telescopes with 12 m diameter reflector mounting Davies-Cotton optics, with 8° FoV cameras made of 0.18° pixels; 5 telescopes with 24 m reflector mounting parabolic optics, with 5° FoV camera made of 0.09° pixels.

- Array C: 55 telescopes with 12 m diameter reflector moulting Davies-Cotton optics, with 8° FoV cameras made of 0.18° pixels.

- Array E: 32 telescopes with 7 m diameter Davies-Cotton optics, 10° FoV and 0.25° pixels; 23 telescopes of 12 m diameter reflector mouton Davies-Cotton optics, with 8° FoV cameras

made of 0.18° pixels; 4 telescopes with 24 m reflector mounting parabolic optics, with 5° FoV camera made of 0.09° pixels.

Differences in sensitivity between arrays are due to the number of detectors of each kind that are used, and their spatial layout. All three considered layouts can be found in Fig. 5.2, and their corresponding differential sensitivities in Fig. 5.3.

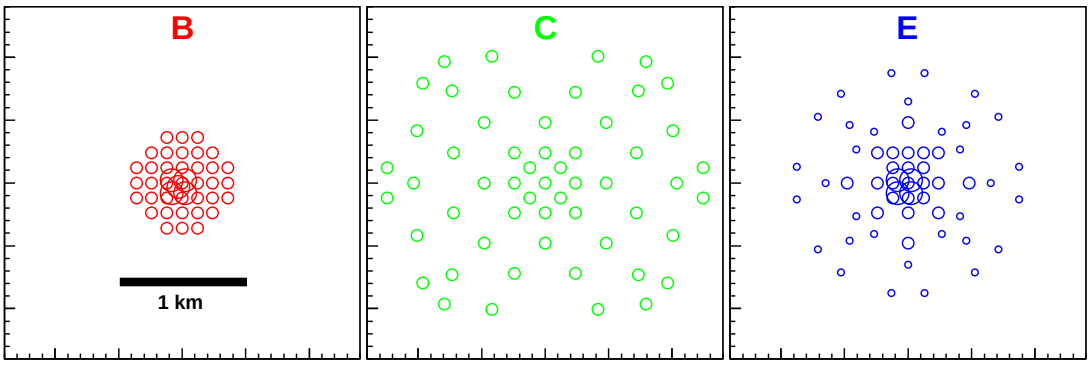

Figure 5.2: Three possible CTA configurations, labeled B, C, and E arrays. B array would consist on 42 telescopes (5 telescopes of 24 m diameter and 37 telescopes of 12 m diameter); C array would consist on 55 telescopes of 12 m diameter; E array would consist on 59 telescopes (4 telescopes of 24 m diameter, 23 telescopes of 12 m diameter, and 32 telescopes of 7 m diameter). The size of telescope's reflector is represented by the size of the circle. Figure extracted from [386].

In the next section, the prospects of detection of dark matter subhalos with CTA will be studied. The capabilities of these three different array layouts will be tested thanks to their simulated responses: γ-ray effective areas and background rates provided by the CTA Consortium [386]. It should be mentioned that all considered layouts correspond to possible configurations for the southern array. Since the northern and southern arrays are planned to present similar performances in the low and mid energy ranges, the following results can be also interpreted in terms of the northern array.

5.2 Detection prospects of point-like dark matter sources

The dark matter detection prospects with CTA requires to probe the capabilities of the system to various possible targets: the search in dSph galaxies and other Galactic Halo substructures, the Galactic Halo in the vicinities of the Galactic Center, the Galactic Center itself, galaxy clusters; the search of spatial signals in the γ-ray background through anisotropies; the search for dark matter emission lines; the search for axion dark matter in the high energy spectra of distant AGN, etc. In the following, only targets which could be considered point-like sources for CTA, and whose emission is due to WIMP dark matter annihilation, will be studied. These targets could be identified with dark matter subhalos in the Galactic Halo fulfilling the previous conditions.

In order to quantify the detection prospects of those dark matter subhalos with CTA, a hypothetical γ-ray spectrum from dark matter annihilation must be compared with the expected CTA performance. Consequently, a generic dark matter emission spectrum was assumed

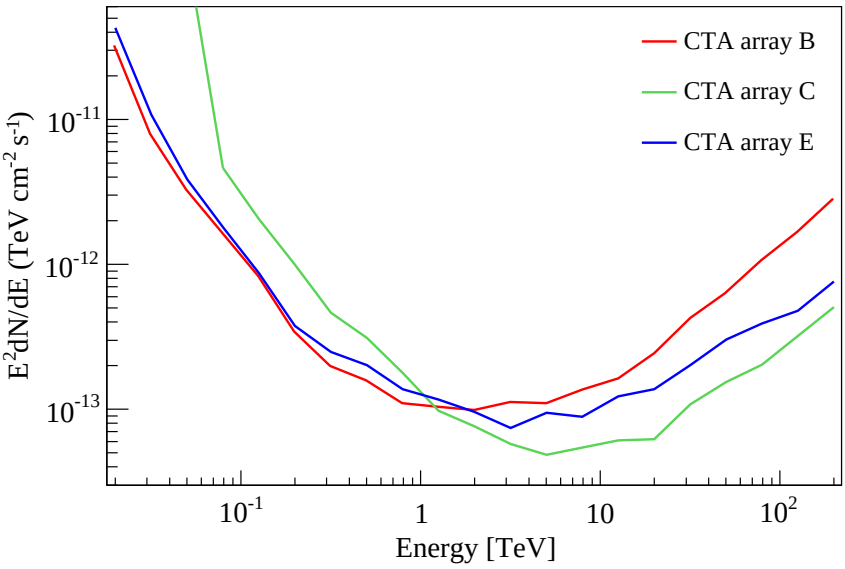

Figure 5.3: Simulated differential sensitivity of CTA for the three considered arrays.

following the prescriptions from Sec. 1.4.3.2:

$$\phi(E, \Delta\Omega) = J(\Delta\Omega) \times \phi^{PP}(E) = J(\Delta\Omega) \times \frac{1}{4\pi} \frac{\langle\sigma_{\rm ann} v\rangle}{2m^2_{\rm DM}} \sum_{i=1}^{n} B_i \frac{dN_i^\gamma}{dE}, \tag{5.1}$$

where $\langle\sigma_{\rm ann} v\rangle$ is the dark matter particle annihilation cross section, $m_{\rm DM}$ is the particle mass, $\frac{dN_i^\gamma}{dE}$ is the photon spectrum per annihilation through channel i, and B_i is the i channel branching ratio. The astrophysical factor, $J(\Delta\Omega)$, is the integrated dark matter density squared along the line-of-sight, considering a solid angle $\Delta\Omega$ (see Eq. 1.25).

There are many unknown variables in the former expression. For simplicity, a number of assumptions to build a set of reasonable dark matter spectra were made. First, the dark matter particle is considered to be a WIMP whose freeze-out in standard cosmology implies an annihilation cross section of $\langle\sigma_{\rm ann} v\rangle \sim 3\times10^{-26}{\rm cm}^3{\rm s}^{-1}$ (see Sec. 1.3). For the photon spectra per annihilation, the analytical expressions from [145] for the channels $b\bar{b}$, W^+W^-, $\tau^+\tau^-$, and $\mu^+\mu^-$ respectively were used. Throughout the work, branching ratios B_i of 100% are fixed, assuming that the annihilation proceeds entirely through each of the considered channel. As for the dark matter particle mass, a range of possible masses for the dark matter particle $m_{\rm DM}$, that spans from 50 GeV to 10 TeV, was considered. The lower limit corresponds to a conservative energy threshold for CTA, also motivated by the current experimental lower limits from accelerator data for supersymmetric WIMPs [396]. The upper limit is justified by theoretical arguments (see, *e.g.*, [57]).

As a consensus within the IACT field, a detection of a γ-ray signal is considered statistically significant if it exceeds 5 standard deviations (5σ) over the background events, following the standard formalism (see [306]). In order to survey the CTA capabilities to γ-rays detection from dark matter annihilation at a specific subhalo object, we evaluate the statistical significance of the dark matter signal as a function of the dark matter particle mass $m_{\rm DM}$ and the astrophysical factor J, considering the above-mentioned four different annihilation channels. The γ-ray excess

rate R_{exc} over a certain energy threshold E_{th} can be computed from the effective area of the instrument $A_{eff}(E)$ and the differential spectrum of the source $\phi(E, \Delta\Omega)$ (Eq. 5.1), which includes all the aforementioned dependencies, as:

$$R_{exc}(E_{th}) = \int_{E_{th}}^{\infty} \phi(E, \Delta\Omega) A_{eff}(E)\, dE = \int_{E_{th}}^{\infty} J(\Delta\Omega) \times \frac{1}{4\pi} \frac{\langle \sigma_{\rm ann} v \rangle}{2m_{\rm DM}^2} \sum_{i=1}^{n} B_i \frac{dN_i^{\gamma}}{dE} A_{eff}(E)\, dE \tag{5.2}$$

The background rate over a certain energy threshold E_{th}, in the same way as the effective area of the instrument $A_{eff}(E)$, is obtained from the MC simulations, and thus depends on the array layout. It can be expressed as:

$$R_{bkg}(E_{th}) = \int_{E_{th}}^{\infty} \frac{dR_{bkg}}{dE}\, dE. \tag{5.3}$$

Consequently, inserting $N_{on} = (R_{exc} + R_{bkg}) \times t$ and $N_{off} = R_{bkg} \times t$ into Eq. 2.17, the significance of detection turns to depend on the dark matter spectrum and the array layout. These dependencies are exploited in two different ways to present the CTA dark matter detection prospects. First, the astrophysical factor J required to reach a statistical significance of 5σ is obtained for different arrays and different annihilation channels. Second, the prospects of detection for a set of well known dwarf spheroidal galaxies is studied by introducing the so-called flux *boost factor* required to meet a detection. In both approaches observing times of 250 hours are considered, corresponding to a typical long-term observation program in the IACT context, as well as a number of 5 *off* regions ($\kappa^{-1} = 5$ in Eq. 2.17).

An example of hypothetical spectra for different annihilation channels for a WIMP of mass $m_{\rm DM} = 1$ TeV forming a dark matter subhalo of astrophysical factor $J = 9 \times 10^{20}$ GeV^2, is shown in Fig. 5.4. In the case of a dark matter particle annihilating to $\tau^+\tau^-$, such a dark matter subhalo would be detected by CTA after 50 hours observing time.

5.2.1 Detection limits in terms of minimum astrophysical factors

As already mentioned, a way to show the CTA capabilities for dark matter detection is to evaluate the minimum astrophysical factor J_{min} required for a 5σ detection in a certain amount of observing time, which in the current case was set to 250 hours. Once the array layout is fixed, and so they are the specific effective area and the background rate, J_{min} depends on the dark matter particle mass $m_{\rm DM}$ and the annihilation channel. The J_{min} evolution as a function of the particle mass is shown in Fig. 5.5 for the three considered arrays and two different annihilation channels, namely, to $b\bar{b}$ and $\tau^+\tau^-$. As a general conclusion for these three layouts, it can be said that CTA is more sensitive to a dark matter particle mass in the range from 300 GeV to 1 TeV. The smallest J_{min} values are provided by the array B, turning this layout the most sensitive for dark matter searches, even for few TeV mass WIMPs. Array E results are comparable to array B's, although they show a slightly less sensitive performance. Array C performs significantly worse at low energies and tends to match array B and E at TeV energies. This behavior was expected since array C is optimized for the several TeV energy range, performing much better than the other two layouts in that region [386]. As can be seen from Fig. 5.4, annihilation to $\tau^+\tau^-$ provides harder spectral shapes and a more numerous population of photons close the WIMP cut-off as compared to the $b\bar{b}$. Therefore, J_{min} values associated to the annihilation channel $\tau^+\tau^-$ are smaller than those associated to the $b\bar{b}$ channel. In order to put these values in context, it is worth mentioning that known dwarf galaxies span in a range between 4×10^{17}

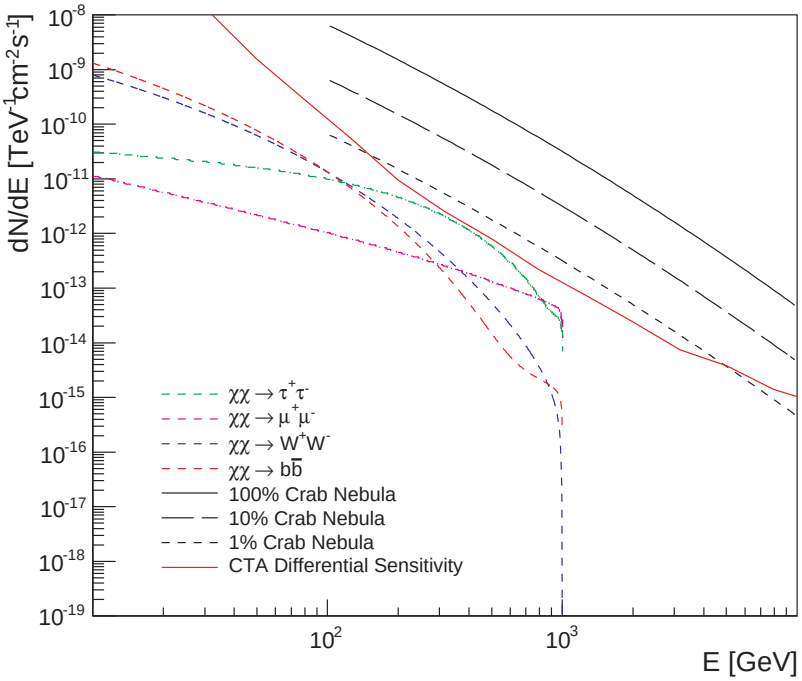

Figure 5.4: Dark matter spectra for $b\bar{b}$, W^+W^-, $\tau^+\tau^-$, and $\mu^+\mu^-$ channels, following [145]. An astrophysical factor $J = 9 \times 10^{20}$ GeV^2, an annihilation cross section $< \sigma v >= 3 \times 10^{-26}$ cm^{3}s^{-1}, and $m_{\rm DM} = 1$ TeV were assumed. The red solid line depicts CTA differential sensitivity for 50 hours of observation time (array E). With such a high astrophysical factor, if the dark matter particle annihilated exclusively to $\tau^+\tau^-$, it would be detected by CTA with and exposure of 50 hours. The lines indicate the 100%, 10% and 1% Crab Nebula differential flux [344].

GeV^2 cm^{-5} for the Carina dSph galaxy [329], and 1.8×10^{19} GeV^2 cm^{-5} for Segue 1 ultra-faint dSph galaxy [371]. The effect that the different annihilation channels have over the J_{min} parameter is illustrated in Fig. 5.6. In the figure, only the array B was used while four different channels were considered, namely, annihilation exclusively to $\tau^+\tau^-$, $b\bar{b}$, $\mu^+\mu^-$, or W^+W^-.

5.2.2 Detection limits in terms of boost factors

The next way to evaluate the prospects of dark matter detection is by means of the *boost factor* B_F. This B_F is defined as the ratio of the minimum astrophysical factor J_{min} to the estimated astrophysical factor J_{obs} from observations, for a particular WIMP mass and an observing time of 250 hours. The approach is justified by the fact that one current conjecture in this field is that the actual signal due to dark matter might be enhanced with respect to classical calculations. This intrinsic boost in the flux could be provided by the effect of substructures within the subhalos, which enhances the astrophysical factor [171] and/or by the *Sommerfeld effect* which enhances the particle physics term [162].

The measured astrophysical factors assume an angular integration region of $\Delta\Omega = 10^{-5}$ sr, corresponding to the typical PSF of the current generation of IACTs. Although Monte Carlo simulations predict a relative improvement of the CTA PSF as compared to the current generation of IACTs [386], which would require the considered J_{obs} to be recomputed by changing the angular integration region to a smaller one, the changes would not be very significant (see

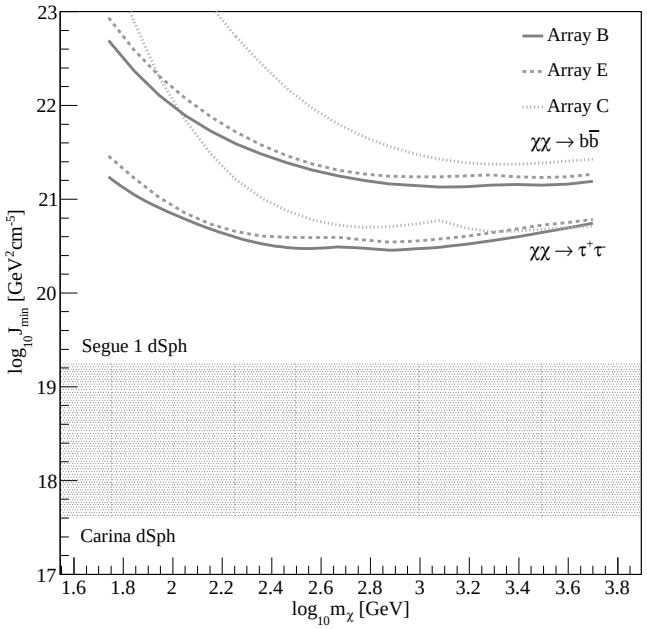

Figure 5.5: Minimum astrophysical factor J_{min} for a 5σ detection with CTA as a function of WIMP mass $m_{\rm DM}$. Results for three different array configurations are shown: array B, C, and E. WIMPs annihilating exclusively to $\tau^+\tau^-$ or $b\bar{b}$, with a typical annihilation cross section of $\langle\sigma_{\rm ann}v\rangle \sim 10^{-26}{\rm cm}^3{\rm s}^{-1}$ were assumed. The shaded region illustrates the current estimated values from Carina to Segue 1 dSph galaxies.

Fig. 3.17). There would be an overall decrease of the J_{obs} due to the smaller integration region, but the large uncertainties on the calculation of this factor would render these changes negligible. Thus, the results should be considered as an order of magnitude approximation to the problem.

The set of selected dSph galaxies, together with their estimated astrophysical factors J_{obs}, can be found in Table 5.1. A distribution of the minimum B_F for the case of a 1 TeV mass dark matter particle annihilating to $\tau^+\tau^-$ for the array B configuration is shown in Fig. 5.7. The ultra-faint dSph Segue 1 appears to be one of the most attractive dark matter targets from the halo modelling of [371], although further accurate modelling from stellar dynamics is needed. Considering a $B_F \geq 16$ over the current J_{obs} for Segue 1, a dark matter signal could be detected in 250 hours of CTA observation time.

5.3 Conclusions and outlook

A study of the prospects of dark matter detection with CTA in the figure of γ-ray point-like sources has been presented using expected instrument sensitivities from MC simulations. This γ-ray point-like sources could be found in the general shape of galactic dark matter clumps or the particular type of objects the satellite dSph galaxies form.

In order to survey the CTA capabilities of dark matter detection, the statistical significance of a hypothetical dark matter signal has been evaluated as a function of the dark matter particle mass $m_{\rm DM}$ and the source astrophysical factor J, considering different possible annihilation

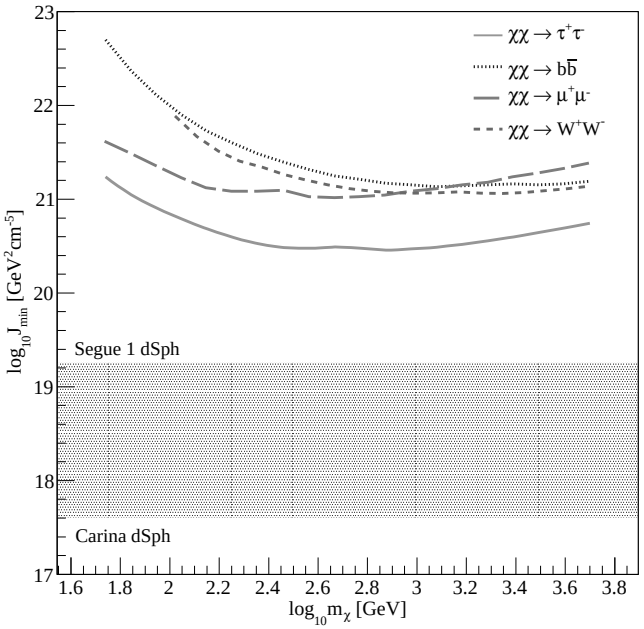

Figure 5.6: Minimum astrophysical factor J_{min} for a 5σ detection with CTA as a function of WIMP mass $m_{\rm DM}$. WIMP annihilation entirely into $\tau^+\tau^-$, $b\bar{b}$, $\mu^+\mu^-$, or W^+W^- were considered. A typical annihilation cross section of $\langle\sigma_{\rm ann}v\rangle \sim 10^{-26}{\rm cm}^3{\rm s}^{-1}$ was assumed. The shaded region illustrates the current estimated values from Carina to Segue 1 dSph galaxies. The results are for CTA array B and an observation time of 250 hours.

Table 5.1: Astrophysical factors for the selected set of dSph.

Source	Reference	Profile	J_{obs}	B_F
Carina	[329]	NFW	4.0×10^{17}	700
Boötes 1	[327]	NFW	1.1×10^{18}	250
Draco	[327]	NFW	1.5×10^{18}	200
Ursa Minor	[327]	NFW	2.7×10^{18}	100
Sculptor	[329]	NFW	4.0×10^{18}	75
Willman 1	[327]	NFW	8.4×10^{18}	35
Segue 1	[3]	Einasto	1.8×10^{19}	16

Astrophysical factors for the set of dSph galaxies considered for Fig. 5.7, as well as the required B_F to match a detection in 250 hours of CTA observation time for a 1 TeV dark matter particle annihilating to $\tau^+\tau^-$. The integration solid angle corresponds to a $\Delta\Omega = 10^{-5}$ sr ($\sim 0.1^\circ$ PSF) in all the cases. The B_F are computed for the array B configuration.

channels. Two different ways to present the results were chosen. In the first one, the minimum astrophysical factor J_{min} required to reach a statistical significance of 5σ, assuming an effective observation time of 250 hours, was computed. The main results from this first approach can be found in Fig. 5.5 and Fig. 5.6, where it can be clearly seen that, for the studied energy range, the arrays B and E are more sensitive for GeV-mass dark matter particles than array C, while for TeV-mass dark matter particles this difference is not that significant any more. Additionally,

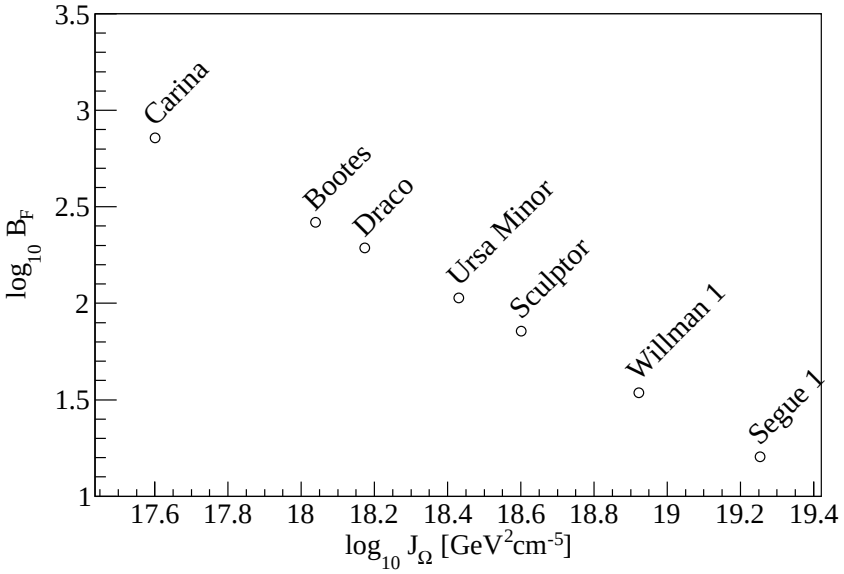

Figure 5.7: Minimum boost factor B_F as a function of astrophysical factor J for a set of 7 well-studied dSph galaxies, for a putative 1 TeV WIMP mass annihilating to $\tau^+\tau^-$. The minimum requirement is a 5σ detection in 250 hours by CTA (array B). The least strict boost is for the ultra-faint Segue 1 that would only require $B_F \geq 16$.

dark matter annihilation detection could be realized, within an observation time of 250 hours, for subhalos with astrophysical factors $J \geq 4 \times 10^{20}$ GeV^2 cm^{-5} assuming a WIMP dark matter particle with a mass around 1 TeV 100% annihilating into $\tau^+\tau^-$. In the second approach, the so-called *boost factor* B_F, defined as the ratio between the aforementioned J_{min} and the observational astrophysical factor J_{obs}, was calculated for a set of well known dSph galaxies. Fig. 5.7 shows the B_F distribution for the considered set of dSph galaxies. At present, Segue 1 appears as one of the most promising dark matter targets. Actually, a dark matter signal could be detected in 250 hours of observation time with a $B_F \geq 16$ for a dark matter particle with mass in the range from 300 GeV to 1 TeV 100% annihilating into $\tau^+\tau^-$. However, further work is required to refine the calculation of its J_{obs} which could affect the estimated B_F value. From these results, it is obvious that the search for objects with extreme astrophysical factors must continue. Either less distant subhalos or objects with enhanced density profiles could provide the pursued astrophysical factors required for a detection with CTA. Our knowledge of the Galactic halo will certainly improve with upcoming Southern surveys, similar to the *sdss* ones, that will scan for such subhalos prior or simultaneously to CTA, like the planned SkyMapper Southern Sky Survey [384].

As a final remark, it should be emphasized that the results presented in this chapter[1], should be considered as conservative limits from the observational point of view. Further studies and design improvements are being introduced in the final CTA configuration which could eventually change in a significant way the arrays performance. As an example, the used MC do not consider the possible contribution of a noteworthy increase of telescope units proposed by the US part of the CTA Consortium. Nonetheless, this study clearly illustrates the tremendous impact that CTA could make on indirect dark matter searches over the upcoming years.

[1]These results will be eventually published within an *Astroparticle Physics Special Issue* in preparation.

Chapter 6

Conclusions and Outlook

The presented work reports on indirect dark matter searches performed on dSph galaxies, and possible dark matter subhalos of the Milky Way. The observations were carried our in the high energy band of the electromagnetic spectrum, from X-rays to VHE γ-rays, and thus different instruments were used, namely the MAGIC Telescopes (VHE γ-ray regime), the Fermi-GST (HE γ-ray regime), and the Chandra-XRO. As for the dark matter particle candidates considered, special attention was given to the *sterile neutrino* as a well motivated example of decaying dark matter in the X-ray band, and to the *neutralino*, an annihilating dark matter natural candidate emerging from the supersymmetric extension of the Standard Model of particle physics. The work also presents the study of the dark matter detection prospects for the next generation of Cherenkov telescopes, through the characterization of the sensitivity of the future Cherenkov Telescope Array to dark matter signals in the VHE γ-ray regime.

In the following, the main results and conclusions of this work are presented, along with a brief outlook, for each relevant part of the work.

Dark matter searches in dwarf spheroidal galaxies: The search for dark matter in dwarf spheroidal galaxies has been two folded. First, signatures for a possible annihilating dark matter particle have been searched for in VHE γ-ray observations of Willman 1 and Segue 1 dSph by the MAGIC-I Telescope. Second, searches for spectral lines from a decaying dark matter particle in the X-ray band have been conducted in Chandra-XRO observations of Willman 1.

Concerning the observation in the VHE γ-ray band, no signal was found for any of the surveyed targets. The analyses of the datasets led to the computation of upper limits to the differential and integral fluxes coming from both sources. The upper limits to the integral flux range from 2% to 10% CU in the case of Willman 1, and from 0.5% to 9% CU, depending on the analysis energy threshold. Those limits are unique in the low end of the very high energy γ-ray band due to the lowest energy threshold of MAGIC among the current generation of IACTs. The lack of signal was exploited in terms of indirect dark matter searches by placing corresponding limits to certain mSUGRA models where the *neutralino* is the dark matter particle candidate. In the case of Willman 1, four mSUGRA benchmark models, each of them being a representative point in the parameter space, were considered. The boost factor required to match each point's expected dark matter flux to the corresponding derived upper limits ranges from $B^{ul} =\sim 10^3$ in the case of the $funnel$ region to $B^{ul} =\sim 10^5$ in the case of the $co-annihilation$ region, highlighting the influence of the spectral shape over the detection prospects. Instead of few benchmark points, in the case of Segue 1 an extensive mSUGRA parameter space sampling was performed, simulating more than five million particular points, which covered the region that can provide a *neutralino*

in the mass range equivalent to the typical IACTs energy range. Individual upper limits to the *neutralino* annihilation cross-section were obtained in a point-by-point basis, showing again that the limits are strongly dependent on the energy spectrum of the each parameter space point. Due to the fact that a general exclusion plot to constrain the parameter space cannot be drawn, the results were given in the form of enhancement factors, defined as the ratio between the upper limit to the annihilation cross-section and the characteristic annihilation cross-section obtained for each point of the scanned parameter space. For points of the parameter space fulfilling the cosmological constraints from WMAP data, the enhancement factor average value ranges from 10^4 to 10^5 with a minimum at 10^{-3}, whereas if WMAP cosmological constraints are removed the minimum enhancement factor can be as low as 3.9. Additionally to the mSUGRA models, leptophilic models proposed to accommodate PAMELA electron-positron fraction excess, and allowed by Fermi-LAT constraints, where probed. In this scenario, the upper limits imposed by Segue 1 observations are marginally on tension with leptophilic dark matter annihilating through the $\tau^+\tau^-$ channel. An exclusion of such model would be possible if updated kinematic data on Segue 1 star members increased the astrophysical factor of the source.

It is worth mentioning that there are other models offering dark matter particle candidates that could be identified in the very high energy γ-ray regime. The constraining power of the before mentioned observations should be tested over those candidates too.

The X-ray data on Willman 1 provided by Chandra-XRO observations were analyzed, studying separately the diffuse component and the point-like emission within a FoV enclosing the dSph galaxy core. The main result regarding the point-like source population of that region is that, down to the luminosity limit of the observation, the total number of sources is compatible with a background AGN population. Spectral information for each point-like source favors the before mentioned hypothesis. On top of that, the probability of finding candidate X-ray binaries within Willman 1 inner core was estimated to be extremely low. Concerning the diffuse emission, an exhaustive search for exotic spectral lines, that could be attributed to *sterile neutrino* decay, was performed without any positive finding. The flux from spectral lines in the Chandra-XRO energy band was constrained, and those constraints were translated into limits to the *sterile neutrino* parameter space by considering this particle to be the exclusive component of the dark matter. It was shown that one of the greatest challenges on the identification of exotic spectral lines are the control of instrumental and ordinary astrophysical lines, which are the main contaminant of a possible dark matter signature in this kind of observations.

For the *sterile neutrino* searches, deeper exposures on the best candidates are encouraged. Chandra-XRO and XMM-Newton are the best suited instruments for such searches, being complementary: Chandra-XRO has a better energy resolution, thus fitting better for dark matter decay lines searches, while XMM-Newton is more sensitive to extended emission, which is a crucial feature to check the variation of a possible dark matter signal as a function of the dark matter profile in the target.

These results hitherto presented, that involve a dark matter-motivated interpretation, rely on a proper determination of the astrophysical factor of each corresponding source. Consequently, the uncertainties in such a factor, and also the assumptions made at the time of the dark matter density distribution modelling, must be taken into strong consideration. In order to reduce such uncertainties, a better characterization of the dark matter density profiles of the sources is needed, and this could only be provided by further studies about the kinematics of their star members. Therefore, deepest optical spectroscopic observations on Willman 1 and Segue 1 are encouraged.

Besides the improvement in the characterization of the known targets, it should be noted that

new dSph galaxies may emerge from current and future observational projects (like the extension of the SDSS, or the incoming Skymapper). These potentially new dSph galaxies might be more favorable targets from the dark matter detection point of view.

A very interesting strategy in order to take advantage of the already available dSph data in both, in the X-ray and the very high energy γ-ray bands, is the stacking of the data. This stacking is possible due to the fact that the spectrum from dark matter annihilation or decay must be universal, and that the dark matter density profile seems to be scale-invariant. Moreover, in the case of the *sterile neutrino* more ambitious approaches can be followed: if the *sterile neutrino* forms the Galactic dark matter Halo, its decay line must be present as an irreducible background in all the observations. Thus, the stacking of data from dark patches and regions without detected extended emission (and after point-like source subtraction) may offer a new opportunity for dark matter detection. In principle, this strategy could be also considered for observations in the VHE γ-ray band but, due to the complexity of the IACTs' background determination, its realization may be much more complicated, and the expected signal may be below the statistical error inherent to the technique.

With the advent of a new generation of more sensitive instruments in both, the x-ray band (like the ixo project), and the VHE γ-rayband (like the CTA project), an eventual detection might be closer. In the worst case, the presented limits could be significantly improved and some proposed dark matter candidates could be ruled out. Consequently, detection prospect studies for this new generation of instruments is are encouraged.

Dark matter searches in unassociated Fermi objects: A thorough search was developed in order to select possible dark matter clump candidates out of the 1FGL Catalog unassociated objects. The search was performed under the hypothesis of a dark matter particle with such a large mass that the identifying cut-off of its annihilation spectrum is located beyond the upper end of Fermi-LAT energy range, and within the reach of the IACTs. Such a search, consists of several steps: a selection of dark matter clump-like objects based on the 1FGL Catalog parameters; a dedicated search for possible counterparts in the main astronomical catalogs and mission archives covering all the available electromagnetic spectrum; a study of the Fermi-LAT HE γ-ray photons from each source and its surroundings; and the calculation of the estimated detection time with the MAGIC Telescopes. The outcome of such search was a total of six dark matter clump candidates, that could be observed at MAGIC latitude, out of the 1FGL Catalog population.

The best two candidates out of the final list were observed by the MAGIC Telescopes, namely, 1FGL J0338.8+1313 and 1FGL J2347.3+0710. No VHE γ-ray signal was detected for any of them after short observations ($\lesssim$10 h each). Competitive upper limits to their differential and integral spectra were derived. The upper limits to the differential flux obtained for 1FGL J0338.8+1313 disfavors a direct extrapolation of the Fermi- flux beyond 200 GeV, whereas the upper limits to the differential flux obtained for 1FGL J2347.3+0710 do not favor a direct extrapolation beyond 400 GeV. Consequently, a possible curvature or cut-off at Fermi-LAT HE range can be suggested in both cases. A confirmation of such spectral behavior can only be stated if deeper observations are carried out in these sources. However, these conclusions rely on 1FGL Catalog results, and should be reconsidered once updated spectral data on these sources, coming from the 2FGL Catalog, are released.

During the dedicated counterpart search, Swift-XRT data from both sources were analyzed. The fields corresponding to the Fermi-LAT error regions were free of any X-ray point-like source. While for 1FGL J0338.8+1313 no evident point-like sources were present in the entire Swift-

XRT FoV, a bright X-ray source was detected close to the 1FGL J2347.3+0710 Fermi-LAT error contour. Consequently, 1FGL J2347.3+0710 classification as good dark matter clump candidate has to be reconsidered once its possible association with the bright Swift-XRT source is clarified.

The developed selection procedure can be applied to the 2FGL Catalog in order to propose new candidates or to confirm already selected targets. Moreover, the detection prospects can be evaluated not only for the MAGIC Telescopes but also for the future . Besides the proposal of targets for VHE γ-rayobservations, the selection method can be also used to propose X-ray observations on high galactic latitude unassociated Fermi objects with the same motivation: these sources might be dark matter clump candidates that, in case the dark matter constituent is the *sterile neutrino*, may produce identifying X-ray lines potentially detectable with sensitive X-ray telescopes.

It should be mentioned the great potential that a multiwavelength approach to the dark matter identification can offer. It has been shown in this work the synergy between different γ-ray telescopes was able to provide with new dark matter motivated astrophysical targets. Consequently, to widen the search energy window and to add different energy bands must be encouraged in the pursue for the dark matter particle identification.

Dark matter prospects for the next generation of Cherenkov telescopes: The prospects of dark matter detection with the future Cherenkov Telescope Array, as the most promising project for the next generation of Cherenkov telescopes, have been studied. Particularly, the planned instrument sensitivity to point-like sources, whose γ-ray emission was produced by GeV-mass dark matter annihilation, were considered. This generic source may represent, as an approximation, the expected dark matter flux from dSph galaxies, and other galactic dark matter clumps.

MC simulations of the telescope response have been used to survey the CTA capabilities for dark matter detection. Such capabilities have been tested as a function of the dark matter particle mass and the source astrophysical factor J, also considering four different annihilation channels. On top of that, several possible array configurations have been considered (named B, C, and E array), with the aim of finding out the best layout for dark matter searches.

The sensitivity of CTA to this kind of sources has been evaluated in two different ways: in terms of the minimum *astrophysical factor* J_{min} needed to meet a detection in a given observation time ($T_{obs} = 250$ h), and in terms of the minimum *boost factor* the fluxes from a set o known dSph galaxies would require to reach a detection considering the same amount of observation time. The main result from that first approach is that, for the studied energy range, the array B is the most sensitive to GeV-mass dark matter, followed by array E, which is slightly less sensitive in this energy range. The sensitivity of array C to GeV-mass dark matter particles is significantly worse than the two previous arrays. However, for few TeV-mass dark matter particles the performances of the three different arrays are very similar. It has been shown the influence of the annihilation channel in the prospects of detection. Eventually, in the most optimistic case, namely, a dark matter particle of mass in the range from 300 GeV to 1 TeV 100% annihilating into $\tau^+\tau^-$, would be detected by CTA array B in 250 h observation time, if a dark matter target offering an astrophysical factor of $J \geq 4 \times 10^{20}$ GeV^2 cm^{-5} was found. The main results from the second approach were obtained under the previous optimistic case, considering the same array B configuration, and the same observation time. For the most promising promising dark matter target so far, the dSph galaxy Segue 1, a detection of a dark matter signal could be met if the expected source from the source would be increased by a *boost factor* $B_F \geq 16$. It should be noted that such low *boost factor* might be reached if the effect of

the substructures within the dSph galaxy dark matter density distribution is taken into account. However, this result relies on a proper characterization of the observed *astrophysical factor* of the source which, in the case of Segue 1, suffers from large uncertainties that should be reduced in the future by deepest optical spectroscopic observations.

Finally, it must be noted that these results should be considered as conservative limits from the observational point of view. The final CTA design is not fixed yet. Further studies and design improvements may enhance the CTA performance, and increase its sensitivity to dark matter signals. Albeit conservatives, these results show the great contribution that CTA would be able to offer to the indirect dark matter searches in the near future. CTA will be the most powerful instrument to search for this elusive component of the Universe in the VHE γ-rayband.

Appendix A

Extended Atmospheric Showers

Very high energy cosmic rays and γ-rays that impinge the Earth's atmosphere are absorbed through the generation of extended atmospheric showers (EASs) of secondary photons and particles. Cosmic ray absorption would develop hadronic showers while γ-ray absorption would develop purely electromagnetic showers. In either case, the EASs are characterized by extensions over several kilometers in length and up to hundreds of meters in width, with a maximum number of produced particles and photons typically located at 0.2 – 0.3 atmospheric mass fraction (between 8 and 12 km in the case of vertical incidence). A large fraction of the shower's charged particles move faster than light in the medium, thus emitting Cherenkov photons. The morphology of hadronic showers and pure electromagnetic showers are not equal, nor the corresponding Cherenkov emission, thus allowing for discrimination among them. In the following, a brief description of γ-ray and cosmic ray induced EASs, as well as some comments on the Cherenkov effect, will be presented.

A.1 Extended atmospheric showers from gamma-rays

When a γ-ray impinges the atmosphere it is converted into an electron positron pair in the vicinities of an atmospheric nucleus. The generated electron and positron pair loose energy through the emission of high energy bremsstrahlung photons again in the presence of atmospheric nuclei. These high energy bremsstrahlung photons create more electron positron pairs in turn, and so on. These processes are repeated, creating a shower of electrons, positrons, and photons with reduced energy in every step, until the bremsstrahlung emission turns out to be less probable than the ionization as energy loss mechanism for the charged particles (below the critical energy of $E_c = 83$ MeV, ionization losses dominate). Since only photons, electrons, and positrons take part in the shower development, this kind of showers are called pure electromagnetic showers. A simplified diagram for an electromagnetic shower is shown in Fig. A.1.

The most common models to describe the electromagnetic shower development assumes certain simplifications:

- The radiation length for ultrarrelativistic electrons[1], and the mean free path of photons[2] with similar energies are equal, so the number of photons, electrons, and positrons after n-radiation/absorption lengths is 2^n.

[1]The radiation length is defined as the mean covered distance after which the energy of the charged particle is reduced by a factor e due to bremsstrahlung radiation.

[2]The mean free path of photons is defined as the distance covered by a population of photons after which the total number of photons is reduced by a factor e due to electron-positron pair production.

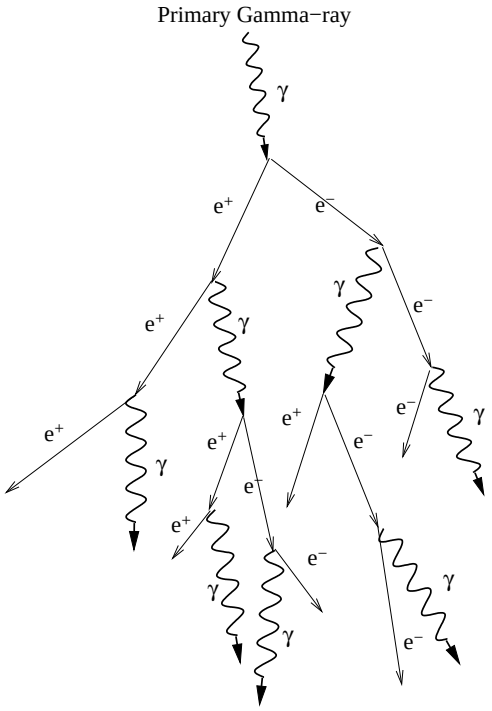

Figure A.1: Schematic figure of an electromagnetic EAS. This kind of showers are initiated by the absorption of γ-ray photons via pair production. Figure extracted from [201].

- The energy shared by the particle and the bremsstrahlung photon, or by the electron and positron out of a pair creation, is equally distributed, so the energy for each constituent decreases as $E_0/2^n$ after n-radiation/absorption lengths, where E_0 is the primary γ-ray energy.

It can be shown (see [413; 414]) that the number of electrons above the aforementioned critical energy E_c can be obtained as:

$$N_e(s) = \frac{0.31}{\sqrt{\ln(E/E_0)}} e^{T(-1.5\ \ln(s))}, \tag{A.1}$$

where s is the so-called shower age, and T is the atmospheric depth expressed in radiation lengths. The shower age s is a function of the atmospheric depth T, and it is defined as:

$$s = \frac{3T}{T + 2\ln\left(\frac{E_\gamma}{E_c}\right)} \tag{A.2}$$

The atmospheric depth T depends on the assumed atmospheric model. In the case of an isothermal atmosphere it reads:

$$T = T_0 e^{(-\frac{h}{h_0})}, \tag{A.3}$$

where H is the height above sea level, h_0=8400 m is the so-called scale-height at 290 K temperature, and T_0 is defined as:

$$T_0 = \frac{X_{air}}{X_0 \cos\theta}, \tag{A.4}$$

where X_{air} is the column height of air at sea level (≈ 1013 g/cm^2), X_0 is the electrons radiation length in air (37.2 g cm^{-2}), and θ the incident angle of the electromagnetic shower. In Fig. A.2, the longitudinal development of electromagnetic showers of different energy primary γ-rays is shown in terms of the shower size (the number or electrons and positrons) versus the shower depth.

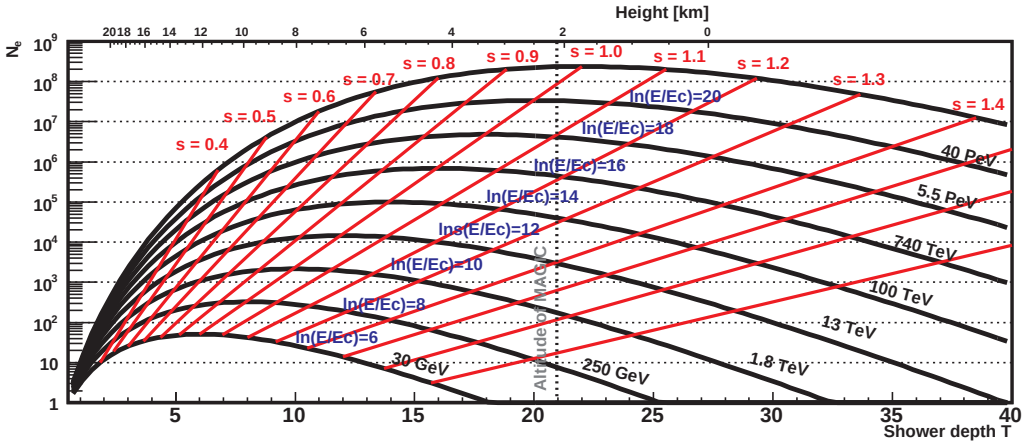

Figure A.2: γ-ray induced EAS longitudinal development, described by the shower size N_e as a function of the shower depth T. The red lines define points sharing the same shower age s. The altitude of MAGIC above the sea level is depicted by the dotted black line. Figure extracted from [201].

The lateral distribution of the shower ρ_N can be described in the regime $1 \leq s \leq 1.4$ as

$$\rho_N(r, E, T) = \frac{N_e(E, T)}{r_M^2} f(r), \tag{A.5}$$

where r_M is the Moliere radius ($\sim$ 78 m at sea level) and $f(r)$ is the Nishimura-Kamata-Greisen formula:

$$f(r) = \frac{\Gamma(4.5 - s)}{2\pi\Gamma(s)\Gamma(4.5 - 2s)} \left(\frac{r}{r_M}\right)^{s-2} \left(1 + \frac{r}{r_M}\right)^{s-4.5}, \tag{A.6}$$

where Γ is the Gamma function. ρ_N thus provides the density of electrons and positrons as a function of the distance to the shower axis r, the energy of the primary γ-ray E, and the shower depth T.

A.2 Extended atmospheric showers from cosmic rays

Cosmic rays, mainly protons (helium and heavier elements to a less extent), are also absorbed by the atmosphere due to hadronic collisions with atmospheric nuclei. Hadronic showers are more complex than electromagnetic showers, due to the large variety of products out of the collisions: pions ($\sim$ 90%), kaons ($\sim$ 10%), and other marginally nucleons. Some of these products continue colliding with other atmosphere nuclei, some others decay, and the reactions keep going until the available energy per particle goes below the pion production threshold ($\sim$ 1 GeV), when ionization losses start to dominate. Fig. A.3 shows a simplified diagram of a cosmic ray initiated shower.

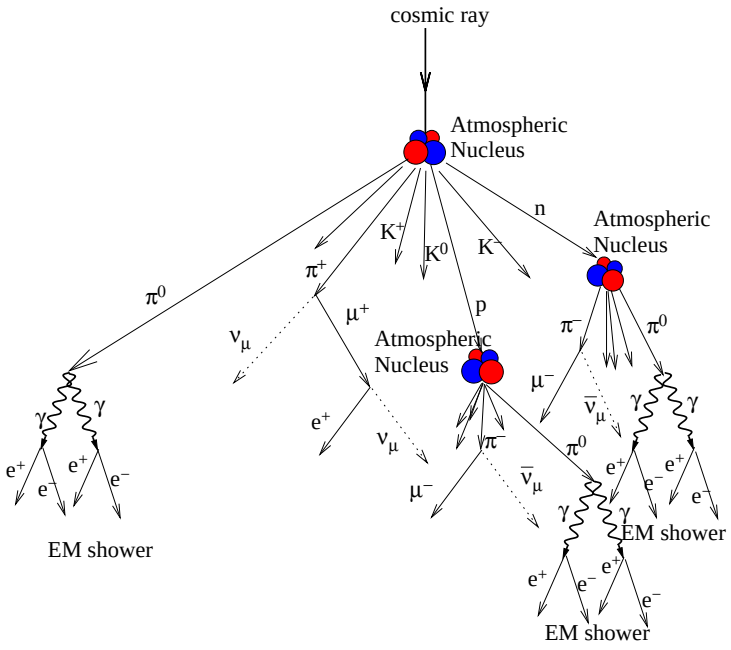

Figure A.3: Schematic figure of an hadronic shower. Since heavy hadrons can present high transverse momentum that is transferred to the products, the shower width is broadened as compared to a pure electromagnetic EAS. Figure extracted from [201].

The hadronic showers can be described as the sum of three contributions: the hadronic core, the muonic component, and the electromagnetic component.

- The hadronic core consist of nucleons and charged mesons. The later eventually decay into muons and neutrinos, although neutral pions are also produced in kaon decays ($K^{\pm} \rightarrow \pi^{\pm} + \pi^0$).
- The muonic component is basically formed by muons from the hadronic core. These muons lose energy by ionization, and also generate Cherenkov photons. They travel large distances until their decay to electrons, thus removing part of the energy from the core of the shower. The subsequent electrons generate electromagnetic showers in turn, thus broadening the hadronic shower width with respect to pure electromagnetic showers.
- The electromagnetic component is partially due to the before mentioned electron-induced showers. However, the main contribution arises from the high energy photons produced by the decay of neutral pions ($\pi^0 \rightarrow 2\gamma$) that takes place in the hadronic core.

Attending to certain models that try to characterize the hadronic shower [414], the position of the maximum of the shower X_{max} is related to the hadronic interaction length λ_{hi}, the energy of the primary cosmic ray E_0, the critical energy E_c (see Sec. A.1), and the number of nucleons A of the cosmic ray:

$$X_{max} = \lambda_{hi} \ln \left(\frac{E_0}{A E_c} \right) . \tag{A.7}$$

Consequently, for a given energy E_0, the heavier the cosmic ray the higher the shower maximum. Besides, the hadronic interaction length in air ($\lambda_{hi} \approx 90$ g cm^{-2}) is larger that the

γ-ray interaction length by a factor of more than two. Thus, the hadronic shower maximum is located closer to the ground than the electromagnetic shower maximum. It is worth mentioning that the radiation length for hadrons ($\lambda_{hr} \approx 37$ g cm^{-2}) is smaller than the interaction length. This fact produces a broadening of the hadronic showers as compared to the pure electromagnetic ones, where both, the interaction (λ_{ei}) and the radiation (λ_{er}) lengths are similar ($\lambda_{ei} \approx 1.3\lambda_{er}$).

A.3 The Cherenkov effect

When a charged particle travels through a dielectric transparent medium with a speed faster than the speed of light in that medium, Cherenkov photons are produced [415]. This condition is met if the medium presents a refractive index $n > 1$ and the particle velocity is $v > c/n$. A charged particle moving through a transparent medium polarizes it. If the particle moves slower than the speed of light in the medium, the net polarization field is null due to the symmetric arrangement of the dipoles. If the particle speed is larger than the light speed in the medium, then the polarization gets asymmetric and a net field is created (see Fig. A.4a). Since the field inductor (the charged particle) is faster than the field propagation itself, then a shock wave of in-phase reorientation of dipoles is generated, which originates the Cherenkov photon emission (see Fig. A.4b).

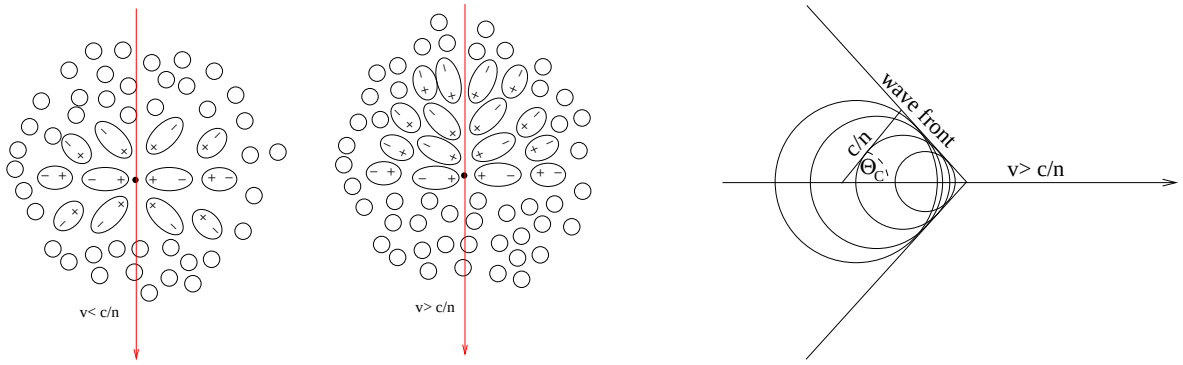

(a) Medium polarization **(b)** Cherenkov shock wave front

Figure A.4: Schematic simplification of the Cherenkov effect. Fig. A.4a: Medium polarization due to a charged particle traveling slower (*left*) and faster (*right*) than the speed of light through the medium. Fig. A.4b: Shock wave of in-phase reorientation of dipoles, origin of the Cherenkov photons. Figures extracted from [270].

Attending to the geometrical argument shown in Fig. A.4b, the Cherenkov photons are emitted in a cone characterized by a certain angle θ, called the Cherenkov angle. By applying the Huygens principle, and considering the charged particle recoil due to the photon emission, the Cherenkov angle can be expressed as:

$$cos\theta = \frac{1}{n\beta} + \frac{\hbar k}{2p}\left(1 - \frac{1}{n^2}\right), \tag{A.8}$$

where β is the particle speed in units of the speed of light, k is the Cherenkov photon momentum, and p is the charged particle momentum. Since the photon momentum is much

smaller than the charged particle momentum, Eq A.3 can be approximated by:

$$cos\theta = \frac{1}{n\beta}. \tag{A.9}$$

Consequently, the charged particle minimum speed in order to emit Cherenkov photons is $\beta_{min} = n^{-1}$, and the maximum value of the Cherenkov angle, obtained for ultra-relativistic particles ($\beta \approx 1$), is $\theta_{max} = \cos^{-1}(n^{-1})$. The minimum energy a particle should posses in order to produce Cherenkov photons is then:

$$E_C^{thr} = \frac{m_0 c^2}{\sqrt{1-\beta_{min}^2}} = \frac{m_0 c^2}{\sqrt{1-(1/n)^2}}, \tag{A.10}$$

where m_0 is the rest mass of the particle. Thus, at sea level ($n \approx 1.00029$), that minimum energy is 21 MeV, 4.4 GeV, and 39 GeV for electrons, muons, and protons respectively. However, it should be noted that the atmosphere refractive index is not constant but changes with the height, since it is related to the air density. For an isothermal atmosphere as the one described by Eq. A.1, the refractive index can be expressed as:

$$n(h) = 1 + n_0 e^{-\frac{h}{h_0}}, \tag{A.11}$$

where $n_0 = 2.9 \times 10^{-4}$. Consequently, the maximum Cherenkov angle reads:

$$\theta_{max} \approx \sqrt{2n_0} e^{-\frac{h}{2h_0}}, \tag{A.12}$$

and the the minimum particle energy for Cherenkov photon emission is:

$$E_C^{thr} \approx \frac{m_0 c^2}{\sqrt{2n_0}} e^{\frac{h}{2h_0}}. \tag{A.13}$$

As a consequence, the maximum Cherenkov angle in the upper atmosphere, for a vertical incidence charged particle, is less than 1°, increasing as the particle moves down to 1° at 8 km height, and reaches 1.4° at sea level. The lateral distribution of Cherenkov photons at ground can be computed by integrating the Cherenkov cones intersecting with the ground along the particle's tracks. The intersection radius for vertical incidence of ultra-relativistic particles is:

$$R_C(h) = (h - h_{obs}) \tan\theta_{max}, \tag{A.14}$$

where h_{obs} is the observation altitude. The aforementioned integration, applied to an electromagnetic shower, concludes that a typical shower creates a Cherenkov light pool with a maximum density of photons concentrated at a radius of ~ 120 m, decreasing to the center, and exponentially falling to larger radii.

As for the Cherenkov spectrum, the number of photons emitted for unit distance $\mathrm{d}x$, and wavelength interval $\mathrm{d}\lambda$, by a particle of charge ze and speed β can be expressed as [416]:

$$\frac{\mathrm{d}^2 N}{\mathrm{d}x \mathrm{d}\lambda} = \frac{2\pi\alpha z^2}{\lambda^2}\left(1 - \frac{1}{\beta^2 n^2(\lambda)}\right). \tag{A.15}$$

The Cherenkov spectrum ranges from the infrared to the ultraviolet regime but it suffers from atmospheric absorption too, changing the energy distribution of Cherenkov photons at

ground in such a way that the maximum emission is located at $\lambda \approx 330$ nm (blueish light). The main factors that rule that spectral distortion are the following: upper atmospheric ozone dissociation ($O_3 + \gamma \rightarrow O_2 + O$), that absorbs wavelengths smaller than 290 nm; infrared absorption by H_2O and CO_2 molecules, that cut off wavelengths larger than 800 nm; and the scattering off atmospheric particles like the Rayleigh scattering off air molecules, and the Mie scattering off aerosol particles.

Further information about extended air showers and their implication in the IACT technique can be found in [270] and references therein.

Appendix B

Restricciones sobre Materia Oscura a partir de Observaciones Astrofísicas de Alta Energía

Hay fuertes evidencias observables que apuntan hacia la existencia de materia oscura en el Universo. En el paradigma del Modelo Cosmológico Estándar, un 83% del contenido total de materia del Universo no puede ser explicado en términos de materia ordinaria, requiriendo la introducción de un componente adicional no bariónico. Sin lugar a dudas, el conocimiento de dicha materia oscura es uno de los principales problemas abiertos de la ciencia contemporánea.

La búsqueda de materia oscura se está realizando paralelamente en tres frentes distintos. El primero pretende generar la partícula constituyente de la materia oscura en grandes aceleradores de partículas. El segundo pretende detectar la partícula de materia oscura mediante sus colisiones con la materia ordinaria. El tercero intenta detectar la partícula de materia oscura a través de señales indirectas, como el estudio de los productos ordinarios generados tras una posible aniquilación o desintegración de la partícula de materia oscura.

El presente trabajo refleja ejemplos prácticos de búsqueda indirecta de materia oscura en objetos astrofísicos tales como galaxias esferoidales enanas o posibles subhalos de materia oscura de la Vía Láctea.

B.1 Introducción

Para contextualizar la búsqueda indirecta de materia oscura a partir de observaciones astrofísicas de alta energía, hay que introducir el paradigma cosmológico actual, fundamentado sustancialmente en la existencia de este tipo de materia, así como presentar las señales esperadas de la misma que sean susceptibles de ser detectadas en el rango energético considerado.

B.1.1 El paradigma de la materia oscura

La existencia de la materia oscura se ve fundamentada por dos hechos observacionales independientes: las curvas de rotación de galaxias y cúmulos de galaxias por una parte, y las lentes gravitacionales por otra.

- Las curvas de rotación de galaxias y cúmulos de galaxias exponen la variación de la velocidad radial de sus miembros constituyentes (estrellas o galaxias respectivamente) en

función de su distancia al centro de gravedad del sistema. Asumiendo una distribución de materia esféricamente simétrica, al igual que la aplicabilidad de la gravitación newtoniana, la dependencia radial de la velocidad de un miembro del sistema dentro de la distribución de materia es $v(r) \propto r$, mientras que la dependencia radial de la velocidad de un miembro alejado de la disribución de materia es $v(r) \propto r^{-1/2}$. Contrariamente a lo esperado, las observaciones indican que la velocidad radial de miembros del sistema alejados de la distribución de materia, lejos de ser inversamente proporcional a la raíz cuadrada de la distancia, toma un valor constante. Este fenómeno, habitualmente conocido como curva de rotación plana, implica la existencia de un componente no visible de materia, que se extiende en un volumen mucho mayor que el formado por la materia visible, que domina la dinámica de los cuerpos visibles más alejados del sistema (véase, por ejemplo, [11]).

- Conforme a la teoría de la Relatividad General, la trayectoria de los fotones sigue las deformaciones del espacio-tiempo producidas por las distribuciones de densidad-energía presentes. Como consecuencia, los objetos masivos pueden actuar como lentes gravitacionales que pueden modificar el flujo aparente y la forma de los objetos astronómicos. La teoría de lentes gravitacionales se ha desarrollado hasta un punto tal que es capaz de reconstruir la distribución de masa que origina la lente gravitacional a partir de las imágenes distorsionadas por dicha lente. Esta reconstrucción es más precisa en el caso de lentes gravitacionales fuertes, es decir, objetos supermasivos como cúmulos de galaxias interpuestos entre una fuente brillante, como un cuásar, y el observador. La masa de cúmulos de galaxias reconstruída a través de este tipo de observaciones es mayor, en factores que llegan a la centena, que la masa visible del sistema completo (véase, por ejemplo, [14]).

El Modelo Cosmológico Estándar es un paradigma cosmológico bien establecido, fruto de más de un siglo de desarrollo de la cosmología teórica, fuertemente soportado por la reciente explosión de la cosmología observacional (véase, por ejemplo, [18]). Dicho modelo está construído sobre los cimientos del principio cosmológico, el cual asume homogeneidad e isotropía en el Universo a gran escala, así como sobre la Relatividad General, la singularidad inicial del Big Bang y la posterior época de inflación. La cosmología observacional, basada en el estudio de la radiación de fondo de microondas, las oscilaciones acústicas de bariones y las observaciones de supernovas de tipo Ia han sido capaces de concretar el Modelo Cosmológico Estándar originando conclusiones sorprendentes: el Universo presenta una geometría espacial global plana, y su contenido de energía-densidad se desglosa como un 4% de materia bariónica, un 23% de materia oscura y un impresionante 73% de energía oscura, componente este último más sorprendente y desconocido si cabe que la propia materia oscura (véase, por ejemplo, [29]).

La materia oscura tiene el papel fundamental de dirigir la formación de estructuras a gran escala en el Universo, puesto que su desacoplo fue anterior al de la materia bariónica, quedando expuesta a la gravedad antes que esta última. El camino libre medio de las partículas de materia oscura caracteriza las escalas mínimas de formación de estructuras. De esta forma, los distintos candidatos a partículas de materia oscura pueden clasificarse como fríos, calientes o templados.

- Materia oscura fría: se dice de la materia oscura cuya velocidad en el momento del desacoplo no era relativista, de forma que su recorrido libre medio suele ser corto, pudiendo amplificar fluctuaciones de densidad a escalas terrestres. Esto puede estar en conflicto con las observaciones, ya que aún no se han detectado fluctuaciones en la distribución de materia oscura a escalas menores que la de las galaxias esferoidales enanas. El neutralino es un típico ejemplo de materia oscura fría.

- Materia oscura caliente: en este caso, la velocidad de las partículas de materia oscura en el momento del desacoplo era relativista, provocando un gran recorrido libre medio, formando primero las estructuras en la escala del Mpc, lo cual parece en contradicción con las observaciones. Los neutrinos estándar se pueden clasifican dentro de este tipo de materia oscura.

- Materia oscura templada: este tipo de materia oscura está a medio camino entre las dos anteriores. Los recorridos libres medios de este tipo de partículas tienen el tamaño típico de galaxias. A escalas mayores se comporta igual que la materia oscura fría, pero a escalas menores genera muchas menos estructuras. Los neutrinos estériles pertenecen a este grupo.

B.1.1.1 Candidatos a partícula de materia oscura

Hay una gran multitud de candidatos a partícula de materia oscura. Muchos de ellos son candidatos *ad hoc*, que emergen de modelos diseñados con el propósito de solucional el problema del constituyente de la materia oscura. Otros candidatos son los llamados *naturales*, que son aquellos surgidos espontáneamente de modelos que atacan otros problemas distintos de la física. En cualquiera de los casos, un candidato a materia oscura ha de cumplir ciertos requisitos [50]: ha de poder reproducir la densidad primordial, ha de ser cosmológicamente estable, no ha de acoplarse directamente al sector electromagnético, ha de poder alimentar la formación de estructuras a gran escala, y ha de preservar la nucleosístesis primordial y la evolución estelar.

Dos ejemplos de candidatos *naturales* bien motivados, considerados a lo largo de este trabajo, son el neutralino y el neutrino estéril.

Neutrino estéril: Los neutrinos estériles son fermiones de interacción débil, contrapartida dextrógira de los neutrinos estándar, originados en extensiones mínimas del Modelo Estándar diseñadas para explicar la masa de los neutrinos estándar [75]. El más ligero de los neutrinos estériles sería cosmológicamente estable si su masa fuera de unos pocos keV, convirtiéndose en un buen candidato a partícula de materia oscura templada [79].

Su desintegración fundamental sería a tres neutrinos estándar, señal actualmente indetectable por la baja energía de los neutrinos producto. El modo secundario de desintegración sería un proceso a dos cuerpos de constante de desintegración [80]:

$$\Gamma_{\nu_s \to \nu\gamma} = \frac{9}{256} \frac{\alpha_{EM} G_F^2}{4\pi^4} \sin^2(\theta) m_{\nu_s}^5, \tag{B.1}$$

donde α_{EM} es la constante de estructura fina, G_F es la constante de Fermi, m_{ν_s} es la masa del neutrino estéril y θ es el ángulo de mezcla. Los fotones originados tendrían energías $E_\gamma = m_{\nu_s}/2$, y la línea se vería ensanchada en función de la velocidad de dispersión de los neutrinos estériles. Por lo tanto, regiones de alta densidad de materia oscura podría generar líneas de rayos X detectables en el rango 0.1–100 keV [79; 81].

Neutralino: El hipotético neutralino es la partícula masiva de interacción débil (WIMP, del inglés *weakly interacting massive particle*) más prometedora y estudiada. Dicha partícula puede emerger en el marco de la teoría de extensión supersimétrica del Modelo Estándar (véase, por ejemplo, [58; 59]). Esta última teoría, que duplica el número de partículas del Modelo Estándar asignando a cada fermión un compañero bosónico supersimétrico y viceversa, fue desarrollada para solucionar el problema de jerarquía [60] y la unificación de los acoplos gauge a muy alta energía [61]. Si a dicha teoría se le impone la conservación de cierta simetría (R-paridad), la

partícula supersimétrica más ligera (LSP, del inglés *lightest supersymmetric particle*) sería estable y ejercería de candidato ideal a partícula de materia oscura fría [62]. En modelos simplificados de supersimetría, como el modelo de mínima supergravedad (mSUGRA, véase [65]), el papel de la LSP lo juega el neutralino en la mayor parte del espacio de parámetros del modelo.

Las partículas supersimétricas de los fermiones del Modelo Estándar producen seis autoestados de masa diferentes como combinaciones lineares de las mismas: dos estados cargados, denominados charginos ($\tilde{\chi}^{+,-}_{1,2}$) y cuatro estados neutros ($\tilde{\chi}^{0}_{1,2,3,4}$), denominados neutralinos. El más ligero de éstos últimos ($\tilde{\chi}^{0}_{1}$ o simplemente χ) recibe el nombre de neutralino por abuso del lenguaje. El neutralino es una superposición lineal del wino ($\tilde{W}$), del bino ($\tilde{B}$) y del los higgsinos neutros ($\tilde{H}^{0}_{1,2}$). El peso que tiene cada cual en la combinación lineal depende del punto del espacio de parámetros de supersimetría.

Los neutralinos son partículas de Majorana, permitiendo pues su aniquilación a partículas del Modelo Estándar y la posibilidad consecuente de poder generar señales detectables. Su sección eficaz de aniquilación ($\langle\sigma_{ann}v\rangle$ en Ec. B.2) depende también del punto del espacio de parámetros del modelo.

B.1.2 Busqueda indirecta de materia oscura mediante astrofísica de altas energías

La búsqueda indirecta de materia oscura se basa en la detección de partículas del Modelo Estándar originadas tras la aniquilación o desintegración de partículas de materia oscura, para la posterior identificación y reconstrucción de propiedades de la misma. Si la masa de la partícula se ubica en el el rango de las altas energías, las técnicas de detección y los posibles fondos de una hipotética señal, serán compartidos con los de la astrofísica de altas energías. Este trabajo se centra en la búsqueda indirecta de materia oscura en fuentes individuales, a través de fotones como partículas mensajeras, principalmente rayos γ de alta y muy alta energía y en un menor grado rayos X. Convencionalmente, los rayos γ de alta energía se consideran aquellos cuyas energías están entre los 100 MeV y los 100 GeV, mientras que los rayos γ de muy alta energía son aquellos cuya energía supera los 100 GeV.

B.1.2.1 Flujos esperados por aniquilación o desintegración de materia oscura

El flujo diferencial de fotones producido por aniquilación o desintegración de materia oscura, medido por un determinado detector, depende de la distribución de densidad de materia oscura en la fuente, pero también de las características instrumentales del detector, principalmente su resolución energética y angular.

Aniquilación de materia oscura: El flujo integral producido por aniquilación de materia oscura sobre una determinada energía umbral E_0, puede describirse como el producto de dos términos, a saber, el factor de física de partículas $\Phi^{PP}(> E_0)$ y el factor astrofísico $J_{ann}(\Delta\Omega)$:

$$\begin{aligned}\Phi_{DM}(> E_0, \Delta\Omega) &= \Phi^{PP}(> E_0) \times J_{ann}(\Delta\Omega) \\ &= \frac{1}{4\pi}\frac{\langle\sigma_{ann}v\rangle}{2m^2_{DM}}\int_{E_0}^{m_{DM}}\sum_{i=1}^{n} B^i\frac{dN^i_\gamma}{dE}dE \times \int_{\Delta\Omega}\int_{los}\rho^2_{DM}(r(s,\Omega))dsd\Omega,\end{aligned} \tag{B.2}$$

donde $\langle\sigma_{ann}v\rangle$ es la sección eficaz de aniquilación, m_{DM} es la masa de la partícula de materia oscura y $\sum_{i=1}^{n} B^i dN^i_\gamma/dE = dN_\gamma/dE$ es la suma sobre todos los n posibles canales de aniquilación

generando fotones (B^i es la contribución individual de cada canal, de forma que $\sum_{i=1}^{n} B^i = 1$). En este caso, el factor astrofísico resulta de la integración del cuadrado de la densidad de materia oscura a lo largo de la línea de visión.

En caso de que se realice una observación en la cual se espere la detección del flujo descrito anteriormente, pero no se produzca, se pueden calcular límites superiores al mismo aplicando la siguiente expresión:

$$\Phi_{DM}^{UL}(> E_0) = \frac{N^{UL}(> E_0)}{T_{obs} \int_0^\infty \phi_{DM}(E) A_{eff}(E) dE} \int_{E_0}^{\infty} \phi_{DM}(E) dE, \tag{B.3}$$

donde ϕ_{DM} es la forma diferencial de la Ec. B.2, $N^{UL}(> E_0)$[1] es el límite superior a los sucesos de exceso, T_{obs} es el tiempo de observación, E_0 es la energía umbral de análisis y $A_{eff}(E)$ es el área efectiva de análisis. De esta forma, se pueden imponer límites a la sección eficaz de aniquilación una vez conocidos los flujos esperados y los límites observados del mismo:

$$\langle \sigma_{\rm ann} v \rangle^{UL} = \frac{4\pi 2 m_{DM}^2 \Phi^{UL}(> E_0)}{J(\Delta\Omega)_{ann} \int_{E_0}^{m_{DM}} \sum_{i=1}^{n} B^i \frac{dN_\gamma^i}{dE} dE}. \tag{B.4}$$

Desintegración de materia oscura: Este escenario es especialmente interesante cuando la aniquilación se produce a dos cuerpos y una línea espectral puede producirse. El flujo de dicha línea puede describirse como el producto de dos factores:

$$\Phi(\Delta\Omega) = \Gamma \times J_{dec}(\Delta\Omega) = \Gamma \times \int_{\Delta\Omega} \int_{los} \rho_{DM}(r(s,\Omega)) ds d\Omega, \tag{B.5}$$

donde Γ es el ritmo de desintegración, en el cual reside codificada la información correspondiente a la física de la partícula de materia oscura y es universal para todas las fuentes. $J_{dec}(\Delta\Omega)$ es el factor astrofísico, el cual incluye la contribución astrofísica particular de cada fuente y que consiste en la integración de la densidad de materia oscura de la fuente a lo largo de la línea de visión.

Análogamente al caso de aniquilación de materia oscura, si no hay detección de ninguna línea de emisión, sino un límite superior al flujo de la misma, se puede limitar a su vez el ritmo de desintegración de la forma:

$$\Gamma^{UL} = \frac{\Phi^{UL}}{\int_{\Delta\Omega} \int_{los} \rho_{DM}(r(s,\Omega)) ds d\Omega}. \tag{B.6}$$

Para tener en cuenta las características del detector, el ritmo de desintegración Γ en la Ec. B.5 y el término de física de partículas Φ^{PP} en la Ec. B.2, han de ser convolucionados con la función de resolución energética correspondiente. De la misma forma, la distribución de densidad de materia oscura ha de ser convolucionada con la función de resolución angular en ambas Ecs. B.5 y B.2. Estas dependencias afectan consecuentemente a los límites que se puedan llegar a imponer sobre el ritmo de desintegración (Ec. B.6) o la sección eficaz de aniquilación (Ec. B.4).

[1] A lo largo de este trabajo, el límite superior a los sucesos de exceso $N^{UL}(> E_0)$ ha sido siempre obtenido utilizando el método de Rolke et al. [308] considerando un nivel de confianza del 95%.

B.1.2.2 Breve descripción de los detectores

Las búsquedas de neutralinos o, más generalmente WIMPs, se realizan en el rango energético de rayos γ de alta y muy alta energía, por lo que los telescopios Cherenkov y los telescopios de rayos γ a bordo de satélites son los instrumentos más adecuados. Las búsquedas de neutrinos estériles se producen en el rango de rayos X, por lo que los telescopios de rayos X a bordo de satélites son los instrumentos más indicados. A continuación se desciben brevemente los instrumentos utilizados en las distintas búsquedas que conforman este trabajo.

Los telescopios MAGIC: Los telescopios MAGIC [248] son un sistema de dos telescopios IACT (del inglés *imaging atmospheric Cherenkov technique*, técnica Cherenkov de imagen atmosférica), ubicados en el Observatorio del Roque de los Muchachos, en la isla canaria de La Palma, cuyos reflectores de 17 metros de diámetro les hacen los más grandes telescopios IACTs hasta la fecha. Su técnica de detección se basa en obtener imágenes de las cascadas electromagnéticas producidas por los rayos γ cuando penetran en la atmósfera. En dichas cascadas electromagnéticas se produce emisión de fotones Cherenkov, puesto que las partículas que forman la cascada (pares electrón-positrón) viajan más rápido que la velocidad de la luz en el medio. La reconstrucción de la imagen de la cascada permite obtener información acerca del rayo γ primario, básicamente su energía y dirección de llegada. Esta técnica permite, en el caso de MAGIC, un umbral inferior de energía de pocas decenas de GeV y superior de pocas decenas de TeV, aportando un gran área efectiva de detección ($\sim 10^5$ m^2). Su principal fondo son las cascadas atmosféricas iniciadas por rayos cósmicos, principalmente protones, cuyos fotones Cherenkov también forman imágenes en las cámaras de los telecopios. Estas cascadas denominadas hadrónicas, tienen una incidencia 10^4 veces superior a la de los rayos γ de muy alta energía. Dicho fondo es reducido posteriormente vía análisis.

El satélite Fermi-GST: El satélite Fermi-GST [246] (del inglés *Gamma-ray Space Telescope*, telescopio espacial de rayos γ) lleva dos instrumentos científicos a bordo, el monitor de GRBs (Fermi-GBM) y el telescopio de gran área (Fermi-LAT [257]). Éste último consiste en un telescopio de producción de pares, donde los rayos γ incidentes son convertidos en un par electrón-positrón, de cuyas trazas se reconstruye la posición de llegada del rayo γ, y que acaban depositando su energía en un calorímetro de centelleo, de donde se reconstruye la energía del rayo γ. Fermi-LAT es sensible a rayos γ de alta energía, desde 30 MeV hasta 300 GeV, aunque su área efectiva limitada ($\sim$1 m^2) reduce dramáticamente su sensibilidad por encima de los 100 GeV.

El satélite Chandra-XRO: El satélite Chandra-XRO [311] (del inglés, *X-Ray Observatory*, observatorio de rayos X) es, junto con el satélite XMM-Newton [312] el instrumento para la exploración astrofísica en rayos X más sensible actualmente. Está provisto de una capacidad de imagen con una resolución posicional mejor que el segundo de arco y espectroscopía de alta resolución en el rango desde 0.08 keV a 10 keV. Consiste en un sistema de espejos de alta resolución (HRMA) que focaliza los rayos X en un módulo de instrumentos científicos. En dicho módulo se ubica una cámara de alta resolución (HRC) y un espectrómetro avanzado de imagen CCD (ACIS).

B.2 Búsqueda de materia oscura en galaxias esferoidales enanas

En el marco de la teoría de formación jerárquica de estructuras en el Universo, las galaxias esferoidales enanas se proponen como subestructuras de los halos galácticos de materia oscura [170; 315]. Las galaxias esferoidales enanas satélites de la Vía Láctea son objetivos muy prometedores para la búsqueda indirecta de materia oscura por varias razones:

- La dinámica de las estrellas que conforman estos objetos permiten inferir su contenido de materia oscura, mostrando a estos objetos como los sistemas astrofísicos más dominados por la materia oscura en el Universo [13].
- Debido a su gran cociente masa-luz y sus grandes radios de luminosidad media $r_{1/2}$, no se espera que la materia bariónica influya significativamente en la distribución de materia oscura.
- No se esperan grandes emisores de rayos γ ni de rayos X entre la población de objetos que conforman este tipo de galaxias. Por lo tanto, un fondo astrofísico convencional que pudiera ocultar una posible señal de materia oscura no es esperado [2; 325]. Además, la mayoría de galaxias esferoidales enanas presentan altas latitudes galácticas, donde una posible contaminación del fondo galáctico es muy reducida.
- Son objetos bien localizados y relativamente cercanos, muchas de ellas a distancias menores que 100 kpc, lo que hace que pese a sus flujos intrínsicos bajos el flujo esperado en la posición del observador sea el mayor comparado con el resto de posibles objetos conocidos para búsquedas indirectas (exceptuando el Centro Galáctico) [175].

Hasta la fecha se han producido múltiples observaciones de estos objetos en la banda de rayos γ de alta y muy alta energía en busca de materia oscura (en la figura de WIMPs de masas en el rango GeV-TeV) por parte de los telescopios Whipple [272], MAGIC [1; 3; 326], HESS [328; 329], VERITAS [327] y Fermi-LAT [268].

Al igual, varias observaciones en rayos X de estos objetos se han producido en busca de materia oscura en el rango keV. Estas observaciones han sido llevadas a cabo por los telescopios Chandra-XRO [2; 86; 330], XMM-Newton [83; 84] y Swift [85].

Para este trabajo se han utilizado observaciones de dos galaxias esferoidales enanas: Willman 1, incluyendo datos de MAGIC-I y Chandra-XRO, y Segue 1, considerando datos de MAGIC-I.

Willman 1 Willman 1 fue un descubrimiento del año 2005, surgido de los datos de medicin digital de cielo (SDSS, acrónimo del inglés *Sloan Digital Sky Survey*, véase [40]) como una débil sobredensidad de estrellas en la banda R [319], a una distancia de 38 kpc en dirección a la constelación de Ursa Major. Gracias a observaciones posteriores del telescopio Keck II [417] se pudo inferir su cociente masa-luminosidad, que con un valor de $\sim 700 M_{\odot}/L_{\odot}$ [331] fue durante un tiempo el objeto conocido más dominado por la materia oscura y el mejor candidato para búsquedas indirectas de materia oscura [13; 334]. Su naturaleza ha estado sujeta a debate. Se ha sugerido que Willman 1 pudiera ser un cúmulo estelar [335]. Los últimos datos espectroscópicos de sus estrellas miembro indican que Willman 1 es, con alta probabilidad, una galaxia esferoidal enana, pero con posibilidades de que su estructura interna haya sido afectada por fuerzas de marea y que no esté en equilibrio dinámico [332]. Datos más precisos y un aumento de la población de estrellas miembro de Willman 1 serán necesarios para una mejor caracterización dinámica del objeto.

Segue 1 En el año 2009, y a partir de los datos de la extensión del programa SDSS para la exploración y entendimiento galácticos (SEGUE, acrónimo del inglés *SDSS Extension for Galactic Understanding and Exploration*, véase [336]) y una posterior observación del telescopio Subaru [337], el objeto denominado Segue 1 fue descubierto e inicialmente clasificado como un cúmulo estelar [321]. Segue 1 se ubica a 23 kpc de distancia en dirección a la corriente de Sagitario, lo que hace muy complicado la identificación de sus estrellas miembro del fondo de estrellas de la corriente. La naturaleza de Segue 1 ha sido materia de gran debate y controversia [321; 338; 339; 340], puesto que sus principales características están ubicadas en la frontera entre cúmulos globulares y galaxias esferoidales enanas. Observaciones más profundas del telescopio Keck II aumentaron la población de estrellas miembro identificadas de 24 a 71, mejorando a su vez los datos cinemáticos de las mismas. Como principal conclusión de esta nueva observación Segue 1 fue finalmente clasificado como una galaxia esferoidal enana ultra ténue, atribuyéndo a su vez el título de objeto más dominado por materia oscura del Universo, con un cociente masa-luminosidad estimado en 3400 $M_\odot/L_\odot$ [341; 342], y no superado hasta la fecha. Este elevado valor del cociente masa-luminosidad presenta grandes incertidumbres que deberán de ser reducidas mediante futuras observaciones más profundas del objeto.

B.2.1 Búsqueda de materia oscura en Willman 1 con MAGIC

Willman 1 fue observada por MAGIC-I entre enero y marzo de 2008, por un tiempo total de 15.5 horas de datos de buena calidad. No hubo detección de señal de rayos γ por encima de una energía umbral de análisis de 100 GeV.

La falta de señal permitió el cálculo de límites superiores al flujo, los cuales consideraron tanto espectros descritos por leyes de potencia como espectros particulares de modelos de emisión por aniquilación de materia oscura. Los límites al flujo integral basados en leyes de potencias resultaron del orden de 10^{-12} cm^{-2}s^{-1}, variando desde un 2% a un 10% en unidades del flujo integrado de la Nebulosa del Cangrejo (C.U.), dependiendo del umbral de energía de análisis. Los límites correspondientes al flujo diferencial pueden ser encontrados en la Tabla B.1 y están ilustrados en la Fig. B.1.

Tabla B.1: Límites de MAGIC al flujo diferencial de Willman 1.

ΔE [TeV]	$N_{\rm ON}$	$N_{\rm OFF}$	$\sigma_{\rm Li,Ma}$ 95% C.L.	N_{exc}^{UL}	$d\Phi^{UL}/dE$ [TeV^{-1}cm^{-2}s^{-1}]				
					$\Gamma=-1.0$	$\Gamma=-1.5$	$\Gamma=-2.0$	$\Gamma=-2.5$	$\Gamma=-3.0$
0.1, 0.32	53167	53555	-1.2	639.2	1.4×10^{-10}	1.5×10^{-10}	1.7×10^{-10}	2.1×10^{-10}	2.7×10^{-10}
0.32, 1	703	645	1.6	192	1.0×10^{-11}	1.1×10^{-11}	1.2×10^{-11}	1.4×10^{-11}	1.7×10^{-11}
1, 3.2	105	114	-0.6	26	6.0×10^{-13}	6.2×10^{-13}	6.8×10^{-13}	8.0×10^{-13}	1.0×10^{-12}
3.2, 10	8	8	0.0	10	7.1×10^{-14}	7.4×10^{-14}	8.1×10^{-14}	9.3×10^{-14}	1.1×10^{-13}

Límites de MAGIC al flujo diferencial de Willman 1, a un nivel de confianza del 95% en unidades de TeV^{-1}cm^{-2}s^{-1}. Se han asumido cuatro leyes de potencia diferentes para el cálculo de los límites, así como cuatro intervalos de energía distintos.

Los límites al flujo integral calculados para espectros diferenciales de emisión originada por aniquilación de materia oscura se basan en modelos representativos de cuatro regiones del espacio de parámetros de mSUGRA [346], denominadas regiones *bulk, focus point, funnel,* y de coaniquilación (denotadas por I', F_*, K' y J' respectivamente). A partir del factor de física de partículas Φ^{PP} correspondiente a cada uno de los modelos anteriores, y el factor astrofísico

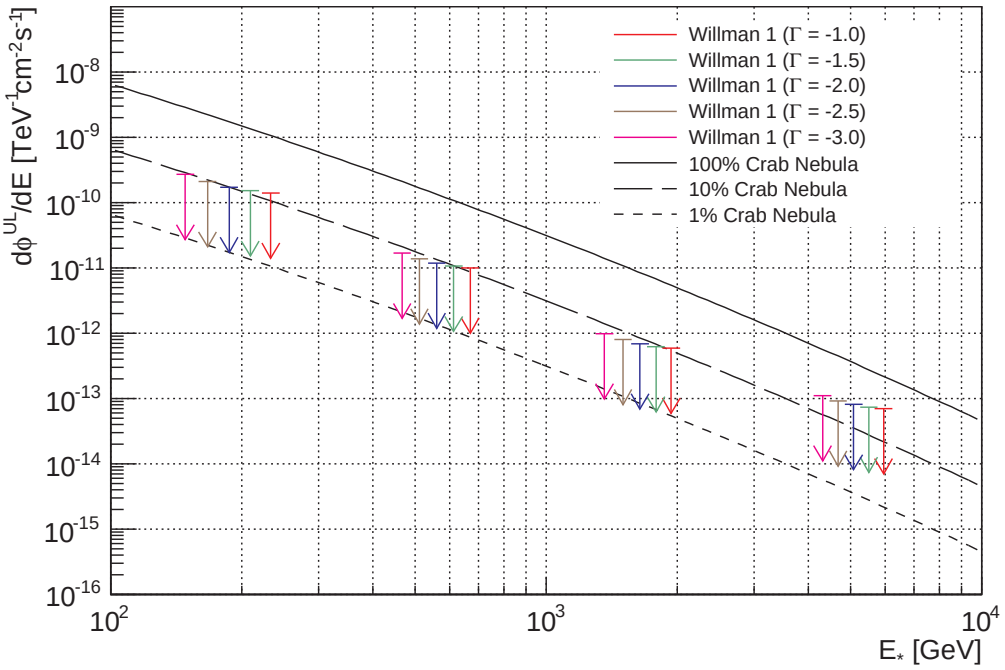

Figura B.1: Límites al flujo diferencial de Willman 1 a partir de datos de MAGIC. Los valores concretos pueden verse en la Tabla 3.4. El espectro diferencial de la Nebulosa del Cangrejo observado por MAGIC [344] es mostrado como referencia (línea sólida al 100%, línea discontinua ancha al 10%, línea discontinua estrecha al 1%).

de Willman 1, calculado siguiendo las parametrización extraída de [13], se obtuvieron los flujos integrales esperados $\Phi^{est}(E > 100\ GeV) = J(\Delta\Omega)\Phi^{PP}(E > 100\ GeV)$ para cada modelo representativo. A partir de los datos y los espectros esperados de cada modelo se calcularon los límites al flujo integral de cada modelo representativo aplicando la Ec. B.3. Finalmente, se calcularon los factores de aumento mínimos necesarios para que el flujo esperado alcanzara los límites observacionales en cada uno de los casos. Los valores del flujo esperado Φ^{est}, el límite observacional al flujo Φ^{ul} y el factor de aumento mínimo B_F para cada modelo representativo se pueden encontrar en la Tabla B.2.

B.2.1.1 Conclusiones

Atendiendo a los factores de aumento mínimo obtenidos, se ve claramente que la región *funnel* (modelo K') produce una menor distancia entre el flujo teórico estimado y el límite observacional ($B_F = 2.6 \times 10^3$). Las regiones *bulk* y *focus point* (I' y F^* respectivamente) producen similares factores de aumento mínimo, mientras que la región de coaniquilación es la que mayor distancia presenta entre el flujo teórico estimado y el límite observacional ($B_F = 1.3 \times 10^5$), básicamente debido a la baja sección eficaz de aniquilación característica de esta región.

Es importante recalcar que los resultados aquí obtenidos se aplican a puntos representativos del espacio de parámetros de mSUGRA, no al modelo en su totalidad. Para una mayor generalización de los resultados sería necesario un barrido del espacio de parámetros que explorara éste en mayor profundidad. Por otra parte, la estimación del flujo teórico adolece de una gran

Tabla B.2: Límites a los factores de aumento para flujos esperados en Willman 1.

	$\Phi^{est}(E > 100$ GeV) $[\mathrm{cm}^{-2}\mathrm{s}^{-1}]$	$\Phi^{ul}(E > 100$ GeV) $[\mathrm{cm}^{-2}\mathrm{s}^{-1}]$	B_F
I'	2.64×10^{-16}	9.87×10^{-12}	3.7×10^4
J'	4.29×10^{-17}	5.69×10^{-12}	1.3×10^5
K'	2.32×10^{-15}	6.83×10^{-12}	2.9×10^3
F^*	2.09×10^{-16}	7.13×10^{-12}	3.4×10^4

Comparación entre flujos integrales estimados Φ^{est} sobre 100 GeV para los distintos modelos de materia oscura considerados y el límite al flujo integral Φ^{ul} sobre 100 GeV impuesto por las observaciones de Willman 1 por MAGIC. También se muestra el límite a los factores de aumento necesarios para igualar ambos flujos B_F.

incertidumbre proveniente del cálculo del factor astrofísico de Willman 1. Esta incertidumbre tiene origen en el modelado de la distribución de densidad de materia oscura de Willman 1. Dicho modelado es obtenido a partir de un ajuste al potencial gravitatorio del sistema, que es a su vez determinado por estudios de la dinámica estelar de la galaxia esferoidal enana. En el caso de Willman 1 tan sólo se dispone de datos dinámicos de 45 estrellas miembro (por ejemplo, la galaxia esferoidal enana Draco posee más de mil estrellas miembro detectadas y sus correspondientes datos dinámicos). Aparte, hay que tener en cuenta la posibilidad de que el sistema no esté en completo equilibrio dinámico, lo cual afectaría al método de obtención del factor astrofísico, que es aplicable bajo el supuesto de sistemas en equilibrio. Por lo tanto, observaciones más profundas en el rango óptico son necesarias para aclarar el estado real de Willman 1, así como para incrementar la población de sus estrellas miembro.

Los resultados aquí presentados fueron publicados en la revista científica internacional Astrophysical Journal [1].

B.2.2 Búsqueda de materia oscura en Willman 1 con Chandra-XRO

El observatorio espacial de rayos X Chandra observó la galaxia esferoidal enana Willman 1 durante enero de 2010. Las observaciones se realizaron con el espectrómetro avanzado de imagen ACIS. El tiempo de observación tras rechazar periodos de tiempo de mala calidad fue de 100.68 ks. Se realizaron dos análisis complementarios y enfocados en la región central de Willman 1, correspondiente a un área circular de radio $5'$ centrada en la posición nominal de la galaxia esferoidal enana. Dicha región, considerando una distacia a Willman 1 de 38 kpc, se traduce en un área de radio 55 pc, superior al radio de luminosidad media $r_{1/2}$ del objeto. Sendos análisis corresponden a un análisis de fuentes puntuales y a un análisis de la componente difusa.

El análisis de fuentes puntuales tiene como objeto estudiar las posibles fuentes astrofísicas de alta energía presentes en la región central de Willman 1 y que formen parte de sistema. Este estudio es de especial importancia para verificar que las galaxias esferoidales enanas, ejemplificadas en el presente objeto, son objetos libres de fuentes astrofísicas convencionales que pudieran generar emisión de alta energía y que, eventualmente, pudieran ser un fondo irreducible para una posible señal originada por desintegración o aniquilación de materia oscura. 26 fuentes puntuales fueron detectadas en el rango de energías de 0.5 keV a 6.0 keV, de las cuales 10 coinciden posicionalmente con objetos en el catálogo óptico SDSS DR7 [356]: 4 cuásares, 3 galaxias de otro tipo y 3 estrellas. El número de fuentes puntuales no difiere significativamente del número de AGNs de fondo que se esperan para una observación de esta profundidad, que

asciende a 24 ± 3 AGNs de fondo para una región del tamaño de la estudiada [359]. El diagrama color-magnitud también fue obtenido, no identificándose claramente ningún sistema binario que pudiese pertenecer a Willman 1. Cuando la estadística de fotones fue suficiente, se obtuvieron los espectros, todos ellos compatibles con los esperados para una población de AGNs. También se calculó la probabilidad de presencia de sistemas binarios de rayos X siguiendo el método desarrollado en [365], siendo ésta despreciable para el límite de luminosidad de la observación.

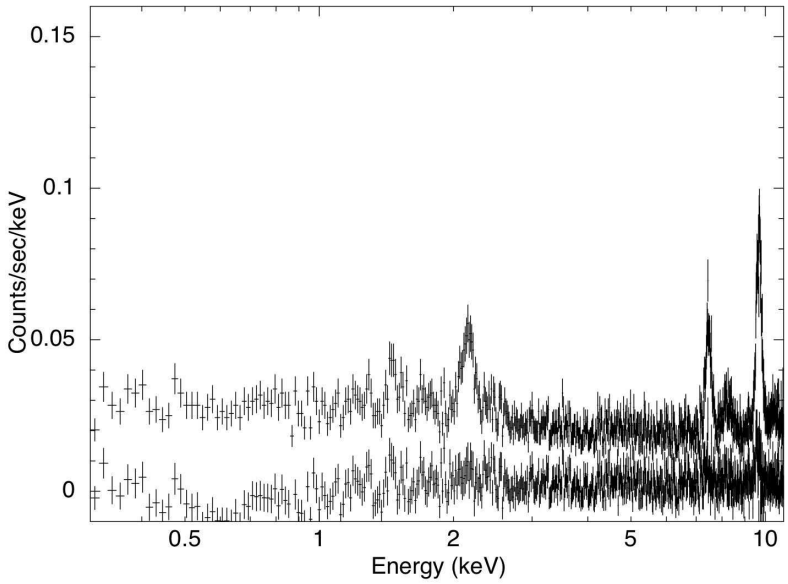

Figura B.2: Espectro de los datos del detector ACIS-I de Chandra extraído de una región circular de radio $5'$ centrada en Willman 1. *Arriba:* datos anteriores a la extracción del fondo. La aparición de líneas instrumentales, incluyendo las originadas por Si K α (1.74 keV), Au M α, β (2.1–2.2 keV), Ni K α (7.47 keV) y Au L α (9.67 keV), es manifiesta. *A*bajo: Espectro tras la extracción del fondo.

La componente difusa de rayos X provenientes de Willman 1 puede estar dominada por una población de fuentes no resueltas o por algún componente gaseoso complejo [349]. Sin embargo, también pudiera ser que hubiera cierta contribución por parte de líneas de desintegración de neutrinos estériles si los mismos fueran el principal ingrediente de la materia oscura. De cara a analizar la componente difusa de esta observación se extrajeron todas las fuentes resueltas dentro del área de estudio. Para la obtención del espectro difuso, el fondo fue substraído siguiendo los métodos estándar para el análisis de datos de Chandra-XRT [350]. Antes de la substracción del fondo, el espectro se ve dominado por líneas instrumentales como las líneas de transición Si K α (1.74 keV), Au M α, β (2.1–2.2 keV), Ni K α (7.47 keV), y Au L α (9.67 keV). Dichas líneas instrumentales se ven muy reducidas tras la substracción del fondo, como puede verse en la Fig. B.2. Al no existir ninguna línea no instrumental manifiesta, se calcularon límites a la posible emisión de líneas de desintegración de neutrino estéril siguiendo los procedimientos habituales para este tipo de cálculos (véase, por ejemplo, [351; 352]). A partir de dichos límites se pudo restringir el espacio de parámetros de neutrino estéril para masas 1.6 keV $< m_\nu <$ 16.0 keV en función del ángulo de mezcla θ, teniendo en cuenta las Ec. B.6 y B.1. Dichas restricciones se ven ilustradas en la Fig. B.3.

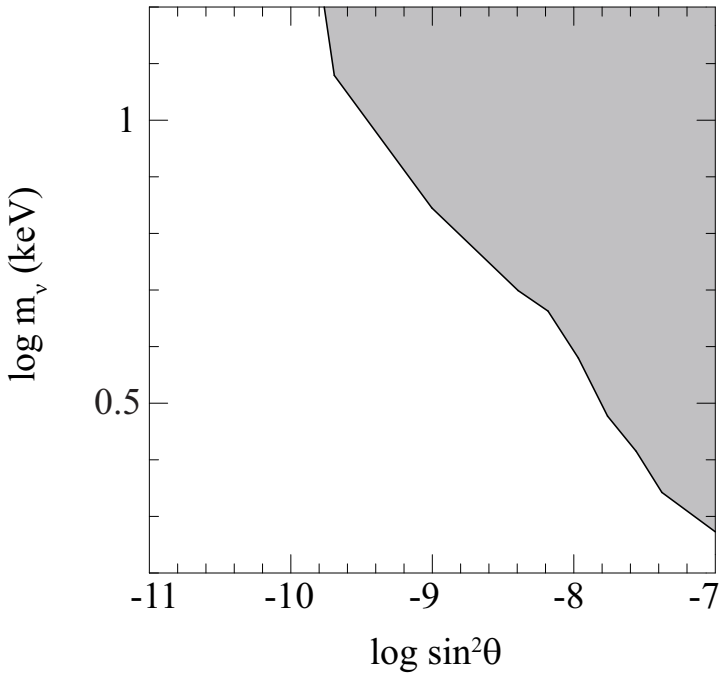

Figura B.3: Restriciones al espacio de parámetros del neutrino estéril a partir de las observaciones de Chandra sobre Willman 1. La región superior derecha quedaría excluída por estas observaciones.

Un análisis previo de este mismo conjunto de datos, condujo al presunto descubrimiento de una línea exótica compatible con una línea de emisión generada por la desintegración de neutrinos estériles de masa $m_\nu \approx 5$ keV [86]. Sin embargo, el análisis presentado en este trabajo no fue capaz de obtener la misma conclusión. De hecho, una inspección cuidadosa del espectro tras las substracción del fondo muestra residuos de líneas espectrales en las cercanías de la energía correspondiente a una deficiente extracción de líneas instrumentales (Au M α, β) en las cercanías de la supuesta línea exótica, ubicada en ~ 2.5 keV. A parte de ello, la condición exótica de la supuesta línea podría tener una explicación convencional, puesto que es coincidente con la línea de transición del azufre completamente ionizado S XV α, ubicada en 2.45 keV y detectada rutinariamente en plasmas calientes [354; 355].

B.2.2.1 Conclusiones

El análisis de la componente difusa de la observación de Willman 1 llevada a cabo por Chandra-XRO no ha encontrado ninguna línea de emisión evidente que no pudiera ser atribuída a las líneas experimentales características del instrumento, en contraposición a análisis anteriores donde se anunciaba la detección de una línea exótica atribuída presuntamente a desintegración de neutrinos estériles [86]. Los límites superiores al flujo de líneas espectrales no instrumentales han permitido restringir el espacio de parámetros del neutrino estéril, asumiendo esta partícula como el componente fundamental de la materia oscura en el Universo. Debido a la dificultad de mejorar los actuales límites con la instrumentación disponible actualmente [81], sería interesante estudiar las perspectivas de detección de neutrinos estériles con las próximas generaciones de telescopios espaciales de rayos X [366]. Se ha mostrado que cualquier búsqueda de líneas exóticas en este rango energético ha de tener en cuenta la superposición de las líneas instrumentales, a la vez que la posible contaminación de líneas de emisión de plasmas que pudieran emular una

señal de desintegración de materia oscura.

Adoptando una distancia estimada de 38 kpc, y teniendo en cuenta el límite de luminosidad obtenido por esta observación de 10^{32} erg s^{-1} en la banda de energía de 0.5–2.0 keV, pudiera ser que la mayoría de fuentes puntuales de rayos X pertenecientes al sistema emitiesen por debajo de dicha luminosidad. Sin embargo, el ritmo de encuentros calculado indica una probabilidad muy baja de formación de sistemas binarios en Willman 1. Los resultados del diagrama color-magnitud y los espectros obtenidos para las fuentes con estadística suficiente para poder haber sido analizadas también rechazan que parte significantiva de la población de fuentes puntuales sean sistemas binarios de rayos X pertenecientes a Willman 1. De hecho, la totalidad de fuentes podría ser atribuída al fondo de AGNs.

Los resultados presentandos han sido hechos públicos a la comunidad científica internacional [2].

B.2.3 Búsqueda de materia oscura en Segue 1 con MAGIC

La galaxia esferoidal enana Segue 1 ha sido observada por MAGIC-I entre noviembre de 2008 y marzo de 2009. El tiempo de observación total acumulado asciende a 43.2 horas, de las cuales 29.4 horas pasaron los criterios de calidad impuestos. No se detectó ningún exceso de rayos γ de muy alta energía, proveniente de la posición nominal de la fuente, en el rango energético de sensibilidad de MAGIC-I, situándose el umbral de energía de esta observación en 100 GeV.

Dada la falta de señal, se calcularon límites al flujo integral y diferencial de la fuente considerando el caso genérico de una emisión descrita por una ley de potencia (considerándose distintos índices espectrales). Los resultados quedan resumidos en la Tabla B.3 e ilustrados en la Fig. B.4 para el caso de los límites integrales, y en la Tabla B.4 y Fig. B.5 para el caso de los límites al flujo diferencial. Los resultados son compatibles con los publicados para otras galaxias esferoidales enanas observadas anteriormente por IACTs.

Tabla B.3: Límites de MAGIC al flujo integral de Segue 1.

E_0 [GeV]	N_{ON}	N_{OFF}	N_{exc}^{UL} 95% C.L.	$\sigma_{\mathrm{Li,Ma}}$	Φ^{UL} $\times 10^{-12}[\mathrm{cm}^{-2}\mathrm{s}^{-1}]$					
					$\Gamma=-1.0$	$\Gamma=-1.5$	$\Gamma=-1.8$	$\Gamma=-2.0$	$\Gamma=-2.2$	$\Gamma=-2.4$
100	52978	53301	453	-0.99	7.5 (1.4)	8.8 (1.6)	10.5 (2.0)	11.6 (2.2)	12.7 (2.4)	13.7 (2.5)
126	18835	19233	174	-2.04	2.8 (0.7)	3.2 (0.8)	3.6 (0.9)	4.0 (1.0)	4.3 (1.1)	4.6 (1.1)
158	6122	6374	93	-2.25	1.5 (0.5)	1.6 (0.5)	1.8 (0.6)	1.9 (0.6)	2.0 (0.7)	2.1 (0.7)
200	3012	3088	110	-0.97	1.7 (0.8)	1.7 (0.8)	1.9 (0.9)	2.0 (0.9)	2.1 (1.0)	2.2 (1.0)
251	1687	1654	194	0.57	2.9 (1.8)	3.0 (1.9)	3.1 (1.9)	3.2 (2.0)	3.4 (2.1)	3.5 (2.2)
316	1107	1030	250	1.67	3.6 (3.1)	3.7 (3.2)	3.8 (3.3)	3.9 (3.4)	3.9 (3.4)	4.1 (3.6)
398	792	761	147	0.79	2.0 (2.5)	2.0 (2.5)	2.1 (2.6)	2.1 (2.6)	2.2 (2.7)	2.2 (2.7)
501	613	580	140	0.96	1.9 (3.3)	1.9 (3.3)	1.9 (3.3)	1.9 (3.3)	2.0 (3.5)	2.0 (3.5)
631	536	509	124	0.84	1.5 (3.7)	1.5 (3.7)	1.6 (4.0)	1.6 (4.0)	1.6 (4.0)	1.6 (4.0)
794	486	445	146	1.34	1.7 (6.2)	1.8 (6.6)	1.8 (6.6)	1.8 (6.6)	1.8 (6.6)	1.8 (6.6)
1000	411	373	135	1.36	1.6 (8.6)	1.6 (8.6)	1.6 (8.6)	1.6 (8.6)	1.6 (8.6)	1.6 (8.6)

Límites de MAGIC al flujo integral de Segue 1, a un nivel de confianza del 95% en unidades de $10^{-12}\mathrm{cm}^{-2}\mathrm{s}^{-1}$ para seis índices espectrales y diferentes energías umbral de análisis E_0. Los números entre paréntesis indican los límites superiores en porcentaje de unidades de la Nebulosa del Cangrejo [344] sobre la misma energía umbral de análisis.

En el contexto de búsqueda indirecta de materia oscura, se calcularon límites a la sección eficaz de aniquilación del neutralino para un gran número de modelos de mSUGRA. Dichos modelos fueron obtenidos tras simulaciones extensivas que barrieron la región de interes para los

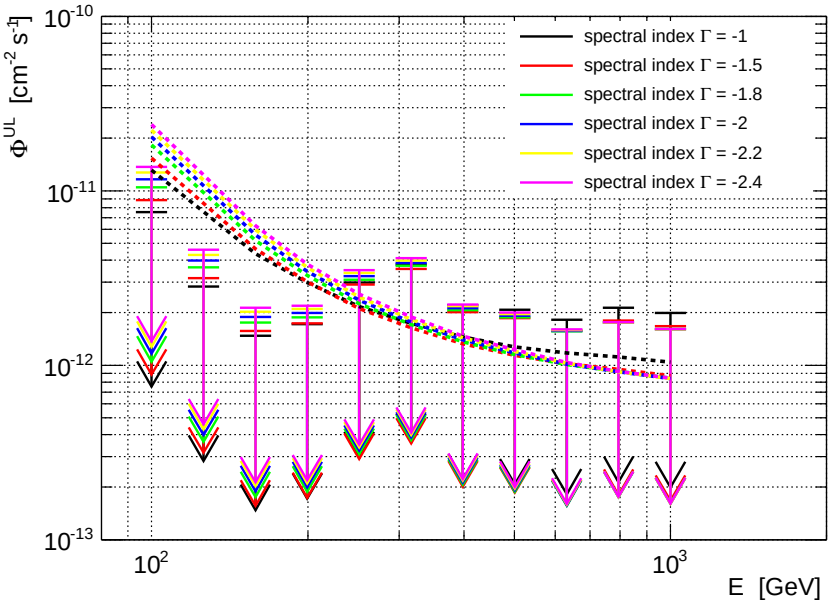

Figura B.4: Límites al flujo integral de Segue 1 a partir de datos de MAGIC, para cuatro índices espectrales distintos y diferentes energías umbral de análisis. Los valores concretos pueden verse en la Tabla B.3. Las líneas discontinuas indican los límites integrales al flujo si se asume una significancia de detección $\sigma_{\mathrm{Li,Ma}} = 0$, ilustrando los efectos de las fluctuaciones de la significancia observada sobre los mismos.

Tabla B.4: Límites de MAGIC al flujo diferencial de Segue 1.

ΔE [TeV]	N_{ON}	N_{OFF}	N_{exc}^{UL} 95% C.L.	$\sigma_{\mathrm{Li,Ma}}$	$d\Phi^{UL}/dE$ [TeV^{-1}cm^{-2}s^{-1}]					
					$\Gamma = -1.0$	$\Gamma = -1.5$	$\Gamma = -1.8$	$\Gamma = -2.0$	$\Gamma = -2.2$	$\Gamma = -2.4$
0.1, 0.32	51871	52271	399	-1.2	4.9×10^{-11}	5.2×10^{-11}	5.5×10^{-11}	5.8×10^{-11}	6.1×10^{-11}	6.5×10^{-11}
0.32, 1	696	657	156	1.1	3.3×10^{-12}	3.4×10^{-12}	3.6×10^{-12}	3.8×10^{-12}	4.0×10^{-12}	4.2×10^{-12}
1, 3.2	99	77	72	1.7	3.5×10^{-13}	3.7×10^{-13}	3.9×10^{-13}	4.0×10^{-13}	4.2×10^{-13}	4.5×10^{-13}
3.2, 10	69	57	48	1.1	5.7×10^{-14}	6.0×10^{-14}	6.4×10^{-14}	6.6×10^{-14}	7.0×10^{-14}	7.4×10^{-14}

Límites de MAGIC al flujo diferencial de Segue 1, a un nivel de confianza del 95% en unidades de TeV^{-1}cm^{-2}s^{-1}. Se han asumido seis leyes de potencia diferentes para el cálculo de los límites, así como seis intervalos de energía distintos.

IACTs del espacio de parámetros de mSUGRA. Se simularon más de 5×10^6 puntos del espacio de parámetros en un barrido descrito en la Tabla B.2.3.

Para cada punto uno de los modelos generados que satisfaciera las restricciones experimentales (modelos físicos), se calculó su límite individual a la sección eficaz de aniquilación, teniendo en cuenta su propio espectro diferencial de aniquilación ($\phi(E)_{DM}$ en Ec. B.3). De esta manera, para cada punto considerado del espacio de parámetros de mSUGRA, se tiene en cuenta su forma espectral individual a la hora de limitar la sección eficaz de aniquilación. Este tratamiento de los datos es totalmente novedoso dentro del campo de investigación particular. Los resultados de este planteamiento muestran la clara dependencia de los límites con el espectro, poniendo de manifiesto que no es conveniente expresar dichos límites en términos de líneas de exclusión que

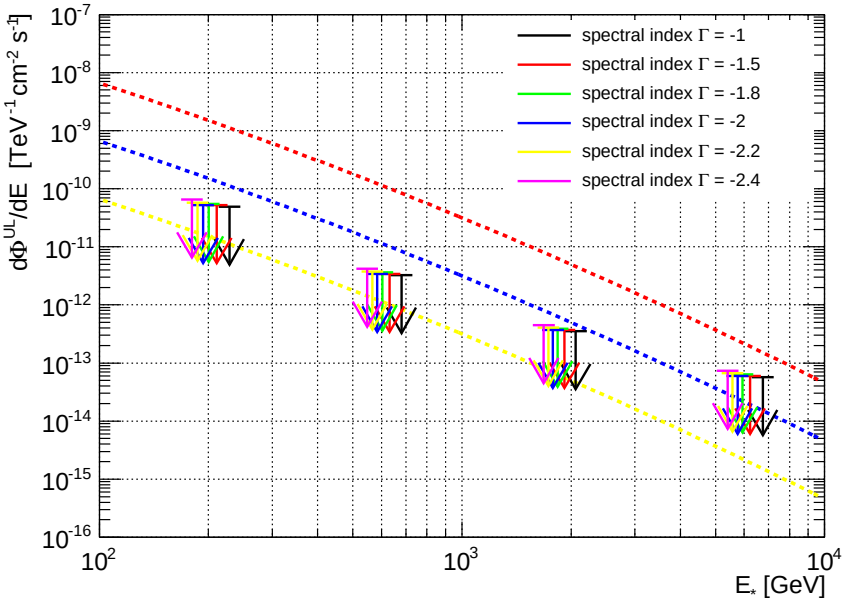

Figura B.5: Límites al flujo diferencial de Segue 1 a partir de datos de MAGIC. Los valores concretos pueden verse en la Tabla B.4. El espectro diferencial de la Nebulosa del Cangrejo observado por MAGIC [344] es mostrado como referencia (línea discontinua roja al 100%, línea discontinua azul al 10%, línea discontinua amarilla al 1%).

Tabla B.5: Rangos del barrido del espacio de parámetros de mSUGRA.

Parametro	Rango	Pasos
m_0	50–5000 GeV	40
$m_{1/2}$	0–5000 GeV	40
$\tan\beta$	2–62	40
A_0	−7000–7000	40
$\mathrm{sign}(\mu)$	$+,-$	2

La región del espacio de parámetros de mSUGRA así restringida genera neutralinos cuyas masas entran en el rango de sensibilidad de MAGIC.

consideren aniquilaciones exclusivas mediante un sólo canal (i.e. con un solo tipo de productos iniciales) (véase Fig. B.6). El uso de líneas de exclusión puede ser aceptable como aproximación tras seleccionar modelos dentro del barrido del espacio de parámetros cuya fracción de aniquilación a un canal determinado sea claramente dominante, como ilustra la Fig. B.6.

La variedad de límites en función de cada espectro individual de aniquilación hace que la mejor manera de presentar los resultados sea en términos del cociente entre el límite observado a la sección eficaz de aniquilación y la sección eficaz de aniquilación resultado de la simulación para cada modelo:

$$\mathrm{ENF} = \langle\sigma_{ann}v\rangle^{UL}/\langle\sigma_{ann}v\rangle, \tag{B.7}$$

donde el acrónimo ENF proviene del inglés *enhancement factor*. Por definición, ENF=1

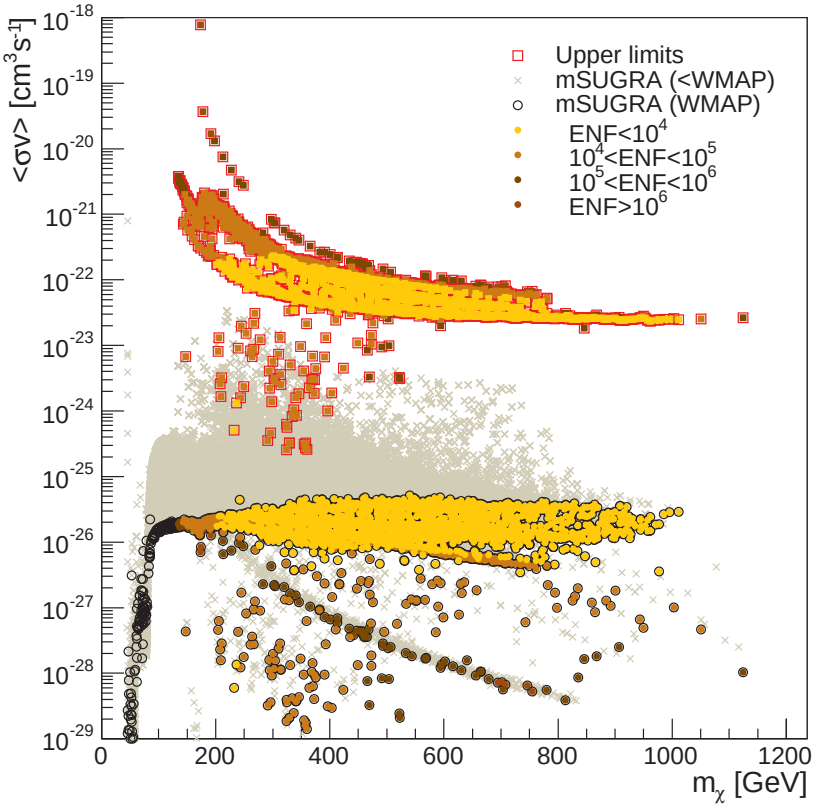

Figura B.6: Límites a la sección eficaz de aniquilación del neutralino por las observaciones de Segue 1 para cada modelo individual simulado. Las cruces grises representan modelos cuya densidad primordial es inferior al valor nominal ofrecido por los datos de WMAP. Las circunferencias negras representan modelos compatibles a 3σ con los resultados de WMAP. Los cuadrados abiertos representan límites a la sección eficaz de aniquilación para cada modelo individual simulado. Los círculos y cuadrados siguen un código de colores en función del factor de aumento para cada modelo.

implicaría la detección del modelo en el tiempo de observación, de forma que valores negativos para el cociente ENF implicarían la exclusión del modelo bajo el supuesto de no detección de la fuente. Los mínimos cocientes ENF obtenidos para modelos compatibles con las restricciones impuestas por los datos de WMAP resultan del orden de 10^3. En promedio, dichos cocientes adquieren valores entre $\sim 10^4$ y $\sim 10^5$. Sin embargo, si se admiten modelos cuya densidad primordial sea inferior a la impuesta por WMAP, la situación es diferente. Bajo el anterior supuesto, los cocientes ENF obtenidos se acercan hasta valores tan bajos como 3.9. En todo caso, hay que remarcar que los neutralinos de dichos modelos no podrían considerarse el componente hegemónico de la materia oscura, sino que sólo formarían una fracción de ésta. En la Fig. B.8 se pueden encontrar las distribuciones de los cocientes ENF para ambos supuestos, así como los correspondientes histogramas.

Adicionalmente, las observaciones de Segue 1 por parte de MAGIC-I han sido utilizadas para comprobar modelos de materia oscura leptofílica favorecidos por el exceso en la fracción de electrones-positrones detectado por el satélite PAMELA. Los límites impuestos por las observaciones de Segue 1 ya se encuentran marginalmente en tensión con uno de los modelos propuestos

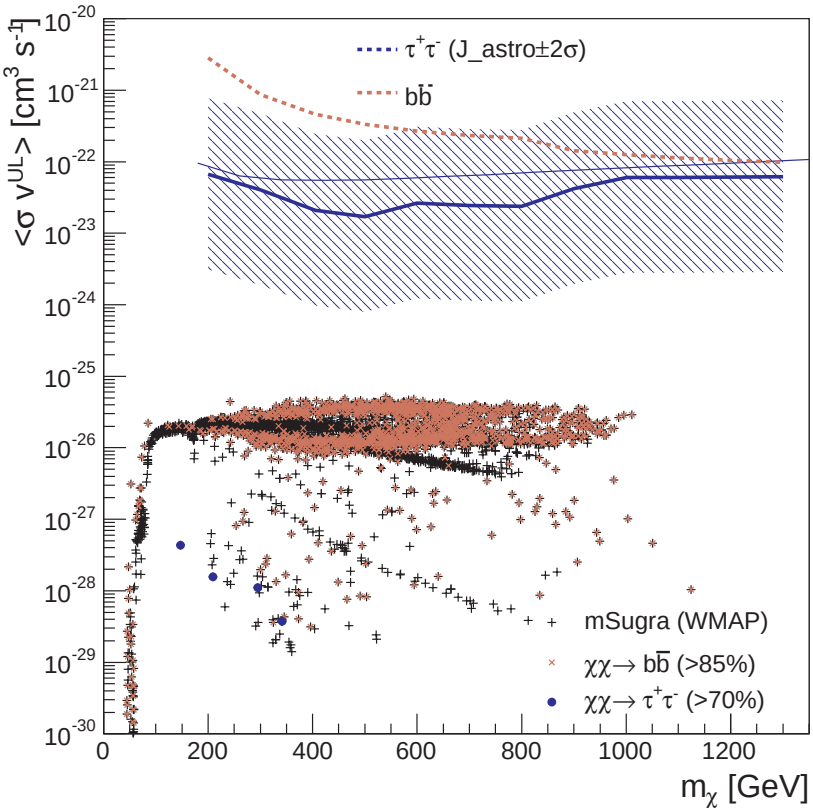

Figura B.7: Límites a la sección eficaz de aniquilación del neutralino a partir de las observaciones de Segue 1 de MAGIC-I. Neutralinos aniquilándose integramente a $b\bar{b}$ o $\tau^+\tau^-$ han sido considerados. Las cruces negras representan modelos de mSUGRA con densidad primordial compatibles a 3σ con los datos de WMAP. Entre dichos modelos, aquéllos cuya aniquilación se produce principalmente a $b\bar{b}$ y $\tau^+\tau^-$ se indican con cruces marrones y puntos azules respectivamente. Los límites superiores para neutralinos aniquilándose exclusivamente en $b\bar{b}$ están representados por la línea discontinua marrón. Las líneas azules representan los límites para la aniquilación exclusiva a $\tau^+\tau^-$ bajo los supuestos de una energía umbral de análisis fija en $E_{th} = 100$ GeV (línea fina) y de una energía umbral optimizada para cada masa m_χ. La banda azul cubre la región originada si se toma en consideración la incertidumbre a 2σ del factor astrofísico de la fuente.

para explicar el exceso anteriormente mencionado si se consideran valores optimistas para el factor astrofísico de Segue 1 dentro de la banda de incertidumbre mostrada en la Fig. B.7. Dicho modelo se caracteriza por una partícula de materia oscura pesada (masa en el rango TeV) que se aniquila exclusivamente siguiendo el canal $\tau^+\tau^-$. Los otros dos modelos comprobados consisten en partículas de materia oscura de alta masa (también en el rango TeV) aniquilándose exclusivamente a $\mu^+\mu^-$, y en partículas de materia oscura aniquilándose a un estado intermedio ϕ de baja masa ($m_\phi = 100$ MeV), que posteriormente decae en un par electrón-positrón. Estos últimos resultados están ilustrados en la Fig. B.9.

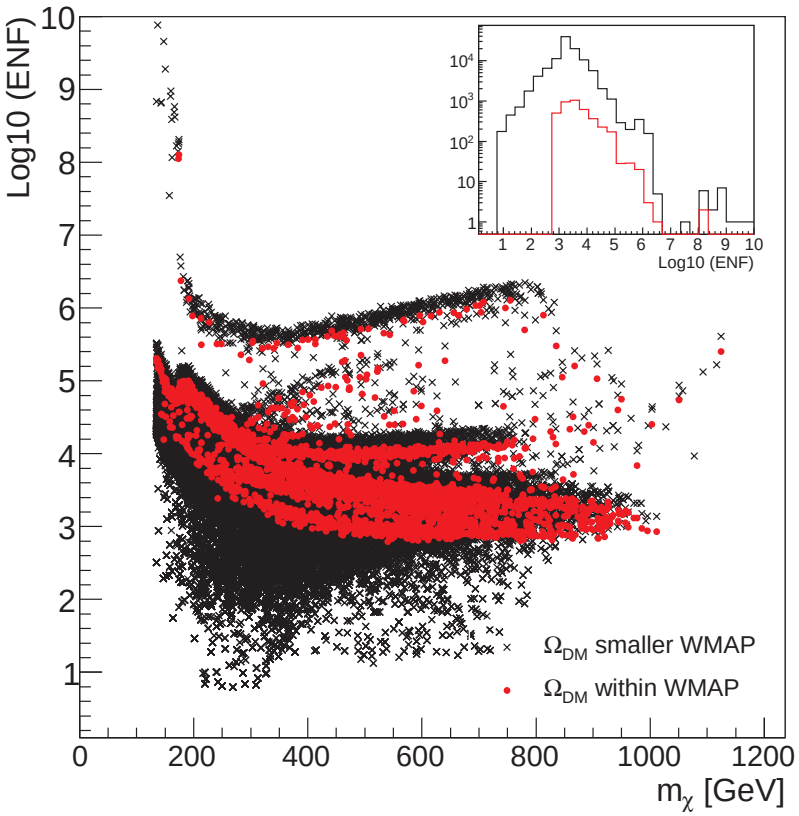

Figura B.8: Distribución de los cocientes ENF generados por las observaciones de Segue 1 en función de la masa del neutralino. Las cruces rojas representan modelos compatibles a 3σ con los resultados de WMAP. Las cruces negras representan modelos cuya densidad primordial es inferior al valor nominal ofrecido por los datos de WMAP. En la esquina superior derecha se representan los histogramas correspondientes a los cocientes ENF para cada uno de esos conjuntos de puntos (mismo código de color).

B.2.3.1 Conclusiones

Los datos de las observaciones de MAGIC-I sobre Segue 1 han sido utilizados para poner límites competitivos al flujo de la fuente considerando una emisión caracterizada por una ley de potencias. En términos de búsquedas de materia oscura, se ha desarrollado un método novedoso que explota la dependencia espectral de los límites al flujo para obtener límites individuales para cada modelo generado en un barrido extensivo de la región del espacio de parámetros de mSUGRA que genera neutralinos de masas compatibles con el rango de sensibilidad de MAGIC. Los resultados se han expresado en términos de límites a la sección eficaz de aniquilación del neutralino así como de los cocientes entre los anteriores límites y las correspondientes secciones eficaces de aniquilación provenientes de la simulación.

La fortaleza de los límites obtenidos depende fuertemente del factor astrofísico que se ha asumido, puesto que el mismo presenta una incertidumbre de un orden de magnitud a 2σ [371]. En todo caso, los resultados aquí presentados también tiene cierta componente conservadora, ya que no se ha considerado el efecto de aumento del flujo esperado que puede ser originado por la presencia de subestructuras de materia oscura dentro de la propia fuente, que puede ser de

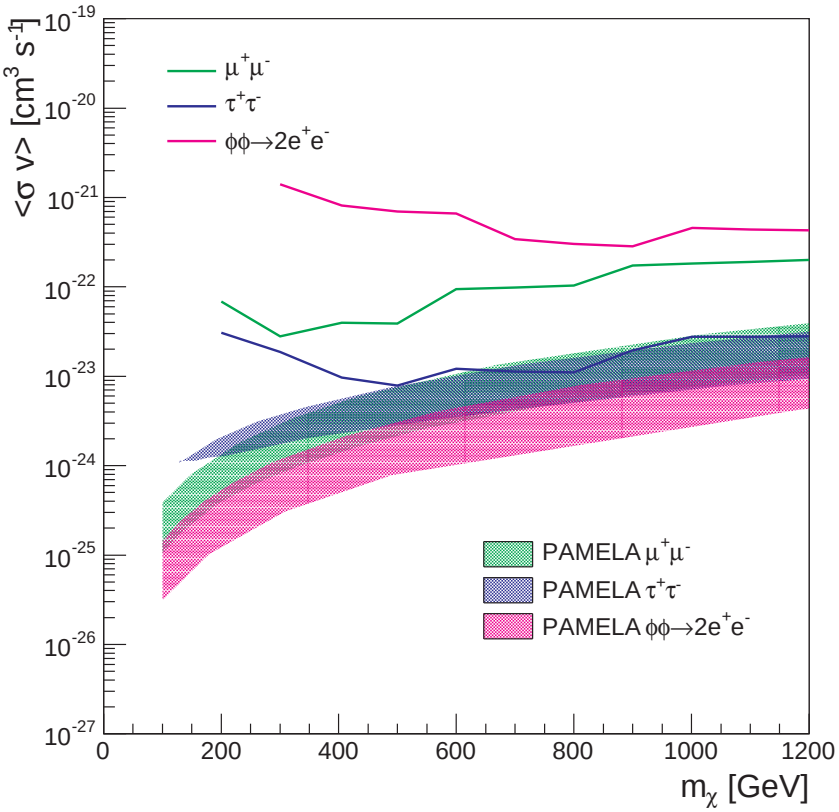

Figura B.9: Líneas de exclusión para partículas de materia oscura aniquilándose exclusivamente a $\mu^+\mu^-$ (línea verde), o $\tau^+\tau^-$ (línea azul), o para partículas de materia aniquilándose a un estado intermedio ligero ϕ desintegrándose a su vez en un par electrón-positrón (línea rosa). Los mismos canales de aniquilación (conservado el código de colores) han sido considerados para mostrar las regiones favorecidas por modelos de materia oscura capaces de justificar el exceso de la fracción de positrones observado por PAMELA (y a su vez restringidas por Fermi-LAT) [371].

hasta un factor 15 para un objeto como Segue 1 [171]. Tampoco se ha tenido en consideración posibles aumentos de flujo provocados por el conocido como *efecto Sommerfeld* [162; 382].

Finalmente, si se comparan los límites obtenidos a partir de las observaciones de Segue 1 con MAGIC-I y aquéllos obtenidos a partir de los datos de Fermi-LAT [374], se llega a la conclusión de que el poder restrictivo de Fermi-LAT domina para partículas de materia oscura de baja masa ($m_{DM} \leq 10^2$ GeV), mientras que MAGIC genera límites más competitivos para partículas de materia oscura de alta masa ($m_{DM} \geq 10^2$ GeV).

Los resultados anteriormente expuestos han sido publicados en la revista científica internacional *Journal of Cosmology and Astroparticle Physics* [3].

B.3 Búsquedas de materia oscura en fuentes de Fermi no asociadas

Las regiones fuertemente dominadas por la materia oscura, que presentan grandes concentraciones de la misma, son buenos objetivos donde desarrollar búsquedas indirectas de materia oscura. Convencionalmente son regiones bien caracterizadas, como el Centro Galáctico, los cúmulos de galaxias, o las galaxias esferoidales enanas. A parte de estos objetos, pueden haber otras regiones de alta concentración de materia oscura que hayan pasado desapercibidas hasta ahora.

Las simulaciones de N-cuerpos de alta resolución indican que los halos galácticos de materia oscura no presentan distribuciones homogéneas y suaves, de monótono crecimiento de la densidad de materia oscura hasta alcanzar un máximo en su centro, sino que exhiben una gran cantidad de subestructuras en todas las escalas de masa resueltas por las simulaciones [38; 171]. Dichas subestructuras, o subhalos, pueden ser tan pequeñas que no hayan podido atraer la suficiente materia bariónica como para iniciar formación estelar y, por lo tanto, hayan sido invisibles para las observaciones astronómicas hasta la fecha. Dichos subhalos de materia oscura podrían encontrarse en regiones cercanas al observador de forma que pudieran ser objetos brillantes en la banda de rayos γ debido a la aniquilación de las partículas de materia oscura que los forman [173]. De una forma similar, sobredensidades de materia oscura han sido predichas en las cercanías de agujeros negros de masa intermedia, pudiendo ser también detectados por el mismo mecanismo de emisión [394].

Puesto que la emisión de rayos γ producida por aniquilación de materia oscura se espera constante, estos subhalos o sobredensidades de materia oscura emergerían en observaciones que monitorizaran todo el cielo durante largos periodos de tiempo [395]. Esto es lo que hace precisamente el satélite Fermi-LAT, y dichos subhalos de materia oscura podrían formar parte de la población de fuentes de Fermi-LAT no detectadas en ninguna otra banda del espectro electromagnético (UFOs, acrónimo del inglés *unassociated Fermi objects*). Muy probablemente, el corte espectral distintivo de la emisión por aniquilación de materia oscura está situado a una energía lo suficientemente grande para que la sensibilidad de Fermi-LAT no sea efectiva de cara a su caracterización (véase, por ejemplo, el límite inferior a la masa del neutralino en [71]), de forma que los instrumentos ideales para hacerlo sean los IACTs.

B.3.1 Búsqueda de posibles subhalos de materia oscura

La sinergia anteriormente propuesta se resume en que los datos de Fermi-LAT pueden esconder fuentes correspondientes a subhalos de materia oscura, cuya caracterización completa, incluyendo la medida de la masa de la partícula de materia oscura, dependería de observaciones de IACTs.

Búsqueda en el catálogo de Fermi La búsqueda de fuentes se basó en el primer catálogo de fuentes puntuales de Fermi [183], elaborado tras once meses de observaciones, el cual contiene 1451 fuentes de rayos γ de alta energía, de las cuales 630 no están asociadas a ninguna posible contrapartida. Sobre dichos 630 UFOs se impusieron los filtros descritos a continuación.

- Las fuentes habían de presentar una alta latitud galáctica para evitar la zona más poblada de UFOs en el catálogo de Fermi: el Plano Galáctico. Los subhalos de materia oscura presentan una distribución homogénea en latitud galáctica, al contrario que los objetos

bariónicos que se aglomeran en dicho plano. UFOs con latitudes galácticas $|b| < 10^{\circ}$ fueron rechazados.

- Los espectros de las fuentes debían de ajustarse a una ley de potencias de índice duro. Los espectros de aniquilación de materia oscura así lo son [145; 343] hasta el corte distintivo a la altura de la masa de la partícula. Fuentes cuyos espectros se decribían por índices espectrales mayores a 2 fueron rechazadas, así como las que se desviaban del ajuste a ley de potencias.

- Las curvas de luz de las fuentes debían ser constantes, es decir, las fuentes no debían de ser variables. Esto viene motivado por el hecho de que la emisión por aniquilación de materia oscura se supone constante, sin presentar variabilidad alguna.

De los 630 UFOs del primer catálogo de Fermi, 93 satisfacieron las anteriores premisas.

Búsqueda de posibles contrapartidas: Una búsqueda extensiva, e independiente a la efectuada por Fermi-LAT, de posibles asociaciones para cada fuente clasificada tras la anterior selección fue realizada. Fueron explorados los principales catálogos astronómicos y archivos de misiones, desde la banda de rayos γ a la banda radio, con la ayuda del archivo de la NASA para astrofísica de altas energías [400]. Las regiones exploradas fueron definidas por áreas circulares, centradas en las posiciones nominales de cada fuente, con un radio conservador de 20', correspondiente al doble del valor de la PSF de Fermi-LAT para energías de 10 GeV [399].

Hay que remarcar que el propósito de esta búsqueda de contrapartidas no era la asociación de fuentes, sino el poder descartar fuentes cuya emisión γ de muy alta energía, caso de ser detectada en observaciones de IACTs, pudiera ser atribuída a una fuente convencional presente en las cercanías del UFO.

Tras esta búsqueda dedicada, 83 fuentes de las 93 evaluadas presentaron algún tipo de posible asociación dentro de la región de búsqueda, por lo que fueron descartadas. Las 10 fuentes restantes, candidatas a ser subhalos de materia oscura, son mostradas en la Fig. B.10.

Estudio de perspectivas de detección por IACTs: La significancia de detección σ es una función dependiente de los sucesos de exceso y fondo o, equivalentemente, los ritmos de adquisición de sucesos de exceso R_{exc} y de fondo R_{bkg} y el tiempo de observación T_{obs}, de forma que $\sigma = \sigma(R_{exc}T_{obs}, R_{bkg}T_{obs})$ (véase [306]). El ritmo de adquisición de sucesos de exceso se obtiene a partir del área efectiva simulada A_{eff} del instrumento y del espectro diferencial asumido $\phi(E, \Delta\Omega)$:

$$R_{exc}(E_{th}) = \int_{E_{th}}^{\infty} \phi(E, \Delta\Omega) A_{eff}(E)\, dE, \tag{B.8}$$

donde E_{th} corresponde a la energía umbral del detector. El ritmo de adquisición de fondo también se obtiene a través del ritmo diferencial de adquisición de fondo simulado, de la forma:

$$R_{bkg}(E_{th}) = \int_{E_{th}}^{\infty} \frac{dR_{bkg}}{dE}\, dE. \tag{B.9}$$

Luego la significancia pasa a depender del espectro diferencial asumido (véase Ec. B.2), la respuesta de cada IACT, codificada ésta en su área efectiva y ritmo de adquisición de fondo característicos, y la energía umbral de análisis E_{th}.

Una fuente se considera detectada por un IACT cuando su significancia de detección cumple $\sigma > 5$. Por lo tanto, conocido el espectro de una fuente determinada y el comportamiento

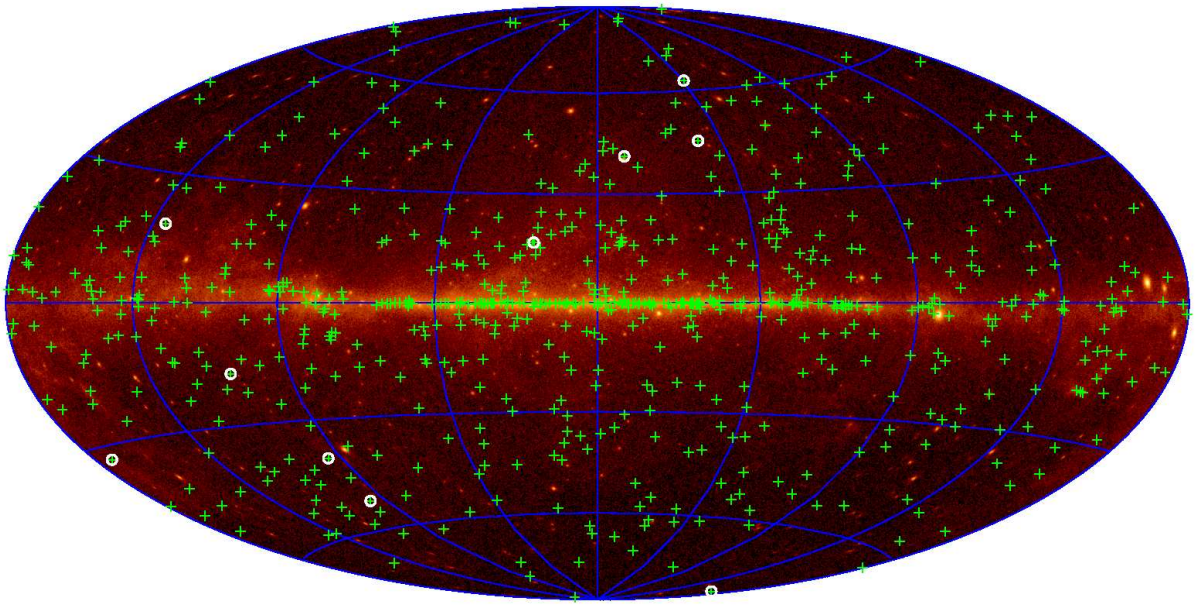

Figura B.10: Cielo completo en proyección Aitoff considerando fotones de Fermi-LAT de energías superiores a 1 GeV. Las cruces verdes indican las posiciones nominales de los 630 objetos no asociados pertenecientes al catálogo 1FGL. Los círculos blancos indican las 10 fuentes candidatas a subhalos de materia oscura.

del instrumento en términos del área efectiva y del ritmo de adquisición de fondo es posible estimar el tiempo de detección de una fuente en función de los ritmos de exceso y fondo $T_{obs} = T_{obs}(R_{exc}, R_{bkg}, \sigma = 5)$.

Para estudiar las perspectivas de detección por IACTs de las fuentes seleccionadas se utilizaron el área efectiva y ritmo de adquisición de fondo de los telescopios MAGIC operando en modo estereoscópico. En relación al espectro de las fuentes, se extrapolaron al rango de energías de MAGIC las parametrizaciones ofrecidas en el catálogo de Fermi-LAT. Se calcularon dos estimaciones del tiempo de detección por cada UFO seleccionado, considerando una energía umbral de análisis de 100 GeV. En la primera, se consideraron para la extrapolación los valores nominales del factor de normalización e índice espectral que caracterizaban los espectros de Fermi-LAT. En la segunda, se consideraron el valor del factor de normalización menos una sigma de su error y el índice espectral más una sigma de su error. Esta última estimación tenía por objeto el incluir los efectos de error de la parametrización espectral de Fermi-LAT en el cálculo de la perspectiva de detección, originando el llamado escenario *pesimista*.

Finalmente, los UFOs que presentaron tiempos de detección superiores a 100 horas en el escenario *pesimista* fueron descartados, quedando seis candidatos finales.

Estudio de fotones de Fermi por encima de 10 GeV: Para cada una de los seis candidatos a subhalo de materia oscura restantes se llevó a cabo un análisis de los fotones de Fermi-LAT de energías superiores a 10 GeV. Se extrajeron dichos fotones una región lo suficientemente extensa como para que incluyese el campo de visión de la cámara de los telescopios MAGIC en su interior (3.5°). De esta manera se comprobó que no hubiese, en ninguno de los casos, ninguna fuente en las cercanías de la candidata que pudiera contaminar el campo de visión, complicando el análisis

de los datos. También se estudiaron los fotones provinientes de la fuente, considerando como tales aquéllos cuyo origen no distaba de la posición nominal de la fuente más de 1.5 veces la resolución angular de Fermi-LAT (a 10 GeV). La existencia de estos fotones ayudó a justificar la extrapolación del flujo de Fermi-LAT.

Finalmente, de las seis fuentes candidatas sólo cuatro eran visibles desde la latitud de MAGIC bajo un ángulo cenital que garantizase una buena energía umbral. Las dos fuentes más prometedoras en términos de detectabilidad y fotones de Fermi-LAT de alta energía fueron observadas, a saber, 1FGL J0338.8+1313 y 1FGL J2347.3+0710. Los candidatos finales observables desde MAGIC se presentan en la Tabla B.6.

Tabla B.6: Posibles subhalos de materia oscura observables por MAGIC.

Fuente	Detectabilidad [h]	Energía de los fotones individuales ($E_{\gamma}^{Fermi-LAT}$ >10 GeV) [GeV]
1FGL J0338.8+1313	3 (41)	12.7, 14.0, 14.2, 18.2, 22.3, 23.7, 29.1, 133.5
1FGL J2347.3+0710	1 (20)	15.6, 45.7, 20.4, 29.2, 86.8, 101.1
1FGL J1312.6+0048	3 (9)	10.0, 10.6, 12.7, 27.0
1FGL J1725.2−0509	5 (36)	14.5, 14.6, 22.4, 35.4, 42.5, 58.3

Posibles subhalos de materia oscura observables por MAGIC. El campo de detectabilidad indica la obtenida para el caso nominal y para el escenario *pesimista*, ésta última entre paréntesis. La energía umbral considerada para el cálculo de la detectabilidad es de E_{thr} = 100 GeV. Sólo son mostrados candidatos cuya detectabilidad en el caso *pesimista* fuera inferior a 100 horas de observación.

B.3.2 Observaciones de la fuente 1FGL J2347.3+0710

La fuente 1FGL J2347.3+0710 se clasificó como buen candidato a subhalo de materia oscura. No se obtuvo ninguna posible contrapartida en la búsqueda dedicada de las mismas en catálogos. A su vez, la numerosa colección de fotones de Fermi-LAT de energías superiores a 10 GeV motivaron la extrapolación del flujo observado por Fermi-LAT al rango de energías de MAGIC para estimar la detectabilidad de la fuente por este último. Dicha estimación ofreció un tiempo de detección para el escenario *pesimista*, descrito anteriormente, de 20 horas. No se detectaron fuentes cercanas ni fondo significativo en el análisis de fotones de alta energía de Fermi-LAT en los alrededores de 1FGL J2347.3+0710. En el análisis de los datos de rayos X del satélite Swift se detectó una fuente puntual en el campo de visión, aunque no compatible con la región de error posicional de Fermi-LAT para la fuente 1FGL J2347.3+0710. El espectro óptico obtenido para dicha fuente sugiere que su naturaleza podría ser la de BL-Lac [410].

Finalmente, la fuente 1FGL J2347.3+0710 fue observada por los telescopios MAGIC en modo estereoscópico durante un tiempo de exposición de 13.3 horas, reducido a 8.3 horas de datos de buena calidad. No se detectó ninguna señal de emisión de rayos γ de alta energía a partir de dichos datos. Posteriormente, se calcularon límites al flujo integral y diferencial de rayos γ de muy alta energía provenientes de la fuente. La Tabla B.7 muestra los límites al flujo diferencial de 1FGL J2347.3+0710 en cuatro rangos de energía y para cuatro leyes de potencia de diferentes índices espectrales. Estos límites diferenciales se presentan también en la Fig. B.11, junto con el flujo diferencial medido por Fermi-LAT.

Debido a los cortes de calidad sobre el tiempo total de exposición, la cantidad total de datos se vio reducida a 8.3 horas, bastante distante de la estimación para la detección en el escenario *pesimista*, que indica una exposición de 20 horas. Debido a ello, una exclusión de la extrapolación

Tabla B.7: Límites superiores al flujo diferencial de la fuente 1FGL J2347.3+0710.

ΔE [TeV]	$N_{\rm ON}/N_{\rm OFF}$	$\sigma_{\rm Li,Ma}$	N_{exc}^{UL} 95% C.L.	$d\Phi^{UL}/dE$ [TeV^{-1}cm^{-2}s^{-1}]				
				$\Gamma=-1.0$	$\Gamma=-1.5$	$\Gamma=-2.0$	$\Gamma=-2.5$	$\Gamma=-3.0$
0.1, 0.32	3519/3411	1.3	389	1.5×10^{-10}	1.6×10^{-10}	1.8×10^{-10}	2.1×10^{-10}	2.5×10^{-10}
0.32, 1	207/208	0.0	48	3.1×10^{-12}	3.3×10^{-12}	3.6×10^{-12}	4.0×10^{-12}	4.6×10^{-12}
1, 3.2	14/22	-1.3	8	1.3×10^{-13}	1.3×10^{-13}	1.4×10^{-13}	1.6×10^{-13}	1.8×10^{-13}
3.2, 10	3/5	-0.7	5	2.1×10^{-14}	2.3×10^{-14}	2.5×10^{-14}	2.9×10^{-14}	3.5×10^{-14}

Límites superiores para el flujo diferencial (nivel de confianza del 95%) en unidades de TeV^{-1}cm^{-2}s^{-1} para cinco leyes de potencia de índices espectrales Γ. Han sido considerados cuatro rangos de energía.

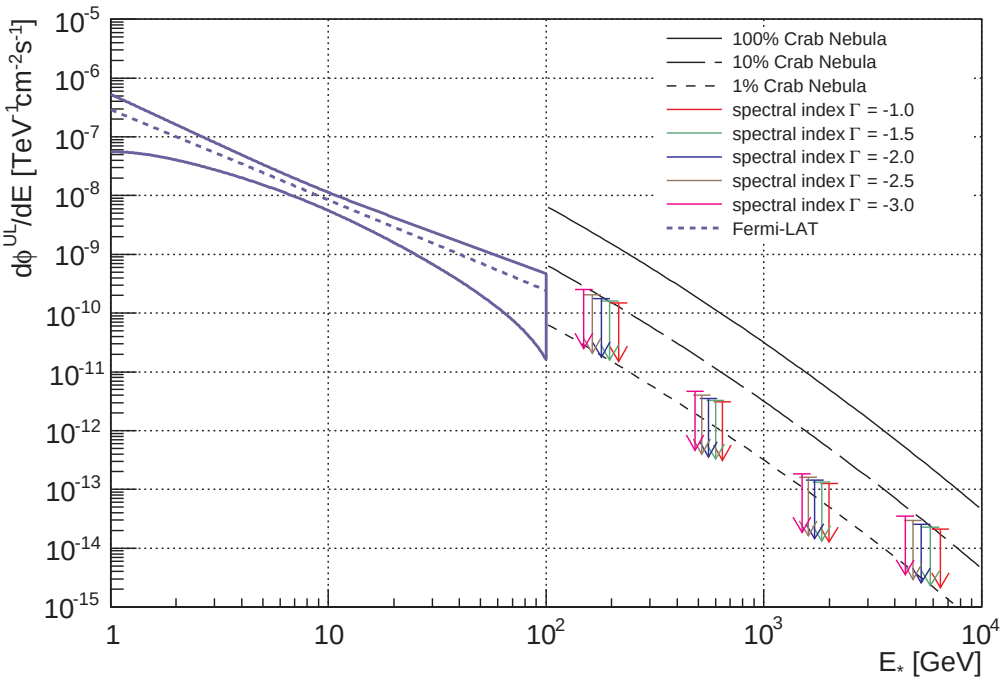

Figura B.11: Espectro diferencial de la fuente 1FGL J2347.3+0710 observado por Fermi-LAT en el rango de rayos γ de alta energía. En el rango de rayos γ de muy alta energía se muestran los límites superiores al flujo de las observaciones de MAGIC. El espectro diferencial de la Nebulosa del Cangrejo medido por MAGIC se muestra como referencia. La banda de error de Fermi-LAT ha sido calculada siguiendo las instrucciones detallandas en [411].

de los datos espectrales de Fermi-LAT al rango energético de MAGIC no puede tener lugar, a no ser que se atienda exclusivamente a los valores nominales de los parámetros que describen el flujo observado por Fermi-LAT y se ignoren sus errores. Si así si hiciera, la Fig. B.11 muestra que la extrapolación de los valores nominales se ve claramente desfavorecida para energías superiores a los 400 GeV. Esto indica la posible existencia de una cierta curvatura espectral que tuviera lugar entre los 100 GeV y los 400 GeV. Dicha curvatura podría ser intrínseca a la emisión de la fuente, pero también podría ser externa a la misma. Una hipótesis de trabajo ha sido la asunción de que las fuentes son locales. De este modo no se ha considerado una posible extinción a muy altas

energías debida a la absorción por parte del EBL. Dicha absorción podría originar la curvatura sugerida por los datos, caso de que la fuente fuera extragaláctica y su desplazamiento al rojo no fuera despreciable. En todo caso, estas conclusiones han de ser revisadas a medida que los datos de Fermi-LAT vayan ofreciendo actualizaciones sobre las parametrizaciones espectrales de las fuentes de su catálogo.

B.3.3 Observaciones de la fuente 1FGL J0338.8+1313

La selección de la fuente 1FGL J0338.8+1313 como posible candidata a subhalo de materia oscura está razonablemente fundamentada. La fuente no posee ninguna contrapartida obvia tras la exhaustiva búsqueda dedicada en catálogos y tampoco hay ninguna fuente brillante en rayos X tras realizar el análisis de los datos de Swift-XRT. De acuerdo con los datos de Fermi-LAT, posee una numerosa población de fotones de energías superiores a 10 GeV, a la vez que no hay ninguna otra fuente brillante ni fondo significativo en este rango de energías. La extrapolación del espectro de 1FGL J0338.8+1313 al rango energético de MAGIC produce una predicción de detección de 41 horas en el escenario *pesimista* definido con anterioridad.

Los telescopios MAGIC observaron la fuente 1FGL J0338.8+1313 en modo estereoscópico durante dicembre de 2010 y enero de 2011, por un tiempo total de observación de 15.3 horas, reducidas a 10.7 horas de datos de buena calidad. El análisis de dichos datos no reveló señal alguna en la banda de rayos γ de muy alta energía. Consecuentemente, se obtuvieron límites al flujo integral y diferencial de rayos γ de muy alta energía provenientes de la fuente. La Tabla B.8 contiene los límites al flujo diferencial de 1FGL J0338.8+1313 en cuatro rangos de energía y para cuatro leyes de potencia de distinto índice espectral. Dichos límites se presentan también en la Fig. B.12, junto con el flujo diferencial medido por Fermi-LAT.

Tabla B.8: Límites al flujo diferencial de la fuente 1FGL0338.8+1313.

ΔE [TeV]	$N_{\rm ON}/N_{\rm OFF}$	$\sigma_{\rm Li,Ma}$	N_{exc}^{UL} 95% C.L.	$d\Phi^{UL}/dE$ [TeV^{-1}cm^{-2}s^{-1}]				
				$\Gamma=-1.0$	$\Gamma=-1.5$	$\Gamma=-2.0$	$\Gamma=-2.5$	$\Gamma=-3.0$
$0.1, 0.32$	3271/3342	-0.9	120	3.6×10^{-11}	3.9×10^{-11}	4.3×10^{-11}	5.0×10^{-11}	6.0×10^{-11}
$0.32, 1$	205/214	-0.4	39	1.9×10^{-12}	2.0×10^{-12}	2.2×10^{-12}	2.5×10^{-12}	2.9×10^{-12}
$1, 3.2$	18/16	0.3	18	2.2×10^{-13}	2.4×10^{-13}	2.6×10^{-13}	2.9×10^{-13}	3.3×10^{-13}
$3.2, 10$	1/3	-1.0	4	1.1×10^{-14}	1.2×10^{-14}	1.3×10^{-14}	1.5×10^{-14}	1.8×10^{-14}

Límites al flujo differencial (nivel de confianza del 95%) en unidades de TeV^{-1}cm^{-2}s^{-1} para cinco leyes de potencia de índices espectra Γ. Han sido considerados cuatro rangos de energía.

El tiempo de observación que generó datos de buena calidad se encuentra muy por debajo de las estimaciones de detección del escenario *pesimista* (10.7 horas y 41 horas, respectivamente). Por ello no es posible aún descartar la extrapolación del flujo obervado por Fermi-LAT al rango energético de MAGIC si se consideran las incertidumbres en la caraterización espectral de la fuente por parte de Fermi-LAT. Aún así, los datos de MAGIC no son compatibles con la extrapolación de los valores nominales de los parámetros espectrales de Fermi-LAT, desfavoreciendo una extrapolación de los mismos por encima de 200 GeV. Este hecho puede apuntar una posible curvatura en el espectro de la fuente. Hay que remarcar que dicha curvatura podría no ser intrínseca a la emisión de la fuente. Una de las hipótesis iniciales de la búsqueda es que las fuentes son locales, de forma que la posible extinción por EBL no se ha tenido en consideración, pero pudiera darse el caso de que la fuente fuera realmente extragaláctica y que la curvatura que

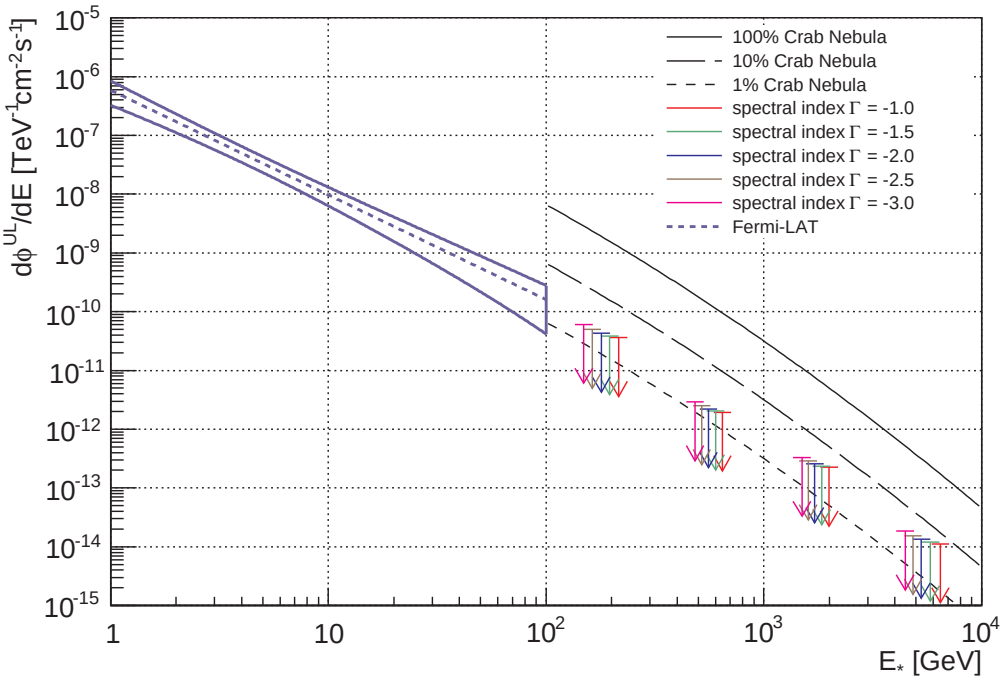

Figura B.12: Espectro diferencial de la fuente 1FGL J0338.8+1313 observado por Fermi-LAT en el rango de rayos γ de alta energía. En el rango de rayos γ de muy alta energía se muestran los límites al flujo de las observaciones de MAGIC. El espectro diferencial de la Nebulosa del Cangrejo medido por MAGIC se muestra como referencia. La banda de error de Fermi-LAT ha sido calculada siguiendo las instrucciones detallandas en [411].

se intuye a partir de los datos presentados pueda ser justificada a través de dicha extinción. En todo caso, esta conclusión ha de ser revisada una vez que se actualicen los ajustes espectrales de 1FGL J0338.8+1313 gracias al aumento de estadística en los datos de Fermi-LAT.

B.3.4 Conclusiones

Se ha presentado un método de búsqueda de posibles subhalos de materia oscura en el catálogo de Fermi-LAT, con el propósito de la caracterización de los mismos a mayores energías por parte de IACTs. Dicha estrategia se basa en la posibilidad fundamentada de que la partícula de materia oscura posea una masa lo suficientemente alta como para que Fermi-LAT no tenga alcance suficiente para caracterizar el corte espectral distintivo de las emisiones de aniquilación de materia oscura.

Se han estudiado las perspectivas de detección por parte de los telescopios MAGIC, en modo de observación estereoscópica. También se ha estudiado la población de fotones de Fermi-LAT de energías superiores a 10 GeV, con objecto de investigar posibles fondos no deseados de cara a realizar observaciones con IACTs. A la vez, los fotones de Fermi-LAT de alta energía, provenientes de las fuentes, han motivado la extrapolación de flujos de Fermi-LAT a la zona de solapamiento con MAGIC.

De las 1451 fuentes del primer catálogo de Fermi-LAT, 4 han superado todos los requisitos impuestos para poder ser observadas por MAGIC como candidatas a subhalos de materia oscura.

Dos de ellas han sido finalmente observadas por MAGIC, a saber, 1FGL J2347.3+0710 y 1FGL J0338.8+1313, por tiempos de 8.3 y 10.7 horas efectivas respectivamente. Ninguna observación concluyó en detección. En ambos casos los límites al flujo calculados sugieren cierta curvatura necesaria en los espectros. Serán necesarias observaciones más profundas para descubrir la verdadera naturaleza de dichas fuentes.

Merece la pena señalar que la búsqueda indirecta de materia oscura puede beneficiarse ampliamente de programas de observación en diversas bandas espectrales.

El trabajo de búsqueda de posibles subhalos de materia oscura en el catálogo de Fermi-LAT ha sido presentado a la comunidad científica en el simposio anual de Fermi-LAT de 2011 [4]. Los análisis de las dos fuentes candidatas observadas por los telescopios MAGIC se han presentado a la comunidad científica en el congreso internacional de rayos cósmicos (ICRC) de 2011 [5].

B.4 Perspectivas de detección de materia oscura con la nueva generación de telescopios Cherenkov

La actual generación de telescopios Cherenkov ha desarrollado un gran trabajo en lo que a búsquedas indirectas de materia oscura se refiere, ofreciendo restricciones competitivas, llevando a los instrumentos hasta sus límites de sensibilidad. Hoy día, la próxima generación de telescopios Cherenkov está liderada por el ambicioso proyecto CTA [412] (matriz de telescopios Cherenkov, acrónimo del inglés, Cherenkov Telescope Array).

Aún en fase de desarrollo, el concepto de CTA consiste en desarrollar matrices de varias decenas de telescopios Cherenkov. Idealmente, CTA tendrá una cobertura total del cielo, puesto que el proyecto propone dos matrices asimétricas ubicadas en sendos hemisferios: una matriz norte dedicada a la observación de objectos extragalácticos y una matriz dedicada al estudio de objetos tanto galácticos como extragalácticos. El proyecto mejorará la sensibilidad de los actuales IACTs, como MAGIC, HESS y VERITAS, en un factor 5–10 en el rango de energías desde 100 GeV a pocas decenas de TeV, a la vez que extenderá el rango de energía cubierto por los mismos, presentando una mejor resolución energética y angular [386]. Caracterizar dichas mejoras es un proceso complejo que ha de tener en consideración múltiples variables, desde las características técnicas de los instrumentos (diseño de las cámaras, reflectores, *trigger*, grabado de datos, etc.), hasta el número y disposición geométrica de los mismos, es decir, la configuración de la matriz. Gracias a un detallado trabajo de simulaciones Montecarlo [386], es posible estudiar la hipotética respuesta de distintas configuraciones de CTA frente a una emisión de rayos γ caraterizada por un determinado espectro diferencial.

B.4.1 Perspectivas de detección de fuentes puntuales de materia oscura

Las perspectivas de detección de materia oscura por CTA requieren de la evaluación del sistema frente a las distintas estrategias de búsqueda planteadas: búsqueda en galaxias eferoidales enanas y otras subestructuras del Halo Galáctico, búsqueda en el Centro Galáctico o en el propio Halo Galáctico, búsqueda en cúmulos de galaxias, búsqueda de señales espaciales en la distribución del fondo de rayos γ, búsqueda de líneas de emisión, etc. En el presente trabajo, se ha estudiado la sensibilidad de CTA frente a fuentes puntuales que presenten espectros diferenciales característicos a la emisión producida por aniquilación de materia oscura. Dichas fuentes podrían ser subhalos de materia oscura cuya emisión no resultara extensa en función de la resolución angular de CTA.

El método elegido para poder evaluar la sensibilidad de CTA a fuentes puntuales de materia oscura se basa en la obtención de significancias de detección para distintos espectros diferenciales de materia oscura siguiendo el método presentado en la anterior Sec. B.3.1. En el presente caso, el espectro diferencial asumido (véase Ec. B.2) pasa a ser el espectro esperado de materia oscura y cada configuración de la matriz de telescopios genera un área efectiva y un ritmo diferencial de adquisicion de fondo distintos. Debido a la gran cantidad de variables que caracterizan la posible emisión de una fuente de materia oscura, ciertas hipótesis respecto al espectro han sido consideradas: se asume un valor típico para la sección eficaz de aniquilación $\langle\sigma_{\rm ann}v\rangle \sim 3\times10^{-26}$ cm^{3}s^{-1}, fundamentado en criterios cosmológicos [57]; se consideran aniquilaciones exclusivas a un sólo canal, $b\bar{b}$, W^+W^-, $\tau^+\tau^-$, o $\mu^+\mu^-$, siguiendo parametrizaciones analíticas [145]; el rango de masas considerado para la partícula de materia oscura es de 50 GeV a 10 TeV, coincidiendo el límite inferior con una estimación conservadora de la energía umbral de CTA y restricciones experimentales sobre WIMPs supersimétricos [71] y el límite superior con restricciones teóricas de los mismos [57]. El tiempo de observación se ha querido fijar en 250 horas, que correspondería al tiempo de observación asignado habitualmente para programas profundos en la generación actual de IACTs. Este tiempo puede ser invertido en una sola fuente o repartido entre fuentes de similar naturaleza. Por otra parte, se han cosiderado tres configuraciones posibles para la matriz de CTA, descritas en [386]:

- Configuración B: telescopios con reflectores de 12 m (37 unidades) y 24 m (5 unidades) de diámetro.
- Configuración C: telescopios con reflectores de 12 m (55 unidades) de diámetro.
- Configuración E: telescopios con reflectores de 7 m (32 unidades), 12 m (23 unidades) y 24 m (4 unidades) de diámetro.

De esta forma, una vez fijados las distintas configuraciones de la matriz y el canal de aniquilación, se pueden estudiar las perspectivas de detección en función de la masa del WIMP y el factor astrofísico de la fuente. Se ha querido presentar los resultados en términos de mínimos factores astrofísicos necesarios para obtener la detección de la fuente, así como de los aumentos mínimos necesarios sobre factores astrofísicos de galaxias esferoidales conocidas que generarían una detección a su vez.

B.4.1.1 Límites de detección en términos de mínimos factores astrofísicos

La obtención del factor astrofísico mínimo J_{min} que generaría una señal al nivel de 5σ, en función de la masa de la partícula de materia oscura, del canal de aniquilación y del tiempo de observación, fijado en este caso en $T_{obs} = 250$ h, resulta un buen indicador para evaluar la capacidad de detección de CTA frente a fuentes puntuales de materia oscura.

La evolución de dicho factor astrofísico mínimo en función de la masa de la partícula de materia oscura se muestra en la Fig. B.13 para las tres configuraciones de matriz seleccionadas. Dos canales de aniquilación han sido considerados, a saber, aniquilación a $b\bar{b}$ y a $\tau^+\tau^-$. Como conclusión general a la vista de estos resultados, puede decirse que, independientemente de la configuración elegida, CTA es más sensible a una partícula de materia oscura de masa en el rango de 300 GeV a 1 TeV. Los valores de factor astrofísico mínimo más pequeños son originados para la configuración tipo B, convirtiendo a esta disposición de telescopios como la más sensible para búsquedas de materia oscura, incluso para valores de masas por encima del TeV. Los resultados de la configuracion tipo E son muy similares a los obtenidos por el tipo B, aunque

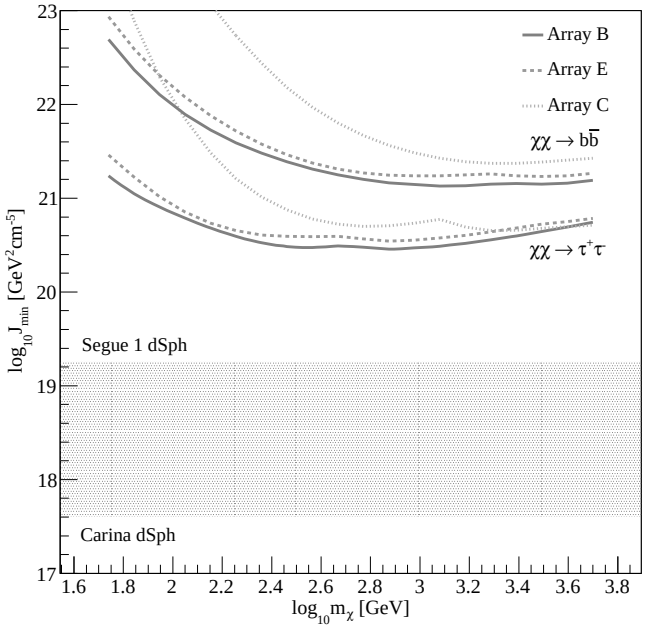

Figura B.13: Mínimo factor astrofísico J_{min} que produciría una detección al nivel de 5σ en función de la masa del WIMP m_χ. Los resultados mostrados corresponden a tres posibles configuraciones distintas de CTA: configuración B, C, y E. La aniquilación de WIMPs siguiendo al canal $\tau^+\tau^-$ y una típica sección eficaz de aniquilación de $\langle\sigma_{\rm ann}v\rangle \sim 10^{-26}$ cm^{3}s^{-1} son asumidas. La región sombreada ilustra el rango de valores de factor astrofísico típico para las galaxias esferoidales enanas conocidas, desde el mínimo de Carina al máximo de Segue 1.

sin mejorar a estos últimos. La configuración tipo C se comporta mucho peor a bajas energías que estos dos primeros, y tiende a mostrar resultados similares a muy altas enegías (en el rango TeV). Este último resultado no es sorprendente, pues la configuración tipo C está especialmente diseñada para optimizar su respuesta a muy altas energías y tiene una mayor sensibilidad que las configuraciones C y E en el rango de energías de varios TeV [386].

El espectro de fotones de una aniquilación a $\tau^+\tau^-$ es más duro que el de una aniquilación a $b\bar{b}$, generando más fotones cercanos al corte espectral producido por la masa de la partícula. Esto hace que los valores de los factores astrofísicos mínimos asocados al primero de los canales sean significativamente menores que los asociados al segundo. Para profundizar en la diferente respuesta de CTA a los diversos canales de aniquilación, en la Fig. B.14 se representan los factores astrofísicos mínimos para cuatro diferentes, a saber, $\tau^+\tau^-$, $b\bar{b}$, $\mu^+\mu^-$, y W^+W^-, para la configuración de matriz tipo B.

B.4.1.2 Límites de detección en términos de factores de aumento mínimo

La siguiente manera de ilustrar la capacidad de detección de materia oscura en fuentes puntuales de CTA es a través del llamado factor de aumento mínimo B_F. Dicho factor B_F se define como el cociente entre el factor astrofísico mínimo J_{min} y el factor astrofísico derivado tras observaciones J_{obs} de sistemas conocidos. El factor de aumento mínimo hereda las dependencias de J_{min}, de forma que es función de la masa de la partícula de materia oscura, el canal de aniquilación, el

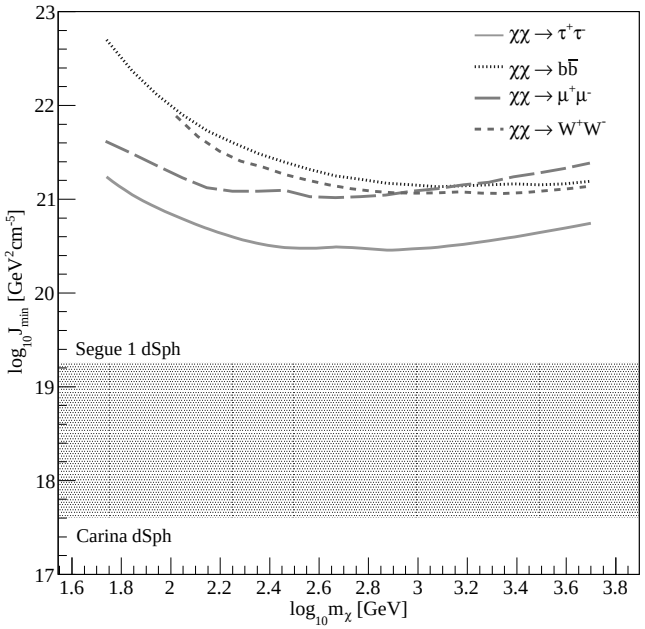

Figura B.14: Mínimo factor astrofísico J_{min} que produciría una detección al nivel de 5σ en función de la masa del WIMP m_χ, e función de distintos canales de aniquilación. Los canales considerados son $\tau^+\tau^-$, $b\bar{b}$, $\mu^+\mu^-$, or W^+W^-. La aniquilación se considera íntegra a un solo canal. Se asume una típica sección eficaz de aniquilación de $\langle\sigma_{\rm ann}v\rangle \sim 10^{-26}$ cm^{3}s^{-1}. La región sombreada ilustra el rango de valores de factor astrofísico típico para las galaxias esferoidales enanas conocidas, desde el mínimo de Carina al máximo de Segue 1. Los resultados corresponden a una configuración B y a un tiempo de observación de 250 horas.

tiempo de observación y la configuración de la matriz de telescopios.

La introducción de este factor de aumento mínimo se ve físicamente motivada por la posibilidad de que el flujo esperado de fotones originados por aniquilación de materia oscura se vea incrementado por efectos de inclusión de subestructuras en la distribución de densidad de materia oscura (ρ_{DM} en Ec. B.2), lo cual incrementaría el factor astrofísico [171], y/o por el conocido como efecto Sommerfeld, el cual incrementaría el término de física de partículas [162] (Φ^{PP} en Ec. B.2).

Tras considerar un tiempo de observación de $T_{obs} = 250$ h y un conjunto de siete galaxias esferoidales enanas con factores astrofísicos observados disponibles, se calcularon los factores de aumento mínimo B_F. Dichos factores, para el escenario optimista donde la partícula de materia oscura tuviera una masa de 1 TeV, se aniquilara exclusivamente a $\tau^+\tau^-$, y la configuración de la matriz de CTA fuera de tipo B, se muestran en la Tabla B.9 y en la Fig. B.15. La galaxia esferoidal enana Segue 1 se presenta como la fuente más prometedora para la búsqueda de materia oscura con CTA. En su caso particular, un factor de aumento mínimo $B_F = 16$ provocaría que la señal de materia oscura proveniente de la fuente fuera detectada tras 250 horas de observación de CTA.

Los factores astrofísicos observados que se han considerado asumen una región angular de integración de $\Delta\Omega = 10^{-5}$ sr, correspondiente a la PSF típica de la generación actual de telescopios Cherenkov. Las simulaciones Montecarlo predicen para la PSF de CTA una mejora significativa

respecto a esta anterior [386], con lo cual el factor astrofísico debería de ser recalculado teniendo en cuenta la reducción correspondiente de la región angular de integración. Aún así, el cambio no sería determinante. Los factores astrofísicos observados J_{obs} reducirían sus valores, pero las grandes incertidumbres que acompañan al cálculo de esta cantidad harían de estas variaciones algo poco significativo. De hecho, debido a las considerables incertidumbres antes comentadas, los resultados presentados en esta sección deberían de ser considerados como una aproximación de orden de magnitud al problema.

Tabla B.9: Mínimos factores de aumento para un conjunto de galaxias esferoidales enanas.

Fuente	Referencia	Perfil	$J_{obs}(\Delta\Omega)$ $[\mathrm{GeV}^2\mathrm{cm}^{-5}]$	B_F
Carina	[329]	NFW	4.0×10^{17}	700
Boötes 1	[327]	NFW	1.1×10^{18}	250
Draco	[327]	NFW	1.5×10^{18}	200
Ursa Minor	[327]	NFW	2.7×10^{18}	100
Sculptor	[329]	NFW	4.0×10^{18}	75
Willman 1	[327]	NFW	8.4×10^{18}	35
Segue 1	[3]	Einasto	1.8×10^{19}	16

Factores astrofísicos observados para el conjunto de galaxias esferoidales enanas considerado en la Fig. B.15. También se muestra el factor de aumento mínimo B_F necesario para alcanzar una detección en 250 horas de observación con CTA para el caso de una partícula de materia oscura de $m_{DM} = 1$ TeV aniquilándose exclusivamente a $\tau^+\tau^-$. El ángulo sólido de integración es de $\Delta\Omega = 10^{-5}$ sr ($\sim 0.1^\circ$ PSF). NFW es el acrónimo del perfil tipo Navarro-Frenk-White. Los factores B_F están calculados para una configuración tipo B.

B.4.2 Conclusiones

Se ha realizado un estudio de perspectivas de detección de fuentes puntuales de materia oscura para la próxima generación de telescopios Cherenkov, particularizada en el proyecto en desarrollo CTA.

Para dicho observatorio futuro existen simulaciones Montecarlo que caracterizan el área efectiva del mismo, así como el ritmo diferencial de adquisición de fondo, en función de distintas configuraciones de matrices de telescopios propuestas. Se han evaluado tres de dichas configuraciones, a saber, la configuración tipo B, tipo C y tipo E, en función del factor astrofísico mínimo que produciría una detección para un tiempo de observación de 250 horas. Dicho factor astrofísico mínimo depende a su vez del canal de aniquilación característico de la partícula de materia oscura, así como de su masa. También se han presentado los resultados en términos del factor de aumento mínimo requerido a los flujos esperados de galaxias esferoidales enanas conocidas, para generar una detección en el mismo tiempo de observación de 250 horas.

La principal conclusión de la evaluación en términos de factor astrofísico mínimo es que la configuración de matriz tipo B es la más sensible a partículas de materia oscura de masas en el rango de 50 GeV a unos pocos TeV, banda donde podría ubicarse, por ejemplo, la masa de un neutralino. A parte de ello, se ha comprobado que el escenario más prometedor de cara a una futura detección incluiría una partícula de materia oscura de masa localizada en el intervalo de 300 GeV a 1 TeV aniquilándose exclusivamente a $\tau^+\tau^-$. La principal conclusión respecto a los factores de aumento mínimo es que, para el caso de la galaxia esferoidal enana Segue 1,

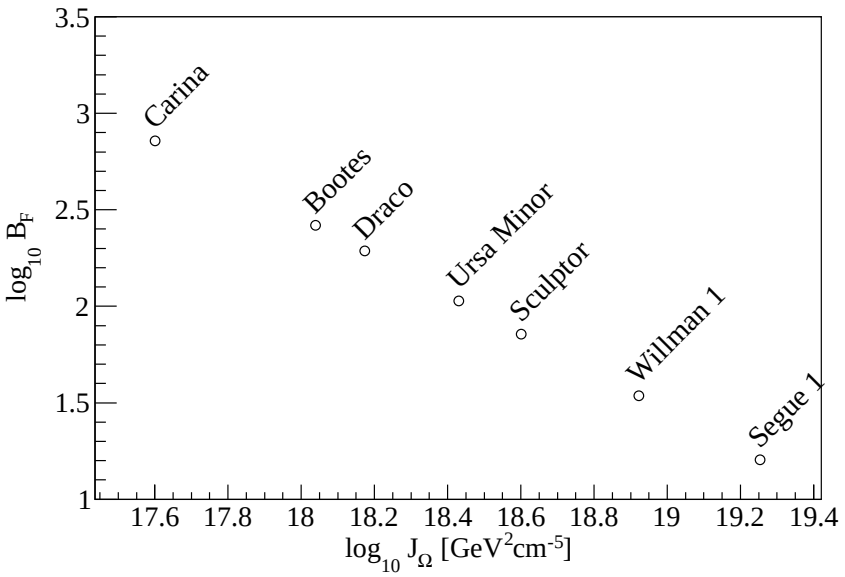

Figura B.15: Factor de aumento mínimo B_F en función del factor astrofísico J para un conjunto de 7 galaxias esferoidales bien caracterizadas. Se considera un WIMP de 1 TeV de masa cuya aniquilación se produce íntegramente mediante el canal $\tau^+\tau^-$. El requisito impuesto es una deteción al nivel de 5 en 250 horas de observación. El factor de aumento mínimo más prometedor corresponde a Segue 1, la cual tan sólo requerirá $B_F \geq 16$.

dicho factor sería tan sólo $B_F \sim 16$. Ello implica que si el flujo debido a aniquilación de materia oscura en Segue 1 aumentara en un factor 16 o mayor, se podría detectar la fuente en un tiempo de observación de 250 horas en el escenario propuesto anteriormente.

A pesar de que los valores obtenidos de factores astrofísicos mínimos puedan parecer lejanos a los factores astrofísicos observados en la mayoría de galaxias esferoidales enanas, esto no implica *a priori* que sean valores irreales. De hecho, parte de las fuentes puntuales de materia oscura pudieran ser, por ejemplo, subestructuras de materia oscura del Halo Galáctico que, por su cercanía al observador, generasen altos factores astrofísicos.

Como apunte final, se ha de enfatizar que los resultados anteriormente presentados han de ser considerados límites conservadores. CTA no es un proyecto cerrado aún, así que nuevos estudios y mejoras de diseño pueden ser todavía añadidos a la configuración del instrumento, los cuales pueden acarrear cambios significativos en su sensibilidad final. Por ejemplo, las simulaciones Montecarlo utilizadas no consideran la contribución a la configuración final de CTA de la parte norteamericana del consorcio, cuya propuesta consiste en un aumento significativo del número de telescopios medianos de la matriz. En todo caso, este estudio presenta el gran impacto que CTA podría tener en el ámbito de búsquedas indirectas de materia oscura en comparación con la generación actual de IACTs.

El trabajo sobre el estudio de perspectivas de detección de materia oscura con CTA ha generado la publicación [6] y será incluído en una entrega especial dedicada a CTA de la revista internacional especializada *Astroparticle Physics*.

Appendix C

Publications

Author's list of publications during his PhD studentship, by the thesis publication date.

C.1 Publications in refereed journals

- J. Aleksic *et al.* (including D. Nieto) [The MAGIC Collaboration], *Searches for Dark Matter annihilation signatures in the Segue 1 satellite galaxy with the MAGIC-I telescope*, JCAP **1106** (2011) 035. [arXiv:1103.0477[astro-ph.HE]].

- J. Aleksic *et al.* (including D. Nieto) [The MAGIC Collaboration], *A search for Very High Energy gamma-ray emission from Scorpius X-1 with the MAGIC telescopes*, Astrophys. J. **735** (2011) L5.
[arXiv:1103.5677[astro-ph]].

- J. Aleksic *et al.* (including D. Nieto) [The MAGIC Collaboration], *MAGIC observations and multiwavelength properties of the quasar 3C279 in 2007 and 2009*, Astron. Astrophys. **530** (2011) A4.
[arXiv:1101.2522[astro-ph]].

- J. Aleksic *et al.* (including D. Nieto) [The MAGIC Collaboration], *MAGIC discovery of VHE Emission from the FSRQ PKS 1222+21*, Astrophys. J. **730** (2011) L8.
[arXiv:1101.4645[astro-ph]].

- V.A. Acciari *et al.* (including D. Nieto) [The VERITAS and MAGIC Collaborations], *Spectral Energy Distribution of Markarian 501: Quiescent State vs. Extreme Outburst*, Astrophys. J. **729** (2011) 2. [arXiv:1012.2200 [astro-ph]].

- J. Aleksić *et al.* (including D. Nieto) [The MAGIC Collaboration], *Observations of the Blazar 3C 66A with the MAGIC Telescopes in Stereoscopic Mode*, Astrophys. J. **726** (2011) 58. [arXiv:1010.0550 [astro-ph.HE]].

- A. A. Abdo *et al.* (including D. Nieto) [The Fermi-LAT, MAGIC and VERITAS Collaborations] *Insights into the High-energy gamma-ray Emission of Markarian 501 from Extensive Multifrequency Observations in the Fermi Era*, Astrophys. J. **727** (2011) 129

- J. Aleksić *et al.* (including D. Nieto) [The MAGIC Collaboration], *Detection of very high energy gamma-ray emission from the Perseus cluster head-tail galaxy IC 310 by the MAGIC telescopes*, Astrophys. J. Lett. **723** (2010) L207-212, [arXiv:1009.2155 [astro-ph.HE]].

- J. Aleksić *et al.* (including D. Nieto) [The MAGIC Collaboration], *MAGIC Upper Limits for two Milagro-detected, Bright Fermi Sources in the Region of SNR G65.1+0.6*, Astrophys. J. **725** (2010) 1629-1632. [arXiv:1007.3359 [astro-ph.HE]].
- J. Aleksić *et al.* (including D. Nieto) [The MAGIC Collaboration], *Magic constraints on Gamma-ray emission from Cygnus X-3*, Astrophys. J. **721** (2010) 843-855. [arXiv:1005.0740 [astro-ph.HE]].
- J. Aleksić *et al.* (including D. Nieto) [The MAGIC Collaboration], *MAGIC observation of the GRB080430 afterglow*, Astron. Astrophys. **517** (2010) A5, [arXiv:1004.3665 [astro-ph.HE]].
- J. Aleksić *et al.* (including D. Nieto) [The MAGIC Collaboration], *Search for an extended VHE gamma-ray emission from Mrk 421 and Mrk 501 with the MAGIC Telescope*, Astron. Astrophys. **524** (2010) 77, [arXiv:1004.1093 [astro-ph.HE]].
- J. Aleksić *et al.* (including D. Nieto) [The MAGIC Collaboration], *MAGIC TeV Gamma-Ray Observations of Markarian 421 during Multiwavelength Campaigns in 2006*, Astron. Astrophys. **519** (2010) A32.
[arXiv:1001.1291 [astro-ph.CO]].
- J. Aleksić *et al.* (including D. Nieto) [The MAGIC Collaboration], *Simultaneous multi-frequency observation of the unknown redshift blazar PG 1553+113 in March-April 2008*, Astron. Astrophys. **515** (2010) A76. [arXiv:0911.1088 [astro-ph.HE]].
- H. Anderhub *et al.* (including D. Nieto) [The MAGIC Collaboration], *Search for Very High Energy Gamma-ray Emission from Pulsar-Pulsar Wind Nebula Systems with the MAGIC Telescope*, Astrophys. J. **710** (2010) 828-835.
- H. Anderhub *et al.* (including D. Nieto) [The MAGIC Collaboration], *Correlated X-ray and Very High Energy emission in the gamma-ray binary LS I +61 303*, Astrophys. J. **706** (2009) L27-L32.
[arXiv:0910.4381 [astro-ph.HE]].
- H. Anderhub *et al.* (including D. Nieto) [The MAGIC Collaboration], *Simultaneous Multiwavelength observation of Mkn 501 in a low state in 2006*, Astrophys. J. **705** (2009) 1624-1631.
[arXiv:0910.2093 [astro-ph.HE]].
- H. Anderhub *et al.* (including D. Nieto) [The MAGIC Collaboration], *Discovery of very High Energy gamma-Rays from the Blazar S5 0716+714*, Astrophys. J. Lett. **704** (2009) L129-133,
[arXiv:0907.2386 [astro-ph.CO]].
- J. Aleksić *et al.* (including D. Nieto) [The MAGIC Collaboration], *MAGIC Gamma-Ray Telescope Observation of the Perseus Cluster of Galaxies: Implications for Cosmic Rays, Dark Matter and NGC 1275*, Astrophys. J. **710** (2010) 634-647. [arXiv:0909.3267 [astro-ph.HE]].
- V. A. Acciari *et al.* (including D. Nieto) [The VERITAS and the MAGIC Collaborations], *Simultaneous Multiwavelength Observations of Markarian 421 During Outburst*, Astrophys. J. **703** (2009) 169 [arXiv:0907.3923 [astro-ph.HE]].

- V. A. Acciari *et al.* (including D. Nieto) [The VERITAS, HESS and MAGIC Collaborations, the VLBA Monitoring Team], *Radio Imaging of the Very-High-Energy Gamma-Ray Emission Region in the Central Engine of a Radio Galaxy,* Science **325** (2009) 444-448. [arXiv:0908.0511 [astro-ph.HE]].

- H. Seta *et al.* (including D. Nieto) [The KANATA and MAGIC Collaboration], *Suzaku and Multi-wavelength Observations of OJ 287 during the Periodic Optical Outburst in 2007*, Publ. Astr. Soc. Jap. **61** (2009) 1011 [arXiv:0906.0234 [astro-ph.CO]].

- H. Anderhub *et al.* (including D. Nieto) [The MAGIC Collaboration], *Search for VHE γ-ray emission from the globular cluster M13 with the MAGIC telescope*, Astrophys. J. **702** (2009) 266-269.
[arXiv:0905.2427 [astro-ph.HE]].

- J. Albert *et al.* (including D. Nieto) [The MAGIC Collaboration], *MAGIC Observations of PG 1553+113 during a Multiwavelength Campaign in July 2006*, Astron. Astrophys. **493** (2009) 467,
[arXiv:0812.3037 [astro-ph]].

- I. Donnarumma *et al.* (including D. Nieto) [The AGILE, GASP-WEBT, MAGIC and VERITAS Collaborations], *The June 2008 flare of Markarian 421 from optical to TeV energies*, Astrophys. J. **691** (2009) L13-L19. [arXiv:0812.1500 [astro-ph]].

- H. Anderhub *et al.* (including D. Nieto) [The MAGIC Collaboration], *MAGIC upper limits to the VHE gamma-ray flux of 3C454.3 in high emission state*, Astron. Astrophys. **498** (2009) 83, [arXiv:0811.1680 [astro-ph]].

- E. Aliu *et al.* (including D. Nieto) [The MAGIC Collaboration], *Discovery of a very high energy gamma-ray signal from the 3C 66A/B region*, Astrophys. J. Lett. **692** (2009) L29 [arXiv:0810.4712 [astro-ph]].

- E. Aliu *et al.* (including D. Nieto) [The MAGIC Collaboration], *Improving the performance of the single-dish Cherenkov telescope MAGIC through the use of signal timing*, Astropart. Phys. **30** (2009) 293-305.
[arXiv:0810.3568 [astro-ph]].

- E. Aliu *et al.* (including D. Nieto) [The MAGIC Collaboration], *Upper limits on the VHE gamma-ray emission from the Willman 1 satellite galaxy with the MAGIC Telescope* , Astrophys. J. **697** (2009) 1299-1304. [arXiv:0810.3561 [astro-ph]].

- E. Aliu *et al.* (including D. Nieto) [The MAGIC Collaboration], *Observation of pulsed gamma-rays above 25 GeV from the Crab pulsar with MAGIC*, Science **322** (2008) 1221-1224. [arXiv:0809.2998 [astro-ph]].

- E. Aliu *et al.* (including D. Nieto) [The MAGIC Collaboration], *First bounds on the high-energy emission from isolated Wolf-Rayet binary systems*, Astrophys. J. **685** (2008) L71-L74. [arXiv:0808.1832 [astro-ph]].

- E. Aliu *et al.* (including D. Nieto) [The MAGIC Collaboration], *Very-High-Energy Gamma Rays from a Distant Quasar: How Transparent Is the Universe?*, Science **320** (2008) 1752. [arXiv:0807.2822 [astro-ph]].

- J. Albert *et al.* (including D. Nieto) [The MAGIC Collaboration], *Periodic very high energy gamma-ray emission from LS I +61 303 observed with the MAGIC telescope*, Astrophys. J. **693** (2009) 303-310. [arXiv:0806.1865 [astro-ph]].
- J. Albert *et al.* (including D. Nieto) [The MAGIC Collaboration], *MAGIC Observations of a 13-Day Flare Complex in M87 in February 2008*, Astrophys. J. **685** (2008) L23-L26. [arXiv:0806.0988 [astro-ph]].
- J. Albert *et al.* (including D. Nieto) [The MAGIC Collaboration], *Multi-wavelength (radio, X-ray and gamma-ray) observations of the gamma-ray binary LS I +61 303*, Astrophys. J. **684** (2008) 1351-1358. [arXiv:0801.3150 [astro-ph]].
- G. Tagliaferri *et al.* (including D. Nieto) [The MAGIC Collaboration], *Simultaneous multiwavelength observations of the blazar 1ES1959+650 at a low TeV flux*, Astrophys. J. **679** (2008) 1029
  [arXiv:0801.4029 [astro-ph]].
- J. Albert *et al.* (including D. Nieto) [The MAGIC Collaboration], *Upper limit for gamma-ray emission above 140-GeV from the dwarf spheroidal galaxy Draco*, Astrophys. J. **679** (2008) 428-431.
  [arXiv:0711.2574 [astro-ph]].
- J. Albert *et al.* (including D. Nieto) [The MAGIC Collaboration], *Implementation of the Random Forest Method for the Imaging Atmospheric Cherenkov Telescope MAGIC*, Nucl. Instrum. Meth. **A588** (2008) 424-432. [arXiv:0709.3719 [astro-ph]].
- J. Albert *et al.* (including D. Nieto) [The MAGIC Collaboration], J. Ellis *et al.*, *Probing Quantum Gravity using Photons from a flare of the active galactic nucleus Markarian 501 Observed by the MAGIC telescope*, Phys. Lett. **B668** (2008) 253-257. [arXiv:0708.2889 [astro-ph]].
- J. Albert *et al.* (including D. Nieto) [The MAGIC Collaboration], *Unfolding of differential energy spectra in the MAGIC experiment*, Nucl. Instrum. Meth. **A583** (2007) 494-506. [arXiv:0707.2453 [astro-ph]].
- J. Albert *et al.* (including D. Nieto) [The MAGIC Collaboration], *Systematic search for VHE gamma-ray emission from X-ray bright high-frequency BL Lac objects*, Astrophys. J. **681** (2008) 944-953.
  [arXiv:0706.4453 [astro-ph]].
- J. Albert *et al.* (including D. Nieto) [The MAGIC Collaboration], *MAGIC observations of the unidentified TeV gamma-ray source TeV J2032+4130*, Astrophys. J. **675** (2008) L25-L28.
  [arXiv:0801.2391 [astro-ph]].
- J. Albert *et al.* (including D. Nieto) [The MAGIC Collaboration], *VHE Gamma-Ray Observation of the Crab Nebula and Pulsar with MAGIC*, Astrophys. J. **674** (2008) 1037-1055. [arXiv:0705.3244 [astro-ph]].
- J. Albert *et al.* (including D. Nieto) [The MAGIC Collaboration], *Variable VHE gamma-ray emission from Markarian 501*, Astrophys. J. **669** (2007) 862-883. [arXiv:0702008 [astro-ph]].

- J. Albert *et al.* (including D. Nieto) [The MAGIC Collaboration], *FADC signal reconstruction for the MAGIC Telescope*, Nucl. Instrum. Meth. **A594** (2008) 407-419. [arXiv:0612385 [astro-ph]].

- J. Albert *et al.* (including D. Nieto) [The MAGIC Collaboration], *Discovery of Very High Energy gamma-rays from 1ES1011+496 at z=0.212*, Astrophys. J. **667** (2007) L21-L23. [arXiv:0706.4435 [astro-ph]].

- J. Albert *et al.* (including D. Nieto) [The MAGIC Collaboration], *Very High Energy Gamma-ray Radiation from the Stellar-mass Black Hole Cygnus X-1*, Astrophys. J. **665** (2007) L51 [arXiv:0706.1505 [astro-ph]].

- J. Albert *et al.* (including D. Nieto) [The MAGIC Collaboration], *Discovery of VHE Gamma Radiation from IC443 with the MAGIC Telescope*, Astrophys. J. **664** (2007) L87-L90. [arXiv:0705.3119 [astro-ph]].

C.2 Publications in non-refereed journals

- D. Nieto, N. Mirabal, *Willman 1: An X-ray shot in the dark with Chandra* (2011). [arXiv:1003.3745[astro-ph.CO]].

- N. Mirabal, D. Nieto, S. Pardo, *The exotic fraction among unassociated Fermi sources* (2010).
[arXiv:1007.2644 [astro-ph.HE]].

C.3 Public conferences contributions

- D. Nieto *et al.* [for the MAGIC Collaboration], *The search for galactic dark matter clumps with Fermi and MAGIC*, 32^{nd} International Cosmic Ray Conference, Beijing, China (2011). [arXiv:1109.5935 [astro-ph.HE]].

- D. Nieto *et al.* [for the CTA Consortium], *On the detectability of dwarf galaxies with the Cherenkov Telescope Array*, 32^{nd} International Cosmic Ray Conference, Beijing, China (2011).[arXiv:1111.2183[astro-ph.HE]].

- J. Aleksić, [...], D. Nieto [for the MAGIC Collaboration], *Segue 1: the best dark matter candidate dwarf galaxy surveyed by MAGIC*, 32^{nd} International Cosmic Ray Conference, Beijing, China (2011). [arXiv:1109.6781 [astro-ph.CO]].

- D. Nieto *et al.*, *A search for possible Dark Matter subhalos as IACT targets in the First Fermi Catalog* (poster), Third Fermi Symposium, Rome, Italy (2011). [arXiv:1110.4744[astro-ph.HE]].

- D. Nieto [for the MAGIC Collaboration], *Indirect Dark Matter Searches with MAGIC*, Ninth UCLA Symposium on Sources and Detection of Dark Matter and Dark Energy in the Universe, Marina del Rey CA (2010).

- D. Nieto and J. A. R. Cembranos, *Dark Matter: evidences, theories and searches*, Dark Matter Awareness Week, Universidad Complutense de Madrid (2010).

- D. Nieto and N. Mirabal, *An X-Ray search for the sterile neutrino in Willman-1* (poster), IX Spanish Society of Astronomy Meeting, Madrid (2010).
- D. Nieto [on behalf of the MAGIC Collaboration] *Indirect Dark Matter Searches with MAGIC*, IX Spanish Society of Astronomy Meeting, Madrid (2010).
- D. Nieto and N. Mirabal, *Willman-1 in X-rays*, Second MultiDark Workshop, IFCA Santander (2010).
- I. Oya (Author),[...],D. Nieto (co-Author) *et al.*, *Data Quality Check and On-Site Analysis of the MAGIC Telescope*, Highlights of Spanish Astrophysics V, (2010) 519.
- S. Lombardi (Author),[...], D. Nieto(Co-Author) *et al.* [for the MAGIC Collaboration], *Search for Dark Matter signatures with MAGIC-I and prospects for MAGIC Phase-II*, 31^{st} International Cosmic Ray Conference, Lódź (2009). [arXiv:0907.0738 [astro-ph.HE]].
- I. Reichardt (Author),[...], D. Nieto *et al.* [for the MAGIC Collaboration], *The MAGIC Data Center*, 31^{st} International Cosmic Ray Conference, Lódź (2009). [arXiv:0907.0968 [astro-ph.IM]].
- C. Malagon, J. A. Barrio, D. Nieto *et al.*, *Classification Methods for MAGIC Telescope Images on a Pixel-by-pixel base*, 30^{th} International Cosmic Ray Conference, **3** (2008) 1473-1476.
- C. Malagon, J. A. Barrio, D. S. Parcerisa, D. Nieto, *Representations and image classification methods for Cherenkov telescopes*, AIP Conf. Proc. **1018** (2008) 184-185.
- S. Lombardi (Author),[...], D. Nieto (Co-Author) *et al.* [for the MAGIC Collaboration], *Indirect Dark Matter searches with MAGIC Telescope*, Heidelberg Gamma-ray Symposium, (2008).

C.4 Internal MAGIC collaboration contributions

- I. Oya, D. Nieto *et al.*, *MAGIC On-Site Analysis Program*, MAGIC-TDAS **09-03** (2009).
- I. Oya, [...], D. Nieto *et al.*, *MAGIC Data Check Program*, MAGIC-TDAS **09-02** (2009).
- D. Nieto, *Report on the Unassociated Fermi Objects observations*, MAGIC Collaboration Meeting, Split (2010).
- D. Nieto, *Status of the On-Site Analysis*, MAGIC Collaboration Meeting, Split (2010).
- D. Nieto, *Introduction to the On-Site Analysis*, MAGIC Stereo Workshop, Dortmund (2010).
- D. Nieto, *Status of the On-Site Analysis*, MAGIC Collaboration Meeting, Munich (2010).

List of Figures

List of Tables

Acronyms

1FGL First Fermi Catalog. 143–145, 147–149, 155, 156, 160, 164, 166, 168, 183

2FGL Second Fermi Catalog. 158, 160, 183, 184

AGN Active Galactic Nuclei. 39, 42, 49, 51–53, 59, 60, 96, 119–121, 139, 142, 147, 173, 182

ATIC Advanced Thin Ionization Calorimeter. 33

BAO Baryon Acoustic Oscillations. 10, 12

BBN Big Bang Nucleosynthesis. 16, 25

Callisto CALibrate LIght Signals and Time Offsets. 72

CCM Concordance Cosmological Model. 8–15, 99

CIAO Chandra-XRO Interactive Analysis of Observations. 113, 117, 119, 120

CL Confidence Level. 30, 38, 93, 94, 108, 109, 125, 127, 156, 158, 159, 166, 167

CMB Cosmic Microwave Background. 10, 14–16, 24, 25, 47

cMSSM constrained Minimal Super-Symmetric Model. 18, 19, 21, 31, 129

COBE Cosmic Background Explorer. 10

CoG Center of Gravity. 73–76, 82

CTA Cherenkov Telescope Array. 171–179, 183–185

CU Crab Nebula Units. 87, 111, 123, 138, 181

DAQ Data Acquisition System. 66, 67, 78

dSph dwarf Spheroidal. 7, 13, 23, 24, 36–40, 60, 99–103, 128, 137–140, 142, 173, 176–179, 181–185

EAS Extended Atmospheric Shower. 56–58, 61, 62, 65

EBL Extragalactic Background Light. 39, 48, 49, 53, 54, 147, 160, 168

FADC Flash Analog to Digital Converter. 66, 69, 71

FLRW Friedman-Lemaitre-Robertson-Walker. 9

FoV Field of View. 57, 58, 64–66, 82, 83, 89, 97, 113, 121, 124, 146, 151–153, 159–162, 172, 173, 182, 184

GBM Gamma-ray Burst Monitor. 54, 58

GRB Gamma-Ray Burst. 44, 48, 53, 54, 58, 59

GST Gamma-ray Space Telescope. 56, 58, 59, 143, 145, 181

H.E.S.S. High Energy Stereoscopic System. 33, 37, 38, 49–51, 54, 57, 64, 92, 101, 171

HE High Energy. 37, 40, 49–51, 53–56, 59, 63, 142, 143, 145–149, 151, 158, 160, 166, 169, 181, 183

IACTs Imaging Atmospheric Cherenkov Telescopes. 60–62, 64, 101, 132, 137–139, 141–144, 147, 177, 181–183

IC Inverse Compton. 46, 50–52, 54, 95

IXO International X-ray Observatory. 140

LAT Large Area Telescope. 33, 39, 48–54, 56, 58–60, 101, 138, 141–153, 156, 158, 160–163, 166, 168, 169, 182–184

LSP Lightest Super-Symmetric Particle. 18, 19, 22, 26, 27, 129, 130

LUT Look-Up Table. 79, 83, 84, 154, 155, 163

MAGIC Major Atmospheric Imaging Cherenkov. 33, 37–39, 41, 49–54, 57, 61, 64–68, 72, 76, 78, 79, 82–88, 90–93, 95, 99, 101, 103, 104, 106–112, 121–131, 134, 136–138, 140, 141, 143, 148, 149, 151–169, 171, 181, 183, 184

MARS MAGIC Analysis and Reconstruction Software. 70, 76

MC Monte Carlo. 77, 79–81, 83–85, 87, 89, 91, 95, 105, 122, 124, 129, 154, 156, 171, 175, 178, 179, 184

Melibea MErge and Link Image parameter Before Energy Analysis. 81, 83

Merpp Merging and Preprocessing Program. 71

MOND Modified Newtonian Dynamics. 15

MSSM Minimal Super-Symmetric Model. 18, 19, 22

mSUGRA minimal SUper-GRAvity. 19, 21, 27, 38, 110–113, 128–133, 136–140, 181, 182

NSBL Night-Sky Background Light. 63, 67–69, 72, 79, 95, 105, 122, 153, 162

PAMELA Payload for Antimatter Matter Exploration and Light-nuclei Astrophysics. 33, 34, 135–137, 139, 182

PMT Photo-Multiplier Tube. 65, 66, 79, 95

PSF Point Spread Function. 78–80, 89, 90, 105, 107, 110, 126, 140, 145, 147, 154, 156, 157, 163, 165, 169, 177, 178

QE Quantum Efficiency. 65, 66, 95

RF Random Forest. 79–84, 105, 122, 154, 163

RMS Root Mean Squared. 73, 75, 83

SDSS Sloan Digital Sky Survey. 99–102, 118, 140, 183

SED Spectral Energy Distribution. 51–53, 70, 92

SEGUE Sloan Extension for Galaxy Understanding and Exploration. 102

Star STandard Analysis and Reconstruction. 76

SUSY Super-Symmetry. 129

TeVeS Tensor-Vector-Scalar gravity. 15

TS Test Statistics. 89, 90, 156, 163

UFO Unassociated Fermi Object. 142, 144–147, 151, 168, 169

VERITAS Very Energetic Radiation Imaging Telescope Array System. 49, 51, 52, 54, 57, 64, 101, 171

VHE Very High Energy. 38–40, 48–51, 53–55, 63, 68, 69, 71, 79, 87, 99, 101, 106, 113, 121, 125, 137, 138, 140–142, 147, 155, 156, 163, 168, 169, 181, 183–185

WIMP Weakly Interacting Massive Particle. 16, 25, 30–32, 36, 37, 39, 101, 110, 113, 132–134, 138, 139, 144, 149, 173–179

WMAP Wilkinson Microwave Anisotropy Probe. 10–12, 14, 19, 24, 32, 130, 131, 133–135, 137–139, 182

XRO X-Ray Observatory. 96, 99, 101, 113–119, 121, 139, 140, 145, 181, 182

XRT X-Ray Telescope. 145, 151–153, 158, 160–162, 166, 168, 169, 183, 184

ZA Zenith Angle. 77

References

[1] **MAGIC** Collaboration, E. Aliu *et. al.*, *MAGIC upper limits on the VHE gamma-ray emission from the satellite galaxy Willman 1*, *ApJ* **697** (2009) 1299–1304, [arXiv:0810.3561]. 3, 101, 135, 201, 204

[2] D. Nieto and N. Mirabal, *Willman 1: an X-ray shot in the dark with Chandra*, *ArXiv e-prints* (2011) [arXiv:1003.3745]. 3, 100, 101, 201, 205

[3] **MAGIC** Collaboration, J. Aleksić *et. al.*, *Searches for dark matter annihilation signatures in the Segue 1 satellite galaxy with the MAGIC-I telescope*, *JCAP* **6** (June, 2011) 35, [arXiv:1103.0477]. 3, 101, 178, 201, 209, 219

[4] D. Nieto, V. Martínez, N. Mirabal, J. A. Barrio, K. Satalecka, S. Pardo, and I. Lozano, *A search for possible dark matter subhalos as IACT targets in the First Fermi-LAT Source Catalog*, *III Fermi-LAT Symposium, Rome* (Oct., 2011) [arXiv:1110.4744]. 3, 215

[5] D. Nieto *et. al.*, *The search for galactic dark matter clump candidates with Fermi and MAGIC*, *ArXiv e-prints* (Sept., 2011) [arXiv:1109.5935]. 3, 215

[6] **CTA** Collaboration, D. Nieto *et. al.*, *Dark Matter Prospects for the Cherenkov Telescope Array*, *Proceedings of the 32nd International Cosmic Ray Conference* (2011) [arXiv:1111.2183]. 3, 220

[7] E. Öpik, *Selective absorption of light in space, and the dynamics of the universe*, *Bull. de la Soc. Astr. de Russie* **21** (1915) 150. 5

[8] J. C. Kapteyn, *First Attempt at a Theory of the Arrangement and Motion of the Sidereal System*, *ApJ* **55** (1922) 302. 5

[9] J. H. Jeans, *The motions of stars in a Kapteyn universe*, **82** (Jan., 1922) 122–132. 5

[10] F. Zwicky, *Die Rotverschiebung von extragalaktischen Nebeln*, *Helvetica Physica Acta* **6** (1933) 110–127. 5, 6

[11] K. G. Begeman, A. H. Broeils, and R. H. Sanders, *Extended rotation curves of spiral galaxies - Dark haloes and modified dynamics*, **249** (Apr., 1991) 523–537. 6, 196

[12] J. N. Bahcall, C. Flynn, and A. Gould, *Local dark matter from a carefully selected sample*, *ApJ* **389** (Apr., 1992) 234–250. 7

[13] L. E. Strigari, S. M. Koushiappas, J. S. Bullock, M. Kaplinghat, J. D. Simon, M. Geha, and B. Willman, *The Most Dark-Matter-dominated Galaxies: Predicted Gamma-Ray Signals from the Faintest Milky Way Dwarfs*, **678** (2008) 614. 7, 38, 99, 100, 101, 110, 201, 203

[14] P. Schneider, J. Ehlers, and E. E. Falco, *Gravitational Lenses*. Springer–Verlag, 1992. 7, 196

[15] L. A. Moustakas *et. al.*, *Strong gravitational lensing probes of the particle nature of dark matter*, in *astro2010: The Astronomy and Astrophysics Decadal Survey*, vol. 2010 of *Astronomy*, p. 214, 2009. arXiv:0902.3219. 7

[16] N. Kaiser and G. Squires, *Mapping the dark matter with weak gravitational lensing*, *ApJ* **404** (Feb., 1993) 441–450. 8

[17] J. Wambsganss, *Microlensing Search for Dark Matter at all Mass Scales*, in *Gravitational Lensing Impact on Cosmology* (Y. Mellier & G. Meylan, ed.), vol. 225 of *IAU Symposium*, pp. 321–332, June, 2005. 8

[18] S. Weinberg, *Cosmology*. Oxford University Press, 2008. 8, 196

[19] G. Gamow, *The Evolution of the Universe*, **162** (Oct., 1948) 680–682. 10

[20] A. A. Penzias and R. W. Wilson, *A Measurement of Excess Antenna Temperature at 4080 Mc/s.*, *ApJ* **142** (July, 1965) 419–421. 10

[21] NASA, "WMAP Home Page." http://map.gsfc.nasa.gov/, 2011. 10

[22] ESA, "Plank Home Page." http://www.rssd.esa.int/index.php?project=Planck, 2011. 10

[23] N. Jarosik *et. al.*, *Seven-year Wilkinson Microwave Anisotropy Probe (WMAP) Observations: Sky Maps, Systematic Errors, and Basic Results*, *ApJS* **192** (Feb., 2011) 14–+, [arXiv:1001.4744]. 11

[24] D. Larson *et. al.*, *Seven-year Wilkinson Microwave Anisotropy Probe (WMAP) Observations: Power Spectra and WMAP-derived Parameters*, *ApJS* **192** (Feb., 2011) 16–+, [arXiv:1001.4635]. 11

[25] **SDSS** Collaboration, W. J. Percival *et. al.*, *Baryon acoustic oscillations in the Sloan Digital Sky Survey Data Release 7 galaxy sample*, **401** (Feb., 2010) 2148–2168, [arXiv:0907.1660]. 10

[26] **Supernova Cosmology Project** Collaboration, P. Astier *et. al.*, *The Supernova Legacy Survey: measurement of Ω_M, Ω_Λ and w from the first year data set*, *A&A* **447** (Feb., 2006) 31–48, [astro-ph/0510447]. 10

[27] **Supernova Cosmology Project** Collaboration, M. Kowalski *et. al.*, *Improved Cosmological Constraints from New, Old, and Combined Supernova Data Sets*, *ApJ* **686** (Oct., 2008) 749–778, [arXiv:0804.4142]. 10

[28] M. Hicken *et. al.*, *Improved Dark Energy Constraints from ˜100 New CfA Supernova Type Ia Light Curves*, *ApJ* **700** (Aug., 2009) 1097–1140, [arXiv:0901.4804]. 10

[29] E. Komatsu *et. al.*, *Seven-year Wilkinson Microwave Anisotropy Probe (WMAP) Observations: Cosmological Interpretation*, "" **192** (Feb., 2011) 18–+, [arXiv:1001.4538]. 11, 12, 130, 133, 196

[30] S. Dodelson, *Modern Cosmology*. Academic Press, 2003. 12

[31] J. R. Primack, *Whatever Happened to Hot Dark Matter?*, *ArXiv Astrophysics e-prints* (Dec., 2001) [astro-ph/0112336]. 13

[32] V. Springel, C. S. Frenk, and S. D. M. White, *The large-scale structure of the Universe*, *Nature* **440** (Apr., 2006) 1137–1144, [astro-ph/0604561]. 13

[33] M. Götz and J. Sommer-Larsen, *Galaxy formation: Warm dark matter, missing satellites, and the angular momentum problem*, **284** (Apr., 2003) 341–344, [astro-ph/0210599]. 13, 23

[34] J. R. Primack, *Cosmology: small-scale issues*, *New Journal of Physics* **11** (Oct., 2009) 105029, [arXiv:0909.2247]. 13

[35] R. M. Dunstan, K. N. Abazajian, E. Polisensky, and M. Ricotti, *The Halo Model of Large Scale Structure for Warm Dark Matter*, *ArXiv e-prints* (Sept., 2011) [arXiv:1109.6291]. 13

[36] V. Springel, S. D. M. White, A. Jenkins, C. S. Frenk, N. Yoshida, L. Gao, J. Navarro, R. Thacker, D. Croton, J. Helly, J. A. Peacock, S. Cole, P. Thomas, H. Couchman, A. Evrard, J. Colberg, and F. Pearce, *Simulations of the formation, evolution and clustering of galaxies and quasars*, *Nature* **435** (June, 2005) 629–636, [astro-ph/0504097]. 13

[37] M. Zemp, *The Structure of Cold Dark Matter Halos: Recent Insights from High Resolution Simulations*, *Modern Physics Letters A* **24** (2009) 2291–2305, [arXiv:0909.4298]. 13

[38] V. Springel, J. Wang, M. Vogelsberger, A. Ludlow, A. Jenkins, A. Helmi, J. F. Navarro, C. S. Frenk, and S. D. M. White, *The Aquarius Project: the subhaloes of galactic haloes*, *Mon.Not.Roy.Astron.Soc.* **391** (Dec., 2008) 1685–1711, [arXiv:0809.0898]. 13, 36, 99, 209

[39] **The 2dF Galaxy Redshift Survey** Collaboration, "The 2dF Galaxy Redshift Survey Home Page." http://magnum.anu.edu.au/~TDFgg/, 2011. 14

[40] **The Sloan Digital Sky Survey** Collaboration, "The SDSS Home Page." http://www.sdss.org, 2011. 14, 99, 201

[41] J. Huchra, M. Davis, D. Latham, and J. Tonry, *A survey of galaxy redshifts. IV - The data*, *ApJS* **52** (June, 1983) 89–119. 14

[42] The Virgo Consortium, "The Millenium Simulation Home Page." http://www.mpa-garching.mpg.de/millennium/, 2011. 14

[43] L. Perivolaropoulos, *LCDM: Triumphs, Puzzles and Remedies*, *ArXiv e-prints* (Apr., 2011) [arXiv:1104.0539]. 13

[44] M. Milgrom, *A modification of the Newtonian dynamics as a possible alternative to the hidden mass hypothesis.*, **270** (1983) 365–370. 15

[45] J. D. Bekenstein, *Erratum: Relativistic gravitation theory for the modified Newtonian dynamics paradigm [Phys. Rev. D 70, 083509 (2004)]*, *Phys.Rev.D* **71** (Mar., 2005) 069901. 15

[46] K. Gödel, *An Example of a New Type of Cosmological Solutions of Einstein's Field Equations of Gravitation*, *Reviews of Modern Physics* **21** (July, 1949) 447–450. 15

[47] F. Hoyle, G. Burbidge, and J. V. Narlikar, *The Basic Theory Underlying the Quasi-Steady-State Cosmology*, *Royal Society of London Proceedings Series A* **448** (Feb., 1995) 191–212. 15

[48] C. H. Brans, *The roots of scalar-tensor theory: an approximate history*, *ArXiv General Relativity and Quantum Cosmology e-prints* (June, 2005) [gr-qc/0506063]. 15

[49] A. Blanchard, M. Douspis, M. Rowan-Robinson, and S. Sarkar, *An alternative to the cosmological "concordance model"*, **412** (Dec., 2003) 35–44, [astro-ph/0304237]. 15

[50] M. Taoso, G. Bertone, and A. Masiero, *Dark matter candidates: a ten-point test*, *JCAP* **3** (Mar., 2008) 22–+, [arXiv:0711.4996]. 15, 197

[51] K. M. Zurek, *Multicomponent dark matter*, *Phys.Rev.D* **79** (June, 2009) 115002–+, [arXiv:0811.4429]. 15

[52] L. Roszkowski, *Particle dark matter - A theorist's perspective*, *Pramana* **62** (Feb., 2004) 389–+, [hep-ph/0404052]. 17

[53] R. J. Scherrer and M. S. Turner, *On the relic, cosmic abundance of stable, weakly interacting massive particles*, *Phys.Rev.D* **33** (Mar., 1986) 1585–1589. 16

[54] J. Ellis, *Particle Candidates for Dark Matter*, *Physica Scripta Volume T* **85** (2000) 221–230, [astro-ph/9812211]. 17

[55] L. Bergström, *Non-baryonic dark matter: observational evidence and detection methods*, *Reports on Progress in Physics* **63** (May, 2000) 793–841, [hep-ph/0002126]. 17

[56] G. Bertone, D. Hooper, and J. Silk, *Particle dark matter: Evidence, candidates and constraints*, *Phys.Rept.* **405** (2005) 279–390, [hep-ph/0404175]. 17, 19, 20

[57] B. Gianfranco, ed., *Particle Dark Matter*. Cambridge University Press, first published ed., 2010. 17, 24, 26, 29, 174, 216

[58] P. Fayet and S. Ferrara, *Supersymmetry*, *Phys. Rept.* **32** (1977) 249–334. 17, 197

[59] H. P. Nilles, *Supersymmetry, Supergravity and Particle Physics*, *Phys. Rep.* **110** (1984) 1–162. 17, 19, 197

[60] E. Witten, *Mass hierarchies in supersymmetric theories*, *Phys.Lett.B* **105** (1981), no. 4 267 – 271. 17, 197

[61] J. Ellis, S. Kelley, and D. V. Nanopoulos, *Constraints from gauge coupling unification on the scale of supersymmetry breaking*, *Phys.Lett.B* **287** (Aug., 1992) 95–100, [hep-ph/9206203]. 18, 197

[62] J. R. Ellis, J. Hagelin, D. V. Nanopoulos, K. A. Olive, and M. Srednicki, *Supersymmetric Relics from the Big Bang*, *Nucl.Phys.* **B238** (1984) 453–476. 18, 198

[63] J. Edsjö, *Aspects of Neutrino Detection of Neutralino Dark Matter*. PhD thesis, Uppsala Univ. (preprint hep-ph/9704384), (1997), Oct., 1997. 18, 20

[64] **Super-Kamiokande** Collaboration, H. Nishino *et. al.*, *Search for Proton Decay via $pe^+\pi^0$ and $p\mu^+\pi^0$ in a Large Water Cherenkov Detector*, **102** (Apr., 2009) 141801, [arXiv:0903.0676]. 18

[65] A. H. Chamseddine, R. L. Arnowitt, and P. Nath, *Locally Supersymmetric Grand Unification*, **49** (1982) 970. 19, 198

[66] J. Ellis, T. Falk, K. A. Olive, and Y. Santoso, *Exploration of the MSSM with non-universal Higgs masses*, *Nuclear Physics B* **652** (Mar., 2003) 259–347, [hep-ph/0210205]. 19

[67] J. Ellis, K. A. Olive, and P. Sandick, *What if supersymmetry breaking appears below the GUT scale?*, *Phys.Lett.B* **642** (Nov., 2006) 389–399, [hep-ph/0607002]. 19

[68] C. F. Berger, J. S. Gainer, J. L. Hewett, and T. G. Rizzo, *Supersymmetry without prejudice*, *Journal of High Energy Physics* **2** (Feb., 2009) 23, [arXiv:0812.0980]. 19

[69] O. Buchmueller, R. Cavanaugh, D. Colling, A. de Roeck, M. J. Dolan, J. R. Ellis, H. Flächer, S. Heinemeyer, G. Isidori, D. Martínez Santos, K. A. Olive, S. Rogerson, F. J. Ronga, and G. Weiglein, *Supersymmetry and dark matter in light of LHC 2010 and XENON100 data*, *European Physical Journal C* **71** (Aug., 2011) 1722–+, [arXiv:1106.2529]. 21

[70] T. Bringmann, L. Bergstrom, and J. Edsjo, *New Gamma-Ray Contributions to Supersymmetric Dark Matter Annihilation*, *JHEP* **0801** (2008) 049, [arXiv:0710.3169]. 21, 141

[71] **Particle Data Group** Collaboration, K. Nakamura *et. al.*, *Review of particle physics*, *J.Phys.G* **G37** (2010) 075021. 22, 42, 43, 210, 216

[72] T. Falk, K. A. Olive, and M. Srednicki, *Heavy sneutrinos as dark matter*, *Phys.Lett.B* **339** (Nov., 1994) 248–251, [hep-ph/9409270]. 22

[73] J. L. Feng, *Dark Matter Candidates from Particle Physics and Methods of Detection*, *Ann.Rev.Astron.Astrophys.* **48** (2010) 495, [arXiv:1003.0904]. 22

[74] K.-Y. Choi, L. Covi, J. E. Kim, and L. Roszkowski, *Axino Cold Dark Matter Revisited*, *ArXiv e-prints* (Aug., 2011) [arXiv:1108.2282]. 22

[75] T. Asaka, S. Blanchet, and M. Shaposhnikov, *The νMSM, dark matter and neutrino masses [rapid communication]*, *Phys.Lett.B* **631** (Dec., 2005) 151–156, [hep-ph/0503065]. 22, 197

[76] S. Dodelson and L. M. Widrow, *Sterile-neutrinos as dark matter*, **72** (1994) 17–20, [hep-ph/9303287]. 23

[77] X. Shi and G. M. Fuller, *New Dark Matter Candidate: Nonthermal Sterile Neutrinos*, **82** (Apr., 1999) 2832–2835, [astro-ph/9810076]. 23

[78] T. Asaka and M. Shaposhnikov, *The nuMSM, dark matter and baryon asymmetry of the universe*, *Phys.Lett.B* **620** (2005) 17–26, [hep-ph/0505013]. 23

[79] A. Dolgov and S. Hansen, *Massive sterile neutrinos as warm dark matter*, *Astropart.Phys.* **16** (2002) 339–344, [hep-ph/0009083]. 23, 114, 197

[80] P. B. Pal and L. Wolfenstein, *Radiative decays of massive neutrinos*, *Phys. Rev. D* **25** (Feb, 1982) 766–773. 23, 197

[81] K. Abazajian, G. M. Fuller, and W. H. Tucker, *Direct detection of warm dark matter in the X-ray*, *ApJ* **562** (2001) 593–604, [astro-ph/0106002]. 23, 114, 121, 197, 205

[82] H. Yuksel, J. F. Beacom, and C. R. Watson, *Strong Upper Limits on Sterile Neutrino Warm Dark Matter*, **101** (2008) 121301, [arXiv:0706.4084]. 23, 114

[83] A. Boyarsky, O. Ruchayskiy, D. Iakubovskyi, M. G. Walker, S. Riemer-Sorensen, *et. al.*, *Searching for dark matter in X-rays: how to check the dark matter origin of a spectral feature*, *MNRAS* **407** (2010) 1188–1202, [arXiv:1001.0644]. 23, 101, 114, 117, 201

[84] M. Loewenstein, A. Kusenko, and P. L. Biermann, *New Limits on Sterile Neutrinos from Suzaku Observations of the Ursa Minor Dwarf Spheroidal Galaxy*, **700** (2009) 426–435, [arXiv:0812.2710]. 23, 101, 114, 201

[85] N. Mirabal, *Swift observation of Segue 1: constraints on sterile neutrino parameters in the darkest galaxy*, *Mon.Not.Roy.Astron.Soc.* **409** (Nov., 2010) L128–L131, [arXiv:1010.4706]. 23, 101, 114, 201

[86] M. Loewenstein and A. Kusenko, *Dark Matter Search Using Chandra Observations of Willman 1, and a Spectral Feature Consistent with a Decay Line of a 5 keV Sterile Neutrino*, **714** (2010) 652–662, [arXiv:0912.0552]. 23, 101, 114, 116, 117, 201, 205

[87] A. Boyarsky, O. Ruchayskiy, and D. Iakubovskyi, *A lower bound on the mass of dark matter particles*, *JCAP* **3** (Mar., 2009) 5–+, [arXiv:0808.3902]. 23

[88] M. Viel, G. D. Becker, J. S. Bolton, M. G. Haehnelt, M. Rauch, and W. L. W. Sargent, *How Cold Is Cold Dark Matter? Small-Scales Constraints from the Flux Power Spectrum of the High-Redshift Lyman-α Forest*, **100** (Feb., 2008) 041304–+, [arXiv:0709.0131]. 23

[89] S. Fukuda *et. al.*, *Determination of solar neutrino oscillation parameters using 1496 days of Super-Kamiokande-I data*, *Phys.Lett.B* **539** (July, 2002) 179–187, [hep-ex/0205075]. 24

[90] O. Klein, *On the problem of unity in physics*, *Sitzungsber. Preuss. Akad. Wiss. Berlin (Math. Phys.)* **1921** (1921) 966–972. 24

[91] O. Klein, *Quantum theory and five-dimensional theory of relativity*, *Z. Phys.* **37** (1926) 895–906. 24

[92] T. Appelquist, H. Cheng, and B. A. Dobrescu, *Bounds on universal extra dimensions*, *Phys.Rev.D* **64** (Aug., 2001) 035002, [hep-ph/0012100]. 25

[93] G. Servant and T. M. P. Tait, *Is the lightest Kaluza-Klein particle a viable dark matter candidate?*, *Nucl.Phys.B* **650** (Feb., 2003) 391–419, [hep-ph/0206071]. 25

[94] R. D. Peccei and H. R. Quinn, *CP conservation in the presence of pseudoparticles*, **38** (June, 1977) 1440–1443. 25

[95] M. A. Sánchez-Conde, D. Paneque, E. Bloom, F. Prada, and A. Domínguez, *Hints of the existence of axionlike particles from the gamma-ray spectra of cosmological sources*, *Phys.Rev.D* **79** (June, 2009) 123511–+, [arXiv:0905.3270]. 25, 39

[96] M. Schmaltz and D. Tucker-Smith, *Little Higgs Theories*, *Annual Review of Nuclear and Particle Science* **55** (Dec., 2005) 229–270, [hep-ph/0502182]. 25

[97] W. Shepherd, T. M. P. Tait, and G. Zaharijas, *Bound states of weakly interacting dark matter*, *Phys.Rev.D* **79** (Mar., 2009) 055022–+, [arXiv:0901.2125]. 25

[98] J. March-Russell and S. M. West, *WIMPonium and boost factors for indirect dark matter detection*, *Phys.Lett.B* **676** (June, 2009) 133–139, [arXiv:0812.0559]. 25

[99] J. L. Feng, A. Rajaraman, and F. Takayama, *Superweakly Interacting Massive Particles*, **91** (July, 2003) 011302–+, [hep-ph/0302215]. 25

[100] J. L. Feng and J. Kumar, *Dark-Matter Particles without Weak-Scale Masses or Weak Interactions*, **101** (Dec., 2008) 231301–+, [arXiv:0803.4196]. 25

[101] E. W. Kolb, D. J. H. Chung, and A. Riotto, *WIMPZILLAS!*, in *Dark matter in Astrophysics and Particle Physics* (H. V. Klapdor-Kleingrothaus & L. Baudis, ed.), pp. 592–+, 1999. hep-ph/9810361. 26

[102] L. Hui and E. D. Stewart, *Superheavy dark matter from thermal inflation*, *Phys.Rev.D* **60** (July, 1999) 023518–+, [hep-ph/9812345]. 26

[103] V. Berezinsky, M. Kachelrieß, and A. Vilenkin, *Ultrahigh energy cosmic rays without greisen-zatsepin-kuzmin cutoff*, **79** (Dec, 1997) 4302–4305. 26

[104] J. A. Cembranos, A. Dobado, and A. L. Maroto, *Brane-World Dark Matter*, **90** (June, 2003) 241301–+, [hep-ph/0302041]. 26

[105] J. A. R. Cembranos, J. L. Diaz-Cruz, and L. Prado, *Impact of DM direct searches and the LHC analyses on branon phenomenology*, *ArXiv e-prints* (Oct., 2011) [arXiv:1110.0542]. 26

[106] E. A. Baltz, M. Battaglia, M. E. Peskin, and T. Wizansky, *Determination of dark matter properties at high-energy colliders*, *Phys.Rev.D* **74** (Nov., 2006) 103521, [hep-ph/0602187]. 27

[107] E. O. of Nuclear Research, "LHC Homepage." http://public.web.cern.ch/public/en/LHC/LHC-en.html, 2011. 27

[108] European Organization of Nuclear Research, "ATLAS Homepage." http://www.atlas.ch/, 2011. 27

[109] European Organization of Nuclear Research, "CMS Homepage." http://cms.web.cern.ch/, 2011. 27

[110] ATLAS Collaboration, *Search for new phenomena in final states with large jet multiplicities and missing transverse momentum using sqrt(s)=7 TeV pp collisions with the ATLAS detector*, *ArXiv e-prints* (Oct., 2011) [arXiv:1110.2299]. 27

[111] D. G. Cerdeño and A. M. Green, *Direct detection of WIMPs*, pp. 347–+. Cambridge University Press, 2010. 28

[112] **IGEX** Collaboration, Irastorza *et. al.*, *Present Status of Igex Dark Matter Search at Canfranc Underground Laboratory*, in *Identification of Dark Matter* (N. J. C. Spooner & V. Kudryavtsev, ed.), pp. 308–313, Mar., 2003. astro-ph/0211535. 29

[113] **TEXONO** Collaboration, S. T. Lin *et. al.*, *New limits on spin-independent and spin-dependent couplings of low-mass WIMP dark matter with a germanium detector at a threshold of 220 eV*, *ArXiv e-prints* (Dec., 2007) [arXiv:0712.1645]. 29

[114] **CoGeNT** Collaboration, C. E. Aalseth *et. al.*, *Results from a Search for Light-Mass Dark Matter with a p-Type Point Contact Germanium Detector*, *Phys.Rev.Lett* **106** (Apr., 2011) 131301, [arXiv:1002.4703]. 29, 30

[115] **DAMA/LIBRA** Collaboration, R. Bernabei *et. al.*, *First results from DAMA/LIBRA and the combined results with DAMA/NaI*, *European Physical Journal C* **56** (Aug., 2008) 333–+, [arXiv:0804.2741]. 29, 30

[116] **CDMS** Collaboration, Z. Ahmed *et. al.*, *Search for inelastic dark matter with the CDMS II experiment*, *Phys.Rev.D* **83** (June, 2011) 112002–+, [arXiv:1012.5078]. 29

[117] **EDELWEISS** Collaboration, E. Armengaud *et. al.*, *Final results of the EDELWEISS-II WIMP search using a 4-kg array of cryogenic germanium detectors with interleaved electrodes*, *Phys.Lett.B* **702** (Aug., 2011) 329–335, [arXiv:1103.4070]. 29

[118] **CRESST** Collaboration, G. Angloher *et. al.*, *Results from 730 kg days of the CRESST-II Dark Matter Search*, *ArXiv e-prints* (Sept., 2011) [arXiv:1109.0702]. 29

[119] **ROSEBUD** Collaboration, J. Amaré *et. al.*, *Recent developments on scintillating bolometers for WIMP searches: ROSEBUD status*, *J.Phys.Conf.Series* **39** (May, 2006) 133–135. 29

[120] **XMASS** Collaboration, Y. Kim *et. al.*, *The status and background considerations of XMASS experiment*, *AIP Conf.Proc.* **897** (2007) 79–84. 29

[121] **DEAP-CLEAN** Collaboration, M. Boulay *et. al.*, *Dark matter search at SNOLAB with DEAP-1 and DEAP/CLEAN-3600*, *J.Phys.Conf.Series* **136** (2008) 042081. 29

[122] **XENON100** Collaboration, E. Aprile *et. al.*, *First Dark Matter Results from the XENON100 Experiment*, *Phys.Rev.Lett* **105** (2010) 131302, [arXiv:1005.0380]. 29

[123] **ZEPLIN** Collaboration, D. Y. Akimov *et. al.*, *WIMP-nucleon cross-section results from the second science run of ZEPLIN-III*, *ArXiv e-prints* (Oct., 2011) [arXiv:1110.4769]. 29

[124] **WArP** Collaboration, R. Brunetti *et. al.*, *WARP liquid argon detector for dark matter survey*, **49** (May, 2005) 265–269, [astro-ph/0405342]. 29

[125] C. Regenfus *et. al.*, *The argon dark matter experiment (ArDM)*, *J.Phys.Conf.Series* **203** (Jan., 2010) 012024, [arXiv:0912.2962]. 29

[126] **DRIFT** Collaboration, E. Daw, A. Dorofeev, J. Fox, J.-L. Gauvreau, C. Ghag, *et. al.*, *The DRIFT Dark Matter Experiments*, arXiv:1110.0222. * Temporary entry *. 29

[127] **DMTPC** Collaboration, S. Ahlen, J. Battat, T. Caldwell, C. Deaconu, D. Dujmic, *et. al.*, *First Dark Matter Search Results from a Surface Run of the 10-L DMTPC Directional Dark Matter Detector*, *Phys.Lett.B* **695** (2011) 124–129, [arXiv:1006.2928]. 29

[128] **MIMAC** Collaboration, D. Santos, J. Billard, G. Bosson, J. Bouly, O. Bourrion, *et. al.*, *MIMAC : A micro-tpc matrix for directional detection of dark matter*, *J.Phys.Conf.Ser.* **309** (2011) 012014, [arXiv:1102.3265]. * Temporary entry *. 29

[129] **NEWAGE** Collaboration, K. Miuchi, H. Nishimura, K. Hattori, N. Higashi, C. Ida, *et. al.*, *First underground results with NEWAGE-0.3a direction-sensitive dark matter detector*, *Phys.Lett.* **B686** (2010) 11–17, [arXiv:1002.1794]. 29

[130] **COUPP** Collaboration, E. Ramberg *et. al.*, *Developing a 60 kg bubble chamber for dark matter detection*, *Nucl.Instrum.Meth.A* **623** (Nov., 2010) 454–456. 29

[131] **EURECA** Collaboration, H. Kraus *et. al.*, *Eureca the european future of dark matter searches with cryogenic detectors*, *Nuclear Physics B - Proceedings Supplements* **173** (2007), no. 0 168 – 171. 29

[132] **DARWIN** Collaboration, L. Baudis *et. al.*, *DARWIN: dark matter WIMP search with noble liquids*, in *Proceedings of Identification of Dark Matter 2010 (IDM 2010)*, 2010. arXiv:1012.4764. 29

[133] R. Bernabei *et. al.*, *New results from DAMA/LIBRA*, *European Physical Journal C* **67** (May, 2010) 39–49, [arXiv:1002.1028]. 30

[134] C. E. Aalseth *et. al.*, *Search for an Annual Modulation in a p-Type Point Contact Germanium Dark Matter Detector*, *Phys.Rev.Lett* **107** (Sept., 2011) 141301–+, [arXiv:1106.0650]. 30

[135] T. Schwetz and J. Zupan, *Dark matter attempts for CoGeNT and DAMA*, *JCAP* **8** (Aug., 2011) 8–+, [arXiv:1106.6241]. 30

[136] M. Farina, D. Pappadopulo, A. Strumia, and T. Volansky, *Can CoGeNT and DAMA Modulations Be Due to Dark Matter?*, *ArXiv e-prints* (July, 2011) [arXiv:1107.0715]. 30

[137] K. Blum, *DAMA vs. the annually modulated muon background*, *ArXiv e-prints* (Oct., 2011) [arXiv:1110.0857]. 30

[138] **XENON100** Collaboration, E. Aprile *et. al.*, *Dark Matter Results from 100 Live Days of XENON100 Data*, *ArXiv e-prints* (Apr., 2011) [arXiv:1104.2549]. 31

[139] T. A. Porter, R. P. Johnson, and P. W. Graham, *Dark Matter Searches with Astroparticle Data*, *ArXiv e-prints* (Apr., 2011) [arXiv:1104.2836]. 31

[140] D. P. Finkbeiner, *Microwave Interstellar Medium Emission Observed by the Wilkinson Microwave Anisotropy Probe*, *ApJ* **614** (Oct., 2004) 186–193, [astro-ph/0311547]. 32

[141] D. P. Finkbeiner, *WMAP Microwave Emission Interpreted as Dark Matter Annihilation in the Inner Galaxy*, *ArXiv Astrophysics e-prints* (Sept., 2004) [astro-ph/0409027]. 32

[142] M. Kaplinghat, D. J. Phalen, and K. M. Zurek, *Pulsars as a source of the WMAP haze*, *JCAP* **12** (Dec., 2009) 10, [arXiv:0905.0487]. 32

[143] S. Colafrancesco, S. Profumo, and P. Ullio, *Detecting dark matter WIMPs in the Draco dwarf: A multiwavelength perspective*, *Phys.Rev.D* **75** (Jan., 2007) 023513, [astro-ph/0607073]. 32

[144] T. Linden, D. Hooper, and F. Yusef-Zadeh, *Dark Matter and Synchrotron Emission from Galactic Center Radio Filaments*, *ApJ* **741** (Nov., 2011) 95, [arXiv:1106.5493]. 32

[145] J. A. R. Cembranos, A. de La Cruz-Dombriz, A. Dobado, R. A. Lineros, and A. L. Maroto, *Photon spectra from WIMP annihilation*, *"Phys.Rev.D"* **83** (Apr., 2011) 083507–+, [hep-ph/1009.4936]. 32, 132, 144, 156, 174, 176, 210, 216

[146] R. Essig, N. Sehgal, and L. E. Strigari, *Bounds on Cross-sections and Lifetimes for Dark Matter Annihilation and Decay into Charged Leptons from Gamma-ray Observations of Dwarf Galaxies*, *Phys.Rev.* **D80** (2009) 023506, [hep-ph/0902.4750]. 32, 132

[147] F. Halzen and D. Hooper, *The indirect search for dark matter with IceCube*, *New Journal of Physics* **11** (Oct., 2009) 105019, [arXiv:0910.4513]. 33, 39

[148] **IceCube** Collaboration, R. Abbasi *et. al.*, *Search for dark matter from the Galactic halo with the IceCube Neutrino Telescope*, *Phys.Rev.D* **84** (July, 2011) 022004, [arXiv:1101.3349]. 33

[149] B. J. Teegarden *et. al.*, *INTEGRAL SPI Limits on Electron-Positron Annihilation Radiation from the Galactic Plane*, *ApJ* **621** (Mar., 2005) 296–300, [astro-ph/0410354]. 33

[150] N. Prantzos, C. Boehm, A. M. Bykov, R. Diehl, K. Ferrière, N. Guessoum, P. Jean, J. Knoedlseder, A. Marcowith, I. V. Moskalenko, A. Strong, and G. Weidenspointner, *The 511 keV emission from positron annihilation in the Galaxy*, *Reviews of Modern Physics* **83** (July, 2011) 1001–1056, [arXiv:1009.4620]. 33

[151] J. Chang, J. Adams, H. Ahn, G. Bashindzhagyan, M. Christl, *et. al.*, *An excess of cosmic ray electrons at energies of 300-800 GeV*, *Nature* **456** (2008) 362–365. 33, 34

[152] **MAGIC** Collaboration, D. Borla Tridon *et. al.*, *Measurement of the cosmic electron plus positron spectrum with the MAGIC telescopes*, *ArXiv e-prints* (Oct., 2011) [arXiv:1110.4008]. 33

[153] **PAMELA** Collaboration, O. Adriani *et. al.*, *An anomalous positron abundance in cosmic rays with energies 1.5-100 GeV*, *Nature* **458** (2009) 607–609, [astro-ph/0810.4995]. 33, 34, 135

[154] M. Cirelli, M. Kadastik, M. Raidal, and A. Strumia, *Model-independent implications of the e+-, anti-proton cosmic ray spectra on properties of Dark Matter*, *Nucl.Phys.* **B813** (2009) 1–21, [hep-ph/0809.2409]. 33, 135

[155] M. Kadastik, M. Raidal, and A. Strumia, *Enhanced anti-deuteron Dark Matter signal and the implications of PAMELA*, *Phys.Lett.B* **683** (Jan., 2010) 248–254, [arXiv:0908.1578]. 33

[156] A. V. Kravtsov, A. A. Klypin, J. S. Bullock, and J. R. Primack, *The Cores of dark matter dominated galaxies: Theory versus observations*, **502** (1998) 48, [astro-ph/9708176]. 35

[157] M. Persic, P. Salucci, and F. Stel, *The Universal rotation curve of spiral galaxies: 1. The Dark matter connection*, *Mon.Not.Roy.Astron.Soc.* **281** (1996) 27, [astro-ph/9506004]. 35

[158] J. F. Navarro, C. S. Frenk, and S. D. White, *A Universal density profile from hierarchical clustering*, **490** (1997) 493–508, [astro-ph/9611107]. 36

[159] B. Moore, T. R. Quinn, F. Governato, J. Stadel, and G. Lake, *Cold collapse and the core catastrophe*, *Mon.Not.Roy.Astron.Soc.* **310** (1999) 1147–1152, [astro-ph/9903164]. 36, 99

[160] J. F. Navarro, A. Ludlow, V. Springel, J. Wang, M. Vogelsberger, S. D. M. White, A. Jenkins, C. S. Frenk, and A. Helmi, *The diversity and similarity of simulated cold dark matter haloes*, *Mon.Not.Roy.Astron.Soc.* **402** (Feb., 2010) 21–34, [arXiv:0810.1522]. 36

[161] J. Hisano, S. Matsumoto, and M. M. Nojiri, *Explosive Dark Matter Annihilation*, **92** (Jan., 2004) 031303, [hep-ph/0307216]. 36

[162] M. Lattanzi and J. I. Silk, *Can the WIMP annihilation boost factor be boosted by the Sommerfeld enhancement?*, *Phys.Rev.* **D79** (2009) 083523, [arXiv:0812.0360]. 36, 113, 138, 177, 209, 218

[163] D. P. Finkbeiner, L. Goodenough, T. R. Slatyer, M. Vogelsberger, and N. Weiner, *Consistent Scenarios for Cosmic-Ray Excesses from Sommerfeld-Enhanced Dark Matter Annihilation*, *ArXiv e-prints* (Nov., 2010) [arXiv:1011.3082]. 36, 135

[164] J. Diemand, M. Kuhlen, and P. Madau, *Dark matter substructure and gamma-ray annihilation in the Milky Way halo*, **657** (2007) 262–270, [astro-ph/0611370]. 36

[165] **Whipple** Collaboration, K. Kosack *et. al.*, *TeV Gamma-Ray Observations of the Galactic Center*, *ApJL* **608** (June, 2004) L97–L100, [astro-ph/0403422]. 37, 49

[166] **CANGAROO** Collaboration, K. Tsuchiya *et. al.*, *Detection of Sub-TeV Gamma Rays from the Galactic Center Direction by CANGAROO-II*, *ApJL* **606** (May, 2004) L115–L118, [astro-ph/0403592]. 37

[167] **H.E.S.S.** Collaboration, F. Aharonian *et. al.*, *H.e.s.s. observations of the galactic center region and their possible dark matter interpretation*, *Phys.Rev.Lett* **97** (Nov, 2006) 221102. 37, 142

[168] **MAGIC** Collaboration, J. Albert *et. al.*, *Observation of Gamma Rays from the Galactic Center with the MAGIC Telescope*, *ApJ* **638** (2006) L101–L104, [astro-ph/0512469]. 37, 49, 50, 142

[169] A. Abramowski *et. al.*, *Search for a Dark Matter Annihilation Signal from the Galactic Center Halo with H.E.S.S.*, *Phys.Rev.Lett* **106** (Apr., 2011) 161301–+, [arXiv:1103.3266]. 37, 38

[170] L. E. Strigari, S. M. Koushiappas, J. S. Bullock, and M. Kaplinghat, *Precise constraints on the dark matter content of Milky Way dwarf galaxies for gamma-ray experiments*, *Phys.Rev.D* **75** (Apr., 2007) 083526, [astro-ph/0611925]. 38, 99, 100, 201

[171] J. Diemand, M. Kuhlen, P. Madau, M. Zemp, B. Moore, *et. al.*, *Clumps and streams in the local dark matter distribution*, *Nature* **454** (2008) 735–738, [arXiv:0805.1244]. 38, 99, 138, 142, 144, 176, 209, 218

[172] V. Springel, S. White, C. Frenk, J. Navarro, A. Jenkins, *et. al.*, *Prospects for detecting supersymmetric dark matter in the Galactic halo*, *Nature* **456N7218** (2008) 73–80. 38, 142, 144

[173] L. Pieri, G. Bertone, and E. Branchini, *Dark Matter Annihilation in Substructures Revised*, *Mon.Not.Roy.Astron.Soc.* **384** (2008) 1627, [arXiv:0706.2101]. 39, 142, 210

[174] G. M. Voit, *Tracing cosmic evolution with clusters of galaxies*, *Reviews of Modern Physics* **77** (Apr., 2005) 207–258, [astro-ph/0410173]. 39

[175] M. A. Sanchez-Conde, M. Cannoni, F. Zandanel, M. E. Gomez, and F. Prada, *Dark matter searches with Cherenkov telescopes: nearby dwarf galaxies or local galaxy clusters?*, *ArXiv e-prints* (Apr., 2011) [arXiv:1104.3530]. 39, 100, 201

[176] **Fermi-LAT** Collaboration, S. Zimmer *et. al.*, *A Combined Analysis of Clusters of Galaxies - Gamma Ray Emission from Cosmic Rays and Dark Matter*, *ArXiv e-prints* (Oct., 2011) [arXiv:1110.6863]. 39

[177] **MAGIC** Collaboration, J. Aleksić *et. al.*, *MAGIC Gamma-ray Telescope Observation of the Perseus Cluster of Galaxies: Implications for Cosmic Rays, Dark Matter, and NGC 1275*, *ApJ* **710** (Feb., 2010) 634–647, [arXiv:0909.3267]. 39

[178] **VERITAS** Collaboration, N. Galante *et. al.*, *Observation of Radio Galaxies and Clusters of Galaxies with VERITAS*, *ArXiv e-prints* (July, 2009) [arXiv:0907.5000]. 39

[179] **H.E.S.S.** Collaboration, W. Domainko, W. Benbow, J. A. Hinton, *et. al.*, *H.E.S.S. observations of galaxy clusters*, in *International Cosmic Ray Conference*, vol. 3 of *International Cosmic Ray Conference*, pp. 953–956, 2008. arXiv:0708.1384. 39

[180] A. Boyarsky, A. Neronov, O. Ruchayskiy, and M. Shaposhnikov, *Restrictions on parameters of sterile neutrino dark matter from observations of galaxy clusters*, *Phys.Rev.D* **74** (Nov., 2006) 103506, [astro-ph/0603368]. 39

[181] M. Fornasa, M. Taoso, and G. Bertone, *Gamma rays from dark matter minispikes in the Andromeda Galaxy M31*, *Phys.Rev.D* **76** (Aug., 2007) 043517, [astro-ph/0703757]. 39

[182] M. Gorchtein, S. Profumo, and L. Ubaldi, *Probing dark matter with active galactic nuclei jets*, *Phys.Rev.D* **82** (Oct., 2010) 083514, [arXiv:1008.2230]. 39

[183] **Fermi-LAT** Collaboration, A. A. Abdo *et. al.*, *Fermi Large Area Telescope First Source Catalog*, *ApJS* **188** (2010) 405–436, [arXiv:1002.2280]. 40, 143, 210

[184] S. Ando, E. Komatsu, T. Narumoto, and T. Totani, *Dark matter annihilation or unresolved astrophysical sources? Anisotropy probe of the origin of the cosmic gamma-ray background*, *Phys.Rev.D* **75** (Mar., 2007) 063519, [astro-ph/0612467]. 40

[185] M. Fornasa, J. Zavala, M. A. Sanchez-Conde, F. Prada, and M. Vogelsberger, *Dark Matter implications of the Fermi-LAT measurement of anisotropies in the diffuse gamma-ray background: status report*, *ArXiv e-prints* (Oct., 2011) [arXiv:1110.0324]. 40, 60

[186] M. Longair, *High energy astrophysics*. Cambridge University Press, 2011. 41, 49

[187] Perkins, D., *Particle Astrophysics*. Oxford University Press., 2011. 41

[188] Hess, V.F., *Observations of the penetrating radiation on seven balloon flights*, *Physik Z.* **13** (1912) 1084. 42

[189] **Pierre Auger** Collaboration, J. Abraham *et. al.*, *Correlation of the Highest-Energy Cosmic Rays with Nearby Extragalactic Objects*, *Science* **318** (Nov., 2007) 938–, [arXiv:0711.2256]. 42

[190] **Pierre Auger** Collaboration, J. Abraham *et. al.*, *Astrophysical Sources of Cosmic Rays and Related Measurements with the Pierre Auger Observatory*, *ArXiv e-prints* (June, 2009) [arXiv:0906.2347]. 42

[191] N. Mirabal and I. Oya, *Correlating Fermi gamma-ray sources with ultra-high-energy cosmic rays*, **405** (June, 2010) L99–L101, [arXiv:1002.2638]. 42

[192] B. T. Cleveland, T. Daily, R. Davis, Jr., J. R. Distel, K. Lande, C. K. Lee, P. S. Wildenhain, and J. Ullman, *Measurement of the Solar Electron Neutrino Flux with the Homestake Chlorine Detector*, *ApJ* **496** (Mar., 1998) 505. 43

[193] K. Hirata, T. Kajita, M. Koshiba, M. Nakahata, and Y. Oyama, *Observation of a neutrino burst from the supernova SN1987A*, *Physical Review Letters* **58** (Apr., 1987) 1490–1493. 43

[194] **IMB** Collaboration, C. B. Bratton *et. al.*, *Angular distribution of events from sn1987a*, *Phys.Rev.D* **37** (Jun, 1988) 3361–3363. 43

[195] F. Halzen and D. Hooper, *High-energy neutrino astronomy: the cosmic ray connection*, *Reports on Progress in Physics* **65** (2002), no. 7 1025. 43

[196] **Antares** Collaboration, "Antares Homepage." http://antares.in2p3.fr/, 2011. 43

[197] **IceCube** Collaboration, "IceCube Neutrino Observatory Homepage." `http://icecube.wisc.edu/`, 2011. 43

[198] The IceCube Collaboration, *IceCube - Astrophysics and Astroparticle Physics at the South Pole*, *ArXiv e-prints* (Nov., 2011) [`arXiv:1111.5188`]. 44

[199] **LIGO** Collaboration, "LIGO Homepage." `http://ligo.org/`, 2011. 44

[200] ESA, "LISA Homepage." `http://sci.esa.int/lisa`, 2011. 44

[201] I. Oya, *Observations of Active Galactic Nuclei with the MAGIC Telescope*. PhD dissertation, Universidad Complutense de Madrid, Atomic and Nuclear Physics Department, 2010. 45, 53, 188, 189, 190

[202] Dwek, E. and Krennrich, F., *Simultaneous Constraints on the Spectrum of the Extragalactic Background Light and the Intrinsic TeV Spectra of Markarian 421, Markarian 501, and H1426+428*, *ApJ* **618** (2005) 657–674. 48

[203] **Fermi-LAT** Collaboration, The Fermi-LAT Collaboration, *Fermi Large Area Telescope Second Source Catalog*, *ArXiv e-prints* (Aug., 2011) [`arXiv:1108.1435`]. 49, 53, 59, 60

[204] S. Wakely and D. Horan, "TeVCat Online Gamma-Ray Catalog." `http://tevcat.uchicago.edu/`, 2011. 49, 50, 53

[205] **Fermi-LAT** Collaboration, A. A. Abdo *et. al.*, *Fermi/Large Area Telescope Bright Gamma-Ray Source List*, *ApJS* **183** (July, 2009) 46–66, [`arXiv:0902.1340`]. 49

[206] **HESS** Collaboration, Aharonian, F., and others, *Very high energy gamma rays from the direction of Sagittarius A**, *A&A* **425** (2004) L13–L17. 49

[207] **Fermi-LAT** Collaboration, M. Ackermann *et. al.*, *A Cocoon of Freshly Accelerated Cosmic Rays Detected by Fermi in the Cygnus Superbubble*, *Science* **334** (Nov., 2011) 1103–1107. 50, 59

[208] **Whipple** Collaboration, Weekes, T.C., and others, *Observation of TeV gamma rays from the Crab nebula using the atmospheric Cerenkov imaging technique*, *ApJ* **342** (1989) 379–395. 50, 63

[209] Bosch-Ramon, V., and others, *The radio to TeV orbital variability of the microquasar LS I +61 303*, *A&A* **459** (2006) L25–L28. 51

[210] Maraschi, L. and Treves, A., *A model for LS I 61° 303*, *MNRAS* **194** (1981) 1–5. 51

[211] **H.E.S.S.** Collaboration, Aharonian, F., and others, *Discovery of the Binary Pulsar PSR B1259-63 in Very-High-Energy Gamma Rays around Periastron with H.E.S.S*, *A&A* **442** (2005) 1–10. 51

[212] **H.E.S.S.** Collaboration, Aharonian, F., and others, *Discovery of Very High Energy Gamma Rays Associated with an X-ray Binary*, *Science* **309** (2005) 746–749. 51

[213] **MAGIC** Collaboration, Albert, J., and others, *Variable Very-High-Energy Gamma-Ray Emission from the Microquasar LS I +61 303*, *Science* **312** (2006) 1771–1773. 51

[214] **MAGIC** Collaboration, Albert, J., and others, *Periodic very high energy gamma-ray emission from LS I +61 303 observed with the MAGIC telescope*, *ApJ* **693** (2009) 303–310. 51

[215] **Fermi-LAT** Collaboration, A. A. Abdo *et. al.*, *Fermi LAT Observations of LS I +61*deg*303: First Detection of an Orbital Modulation in GeV Gamma Rays*, *ApJL* **701** (Aug., 2009) L123–L128, [arXiv:0907.4307]. 51

[216] **Fermi-LAT** Collaboration, A. A. Abdo *et. al.*, *Modulated High-Energy Gamma-Ray Emission from the Microquasar Cygnus X-3*, *Science* **326** (Dec., 2009) 1512–. 51

[217] Kennel, C.F. and Coroniti, F.V., *Magnetohydrodynamic model of Crab nebula radiation*, *ApJ* **283** (1984) 710–730. 51

[218] **MAGIC** Collaboration, Aliu. E., and others, *Observation of Pulsed γ-Rays Above 25 GeV from the Crab Pulsar with MAGIC*, *Science* **322** (2008) 1221. 51, 68

[219] **MAGIC** Collaboration, J. Aleksić *et. al.*, *Phase-resolved energy spectra of the Crab Pulsar in the range of 50-400 GeV measured with the MAGIC Telescopes*, *ArXiv e-prints* (Sept., 2011) [arXiv:1109.6124]. 51, 52

[220] A. Nepomuk Otte and for the VERITAS Collaboration, *First Detection of a Pulsar above 100 GeV*, *ArXiv e-prints* (Nov., 2011) [arXiv:1111.6610]. 51

[221] R. W. Romani, *Gamma-Ray Pulsars: Radiation Processes in the Outer Magnetosphere*, *ApJ* **470** (Oct., 1996) 469. 51

[222] A. G. Muslimov and A. K. Harding, *High-Altitude Particle Acceleration and Radiation in Pulsar Slot Gaps*, *ApJ* **606** (May, 2004) 1143–1153, [astro-ph/0402462]. 51

[223] H. J. Pletsch *et. al.*, *Discovery of Nine Gamma-Ray Pulsars in Fermi-LAT Data Using a New Blind Search Method*, arXiv:1111.0523. 51

[224] D. Pooley, W. Lewin, S. Anderson, H. Baumgardt, A. Filippenko, *et. al.*, *Dynamical formation of close binary systems in globular clusters*, **591** (2003) L131–L134, [astro-ph/0305003]. 51, 120

[225] A. A. Abdo *et. al.*, *A population of gamma-ray emitting globular clusters seen with the Fermi Large Area Telescope*, *A&A* **524** (Dec., 2010) A75. 51

[226] **H.E.S.S.** Collaboration, A. Abramowski *et. al.*, *Very-high-energy gamma-ray emission from the direction of the Galactic globular cluster Terzan 5*, *ArXiv e-prints* (June, 2011) [arXiv:1106.4069]. 52

[227] A. Pinzke, C. Pfrommer, and L. Bergstrom, *Prospects of detecting gamma-ray emission from galaxy clusters: cosmic rays and dark matter annihilations*, *ArXiv e-prints* (May, 2011) [arXiv:1105.3240]. 53

[228] M. Ackermann *et. al.*, *GeV Gamma-ray Flux Upper Limits from Clusters of Galaxies*, *ApJL* **717** (July, 2010) L71–L78, [arXiv:1006.0748]. 53

[229] **MAGIC** Collaboration, J. Aleksić *et. al.*, *Constraining Cosmic Rays and Magnetic Fields in the Perseus Galaxy Cluster with TeV observations by the MAGIC telescopes*, *ArXiv e-prints* (Nov., 2011) [arXiv:1111.5544]. 53

[230] Urry, C.M. and Padovani, P., *Unified Schemes for Radio Sources*, *Publications of the Astronomical Society of the Pacific* **107** (1995) 803. 53

[231] **MAGIC** Collaboration, J. Albert *et. al.*, *Probing quantum gravity using photons from a flare of the active galactic nucleus Markarian 501 observed by the MAGIC telescope*, *Phys.Lett.B* **668** (Oct., 2008) 253–257, [arXiv:0708.2889]. 53

[232] R. C. Gilmore, R. S. Somerville, J. R. Primack, and A. Domínguez, *Semi-analytic modeling of the EBL and consequences for extragalactic gamma-ray spectra*, *ArXiv e-prints* (Apr., 2011) [arXiv:1104.0671]. 53, 168

[233] Klebesadel, R, Strong, I, and Olson, R, *Observations of gamma-ray bursts of cosmic origin*, *ApJ* **182** (1973) L85. 53

[234] Costa, E., et al, *Discovery of an X-ray afterglow associated with the big γ-ray burst of 28 February 1997*, *Nature* **387** (1997) 783–785. 53

[235] H. Ziaeepour, *A systematic description of shocks in gamma-ray bursts - I. Formulation*, **397** (July, 2009) 361–385, [arXiv:0812.3277]. 54

[236] **Fermi-LAT** Collaboration, M. Ackermann *et. al.*, *Fermi Observations of High-energy Gamma-ray Emission from GRB 090217A*, *ApJL* **717** (July, 2010) L127–L132, [arXiv:1007.3409]. 54

[237] **MAGIC** Collaboration, A. Carosi *et. al.*, *MAGIC low energy observation of GRB090102 afterglow*, *ArXiv e-prints* (Oct., 2011) [arXiv:1110.6848]. 54

[238] Amati, L., et al, *Intrinsic spectra and energetics of BeppoSAX Gamma-Ray Bursts with known redshifts*, *A&A* **390** (2002) 81. 54

[239] **HESS** Collaboration, Acero, F., and others, *Detection of Gamma Rays from a Starburst Galaxy*, *Science* **326** (2009) 1080. 54

[240] **VERITAS** Collaboration, V. A. Acciari *et. al.*, *A connection between star formation activity and cosmic rays in the starburst galaxy M82*, *Nature* **November 1** (2009). 54

[241] **Fermi-LAT** Collaboration, A. A. Abdo *et. al.*, *Detection of Gamma-Ray Emission from the Starburst Galaxies M82 and NGC 253 with the Large Area Telescope on Fermi*, *ApJL* **709** (Feb., 2010) L152–L157, [arXiv:0911.5327]. 54

[242] **MAGIC** Collaboration, J. Albert *et. al.*, *First Bounds on the Very High Energy γ-Ray Emission from Arp 220*, *ApJ* **658** (Mar., 2007) 245–248, [astro-ph/0611786]. 54

[243] R. Wagner, "VHE Gamma-ray Sky Map and Source Catalog." http://www.mpp.mpg.de/~rwagner/sources/, 2011. 55

[244] M. Doro, *Novel Reflective Elements and Indirect Dark Matter Searches for MAGIC II and Future IACTs*. PhD dissertation, Università degli studi di Padova, Physics Department Galileo Galilei, 2009. 55

[245] ESA, "The INTEGRAL Homepage." http://www.sciops.esa.int/index.php?project=INTEGRAL&page=index, 2011. 56

[246] NASA, "Fermi science tools: Cicerone." http://fermi.gsfc.nasa.gov, 2011. 56, 58, 59, 142, 200

[247] **Hagar** Collaboration, "Hagar Telescope Homepage." http://www.iiap.res.in/iao_hagar, 2011. 56

[248] **MAGIC** Collaboration, "The MAGIC Telecopes Homepage." http://wwwmagic.mppmu.mpg.de/, 2011. 57, 60, 64, 200

[249] **H.E.S.S.** Collaboration, "H.E.S.S. Homepage." http://www.mpi-hd.mpg.de/hfm/HESS/, 2011. 57, 64

[250] **VERITAS** Collaboration, "VERITAS Homepage." http://veritas.sao.arizona.edu/, 2011. 57, 64

[251] **MILAGRO** Collaboration, "The Milagro Gamma-Ray Observatory Homepage." http://www.lanl.gov/milagro/, 2011. 57

[252] **HAWC** Collaboration, "HAWC Homepage." http://hawc.umd.edu/, 2011. 57

[253] **Tibet-AS** Collaboration, "Tibet-AS Gamma Experiment Homepage." http://www.icrr.u-tokyo.ac.jp/em/, 2011. 57

[254] **Argo-YBJ** Collaboration, "Argo-YBJ Homepage." http://argo.na.infn.it/, 2011. 57

[255] **HiRes** Collaboration, "HiRes Homepage." http://www.cosmic-ray.org/, 2011. 57

[256] **Pierre Auger** Collaboration, "The Pierre Auger Observatory Homepage." http://www.auger.org/, 2011. 57

[257] **Fermi-LAT** Collaboration, "The Fermi Large Area Telescope Homepage." http://www-glast.stanford.edu/, 2011. 58, 200

[258] **Fermi-LAT** Collaboration, W. Atwood *et. al.*, *The Large Area Telescope on the Fermi Gamma-ray Space Telescope Mission*, *ApJ* **697** (2009) 1071–1102, [arXiv:0902.1089]. 59

[259] M. Su, T. R. Slatyer, and D. P. Finkbeiner, *Giant Gamma-ray Bubbles from Fermi-LAT: Active Galactic Nucleus Activity or Bipolar Galactic Wind?*, *ApJ* **724** (Dec., 2010) 1044–1082, [arXiv:1005.5480]. 59

[260] **Fermi-LAT** Collaboration, A. A. Abdo *et. al.*, *Gamma-Ray Flares from the Crab Nebula*, *Science* **331** (Feb., 2011) 739–, [arXiv:1011.3855]. 59

[261] **Fermi-LAT** Collaboration, A. A. Abdo *et. al.*, *A Population of Gamma-Ray Millisecond Pulsars Seen with the Fermi Large Area Telescope*, *Science* **325** (Aug., 2009) 848–. 59

[262] **Fermi-LAT** Collaboration, A. A. Abdo *et. al.*, *Fermi Observations of High-Energy Gamma-Ray Emission from GRB 080916C*, *Science* **323** (Mar., 2009) 1688–. 59

[263] **Fermi-LAT** Collaboration, M. Ackermann *et. al.*, *Measurement of Separate Cosmic-Ray Electron and Positron Spectra with the Fermi Large Area Telescope*, *Phys.Rev.Lett* **108** (Jan., 2012) 011103, [arXiv:1109.0521]. 59

[264] **Fermi-LAT** Collaboration, A. A. Abdo *et. al.*, *The Fermi-LAT High-Latitude Survey: Source Count Distributions and the Origin of the Extragalactic Diffuse Background*, *ApJ* **720** (Sept., 2010) 435–453, [arXiv:1003.0895]. 60

[265] **Fermi-LAT** Collaboration, A. A. Abdo *et. al.*, *Constraints on cosmological dark matter annihilation from the Fermi-LAT isotropic diffuse gamma-ray measurement*, *JCAP* **4** (Apr., 2010) 14, [arXiv:1002.4415]. 60

[266] **Fermi-LAT** Collaboration, A. Abdo *et. al.*, *Fermi Large Area Telescope Search for Photon Lines from 30 to 200 GeV and Dark Matter Implications*, *Phys.Rev.Lett* **104** (Mar., 2010) 091302, [arXiv:1001.4836]. 60

[267] **Fermi-LAT** Collaboration, M. Ackermann *et. al.*, *Constraints on dark matter annihilation in clusters of galaxies with the Fermi large area telescope*, *JCAP* **5** (May, 2010) 25, [arXiv:1002.2239]. 60

[268] **Fermi-LAT** Collaboration, M. Ackermann *et. al.*, *Constraining dark matter models from a combined analysis of Milky Way satellites with the Fermi-LAT*, *ArXiv e-prints* (Aug., 2011) [arXiv:1108.3546]. 60, 101, 201

[269] **Fermi-LAT** Collaboration, M. Ajello *et. al.*, *Constraints on dark matter models from a Fermi LAT search for high-energy cosmic-ray electrons from the Sun*, *Phys.Rev.D* **84** (2011) 032007, [arXiv:1107.4272]. 60

[270] M. Lopez, *Astronomía Gamma con el Telescopio MAGIC: Observaciones de la Nebulosa y Pulsar del Cangrejo*. PhD dissertation, Universidad Complutense de Madrid, Atomic and Nuclear Physics Department, 2006. 62, 191, 193

[271] **VERITAS** Collaboration, J. Kildea *et. al.*, *The whipple observatory 10m gamma-ray telescope, 1997 - 2006*, *Astroparticle Physics* **28** (2007), no. 2 182 – 195. 64

[272] M. Wood *et. al.*, *A Search for Dark Matter Annihilation with the Whipple 10 m Telescope*, *ApJ* **678** (May, 2008) 594–605, [arXiv:0801.1708]. 64, 101, 138, 201

[273] **HEGRA** Collaboration, G. Pühlhofer *et. al.*, *The technical performance of the HEGRA system of imaging air Cherenkov telescopes*, *Astroparticle Physics* **20** (Dec., 2003) 267–291, [astro-ph/0306123]. 64

[274] **HEGRA** Collaboration, F. A. Aharonian *et. al.*, *The Energy Spectrum of TEV Gamma Rays from the Crab Nebula as Measured by the HEGRA System of Imaging Air Cerenkov Telescopes*, *ApJ* **539** (Aug., 2000) 317–324, [astro-ph/0003182]. 64

[275] A. Barrau *et. al.*, *The CAT imaging telescope for very-high-energy gamma-ray astronomy.*, *Nucl.Instrum.Meth.A* **416** (Oct., 1998) 278–292, [astro-ph/9804046]. 64

[276] A. Djannati-Atai *et. al.*, *Very High Energy Gamma-ray spectral properties of MKN 501 from CAT Čerenkov telescope observations in 1997*, **350** (Oct., 1999) 17–24, [astro-ph/9906060]. 64

[277] J. Hinton, *Ground-based gamma-ray astronomy with Cherenkov telescopes*, *New Journal of Physics* **11** (May, 2009) 055005–+, [arXiv:0803.1609]. 64

[278] Doro, M. *et. al.*, *The reflective surface of the MAGIC telescope*, **595** (2008) 200–203. 64

[279] D. Bastieri, J. Arnold, C. Baixeras, and et al., *The reflecting surface of the MAGIC-II Telescope*, in *International Cosmic Ray Conference*, vol. 3 of *International Cosmic Ray Conference*, pp. 1547–1550, 2008. arXiv:0709.1372. 64

[280] A. Biland, M. Garczarczyk, H. Anderhub, *et. al.*, *The Active Mirror Control of the MAGIC Telescopes*, in *International Cosmic Ray Conference*, vol. 3 of *International Cosmic Ray Conference*, pp. 1353–1356, 2008. arXiv:0709.1574. 65

[281] T. Bretz, D. Dorner, R. M. Wagner, and P. Sawallisch, *The drive system of the major atmospheric gamma-ray imaging Cherenkov telescope*, *Astrop.Phys.* **31** (Mar., 2009) 92–101, [arXiv:0810.4593]. 65

[282] D. Borla Tridon *et. al.*, *Performance of the Camera of the MAGIC II Telescope*, *ArXiv e-prints* (June, 2009) [arXiv:0906.5448]. 66

[283] MAGIC Collaboration: Florian Goebel, H. Bartko, E. Carmona, N. Galante, T. Jogler, R. Mirzoyan, J. A. Coarasa, and M. Teshima, *Upgrade of the MAGIC Telescope with a Multiplexed Fiber-Optic 2 GSamples/s FADC Data Acquisition system*, *ArXiv e-prints* (Sept., 2007) [arXiv:0709.2363]. 66, 67

[284] D. Tescaro, J. Aleksic, M. Barcelo, M. Bitossi, J. Cortina, M. Fras, D. Hadasch, J. M. Illa, M. Martinez, D. Mazin, R. Paoletti, R. Pegna, and for the MAGIC Collaboration, *The readout system of the MAGIC-II Cherenkov Telescope*, *ArXiv e-prints* (July, 2009) [arXiv:0907.0466]. 67

[285] M. Rissi, N. Otte, T. Schweizer, and M. Shayduk, *A New Sum Trigger to Provide a Lower Energy Threshold for the MAGIC Telescope*, *IEEE Transactions on Nuclear Science* **56** (Dec., 2009) 3840–3843. 68

[286] V. P. Fomin, A. A. Stepanian, R. C. Lamb, D. A. Lewis, P. M., and T. C. Weekes, *New methods of atmospheric Cherenkov imaging for gamma-ray astronomy. 1: The False source method*, *Astropart.Phys.* **2** (1994) 137. 69, 82, 122, 153, 162

[287] Bretz, T. and Wagner, R.M., *The MAGIC Analysis and Reconstruction Software*, *Proceedings of the 28th International Cosmic Ray Conference, Tsukuba, japan* **5** (2003) 2947–2950. 70

[288] **MAGIC** Collaboration, S. Lombardi, K. Berger, P. Colin, A. Diago Ortega, S. Klepser, *et. al.*, *Advanced stereoscopic gamma-ray shower analysis with the MAGIC telescopes*, *ArXiv e-prints* (Sept., 2011) [arXiv:1109.6195]. 70

[289] The ROOT Team, "ROOT, a Data Analysis Framework." http://root.cern.ch/, 2011. 70

[290] R. Zanin, D. Mazin, E. Carmona, P. Colin, J. Cortina, T. Jogler, S. Klepser, A. Moralejo, Julian Sitarek for the MAGIC collaboration, D. Horns, and M. Meyer, *MAGIC measurement of the Crab Nebula spectrum over three decades in energy*, *ArXiv e-prints* (Oct., 2011) [arXiv:1110.2987]. 71

[291] M. Tavani *et. al.*, *Discovery of Powerful Gamma-Ray Flares from the Crab Nebula*, *Science* **331** (Feb., 2011) 736–, [arXiv:1101.2311]. 71

[292] **MAGIC** Collaboration, J. Albert *et. al.*, *FADC signal reconstruction for the MAGIC telescope*, *Nucl.Instrum.Meth.A* **594** (Sept., 2008) 407–419, [0612385]. 71

[293] R. Mirzoyan, *On the Calibration Accuracy of Light Sensors in Atmospheric Cherenkov Fluorescence and Neutrino Experiments*, in *International Cosmic Ray Conference*, vol. 7 of *International Cosmic Ray Conference*, p. 265, 1997. 72

[294] Hillas, A.M., *Cherenkov Images of EAS produced by primary gamma rays and by nuclei*, *Proceedings of the 19th International Cosmic Ray Conference, La Jolla* **3** (1985) 445. 73, 122

[295] **HEGRA** Collaboration, A. Kohnle *et. al.*, *Stereoscopic imaging of air showers with the first two HEGRA Cherenkov telescopes*, *Astroparticle Physics* **5** (Aug., 1996) 119–131. 76

[296] I. Oya, R. de los Reyes, D. Nieto, *et. al.*, *MAGIC Data Check Program*, Internal TDAS Document 09-02, MAGIC Collaboration, 2009. 76

[297] D. Heck, J. Knapp, J. N. Capdevielle, G. Schatz, and T. Thouw, *CORSIKA: a Monte Carlo code to simulate extensive air showers.* Forschungszentrum Karlsruhe GmbH, Feb., 1998. 77

[298] P. Majumdar, A. Moralejo, C. Bigongiari, O. Blanch, and D. Sobczynska, *Monte Carlo simulation for the MAGIC telescope*, in *International Cosmic Ray Conference*, vol. 5 of *International Cosmic Ray Conference*, p. 203, 2005. 79

[299] E. Carmona, P. Majumdar, A. Moralejo, and et al., *Monte Carlo Simulation for the MAGIC-II System*, in *International Cosmic Ray Conference*, vol. 3 of *International Cosmic Ray Conference*, pp. 1373–1376, 2008. arXiv:0709.2959. 79

[300] L. Breiman, *Random forests*, *Machine Learning* **45** (2001) 5–32. 10.1023/A:1010933404324. 79

[301] de Naurois, M. and Rolland, M., *A high performance likelihood reconstruction of gamma-rays for Imaging Atmospheric Cherenkov Telescopes*, *Astrop. Phys.* **32** (2009) 231–252. 80

[302] **MAGIC** Collaboration, J. Albert *et. al.*, *Implementation of the Random Forest method for the Imaging Atmospheric Cherenkov Telescope MAGIC*, *Nucl.Instrum.Meth.A* **588** (Apr., 2008) 424–432, [arXiv:0709.3719]. 80

[303] C. Gini, *Measurement of inequality of income*, *Economic Journal* **31** (1921) 22–43. 80

[304] **MAGIC** Collaboration, J. Aleksić *et. al.*, *Search for an extended VHE γ-ray emission from Mrk 421 and Mrk 501 with the MAGIC Telescope*, *A&A* **524** (Dec., 2010) A77, [arXiv:1004.1093]. 82

[305] **MAGIC** Collaboration, J. Aleksić *et. al.*, *Performance of the MAGIC stereo system obtained with Crab Nebula data*, *ArXiv e-prints* (Aug., 2011) [arXiv:1108.1477]. 84, 91, 95

[306] T.-P. Li and Y.-Q. Ma, *Analysis methods for results in gamma-ray astronomy*, **272** (1983) 317–324. 85, 124, 174, 211

[307] **MAGIC** Collaboration, J. Albert *et. al.*, *Unfolding of differential energy spectra in the MAGIC experiment*, *Nucl.Instrum.Meth.A* **583** (2007) 494–506, [astro-ph/0707.2453]. 92

[308] W. A. Rolke, A. M. Lopez, and J. Conrad, *Limits and confidence intervals in the presence of nuisance parameters*, **A551** (2005) 493–503, [physics/0403059]. 93, 106, 125, 156, 199

[309] S. Arnaud, K. and Siemiginowska, A., eds., *Handbook of X-Ray Astronomy*. Cambridge University Press., 2011. 95

[310] P. Fabian, A.C. and Blandford, R.D., eds., *Frontiers of X-Ray Astronomy*. Cambridge University Press., 2011. 95

[311] NASA, "Chandra X-ray Observatory Homepage." http://chandra.si.edu/, 2011. 96, 200

[312] ESA, "XMM-Newton Science Operation Center." http://xmm.esac.esa.int/, 2011. 96, 200

[313] M. C. Weisskopf, B. Brinkman, C. Canizares, G. Garmire, S. Murray, and L. P. Van Speybroeck, *An Overview of the Performance and Scientific Results from the Chandra X-Ray Observatory*, **114** (Jan., 2002) 1–24, [astro-ph/0110308]. 96

[314] D. A. Schwartz, *The Development and Scientific Impact of the Chandra X-Ray Observatory*, *International Journal of Modern Physics D* **13** (2004) 1239–1247, [astro-ph/0402275]. 97

[315] A. A. Klypin, A. V. Kravtsov, O. Valenzuela, and F. Prada, *Where are the missing Galactic satellites?*, **522** (1999) 82–92, [astro-ph/9901240]. 99, 100, 201

[316] A. V. Kravtsov, O. Y. Gnedin, and A. A. Klypin, *The Tumultuous Lives of Galactic Dwarfs and the Missing Satellites Problem*, **609** (July, 2004) 482–497, [astro-ph/0401088]. 99

[317] G. Gilmore, M. I. Wilkinson, R. F. Wyse, J. T. Kleyna, A. Koch, *et. al.*, *The Observed properties of Dark Matter on small spatial scales*, **663** (2007) 948–959, [astro-ph/0703308]. 99

[318] H. Shapley, *A stellar system of a new type*, *Harvard College Obs. Bull.* **908** (1938) 1–11. 99

[319] B. Willman, M. R. Blanton, A. A. West, J. J. Dalcanton, D. W. Hogg, *et. al.*, *A New Milky Way companion: Unusual globular cluster or extreme dwarf satellite?*, *Astron.J.* **129** (2005) 2692–2700, [astro-ph/0410416]. 99, 101, 116, 118, 201

[320] B. Willman, J. J. Dalcanton, D. Martinez-Delgado, A. A. West, M. R. Blanton, D. W. Hogg, J. C. Barentine, H. J. Brewington, M. Harvanek, S. J. Kleinman, J. Krzesinski, D. Long, E. H. Neilsen, Jr., A. Nitta, and S. A. Snedden, *A New Milky Way Dwarf*

Galaxy in Ursa Major, *Astrophys.J.L.* **626** (June, 2005) L85–L88, [astro-ph/0503552]. 99

[321] V. Belokurov *et. al.*, *Cats and Dogs, Hair and A Hero: A Quintet of New Milky Way Companions*, **654** (2007) 897–906, [astro-ph/0608448]. 100, 102, 202

[322] J. D. Simon and M. Geha, *The Kinematics of the Ultra-Faint Milky Way Satellites: Solving the Missing Satellite Problem*, **670** (2007) 313–331, [astro-ph/0706.0516]. 100, 103

[323] B. J. Pritzl, K. A. Venn, and M. Irwin, *A Comparison of Elemental Abundance Ratios in Globular Clusters, Field Stars, and Dwarf Spheroidal Galaxies*, *Astrophys. J.* **130** (Nov., 2005) 2140–2165, [astro-ph/0506238]. 100

[324] P. Madau, J. Diemand, and M. Kuhlen, *Dark matter subhalos and the dwarf satellites of the Milky Way*, astro-ph/0802.2265. 100

[325] M. L. Mateo, *Dwarf Galaxies of the Local Group*, **36** (1998) 435–506, [astro-ph/9810070]. 100, 201

[326] **MAGIC** Collaboration, J. Albert *et. al.*, *Upper limit for gamma-ray emission above 140-GeV from the dwarf spheroidal galaxy Draco*, *ApJ* **679** (2008) 428–431, [astro-ph/0711.2574]. 101, 135, 137, 138, 201

[327] **VERITAS** Collaboration, V. A. Acciari *et. al.*, *VERITAS Search for VHE Gamma-ray Emission from Dwarf Spheroidal Galaxies*, *ApJ* **720** (2010) 1174–1180, [astro-ph.CO/1006.5955]. 101, 138, 178, 201, 219

[328] **H.E.S.S.** Collaboration, F. Aharonian *et. al.*, *Observations of the Sagittarius Dwarf galaxy by the H.E.S.S. experiment and search for a Dark Matter signal*, *Astrop.Phys.* **29** (2008) 55–62, [astro-ph/0711.2369]. 101, 137, 138, 201

[329] **H.E.S.S.** Collaboration, A. Abramowski *et. al.*, *H.E.S.S. constraints on Dark Matter annihilations towards the Sculptor and Carina Dwarf Galaxies*, *ArXiv e-prints* (Dec., 2010) [astro-ph.HE/1012.5602]. 101, 176, 178, 201, 219

[330] S. Riemer-Sorensen and S. H. Hansen, *Decaying dark matter in Draco*, *ArXiv e-prints* (Jan., 2009) [astro-ph.CO/0901.2569]. 101, 201

[331] N. Martin, R. Ibata, S. Chapman, M. Irwin, and G. Lewis, *A Keck/DEIMOS spectroscopic survey of faint Galactic satellites: Searching for the least massive dwarf galaxies*, *Mon.Not.Roy.Astron.Soc.* **380** (2007) 281–300, [astro-ph/0705.4622]. 101, 120, 201

[332] B. Willman, M. Geha, J. Strader, L. E. Strigari, J. D. Simon, *et. al.*, *Willman 1 - a probable dwarf galaxy with an irregular kinematic distribution*, *Astron.J. (submitted)* (2010) [astro-ph.GA/1007.3499]. 101, 102, 120, 121, 201

[333] Keck Observatory, "DEIMOS Home Page." http://www2.keck.hawaii.edu/inst/deimos/, 2011. 101, 103

[334] F. Sanchez-Salcedo and X. Hernandez, *Tidal radii and escape speeds in dwarf spheroidal galaxies under MOND and dark halos compared*, **667** (2007) 878–890, [astro-ph/0702443]. 101, 201

[335] M. Siegel, M. Shetrone, and M. Irwin, *Trimming Down the Willman 1 dSph*, astro-ph/0803.2489. 102, 201

[336] **SDSS-II SEGUE** Collaboration, B. Yanny *et. al.*, *SEGUE: A Spectroscopic Survey of 240,000 Stars with g = 14-20*, *Astron.J.* **137** (May, 2009) 4377–4399, [astro-ph.GA/0902.1781]. 102, 202

[337] National Astronomical Observatory of Japan, "Subaru Telescope Homepage." http://www.naoj.org/, 2011. 102, 202

[338] M. Niederste-Ostholt, V. Belokurov, N. W. Evans, G. Gilmore, R. F. G. Wyse, and J. E. Norris, *The origin of Segue 1*, *Mon.Not.Roy.Astron.Soc.* **398** (Oct., 2009) 1771–1781, [astro-ph.GA/0906.3669]. 102, 202

[339] M. Geha, B. Willman, J. D. Simon, L. E. Strigari, E. N. Kirby, *et. al.*, *The Least Luminous Galaxy: Spectroscopy of the Milky Way Satellite Segue 1*, **692** (2009) 1464–1475, [astro-ph/0809.2781]. 102, 202

[340] M. Xiang-Gruess, Y. Lou, and W. J. Duschl, *Dark matter dominated dwarf disc galaxy Segue 1*, *Mon.Not.Roy.Astron.Soc.* **400** (Nov., 2009) L52–L56, [astro-ph.CO/0909.3496]. 102, 202

[341] J. D. Simon, M. Geha, Q. E. Minor, G. D. Martinez, E. N. Kirby, *et. al.*, *A Complete Spectroscopic Survey of the Milky Way Satellite Segue 1: The Darkest Galaxy*, *Astrophys.J. (submitted)* (2010) [astro-ph.GA/1007.4198]. 103, 202

[342] G. D. Martinez, Q. E. Minor, J. Bullock, M. Kaplinghat, J. D. Simon, *et. al.*, *A Complete Spectroscopic Survey of the Milky Way satellite Segue 1: Dark matter content, stellar membership and binary properties from a Bayesian analysis*, *ArXiv e-prints* (2010) [astro-ph.GA/1008.4585]. 103, 113, 202

[343] G. Bertone, T. Bringmann, R. Rando, G. Busetto, and A. Morselli, *GLAST sensitivity to Point Sources of Dark Matter Annihilation*, *ArXiv Astrophysics e-prints* (Dec., 2006) [astro-ph/0612387]. 107, 144, 145, 156, 210

[344] **MAGIC** Collaboration, J. Albert *et. al.*, *VHE Gamma-Ray Observation of the Crab Nebula and Pulsar with MAGIC*, *ApJ* **674** (2008) 1037–1055, [astro-ph/0705.3244]. 107, 108, 109, 125, 127, 158, 176, 202, 206

[345] M. Battaglia, A. D. Roeck, J. Ellis, F. Gianotti, K. A. Olive, and L. Pape, *Updated post-WMAP benchmarks for supersymmetry*, *European Physical Journal C* **33** (Mar., 2004) 273–296, [hep-ph/0306219]. 110

[346] T. Bringmann, M. Doro, and M. Fornasa, *Dark Matter signals from Draco and Willman 1: Prospects for MAGIC II and CTA*, *JCAP* **0901** (2009) 016, [astro-ph/0809.2269]. 110, 111, 112, 132, 203

[347] M. Kuhlen, J. Diemand, P. Madau, and M. Zemp, *The Via Lactea INCITE Simulation: Galactic Dark Matter Substructure at High Resolution*, *J.Phys.Conf.Ser.* **125** (2008) 012008, [astro-ph/0810.3614]. 113, 142

[348] NASA, "Chandra Interactive Analysis of Observations Software." http://cxc.cfa.harvard.edu/ciao/, 2011. 113

[349] C. Hui, K. Cheng, and R. E. Taam, *Diffuse X-ray emission in globular cluster cores*, **700** (2009) 1233–1241, [astro-ph.HE/0905.2908]. 114, 204

[350] NASA, "The ACIS "Blank-Sky" Background Files." http://cxc.harvard.edu/ciao/threads/acisbackground/index.html, 2011. 115, 204

[351] N. Mirabal, F. Paerels, and J. Halpern, *High resolution grating spectroscopy of GRB 020405 with Chandra LETGS*, **587** (2003) 128–134, [astro-ph/0209516]. 115, 205

[352] S. Riemer-Sorensen, S. H. Hansen, and K. Pedersen, *Sterile neutrinos in the Milky Way: Observational constraints*, **644** (2006) L33–L36, [astro-ph/0603661]. 115, 121, 205

[353] J. C. Raymond and B. W. Smith, *Soft X-ray spectrum of a hot plasma*, **35** (1977) 419–439. 117

[354] U. Hwang *et. al.*, *A Million Second Chandra View of Cassiopeia A*, *ApJL* **615** (Nov., 2004) L117–L120, [astro-ph/0409760]. 117, 205

[355] D. Henley, M. Corcoran, J. Pittard, I. Stevens, K. Hamaguchi, *et. al.*, *Chandra X-ray Grating Spectrometry of Eta Carinae near X-ray Minimum: I. Variability of the Sulfur and Silicon Emission Lines*, **680** (2008) 705, [astro-ph/0801.4779]. 117, 205

[356] **SDSS** Collaboration, K. N. Abazajian *et. al.*, *The Seventh Data Release of the Sloan Digital Sky Survey*, *ApJS* **182** (2009) 543–558, [astro-ph/0812.0649]. 118, 119, 204

[357] G. T. Richards, A. D. Myers, A. G. Gray, R. N. Riegel, R. C. Nichol, *et. al.*, *Efficient Photometric Selection of Quasars from the Sloan Digital Sky Survey: II. 1,000,000 Quasars from Data Release Six*, **180** (2009) 67–83, [astro-ph/0809.3952]. 118, 119

[358] R. Giacconi, P. Rosati, P. Tozzi, M. Nonino, G. Hasinger, *et. al.*, *First results from the x-ray and optical survey of the Chandra Deep Field South*, **551** (2001) 624–634, [astro-ph/0007240]. 119

[359] B. Luo, F. Bauer, W. Brandt, D. Alexander, B. Lehmer, *et. al.*, *The Chandra Deep Field-South Survey: 2 Ms Source Catalogs*, **179** (2008) 19–36, [astro-ph/0806.3968]. 119, 204

[360] G. Ramsay and K. Wu, *A search for stellar X-ray sources in the Sagittarius and Carina dwarf galaxies. 1. X-ray observations*, *Astron.Astrophys.* **459** (2006) 777–781, [astro-ph/0609116]. 119

[361] C. Heinke, J. Grindlay, P. Edmonds, D. Lloyd, S. Murray, *et. al.*, *A chandra x-ray study of the globular cluster m80*, **598** (2003) 516–526, [astro-ph/0305443]. 119

[362] J. E. Grindlay, C. Heinke, P. D. Edmonds, and S. S. Murray, *High-Resolution X-ray Imaging of a Globular Cluster Core: Compact Binaries in 47Tuc*, *Science* **292** (June, 2001) 2290–2295, [astro-ph/0105528]. 119

[363] K. A. Arnaud, *Astronomical Data Analysis Software and Systems V*, vol. 101 of *Conference Series*. Astron. Soc. Pac., San Francisco, 1996. 120

[364] D. Haggard, A. M. Cool, and M. B. Davies, *A Chandra Study of the Galactic Globular Cluster Omega Centauri*, **697** (2009) 224–236, [astro-ph.HE/0902.2397]. 120

[365] F. Verbunt, *Binary Evolution and Neutron Stars in Globular Clusters*, vol. 296 of *Conference Series*. Astron. Soc. Pac., San Francisco, 2003. 120, 204

[366] J. den Herder, A. Boyarsky, O. Ruchayskiy, K. Abazajian, C. Frenk, *et. al.*, *The Search for decaying Dark Matter*, astro-ph.C/0906.1788. 121, 205

[367] J. J. Condon, W. Cotton, E. Greisen, Q. Yin, R. Perley, *et. al.*, *The NRAO VLA Sky survey*, *Astron.J.* **115** (1998) 1693–1716. 121

[368] S. Lombardi, *Development of analysis tools for the MAGIC Telescopes and observation of the Segue 1 Satellite Galaxy with the MAGIC-I Telescope.* PhD dissertation, Università degli studi di Padova, Physics Department Galileo Galilei, 2010. 124, 129

[369] **MAGIC** Collaboration, E. Domingo-Santamaria, J. Flix Molina, V. Scalzotto, W. Wittek, and J. Rico, *The DISP analysis method for point-like or extended gamma source searches / studies with the MAGIC telescope*, *Proceedings of the International Cosmic Ray Conference* (2005) [astro-ph/0508274]. 125

[370] L. E. Strigari. Private communication, 2010. 128

[371] R. Essig, N. Sehgal, L. E. Strigari, M. Geha, and J. D. Simon, *Indirect Dark Matter Detection Limits from the Ultra-Faint Milky Way Satellite Segue 1*, *Phys.Rev.* **D82** (2010) 123503, [astro-ph.CO/1007.4199]. 128, 131, 133, 136, 137, 138, 176, 177, 209

[372] P. Gondolo, J. Edsjo, P. Ullio, L. Bergstrom, M. Schelke, *et. al.*, *DarkSUSY: Computing supersymmetric dark matter properties numerically*, *JCAP* **0407** (2004) 008, [astro-ph/0406204]. 130

[373] H. Baer, F. E. Paige, S. D. Protopescu, and X. Tata, *ISAJET 7.69: A Monte Carlo Event Generator for pp, p(bar)p, and e+e- Reactions*, *ArXiv e-prints* (Dec., 2003) [hep-ph/0312045]. 130

[374] A. Abdo, M. Ackermann, M. Ajello, W. Atwood, L. Baldini, *et. al.*, *Observations of Milky Way Dwarf Spheroidal galaxies with the Fermi-LAT detector and constraints on Dark Matter models*, *ApJ* **712** (2010) 147–158, [astro-ph.CO/1001.4531]. 132, 138, 209

[375] L. Bergstrom, P. Ullio, and J. H. Buckley, *Observability of gamma-rays from dark matter neutralino annihilations in the Milky Way halo*, *Astropart.Phys.* **9** (1998) 137–162, [astro-ph/9712318]. 135

[376] N. Arkani-Hamed, D. P. Finkbeiner, T. R. Slatyer, and N. Weiner, *A Theory of Dark Matter*, *Phys.Rev.D* **79** (2009) 015014, [hep-ph/0810.0713]. 135, 136

[377] M. Pospelov and A. Ritz, *Astrophysical Signatures of Secluded Dark Matter*, *Phys.Lett.* **B671** (2009) 391–397, [arXiv:0810.1502]. 135

[378] I. Cholis, D. P. Finkbeiner, L. Goodenough, and N. Weiner, *The PAMELA Positron Excess from Annihilations into a Light Boson*, *JCAP* **0912** (2009) 007, [astro-ph/0810.5344]. 135

[379] I. Cholis, G. Dobler, D. P. Finkbeiner, L. Goodenough, and N. Weiner, *The Case for a 700+ GeV WIMP: Cosmic Ray Spectra from ATIC and PAMELA*, *Phys.Rev.* **D80** (2009) 123518, [astro-ph/0811.3641]. 135

[380] L. Bergstrom, J. Edsjo, and G. Zaharijas, *Dark matter interpretation of recent electron and positron data*, **103** (2009) 031103, [astro-ph.HE/0905.0333]. 135

[381] P. Meade, M. Papucci, A. Strumia, and T. Volansky, *Dark Matter Interpretations of the e+- Excesses after FERMI*, *Nucl.Phys.* **B831** (2010) 178–203, [hep-ph/0905.0480]. 135

[382] L. Pieri, M. Lattanzi, and J. Silk, *Constraining the dark matter annihilation cross-section with Cherenkov telescope observations of dwarf galaxies*, *Mon.Not.Roy.Astron.Soc.* **399** (Nov., 2009) 2033–2040, [astro-ph.HE/0902.4330]. 138, 209

[383] **H.E.S.S.** Collaboration, F. Aharonian *et. al.*, *A Search for a Dark Matter Annihilation Signal Toward the Canis Major Overdensity with H.E.S.S.*, *ApJ* **691** (Jan., 2009) 175–181, [astro-ph/0809.3894]. 138

[384] S. C. Keller, B. P. Schmidt, M. S. Bessell, P. G. Conroy, P. Francis, A. Granlund, E. Kowald, A. P. Oates, T. Martin-Jones, T. Preston, P. Tisserand, A. Vaccarella, and M. F. Waterson, *The SkyMapper Telescope and The Southern Sky Survey*, *Publications of the Astronomical Society of Australia* **24** (May, 2007) 1–12, [astro-ph/0702511]. 140, 179

[385] X. Barcons *et. al.*, *International X-ray Observatory (IXO) Assessment Study Report for the ESA Cosmic Vision 2015-2025*, *ArXiv e-prints* (Feb., 2011) [astro-ph.HE/1102.2845]. 140

[386] **CTA Consortium** Collaboration, W. Hoffman and M. Martinez, *Design Concepts for the Cherenkov Telescope Array*, *ArXiv e-prints* (2010) [astro-ph.IM/1008.3703]. 140, 171, 172, 173, 175, 177, 216, 217, 218

[387] G. Bertone, C. Jackson, G. Shaughnessy, T. M. Tait, and A. Vallinotto, *The WIMP Forest: Indirect Detection of a Chiral Square*, *Phys.Rev.* **D80** (2009) 023512, [astro-ph.HE/0904.1442]. 141

[388] L. Pieri, J. Lavalle, G. Bertone, and E. Branchini, *Implications of high-resolution simulations on indirect dark matter searches*, *Phys.Rev.D* **83** (Jan., 2011) 023518–+, [astro-ph.HE/0908.0195]. 141

[389] S. K. Lee, S. Ando, and M. Kamionkowski, *The Gamma-Ray-Flux Probability Distribution Function from Galactic Halo Substructure*, *JCAP* **0907** (2009) 007, [astro-ph/0810.1284]. 141

[390] S. Ando, M. Kamionkowski, S. K. Lee, and S. M. Koushiappas, *Can proper motions of dark-matter subhalos be detected?*, *Phys.Rev.D* **78** (2008) 101301, [astro-ph/0809.0886]. 141

[391] E. A. Baltz, C. Briot, P. Salati, R. Taillet, and J. Silk, *Detection of neutralino annihilation photons from external galaxies*, *Phys.Rev.D* **61** (Dec, 1999) 023514. 141

[392] **MAGIC** Collaboration, J. Aleksić *et. al.*, *MAGIC Gamma-Ray Telescope Observation of the Perseus Cluster of Galaxies: Implications for Cosmic Rays, Dark Matter and NGC 1275*, *ApJ* **710** (2010) 634–647, [arXiv:0909.3267]. 142

[393] J. Stadel, D. Potter, B. Moore, J. Diemand, P. Madau, *et. al.*, *Quantifying the heart of darkness with GHALO - a multi-billion particle simulation of our galactic halo*, astro-ph/0808.2981. 142

[394] G. Bertone, M. Fornasa, M. Taoso, and A. R. Zentner, *Dark Matter Annihilation around Intermediate Mass Black Holes: an update*, *New J.Phys.* **11** (2009) 105016, [astro-ph.HE/0905.4736]. 142, 210

[395] M. Kamionkowski, S. M. Koushiappas, and M. Kuhlen, *Galactic Substructure and Dark Matter Annihilation in the Milky Way Halo*, *Phys.Rev.* **D81** (2010) 043532, [astro-ph.GA/1001.3144]. 142, 210

[396] **Particle Data Group** Collaboration, C. Amsler *et. al.*, *Review of particle physics*, *Phys.Lett.B* **667** (2008) 1–1340. 142, 174

[397] A. Reimer, *The Redshift Dependence of Gamma-Ray Absorption in the Environments of Strong-Line AGNs*, *ApJ* **665** (Aug., 2007) 1023–1029, [astro-ph/0705.1534]. 143

[398] **Fermi-LAT** Collaboration, A. A. Abdo *et. al.*, *Fermi/Large Area Telescope Bright Gamma-Ray Source List*, *ApJS* **183** (July, 2009) 46–66, [astro-ph.HE/0902.1340]. 143

[399] T. Burnett, M. Kerr, and M. Roth, *Measurement of the Fermi-LAT Localization Performance*, astro-ph.HE/0912.3855. 145, 211

[400] NASA, "HEASARC: NASA's Archive of Data on Energetic Phenomena." http://heasarc.gsfc.nasa.gov/, 2011. 145, 211

[401] D. Donato, T. Cheung, and N. Gehrels, *Chandra and Swift Observations of Unidentified Fermi-LAT Objects*, in *AAS/High Energy Astrophysics Division #11*, vol. 42 of *Bulletin of the American Astronomical Society*, pp. 671–+, Feb., 2010. 145, 151

[402] NASA, "HEASARC: NASA's HEASoft Tools." http://heasarc.gsfc.nasa.gov/docs/software/lheasoft, 2011. 145, 151, 161

[403] ASI, "ASDC: ASI's Science Data Center." http://www.asdc.asi.it/, 2011. 146

[404] NASA, "Fermi Science Tools Documentation." http://fermi.gsfc.nasa.gov/ssc/data/analysis/documentation/, 2011. 145

[405] NASA, "Official nasa fermi satellite telescope website." http://fermi.gsfc.nasa.gov/ssc/data/analysis/documentation/Cicerone/, 2011. 146

[406] E. Carmona. Private communication, 2010. 148

[407] **Swift Science Collaboration** Collaboration, N. Gehrels *et. al.*, *The Swift Gamma-Ray Burst Mission*, *AIP Conf.Proc.* **727** (2004) 637–641, [astro-ph/0405233]. 151

[408] NASA, "HEASARC: NASA's Mission Count Rate Simulator." http://heasarc.nasa.gov/Tools/w3pimms.html, 2011. 152, 161

[409] "Michigan-Dartmouth-MIT Observatory." http://www.astro.lsa.umich.edu/obs/mdm/, 2011. 152

[410] J. Halpern. Private communication, 2011. 152, 213

[411] **Fermi-LAT** Collaboration, A. A. Abdo *et. al.*, *Fermi Observations of the Very Hard Gamma-ray Blazar PG 1553+113*, *ApJ* **708** (Jan., 2010) 1310–1320, [astro-ph.HE/0911.4252]. 158, 166, 213, 214

[412] CTA Consortium, "Cherenkov Telescope Array Homepage." www.cta-observatory.org, 2011. 171, 215

[413] Rossi, B. and Greisen, K., *Cosmic Ray Theory*, *Reviews of Modern Physics* **13** (1941) 240–309. 188

[414] Gaisser, T.K., *Cosmic Rays and Particle Physics*. Cambridge University Press., 1990. 188, 190

[415] J. V. Jelly, *Cherenkov radiation and its applications*. Pergamon Press, 1958. 191

[416] Yao, W.M., and others, *Review of particle physics.*, *Journal of Physics G* **33** (2006) 1–1232. 192

[417] Keck Observatory, "Keck Observatory Home Page." http://www.keckobservatory.org/, 2011. 201